Modelling of hydrogen production by chemical looping in a packed bed reactor

Erik Guillermo Resendiz Mora

Submitted in accordance with the requirements for the degree of
Doctor of Philosophy

The University of Leeds
School of Chemical and Process Engineering

June 2021

The candidate confirms that the work submitted is his/her own, except where work which has formed part of jointly-authored publications has been included. The contribution of the candidate and the other authors to this work has been explicitly indicated below. The candidate confirms that appropriate credit has been given within the thesis where reference has been made to the work of others.

Chapter 5 includes work from the jointly authored publication, “Transient Heating of a Packed Bed Comprising Two Different Refractory Materials”, by Erik G. Resendiz Mora, Valerie Dupont, Peter J. Heggs and Tariq Mahmud accepted in the 17th UK Heat Transfer Conference (UKHTC2021) in Manchester, UK. The contribution to this work by the candidate was the literature research, development of the mathematical model, the numerical analysis of the model, coding of the numerical solution and writing the paper. The co-authors provided supervision throughout the development of the work.

Acknowledgements

I would like to express my gratitude to my PhD supervisors Valerie Dupont, Peter J. Heggs and Tariq Mahmud for guiding me through what has been the most challenging, yet rewarding endeavour of my academic life. I would like to specially thank Valerie Dupont, who opened the door for me to come to the University of Leeds and for all her unreserved support when difficult times presented during my stay in Leeds.

I would like to specially thank Peter J. Heggs for all his patience and for continuously motivating me to try and develop my skills and knowledge. Our weekly meetings to discuss and discover more about the mathematical aspects of the numerical solution of Partial Differential Equations were my favourite moments for three years.

I also thank the Chemical Engineering Department at the University of Leeds, particularly Antonia Borissova, Alan Burns, Erik Danso-Boateng and Frank Muller for allowing me to assist in their teaching modules and expand the range of opportunities to develop myself in different aspects, all these experiences certainly contributed to improve my life in the UK.

A special mention to my friends Dave Henry, Lorraine Middlemass, Kevin Tipton and Kaine Varley, thank you for being so kind and help me out to have a wonderful time in England. Also thanks to the people who shared happy moments with me: Flora Brocza, Nina Rangel, Lifita Tande and Francisco Tapia.

To my family, dad, mom and siblings, in special my brother Daniel who could not see this effort come to fruition, I will see you again sometime, somewhere.

And last but not least, thanks to Nelly and Enoc for being really brave to come to the UK, learn a new language on the fly and supporting me throughout this adventure.

Finally, my gratitude extends to CONACyT and SEP in Mexico for their generous financial support and the opportunity of studying abroad.

Abstract

The mathematical modelling of a chemical looping process to produce hydrogen with carbon capture is developed. Two models, one to represent the hydrogen production step known as the Fuel Reactor model, and one to represent the bed regeneration step known as the Air Reactor are proposed and considered as heterogeneous systems, accounting for the phenomenology of separate gas, catalyst, and adsorbent phases.

The heterogeneous Fuel Reactor model is validated with experimental data reported in the open literature for a lab-scale unit. It is also compared with a pseudo-homogeneous model and a pseudo-heterogeneous model previously reported by others, which neglect the potential heat losses due to the various physical limitations to heat transfer from the adsorbent to the catalyst. The comparison is made for systems with small and large particles, and it is found that the outputs from the models compare well in the former case, but significant differences are observed in the latter.

The heterogeneous model is further developed to account for the variation of the adsorbent properties due to the adsorption of CO_2. These variations are accounted for in two different models: one considering the variation of adsorbent porosity only, and another considering the variation of the adsorbent porosity, density, and heat capacity. The results are compared with the base case model, and it is observed that accounting for the variations of the adsorbent properties provides a good fit of the experimental data. Parametric investigations are conducted with the heterogeneous model accounting for the variation of porosity; the study covers the effect of the available heat transfer area, mass flux, feedstock composition, gas and packing temperatures, catalyst and adsorbent densities over the methane conversion, hydrogen purity, hydrogen yield and hydrogen productivity.

The heterogeneous Air Reactor model is validated against experimental data reported in the open literature for a lab-scale unit and applied to conduct a sensitivity study of the Air Reactor. The parametric investigations cover the effect of the mass flux, temperature, the nickel load in the catalyst, the concentration of oxygen in the oxidant agent and the adsorbent and catalyst densities. Additionally, an investigation is conducted to analyse what happens if the bed is loaded with traces of hydrogen at the beginning of the Air Reactor cycle.

Table of Contents

List of Tables

List of Figures

Nomenclature

Letters	Description	Units
A, B	Correlating parameters of the Ergun-type pressure drop equation	–
a, b	Fitting parameters of the diffusivity model of Stendardo et al.	–
A_1, A_2, A_3, A_4	Constants of the numerical solution of the lumped heat transfer model	–
a_S	Surface area per unit of reactor volume	$m^2\ m^{-3}$
a_{S_1}, a_{S_2}	Surface area per unit of reactor volume of packing type 1 and 2	$m^2\ m^{-3}$
b	Equilibrium constant of the calcination model of Escardino et al.	–
b_i	Stoichiometric coefficient of the metallic specie (nickel or nickel oxide) according to the relevant reaction of reduction or oxidation	–
C_{CO_2}	Actual concentration of CO_2	$mol\ m^{-3}$
$C_{CO_2,eq}$	Equilibrium concentration of CO_2	$mol\ m^{-3}$
$C_{0,NiO}$	Initial molar concentration of NiO	$mol\ m^{-3}$
$\bar{C}_{H_2}$	Concentration of H_2 adsorbed in the catalyst in moles per unit of mass	$mol\ kg^{-1}$
$\bar{C}_{H_2,0}$	Initial concentration of H_2 adsorbed in the catalyst in moles per unit of mass	$mol\ kg^{-1}$
C_i	Concentration of the specie "*i*" in the bulk gas (i=CH_4, H_2O, H_2, CO, CO_2, N_2)	$mol\ m^{-3}$
$C_{i,in}$	Concentration of the specie "*i*" in the bulk gas at bed inlet (i=CH_4, H_2O, H_2, CO, CO_2, N_2)	$mol\ m^{-3}$

C_{i,S_1}, C_{i,S_2}	Concentration of i-th component at the surface of packings 1 and 2 (i=CH_4, H_2O, H_2, CO, CO_2, N_2)	$mol\ m^{-3}$
C_{O_2}	Actual concentration of O_2	$mol\ m^{-3}$
$C_{p,b}$	Mass heat capacity of the packing	$J\ kg^{-1}\ K^{-1}$
$C_{p,CaO}$	Mass heat capacity of calcium oxide	$J\ kg^{-1}\ K^{-1}$
$C_{p,CaCO_3}$	Mass heat capacity of calcium carbonate	$J\ kg^{-1}\ K^{-1}$
$C_{p,g}$	Bulk gas mass heat capacity	$J\ kg^{-1}\ K^{-1}$
$C_{p,s}$	Heat capacity of solid materials	$J\ kg^{-1}\ K^{-1}$
$C_{p,0}$	Coefficient of the zero order term of the polynomial expression of heat capacity of solids	$J\ kg^{-1}\ K^{-1}$
$C_{p,1}$	Coefficient of the first order term of the polynomial expression of heat capacity of solids	$J\ kg^{-1}\ K^{-2}$
$C_{p,2}$	Coefficient of the second order term of the polynomial expression of heat capacity of solids	$J\ K\ kg^{-1}$
$C_{p_2,0}$	Initial mass heat capacity of the adsorbent	$J\ K\ kg^{-1}$
C_{p_p}	Combined gas and solid heat capacity of a packing	$J\ kg^{-1}\ K^{-1}$
C_{p_1}, C_{p_2}	Combined gas and solid heat capacity of packing types 1 and 2	$J\ kg^{-1}\ K^{-1}$
C_{01}, C_{02}, C_1, C_2	Constants of the numerical solution of the distributed particle heat transfer model	–
DEN	Term accounting for the adsorption of species in the catalyst surface	–
D_0	Pre-exponential factor of diffusion	
D_b	Bed diameter	m
D_e	Effective diffusivity	$m^2\ s^{-1}$

D_{e,CO_2}	Effective diffusivity of CO_2	$m^2\ s^{-1}$
d_f	Diameter of the furnace	m
$D_{i,m}$	Molecular diffusivity of the specie "*i*" (i=CH_4, H_2O, H_2, CO, CO_2, N_2)	$m^2\ s^{-1}$
d_p	Average packing diameter	m
D_{PL}	Diffusivity of CO_2 in the product layer	$m^2\ s^{-1}$
$d_{p,1}$, $d_{p,2}$	Diameter of packings type 1 and 2	m
d_r	Reactor diameter	m
d_{ri}	Inside reactor diameter	m
d_{ro}	Outside reactor diameter	m
$D_{z,i}$	Axial dispersion coefficient of the specie "*i*" (i=CH_4, H_2O, H_2, CO, CO_2, N_2)	$m^2\ s^{-1}$
E_A	Activation energy	$kJ\ mol^{-1}$
$E_{A,Calc}$	Activation energy of calcination of $CaCO_3$	$kJ\ mol^{-1}$
$E_{A,Carb}$	Activation energy of carbonation of CaO	$kJ\ mol^{-1}$
$E_{CH_{4,c}}$	Activation energy of the reaction of reduction of NiO by the unmixed combustion of CH_4	$kJ\ mol^{-1}$
$E_{CH_{4,p}}$	Activation energy of the reaction of reduction of NiO by the unmixed partial oxidation of CH_4	$kJ\ mol^{-1}$
E_{CO}	Activation energy of the reaction of reduction of NiO with CO	$kJ\ mol^{-1}$
E_{H_2}	Activation energy of the reaction of reduction of NiO with H_2	$kJ\ mol^{-1}$
$E_{A,SMR}$	Activation energy of the steam methane reforming reaction	$kJ\ mol^{-1}$
$E_{A,WGS}$	Activation energy of the water-gas shift reaction	$kJ\ mol^{-1}$

$E_{A,SMRC}$	Activation energy of the complete steam methane reforming reaction	$kJ\ mol^{-1}$
E_D	Activation energy of diffusion	$kJ\ mol^{-1}$
f, h	Represent general functions	–
f_{NiO}	Fraction of free NiO in the OTM	–
G	Gas mass flux	$kg\ m^{-2}\ s^{-1}$
ΔH_{Calc}	Heat of reaction of calcination of $CaCO_3$	$kJ\ mol^{-1}$
ΔH_{Carb}	Heat of reaction of carbonation of CaO	$kJ\ mol^{-1}$
ΔH_j	Heat of reaction of the reactions occurring in the catalyst	$kJ\ mol^{-1}$
ΔH_k	Heat of reaction of the reactions occurring in the adsorbent	$kJ\ mol^{-1}$
ΔH_{Oxi}	Heat of reaction of oxidation of Ni	$kJ\ mol^{-1}$
j_D	Colburn factor for mass transfer	–
j_H	Colburn factor for heat transfer	–
k	Kinetic constant	$various\ units$
k_{Calc}	Kinetic rate constant of calcination of $CaCO_3$	$various\ units$
k_{Carb}	Kinetic constant of carbonation of CaO	$various\ units$
k_{CH_4c}	Kinetic rate constant of the reduction of NiO with CH_4 via unmixed combustion	$m\ s^{-1}$
k_{CH_4p}	Kinetic rate constant of the reduction of NiO with CH_4 via unmixed partial oxidation	$m\ s^{-1}$
k_{CO}	Kinetic rate constant of the reduction of NiO with CO	$m\ s^{-1}$
k_{H_2}	Kinetic rate constant of the reduction of NiO with H_2	$m\ s^{-1}$

k_i	Kinetic rate constant of reduction of NiO or oxidation of Ni, i= CH_4, H_2, CO, O_2	$mol^{0.2}\ m^{0.4} s^{-1}$ for CH_4 $mol^{0.5}\ m^{-0.5} s^{-1}$ for H_2 $mol^{0.2}\ m^{0.4} s^{-1}$ for CO $mol^{0.8}\ m^{-1.4} s^{-1}$ for O_2
k_{Oxi}	Kinetic constant of the reaction of oxidation of nickel	$m\ s^{-1}$
k_s	Kinetic constant for surface reaction of adsorption of CO_2	$m^4\ mol^{-1} s^{-1}$
k_{SMR}	Kinetic constant of the reaction of steam reforming	$mol\ bar^{0.5}\ kg^{-1} s^{-1}$
k_{WGS}	Kinetic constant of the water gas shift reaction	$mol\ bar^{-1}\ kg^{-1} s^{-1}$
k_{SMRC}	Kinetic constant of the complete reaction of steam reforming	$mol\ bar^{0.5}\ kg^{-1} s^{-1}$
K_{SMR}	Equilibrium constant of the steam methane reforming reaction	bar^2
K_{WGS}	Equilibrium constant of water-gas shift reaction	–
K_{SMRC}	Equilibrium constant of the complete steam methane reforming reaction	bar^2
K_i	Adsorption constant of the specie "*i*" i=CH_4,CO,H_2,H	bar
K_{H_2O}	Adsorption constant of water	–
k_x	Conversion dependent factor	–
k_0	Pre-exponential factor of the kinetic constant	$various\ units$
$k_{0,Calc}$	Pre-exponential factor of the kinetic rate constant of calcination of $CaCO_3$	$various\ units$
$k_{0,Carb}$	Pre-exponential factor of the kinetic rate constant of carbonation of CaO	$various\ units$
k_{0,CH_4c}	Pre-exponential factor of the kinetic rate constant the reduction of NiO with CH_4 via unmixed combustion	$various\ units$

k_{0,CH_4p}	Pre-exponential factor of the kinetic rate constant of the reduction of NiO with CH_4 via unmixed partial oxidation	$various\ units$
$k_{0,CO}$	Pre-exponential factor of the kinetic rate constant of the reduction of NiO with CO	$various\ units$
k_{0,H_2}	Pre-exponential factor of the kinetic rate constant of the reduction of NiO with H_2	$various\ units$
$k_{0,Oxi}$	Pre-exponential factor of the kinetic rate constant of oxidation of Ni	$various\ units$
$k_{0,SMR}$	Pre-exponential factor of the kinetic rate constant of steam methane reforming reaction	$various\ units$
$k_{0,WGS}$	Pre-exponential factor of the kinetic rate constant of the water-gas shift reaction	$various\ units$
$k_{0,SMRC}$	Pre-exponential factor of the kinetic rate constant of the complete steam methane reforming reaction	$various\ units$
L_b	Bed length	m
L_0	Pore length in the Random Pore Model	m
M_{CaO}	Molecular weight of calcium oxide	$kg\ mol^{-1}$
M_{CaCO_3}	Molecular weight of calcium carbonate	$kg\ mol^{-1}$
M_{CO_2}	Molecular weight of carbon dioxide	$kg\ mol^{-1}$
M_{Ni}	Molecular weight of nickel	$kg\ mol^{-1}$
M_{NiO}	Molecular weight of nickel oxide	$kg\ mol^{-1}$
M_{O_2}	Molecular weight of oxygen	$kg\ mol^{-1}$
M_1, M_2	Constants of the numerical solution of the distributed particle heat transfer model	$-$
n	Reaction order	$-$

n_i^{in}	Inlet molar flowrate of the specie "*i*" i=CH_4,CO,H_2, CO_2, Ni, $CaCO_3$	$mol\ s^{-1}$
n_i^{out}	Outlet molar flowrate of the specie "*i*" i=CH_4,CO,H_2, CO_2, Ni, $CaCO_3$	$mol\ s^{-1}$
N_{Ca}	Moles of calcium per unit of volume of adsorbent	$mol\ m^{-3}$
P	Bulk gas pressure	bar
$Pe_{i,m}$	Peclet number for the specie "*i*" (i=CH_4, H_2O, H_2, CO, CO_2, N_2)	–
p_i	Partial pressure of the specie "i" (i=CH_4, H_2O, H_2, CO, CO_2, N_2)	bar
$p_{CO_2,eq}$	Equilibrium partial pressure of CO_2	bar
P_{H_2}	Hydrogen purity	%
Pr_{H_2}	Hydrogen productivity	kg
Re	Reynolds number	–
P_{in}	Bulk gas pressure at bed inlet	bar
r_{Calc}	Rate of reaction of calcination of $CaCO_3$	$mol\ kg^{-1}\ s^{-1}$
r_{CaO}	Radius of unreacted core of CaO	m
r_{Carb}	Rate of reaction of carbonation of CaO	$mol\ kg^{-1}\ s^{-1}$
r_{CH_4c}	Reaction rate of reduction of NiO with CH_4 via unmixed combustion	$mol\ kg^{-1}\ s^{-1}$
r_{CH_4p}	Reaction rate of reduction of NiO with CH_4 via unmixed partial oxidation	$mol\ kg^{-1}\ s^{-1}$
r_{CO}	Reaction rate of reduction of NiO with CO	$mol\ kg^{-1}\ s^{-1}$
$r_{g,j}$	Grain radius of the metallic specie "j" j=Ni, NiO, CaO, $CaCO_3$	m
R_g	Ideal gas constant $R_g = 8.314\ J\ mol^{-1}K^{-1} = 8.314 \times 10^{-5}\ bar\ m^3 mol^{-1}K^{-1}$	–

r_{H_2}	Reaction rate of reduction of NiO with H_2	$mol\ kg^{-1}\ s^{-1}$
r_j	Rate of the reactions occurring in the catalyst	$mol\ kg^{-1}\ s^{-1}$
r_k	Rate of the reactions occurring in the adsorbent	$mol\ kg^{-1}\ s^{-1}$
r_{Oxi}	Rate of reaction of oxidation of nickel	$mol\ kg^{-1}\ s^{-1}$
r_{SRM}	Rate of the reaction of steam reforming	$mol\ kg^{-1}\ s^{-1}$
r_{WGS}	Rate of the water gas shift reaction	$mol\ kg^{-1}\ s^{-1}$
r_{SMRC}	Rate of the complete reaction of steam reforming	$mol\ kg^{-1}\ s^{-1}$
r_1, r_2	Radius coordinate in packing types 1 and 2	m
R_1, R_2	Particle radius of packing types 1 and 2	m
Δr_1, Δr_2	Radius-step sizes for packing type 1 and 2	m
Sc_i	Schmidt number for the specie "*i*" (i=CH_4, H_2O, H_2, CO, CO_2, N_2)	$-$
$S_{g,c}$	Initial surface area of the carbonated adsorbent	$m^2\ g^{-1}$
$S_{g,f}$	Initial surface area of the fresh adsorbent or OTM	$m^2\ g^{-1}$
$S_{g,v}$	Adsorbent surface area per unit of volume	$m^2\ m^{-3}$
S_m	Source term of the continuity equation	$kg\ m^{-3}\ s^{-1}$
T	Bulk gas temperature	K
T_f	Furnace temperature	K
T_i	Initial temperature	K
T_{in}	Bulk gas temperature at bed inlet	K

T_{ro}	Temperature at the outside of the reactor wall	K
T_1,T_2	Temperature of packing types 1 and 2	K
$\bar{T}_1$, $\bar{T}_2$	Average temperature of packing types 1 and 2	K
T_{S_1}, T_{S_2}	Temperature at the surface of packings type 1 and 2	K
t	Time coordinate in the Eulerian frame of reference	s
t_P	Time period of the simulation run	s
U	Utilisation factor	–
u_i	Bulk gas interstitial velocity	$m\ s^{-1}$
u_s	Bulk gas superficial velocity	$m\ s^{-1}$
$u_{s,in}$	Bulk gas superficial velocity at bed inlet	$m\ s^{-1}$
U_w	Overall wall heat transfer coefficient	$J\ m^{-2}\ K^{-1}\ s^{-1}$
V_{CaO}	Molar volume of CaO	$m^3\ mol^{-1}$
$\bar{V}_{CaO}$	Volume of CaO in the grain	m^3
$\bar{V}_{CaCO_3}$	Volume of $CaCO_3$ in the grain	m^3
$\bar{V}_{total}$	Volume of the grain	m^3
V_r	Reactor volume	m^3
W_c	Mass of catalyst in the reactor	kg
w_{CaO}	Mass fraction of CaO in the grain	$kg\ kg^{-1}$
w_{CaCO_3}	Mass fraction of $CaCO_3$ in the grain	$kg\ kg^{-1}$
$w_{Ni,0}$	Initial mass fraction of nickel	$kg\ kg^{-1}$
w_{Ni}	Mass fraction of nickel	$kg\ kg^{-1}$
$w_{NiO,0}$	Initial mass fraction of nickel oxide	$kg\ kg^{-1}$
w_{NiO}	Mass fraction of nickel oxide	$kg\ kg^{-1}$
x_{CO_2}	Mole fraction of CO_2	–
$x_{CO_2,eq}$	Equilibrium mole fraction of CO_2	–

X	Molar conversion	–
X_{CaO}	Molar conversion of the calcium oxide	–
$X_{CaO,max}$	Maximum achievable molar conversion of calcium oxide	–
X_{CaCO_3}	Molar conversion of calcium carbonate	–
X_{EKR}	Conversion of CaO at the end of the kinetic regime	
X_i, X_j	Molar conversion of nickel or nickel oxide	–
X_{Ni}	Molar conversion of nickel	–
X_{NiO}	Molar conversion of nickel oxide	–
Y	Dimensionless bed length	
Y_{H_2}	Hydrogen yield	%
YK_r	Dimensionless parameter to assess the likelihood of develop intra-conduction gradients in a packed bed	–
z	Axial coordinate	m
Δz	Length-step size	m
Z	In the Random Pore Model, ratio of volume of the solid phase after the reaction to that before the reaction	–
Z	In the porosity model of the Fuel Reactor is the ratio of the molar volume of calcium carbonate to the molar volume of calcium oxide	–
Z'	In the porosity model of the Air Reactor is the ratio of the molar volume of calcium oxide to the molar volume of calcium carbonate	–

Greek Letters	**Description**	**Units**
α	Convective heat transfer coefficient	$J\ m^{-2}\ K^{-1}\ s^{-1}$

α_i	Convective heat transfer coefficient of particle “i”, where i=1,2	$J\ m^{-2}\ K^{-1}\ s^{-1}$
$\alpha_{e,i}$	Effective heat transfer coefficient of particle “i”, where i=1,2	$J\ m^{-2}\ K^{-1}\ s^{-1}$
α_r	Radiative heat transfer coefficient	$J\ m^{-2}\ K^{-1}\ s^{-1}$
α_w	Wall heat transfer coefficient	$J\ m^{-2}\ K^{-1}\ s^{-1}$
α_1, α_2	Convective heat transfer coefficient of packing types 1 and 2	$J\ m^{-2}\ K^{-1}\ s^{-1}$
$\bar{\alpha}_1$, $\bar{\alpha}_2$	Lumped heat transfer coefficient of packing types 1 and 2	$J\ m^{-2}\ K^{-1}\ s^{-1}$
β	Modified Biot number of the Random Pore Model	$-$
β_1, β_2	Mass transfer coefficient of packing types 1 and 2	$m\ s^{-1}$
γ_1, γ_2	Volumetric fraction of packing type 1 and 2 in the packed bed	$m^3\ m^{-3}$
δ_{CaO}	Average diameter of the calcium oxide grain	m
ε_b	Mean bed voidage	$m^3\ m^{-3}$
ε_f	Emissivity of the furnace	$-$
ε_p	Packing porosity	$m^3\ m^{-3}$
ε_{p_1}, ε_{p_2}	Porosity of packings type 1 and 2	$m^3\ m^{-3}$
$\varepsilon_{p_2,0}$	Initial porosity of the adsorbent (packing type 2)	$m^3\ m^{-3}$
ε_{ro}	Emissivity of the reactor outside wall	$-$
ε_1	End bed voidage	$m^3\ m^{-3}$
ε_∞	Core bed voidage	$m^3\ m^{-3}$
$\varepsilon_{0,a}$	Adsorbent porosity	$m^3\ m^{-3}$
ϵ_1, ϵ_2	Correction factors for the heat transfer coefficient in the lumped model	$-$

η_{Calc}	Effectiveness factor of the reaction of calcination of calcium carbonate	$-$
η_{Carb}	Effectiveness factor of the reaction of carbonation of calcium oxide	$-$
η_j	Effectiveness factor of the reactions occurring in the catalyst	$-$
η_k	Effectiveness factor of the reactions occurring in the adsorbent	$-$
η_{Oxi}	Effectiveness factor of the reaction of oxidation of nickel	$-$
θ	Normalised temperature	$-$
λ_g	Bulk gas thermal conductivity	$J\ m^{-1}\ K^{-1}\ s^{-1}$
λ_{CaO}	Thermal conductivity of calcium oxide	$J\ m^{-1}\ K^{-1}\ s^{-1}$
λ_{CaCO_3}	Thermal conductivity of calcium carbonate	$J\ m^{-1}\ K^{-1}\ s^{-1}$
λ_p	Thermal conductivity of the packing	$J\ m^{-1}\ K^{-1}\ s^{-1}$
$\lambda_{p,e}$	Effective thermal conductivity of the packing	$J\ m^{-1}\ K^{-1}\ s^{-1}$
λ_{p_1}, λ_{p_2}	Thermal conductivity of packing types 1 and 2	$J\ m^{-1}\ K^{-1}\ s^{-1}$
λ_w	Thermal conductivity of reactor wall	$J\ m^{-1}\ K^{-1}\ s^{-1}$
$\lambda_{z,g}$	Effective axial thermal conductivity	$J\ m^{-1}\ K^{-1}\ s^{-1}$
μ_g	Bulk gas viscosity	cP
ν_{ij}	Stoichiometric coefficient of reactions occurring in the catalyst	$-$
ν_{ik}	Stoichiometric coefficient of reactions occurring in the adsorbent	$-$
π	Constant $\pi = 3.141592$ …	$-$
ρ_b	Bulk density of the packed bed	$kg\ m^{-3}$
ρ_{b_1}, ρ_{b_2}	Bulk density of packing types 1 and 2	$kg\ m^{-3}$
ρ_{CaO}	Mass density of calcium oxide	$kg\ m^{-3}$
ρ_{CaCO_3}	Mass density of calcium carbonate	$kg\ m^{-3}$

ρ_g	Mass density of the bulk gas	$kg\ m^{-3}$
$\rho_{m,CaCO_3}$	Molar density of calcium carbonate	$mol\ m^{-3}$
$\rho_{m,j}$	Molar density of the metallic specie "j" (j=Ni, NiO)	$mol\ m^{-3}$
ρ_{p_1}, ρ_{p_2}	Solid density of packing types 1 and 2	$kg\ m^{-3}$
$\rho_{p_2,0}$	Initial mass density of the adsorbent	$kg\ m^{-3}$
σ	Boltzmann constant $\sigma = 5.67x10^{-8}\ Js^{-1}m^{-2}K^{-4}$	–
$\sigma_{0,CaO}$	Initial grain surface area per unit of particle volume	$m^2\ m^{-3}$
τ	Time coordinate in the Lagrangian frame of reference	s
$\Delta\tau, \Delta\tau_1, \Delta\tau_2$	Time-step required to ensure convergence of the numerical solution of the heat transfer problem	
ϕ	Ratio of the mass density of $CaCO_3$ to the mass density of CaO	–
ϕ_{carb}	Thiele module of the carbonation reaction	–
φ_{CaO}	Volumetric fraction of CaO in the grain	$m^3\ m^{-3}$
φ_{CaCO_3}	Volumetric fraction of $CaCO_3$ in the grain	$m^3\ m^{-3}$
ψ	Structural parameter of the Random Pore Model	–
$\Im_{ro\to f}$	Gray body view factor	–
Indexes	**Description**	
b	Reactor bed	
g	Gas phase	
i	i-th component in the fluid	

i	Length coordinate within the computational mesh of the numerical solution of the distributed particle model and the lumped model
I	Number of nodes in the bed length domain
j	j-th reaction at the catalyst
j	Radial coordinate within the particle type 1 in the computational mesh of the numerical solution of the distributed particle model
k	k-th reaction at the adsorbent
k	Radial coordinate within the particle type 2 in the computational mesh of the numerical solution of the distributed particle model
M	Number of nodes in the particle type 1 radius domain
n	Time coordinate within the computational mesh of the numerical solution of the distributed particle model and the lumped model
N	Number of nodes in the time period domain
p	Refers to the particle or pellet
P	Number of nodes in the particle type 2 radius domain
S	Particle surface

Abbreviation	**Description**
a-CLR	Autothermal Chemical Looping Reforming
ATR	Autothermal Reforming
BET	Brunauer-Emmett-Teller
CLC	Chemical Looping Combustion
CLH	Chemical Looping for Hydrogen
CLHG	Chemical Looping for Hydrogen Generation
LEGS	Lime-Enhanced Gasification
OC	Oxygen Carrier
OTM	Oxygen Transfer Material
PDE	Partial Differential Equation
POX	Partial Oxidation
PSA	Pressure Swing Adsorption

RPM	Random Pore Model
SR-CLC	Steam Reforming with Chemical Looping Combustion
SE-CLSMR	Sorption-Enhanced Chemical Looping Steam Methane Reforming
SE-SMR	Sorption-Enhanced Steam Methane Reforming
SMR	Steam Methane Reforming
SR	Steam Reforming
UMR	Unmixed Methane Reforming
WGS	Water-Gas Shift

Chapter 1 Introduction

1.1 Research motivation

The growth of the world population and their requirements of food, water, health and energy represent a big challenge for societies and their future development. The United Nations have recently reported that the population is growing at a rate of 1.18% per cent per year and is expected to be 9.7 billion in 2050 [1], whilst energy consumption would rise up to 802.9 EJ in 2040 [2]. To date, these energy demands have been met primarily with the use of fossil fuels (e.g. coal, oil and natural gas), with the disadvantage that their use is accompanied by the release of the so-called greenhouse gases (CO_2, CH_4, NOx and fluorinated gases) [3] which have brought noxious effects in the form of a global warming that has impacted the environmental equilibrium.

In this context, hydrogen represents a promising alternative, both as an intermediate chemical for food production, and as energy carrier that can play a major role in low carbon mobility [4]. Hydrogen is a relevant substance to many industries; currently it is largely used in the refining industry to up-grade feedstocks and oil products, and in the chemical industry to produce ammonia (NH_3) and methanol (CH_3OH). Moreover, its combustion produces only water in the exhaust, making it a good candidate to generate clean energy in fuel cells or combustion engines [5, 6].

Hydrogen can be produced from renewable and non-renewable sources. Its production from renewable energy currently faces financial (cost), logistic, and regulatory challenges that prevent the widespread use of these technologies [7]. Conversely, the vast majority of hydrogen production is attained from fossil fuels, primarily by the steam reforming of natural gas [8-10], but its production is responsible for large amounts of CO_2 emissions.

Nevertheless, the steady increase of natural gas reserves [11], anticipates that hydrocarbons will remain the primary feedstock to produce hydrogen in the short and mid-term [10]. Furthermore, the development of shale gas formations, which in most cases have a higher content of heavier hydrocarbons in comparison with conventional natural gas, will require the deployment of technologies and process schemes that take advantage of this resource [12]. Consequently, current methods for hydrogen production need to be improved to meet the environmental regulations. In this context, the use of a carbon capture and storage option (CCS)

along with the method of production of hydrogen could be a bridge between the current fossil-based methods and the renewable technology [7].

Among the hydrogen production concepts recently proposed, the chemical looping steam reforming of methane with in situ CO_2 capture (SE-CLSMR) has gained attention lately due to its advantage of integrate the various thermochemical processes occurring in the reactor, yielding an autothermal process, capable of producing a stream with a high purity of hydrogen in a single stage. This concept consists of a reactor working with two different types of materials; an oxygen transfer material (OTM) and a CO_2 sorbent, which work over cycles of alternated feeds of a mixture of fuel/steam and air [13]. In the fuel-steam reaction cycle, the OTM is reduced by partial or complete oxidation of the hydrocarbons present in the feed, if the active metal of the OTM is nickel, the reduced metal also works as catalyst for the reforming reactions. The heat of reaction of reforming is theoretically supplied by the reaction of adsorption of CO_2 which is an exothermic process. The CO_2 sorbent also shifts in a cascade manner the chemical equilibrium of: (i) the OTM reduction reactions, (ii) the water-gas shift reaction (WGS), and (iii) the steam reforming reaction (SR), allowing faster and more complete OTM reduction, and increasing the production of hydrogen. It is also possible that CO_2 capture enhances by equilibrium shift the methanation of the higher hydrocarbons, thus further initiating the cascade of beneficial equilibrium shifts towards higher H_2 yield and purity. During the regeneration cycle, the OTM is oxidised with a sweep gas (commonly air, pure oxygen or steam) and the heat of reaction released is used to heat the bed for the calcination the CO_2 sorbent leading to a theoretically autothermal operation. During the air feed, coke deposited on the catalyst by thermal decomposition undesirable side reactions would also oxidise, thus fully regenerating the OTM whilst providing heat for CO_2 desorption.

Chemical looping can be carried out by switching feed flows over a fixed, packed bed containing the OTM catalyst, or by circulating the solids between reactors with continuous gas feeds. As the technology is meant to apply to the steam reforming industry which relies entirely on packed bed catalytic and sorption technology, it makes sense for ease retrofitting, to focus in this thesis on the alternated gas feed on packed bed configuration. A further incentive for using fixed bed is that, since nickel is the preferred catalyst of the pre-reforming and primary reforming stages in industrial steam reforming plants, as well as an excellent and economic OTM, due to its toxicity and the need for controlling the generation of fine particulates of nickel, the moving bed configuration such as fluidised bed is avoided.

1.2 Research objectives

This research is concerned with the modelling of an adsorptive reactor to produce hydrogen from natural gas from conventional and unconventional sources by a process known as the Sorption Enhanced Chemical Looping Steam Reforming (SE-CLSR). Particularly, with the development of a rigorous mathematical model that accounts for separated phases in the system, i.e. the bulk gas, the catalyst particle, and the adsorbent particle, as well as representing realistically the physical phenomena occurring at the reactor level and at the particle level, specifically the adsorbent. In addition, due to the nature of this process, the heat transfer plays a critical role in attaining an efficient, working system, hence the investigation looks at the heat transfer in fixed beds packed with mixtures of materials exhibiting different transport properties. The specific objectives of the investigation are the following:

- To conduct a thermodynamic analysis of the SE-CLSR process, enabling adiabatic operation of the reactor and determine the feasible operating window as function of the main operating parameters of the process, e.g. temperature, pressure, CaO/C molar ratio, and Ni/CaO molar ratio.
- To develop mathematical models of heat transfer in fixed beds, as well as their numerical solution and assess the relevance of accounting explicitly for the intra-pellet thermal gradients and the situations where this physical phenomena can be neglected or approximated with a simpler model.
- To develop, solve and validate a mathematical model of the Fuel Reactor that accounts for the catalyst and the adsorbent as separated phases, and compare their response to the situation of a homogeneous reactor, and a heterogeneous reactor that accounts for a homogeneous solid phase.
- To incorporate into the base case model the effect of the structural changes taking place in the adsorbent due to the adsorption of carbon dioxide, e.g. the loss of porosity, and the variation of the adsorbent heat capacity and density.
- To develop, solve and validate a mathematical model of the Air Reactor that accounts for the catalyst and the adsorbent as separated phases.
- To conduct a sensitivity analysis with both the Fuel Reactor model and the Air Reactor model to assess the effect of various operating parameters in the reactor performance.

1.3 Structure of the thesis

This thesis is composed of nine chapters including this introduction. **Chapter 2** is divided in three sections, the first part is devoted to reviewing the fundamentals of the steam methane reforming and the sorption-enhanced chemical looping steam reforming; in the second part, the latest advances in the modelling of the SE-CLSMR process are reported, and an the gaps of previous investigations are discussed; the third part comprises a review of the kinetic rate expressions of the various chemical processes involved in the reactor that are required for the model development, i.e. the steam reforming reactions, the carbonation of calcium oxide, the calcination of calcium carbonate, the reduction of nickel oxide and the oxidation of nickel.

Chapter 3 entails the thermodynamic analysis of the SE-CLSMR process. The study is carried out covering a range of values of the main operating parameters of both, the Fuel Reactor and the Air Reactor, including the comparison of the effect of feedstocks with different content of higher hydrocarbons, and the implications of using a pre-reforming stage.

The methodology followed to model the adsorptive reactor is described in **Chapter 4**. The main steps followed to develop the model and the applicable criteria to include or exclude physical considerations from the model are reviewed. The methods of solution of partial differential equations utilised in this research are also described in this chapter, with particular attention to the Finite Differences Method, the Method of Lines and gPROMS, and the Method of Characteristics.

In **Chapter 5**, the development and solution of a mathematical model of the heat transfer in a fixed bed packed with two types of packing materials is presented. The modelling work looks at the relative importance of accounting for the intra-pellet temperature gradients in the prediction of the temperature breakthrough curves and the situations under which they can be neglected in favour of a simpler model. The model solution is developed by applying the Finite Differences Method and the results are validated against the solution of the models obtained in gPROMS by the Method of Lines; the models are then applied to investigate the behaviour of several fixed beds packed with mixtures of spherical pellets with different properties.

The development of the mathematical model of the fuel reactor is presented in **Chapter 6**. The first part of this chapter deals with the development of the base model, and the strategy utilised to find a solution with gPROMS^{TM}. The second part of this chapter deals with the validation of the fuel reactor model, including an assessment of the sensitivity of the reactor model to the various kinetic rate

models reported in Chapter 2, and the results of the comparison of the different reactor models with typical pellet sizes at lab scale and at industrial scale.

In **Chapter 7**, the base model is further developed to include in the mathematical description the variations in the adsorbent properties due to the adsorption of CO_2. The first part of the chapter presents the model equations for the cases of (a) considering only the variation of adsorbent porosity and (b) the variation of adsorbent porosity, density and heat capacity. The validation of the models' output is presented in the second part of **Chapter 7** along with a comparison of the outputs produced with the base case model and the proposed modifications for several variables of the process aiming to determine the minimum level of detail required to fit the experimental data. Finally, the model is applied to conduct a sensitivity analysis of the fuel reactor and the results are presented in the last part **Chapter 7**.

Chapter 8 presents the development and validation of the mathematical model of the Air Reactor, as well as the sensitivity study of this process. In the first part of the chapter, the mathematical equations describing the Air Reactor are presented, along with the detail of the information utilised for the model validation. The second part deals with the analysis of the sensitivity of the Air Reactor model to the kinetic rate expressions of the nickel oxidation and calcium oxide calcination, followed by the results of the validation process. Finally, the results of the sensitivity of the air reactor to the variation of several operating parameters is presented.

Finally, **Chapter 9** presents a summary of the conclusions of this investigation, and the recommendations for future work.

Chapter 2 Literature Review

2.1 Introduction

The pathway to decarbonisation by the extended use of hydrogen throughout the energy system is constrained primarily by the deliverability and the costs associated to the production of hydrogen at the required scales. Various methods to produce hydrogen from a range of feedstocks are available. However, fossil fuels remain as the principal source of H_2, accounting for 95% of the worldwide production [14].

Among the methods to produce hydrogen from fossil fuels, hydrocarbon reforming processes are mature technologies that have been widely applied at the commercial scale for years. There are three reforming methods to produce H_2, namely steam reforming (SR), partial oxidation (POX) and autothermal reforming (ATR) [12, 15]. Of particular interest is the steam reforming of natural gas (SMR), which is regarded as the most reliable technology to meet the H_2 supply demand and currently accounts for largest share of hydrogen worldwide production, followed by the partial oxidation of oil, coal gasification and water electrolysis [7, 12, 16]. Furthermore, steam reforming has the lowest cost of production of high purity hydrogen, albeit with an emission factor of 9.5 kg of CO_2 per kg of H_2 [7], hence, it is reasonable to research possible solutions to reduce its carbon footprint, whilst aiming at a high purity product and a highly efficient process.

This project is aimed to develop a rigorous model to represent an adsorptive-reactor concept know as Sorption-Enhanced Chemical-Looping Steam Reforming (SE-CLSR), therefore, in this chapter the key principles of the commercial Steam Reforming process and the modifications proposed under the SE-CLSR concept, are reviewed in Section 2.2 through 2.4. Section 0 highlights an up to date review of the modelling work that has been carried out to study this particular system with emphasis on those publications presenting dynamic modelling work, along with an assessment of the gaps in the modelling of the sorption enhanced, chemical looping steam reforming process. In section 2.6, a survey of the kinetic rate expressions of the principal processes happening in the SE-CLSR reactor is provided. Finally, in section 0 a summary of the conclusions of the review is given.

2.2 Description of the process

The process of interest in this project is known as the Sorption Enhanced Chemical Looping Steam Reforming (SE-CLSR) and was first proposed by Kumar et al. [17] who referred to it as Unmixed Reforming. The processing concept is an intensification concept that attempts to take advantage of the energy released by the exothermic adsorption of CO_2, utilising it in the endothermic steam reforming processes.

Various processes are involved in this concept, namely, steam reforming, calcium oxide carbonation and calcium carbonate calcination, and oxygen looping material's oxidation and reduction. These processes are arranged within two operating cycles commonly referred to as the fuel and air reactor [17], the details of these processes are addressed in the following sections.

2.2.1 Steam reforming

Steam reforming (SR) is the preferred technology to produce syngas and hydrogen at a large scale with thermal efficiencies up to 85% [14], Figure 2.1 is a diagram of a typical H_2 production plant based on the steam reforming technology. The process is carried out in a number high-alloy reactor tubes filled with catalyst and placed inside a direct fire furnace, operating at temperatures up to 1000°C, pressures up to 40 bar and steam-to-carbon rations between 2 – 4 [18, 19]. The latter is a critical parameter to reduce the likelihood of carbon deposition, a condition that should be avoided to protect the catalyst from deactivating by poisoning and sintering [20].

Examples of feedstocks that are processed in steam reformers are natural gas and naphtha. When processing feedstocks with a high content of heavier hydrocarbons, the plants are equipped with an adiabatic pre-reformer that operates at lower temperatures than the primary reformer, commonly in the range 673–823K [21], and converts the C_{2+} component fraction into a mixture of C_1-components (i.e. methane, carbon monoxide and carbon dioxide) plus H_2O and H_2 through the processes described in Equations (2.1) – (2.3) [22, 23]. This process increases the flexibility of the reforming plant by allowing the processing of heavier feedstocks than natural gas, and reduces the risks of carbon deposition in the primary reformer, enabling high temperature operation, and the potential reduction of the steam-to-carbon ratio [22, 24]. The thermal effects of the pre-reforming process depend upon the content of C_2+ components in the feedstock, for unconventional gas containing a small fraction of these components, the overall process is endothermic [24].

$$C_mH_{n(g)} + mH_2O_{(g)} \rightarrow mCO_{(g)} + \left(m + {}^{n}/_{2}\right)H_{2(g)} \quad \Delta H^0 > 0 \qquad \textbf{(2.1)}$$

$$CO_{(g)} + 3H_{2(g)} \rightarrow CH_{4(g)} + H_2O_{(g)} \quad \Delta H^0 = -206\ kJ\ {mol_{CO}}^{-1} \qquad \textbf{(2.2)}$$

$$CO_{(g)} + H_2O_{(g)} \leftrightarrows CO_{2(g)} + H_{2(g)} \quad \Delta H^0 = -41kJ\ {mol_{CO}}^{-1} \qquad \textbf{(2.3)}$$

The products of the pre-reformer are then fed to the primary reformer, in this reactor the reforming reactions (2.4) and (2.6), along with the water-gas shift reaction (2.5) happen [25]. The energy requirement of the steam reforming process is very high [12, 26], with a standard heat of reaction of 168 kJ mol^{-1}, and its thermal duty is met by the hot flue gases of combustion of a mixture of recycled PSA off-gas toped up with fuel diverted from the desulphurised gas feedstock.

$$CH_{4(g)} + H_2O_{(g)} \leftrightarrows CO_{(g)} + 3H_{2(g)} \quad \Delta H^0 = 206\ kJ\ mol_{CO}^{-1} \qquad \textbf{(2.4)}$$

$$CO_{(g)} + H_2O_{(g)} \leftrightarrows CO_{2(g)} + H_{2(g)} \quad \Delta H^0 = -41kJ\ mol_{CO}^{-1} \qquad \textbf{(2.5)}$$

$$CH_{4(g)} + 2H_2O_{(g)} \leftrightarrows CO_{2(g)} + 4H_{2(g)} \quad \Delta H^0 = 165\ kJ\ mol_{CH_4}^{-1} \qquad \textbf{(2.6)}$$

The conversion of methane and water into syngas in the primary reformer is constrained by the thermodynamic equilibrium, hence, the product of the reforming reactor is usually fed to the Water-Gas Shift reactor(s) where the production of H_2 is maximised [15, 27, 28]. When using two stage WGS, the WGS reactors are operated at high temperature (573–773K), low temperature (483–543K), with a cooling stage in between due to exothermally limited CO conversion, typically over iron oxide/chromium oxide catalyst and a copper-based catalyst, respectively [15, 28]. Finally the product stream undergoes additional purification to achieve the specification of H_2 purity for use in downstream operations [10, 21], common technologies to carry out this purification are pressure-swing adsorption (PSA), chemical absorption, cryogenic, and more recently, membrane processes.

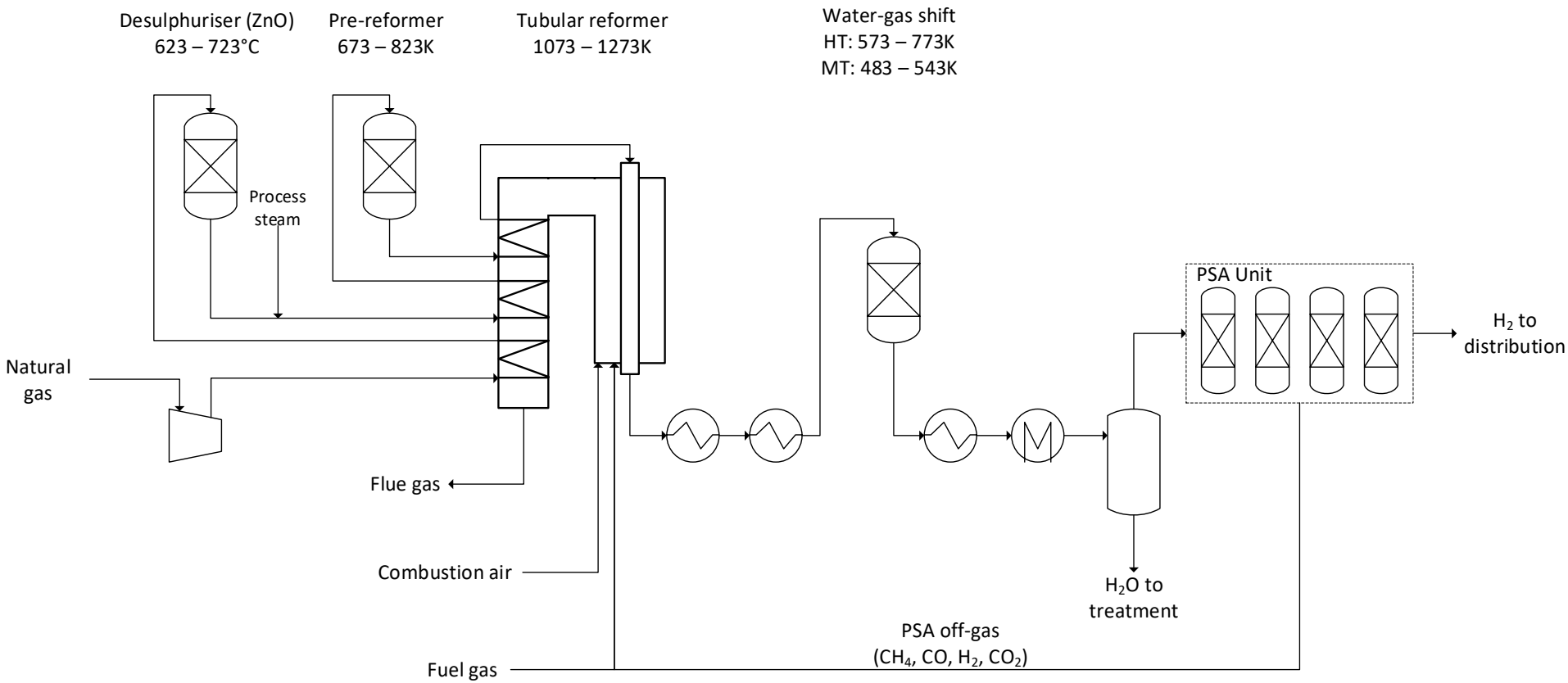

Figure 2.1 Typical process lay-out of a steam methane reforming plant for H_2 production [29].

2.2.2 Sorption Enhanced Steam Methane Reforming (SE-SMR)

Economies of scale lead large SMR plants to operate at pressures 30-40 bar, which result in the steam methane reforming process being limited by the thermodynamic equilibrium, and requires compensating severe operating conditions in the form of high temperatures to achieve methane conversion rarely exceeding 80%. This can cause several operating problems such as catalyst deactivation, carbon formation, increased pressure drop and more expensive materials for the reformer tubes [30].

In the Sorption Enhanced Steam Methane Reforming (SE-SMR) concept these thermodynamic limitations are overcome with the addition of an adsorbent material which selectively captures the CO_2 present in the gaseous bulk [31, 32], enhancing the WGS reaction (2.5), increasing the H_2 production [33, 34], and allowing to operate the reactor at lower temperature than the conventional steam reforming [35], which increases the efficiency and reduces the operating costs in comparison with carbon capture technologies based on solvents [30, 31, 36, 37].

The SE-SMR process is a cyclic operation that works over alternating cycles of reforming/carbonation and calcination [10]. During the reforming/carbonation cycle the adsorbent reacts with the CO_2 produced by the water gas shift stage of the reforming of natural gas and produces a solid carbonate in a separated phase form the main product stream. When the adsorbent is near its maximum adsorption capacity, the regeneration cycle starts, and heat has to be supplied to the process to revert the reaction direction and regenerate the material [32]. Therefore, the adsorbents to be used in this application must have specific properties for multi-cycle operation such as good adsorption capacity, fast adsorption-desorption kinetics, and good thermal and mechanical stability [5, 38, 39]. Table 2.1 summarises some properties of promising adsorbents for SE-SMR.

Among the adsorbents summarised in Table 2.1, calcium oxide exhibits the highest adsorption capacity (0.79 g CO_2/g adsorbent), and the highest heat of reaction per mol of reacted CO_2; in addition it exhibits a fast kinetics in range of temperatures of interests for the coupled application with the steam reforming reactions. Moreover, calcium oxide is cheap and can be found in several natural sources including dolomite and limestone, which are available worldwide; it also exhibits affinity to SO_2 which allows for partial desulphurisation in gas applications [5, 40]. However, this material has the important limitation of a poor stability upon multicyclic operation, presenting a strong tendency to sintering and decay of capture capacity [41-43]. Nevertheless, numerous investigations addressing this problem have been conducted, primarily targeting the use of ceramic materials

as supports to enhance the durability and the multicycle performance of the adsorbent [43-46].

Table 2.1 Adsorption capacity and regenerating temperature of various potential adsorbents for the SE-SMR process [5, 39, 43, 47-49].

Adsorbent	Ca-based	Hydrotalcites	Lithium zirconate	Sodium zirconate	Lithium silicate
Stoichiometric theoretical capacity (g_{CO2}/g_{ads})	0.79	0.022 – 0.033	0.29	0.23	0.37
Adsorption temperature (K)	873 – 1023	673 - 773	973 – 1073	~973	723 – 973
Regenerating temperature (K)	>1073	1173	~1173	~1173	<1023
Heat of adsorption (kJ/mol)	-178	-17	-160	-149	-143
Adsorption	Chemi-sorption	Physi- and chemisorption	Chemi-sorption	Chemi-sorption	Chemi-sorption
Kinetics	Initially fast kinetics	Fast	Slow, improves with the addition of K, Li promoters	Good	Good
Stability	Poor	Good	Good	Good	Good

The chemisorption of CO_2 with CaO is an exothermic process, and is strongly favoured at temperatures ranging from 873–973K and high operating pressures. The process follows the reaction mechanism:

$$CO_{2(g)} + CaO_{(s)} \leftrightarrows CaCO_{3(s)} \quad \Delta H^0 = -178.8\ kJ\ mol_{CaO}^{-1} \qquad \textbf{(2.7)}$$

The high heat of reaction generated by the adsorption of CO_2 benefits the overall thermal balance of the SE-SMR process; the integration of reaction (2.7) with the reforming reactions (2.4) – (2.6) renders a theoretically exothermic process as per reaction (2.8):

$$CH_{4(g)} + 2H_2O_{(g)} + CaO_{(s)} \leftrightarrows CaCO_{3(s)} + 4H_{2(g)} \; \Delta H^0 = -13.9 \; kJ \; mol_{CaO}^{-1} \qquad \textbf{(2.8)}$$

However, the regeneration of the adsorbent represents a challenge due to the high energy required to decompose the $CaCO_3$ [32, 50, 51]. The regeneration process of $CaCO_3$ follows the reverse route of reaction (2.7), and is strongly related to the difference between the CO_2 equilibrium pressure minus the bulk partial pressure of CO_2; if the partial pressure of carbon dioxide in the reactor atmosphere is high, then the temperature of the system needs to be increased to maintain a higher CO_2 equilibrium pressure, hence promoting the calcination of the adsorbent [46]; conversely, at low CO_2 partial pressures, the temperature swing is reduced, yielding a lower energy consumption and potentially a higher thermal efficiency [52]; however, the optimum operating conditions of this process need to be studied in the context of an integrated plant, as the energy and infrastructure required for CO_2 handling might constrain the selection of the operating pressure. Various alternatives to supply the heat of reaction to regenerate the adsorbent have been proposed, these alternatives include the use of hot streams of combustion gases, or high pressure steam, the heat from the combustion of char, and the exothermic oxidation of CaS to $CaSO_4$ in the lime enhanced gasification process (LEGS), and the coupling of a solid oxide fuel cell with the SE-SMR process (ZEG Technology) [50, 52]. The simpler alternative of utilising the heat of combustion of the PSA off-gas toped up by fuel is illustrated in Figure 2.2.

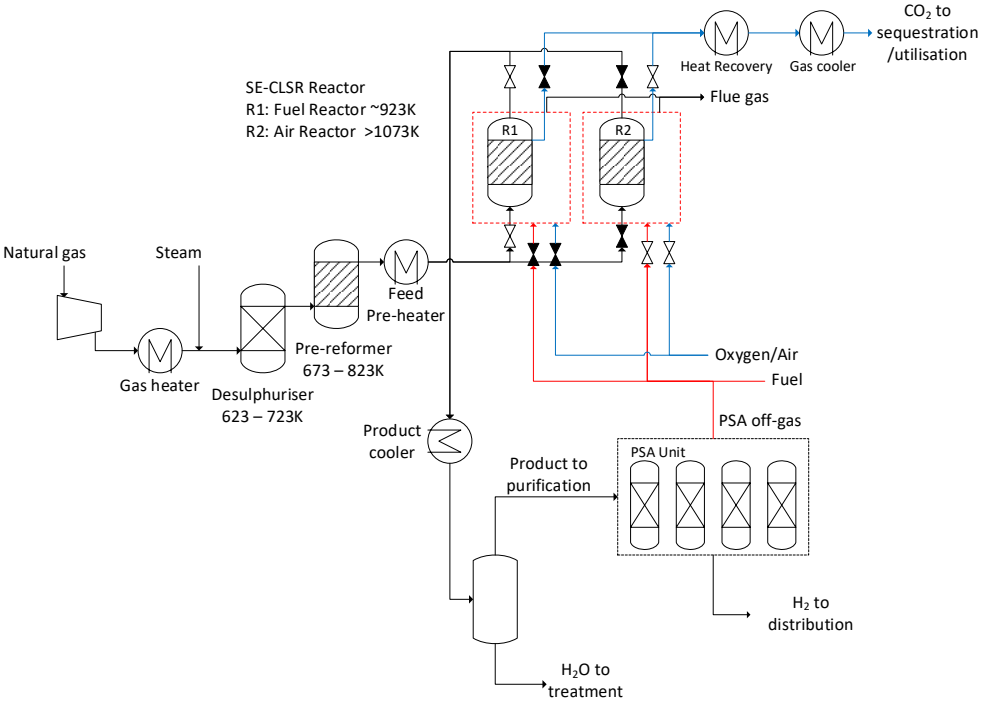

Figure 2.2 Preliminary lay-out of a SE-SMR plant for H_2 production (this work).

2.2.3 Sorption Enhanced Steam Reforming with Chemical Looping (SE-CLSR)

An alternative to supplying the heat of reaction required by the adsorbent regeneration, encompasses the integration of the so called chemical looping combustion process (CLC) along with the SE-SMR process; this method is commonly referred to in the literature as unmixed methane reforming (UMR) or sorption enhanced chemical looping steam methane reforming (SE-CLSMR), and it is based on the work of Kumar et al [17].

In the original CLC concept, the combustion of fuel is attained without mixing the air and the fuel streams, by alternatively passing them over a metal-based material, this implies that the material is subjected to cycles of reduction and oxidation in two stages known as the fuel reactor and the air reactor [13, 17], thus the metal-based material, often referred to as oxygen transfer material (OTM) or oxygen carrier (OC), has to satisfy various requirements to render an attractive process. Among these technical demands are the high reactivity of the OTM in red/ox reactions, high resistance to agglomeration, complete fuel conversion, negligible carbon deposition, and be economical and environmentally friendly [53-55]. Various materials have been proposed as OTM candidates such as perovskites or metal oxides of Fe, Ni, Mn, Ni, Cu and Co [53, 55, 56]. For H_2 production, NiO-based OTMs supported on ceramics such as Al_2O_4, SiO_2, TiO_2, Mg-ZrO_2 and $CaAl_2O_4$, are commonly used due to their high reactivity towards the steam reforming reactions [54, 57].

The coupling of the CLC with the steam reforming reactions and the calcium looping thus renders a process with three steps different from each other that are represented in Figure 2.3. The process follows (a) the reduction of the OTM, (b) the steam reforming of methane with in-situ capture of CO_2, and (c) the regeneration of both the OTM and the adsorbent.

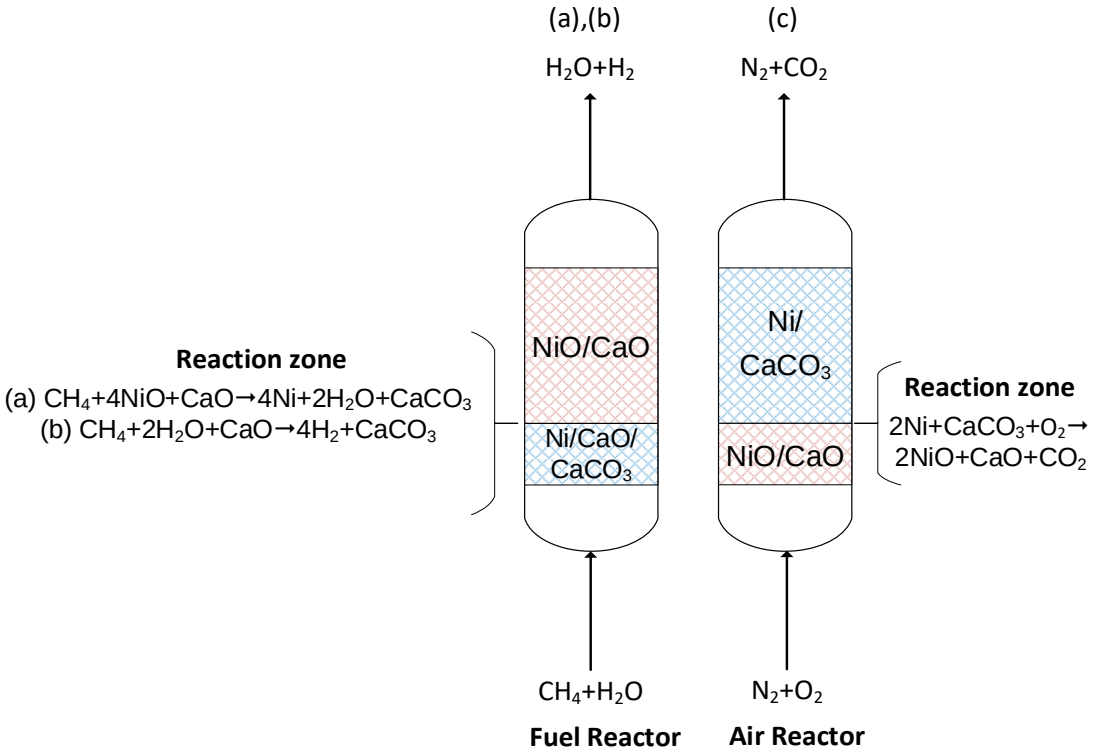

Figure 2.3 Operating steps of the SE-CLSMR reactor [17].

The steps (a) and (b) take place in the fuel reactor [58], the reforming and carbonation reactions stand as described in the previous section; nevertheless, the initial state of the catalyst is in the form of nickel oxide, which is catalytically inert, and should be reduced to the metallic Ni form prior to the start steam reforming reactions [17]; the reduction of NiO can be carried out with the feedstock as the reducing agent, as it contains traces of H_2 and CO which help to initiate the process, in fact, NiO have shown little to non-activity with methane when the material is fully oxidised [57]. This stage works as a step of activation of the catalyst and follows the mechanisms represented in Equations (2.13)–(2.15). When some degree of reduction of the nickel oxide has been achieved, the steam reforming takes place through the chemical mechanism described by Equations (2.4)–(2.6) which increases the concentration of H_2 in the reactor, thus promoting the reduction of any remaining oxidised nickel down the bed [59]; simultaneously, the CO_2 produced in the reforming process is adsorbed by the Ca-based adsorbent as per reaction (2.7).

In summary, the following reactions take place during the fuel reactor:

I) Steam reforming of methane:

$$CH_{4(g)} + H_2O_{(g)} \leftrightarrows CO_{(g)} + 3H_{2(g)} \quad \Delta H^0 = 206\ kJ\ mol^{-1}_{CH_4} \qquad \textbf{(2.9)}$$

II) Water-gas shift:

$$CO_{(g)} + H_2O_{(g)} \leftrightarrows CO_{2(g)} + H_{2(g)} \quad \Delta H^0 = -41\ kJ\ mol_{CO}^{-1} \qquad \textbf{(2.10)}$$

III) Steam reforming of methane (complete reaction):

$$CH_{4(g)} + 2H_2O_{(g)} \leftrightarrows CO_{2(g)} + 4H_{2(g)} \quad \Delta H^0 = 165\ kJ\ mol_{CH_4}^{-1} \qquad \textbf{(2.11)}$$

IV) NiO reduction with CH_4 via Unmixed Combustion (UC):

$$CH_{4(g)} + 4NiO_{(s)} \leftrightarrows CO_{2(g)} + 2H_2O_{(g)} + 4Ni_{(s)} \quad \Delta H^0 = 31\ kJ\ mol_{CH_4}^{-1} \qquad \textbf{(2.12)}$$

V) NiO reduction with CH_4 via Unmixed Partial Oxidation (UPO):

$$CH_{4(g)} + NiO_{(s)} \leftrightarrows CO_{(g)} + 2H_{2(g)} + Ni_{(s)} \quad \Delta H^0 = 203\ kJ\ mol_{CH_4}^{-1} \qquad \textbf{(2.13)}$$

VI) NiO reduction with CO:

$$CO_{(g)} + NiO_{(s)} \leftrightarrows CO_{2(g)} + Ni_{(s)} \quad \Delta H^0 = -43\ kJ\ mol_{CO}^{-1} \qquad \textbf{(2.14)}$$

VII) NiO reduction with H_2:

$$H_{2(g)} + NiO_{(s)} \leftrightarrows H_2O_{(g)} + Ni_{(s)} \quad \Delta H^0 = -2\ kJ\ mol_{NiO}^{-1} \qquad \textbf{(2.15)}$$

VIII) Sorbent carbonation:

$$CO_{2(g)} + CaO_{(s)} \leftrightarrows CaCO_{3(s)} \quad \Delta H^0 = -178.8\ kJ\ mol_{CaO}^{-1} \qquad \textbf{(2.16)}$$

When the adsorbent is nearly saturated the step (c) starts and the reactor operating mode is switched to the air reactor, during which the solid materials undergo regeneration [10, 58]. An oxidising agent, e.g. air, oxygen, is passed over the packed bed oxidising the nickel to form nickel oxide releasing heat that is partially utilised to heat up the bed and provide the heat of reaction necessary to decompose the calcium carbonate formed during the adsorption of CO_2 [13, 17]. This processes are represented in Equations (2.17) and (2.18) as:

$$CaCO_{3(s)} \leftrightarrows CO_{2(g)} + CaO_{(s)} \quad \Delta H^0 = 178.8\ kJ\ mol_{Ca}^{-1} \qquad \textbf{(2.17)}$$

$$2Ni_{(s)} + O_{2(g)} \leftrightarrows 2NiO_{(s)} \quad \Delta H^0 = -480\ kJ\ mol_{O_2}^{-1} \qquad \textbf{(2.18)}$$

The re-oxidation of nickel with air produces a stream composed of primarily N_2 and CO_2 which require to be separated prior to capturing or utilising the CO_2. This can be avoided using pure oxygen which in fact seems to increase the thermal efficiency of the reactor whilst producing a stream of pure CO_2, however, with the associated costs of the oxygen production plant [60].

The integration of the SE-CLSMR reactor within a H_2 production plant is illustrated in Figure 2.4. Similar advantages with respect to the conventional process are observed between the SE-CLSMR and the SE-SMR processes, namely the lower operating temperature of the reactor during the steam reforming of methane and the integration of the WGS process within the same environment of the SE-CLSMR reactor. The main difference of the SE-CLSMR and the SE-SMR shown in Figure 2.2 is the infrastructure required to supply the oxidising agent to the reactor during the regeneration cycle, and the equipment required to handle the exhaust gas produced.

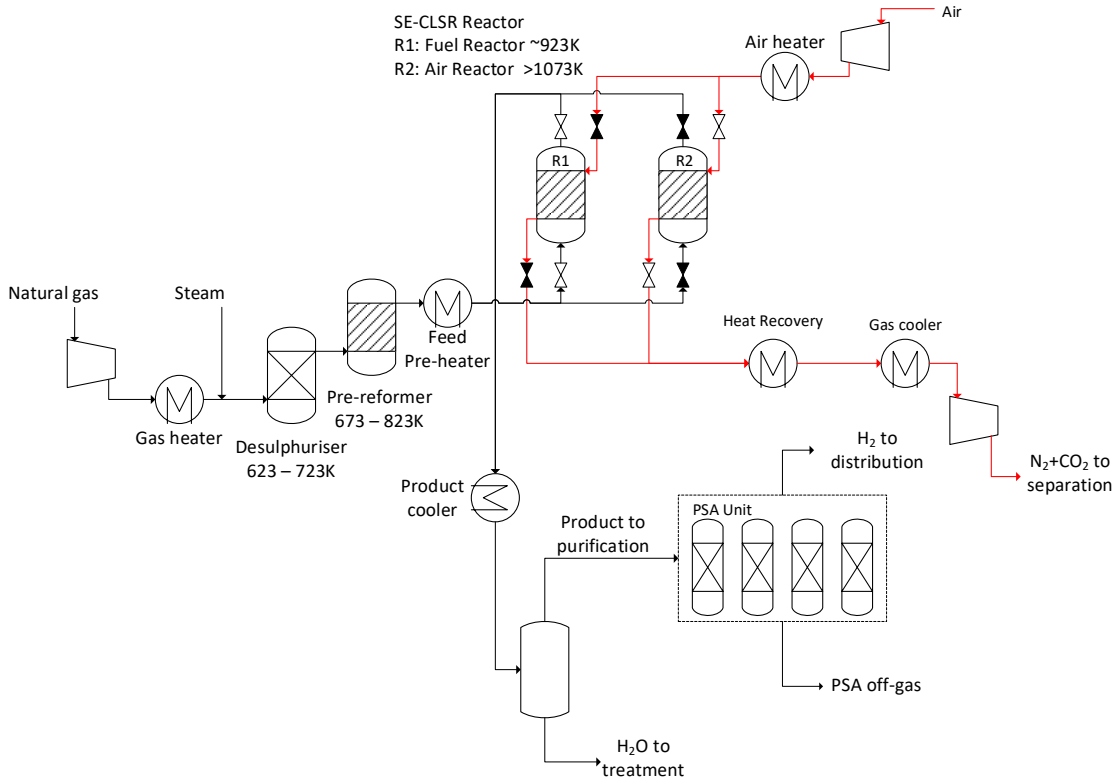

Figure 2.4 Preliminary lay-out of a SE-CLSMR plant for H_2 production (this work).

2.3 Side processes in the SE-CLSR concept

Various side reactions can happen in the Fuel Reactor along with the main processes of interest. At the catalyst active sites the following reactions can

I) Dry methane reforming

$$CH_{4(g)} + CO_{2(g)} \leftrightarrows 2CO_{(s)} + 2H_{2(g)} \quad \Delta H^0 = 246.9\ kJ\ mol_{CH_4}^{-1} \qquad \textbf{(2.19)}$$

II) Boudouard reaction

$$2CO_{(g)} \leftrightarrows C_{(s)} + CO_{2(g)} \quad \Delta H^0 = -171.5\ kJ\ mol_{CO_2}^{-1} \qquad \textbf{(2.20)}$$

III) Methane and higher hydrocarbons decomposition

$$CH_{4(g)} \leftrightarrows C_{(s)} + 2H_{2(g)} \quad \Delta H^0 = 75.3\ kJ\ mol^{-1}_{CH_4} \tag{2.21}$$

$$C_m H_{n(g)} \rightarrow mC_{(s)} + n/2\ H_{2(g)} \quad \Delta H^0 > 0\ kJ\ mol^{-1} \tag{2.22}$$

IV) Carbon gasification with steam, hydrogen and carbon dioxide

$$C_{(s)} + H_2O_{(g)} \leftrightarrows CO_{(g)} + H_{2(g)} \quad \Delta H^0 = 132\ kJ\ mol^{-1}_{C_{(S)}} \tag{2.23}$$

$$C_{(s)} + 2H_{2_{(g)}} \leftrightarrows CH_{4(g)} \quad \Delta H^0 = -75.3\ kJ\ mol^{-1}_{C_{(S)}} \tag{2.24}$$

$$C_{(s)} + CO_{2(g)} \leftrightarrows 2CO_{(g)} \quad \Delta H^0 = 171.5\ kJ\ mol^{-1}_{C_{(S)}} \tag{2.25}$$

The risk of carbon formation must be eliminated of the industrial application as it can lead to undesirable deposits of whisker and gum carbon within the structure of the catalyst promoting deactivation and attrition [22, 24, 61]; the former type is likely to form at temperatures greater than 720 K and can cause breakage of the catalyst and blockage of the reformer, resulting in different operational issues such a higher pressure drop throughout the packed bed, and poor distribution of heat, resulting in the formation of hot spots, hot bands or overly hot tubes, which affects the mechanical integrity of the reactor tubes, and increases the risk of failure [62, 63]; the latter type is formed at temperatures lower than 770 K and it promotes catalyst deactivation, causing a continuous displacement of the temperature profile in the direction of flow [19, 62].

The likelihood of carbon formation is particularly higher when the feedstock contains a higher fraction of C_{2+} components, and the system is operated at low steam-to-carbon ratios [19, 24]. In these cases the potential of carbon formation is reduced using catalysts promoted with alkali metals, as they enhance the adsorption of water helping to reduce the concentration of species that promote carbon formation at the nickel crystals' surface, such as CO_2 [19, 24, 64]. In addition, the pre-reforming of the feedstocks allows the conversion of the heavier hydrocarbons as reported in section 2.2.1, thus reducing the risk of carbon formation [19].

In the SE-CLSMR process the concentration of the species that promote carbon formation are low due to the adsorption of CO_2. Whilst the concentrations of the species that promote carbon gasification are high, provided that a high steam-to-carbon ratio is selected, this condition affect the kinetic thresholds of both carbon formation and gasification as illustrated in Figure 2.5. The curves presented in Figure 2.5 have been calculated in the present work for the conventional steam

reforming of methane, and the SE-CLSMR processes, with the constants derived by Snoeck et al. [61, 63], at equilibrium, 10 bar and temperatures ranging from 823–998 K. The removal of CO_2 from the reacting stream seems to promote an operating condition in which the rate of gasification with H_2 and H_2O are favoured over rate of carbon formation, thus indicating that the probability of these events in the SE-CLSMR reactor is low. This was theoretically demonstrated by Rout et al. [65], who obtained negative rates of carbon formation in the simulation of the SE-SMR process in a packed bed reactor.

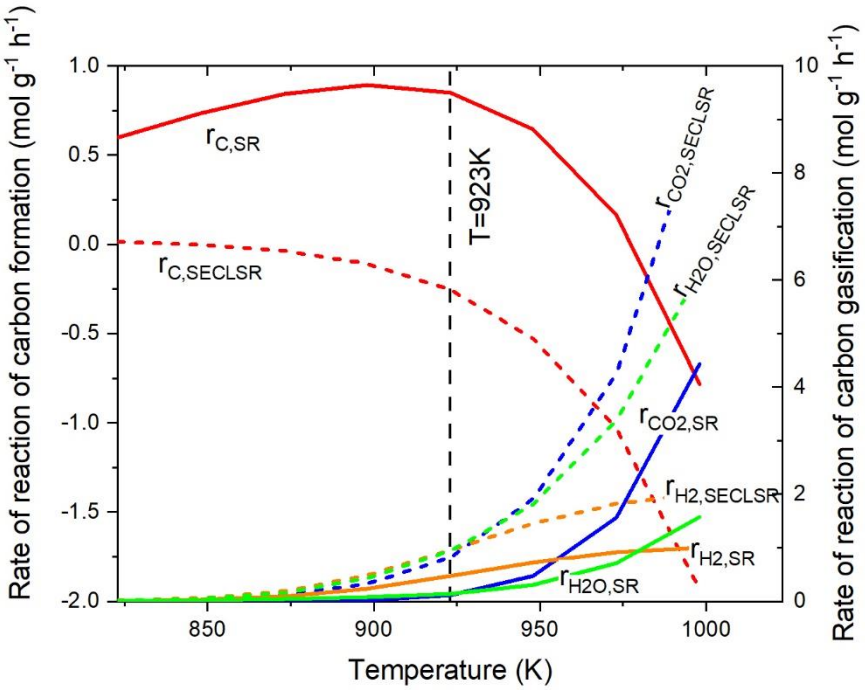

Figure 2.5 Rate of reaction of the formation and gasification of carbon calculated with the equilibrium compositions of the SE-CLSMR and SMR processes at 5 bar and S/C=3 (this work).

The Ca-based adsorbent can react with water to form the respective hydrate, the stoichiometric reaction is represented as:

$$CaO_{(s)} + H_2O_{(g)} \leftrightarrows Ca(OH)_{2(g)} \quad \Delta H^0 = -109\ kJ\ mol_{CaO}^{-1} \qquad \textbf{(2.26)}$$

The hydration of CaO is defined by the operating conditions of the reactor, as can be seen in Figure 2.6, which is a plot of the thermodynamic limits for the carbonation and hydration of CaO. Previous studies analysing the optimum operating conditions of the SE-CLSMR process suggest that the best reactor performance is achieved at low pressures and in temperature ranges that vary from 700 K up to 1023 K [10, 51, 56, 60, 66-68]. For the processing of methane, some agreement has been reached regarding the optimum temperature being around 923 K [51, 56, 60, 68]; at this temperature, the threshold for CaO hydration

water partial pressure greater than 9.53 bar is shown in Figure 2.6, thus, the hydration of calcium oxide is unlikely when operating at low pressures at 923 K. Conversely, at high pressures the adsorbent will undergo a competition between the mechanisms of carbonation and hydration. Nevertheless, some studies have suggested the hydration of the CaO adsorbent as a step to enhance its capture capacity [69]; in this scheme reaction (2.26) is in fact an intermediate step of the carbonation process, followed by the following reaction:

$$Ca(OH)_{2(s)} + CO_{2(g)} \leftrightarrows CaCO_{3(s)} + H_2O_{(g)} \quad \Delta H^0 = -79\ kJ\ mol^{-1}_{Ca(OH)_{2(S)}} \qquad \textbf{(2.27)}$$

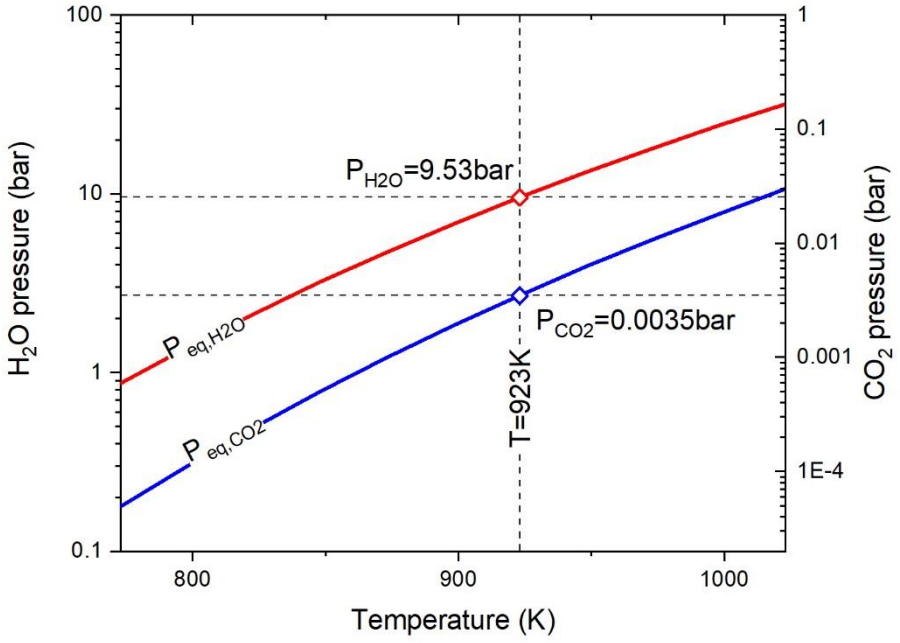

Figure 2.6 Thermodynamic equilibria of CaO carbonation and hydration [70].

2.4 Reactor types for Chemical Looping reactor with and without carbon capture.

The chemical-looping technology can be carried out in both fluidised and fixed bed reactors [54, 71, 72]. Circulating Fluidised Bed Reactors have been proposed for H_2 production with and without sorbent for carbon capture [41, 55, 56, 73-75]. In this type of reactor configuration, the solid materials are continuously circulated between the fuel and air reactors, in cycles of reduction and oxidation of the oxygen carrier and the carbonation and calcination of the CO_2 adsorbent. Some configurations for hydrogen production have been proposed in fluidised systems without adsorption of CO_2, e.g. autothermal chemical looping (a-CLR), steam reforming with chemical looping combustion (SR-CLC) and chemical looping for

hydrogen production (CLH) [53, 76-78]. Other investigations have researched the coupling of the adsorption looping with the conventional steam reforming for hydrogen production in fluidised reactors [41, 73, 75], whilst the regeneration of the adsorbent was simulated using steam as sweep gas [75]. A third category of the application of circulating beds in H_2 generation is known as chemical looping for hydrogen generation (CLHG); in this system three beds are required namely the fuel reactor, the air reactor and the steam reforming reactor. This configuration is aimed at the production of hydrogen with carbon capture without circulating a CO_2-adsorbent in the system [53].

Fluidised bed reactors are a proven technology that allows for continuous operation, and provide a best temperature distribution which is important in terms of heat management [79]. However, the recirculation of particles between reactors can increase the probability of producing solid fines which can be carried over with the gas product stream leading to operational issues such as failures in dynamic equipment located downstream the Chemical Looping process and even a permanent mechanical damage to those equipment. Moreover, the application of fluidised systems to hydrogen production requires a NiO-based material which is highly reactive with methane, the circulation of this type of particles poses potential health and environmental risks, in addition to the associated high costs of losing nickel to the atmosphere [53, 76, 77]. Furthermore, the available modelling investigations showed that the high velocities required for the transport of solids in circulating fluidised beds may limit the re-oxidation of the oxygen carrier, thus impacting the performance of the fuel reactor [76]. Conversely, in [80], a high performance and utilisation of the oxygen carrier is reported to be superior in a bubbling fluidised reactor in comparison to the equivalent fixed bed reactor. Moreover, low rates of attrition have been reported for the application of bubbling fluidised reactor for a SE-SMR reactor [75].

Chemical Looping Reforming with and without in-situ carbon capture has also been analysed in packed bed reactor concepts [6, 31, 32, 35, 50, 54, 59, 65, 68, 81]. Packed bed reactors consist of a stationary solid bed that allows for the operation of an intrinsically separated stream of gas and therefore, a lower risk of carry over solid fines downstream or to the atmosphere [81, 82]. In this reactor configuration, it is required to periodically operate a minimum of two reactors to allow for continuous operation [80, 82]. Additional advantages of fixed bed reactors in comparison with fluidised bed reactors are the flexibility to operate at high pressures, and ease to scale-up the system. However, the packed bed reactors present some drawbacks such as the formation of hot-spots in exothermic processes, the deposition of carbon in the catalyst, the potential of catalyst deactivation by poisoning and sintering, the possibility of flow

maldistribution and a large pressure drop [76, 83]. Table 2.2 summarises the main features of packed and fluidised bed reactor technologies.

Table 2.2 Comparison of the advantages and disadvantages of fixed bed reactor and fluidised bed reactors in chemical looping applications [76, 77, 79, 81, 82].

Criteria	Advantages	Disadvantages
Fixed bed	High pressure operation	Poor heat transfer characteristics
	Gas and solid phases are inherently separated	Hot spots with exothermic reaction
	Compact technology	Large temperature gradients
	Low risk of particle attrition	Channelling possible
	Low active weight content in OC (up to 20%)	Periodic switching of gas flows for reduction/calcination and oxidation/carbonation.
	Avoidance of leakage harmful particles to the environment	Long periods for heat-up
	No mobile parts	Require large pellets to reduce pressure drop
		Low effectiveness due to high intra-pellet diffusion.
Fluidised bed	Good heat transfer characteristics	Issues with high pressure operation
	Better temperature distribution	Equipment erosion due to solids circulation
	Good gas solid contact and mixing	Difficult gas-solid separation
	Minimises the chances of hot spots in exothermic reactions	Higher active weight content in OC (up to 40%)
	Small temperature gradients between Fuel Reactor and Air Reactor.	High dust content in gas phase
	Broad particle-size distribution	High risk of attrition and agglomeration
		Risk of de-fluidisation
		Risk of leakage of harmful OC particles to the environment
		Mobile parts

2.5 Literature review in modelling of the SE-CLSR process.

Much progress has been made in the modelling of the sorption enhanced-chemical looping steam reforming of methane (SE-CLSRM) on the basis of the original concept proposed by Kumar et al. [17], and modifications obtained by introducing different adsorbents and oxygen carriers. These efforts have looked at the application of this technology both in packed bed and fluidised reactors. Because of the relevance of the packed bed technology in the current state-of-the-art hydrogen plants, this review will be focused on the investigations aimed to analyse SE-CLSR in packed beds.

Xiu et al. [35] developed a pseudo-homogeneous model to analyse the sorption enhanced steam reforming of methane without chemical looping, and studied the effect of operating conditions on the performance of the process, reporting hydrogen purities of 90–98% at temperatures between 723–763 K and pressures between 223–891 kPa. The solution of the model was obtained with the orthogonal collocation method, although the authors did not provide details of their numerical solution.

Ochoa-Fernandez et al. [31] reported the application of a pseudo-homogeneous model to simulate the SE-SMR process considering a Ni-based catalyst and lithium zirconate adsorbent (Li_2ZrO_3), their results indicated a purity higher than 95%. Their model considered axial dispersion in the reactor but neglected the velocity and density gradients due to the change in the system's total mass. The solution of the model was attained by the method of lines, the spatial derivatives were approximated by finite differences but used different discretisation orders for the convective and dispersive terms which can introduce errors in the final solution.

Fernandez et al. [6, 50] considered a system with a Ni-based catalyst and a Ca-based adsorbent and conducted a parametric study of the SE-SMR with and without chemical looping. The scenario with chemical looping considered the reduction of copper to generate the heat of reaction necessary for the calcination of $CaCO_3$, however, their study focused only on the effect of the operating parameters during the fuel reactor stage of the cycle and did not show results of the dynamics of the bed regeneration. Similarly to previous studies, their results showed a high purity of hydrogen ranging between 85–95% for the process without chemical looping, and proposed an operating window for temperature (923 – 1023 K), pressure (5 – 15 bar) and steam-to-carbon ratio (3 – 6). The mathematical model considered a pseudo-homogeneous plug flow reactor and the pressure drop was estimated with the Ergun equation, the mass balance equations showed that the researchers considered axial variation of the

superficial velocity. However, no details of additional considerations to calculate this variable were provided. Nevertheless, based on a subsequent publication [44] by the same group, it is suspected that they considered constant velocity throughout the packed bed. The authors did not provide details of the method of solution utilised to solve their model, however, it is inferred that they used the method of lines as they mentioned the use a of an ODE solver in Matlab. In a subsequent paper [52], they analysed the cyclic operation of the reactor, providing the guidelines to attain an operable system. The reported efficiencies for this system were 62.5% and 87.5% for hydrogen production and carbon capture respectively.

Rout and Jakobsen [65] discussed the advantages of a bi-functional particle with catalyst and adsorbent properties applied to the SE-SMR process. They proposed a pellet model to study the performance of the hypothetical particle and concluded that the particle temperature behaves isothermally although with pressure gradients. In addition, their model results confirmed that the physics of the process is diffusion-dominated at the particle level, and determined values of the effectiveness of the carbonation reaction around 0.8. They also simulated a pseudo-homogeneous reactor with axial dispersion, and accounting for the axial variation of gas velocity and density; the pressure drop was estimated with the Ergun equation. The model was solved by the least-squares spectral and spectral element methods. The reactor model was applied to study the effect of operating conditions on the SE-SMR process, their model predicted the absence of carbon formation both in the particle and along the packed bed, and hydrogen purity above 90% under the simulated conditions.

Lugo and Wilhite [33] compared two single-pellet designs, namely the core-shell and the uniform distributed design with the two pellet design in their application to the sorption enhanced steam reforming of methane, without chemical looping. In this study, a heterogeneous model was considered accounting explicitly for the concentration and temperature gradients at the particle level. They found that the uniformly distributed pellet design rendered a higher performance in comparison with the core-shell and the two pellet design. This model was implemented and solved in the commercial software Comsol® which works with the finite element method (FEM).

Abbas et al. [68] analysed the SE-CLSMR process with a pseudo-heterogeneous model that considered steady state mass transfer between the fluid and the solid phase and a dynamic evolution of the solid temperature. This model assumed homogeneous local temperature and concentration profile to characterise the processes happening at both, the catalytic and the adsorbent. In addition, the model, assumed axial dispersion and constant mass flux throughout the system.

The authors applied this model to simulate a SE-CLSMR reactor over a wide range of operating conditions and reported similar results of reactor performance in comparison to previous modelling studies. In this investigation the model was solved in gPROMS® which is based in the method of lines.

The majority of the previous simulation studies of the SE-SMR and SE-CLSMR processes have been conducted assuming a single local temperature and concentration profile between the adsorbent and the catalyst, either following the homogeneous or heterogeneous approach. This assumption might be valid for a small pellets, considering the error that is introduced by incorporating heat and mass transfer correlations. However, it does not afford for a realistic representation of the physics of the system, except in those cases where a single multifunctional particle has been proposed. During the process, the kinetic rates of the reforming reactions and of the carbonation of the adsorbent are affected by the concentration and temperature profiles at each particle; the actual value of these rates can be overestimated by the homogeneous approach, as this model assumes intimate contact between the different phases. Yet, lower values are expected given the possible inter and intra-particle resistances to mass and heat transfer. The previous modelling work have addressed these effects by incorporating effectiveness factors whose role is to reduce the rates at which mass and heat are generated or consumed.

Nevertheless, in this work we consider that the dynamics of each process is likely to affect the performance of the SE-CLSMR reactor, particularly as the pellets' sizes approach the sizes required at industrial scale. At this condition, the inter- and intra-particle effects are larger and might control the transfer processes, impacting the transport of heat of reaction from the adsorbent where the exothermic process happens, towards the gas, and from the gas towards the catalyst where the endothermic processes take place. In addition, it is well documented that the gas-solid heat transfer is limited by the intra-pellet effects [84], hence under certain flow conditions, a higher surface temperature at the adsorbent temperature can be expected with respect to the gas temperature, and with respect to the surface temperature at the catalyst.

Thus, this work looks at a mathematical model that accounts explicitly for separate CO_2 sorbent and oxygen transfer catalyst particles, in order to incorporate the dynamics of each chemical and thermal process and verify its impact onto the simulation results. Moreover, during the adsorption of CO_2 the adsorbent is subjected to timely dependent structural changes (e.g. changes in porosity, density and heat capacity), the effect of the changes in porosity has been accounted for in a previous modelling investigations of the SE-SMR in fluidised beds [41], and in the context of the comparison of the performance of a

multifunctional pellet [85], however none of the effects were incorporated in the context of SE-CLSMR models in packed bed reactors, therefore this work will investigate its effect in the performance of the packed bed reactor.

2.6 Reaction kinetics

Reactor modelling and design requires information of the kinetic rates of the various processes carried out. Numerous kinetic rate expressions have been proposed and their kinetic parameters derived from experiments performed at different conditions and a variety of reaction mechanisms. In this section, a review of available expressions of kinetic rates for the steam reforming processes, the carbonation of CaO, the calcination of $CaCO_3$, the reduction of NiO, and oxidation of Ni is presented.

2.6.1 Steam reforming

The kinetics of the Steam Reforming for methane and higher hydrocarbons has been widely reported in experimental and modelling research [18, 23, 86-88]. Different types of models have been used to represent the kinetics of this process including power law models, however, the vast majority of current research relies on Langmuir-Hinshelwood-Hougen-Watson (LHHW) type expressions, primarily those proposed by Xu and Froment [86].

The intrinsic kinetic expressions by Xu and Froment [86] was developed based on the assumption that the overall reaction rate for this process was controlled by the reforming reactions previously presented in Equations (2.4) – (2.6). The kinetic expression have the following form:

$$r_{SRM} = \frac{k_{SRM}}{p_{H_2}^{2.5}} \frac{\left(p_{CH_4} p_{H_2O} - \frac{p_{H_2}^3 p_{CO}}{K_{SRM}}\right)}{DEN^2} \tag{2.28}$$

$$r_{WGS} = \frac{k_{WGS}}{p_{H_2}} \frac{\left(p_{CO} p_{H_2O} - \frac{p_{H_2} p_{CO_2}}{K_{WGS}}\right)}{DEN^2} \tag{2.29}$$

$$r_{SRMC} = \frac{k_{SRMC}}{p_{H_2}^{3.5}} \frac{\left(p_{CH_4} p_{H_2O}^2 - \frac{p_{H_2}^4 p_{CO_2}}{K_{SRMC}}\right)}{DEN^2} \tag{2.30}$$

$$DEN = 1 + K_{CO} p_{CO} + K_{H_2} p_{H_2} + K_{CH_4} p_{CH_4} + \frac{K_{H_2O} p_{H_2O}}{p_{H_2}} \tag{2.31}$$

Where r_{SRM}, r_{WGS},r_{SRMC}, k_{SRM}, k_{WGS},k_{SRMC}, and K_{SRM}, K_{WGS},K_{SRMC} are the rates of reaction, the kinetic constants and the equilibrium constants of reactions (2.4), (2.5) and (2.6), respectively; p_i represents the partial pressure of the "i" specie at the pore of the catalyst, and K_i is the adsorption constant of each sorbate.

Soliman et al. [87] studied the intrinsic kinetics of a Nickel/Calcium Aluminate catalyst. They suggested a similar mechanism to that proposed by Xu and Froment [86], with the exception that they assumed the adsorption of water steam at the catalyst surface, and that the adsorbed carbon monoxide reacts with the adsorbed steam rather than with oxygen. Their final model resulted from the consideration that the formation of CO_2 from CH_4 controls the kinetic rate, giving:

$$r_{SRM} = 0 \tag{2.32}$$

$$r_{WGS} = \frac{k_{WGS}}{p_{H_2}^{2.5}} \frac{\left(p_{CO}p_{H_2O} - \frac{p_{H_2}p_{CO_2}}{K_{WGS}}\right)}{DEN^2} \tag{2.33}$$

$$r_{SRMC} = \frac{k_{SRMC}}{p_{H_2}^{3.5}} \frac{\left(p_{CH_4}p_{H_2O}^2 - \frac{p_{H_2}^4 p_{CO_2}}{K_{SRM}K_{WGS}}\right)}{DEN^2} \tag{2.34}$$

$$DEN = 1 + K_{CO}p_{CO} + \frac{K_{H_2O}p_{H_2O}}{p_{H_2}} \tag{2.35}$$

Hou and Hughes [88] derived similar kinetic expressions of the LHHW type for a Ni-catalyst supported in α-Al_2O_3, considering a kinetic mechanism in which the rate controlling steps are the formation of CO and CO_2 from intermediate species formed from the adsorption of methane and water steam. After fitting the experimental data they proposed the following model:

$$r_{SRM} = \frac{k_{SRM}}{p_{H_2}^{1.25}} \frac{\left(p_{CH_4}p_{H_2O}^{0.5} - \frac{p_{H_2}^3 p_{CO}}{K_{SRM}p_{H_2O}^{0.5}}\right)}{DEN^2} \tag{2.36}$$

$$r_{WGS} = \frac{k_{WGS}}{p_{H_2}^{0.5}} \frac{\left(p_{CO}p_{H_2O}^{0.5} - \frac{p_{H_2}p_{CO_2}}{K_{WGS}p_{H_2O}^{0.5}}\right)}{DEN^2} \tag{2.37}$$

$$r_{SRMC} = \frac{k_{SRMC}}{p_{H_2}^{1.75}} \frac{\left(p_{CH_4}p_{H_2O} - \frac{p_{H_2}^4 p_{CO_2}}{K_{SRMC}p_{H_2O}}\right)}{DEN^2} \tag{2.38}$$

$$DEN = 1 + K_{CO}p_{CO} + K_H p_H^{0.5} + \frac{K_{H_2O}p_{H_2O}}{p_{H_2}} \quad \textbf{(2.39)}$$

Abbas et al. [89] investigated the steam reforming kinetics over a Ni-catalyst supported in α-Al_2O_3 and fitted their experimental data to Equations (2.28) – (2.30), from which they estimated values of the pre-exponential factor and activation energy for each of the three main reforming reactions. However, in their parameter estimation scheme, they did not consider the fitting of the adsorption enthalpy and the pre-exponential factor of the adsorption constant. A summary of the model parameters of the previously reported this model and those previously reported is provided in Table 2.3.

Table 2.3 Summary of kinetic parameters of steam methane reforming.

Source	Xu and Froment [86]	Soliman et al. [87]	Hou and Hughes [88]	Abbas et al. [89]
Catalyst	$Ni/MgAl_2O_4$	$Ni/CaAl_2O_4$	$Ni/\alpha\text{-}Al_2O_3$	$Ni/\alpha\text{-}Al_2O_3$
Nickel content	15%	Not available	15 – 17%	18%
Experimental conditions				
Steam Reforming				
Temperature (K)	773 – 848	748 – 823	748 - 823	823 – 973
Pressure (bar)	3 – 15	1 – 3	1.2 – 6	1
S/C ratio (-)	3.0 – 5.0	2.4 – 5.9	4.0 – 7.1	3.1
Revers WGS				
Temperature (K)	573 – 673	598 – 673	598 – 673	573 – 648
Pressure (bar)	3 – 10	2.2 – 2.4	1.2	1
H_2/CO_2 ratio (-)	0.5, 1.0	0.6 – 1.0	0.5, 0.75	n/a
Activation Energy				
$E_{A,SMR}$ (kJ mol^{-1})	240.1	0	209.2	257.0
$E_{A,WGS}$ (kJ mol^{-1})	67.3	32.6	15.4	89.2
$E_{A,SMRC}$ (kJ mol^{-1})	243.9	185.89	109.4	236.7
Pre-exponential factor[1]				
$k_{0,SMR}$	1.17×10^{15}	0	1.87×10^{12}	5.19×10^{12}
$k_{0,WGS}$	5.43×10^{5}	4.14×10^{4}	60.28	9.9×10^{6}
$k_{0,SMRC}$	2.83×10^{14}	1.19×10^{12}	3.46×10^{6}	1.32×10^{13}
Adsorption enthalpy				
ΔH_{CO} (kJ mol^{-1})	-70.65	-19.86	-140.0	-
ΔH_{H2} (kJ mol^{-1})	-82.90		-93.4	-
ΔH_{CH4} (kJ mol^{-1})	-38.28			-
ΔH_{H2O} (kJ mol^{-1})	88.68	54.43	15.9	-
Pre-exponential factor				
$A(K_{CO})$ (bar^{-1})	8.23×10^{-5}	2.94	5.13×10^{-11}	-
$A(K_{H2})$ (bar^{-1})	6.12×10^{-9}		5.68×10^{-8}	-
$A(K_{CH4})$ (bar^{-1})	6.65×10^{-4}			-
$A(K_{H2O})$ (-)	1.77×10^{5}	6.00×10^{4}	9.25	-

[1] The units of $k_{0,SMR}$, $k_{0,WGS}$, and $k_{0,SMRC}$ vary for each model as follows:
Xu and Froment/Abbas et al.: $k_{0,AMR}$, $k_{0,SMRC}$ are in mol $bar^{0.5}$ kg^{-1} s^{-1}, $k_{0,WGS}$ in mol bar^{-1} kg^{-1} s^{-1}.
Soliman: $k_{0,WGS}$, $k_{0,SMRC}$ are given in mol $bar^{0.5}$ kg^{-1} s^{-1}.
Hou and Hughes: $k_{0,SMR}$, $k_{0,SMRC}$ are in mol $bar^{-0.25}$ kg^{-1} s^{-1}, $k_{0,WGS}$ in mol bar^{-1} kg^{-1} s^{-1}.

2.6.2 Non-catalytic processes

Non-catalytic systems are relevant processes for the SE-CLSMR reactor. During non-catalytic solid-gas reactions, a moles of a gaseous reactant A react with b moles of a solid reactant B, producing c moles of a solid product C and g moles of a gaseous product G, its general mechanism is represented by [90]:

$$aA(g) + bB(s) \leftrightarrows cC(s) + gG(g) \quad \textbf{(2.40)}$$

The kinetic of this type of processes has been widely studied and different models have been produced. Generally speaking, the kinetics of solid-gas non-catalytic reactions can be expressed as [90]:

$$\frac{dX}{dt} = kf(X)h(P) \quad \textbf{(2.41)}$$

Where k is the kinetic constant, $f(X)$ is a function of the solid conversion describing the reaction mechanism and $h(P)$ is a pressure correction function. The kinetic constant k is typically described by an Arrhenius-type function of the temperature as [91]:

$$k = k_0 e^{\left(-\frac{E_A}{R_g T}\right)} \quad \textbf{(2.42)}$$

Where k_0 is the pre-exponential factor for the non-catalytic process kinetics, E_A is the activation energy, R_g is the gas constant and T is the local temperature. The functional form of $f(X)$ depends on the selected reacting mechanism of the solid [92], e.g. an uniform conversion model, a shrinking core model, a grain model, a random pore model or a nucleation and nuclei model. Summaries of the various expressions for $f(X)$ have been provided in [90, 93, 94], however, its analysis is beyond the scope of this thesis and this review is focused on the specific kinetic rate expressions proposed for the non-catalytic solid-gas reactions relevant to the SE-CLSMR process.

2.6.2.1 Calcium oxide carbonation

The carbonation of CaO has been widely studied. The results of several investigations have suggested that the general mechanism of this process proceeds by an initially kinetic controlled regime, followed by a diffusion-controlled stage [90, 95]. The kinetic regime has been shown to be influenced by the pressure difference between the bulk pressure and the equilibrium pressure of CO_2 [90, 95, 96] at low partial pressures, however, no general consensus has been reached regarding the threshold at which the reaction becomes independent of the pressure level.

Numerous attempts to develop a kinetic rate expression for the adsorption of CO_2 in CaO have been made. The models produced have been mainly of the grain and random pore model types; in addition, some empirical attempts have been reported.

Bhatia and Perlmutter [95] suggested that the behaviour of CaO during the carbonation was intrinsically related to the internal pore structure of the solid, and developed a random pore model (RPM) for each regime of the process to represent the experimental data of the carbonation of lime. For the kinetic regime they proposed the following expression [97]:

$$\frac{dX_{CaO}}{dt} = \frac{k_s S_{g,f}\left(C_{CO_2} - C_{CO_2,eq}\right)(1 - X_{ads})\sqrt{1 - \psi ln(1 - X_{ads})}}{\left(1 - \varepsilon_{0,a}\right)} \qquad \textbf{(2.43)}$$

In Equation (2.43) X_{CaO} represents the conversion of the adsorbent, k_s is the kinetic constant for surface reaction, $S_{g,f}$ is the surface area of CaO, C_{CO_2} and $C_{CO_2,eq}$ are the actual and equilibrium concentrations of CO_2, ε_0 is the adsorbent porosity and ψ is the structural parameter. As the reaction progresses and a product layer is formed, the carbonation kinetics becomes controlled by diffusion, the instantaneous local rate is then calculated from [95]:

$$\frac{dX_{CaO}}{dt} = \frac{k_s S_{g,f} C_s \sqrt{1 - \psi ln(1 - X_{ads})}}{\left(1 - \varepsilon_{0,a}\right)\left[1 + \frac{\beta Z}{\psi}\left(\sqrt{1 - \psi ln(1 - X_{ads})} - 1\right)\right]} \qquad \textbf{(2.44)}$$

The additional parameters β and Z in Equation (2.44) are the modified Biot number and the ratio of volume of the solid phase after the reaction to that before the reaction. Equations (2.43) and (2.44) show the dependence of the conversion of the adsorbent with the structural parameter ψ, this parameter is a measure of the structure of the pore [98] and is defined as:

$$\psi = \frac{4\pi L_0 (1 - \varepsilon)}{S_{g,v}^2} \qquad \textbf{(2.45)}$$

Where L_0, $S_{g,v}$ and $\varepsilon_{0,a}$ are the pore length, the initial surface area per unit of volume and the adsorbent porosity, and are calculated from mercury porosimetry data [95, 98]. The RPM and other modified and simplified versions, have been fitted to experimental data of CaO conversion by other researchers [98-101], a summary of the kinetics parameters is presented in Table 2.4.

The premises of the RPM seem to represent well the physical situation of the carbonation of CaO, however, from the modelling standpoint, its implementation seems rather complex. The mathematical structure of this model is a challenge itself due to the non-linearity imposed by the use of logarithms and fractional

powers, this is a barrier to its implementation as this model is to be coupled with partial differential equations (PDE). Moreover, the piecewise formulation is difficult to implement, primarily because there is not a clear threshold where the kinetic regime ends and the diffusion controlled regime starts. In addition, the large set of parameters needed to solve the model is not always available for the specific materials to be simulated, thus, the application of this model would carry and propagate errors from the use of published parameters that do not match those of the specific material being simulated.

A simpler category of models which are the second most used in recent publications, are based on the grain model originally proposed by Szekely [102]. The grain model considers the pellet as a collection of spherical grains of uniform size which react progressively from the outside toward the centre of the particle [102, 103]. Unlike the random pore model, this type of models does not consider the structural changings of the particle explicitly, instead, a decreasing diffusion model is typically used to account for the sintering of materials and the structural changes due to the progress of the reaction.

Sun et al. [96] researched the intrinsic kinetics of the carbonation of calcium oxide at atmospheric and pressurised conditions and correlated their experimental data to a grain model. They reported a first order dependence of the reaction rate with the partial pressure of CO_2 (p_{CO_2}) when the pressure difference with respect to the equilibrium pressure of the CO_2 ($p_{CO_{2,eq}}$) was lower than 0.1 bar, at the relevant operating temperature. At higher pressure differences, the experimental conversion of the CaO-adsorbent (X_{CaO}) showed no dependence upon the partial pressure of CO_2. The conversion model is then formulated as a piecewise expression as:

$$\frac{dX_{CaO}}{dt(1-X_{CaO})} = k_{Carb} S_{g,f} M_{CaO} \left(p_{CO_2} - p_{CO_{2,eq}}\right) \text{ if } \left(p_{CO_2} - p_{CO_{2,eq}}\right) < 0.1bar \qquad \textbf{(2.46)}$$

$$\frac{dX_{CaO}}{dt(1-X_{CaO})} = k_{Carb} S_{g,f} M_{CaO} \text{ if } \left(p_{CO_2} - p_{CO_{2,eq}}\right) > 0.1bar \qquad \textbf{(2.47)}$$

The kinetic model represented in equations (2.46) and (2.47) relates the CaO-adsorbent conversion (X_{CaO}) to the partial pressure of CO_2 (p_{CO_2}) and the equilibrium pressure of CO_2 ($p_{CO_{2,eq}}$). Additional parameters in this model are the adsorbent surface area ($S_{g,f}$) and the molecular weight of calcium oxide (M_{CaO}). This model is simpler than the RPM presented in Equations (2.43) and (2.44), however, it is strictly only applicable at the early stages of the process. Nevertheless, various researchers have applied this model to analyse their experimental data [42, 104, 105], see Table 2.4 for information regarding the kinetic parameters.

Stendardo and Foscolo [106] developed a single grain model that accounts for the kinetic and the product layer diffusion regimes. The development considered a first order reaction with respect to the concentration of CO_2, regardless of the pressure in the system, the model is as follows:

$$\frac{dX_{CaO}}{dt} = \frac{\sigma_{0,CaO} k_s (1 - X_{CaO})^{2/3} \left(C_{CO_2} - C_{CO_2,eq}\right)}{1 + \frac{N_{Ca} k_s}{2D_{PL}} \delta_{CaO} \sqrt[3]{1 - X_{CaO}} \left(1 - \sqrt[3]{\frac{1 - X_{CaO}}{1 - X_{CaO} + X_{CaO} Z}}\right)} \quad \textbf{(2.48)}$$

where $\sigma_{0,CaO}$ is the initial grain surface area per unit of particle volume, k_s is the intrinsic kinetic constant, N_{Ca} are the moles of calcium per unit of volume of adsorbent, D_{PL} is the product layer diffusivity of CO_2, Z is the ratio of the molar volume of $CaCO_3$ to the molar volume of CaO and δ_{CaO} is the average diameter of the CaO grains.

Unlike the model by Sun et al. [96], the model presented in Equation (2.48) covers the whole range of conversion of the adsorbent; note that at very low conversion values (i.e. the process is kinetically controlled), the denominator approaches the limiting value of 1, yielding a simpler equation similar to Equation (2.46) for the kinetic regime. When X_{CaO} increases, the product layer diffusion controls the process; at this point, the particle has undergone a reduction of porosity and pore size due to the formation of a less dense product layer. Equation (2.48) accounts for this changes through the parameter D_{PL} which expresses the diffusion decrease as a function of the initial diffusion and the adsorbent conversion as:

$$D_{PL} = D_{PL,0} e^{(-a X_{CaO}{}^b)} \quad \textbf{(2.49)}$$

Where $D_{PL,0}$ is the initial solid diffusion of CO_2, a and b are fitting parameters.

Non-structural models or empirical models have been also proposed to correlate the experimental data of the carbonation reaction. Lee [107] proposed an apparent kinetic model and provided kinetic constants and activation energies from the correlation of the experimental data from Bhatia and Perlmutter [95] and Gupta and Fan [108] . Fernandez et al. [6] reported the application to the modelling of SE-SMR of an empirical equation developed by Rodriguez et al. [109] from the interpretation of pilot plant data in a fluidised reactor; although this expression was not developed from a sound theoretical background, however, it was used in a previous investigation by Abbas et al. [68] of this research group at the University of Leeds; this empirical expression is given as:

$$\frac{dX_{CaO}}{dt} = k_{Carb} \left(X_{CaO,max} - X_{CaO}\right) \left(x_{CO_2} - x_{CO_2,eq}\right) \quad \textbf{(2.50)}$$

Table 2.4 summarises the experimental conditions and the kinetic parameters estimated by the various investigations reported above. All these investigations were conducted in the range of temperature of interest for the application of the calcium looping in the SE-CLSR process. Very different order of magnitude of the kinetic constant is observed among all the reported values, which is presumably associated to the different functional form of the rate of conversion proposed in each model. With regards to the activation energy, Bhatia and Perlmutter [95] reported a negligible dependence of this parameter with the temperature, this approach was used too by Stendardo et al. [106] along with their grain model to represent the conversion data of the carbonation of limestone. In those investigations in which a dependence of the kinetic constant with the temperature was founded, similar values in the range of 20 to 30 kJ mol^{-1} are reported, with the exception of the investigation by Jiang et al. [101] who reported a higher value, closer to those obtained for the diffusion controlled stage. The differences in the values can relate to the different experimental conditions used to carry out the experiments.

2.6.2.2 Calcium carbonate calcination

The thermal decomposition of $CaCO_3$ has been widely studied due to its importance in flue gas desulphurisation, hydration of cement and, recently, in the application to calcium looping processes for the capture of CO_2. Table 2.5 summarises several investigations carried out along with the relevant experimental conditions and the estimated kinetic parameters.

The mechanism of this reaction has been considered to proceed as a sharp reacting front moving from the surface of the pellet towards the centre of the particle, encompassing the following rate processes: 1) the heat transfer from the bulk gas to the reaction interphase, 2) the decomposition reaction at the interphase and 3) the mass transfer of CO_2 from the reaction interphase through the product layer, 3) the chemical reaction [110, 111]. However, no general consensus seems to have been reached regarding the reaction the mechanism and a variety of models have been proposed to represent the experimental data [112, 113].

Borgwardt [111] observed that the reaction rate of the decomposition of lime is linearly dependent upon the Brunauer-Emmett-Teller (BTE) area of the sample, and that the diffusion of gas from the reacting interphase towards the gas bulk has no effect for small particles; thus, he proposed an homogeneous model for the conversion of $CaCO_3$ as:

$$\frac{dX_{CaCO_3}}{dt} = k_{Calc} S_{g,c} M_{CaCO_3} \left(1 - X_{CaCO_3}\right) \quad \textbf{(2.51)}$$

Where X_{CaCO_3} represents the fractional conversion of $CaCO_3$, k_{Calc} is the kinetic rate constant of calcination, $S_{g,c}$ is the initial surface area of the carbonated adsorbent, and M_{CaCO_3} is the molecular weight of $CaCO_3$.

Rao et al. [114] determined the kinetic parameters of the decomposition of calcium carbonate from isothermal and non-isothermal experiments based on a grain model and a volume contracting model, respectively. Murthy et al. [115] followed a similar approach but accounted for the thermal intra-conduction effects in the derivation of their set of kinetic parameters. Both investigations relied on a kinetic rate expression of the type:

$$\frac{dX_{CaCO_3}}{dt} = \frac{3k_{Calc}}{\rho_{m,CaCO_3} r_{g,CaCO_3}} \left(1 - X_{CaCO_3}\right)^{2/3} \left(1 - \frac{C_{CO_2}}{C_{CO_2,eq}}\right)^n \quad \textbf{(2.52)}$$

Where $\rho_{m,CaCO_3}$ is the molar density of the carbonated material, $r_{g,CaCO_3}$ is the $CaCO_3$ grain radius, and C_{CO_2} and $C_{CO_2,eq}$ are the bulk and equilibrium CO_2 concentrations.

The effect of carbon dioxide concentration on the kinetics of $CaCO_3$ decomposition is accounted for on the third factor of Equation (2.52). In the analysis of isothermal data Rao et al. [114] found a second order dependence of the kinetics with the concentration of carbon dioxide, i.e. $n = 2$, for temperatures above 1050 K; whereas for lower temperatures the data was better fitted with a value of $n = 1.5$. Murthy et al. [115] on the other hand, proposed a second order dependence.

Escardino et al. [116] studied the effect of the atmosphere over the calcination of several samples of large particles of $CaCO_3$ and applied a grain model accounting for both the kinetic and the diffusional regimes. The model is:

$$\frac{dX_{CaCO_3}}{dt} = \frac{1}{\rho_{m,CaCO_3}} \frac{C_{CO_2,eq} - bC_{CO_2}}{\dfrac{C_{CO_2,eq}}{k_{Calc} S_{g,v} \left(1 - X_{CaCO_3}\right)^{1/3}} + \dfrac{r_p^2 X_{CaCO_3}}{3D_e}} \quad \textbf{(2.53)}$$

In Equation (2.53), the second term in the numerator banishes when there is no presence of CO_2 in the calcinating atmosphere. Otherwise, the effect of the bulk concentration of CO_2 is expressed by the product bC_{CO_2}, where b is regarded as an "equilibrium constant" between the solid surface and the reaction interphase concentrations. In addition, $S_{g,v}$ represents the volumetric BET surface area, and D_e the effective diffusivity which is a fitting parameter of the model.

Table 2.4 Summary of kinetic parameters of CaO carbonation.

Source	Bhatia and Perlmutter [95]	Grasa et al. [98]	Zhou et al. [99]	Nouri et al. [100]	Jiang et al. [101]	Sun et al. [96]	Stendardo and Foscolo [106]	Rodriguez et al. [109]
Adsorbent material	Limestone	Limestone	CaO/ $Ca_9Al_6O_{18}$	CaO	CaO/Al_2O_3	Limestone	Dolomite	-
CaO content (w%)	>97%	-	80%	>99%	-	53.7%		-
Experimental conditions								
Technique	TGA	TGA	TGA	TGA	TGA	TGA/PTGA	TGA	FBR
Sample size (mg)	<1.3	2	10	-	25	4 / 8-11	2	-
Particle size (μm)	81–137	50–75	50–75	-	-	38–45	150–180	< 350
Temp. (K)	823–1023	823–1023	773–973	923–973	823–923	823–1123	823– 1023	-
Press. (bar)	1	1	1	1	1	1/8	1	-
Atmosphere	CO_2-N_2	CO_2-O_2/Air	CO_2-N_2	CO_2-N_2	CO_2	CO_2-He/ CO_2	CO_2	-
Model type	Random Pore	Random Pore	Random Pore	Random Pore	Random Pore	Grain Model	Grain Model	Empirical
Carbonation activation energy (kJ mol^{-1})								
$E_{A,Carb}$ (kinetic control)	0.0	20.3	28.4	29.9	96.0	29.0	0.0	0.0
$E_{A,Carb}$ (product layer control)	88.9 (T<515°C) 179.2 (T>515°C)	163	88.7	-	-	-	-	-
Carbonation pre-exponential factor[1]								
$k_{0,Carb}$ (kinetic control)	5.95×10^{-10}	5.44×10^{-9}	5.66×10^{-9}	2.75×10^{-8}	[2] 1.58×10^{4}	[3] (a)1.67×10^{-2} (b)1.67×10^{-3}	5.95×10^{-10}	0.35
$k_{0,Carb}$ (product layer control)	-	3.87×10^{-6}	1.46×10^{-9}	-	-	-	-	-

[1] The units of the kinetic pre-exponential factor are ($m^4 mol^{-1} s^{-1}$) for all the values of the Random Pore model and the Grain Model of Stendardo and Foscolo, and ($m\ s^{-1}$) for the Empirical model. For the diffusion pre-exponential factor the units are ($m^2 s^{-1}$).

[2] The units of this parameter are not available in the original source.

[3] This grain model is a piecewise expression. Value (a) applies to $P_{CO2} - P_{CO2,eq} < 0.1$ bar and its units are (mol $m^{-2} s^{-1} bar^{-1}$); value (b) applies to $P_{CO2} - P_{CO2,eq} > 0.1$ bar and its units are (mol $m^{-2} s^{-1}$).

Martinez et al. [113] proposed a uniform conversion model to the analysis of the calcination of partially carbonated particles as follows:

$$\frac{dX_{CaCO_3}}{dt} = k_{Calc}\left(1 - X_{CaCO_3}\right)^{2/3}\left(C_{CO_2,eq} - C_{CO_2}\right) \quad \textbf{(2.54)}$$

Other investigations [91, 92] have applied isoconversional methods to study the kinetics of calcination of calcium carbonate, however, the authors have not provided the specifics of the functional expression of the mechanism utilised to fit the experimental data and therefore will not be considered in this thesis.

As shown in Table 2.5 the experimental conditions utilised to study the kinetics of the decomposition of $CaCO_3$ were very different, primarily with respect to the particle size and sweep gases utilised in the investigations. Nevertheless, the reported values of activation energy are of the same order of magnitude with the exception of one of the samples analysed by Martinez et al. [113]. With regards to the pre-exponential factor, the values of Escardino et al. [116] and Martinez et al. [113] are of similar order, but differ considerably from the other investigations. Murthy et al did not provide a value of the pre-exponential factor and will not be considered in this analysis.

2.6.2.3 Nickel oxide reduction and nickel oxidation

The reduction of nickel oxide and the oxidation of nickel have been investigated in the context of different chemical looping applications, primarily chemical looping combustion, hence, the majority of the reports on this subject look at oxygen carriers with a high content of active material.

Abad et al. [117] and Zafar et al. [118] investigated the reactivity of OTM samples loaded with 40 wt.% and 60 wt.% of NiO for Chemical-Looping Combustion applications during cycles of reduction and oxidation. Both investigations proposed a shrinking core model with kinetic control as follows:

$$\frac{dX_j}{dt} = \frac{3b_i k_i C_i^n}{\rho_{m,j} r_{g,j}}\left(1 - X_j\right)^{2/3} \quad \textbf{(2.55)}$$

Where X_j represents the conversion of Nickel or Nickel Oxide, b_i is the stoichiometric coefficient of the metallic specie according to the relevant reaction of reduction or oxidation, $\rho_{m,j}$ and $r_{g,j}$ are model parameters representing the molar density of the active material in the pellet and the grain radius, C_i is the molar concentration of the relevant gas during the reduction/oxidation reactions, and n is the reaction order.

Iliuta et al. [119] researched the kinetics of reduction of a 15 wt.% NiO OTM in a fixed bed reactor with CH_4, H_2 and CO. They found that the volumetric particle

model fitted the experimental data accurately and proposed the following model representing the conversion of nickel oxide:

$$\frac{dX_{NiO}}{dt} = \frac{S_{g,f}(1-X_{NiO})}{C_{0,NiO}}\left[\left(2k_{CH_4c} + k_{CH_4p}\right)C_{CH_4}w_{NiO}w_{Ni} + \left(k_{CO}C_{CO} + k_{H_2}C_{H_2}\right)w_{NiO}\right] \quad \textbf{(2.56)}$$

Table 2.5 Summary of recent investigations of the kinetics of calcination of $CaCO_3$.

Source	Borgwardt [111]	Rao et al. [120]	Murthy et al. [115]	Escardino et al. [116]	Martinez et al. [113]	Fernandez et al. [121]
Adsorbent	Limestone	Comm. calcite	Comm. calcite	Dolomite	Limestone	Limestone
$CaCO_3$ content (wt.%)	95	>98.5	>98.5	99.4	>93.8	37.1–53.2
Experimental conditions						
Technique	Differential Reactor	Thermo-balance	Furnace	TGA	TGA	Drop tube reactor
Sample size (mg)	-	-	-	2	2	
Particle size (μm)	1–90	440–860	8950–17000	450–3600	75–800	<50
Temp. (K)	789–1273	943–1013	1023–1133	975–1216	1093–1183	1063–1273
Press. (bar)	Atm.	Atm.	Atm.	Atm.	Atm.	Atm.
Atmosphere	N_2	N_2	-	CO_2-Air/Air	CO_2-N_2	
Model type	Uniform conversion model	Grain model	Grain model	Grain model	Uniform conversion model	Uniform conversion model
Calcination activation energy (kJ mol^{-1})						
$E_{A,Calc}$	205.0	192.0	175.7	139.0	91.7/ 112.4	195
Calcination pre-exponential factor[1]						
$k_{0,Calc}$	4.11 x 10^7	2.23 x 10^6	-	3.75 x 10^2	[2]2.52 x 10^2/ 2.06 x 10^3	1.6 x 10^6 – 11.9 x 10^6

Where $k_{CH_{4,c}}$ is the kinetic constant of the reduction by the unmixed combustion mechanism of reaction (2.12), $k_{CH_{4,p}}$ is the kinetic constant of the reduction with methane by the unmixed partial oxidation mechanism of reaction (2.13), k_{CO} and k_{H_2} are the kinetic constants of reduction with CO and H_2, and w_{NiO}, w_{Ni} represent the mass fraction of nickel oxide and nickel in kilogram of active material per kilogram of carrier. In addition, $S_{g,f}$ is the B.E.T. surface area of the oxygen carrier and $C_{0,NiO}$ is the initial molar concentration of NiO. The fractions of NiO and Ni are calculated from the following balances:

$$\frac{dw_{NiO}}{dt} = -S_{g,f}M_{NiO}(1-X_{NiO})\left[\left(2k_{CH_4c} + k_{CH_4p}\right)C_{CH_4}w_{NiO}w_{Ni} + \left(k_{CO}C_{CO} + k_{H_2}C_{H_2}\right)w_{NiO}\right] \quad \textbf{(2.57)}$$

[1] The units for this parameter are (mol $m^{-2}s^{-1}$) except where indicated.
[2] The units for this parameter are ($m^3mol^{-1}s^{-1}$).

$$\frac{dw_{Ni}}{dt} = S_{g,f} M_{Ni}(1 - X_{NiO})\left[\left(2k_{CH_4 c} + k_{CH_4 p}\right) C_{CH_4} w_{NiO} w_{Ni} + \left(k_{CO} C_{CO} + k_{H_2} C_{H_2}\right) w_{NiO}\right] \quad \textbf{(2.58)}$$

Zhou et al. [93] conducted a comprehensive theoretical and experimental investigation to determine the most suitable kinetic models of nickel oxide reduction with H_2 and nickel oxidation with air, out of twenty-two expressions of a range of kinetic mechanisms including reaction order, geometrical contraction, diffusion, nucleation and random pore growth. Their investigation concluded that the reduction of nickel oxide is well described by the nucleation and nuclei growth models, whereas the oxidation of nickel is better described by the contracting volume model. However, the researchers did not provide details of the kinetic parameters.

Medrano et al. [57] studied the reactivity of a commercial steam reforming catalyst with a 18 wt.% NiO in low temperature chemical looping applications and observed a loss of reactivity with the increasing conversion of the material and with the decreasing operating temperature. They proposed a shrinking core model with chemical and diffusional control to represent their experimental data as:

$$\frac{dX_j}{dt} = \frac{\dfrac{3C_i^n}{b_i r_{g,j} \rho_{m,j}}}{\dfrac{1}{k_i}\left(1 - X_j\right)^{-\frac{2}{3}} + \dfrac{r_{g,j}}{D}\left(1 - X_j\right)^{-\frac{1}{3}} - \dfrac{r_{g,j}}{D}} \quad \textbf{(2.59)}$$

Where all the variable definitions correspond to those previously given for Equation (2.55), with only a new variable D_e, which is the effective diffusion of the gas, and is expressed as:

$$D_e = D_0 e^{\left(-\frac{E_D}{R_g T} - k_x X_j\right)} \quad \textbf{(2.60)}$$

In Equation (2.60) D_0 is the pre-exponential factor for diffusion, E_D is the activation energy for the diffusive component, and k_x is defined as the conversion dependent factor.

Dueso et al. [122] investigated the reactivity of two Ni-based OTM's supported Al_2O_3 with content of NiO of 18 wt.% and 21 wt.%. They observed that the reactivity of the materials was influenced by the interactions between the NiO and the support, and demonstrated experimentally that the conversion of NiO to Ni during any given cycle is related to the fraction of free NiO in the previous cycle. Moreover, they found that the kinetics was initially very fast due to the reaction of the gas with the free NiO, and progressively slower as the gas reacted with the nickel aluminate ($NiAl_2O_4$) formed from the interaction of the active metal with the

support. Hence, they proposed a piecewise model to represent each stage of the reduction process, comprising an empirical model to represent the reduction of free NiO and a grain model to represent the reduction of the $NiAl_2O_4$. The models are for the reduction of free NiO:

$$\frac{dX_i}{dt} = k_i f_{NiO}^{-1/3} C_i^n \quad \textbf{(2.61)}$$

And for the reduction of $NiAl_2O_4$:

$$\frac{dX_j}{dt} = \frac{3 b_i k_i C_i^n}{\rho_{m,NiAl_2O_4} r_{g,NiAl_2O_4}} \left(1 - X_j\right)^{2/3} \quad \textbf{(2.62)}$$

Where the only new parameter is the free NiO fraction, f_{NiO}. The nomenclature of the remainder variables and parameters is the same as described in the previous models.

The relevant conditions of the experimental work and the kinetic parameters reported for the aforementioned models are summarised in Table 2.6. From all these studies, only those by research groups of Iliuta et al. [119] and Medrano et al. [57] studied the reduction of OTMs within the relevant range of temperatures for the SE-CLSMR application. Moreover, only the former study provides information of the reduction kinetics with methane, whereas the latter study reported no activity of the OTM with methane when the material was in its fully oxidised state, this fact is considered by Iliuta et al. [119] as in their kinetic expressions of the rate of reaction of CH_4 they included the concentration of Ni to obtain a better fit of the experimental data, implying that the fully oxidised state of the OTM would render a zero rate of disappearance of methane. The kinetic parameters of the nickel reduction with models of Abad et al. [117], Zafar et al. [118] and Dueso et al. [122] were derived at temperature ranges well above the temperature of application of the SE-CLSMR technology and their application might produce suspicious results, therefore they are not considered in this modelling work.

Abbas et al. [68] applied and validated the kinetic models of reduction of Iliuta et al. [119] in the context of a SE-CLSMR packed bed reactor and reported a good agreement with the experimental data. Zhou et al. [123] analysed various kinetic models in CLC applications including those by Iliuta et al. [119] and Abad et al. [117] and concluded that the modified volumetric model was superior than the shrinking core model to represent the experimental data. For these reasons, the model of Iliuta et al. previously applied by Abbas et al. [68] in the modelling of SE-CLSMR reactor will be used in this modelling work.

Regarding the kinetic rate expressions of the oxidation of nickel, the models by Dueso et al., and by Medrano et al. appear to be applicable to represent the regeneration of a steam reforming catalyst, based on the active metal content. Nevertheless, all the oxidation models will be tested in Chapter 6 in the context of the SE-CLSMR reactor model.

Table 2.6 Summary of investigations of the kinetics of reduction and oxidation of Ni-based oxygen carriers.

Source	Abad et al. [117]	Zafar et al. [118]	Iliuta et al. [119]	Dueso et al. [122]	Medrano et al. [57]
Support	Al_2O_3	$MgAl_2O_3$	Al_2O_3	α-Al_2O_3	$CaAl_2O_4$
NiO content (w%)	40.0	50.0	15.0	18.0/21.0	18.0
Experimental conditions					
Technique	-	TGA	Fixed bed	TGA	TGA
Sample size (mg)	-	20	100	30 – 70	100
Particle size (μm)	-	125 – 180	140	100 – 300	200 – 300
Temperature (K)	-	1073 – 1273	873 – 1173	1073 – 1223	773 – 1073
Pressure (bar)	-	Atm.	Atm.	Atm.	Atm.
Reducing gas	CH_4, H_2, CO	CH_4	CH_4, H_2, CO	CH_4, H_2, CO	H_2, CO
Oxidising gas	Air	Air	Air	Air	Air
Model type	Shrinking core	Shrinking core	Volumetric model	Empirical/ Changing grain model	Shrinking core
Reduction activation energy (kJ mol^{-1})					
$E_{A,CH4c}$ (via UC)	78.0	114.0	77.4	5.0	-
$E_{A,CH4p}$ (via UPO)	-	-	23.7	-	-
$E_{A,H2}$	26.0	-	26.4	5.0	30.0
$E_{A,CO}$	25.0	-	26.5	5.0	45.0
Reduction pre-exponential factor[3]					
$k_{0,CH4}$ (via UC)	7.1×10^{-1}	2.75	4.66	0.2	-
$k_{0,CH4}$ (via UPO)	-	-	4.18×10^{-3}	-	-
$k_{0,H2}$	9.3×10^{-3}	-	1.31×10^{-4}	0.15	9.0×10^{-4}
$k_{0,CO}$	5.2×10^{-3}	-	1.1×10^{-4}	0.059	3.5×10^{-3}
Reduction reaction order					
n (CH_4 via UC)	0.8	0.4	-	0.2	-
n (CH_4 via UPO)	-	-	-	-	-
n (H_2)	0.5	-	-	0.4	0.6
n (CO)	0.8	-	-	0.6	0.65
Oxidation activation energy					
$E_{A,Oxi}$ (kJ mol^{-1})	7.0	40.0	-	22.0	7.0
Oxidation pre-exponential factor[4]					
$k_{0,Oxi}$	1.8×10^{-3}	5.4×10^{-3}	-	0.084	1.2×10^{-3}
Oxidation reaction order					
n	0.2	1.0	-	0.7	0.9

[3] The units of the pre-exponential factor are (mol^{1-n} m^{3n-2} s^{-1}) for the models of Abad et al., Zafar et al., and Dueso et al.; (m s^{-1}) for the models of Iliuta et al. and Medrano et al.

[4] Idem.

2.7 Concluding remarks

The SE-CLSMR concept shows clear advantages over the conventional SMR, at least, theoretically. Two system proposals were detected in the literature, on one hand a reactor operating with two coupled loops, using Ni-based and Ca-based materials to carry out the operations during the fuel and air cycles. On the other hand, a system operating with three coupled loops, a Ni-looping, a Ca-looping and a Cu-looping. The former seems to be less complicated than the latter, as it requires less steps to complete one cycle of operation of the reactor, however, the main drawback of this configuration is that during the air cycle, the CO_2 to be sequestrated or utilised is diluted with air, if pure oxygen is used to re-oxidise the nickel, then a pure stream of CO_2 can be produced, albeit with a higher CAPEX and OPEX due to the need of the air separation unit. The latter design was proposed to tackle the problem of the dilution of the CO_2 stream. This system is indeed more complicated than the former as various operational conditions need to be meet to produce an undiluted CO_2 stream, and the need of three cycles to operate the system. Moreover, the addition of a third material to the packed bed implies that part of the heat generated by the adsorption of CO_2 will be squandered to heat up the Cu-based material which will act as an inert during the fuel reactor operation. Thus, the system that is modelled in this work corresponds to the design coupling the Ni-looping with the Ca-looping.

The SE-CLSMR concepts, particularly the processes happening during the fuel reactor stage, have been analysed in packed and fluidised bed reactors (PBR and FBR). The comparison of both technologies suggest that the FBRs, particularly the bubbling fluidised reactor, are a better choice to achieve a high integration of the exothermic and the endothermic processes in the system, and increase the likelihood of an autothermal operation. In addition, the smaller pellet sizes required to achieve the fluidisation offer the advantage of reducing the intra-particle transport resistances leading to a better utilisation of the catalyst. However, the drawbacks of this technology may restrict their application due to the various operational, health and environmental risks associated with them. Conversely, packed bed reactors avoid or at the very least, reduce the likelihood of, presenting the noxious impact to the environment, and to the health of plant operators due to toxic material handling and inhalation, albeit with the limitation of a very poor heat transfer, which is critical to deploy an autothermal reactor. Nevertheless, current conventional steam reformers are a packed bed-based technology, and therefore, it makes sense to conceptualise a substitute packed bed technology to avoid a disruptive change of technology in the plant and ease a possible integration of the new reactor by retrofitting.

The modelling of the SE-SMR in packed bed reactors has been widely reported. Less reports have been produced for the modelling of the SE-CLSMR process in a packed bed reactor, which has been reported by two researching groups, one in Spain, and one in the UK. The concept reported by the Spanish group in [6, 50] entails a system with three loops, a Ni-looping, a Cu-looping and a Ca-looping. The model presented by this group is a pseudo-homogeneous model which means that a single local concentration and temperature was assumed for the four distinguishable phases of the system. On the other hand, the model developed in [68] by the UK research group encompasses a reactor combining a Ni-looping and a Ca-looping as the original concept suggested. The modelling work by this group went a step further and considered a pseudo-heterogeneous reactor model, considering intimate contact between the catalyst and the adsorbent, therefore a single local temperature and concentration profile for both materials.

However, the approaches followed in these models oversimplify some aspects of the physics of the problem, particularly the heat transfer between the adsorbent and the catalyst, and the flow field, hence the validity of their predictions might be questionable. The assumption of homogeneity in the packed bed may be unrealistic for a number of reasons, firstly, a homogeneous packed bed is achieved if the heat transfer coefficient is infinite; in packed beds, the main resistance to heat transfer is in the film surrounding the particles, therefore, it can be expected that the temperature varies from one phase to another. Secondly, the structure of the packed bed affects the hydrodynamics of the reactor, and this might cause flow maldistribution, e.g. channelling; since the gas is the heat carrier, the abnormalities in the flow distribution can cause a non-uniform heat transport throughout the solid matrix. Thirdly, the heat transfer between the three phases is a complex function of the temperature and concentration profiles, the pellet sizes, their thermal properties and their geometry, and the volumetric fraction of each material in the bed. These variables affect the rate of heat generated in the adsorbent and heat dissipated in the catalyst during the fuel reactor operation, and vice versa during the air reactor operation. Thus a given packed bed with certain bed properties might result in hot and cold spots in the system, which cannot be identified with a model that assumes homogeneity between the phases. Finally, the prediction of the velocity field is important given the nature of the system. The available models considered constant velocity and constant mass flux; both assumptions are poor as the process entails a relevant change of the total bulk mass in the packed bed due to the sorption of at least one of the gas bulk components (CO_2). This results in an important axial variation

of the density of the fluid and its superficial velocity, affecting the convection of other quantities as mentioned above.

For these reasons this work looks at the development of a model that considers all phases separately, and improves the previous work by incorporating a realistic representation of the flow continuity throughout the packed bed. Additionally, the effects of the structural changes of the adsorbent that modify its textural properties (particularly its porosity), its density and heat capacity, are investigated.

The modelling of the SE-CLSR process involves the use of kinetic models for both catalytic and non-catalytic processes. The catalytic process involved are primarily the well-known steam reforming reactions, and are mostly represented by LHHW type models. Other type of kinetic rate expressions are available but are not considered in this work. A few kinetic parameters were gathered and the sensibility of the different models will be checked in **Chapter 6**.

Chapter 3 Thermodynamic analysis of the SE-CLSMR process

3.1 Introduction

In this chapter the results of the thermodynamic analysis of the SE-CLSMR process are presented. The study rendered the maximum attainable output for methane conversion and hydrogen yield in the Fuel Reactor, and the conversion of nickel and calcium carbonate to their respective oxides in the Air Reactor. These hypothetical limits were obtained from the outlet of both reactors which were calculated with a Gibbs Reactor model available in the software Aspen Plus™. The Gibbs Reactor model is a type of reactor that relies on the minimisation of the Gibbs free energy, yielding the reactor outlet compositions without the need of a reaction set.

Several studies dealing with the thermodynamic analysis of the SE-CLSR process are available in the open literature, however, the majority of these studies have assumed isothermal operation of both, the fuel and the air reactors [51, 56, 60, 67]. The validity of this assumption is questionable as it ignores the thermal effects of the various chemical reactions and can lead to erroneous expectations regarding the potential of the reactor concept. Therefore, an analysis considering adiabatic reactors is developed to assess the effect of temperature, pressure, S/C ratio and NiO/CaO ratio on the Fuel Reactor performance, and the effect of the air temperature, pressure and NiO/CaO ratio on the Air Reactor performance.

3.2 Methodology

The equilibrium simulation is conducted with the aid of the process simulator Aspen Plus™, assuming the following premises:

1. The fuel gas and the air are available at the desired operating pressure of the fuel and air reactors and temperature of 298 K.
2. Water steam is available at the desired operating pressure and the corresponding temperature of saturation.
3. There is availability of hot and cold utilities for the conditioning of the process streams.
4. The pressure drop throughout the reactor is assumed to be negligible.
5. The pressure drop in heat exchangers is set to 0.69 bar unless otherwise specified.
6. The solid components are completely separated from the gas phase in the cyclones.

The simulation flowsheet utilised in this study is shown in Figure 3.1. The process flow starts with the mixing of the fuel gas stream with steam; two samples of gas with different content of C_{2+} hydrocarbons have been considered and their compositions are provided in Table 3.1. After mixing, the temperature of the gaseous mixture is increased up to 723 K, this temperature is selected as it falls within the typical operating temperature range of pre-reformers in steam reforming plants [21]. The thermal duty required to increase the temperature of the pre-reformer feedstock is calculated by means of the Heat Exchanger module labelled PRPH. The preheated feedstock is fed to the pre-reformer PR, which is modelled as an adiabatic Gibbs Reactor module. The product of the PR reactor is obtained at a lower temperature due to the endothermic reforming of the heavier hydrocarbons contained in the feedstock (mostly ethane and propane), hence the heat exchanger unit (FRPH) located downstream of the PR reactor which is used to condition the syngas temperature to the desired temperature of the Fuel Reactor (FR); the operating conditions of the FR reactor are varied in the study giving place to various simulation cases and the operating windows analysed are summarised in Table 3.2. Prior to the heating up of the feedstock, the gas stream is mixed with a stream containing a mixture of CaO and NiO; the latter represents the materials that would be present in the packed bed working as adsorbent and catalyst/OTM, and their thermochemical properties are retrieved from the conventional solid database available in Aspen Plus^{TM}. The stream leaving the FRPH exchanger is then fed to the Fuel Reactor (FR) which is modelled as an adiabatic Gibbs reactor. The reactor product is split into a gas stream containing mainly H_2, H_2O and unreacted CH_4, and a stream containing Ni and $CaCO_3$, this separation is modelled in a cyclone module (S1) which is set-up to obtain complete separation of the phases. The thermal duties required for the conditioning of the product streams of the cyclone are calculated in the heat exchangers H2C and PBH. The H2C exchanger functions as a cooler of the hot gas product and is set to cool the stream down to 298 K. The PBH exchanger is aimed to calculate the duty required to increase the temperature of the hypothetical bed to the temperature level required for the bed regeneration.

The regeneration of the catalyst/OTM and the adsorbent is simulated in the Air Reactor module (AR) which is modelled as an adiabatic Gibbs reactor. The simulation inputs to the AR reactor are a stream of pre-heated air and the stream containing Ni and $CaCO_3$ previously heated up in the PBH exchanger. Prior to enter the AR reactor, the temperature of stream of air is adjusted to the AR reactor temperature in the heat exchanger module ARPH. The AR reactor temperature is dictated by the reactor pressure as this parameter affects the thermodynamic equilibrium of the decomposition of $CaCO_3$, various conditions were simulated as

summarised in Table 3.2. The product stream of the Air Reactor is split using a cyclone unit (S2) that considered a complete separation of the gas and the solid phases; the waste gases containing a mixture of N_2, O_2 and CO_2 are sent to a waste gas cooler (WGC) where their temperature is adjusted for further handling and conditioning. The regenerated materials are cooled down in the PBC unit to the Fuel Reactor temperature to account in the balance for the heat stored in the solids after the Air Reactor cycle that can be used as a source of energy for future heat integration studies.

Table 3.1 Composition of the samples of gas fed utilised in the equilibrium calculations.

Component	UG1 (mole%)	UG2 (mole%)
CH_4	81.5	85.1
C_2H_6	2.8	11.3
C_3H_8	0.4	2.9
n-C_4H_{10}	0.1	0.0
n-C_5H_{12}	0.1	0.0
CO_2	1.0	0.4
N_2	14.1	0.3
HHV (MJ m^{-3})	33.3	42.4

The base case simulation considered the Fuel Reactor to operate at a temperature of 923 K, pressure of 1 bar, S/C ratio of 3, CaO/C ratio of 1 and NiO/CaO ratio 0.5. For the Air Reactor the inlet temperatures of air and the solid stream were set-up at 1123 K, reactor pressure of 1 bar and air-to-Ni ratio of 2.38. Further simulation cases were run considering the operating parameters specified in Table 3.2.

The Fuel Reactor performance was assessed by means of the methane conversion, the hydrogen yield and the hydrogen purity. Methane conversion is defined as the moles of reacted methane divided by the moles of methane fed to the reformer as:

$$X_{CH_4} = \left(\frac{n^{in}_{C_{CH_4}} - n^{out}_{C_{CH_4}}}{n^{in}_{C_{CH_4}}} \right) \times 100 \qquad \textbf{(3.1)}$$

where X_{CH_4} is the molar conversion of CH_4, $n^{in}_{C_{CH_4}}$ is the number of moles of CH_4 fed to the Fuel Reactor and $n^{out}_{C_{CH_4}}$ is the number of moles of CH_4 at the Fuel Reactor outlet; this definition is valid for this analysis since the thermodynamic study is conducted at steady state conditions. Moreover, the type of reactor

utilised to represent the Fuel Reactor is a Gibbs Reactor and thus, no profiles within the reactor are available to possibly evaluate an average conversion. However, Equation (3.1) represents a local or point concentration and might not be representative for a dynamic reactor, in such cases one can look at an integral conversion which would be relevant to assess the length of the cycle required to achieve a desired conversion.

Hydrogen purity in dry basis is defined as the number of moles of hydrogen in the product stream divided by the sum of number of moles of relevant species in product stream except water, thus:

$$\boldsymbol{P_{H_2} = \frac{n_{H_2}^{out}}{n_{CH_4}^{out} + n_{H_2}^{out} + n_{CO_2}^{out} + n_{CO}^{out}} \times 100} \quad \textbf{(3.2)}$$

where P_{H_2} is the hydrogen purity in dry basis, $n_{CH_4}^{out}$, $n_{H_2}^{out}$, $n_{CO_2}^{out}$ and n_{CO}^{out} are the molar flowrates of CH_4, H_2, CO_2 and CO in the Fuel Reactor product stream.

Hydrogen yield is defined as the actual moles of hydrogen produced divided by the stoichiometric moles of hydrogen as:

$$Y_{H_2} = \frac{n_{H_2}^{out}}{4n_{CH_4}^{in}} \times 100 \quad \textbf{(3.3)}$$

The performance of the Air Reactor was measured in terms of the regeneration of the materials, i.e. the conversion of Ni to NiO as expressed in Equation (3.4) and the conversion of $CaCO_3$ to CaO as expressed in (3.5).

$$X_{Ni} = \left(\frac{n_{Ni}^{in} - n_{Ni}^{out}}{n_{Ni}^{in}}\right) \times 100 \quad \textbf{(3.4)}$$

$$X_{CaCO_3} = \left(\frac{n_{CaCO_3}^{in} - n_{CaCO_3}^{out}}{n_{CaCO_3}^{in}}\right) \times 100 \quad \textbf{(3.5)}$$

where X_{NiO} is the molar conversion of Ni to NiO , n_{Ni}^{in} is the molar flowrate of Ni fed to the Air Reactor, n_{Ni}^{out} is the molar flowrate of Ni at the Air Reactor outlet, X_{CaCO_3} is the molar conversion of $CaCO_3$ to CaO, $n_{CaCO_3}^{in}$ is the molar flowrate of $CaCO_3$ fed to the Air Reactor and $n_{CaCO_3}^{out}$ is the molar flowrate of $CaCO_3$ at the Air Reactor outlet.

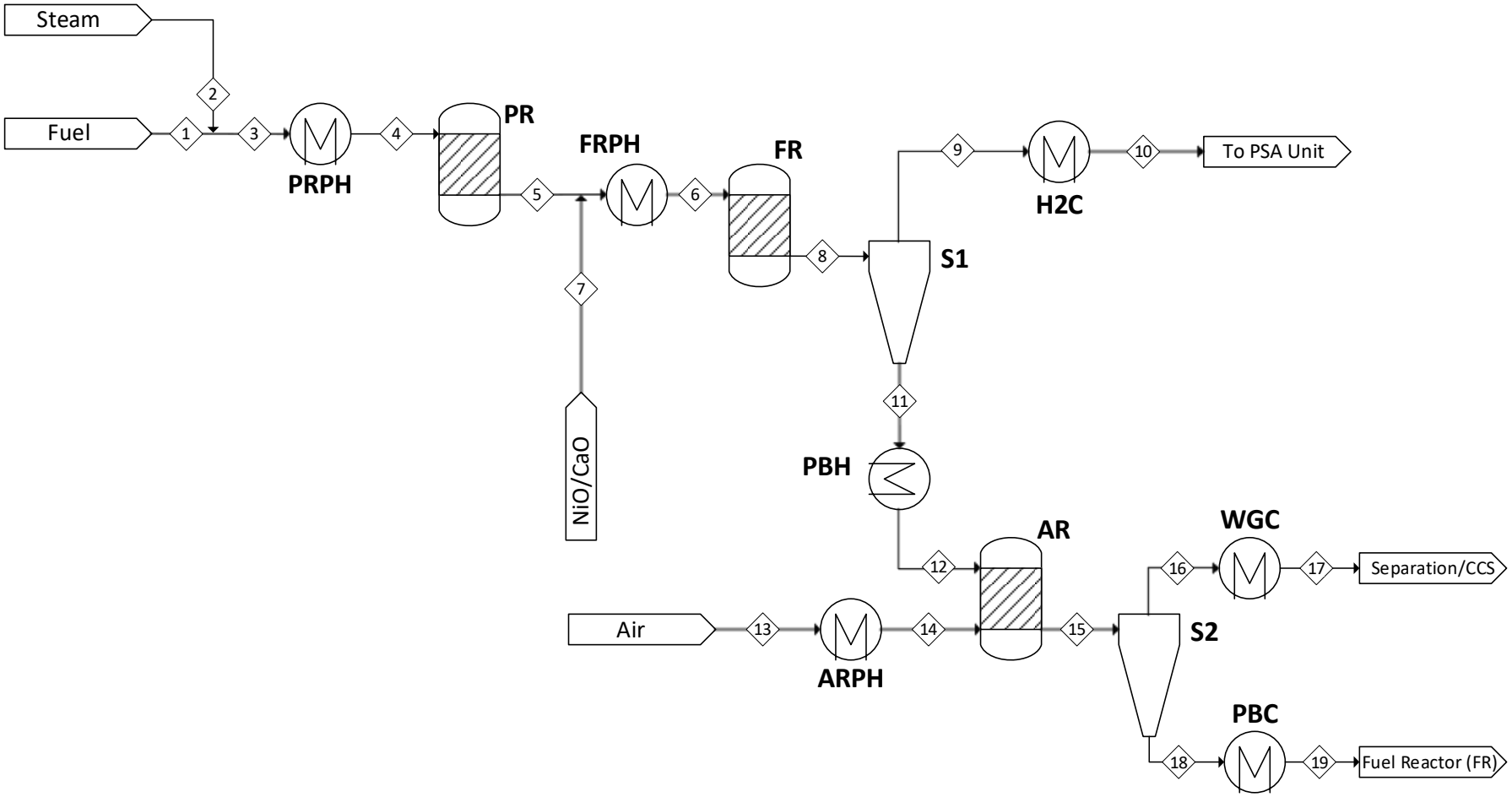

Figure 3.1 Process flow diagram used in the simulation of the Sorption-Enhanced Chemical-Looping Steam Reforming of Natural Gas.

Table 3.2 Description and process specifications of the simulation blocks used in the Aspen Plus flowsheet for the thermodynamic analysis.

Unit	Block ID	Aspen Plus model	Process specifications
Fuel reactor	FR	RGibbs	Calculates the equilibrium compositions of the sorption enhanced steam reforming at the following conditions: pressure = 5–30 bar; temperature = 823–1023 K; S/C ratio = 2–4; NiO/CaO ratio = 0.5, 0.75 and 1.0, and heat duty = 0 kJ s^{-1} (Adiabatic)
Air Reactor	AR	RGibbs	Calculates the equilibrium compositions during the re-oxidation of nickel and calcination of calcium oxide. The operating conditions are: Air/NiO ratio: 1–4; reactor pressure: 1–10bar; air and solid streams inlet temperature: 923–1123 K and heat duty = 0 kJ s^{-1} (Adiabatic)
Pre-reformer	PR	RGibbs	Calculates the equilibrium composition of the pre-reforming stage, operated adiabatically at 5–30 bar.
Pre-reformer heater	PRPH	Heater	Heating up of the feedstock to 723 K at the operating pressure of the pre-reformer.
Fuel Reactor pre-heater	FRPH	Heater	Heating up the syngas produced in the pre-reformer to the Fuel Reactor operating temperature (823–1023K).
Air Rector pre-heater	ARPH	Heater	Heating up the air to the Air Reactor operating temperature (923–1123K) at 1 bar.
Heater to condition the solids to enter the Air Reactor	PBH	Heater	Calculates the utilities required to heat up the solids to the Air Reactor operating temperature (923–1123K).
Cooler to condition the solids to the Fuel reactor temperature	PBC	Heater	Calculates the utilities required to cool down the regenerated materials to the Fuel Reactor operating temperature (823–1023K).
Gas product cooler	H2C	Heater	Calculates the utilities required to cool down the Fuel Reactor gas product to 298K.
Waste gas cooler	WGC	Heater	Calculates the utilities required to cool down the Air Reactor waste gas product to 298K.
Solid separator	S1, S2	Cyclone	Simulates the separation of the gas and solid streams with a split fraction of gas of 100%.

3.3 Results and discussion

3.3.1 Effect of operating temperature and pressure on the Fuel Reactor performance

The advantages of the SE-CLSMR process over the SMR process at various reforming temperatures and pressures is shown in Figure 3.2 and Figure 3.3. Figure 3.2a is a plot of the predicted CH_4 conversion in the SE-CLSMR reactor at various levels of temperature and pressure; similarly, the conversion of CH_4 has been calculated for the conventional SMR and are plotted in Figure 3.2b. A clear trend is shown for both effects, the conversion of CH_4 increases monotonically with the increasing temperature and decreases monotonically with the increasing pressure. This behaviour results from the mixed effect of the chemical equilibrium and the endothermic nature of the reforming process. The complete reaction for both processes (i.e. the SE-CLSMR and the SMR processes) indicates a higher number of molecules in the product, and therefore, as the pressure increases, the equilibrium will move towards the reactants. In addition, due to the endothermicity of the process, an increase in the operating temperature enhances the equilibrium constant, thus shifting the equilibrium towards the products.

It is observed in Figure 3.2a that the SE-CLSMR process renders CH_4 conversions varying in the range 83–96% with the higher conversion attained at the lower pressure as previously mentioned. Conversely, the highest conversion of CH4 achieved in the SMR process would be as high as 90%, operating in the high end of the temperature range analysed. This is clearly a consequence of in-situ adsorption of CO_2. These results are in agreement with those presented by Rydén et al. [56] and more recently, by Antzara et al. [60] and Abbas et al. [68] who conducted studies assuming an isothermal reactor and found similar trends in the ranges of operating temperature and pressure analysed.

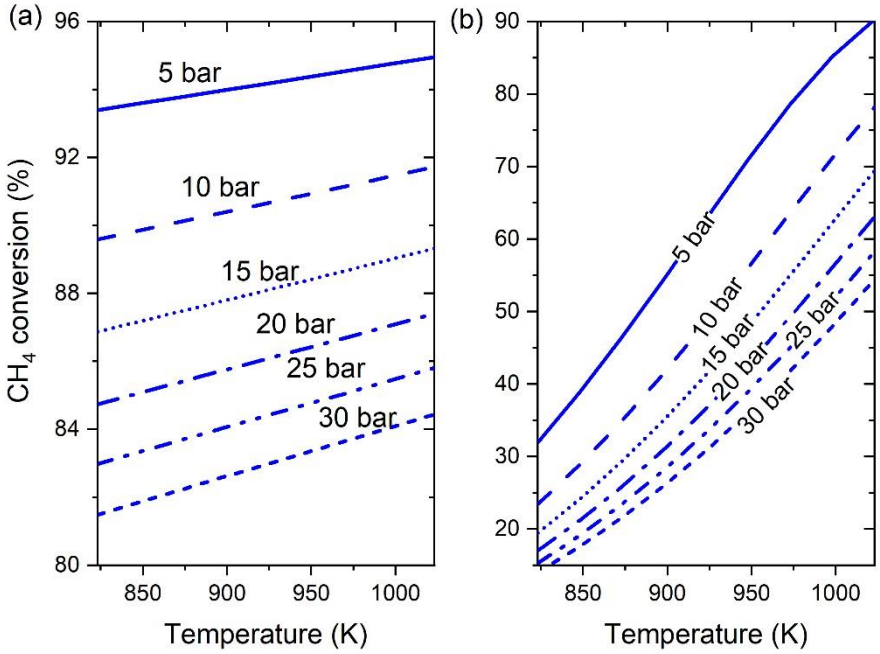

Figure 3.2 (a) CH_4 conversion as function of the reactor temperature and pressure at fixed S/C=3, NiO/CaO=0.5 and CaO/C=1 (b) CH_4 conversion for conventional SMR as function of the reactor temperature and pressure.

The trends of the H_2 yield at various temperature and pressure values are shown in Figure 3.3. Similarly to the CH_4 conversion, the H_2 yield has been plotted for the SE-CLSMR and the SMR processes to illustrate the differences of both processes. Figure 3.3a presents the trends of H_2 yield predicted for the SE-CLSMR reactor. Unlike the CH_4 conversion, the H_2 yield curves exhibit a maximum value in the low to medium pressure range (<10bar), above this pressure, the curves increase monotonically with the increasing temperature. Conversely, the effect of the pressure produces a similar effect on the H_2 yield as that produced on the CH_4 conversion, a higher operating pressure renders a lower H_2 yield.

The effect of the reactor pressure and temperature on the adsorbent conversion is presented in Figure 3.4. Clearly, the adsorbent conversion decreases with the increasing operating pressure. The reason for this behaviour is the shift in the equilibrium of the reforming reactions, a higher pressure will promote the methanation reaction. The effect of the temperature on the adsorbent conversion exhibits a nonmonotonic behaviour, showing a maximum conversion value whose location varies as a function of the operating pressure within the inlet temperature range 873–973K.

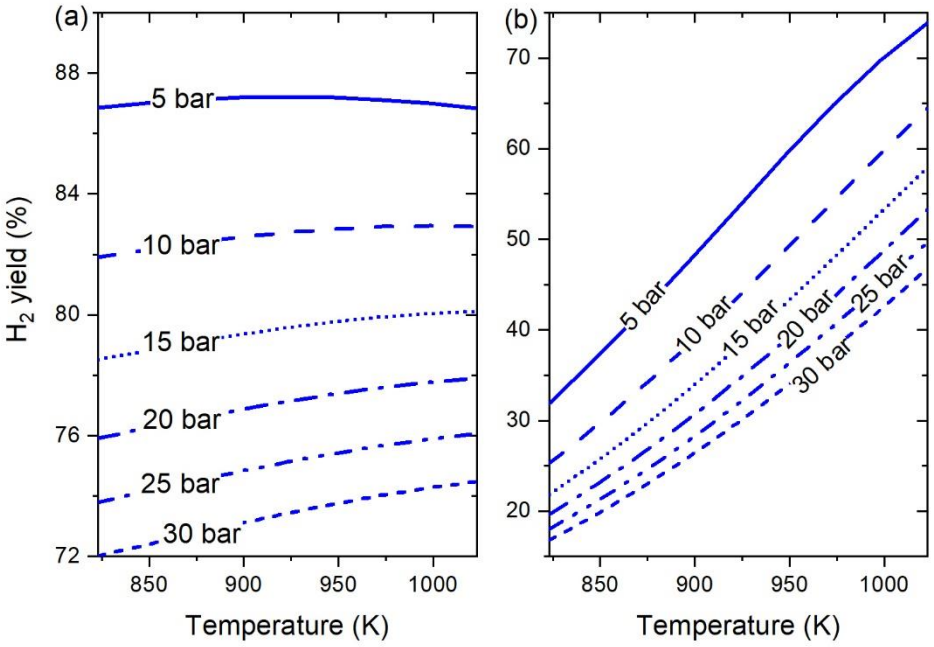

Figure 3.3 (a) H_2 yield as function of the reactor temperature and pressure at fixed S/C=3, NiO/CaO=0.5 and CaO/C=1 (b) H_2 yield for conventional SMR as function of the reactor temperature and pressure.

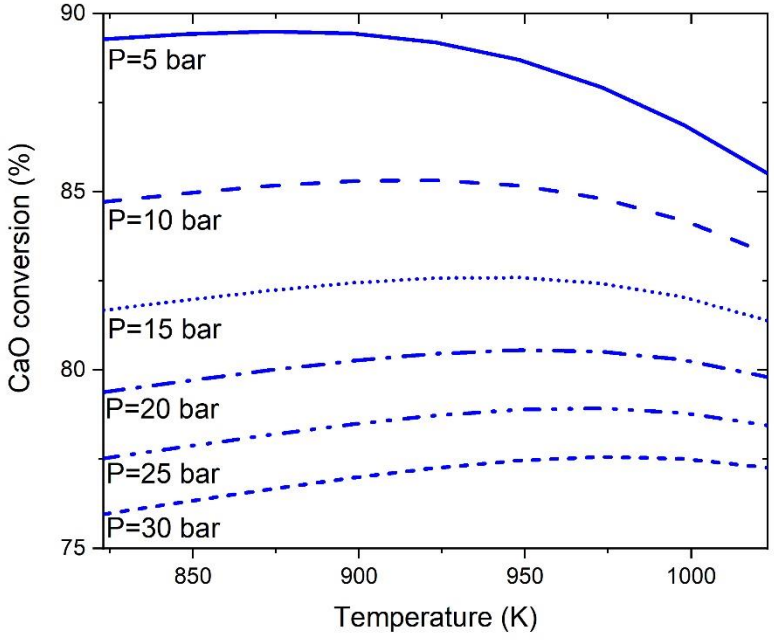

Figure 3.4 Adsorbent conversion as function of the Fuel Reactor temperature and pressure at fixed S/C=3, NiO/CaO=0.5 and CaO/C=1.

3.3.2 Effect of the feedstock on the Fuel Reactor performance

The effect of the composition of the gas fed to the Fuel Reactor was analysed for three operating scenarios including (a) the operation of the Fuel Reactor with a pre-reformed sample of natural gas (sample PUG1), (b) the operation of the Fuel Reactor with a pre-reformed sample of unconventional gas (sample PUG2) and (c) the operation of the Fuel Reactor with a sample of natural gas fed without pre-reforming (sample UG1). For cases (a) and (b), the composition of the stream fed to the Fuel Reactor was determined by simulating the pre-reforming of samples UG1 and UG2 from Table 3.1 at the relevant Fuel Reactor pressure according to the operating conditions listed in Table 3.2, whilst for case (c) the gas composition of sample UG1 provided in Table 3.1 plus the necessary amount of water to keep a S/C ratio of 3 is used directly in the Fuel Reactor simulation block; an example of the composition of the feedstock to the Fuel Reactor is presented in this section are summarised in Table 3.3 considering an operating pressure of 25 bar.

Table 3.3 Fuel Reactor feedstock composition for the operating scenario of 973K and 25 bar.

Component	UG1 (mole%)	PUG1 (mole%)	PUG2 (mole%)
CH_4	18.1	17.8	22.4
C_2H_6	0.6	0.0	0.0
C_3H_8	0.1	0.0	0.0
n-C_4H_{10}	0.0	0.0	0.0
n-C_5H_{12}	0.0	0.0	0.0
H_2	0.0	4.9	5.3
CO	0.0	0.0	0.0
CO_2	0.2	1.7	2.3
N_2	3.1	3.0	0.1
H_2O	77.8	72.6	69.9
HHV[1] (MJ m^{-3})	33.3	26.5	30.6

The effect of the composition on the CH_4 conversion and the H_2 yield obtained in the Fuel Reactor is presented in Figure 3.5a and Figure 3.5b, respectively. In both cases, the higher values of the performance indicators are observed for the operating case (a), followed by case (b) and the lowest performance is exhibited in case(c). The reason for this behaviour is likely to be the content of H_2, CO and

[1] Values of HHV obtained considering a composition free of water.

CO_2 in the feed, that promote an increase in the temperature of the reactor, thus favouring conversion of the fuel.

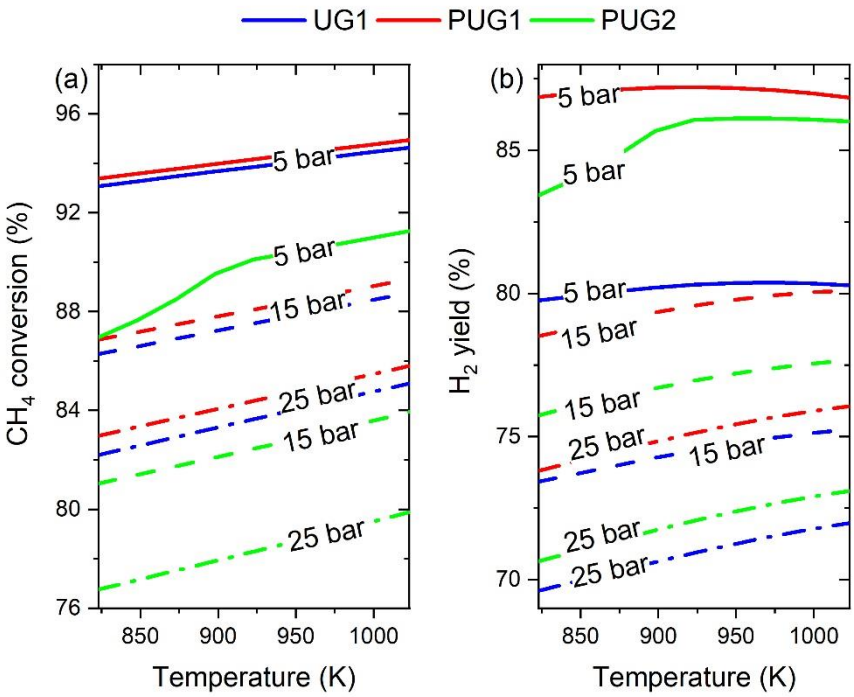

Figure 3.5 (a) CH_4 conversion and (b) H_2 yield in the Fuel Reactor at 5, 15 and 25 bar as a function of the inlet temperature for three different feedstocks.

Figure 3.6 is a plot of the outlet temperature of the gas product as a function of the inlet temperature of the feed gas at 5 bar and 25 bar. In addition the isothermal operating line has been drawn as reference. At 5 bar, the scenarios (a) and (b) will operate exothermally up to 950 K, above this temperature the overall process will be endothermic. Conversely, in the operating scenario (c) i.e. without pre-reforming of natural gas the fuel reactor will operate in an endothermic manner in all the range of temperatures. A similar behaviour is observed at 25 bar, only with a different temperature at which the fuel reactor operation changes from exothermic to endothermic in the operating scenarios (a) with pre-reformed natural gas and (b) with pre-reformed shale gas. It becomes apparent that the presence of H_2, CO and CO_2 in the feed will increase the internal energy of the system due to the reduction reaction of NiO with CO and H_2, the water-gas shift reaction, and to the adsorption of the CO_2. These processes are favoured at lower temperatures due to its exothermic nature, whilst the mechanisms of the reactions of CH_4 are favoured at higher temperatures, thus reducing the temperature of the system.

For the operating scenario without pre-reforming step, the process seems to follow the mechanisms of steam reforming, unmixed partial oxidation and unmixed combustion of methane, all of which are endothermic, thus the

temperature drop observed in Figure 3.6. This result suggests that the integration of the adiabatic pre-reformer step in the process would enhance the operating temperature of the fuel reactor. However, the content of CO_2 in the feed will reduce the adsorbent saturation period and should be considered in the design of a reaction unit.

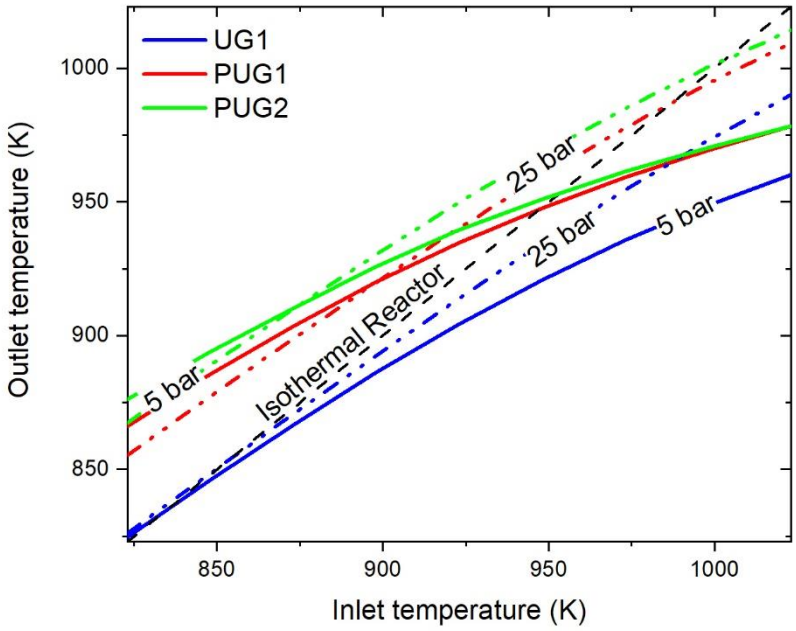

Figure 3.6 Fuel Reactor outlet temperature at 5 and 25 bar as a function of the inlet temperature for three different feedstocks.

3.3.3 Effect of the steam-to-carbon ratio on the Fuel Reactor performance

The effect of the steam-to-carbon ratio on the CH_4 conversion, H_2 yield and H_2 purity in the Fuel Reactor was analysed at 5 bar and 873 K, CaO/C of 1 and S/C varying within the range 2–4, and is illustrated in Figure 3.7. Similar trends as those presented in [68] and [60] were obtained in this assessment. All the performance indicators increase monotonically with the increasing S/C ratio, however, at S/C ratios greater than 3.0 the improvement of the CH_4 conversion, H_2 yield and H_2 purity no longer justifies the extra costs associated to a higher consumption of steam.

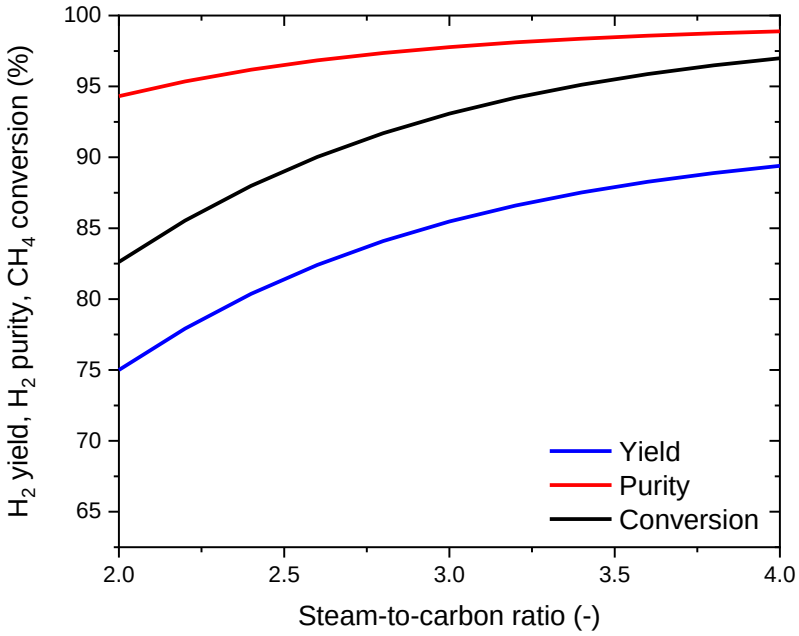

Figure 3.7 H_2 yield, H_2 purity and CH_4 conversion as function of the steam-to-carbon ratio at fixed P=5 bar, T=873.15K, NiO/CaO=0.5 and CaO/C=1.

The selection of the S/C ratio should be a trade between the process efficiency and the process economics, however, care should be taken during the determination of this parameter to avoid falling within the region of carbon formation. The operating conditions required to avoid the carbon deposition region depend on the actual feedstock. As shown before, heavier feedstocks than natural gas, with a higher content of C_{2+} components, e.g. shale gas can be converted in the Fuel Reactor to H_2, however, its processing represent a challenge due to the potential of carbon deposition in the surface of the catalyst/OTM [23, 124]. Carbon deposition can be originated from the decomposition of methane and higher hydrocarbons and from the Boudouard reaction [22], however, the adsorption of CO_2 plays a favourable role in the process, reducing the likelihood of carbon formation. The thermodynamic limit for carbon product was calculated for the Fuel Reactor operating at 5 bar, NiO/CaO molar ratio of 0.5 and CaO/C molar ratio of 1, and is presented in Figure 3.8; for comparison, the equilibrium carbon product limit for the conventional steam methane reforming is shown. As observed in Figure 3.8 operating at S/C>1 ensures an operation away from the carbon product limit for both the SMR and SE-CLSMR processes. The adsorption of CO_2 in the process displaces of the thermodynamic threshold of the SE-CLSMR process to lower steam-to-carbon ratios than those for the conventional SMR. This is consistent with the review presented in **Chapter 2** regarding carbon product limits and with the results of other investigations such as [10].

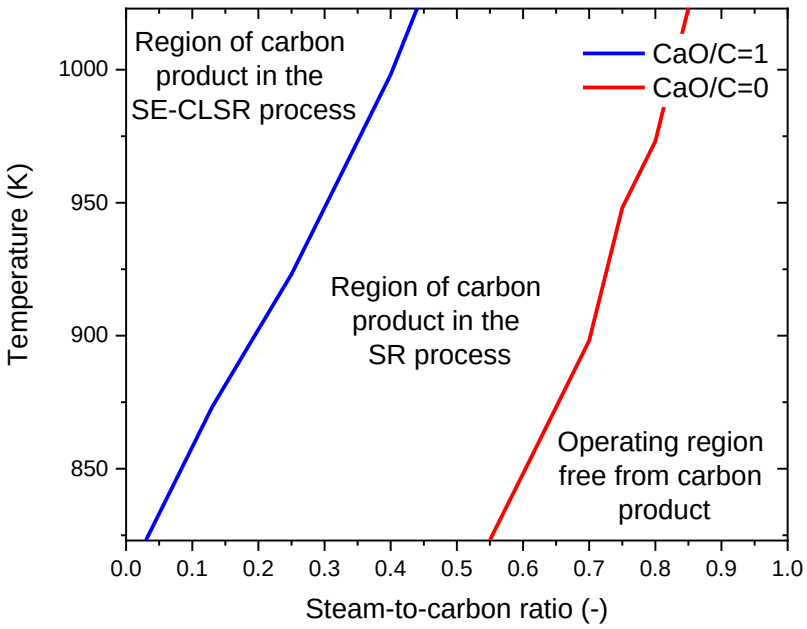

Figure 3.8 Equilibrium carbon product limits for the SE-CLSMR and the SRM processes as a function of the temperature and the S/C ratio at 5 bar.

3.3.4 Effect of the NiO-to-CaO ratio on the Fuel Reactor performance

The effect of NiO-to-CaO ratio upon the H_2 yield and the CH_4 conversion is illustrated in Figure 3.9. By increasing the amount of NiO in the Fuel Reactor, a higher conversion of CH_4 is attained as shown in Figure 3.9a, however, this reduces the H_2 yield as can be observed in Figure 3.9b. This behaviour is presumably due to the mechanisms of reduction of NiO with CH_4, H_2 and CO being favoured, which promotes the unmixed combustion of methane and hydrogen and increase the outlet concentration of CO_2. Similar trends have been previously reported for methane in [56, 60, 67] and for bio-oil in [125].

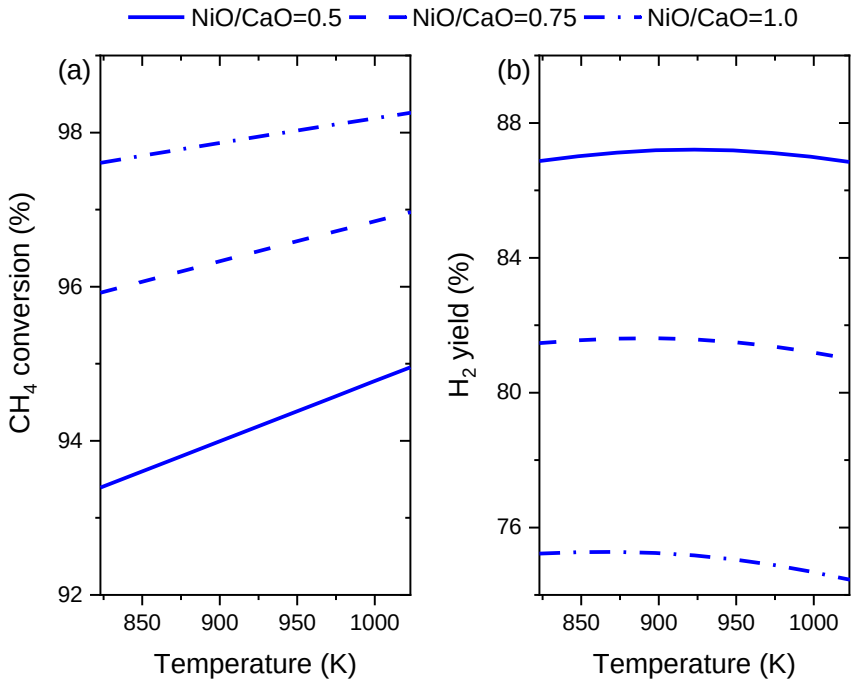

Figure 3.9 (a) CH_4 conversion and (b) H_2 yield, as function of the reactor temperature and NiO/CaO ratio at fixed P=5 bar, S/C=3, and CaO/C=1.

However, a higher NiO/CaO ratio promotes the conversion of the adsorbent, which increases monotonically with the increasing NiO/CaO ratio as illustrated in Figure 3.10a. Moreover, an inspection of the Fuel Reactor outlet temperature indicates that the process will be exothermic for all the range of NiO/CaO ratios simulated (Figure 3.10b); this is desirable from the reactor operation standpoint, although it increases the utilities required to cool down the reactor outlet stream to the required temperature for purification of the final product (i.e. hydrogen), thus increasing the process OPEX. Therefore a trade must be sought between the reactor temperature and the process economics. Since the simulation was conducted assuming an adiabatic reactor, the increase in the Fuel Reactor outlet temperature is due to the absorption of the available heat of reaction of adsorption of CO2, and to a lesser extent of the heat released from the reduction of NiO with H2 and CO. The latter behaviour has been observed experimentally by [119] and [57].

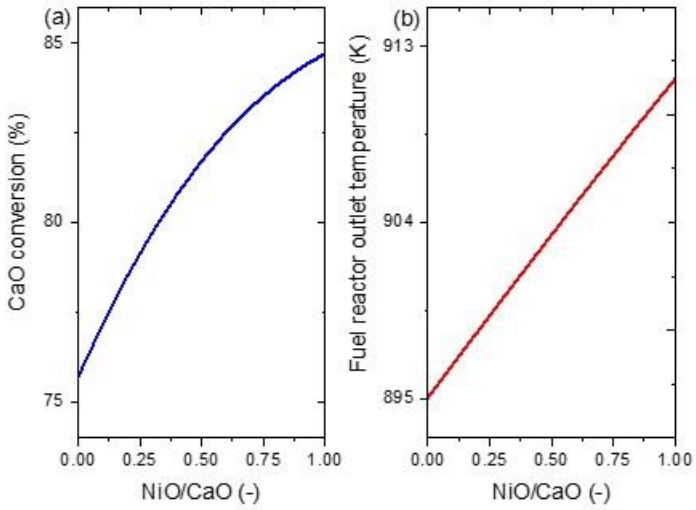

Figure 3.10 Effect of the NiO/CaO ratio on (a) the adsorbent conversion and (b) the reactor outlet temperature and the overall heat balance. The reaction temperature and pressure were fixed at 873K and 5 bar with S/C=3.0.

3.3.5 Effect of the temperature and pressure on the Air Reactor performance

The effect of temperature and pressure on the performance of the Air Reactor was investigated by conducting series of simulations varying the inlet air temperature and pressure, as well as the initial temperature of the solid materials and the reactor pressure, while keeping constant the O_2/Ni molar ratio.

Figure 3.11a is a plot of the conversion of Ni and $CaCO_3$ as a function of their inlet temperature and the air inlet temperature; it is evident that the conversion of Ni is insensitive to the air inlet temperature and the solids temperature, since for all combinations of these parameters a constant value of Ni conversion is predicted. Conversely, the calcination of $CaCO_3$ increases with both, the increasing air inlet temperature and with the increasing inlet solids temperature. However, it is observed that the conversion of this $CaCO_3$ is incomplete within the range of temperatures analysed. It is evident that the energy requirements to achieve complete regeneration of both materials in the Air Reactor is dictated by the equilibrium conditions of the calcination of $CaCO_3$. In the Air Reactor concept, this energy should be supplied by the heat of reaction of the re-oxidation of Ni, however, as shown in Figure 3.11a a high inlet temperature of the solids is required to achieve a high conversion of the adsorbent, this suggest that the available heat of oxidation of nickel might be insufficient to overcome the thermal effects of the calcination of $CaCO_3$ and sustain the regeneration of the adsorbent. This evidently impact the heating utilities required to set up the reactor and the

reactants to the required temperature for regeneration. Figure 3.11b displays the heat inflow required to increase the adsorbent conversion by 1%mole at different reactor and air temperatures. It is evident in Figure 3.11b that the temperature of the air and the materials proportionally affects the heat requirements per unit of conversion of $CaCO_3$, reflecting an obvious impact to the process economics but also suggesting a questionable feasibility of the concept.

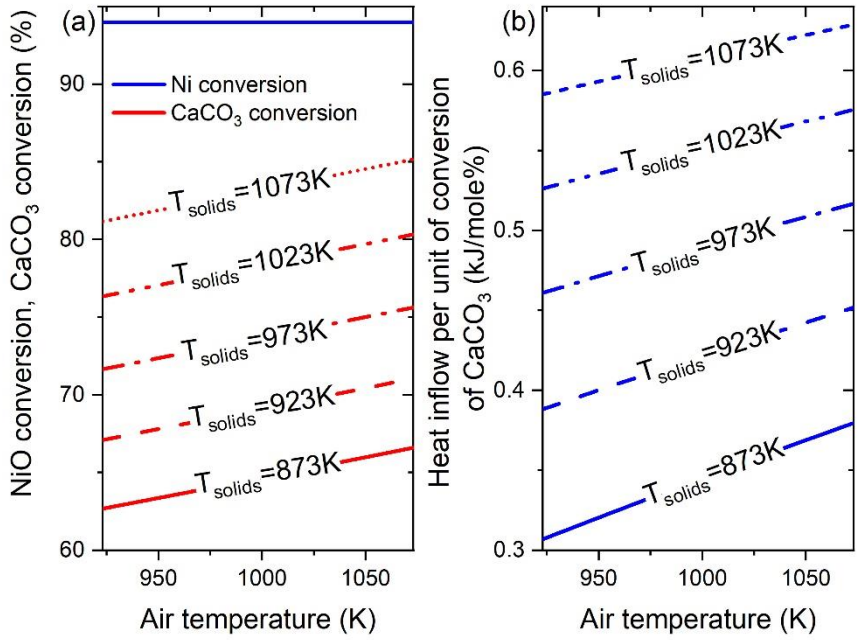

Figure 3.11 (a) $CaCO_3$ and Ni conversion (b) Energy consumption per unit of conversion of $CaCO_3$ in the Air Reactor as a function of the solids temperature and air temperature at fixed $P_{reactor}$=1.013 bar, NiO/CaO=0.5 and O_2/Ni=0.364.

The effect of the pressure is more significant for the calcination of the $CaCO_3$ than for the oxidation of Ni, in fact, similarly to the effect of the temperature, the re-oxidation of Ni is insensitive to the total pressure of the reactor. Figure 3.12a is a plot of the regeneration of the adsorbent as a function of the pressure and the air inlet temperature, maintaining the solids inlet temperature at 1073K and with a O_2/Ni ratio of 0.364. It is clear that if the reactor pressure is increased, the conversion of $CaCO_3$ to CaO reduces owing to the thermodynamic equilibrium of the calcium carbonate decomposition. In addition, a higher air inlet temperature favours the conversion of $CaCO_3$, however, with a penalty of a higher energy consumption in the conditioning of the air and the solid materials. Figure 3.12b displays the heat inflow required to increase the adsorbent conversion by 1%mole at different reactor pressures and air temperatures. Clearly, a higher pressure and temperature will demand a higher energy input to regenerate the adsorbent. Moreover, a higher operating pressure is not only detrimental to the process

performance, as it leads to a lower adsorbent conversion, but as in the case of the Air Reactor operating temperature, a higher operating pressure is undesirable from the process economics standpoint.

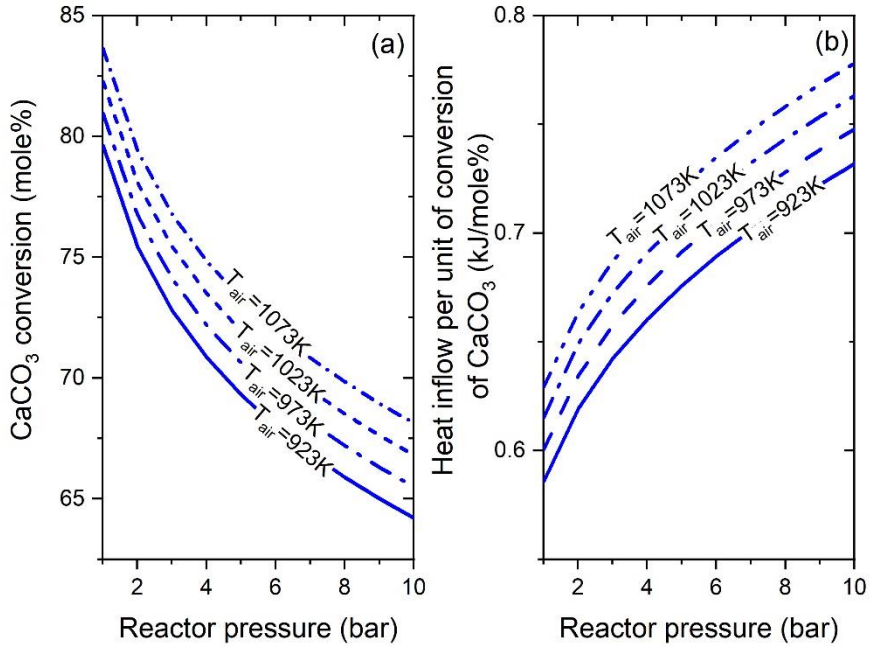

Figure 3.12 (a) Adsorbent conversion and (b) Energy consumption per unit of conversion of $CaCO_3$; as a function of the Air Reactor pressure and air temperature at fixed T_{solid}=1073K, NiO/CaO=0.5 and O_2/Ni=0.364.

3.3.6 Effect of the air flowrate and the NiO/CaO ratio on the Air Reactor performance

The results presented in the previous section indicate that operating the Air Reactor at a high temperature and low pressure yields the best scenario to achieve a high conversion of $CaCO_3$. It was also mentioned that the conversion of nickel is insensitive to the value of such parameters. In this section the effect of the air flowrate is investigated by conducting series of simulations under two scenarios. The scenario (a) looks at a reactor with a NiO-to-CaO ratio of 0.5, air inlet and solids temperatures of 1123 K, and reactor total pressure of 1 bar; the scenario (b) looks at the effect of increasing the NiO/CaO ratio from 0.5 to 0.75.

Figure 3.13a is a plot of the conversion of nickel and calcium carbonate as a function of the O_2/Ni air ratio for case (a). The data indicates that to attain complete conversion of nickel, a O_2/Ni ratio of 0.534, which represents ca. 6.8% of air excess is required; at this condition, a maximum 96.7% conversion of the $CaCO_3$ to CaO is predicted; to achieve a conversion of calcium carbonate >99%, the excess of air jumps from 6.8 to 60%. The implications of this result are the need of larger equipment to supply the required amount of air (higher CAPEX)

and an increase in the operating expenditure due to the energy consumption associated with the handling of a larger volume of both the air at the inlet and the exhaust gas at the outlet. If the NiO/CaO ratio is increased to NiO/CaO=0.75 (see Figure 3.13b), the $CaCO_3$ is fully converted to CaO with a O_2/Ni ratio of 0.392, whereas the complete reoxidation of nickel requires a higher O_2/Ni ratio of 0.532. This is as expected, since more nickel in the reactor represents also more heat of oxidation available to heat up the calcium carbonate and eventually calcinate it.

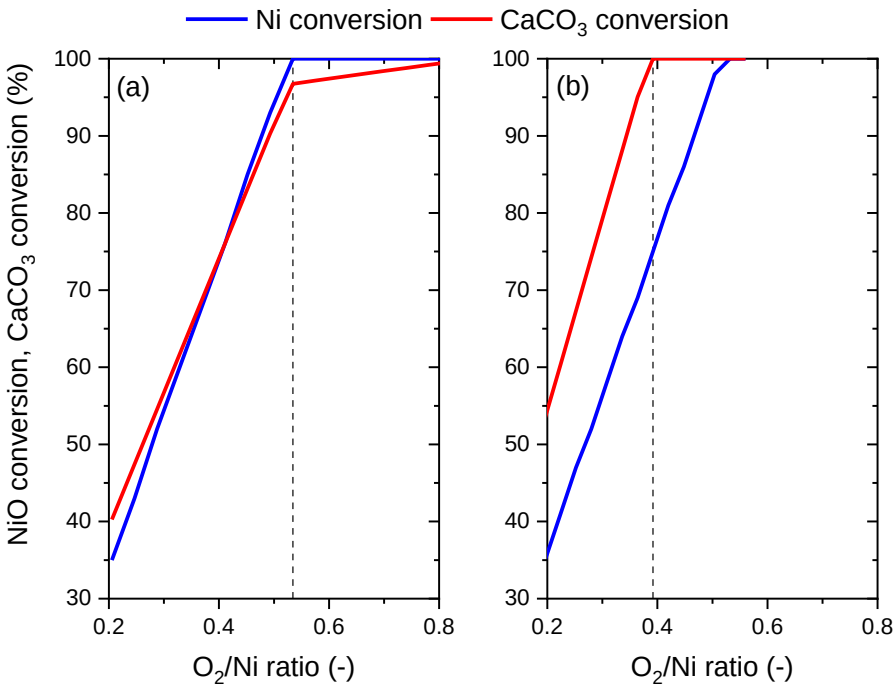

Figure 3.13 NiO and $CaCO_3$ conversion as a function of the O_2/Ni ratio at (a) NiO/CaO ratio fed to the Fuel Reactor of 0.5 and (b) NiO/CaO ratio fed to the Fuel Reactor of 0.75. The inlet temperature of air and solids is set up at 1123 K and the Air Reactor pressure is 1 bar.

3.4 Final comments on the Fuel and Air reactors operating pressure and temperature

The results of the parametric study indicate that the highest performance in both reactors (i.e. Fuel Reactor and Air Reactor) is obtained when they are operated at the lowest pressure level. Both scenarios have advantages and disadvantages with regards to process performance as can be inferred from the data summarised in Table 3.4. In the Fuel Reactor, low pressure operation is constrained by the economics of the process as it would imply additional operating expenditure due to the costs associated with the compression of hydrogen to the required pressure level for purification in the PSA stage and downstream from the PSA to inject the stream into a pipeline for transport or to

feed other processes; in addition, the low specific volume of H_2 implies the necessity of large equipment and piping to condition and handle the product to the relevant downstream operation; this is a serious constrain in revamped plants as in addition to the project budget, the physical space required to integrate the new technology can be a factor in the final design decision. The alternative is to compress the natural gas to the highest acceptable pressure to minimise downstream compression [126], thus reducing the energy requirements for compression (Table 3.4), and its associated costs. However, in this scenario the throughput capacity of the purification step will increase owing to the reduced H_2 purity in the product stream.

The Fuel Reactor operating temperature seems to be dictated by the maximum adsorption of the adsorbent. At each pressure level analysed a maximum conversion of the $CaCO_3$ is predicted, the locus of this maximum conversion varies within the temperature range 873–973K, and it is evident that varying the operating temperature within this range effects the consumption of hot utilities. Hence the operating temperature and pressure of the Fuel Reactor should be selected to maximise the yield and selectivity of H_2, whilst minimise the energy consumption of the integrated system.

Table 3.4 Process indicators and energy consumption to produce 1 mole of hydrogen at 5 and 25 bar.

Parameter	Low pressure operation (5 bar)	High pressure operation (25 bar)
CH_4 conversion (mole%)	93.8	85.1
H_2 purity (mole%)	93.1	90.4
Hot utilities consumption (kJ $mol^{-1}H_2$)	53.5	56.0
Cold utilities consumption (kJ $mol^{-1}H_2$)	94.4	55.2
Compression energy (kJ $mol^{-1}H_2$)	14.2	6.8

Low pressure is preferred for the regeneration of the OTM and adsorbent as the energy required to increase the materials temperature to the desired level to promote the decomposition of the calcium-based adsorbent is associated to the operating pressure of the reactor. A higher pressure would increase this requirement, thus the operating costs of the system. Additional CAPEX and OPEX should be considered in the design to account for conditioning and handling of the waste gas stream produced in the Air Reactor. This stream is mainly composed of N_2, CO_2 and O_2, which need to be separated in order to

obtain stream with a high purity of CO_2 that can be utilised in a range of applications, including its direct use in enhanced oil recovery, as a carbonating agent in the food industry, as a raw material for the chemical and petrochemical industries [127], or injected to geological reservoirs for storage. These costs can include the commissioning of compressors and heat exchangers ahead of the purification unit, with the heating and cooling services, as well as the pressure level required being dependent upon the selected downstream application.

Although the results of this study show promise regarding the conversion of raw materials, the selectivity towards H_2 and the low energy requirements for the reactor operation, further analysis are needed as the decaying of the adsorption capacity over multi-cycling operation is not accounted for in this screening. The loss of adsorption capacity affects the duration of each cycle of hydrogen production and material regeneration, and therefore, the final size of the reactor for a given throughput. Moreover, at each cycle, the availability of heat of adsorption is reduced due to a lower capture capacity of the adsorbent, hence, it is necessary to analyse the multicycle operation and determine the optimal frequency of replacing the deactivated adsorbent with fresh material in order to keep the system operating within the desired level of efficiency.

An additional factor that is likely to affect the performance of this process is the amount of materials other than the active metal oxides working as OTM and adsorbent. Steam reforming catalyst are materials containing about 15–20 wt.% of active phase supported typically in ceramics such as Al_2O_3. Adsorbents, on the other hand, can be applied unsupported, however, their tendency to degrade and lose CO_2 capacity during multicycle operation has launched efforts to find ways of improve their stability, being the use of inert materials one of the options explored [128]. Clearly, the presence of inert material in the bed represents a thermal burden for the process. Adiya et al. [10] included this factor in their simulations and found an increase in the energy requirements per mole of H_2 produced.

3.5 Concluding remarks

A thermodynamic analysis has been conducted to determine the operating windows of the main parameters of the SE-CLSR reactor and its performance indicators have been compared with those of a SMR reactor for the same throughput and operating ranges. At all operating temperatures and pressures, the SE-CLSMR process shows advantages over the conventional SMR process, primarily, a reduction in the operating temperature required to attain a higher conversion of methane and hydrogen yield.

The SE-CLSMR process is favoured at low pressure and temperatures in the range 873–973K, in this temperature range, the maximum adsorbent conversion is achieved at each analysed pressure. However, in the context of a plant the low pressure operation lead to a higher energy consumption per mole of H_2 produced, this is in contrast with the findings by Adiya et al. [10] who suggested a reduction of the operating pressure as a benefit of the lower operating temperature of the SE-CLSR of shale gas. Abbas et al. [68] conducted a similar study for the SE-CLSR of methane, and selected an operating pressure in the high end based on the typical operating pressures at industrial scale.

Previous analyses of the SE-CLSR process for methane and unconventional gas have been conducted assuming a feedstock that is fed without pre-processing to the Fuel Reactor. The results of this study indicate that although it is possible to proceed this way owing to the presence of the CO_2 adsorbent, a better performance is obtained by including the pre-reforming stage within the plant layout. In fact, when a pre-reformed gas is fed to the Fuel Reactor in the range 823–973K, the simulation results indicate an increase in the gas product temperature, thus reducing the energy requirements of the plant. Higher conversion of methane and hydrogen yield are also obtained in this operating scenario. When the content of heavier components (C_2+ fraction) increases, the product temperature is even higher, although the methane conversion and the hydrogen yield are lower. Both cases, however, exhibit a higher performance in comparison to the case where the sample of gas is fed without pre-reforming to the Fuel Reactor. Therefore, for the studies conducted in Chapter 6, the composition of the sample of gas utilised for the dynamic simulations will correspond to that of a pre-reformed gas.

Other relevant parameters analysed included the S/C ratio and the NiO/CaO ratio. For the former, it was shown that a value of S/C>2 would ensure an operation that minimises the risk of presence of carbon in the catalyst surface. Moreover, the performance indicators increase monotonically above this value, however, for values of S/C>3 the benefit obtained per unit of steam put into the

process is lower, and therefore the operation costs can be unjustified. Therefore, a value of S/C=3 is chosen. Regarding the NiO/CaO ratio, mixed results are obtained. In the Fuel Reactor a high NiO/CaO ratio will be in detriment of the hydrogen yield, although it will benefit the conversion of methane and increase the reactor temperature. However, in the Air Reactor, a higher NiO/CaO ratio will help to achieve complete regeneration of the adsorbent.

The Air Reactor should operate at the lowest possible pressure in order to reduce the calcination temperature of the adsorbent. Both, the air temperature and the initial temperature of the materials should be set as high as possible; a preliminary value of 1123K for both phases is found to suffice the requirements to achieve a conversion of the adsorbent greater than 95% and complete reoxidation of nickel with a flow of air about 6.8% in excess and a NiO/CaO ratio of 0.5. Complete conversion of the adsorbent is possible with a NiO/CaO ratio of 0.5, however, an excess of air of ca. 60% is required, thus increasing CAPEX and OPEX due to the larger size of equipment and the increased hot utilities required to condition the air. The final value of the NiO/CaO ratio needs to be determined in the context of the optimisation of the complete plant flowsheet.

Chapter 4 General modelling methodology

4.1 Introduction

The methodology followed in the development of this investigation is entirely computational. Different types of models were produced; the first part of the project looked at the modelling of the heat transfer problem in packed beds comprised of two different refractory materials. The second part of the project dealt with the modelling of the chemical looping reactor both for hydrogen production and for materials regeneration. The modelling methodology followed up in the deployment of such models is provided in the first part of this chapter.

The numerical methods applied to solve the models are reviewed in the second part of the chapter. Particular attention is given to the finite difference method and the method of lines, specifically in the context of the commercial software gPROMS^{TM} which was used to solve the reactor models. In addition, the method of characteristics is revised due to its importance in the determination of the concentration and thermal fronts in the packed bed.

4.2 Modelling methodology

The research carried out in this project followed two main branches, namely, the modelling and simulation of heat transfer in packed beds and the modelling and simulation of the adsorptive reactor in a packed bed.

In general, both objectives were achieved following the work flow shown in Figure 4.1.

4.2.1 Definition of the type of reactor.

There are various types of reactor available to use in the process industry, however, only the packed bed and the fluidised bed are of interest for the application investigated in this project. Some of the main differences between packed bed and fluidised bed reactors have been addressed in **Chapter 2**. Both technologies offer advantages and, in general, the fluidised bed reactor (FBR) seems to represent a better alternative than the packed bed reactor for the SE-CLSMR technology due to its improved heat transfer between phases, which would render a better integration of the heat of adsorption and the heat of reaction of the reforming process.

However, the FBR presents several operational limitations that could increase its CAPEX and OPEX, and thus, hinder its widespread application. Moreover, the

risk of leakage of harmful dusts to the environment (such as nickel) make FBRs less attractive due to the associated risks of damage to the health of operators. In addition, the conventional steam reforming plants are of the packed bed type and therefore, it make sense to study the potential application of the SE-CLSMR process in such type of reactor. For these reasons, the type of reactor selected for this research is the packed bed reactor (PBR).

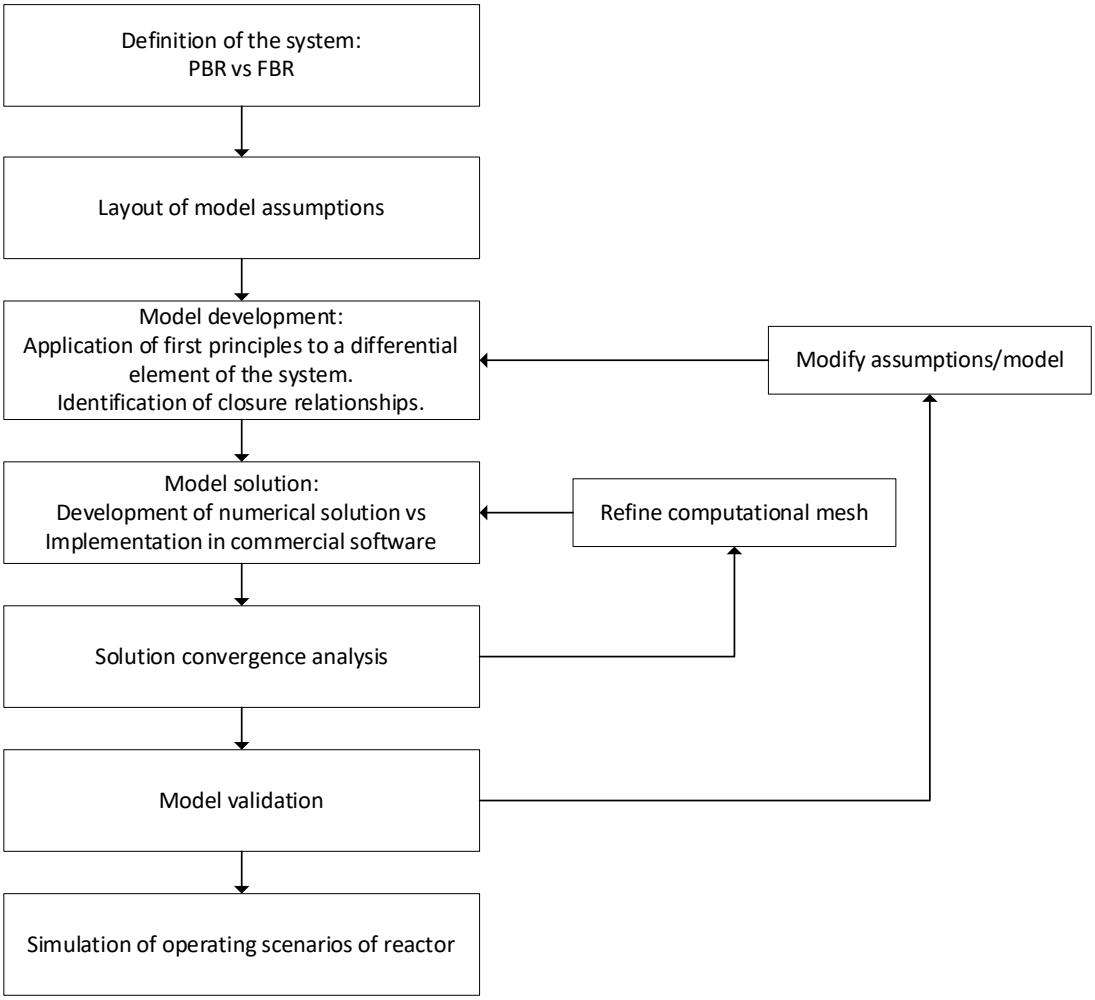

Figure 4.1 Modelling workflow followed in this research project.

4.2.2 Definition of the type of model

Packed bed reactors are complex systems to model due to the random nature of the passages through which the fluid flows and the changing composition of the reactant mixture flowing in it. Rigorously, local variation of the fluid and solid phase properties at each point of the reactor bed is expected. To account for these property and flow field gradients, one should look at the use of modern CFD tools, however, due to the many interrelationships of the system variables, following this path could prove to be very time consuming and computationally expensive.

Instead, simpler modelling approaches like the use of 1D reaction-diffusion models can be used to produce a first picture of the state of the system for several operating conditions. This approach has been commonly applied in the modelling of PBRs and, in particular, in the modelling of the SE-CLSMR process [50, 68].

In order to produce such a simpler model, capable of representing accurately the PBR, several modelling assumptions need to be formulated. This is a critical step in the development of the model, and can originate a range of different models with different degrees of sophistication. In general, two types of models can be produced: homogeneous and heterogeneous [129]. Table 4.1 summarises the possible combinations to produce PBR models.

Table 4.1 Classification of possible reactor models.

Type of Model	Homogeneous	Heterogeneous
Lumped Model	1D Plug Flow Model	1D Plug Flow Model + Inter-pellet resistances
	1D Axial Dispersion Model	1D Plug Flow Model + Axial Dispersion + Inter-pellet resistances
	2D Plug Flow + Radial Dispersion	2D Plug Flow + Radial Dispersion + Inter-pellet resistances
	2D Plug Flow + Radial Dispersion + Axial Dispersion	2D Plug Flow + Radial Dispersion + Axial Dispersion + Inter-pellet resistances
Distributed Particle Model	-	All the combinations of the Lumped Model + Intra-pellet resistances

The different models presented in Table 4.1 can be attained by following practical guidance gained from the accumulated knowledge regarding reactor modelling, such guidelines are:

I. Reactor length-to-particle diameter ratio L_R/d_p.

   The value of the reactor bed length depth provides the basis to assess the possibility of axial dispersion and axial heat conduction. In industrial reactors, the mixing effects are considered negligible when $L_R/d_p > 50$ [79, 129]. More accurate criteria to assess the presence of mixing effects have been proposed [130, 131]; for non-isothermal reactors with cooling or heating at the wall Young and Finlayson [130] derived the following expressions:

$$\frac{r_{A0}\rho_b d_p}{u_s C_{in}} \ll Pe_{m,z} \qquad \textbf{(4.1)}$$

$$\frac{r_{A0}\rho_b d_p(-\Delta H)}{u_s\rho_g C_{p,g}(T_{in}-T_w)} \ll Pe_{h,z} \quad \textbf{(4.2)}$$

where r_{A0} is the reaction rate calculated at inlet conditions, ρ_b is the bed bulk density, d_p is the catalyst pellet diameter, u_s is the superficial velocity, C_{in} is the inlet concentration, ρ_g is the gas density at inlet conditions, C_p is the gas heat capacity at inlet conditions, ΔH is the heat of reaction, T_{in} is the inlet temperature, T_w is the wall temperature, and $Pe_{m,z}$ and $Pe_{h,z}$ are the Peclet numbers for mass and heat dispersion in the axial direction.

Equations (4.1) and (4.2) are applicable when the maximum temperature or conversion are located near the reactor inlet; when the maximum values are located in the interior of the packed bed the following criteria were proposed:

$$max\left|\frac{dX}{d\left(\frac{z}{d_p}\right)}\right| \ll Pe_{m,a} \quad \textbf{(4.3)}$$

$$max\left|\frac{dT'}{d\left(\frac{z}{d_p}\right)}\right| \ll Pe_{h,a} \quad \textbf{(4.4)}$$

Where X is the fractional conversion, T' is the dimensionless reactor temperature, z is the axial position and d_p is the particle diameter. However, the quantities on the left-hand side of Equations (4.3) and (4.4) cannot be readily calculated from the inlet data and thus require approximations based on simulations with a plug flow model.

II. Reactor diameter-to-particle diameter ratio D_b/d_p.

1D models assume that the radial variations of concentration, temperature and velocity can be neglected. This might be an oversimplification, because it is well known that the bed structure is in general non-uniform and exhibits an oscillatory distribution of the bed voidage, which increases from the reactor centreline towards the reactor wall, particularly in packed beds with a low reactor diameter depth [129, 132, 133]. These variations can affect the prediction of important parameters of the reactor such as length needed to achieve a certain conversion level, or the existence and location of hot spots in exothermic processes [134].

However, radial variations can be neglected for large reactor diameter-to-particle diameter ratios fulfilling the condition $D_b/d_p > 30$ [79]. Mears [135] assumed that the radial mass transport effects were negligible in comparison to radial heat transport, based on evidence from previous numerical

investigations and proposed the following criterion to assess the importance of radial temperature variation in systems where the heat transfer resistance at the wall is significant, if the condition is fulfilled, the effect of the temperature variations on the heat generation/dissipation produces an error within 5%:

$$\frac{r_{A0}(1-\varepsilon_b)d_r^2|-\Delta H|}{4\lambda_{e,r}T_w} < \frac{0.4\,R_g T_w/E_A}{1+8d_p/(d_r Bi_w)} \qquad \textbf{(4.5)}$$

Where r_{A0} is the reaction rate calculated at inlet conditions, d_r is the reactor diameter, ε_b is the bed mean voidage, $\lambda_{e,r}$ is the effective radial conductivity, T_w is the wall temperature, E_A is the activation energy, d_p is the particle diameter, R_g is the gas constant and Bi_w is the Biot number evaluated at the wall conditions. If the heat transfer resistance at the wall is negligible, the denominator of the right-hand side approaches 1 and Equation (4.5) reduces to:

$$\frac{r_{A0}(1-\varepsilon_b)d_r^2|-\Delta H|}{4\lambda_{e,r}T_w} < 0.4\,R_g T_w/E_a \qquad \textbf{(4.6)}$$

III. The Mears criteria for inter-pellet heat and mass transfer.
Mears [135] proposed the following criteria to determine presence of inter-pellet transport resistance, if the condition is fulfilled the homogeneous model will deviate less than 5% from the heterogeneous model:

$$\left|\frac{-\Delta H r_{A0} r_p}{\alpha T}\right| < 0.15\frac{R_g T}{E_a} \qquad \textbf{(4.7)}$$

Where α is the heat transfer coefficient, r_p is the particle radius and T is the temperature of the bulk. The remaining parameters stand as previously defined.

IV. The Weisz-Prater criteria for intra-pellet heat and mass transfer.
The Weisz-Prater criteria defined as per Equation (4.8) is utilised to determine the presence of intra-pellet transport resistances. A value of $C_{WP} \ll 1$ indicates the absence of intra-pellet resistances. Conversely if $C_{WP} \gg 1$ the intra-pellet resistances will be severe.

$$C_{WP} = \frac{-r_{A0}\rho_p r_p^2}{D_{e,A}C_{A,S}} \qquad \textbf{(4.8)}$$

Where $D_{e,A}$ is the effective diffusion of the reactant A in the pore of the pellet, $C_{A,S}$ is the concentration of the reactant A at the pellet surface and ρ_p is the pellet density.

As discussed in **Chapter 2**, one of the objectives of this research is to develop a model that predicts the local temperature and concentration profiles in the different phases involved within the system, i.e. this project is looking at a heterogeneous model. The model assumptions will be then laid out considering all relevant physical phenomena such as inter- and intra-particle transport. In addition, relevant assumptions might have to be made to account for local structural changes happening in the materials, owing to the different non-catalytic processes happening in the SE-CLSMR process. The detail of the assumptions taken for each model development will be presented in their respective chapters.

4.2.3 Development of the mathematical model.

The model equations are obtained from the application of mass, energy and momentum balances to an infinitesimal element of the system domain represented in Figure 4.2, and yielded sets of partial differential equations (PDE) along with initial and boundary conditions.

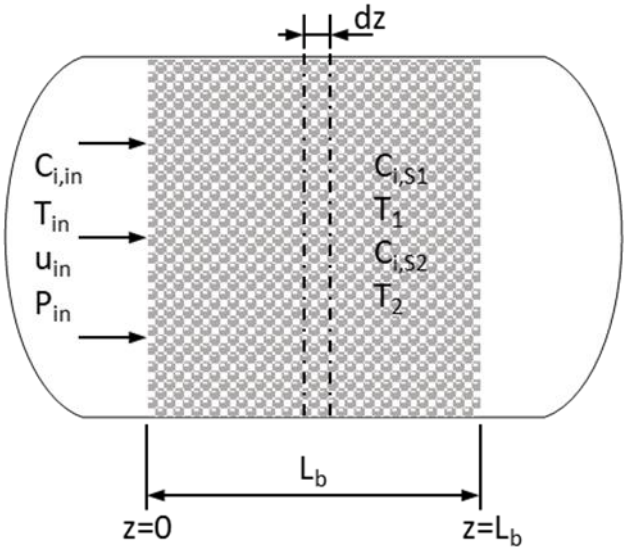

Figure 4.2 Physical domain of the packed bed reactor.

In addition, closure relationships were incorporated to complete the mathematical problem and ensure a well-posed system and obtain a numerical solution.

Let us set as an example of the procedure, the derivation of a model of the heat transfer in a packed bed. The main assumptions of the development are an infinite heat transfer coefficient, negligible temperature gradients in the packing and negligible variation of the bulk properties. Figure 4.3 is a representation of an element of the adsorber of length Δz, where the heat is convected towards and from the element through the cross sectional area A_z.

The balance heat transported by convection in the element is given by the amount of heat ‘in’ minus the amount of heat ‘out’ as:

$$\Delta t A_z u_s \rho_g C_{p,g} (T|_z - T|_{z+\Delta z}) = \Delta t A_z u_s \rho_g C_{p,g} \Delta T \quad \textbf{(4.9)}$$

Where Δt is the time increment, ΔT is the bulk temperature increment, A_z is the cross sectional area of the element, u_s is the superficial velocity, ρ_g is the bulk density and $C_{p,g}$ is the bulk heat capacity. The accumulation of heat in the system is the sum of the accumulation of the specie in the gas phase and in the packing and is given by:

$$\Delta z A_z \varepsilon_b \rho_g C_{p,g} \Delta T + \Delta z A_z \rho_b C_{p,s} \Delta T \quad \textbf{(4.10)}$$

Where ρ_b and $C_{p,s}$ are the packing bulk density and heat capacity, respectively. Hence, the total heat balance is:

$$\Delta z A_z \varepsilon_b \rho_g C_{p,g} \Delta T + \Delta z A_z \rho_b C_{p,s} \Delta T = \Delta t A_z u_s \rho_g C_{p,g} \Delta T \quad \textbf{(4.11)}$$

Dividing by $\Delta z \Delta t A_z \varepsilon_b \rho_g C_{p,g}$ and applying the limit when $\Delta z \to 0$ and $\Delta t \to 0$ the final differential balance is obtained:

$$\frac{\partial T}{\partial t} + \left(\frac{u_i}{1 + \frac{\rho_b C_{p,s}}{\varepsilon_b \rho_g C_{p,g}}} \right) \frac{\partial T}{\partial z} = 0 \quad \textbf{(4.12)}$$

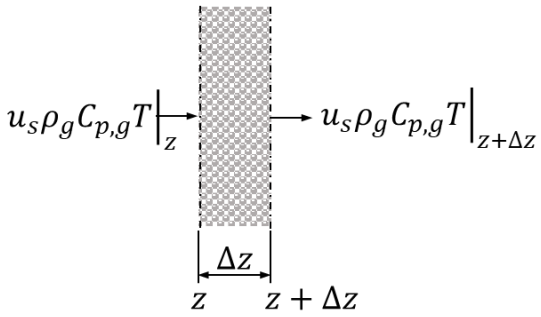

Figure 4.3 Balance of heat over a differential element of the packed bed adsorber.

4.2.4 Model solution and convergence analysis

The model solutions are attained by developing our own algorithm and by implementation of the model in the commercial software gPROMS™ [136]. Details of the techniques utilised for the solution and analysis of the models are reviewed in **Section 4.3**.

The analysis of convergence of the solutions is attained by a trial-and-error approach, solving the model for different mesh sizes and comparing the

simulation results until they are no longer significantly affected by the number of mesh points.

4.2.5 Model validation and sensitivity analysis.

The validation of the models is attained by comparison of the output against published sets of experimental data or against the output of a model solution obtained by a different method. Where there is availability of an analytical solution, it is utilised for validation purposes.

The sensitivity analysis is carried out over operating windows determined from the thermodynamical study of the system. The relevant operating conditions analysed are detailed in **Chapter 6**.

4.3 Numerical solution of the model equations.

Various methods are available to approximate the solution of partial differential equations of the type in Equation (1.13), e.g. method of characteristics (MC), method of lines (MOL), finite differences (FD), finite element (FE), finite volume (FV) and spectral methods (SM) [137-139]. All these methods are applicable to solve PDEs in regular geometry domains such as that of fixed beds. For irregular geometries the finite element and finite volume methods are usually preferred.

Except for the method of characteristics, which is aimed to solve hyperbolic PDEs, all of these methods can be applied to solve both parabolic and hyperbolic PDEs. The mathematical principle underlying these techniques is the approximation of the derivatives, which is based on Taylor approximations for the FDM and FVM [137, 138], piecewise polynomials in the FEM or Fourier series for the SM. The method of characteristics and the method of lines the PDEs into sets of ordinary differential equations (ODE) and then integrate them by the known ODE integrators [139, 140].

Previous modelling investigations of the SE-SMR process in packed bed reactors have applied the method of lines [6, 31, 35, 68], the finite element method [33], and spectral methods [65] to solve the conservation equations. The approximation of the spatial derivative in the conservation equations has been attained by the application of finite differences and orthogonal collocation mainly. In the following sections the basic concepts of the FD and the MOL methods are reviewed due to their relevance in this project. In addition, a note on the Method of Characteristics is made due to its relevance in the analysis of hyperbolic PDEs.

4.3.1 Finite Differences Method

The finite differences method (FDM) is the simplest method to solve sets of partial differential equations. The basic principle of the FDM consist in the approximation of the partial derivatives using differences quotients, transforming the set of PDEs into a set of algebraic equations which are then solved by appropriate techniques for sparse matrixes, for example, the tri-diagonal matrix algorithm [138, 141].

Given a general function of two variables, e.g. $U(t,z)$, the classic approximations for the first and second derivatives of $U(t,z)$ with respect to z at the point $z = z_i$ can be obtained from the application of the Taylor series around $z = z_i$; if it is assumed that the terms of order 3 of higher in the series are negligible, the following formulae for the first and second derivatives are obtained:

$$\left.\frac{\partial U(t,z)}{\partial z}\right|_t \approx \frac{U(t,z_i+\Delta z)-U(t,z_i-\Delta z)}{2\Delta z}+O(\Delta z^2) \qquad \textbf{(4.13)}$$

$$\left.\frac{\partial^2 U(t,z)}{\partial z^2}\right|_t \approx \frac{U(t,z_i+\Delta z)-2U(t,z_i)+U(t,z_i-\Delta z)}{\Delta z^2}+O(\Delta z^2) \qquad \textbf{(4.14)}$$

where Δz is an increment step around the point z_i. Equations (4.13) and (4.14) are central difference approximations to $U'(t,z)$ and $U''(t,z)$, and have a truncation order of $O(\Delta z^2)$, which in practical terms means that the error of the approximated solution will be proportional to the square of the integration step size Δz. Alternatively, the first derivative can be approximated by an upwind or downwind scheme as follows:

$$\left.\frac{\partial U(t,x)}{\partial z}\right|_t \approx \frac{U(t,z_i+\Delta z)-U(t,z_i)}{\Delta z}+O(\Delta z) \qquad \textbf{(4.15)}$$

$$\left.\frac{\partial U(t,x)}{\partial z}\right|_t \approx \frac{U(t,z_i)-U(t,z_i-\Delta z)}{\Delta z}+O(\Delta z) \qquad \textbf{(4.16)}$$

where Equations (4.15) and (4.16) are the forward and backward difference formulae, respectively. These are first order approximations and the truncation error in these formulae is $O(\Delta z)$.

The formulae presented in Equations (4.13) through (4.16) are applied to discretise single or sets of PDEs. In physics problems, these sets are usually functions of two or more independent variables, typically involving time and at least one spatial coordinate of the physical domain of the problem. Consider for example the following parabolic PDE:

$$\frac{\partial U}{\partial t} = \frac{\partial^2 U}{\partial z^2} \qquad \begin{matrix} t > 0, \\ 0 \le z \le L \end{matrix} \tag{4.17}$$

The discretisation of the physical domain of equation (4.17) forms a grid of $N \times I$ computational nodes as displayed in Figure 4.4, where N and I are integer numbers representing the number of points of discretisation along each axis of the domain, and the position of any particular node within the grid is given by a combination of integer numbers n and i. Hence, the actual values of the independent variables can be expressed as the product of the respective variable increment size and the position coordinate, i.e. $t = n\Delta t$ and $z = i\Delta z$.

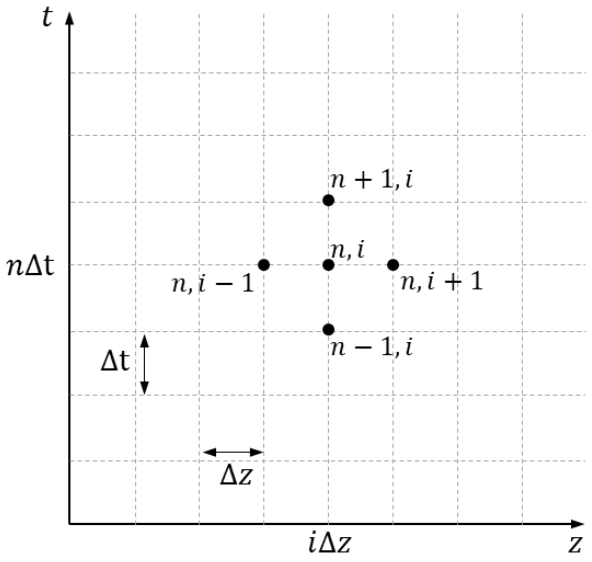

Figure 4.4 Computational mesh obtained by the discretisation of the domain of a function $U(t, x)$.

The approximation of the $U(t, z)$ in (4.17) involves the application of discretisation formulae to the partial derivatives rendering an algebraic relationship that relate unknown values of U, i.e. at time level $n + 1$, with known values of U at time level n. Various approaches can be followed to do this, for example, explicit, semi-implicit or Crank-Nicolson and fully implicit, in which the main difference is the way the second derivative is approximated. These approaches are schematically illustrated in Figure 4.5.

In the explicit method, the approximation of second derivative of U is based on three values of the function U at the n^{th} time level, giving:

$$U_i^{n+1} = U_i^n + r[U_{i-1}^n - 2U_i^n + U_{i+1}^n] \tag{4.18}$$

The semi-implicit or Crank-Nicolson method [142], approximates the second derivative at the midpoint $\left\{n\Delta t, \left(i + \frac{1}{2}\right)\Delta z\right\}$ and calculates $\frac{\partial^2 U}{\partial z^2}$ as the mean of its

finite difference approximations at the levels n and $n+1$, rendering Equation (4.19):

$$-rU_{i-1}^{n+1} + (2+2r)U_i^{n+1} - rU_{i+1}^{n+1} = rU_{i-1}^{n} + (2-2r)U_i^{n} + rU_{i+1}^{n} \quad \textbf{(4.19)}$$

The fully implicit backwards method approximates $\frac{\partial^2 U}{\partial z^2}$ at the $n+1$ time level yielding:

$$-rU_{i-1}^{n+1} + (2+2r)U_i^{n+1} - rU_{i+1}^{n+1} = U_i^{n} \quad \textbf{(4.20)}$$

where U_i^n is the approximated value of $U(t,z)$ at the position (n,i) within the computational grid as illustrated in Figure 4.4, and $r = \Delta t/\Delta z^2$.

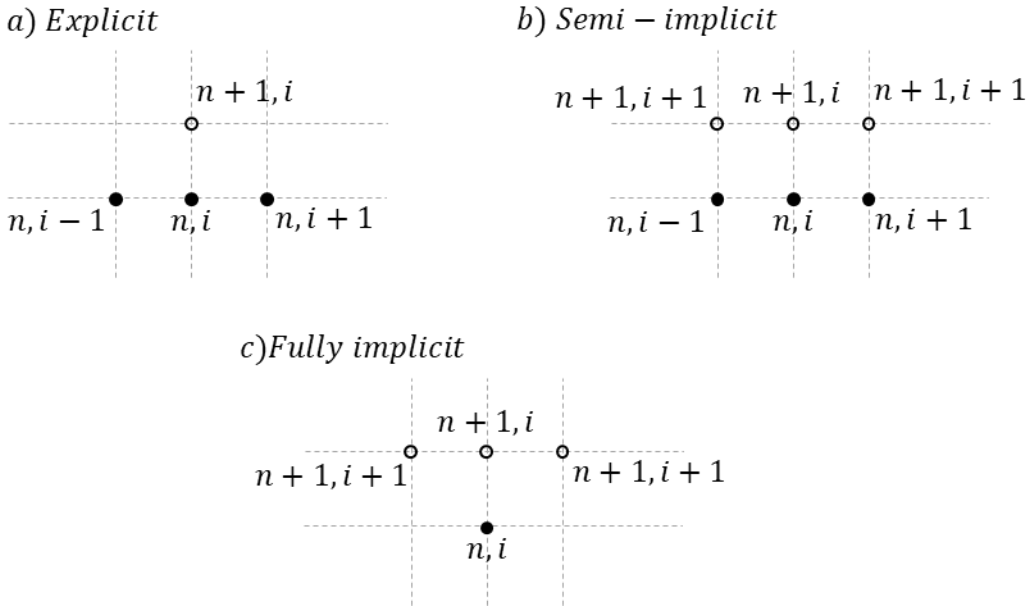

Figure 4.5 Schematic representation of numerical integration algorithms.

The selection of the discretisation scheme is constrained by the stability and convergence of the numerical solution. The explicit scheme is the simplest to implement and the most severely constrained by these issues, hence in order to produce a stable algorithm the implicit and semi-implicit are preferred.

4.3.2 Method of Lines and gPROMS.

The method of lines is a numerical technique that converts partial differential equations into sets of ordinary differential equations (ODE). This is usually attained by transforming the continuous variation of the function with respect to the spatial independent variables into discrete variations, whilst keeping the variations in time as a continuous function, thus replacing the spatial derivatives by an algebraic approximation [139].

The form of the algebraic approximation is not unique and its choice depends on the nature of the problem being approximated, i.e. whether it is a strongly convective or dissipative process. Typically, finite differences discretisation formulae can be applied, although polynomials and piecewise approximations can also be used [139, 143].

The application of the Method of Lines approach to equation (4.17), using the equation (4.14) to approximate the spatial derivative renders the following set of ODE:

$$\begin{aligned} \frac{dU_1(t)}{dt} &= \frac{1}{\Delta z^2}\{U_0 - 2U_1 + U_2\} \\ \frac{dU_2(t)}{dt} &= \frac{1}{\Delta z^2}\{U_1 - 2U_2 + U_3\} \\ &\vdots \\ \frac{dU_{n-1}(t)}{dt} &= \frac{1}{\Delta z^2}\{U_{n-2} - 2U_{n-1} + U_n\} \end{aligned} \qquad \textbf{(4.21)}$$

The set of ordinary differential equations (4.21) is then solved simultaneously by any of the known ODE integrators e.g. Runge-Kutta or Euler.

The method of lines is the base solution technique implemented in the commercial package gPROMS™[136]. gPROMS™ is a general purpose modelling tool designed to model and simulate processes with continuous and discrete characteristics, and can integrate lumped parameters systems and distributed parameter systems within the same modelling environment.

The gPROMS™ package allows the simultaneous solution of large sets of differential algebraic equations (DAE) by means of sophisticated integrators that work over algorithms that adjust the time step-size and integration order automatically maintaining control over the integration error, such as DASOLV. The algorithm of DASOLV consists of a predictor-corrector routine [144]. The predictor step estimates values on new positions of the domain by extrapolation of a polynomial interpolating values of past variables or their derivatives. The corrector step solves a set of non-linear algebraic equations iteratively by a modified Newton method.

The architecture of a gPROMS Model is defined in terms of different entities. The most basic structure to set-up a modelling project in this software uses a Model entity, a Process entity and a set of Variable Types.

The Model Entity is the workspace used to define the model. In this file, all the model parameters, variables and equations, including boundary conditions are defined. The detail of the type of variables i.e. distributed or not distributed should be indicated within the body of this file. For complex models, gPROMS™ might

not find a solution from poor initial estimates and therefore could require of a step-wise initialisation procedure that improves gradually the quality of the initial estimates; this type of procedure should also be implemented in this entity. Figure 4.6 is a view of a basic model in gPROMS™.

```
PARAMETER
    #Gas properties
    gasDensity      AS      REAL
    gasViscosity    AS      REAL
    gasSpecHeat     AS      REAL
    gasThermalCond  AS      REAL
    gasSupVel       AS      REAL
    gasMassFlux     AS      REAL

    #Particle properties
    solDensity      AS      REAL
    solSpecHeat     AS      REAL
    solThermalCond  AS      REAL
    particleRadius  AS      REAL
    bedVoidage      AS      REAL
    pellet_porosity AS      REAL

    specSurface     AS      REAL
    reactorLength   AS      REAL
    TsIn            AS      REAL

DISTRIBUTION_DOMAIN

    zdomain AS [0:reactorLength]

VARIABLE

    Tg              AS DISTRIBUTION(zdomain) OF Temperature
    Tl              AS DISTRIBUTION(zdomain) OF Temperature
```

```
BOUNDARY
# Inlet condition
    Tg(0)=TgIn;
    gasPress(0)=PgIn;

EQUATION
    #Energy balance in the fluid
    FOR z:=0|+ TO reactorLength DO
        gasMassFlux*gasSpecHeat*PARTIAL(Tg(z),zdomain)
          = -heatTransCoeff * specSurface * (Tg(z)-Tl(z));
    END

    FOR z:=0 TO reactorLength DO
        (1-bedVoidage) * ( 1 - pellet_porosity ) * solDensity*solSpecHeat*$Tl(z)
          = heatTransCoeff * specSurface * (Tg(z)-Tl(z));
    END
```

Figure 4.6 Example of a Model Entity in a gPROMS Process Builder model.

The Variable Types are used to define the variables of the model along with their default values, and bounds within which the variables will change during the integration process. gPROMS uses the default estimates to initialise the calculation process, thus, if a variable of the model is not specified within the Variable Types entity, gPROMS will display an error indicating that the variable

type is not defined. Figure 4.7 shows a view of the Variable Types manager and the definition of a Variable Type called “Density”.

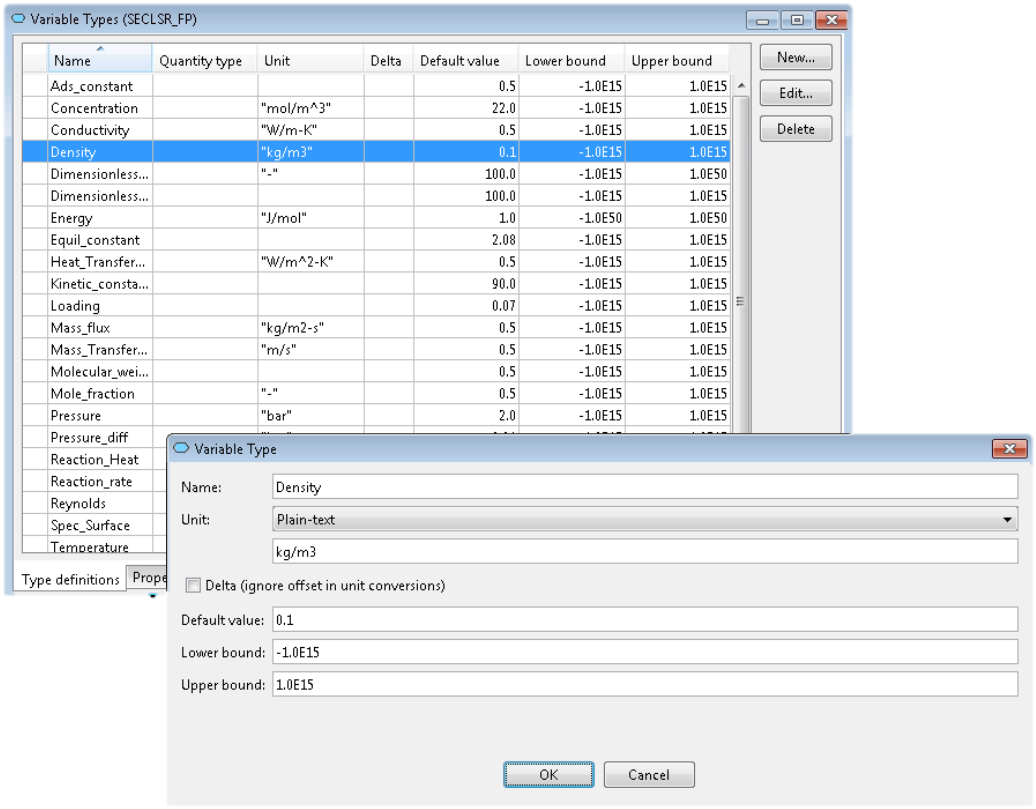

Figure 4.7 View of the Variable Types manager.

The Process Entity (Figure 4.8) is the workspace where the problem to be simulated is defined, it should specify values for all the model parameters, as well as the inlet and initial conditions. In this entity is also specified the method of discretisation for the spatial variables, the order and the number of mesh points utilised to solve the problem. By design, gPROMS™ utilises an implicit approach to handle the time discretisation in dynamic problems, this approach takes advantage of the full capacities of the gPROMS™ algorithm, however, it is possible to implement the temporal derivative in explicit form within the model, thus opening the possibility to define a method of approximation and mesh size for the time coordinate. Nevertheless, the latter approach would render a larger set of algebraic equations with the disadvantage a higher computational and time cost in comparison with the implicit approach and the loss of accuracy due to an unguaranteed control of the temporal discretisation error [143].

```
UNIT FB_1 AS HTM12P_LFR_DLESS
SET
    WITHIN FB_1 DO
        number_of_pellets           :=  2 ;
        gas_density                 :=  6.92 ;              # kg/m3
        gas_viscosity               :=  0.0275;             # cP
        gas_heat_capacity           :=  2597.7 ;            # J/kg-K
        gas_thermal_conductivity    :=  0.1165 ;            # W/m-K
        gas_velocity                :=  1.11 ;              # m/s

        pellet_density              :=  [3630, 3340] ;      # kg/m3
        pellet_heat_capacity        :=  [1195.9, 943.4] ;   # J/kg-K
        pellet_thermal_conductivity :=  [2.1, 8.5] ;        # W/m-K
        pellet_diameter             :=  [0.0130, 0.0130] ;  # m
        pellet_radius               :=  [0.0065, 0.0065] ;  # m
        pellet_porosity             :=  [0.55, 0.52] ;      # dimensionless

        bed_composition             :=  0.0  ;
        reactor_diameter            :=  0.1016 ;            # m
        reactor_length              :=  0.009 ;             # m
        initial_bed_temperature     :=  0 ;

        axialup                     := [CFDM,2,50] ;
    END
ASSIGN
    FB_1.inlet_temperature     :=  1;
INITIAL
    WITHIN FB_1 DO
        FOR z := 0 TO 1 DO
            F1(z) = initial_bed_temperature ;
            F2(z) = initial_bed_temperature ;
        END
        simulation_time = 0 ;
    END
SCHEDULE
    CONTINUE FOR 14.36684
```

Figure 4.8 Example of a Process Entity in a gPROMS Process Builder model.

4.3.3 A note on the method of characteristics.

The method of characteristics is aimed to solve hyperbolic PDE. Abbott [145] regarded the characteristics as the natural choice of a coordinated system to attain a more natural correspondence between the mathematical problem and the physical situation.

Geometrically, the characteristics (also referred to as characteristic directions), are lines that result from the intersection of planar elements defined by PDE. Along these lines, the partial differentials are independent of each other and thus, the equations are reduced to sets of coupled ordinary differential equations that can be solved by an ODE integrator.

The first step in the application of this method to approximate solution of PDE is to determine the characteristic directions $\frac{\partial z}{\partial t}$. Let the following general first order PDE:

$$a\frac{\partial U}{\partial t}+\mathrm{b}\frac{\partial U}{\partial z}=c \qquad \textbf{(4.22)}$$

If the function U is the fluid temperature T, and the constants a, b and c are substituted by $a=1$, $b=\left(\frac{u_i}{1+\frac{\rho_b C_{p,s}}{\varepsilon_b \rho_g C_{p,g}}}\right)$ and $c=0$, Equation (4.22) would represent the pseudo-homogeneous model of heat transfer between a fluid and a solid matrix as:

$$\frac{\partial T}{\partial t}+\left(\frac{v}{1+\frac{\rho_b C_{p,s}}{\varepsilon_b \rho_g C_{p,g}}}\right)\frac{\partial T}{\partial z}=0 \qquad \textbf{(4.23)}$$

If it is assumed that the values of the differentials $\frac{\partial T}{\partial t}$ and $\frac{\partial T}{\partial z}$ can be approximated from an initial set of values of T, then the following relationship should be fulfilled [138]:

$$\frac{\partial T}{\partial t}\mathrm{dt}+\frac{\partial T}{\partial z}\mathrm{dz}=\mathrm{dT} \qquad \textbf{(4.24)}$$

Equations (4.23) and (4.24) can be arranged in matrix form as:

$$\begin{vmatrix} 1 & \frac{u_i}{1+\frac{\rho_b C_{p,s}}{\varepsilon_b \rho_g C_{p,g}}} \\ dt & dz \end{vmatrix} \times \begin{vmatrix} \partial T/\partial t \\ \partial T/\partial z \end{vmatrix} = \begin{vmatrix} 0 \\ dT \end{vmatrix} \qquad \textbf{(4.25)}$$

A single first order PDE will have one characteristic, which is determined from Equation (4.25) based on the trait that Equations (4.23) and (4.24) should be linearly dependent. Thus, equating the determinant of matrix A to zero gives the following characteristic:

$$\frac{dz}{dt}=\frac{u_i}{1+\frac{\rho_b C_{p,s}}{\varepsilon_b \rho_g C_{p,g}}} \qquad \textbf{(4.26)}$$

The mathematical significance of Equation (4.26) is that along this line the partial derivatives are independent of each other, thus, a set of ODEs needs to be solved. Such set is obtained by replacing the independent vector in either of the columns of the matrix in Equation (4.25) and reassessing the determinant, for this case, the solution is:

$$\begin{vmatrix} 1 & 0 \\ dt & dT \end{vmatrix} = 0 \;\rightarrow dT=0 \qquad \textbf{(4.27)}$$

Hence, indicating that along the characteristic, the temperature is constant. This case is the representation of a square step input as the pseudo-homogeneous model assumes an infinite heat transfer coefficient, thus, the saturation of the bed is obtained as the fluid enters the system. The velocity of this thermal front is the physical significance of the characteristic Equation (4.26).

4.4 Concluding remarks

The general modelling methodology has been outlined in this chapter. The workflow utilised in this work is the result of systematic approaches previously identified and applied by many researchers. In this sense, no contribution is made to improve the modelling methods.

A review of the relevant numerical methods to solve PDEs has been conducted. The use of a high level PDE package such as gPROMS^{TM} offers the advantage of a simpler implementation of the mathematical model but at the cost of a limited flexibility. gPROMS^{TM} has several advantages as are the powerful PDE solver and the ability of the package to communicate to third party software such as Multiflash^{TM} and Ansys^{TM}. The former is of particular interest as one of modelling aspects considered in this project is to assess the effect of the gas properties variation along the PBR. However, a gPROMS model solution has to be sought within the software constraints, e.g. gPROMS does not have the ability of using adaptive meshes which would be useful to solve problems with steep moving fronts, like the one covered in this investigation. Conversely, the use of a programming based tool allows the development of fit for purpose solutions based on the particular intricacies of the model, however, this is a very time consuming task that could face several convergence problems, particularly in non-linear stiff systems. For these reasons, although both approaches are used, gPROMS^{TM} is the preferred tool for the development of this project.

Finally, the method of characteristics offer valuable tools for the analysis of the model equations, provided that the system comprises hyperbolic partial differential equations only. In addition it is going to be used as a tool to analyse the certain aspects of the physics of the adsorptive reactor.

Chapter 5 Heat transfer in packed beds

5.1 Introduction

The technical feasibility of the chemical looping reactor proposed in this research depends upon the exchange of heat and mass between the solid pellets and the fluid within the time-scale imposed by the residence time of the gaseous stream throughout the packed bed. While the mass transfer phenomena are primarily limited by the internal diffusion inside the pores of the solid materials, the dynamics of the heat transfer is highly dependent upon the thermal properties of the materials and gaseous stream involved in the exchange, the bed structure and the flow field; therefore, the appropriate selection of the heat transfer mechanisms to be accounted for plays a central role to attain a correct interpretation of the dynamics of the system.

A great deal of research has been devoted to study the problem of heat transfer in fixed beds with the focus of improving the predictive capability of the models in the assessment of thermal regenerators performance. The modelling approaches have considered plug flow systems with intra-conduction effects [146-149], plug flow with axial dispersion and intra-conduction effects [150], and pseudo-homogeneous and the pseudo-heterogeneous models with axial and radial gradients and no intra-conduction effects [151, 152].

In this chapter, the heat transfer operation in a fixed bed randomly packed with spherical pellets of relevant materials for the SE-CLSR process is assessed with the aim of determining the most suitable approach to be considered in the reactor model in **Chapter 6**. Models of heat transfer in fixed beds packed with two types of packing materials are deployed and a numerical solution is provided. The heat transfer mechanisms considered are the fluid-to-particle convection and the intra-pellet conduction. The analysis of various fixed beds packed with combinations of these materials is discussed and the conclusions of this study are presented.

5.2 Eulerian heat transfer model equations

The fixed bed is thought as a pseudo-heterogeneous system. The working fluid is deemed to behave as an ideal plug flow, this approximation is valid as for industrial systems the aspect ratio D_b/d_p is likely to meet the heat dispersion criterion. The pellet materials to be utilised in the reactor exhibit very low thermal conductivity, therefore, the system is likely to develop temperature gradients due to the differences in the rates of heat transfer for each type of particle; this is

accounted for in the model and each particle is modelled by a Fourier type equation, producing a distributed particle model. In addition, the following model assumptions are made:

1. The system modelled in this investigation encompasses a randomly dumped packed bed of two different types of refractory pellets that exchange heat with a hot gas stream as shown in Figure 5.1.
2. The model allows for the calculation of separate heat transfer coefficients for each pellet, depending on their particular sizes and thermal properties.
3. For this study, the pellets are considered as non-porous spheres of constant size; allowance in the model has been made to account for different sizes between pellets; for this case a harmonic average pellet diameter is calculated, hence, a mean bed voidage is considered throughout the bed.
4. The physical properties of the gaseous stream are deemed constant in the range of operating temperature. This assumption is valid as long as the computational experiments are conducted within a temperature change of ~10K.
5. The bed is deemed adiabatic and no radial heat transfer is considered.
6. Axial heat conduction in the pellets and the gases are negligible.
7. Plug flow velocity occurs in the bed.

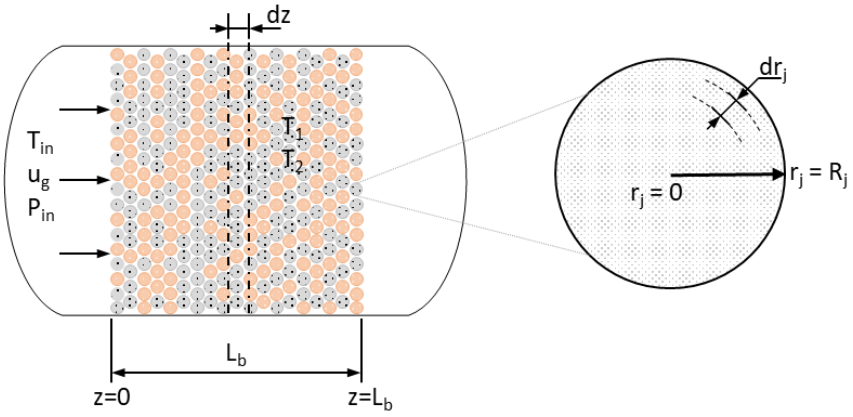

Figure 5.1 Model of a single shot regenerator.

5.2.1 Distributed particle model

From the assumptions previously listed, and by considering a system as shown in Figure 5.1, the fluid energy balance for the problem previously described is defined within the region of interest $t > 0$ and $0 < z \leq L$ as follows:

$$\varepsilon_b \rho_g C_{p,g} \frac{\partial T}{\partial t} + u_s \rho_g C_{p,g} \frac{\partial T}{\partial z} = -\alpha_1 a_{S_1} \left(T - T_1|_{r_1=R_1}\right) - \alpha_2 a_{S_2} \left(T - T_2|_{r_2=R_2}\right) \quad \textbf{(5.1)}$$

And for the solids in the region $t > 0$ and $0 < r_1 < R_1$ and $0 < r_2 < R_2$ as:

$$\rho_{p_1} C_{p_1} \frac{\partial T_1}{\partial t} = \lambda_{p_1} \left(\frac{\partial^2 T_1}{\partial r_1^2} + \frac{2}{r_1} \frac{\partial T_1}{\partial r_1} \right) \quad \textbf{(5.2)}$$

$$\rho_{p_2} C_{p_2} \frac{\partial T_2}{\partial t} = \lambda_{p_2} \left(\frac{\partial^2 T_2}{\partial r_2^2} + \frac{2}{r_2} \frac{\partial T_2}{\partial r_2} \right) \quad \textbf{(5.3)}$$

Where α_1 and α_2 are the heat transfer coefficients for pellets 1 and 2 per unit surface area; a_{S_1} and a_{S_2} are the available areas for heat transfer per unit of volume of bed; u_g, ρ_g and $C_{p,g}$ are the superficial gas velocity, the gas density and the gas heat capacity, respectively; ρ_{p_1}, C_{p_1}, λ_{p_1} and ρ_{p_2}, C_{p_2}, λ_{p_2} are the density, heat capacity and thermal conductivity of pellets 1 and 2, respectively.

For spherical packings the surface areas for pellets 1 and 2 are defined as:

$$a_{S_1} = \frac{6\gamma_1(1-\varepsilon_b)}{d_{p,1}} \text{ and } a_{S_2} = \frac{6\gamma_2(1-\varepsilon_b)}{d_{p,2}} \quad \textbf{(5.4)}$$

Where γ_1 and $\gamma_2 = 1 - \gamma_1$ are the volumetric fractions of the pellets 1 and 2, ε_b is the bed mean voidage and, $d_{p,1}$ and $d_{p,2}$ are the diameters of pellets 1 and 2.

The solution of the model equations (5.1) through (5.3) requires of an additional relationship to couple the physical interaction between the fluid and the solid pellets; such condition is given by the heat fluxes at the surfaces of the particles in the following way:

$$-\lambda_{p_1} \left. \frac{\partial T_1}{\partial r_1} \right|_{r_1 = R_1} = \alpha_1 \left(T_1|_{r_1 = R_1} - T \right)$$
$$\text{and } -\lambda_{p_2} \left. \frac{\partial T_2}{\partial r_2} \right|_{r_2 = R_2} = \alpha_2 \left(T_2|_{r_2 = R_2} - T \right) \quad \textbf{(5.5)}$$

The system is completed with the application of symmetry condition at the centre of each pellet:

$$\left. \frac{\partial T_1}{\partial r_1} \right|_{r_1 = 0} = 0 \text{ and } \left. \frac{\partial T_2}{\partial r_2} \right|_{r_2 = 0} = 0 \quad \textbf{(5.6)}$$

The solution of Equations(5.1), (5.2) and (5.3) depends also upon the initial conditions and the type of forcing function imposed at the entrance of the bed. In this investigation a square-step forcing function is applied at $z = 0$:

$$T(0, t) = T_{in} \quad \textbf{(5.7)}$$

In addition, an initially thermally equilibrated bed is assumed, thus, the initial conditions are presented as a function of the spatial domain at both, the bed and the particle scales:

$$T(x,0) = T_1(x,r_1,0) = T_2(x,r_2,0) = T_i \tag{5.8}$$

5.2.2 Lumped model

If in Equation (5.1) the temperature at the surface of each pellet is replaced by an average pellet temperature, a simplified lumped model is obtained as:

$$\varepsilon_b \rho_g C_{p,g} \frac{\partial T}{\partial t} + u_s \rho_g C_{p,g} \frac{\partial T}{\partial z} = -\bar{\alpha}_1 a_{S_1}(T - \bar{T}_1) - \bar{\alpha}_2 a_{S_2}(T - \bar{T}_2) \tag{5.9}$$

With transfer rate equations:

$$\frac{\partial \bar{T}_1}{\partial t} = \frac{\bar{\alpha}_1 a_{S_1}}{\rho_{b_1} C_{p_1}}(T - \bar{T}_1) \tag{5.10}$$

$$\frac{\partial \bar{T}_2}{\partial t} = \frac{\bar{\alpha}_2 a_{S_2}}{\rho_{b_2} C_{p_2}}(T - \bar{T}_2) \tag{5.11}$$

In Equations (5.9) – (5.11), $\bar{\alpha}_1$ and $\bar{\alpha}_2$ are the heat transfer coefficients for the lumped model and $\bar{T}_1$ and $\bar{T}_2$ are the average temperatures of each pellet, defined for pellet 1 and 2 as:

$$\bar{T}_1(t,z) = \frac{3}{R_1^2}\int_0^{R_1} T_1(t,z,r_1) r_1^2 dr_1 \text{ and}$$
$$\bar{T}_2(t,z) = \frac{3}{R_2^2}\int_0^{R_2} T_2(t,z,r_2) r_2^2 dr_2 \tag{5.12}$$

By integrating Equations (5.2) and (5.3) between the boundary conditions (5.5) and (5.6) the following energy balances at each particle are obtained:

$$\frac{\partial \bar{T}_1}{\partial t} = \frac{3\alpha_1}{R_1 \rho_{p_1} C_{p_1}}\left(T - T_1|_{r_1=R_1}\right) \tag{5.13}$$

$$\frac{\partial \bar{T}_2}{\partial t} = \frac{3\alpha_2}{R_2 \rho_{p_2} C_{p_2}}\left(T - T_2|_{r_2=R_2}\right) \tag{5.14}$$

If we equate Equation (5.10) with (5.13) and Equation (5.11) with (5.14) a definition of the lumped heat transfer coefficient is rendered:

$$\bar{\alpha}_1 = \alpha_1 \frac{\left(T - T_1|_{r_1=R_1}\right)}{(T - \bar{T}_1)} = \alpha_1 \epsilon_1 \qquad \textbf{(5.15)}$$

$$\bar{\alpha}_2 = \alpha_2 \frac{\left(T - T_2|_{r_2=R_2}\right)}{(T - \bar{T}_2)} = \alpha_2 \epsilon_2 \qquad \textbf{(5.16)}$$

In equations (5.15) and (5.16) the correction factors ϵ_1 and ϵ_2 arise as a function of the bulk gas temperature, the average temperature and the temperature at the surface of the particle. These temperatures clearly are functions of time and position in the bed, as well as of the transport properties of the gas and the size of the pellets, whose effects are summarised in the Reynolds number. Therefore, the nature of ϵ_1 and ϵ_2 is dynamic and their evaluation would then require information of the temperature profiles within each particle which are not readily at hand.

An alternative to account for intra-pellet thermal gradients is to use expressions of the type of Equation (5.17) which introduce the effective heat transfer coefficient defined as the sum of individual resistances to heat transfer:

$$\frac{1}{\alpha_{e,i}} = \frac{1}{\alpha_i} + f\left(R_i, \lambda_{p_i}\right) \qquad \textbf{(5.17)}$$

Where $\alpha_{e,i}$ and α_i represent the effective heat transfer coefficient and the convective heat transfer coefficient of the packing type “i”, with i=1,2, and $f\left(R_i, \lambda_{p_i}\right)$ is a packing-shape dependant function reflecting the resistance to heat transfer due to the thermal conductivity of the material. This approach seems to be a solution to avoid the use the intraparticle model and might result inadequate in the analysis of dynamic systems, however its effectiveness to enhance the predictive capabilities will be assessed.

Hence substituting $T_1|_{r_1=R_1}$ by the surface temperature of the pellet type 1, T_{S_1}, and $T_2|_{r_2=R_2}$ by the surface temperature of the pellet type 2, T_{S_2}, and assuming that the average temperatures $\bar{T}_1 = T_{S_1}$ and $\bar{T}_2 = T_{S_2}$, i.e. the thermal conductivity is infinite and the pellets are isothermal, the lumped model is derived for the fluid as:

$$\varepsilon_b \rho_g C_{p,g} \frac{\partial T}{\partial t} + u_s \rho_g C_{p,g} \frac{\partial T}{\partial z} = -\alpha_1 a_{S_1}\left(T - T_{S_1}\right) - \alpha_2 a_{S_2}\left(T - T_{S_2}\right) \qquad \textbf{(5.18)}$$

And for the solids:

$$\frac{\partial T_{S_1}}{\partial t} = \frac{\alpha_1 a_{S_1}}{\rho_{b_1} C_{p_1}}\left(T - T_{S_1}\right) \qquad \textbf{(5.19)}$$

$$\frac{\partial T_{S_2}}{\partial t} = \frac{\alpha_2 a_{S_2}}{\rho_{b_2} C_{p_2}} \left(T - T_{S_2}\right) \quad \textbf{(5.20)}$$

In Equations (5.19) and (5.20) T_{S_1} and T_{S_2} are the temperatures at the surface of each pellet, and the bulk densities are scaled by the mean bed voidage ε_b and the volumetric bed composition γ_1 and γ_2 as follows:

$$\rho_{b_1} = \gamma_1(1 - \varepsilon_b)\rho_{p_1} \text{ and } \rho_{b_2} = \gamma_2(1 - \varepsilon_b)\rho_{p_2} \quad \textbf{(5.21)}$$

In the previous set of equations, it is clear that the conditions $\gamma_1 = 0$ or $\gamma_1 = 1$ reduce the system to the case of a single pellet type.

The solution of the set of PDEs in Equations (5.18) – (5.20) is sought for the same forcing function and initial conditions defined in Equations (5.7) and (5.8), however, the lumped model is distributed only along the axial position in the bed and therefore the initial conditions are re-defined as:

$$T(z, 0) = T_{S_1}(z, 0) = T_{S_2}(z, 0) = T_i \quad \textbf{(5.22)}$$

5.3 Additional data for the numerical solution of the models

The data required for the solution of the models presented in section 5.2 includes the physical properties of the fluid and the solid packings. This information is estimated at inlet conditions and is deemed constant in the range of operation of the packed bed. In addition, information of the mean bed voidage, the heat transfer coefficient and the pressure drop coefficients must be incorporated.

5.3.1 Physical properties

The gas density, specific heat capacity and viscosity of the gas were estimated with the aid of the process simulation tool Aspen Plus™. Two working fluids are considered in this study, namely natural gas and air. The selection of these gases is made to match the properties of those that will operate in the actual reactor, in order to study the heat transfer operation at similar conditions to those that will be simulated in the following chapters. The property method selected to estimate the physical properties of the gases was the Peng-Robinson equation of state with the Boston-Mathias correction, this method is recommended to predict the properties of systems containing hydrogen [153].

With regards to the packings, the physical properties of relevant materials for the reactor such as alumina (Al_2O_3), calcium oxide (CaO) and calcium carbonate ($CaCO_3$) were considered in this analysis; the data utilised for this study is summarised in Table 5.1.

Table 5.1 Physical properties of relevant solid materials [154, 155].

Material	Thermal Conductivity (W m^{-1} K^{-1})	Heat capacity (J kg^{-1} K^{-1}) $C_{p,s} = C_{p,0} + C_{p,1}T + \frac{C_{p,2}}{T^2}$; T in K			Density (kg m^{-3})
		$C_{p,0}$	$C_{p,1}$	$C_{p,2}$	
Ni	68.8	498.6	6.46×10^{-2}	-	8601.9
NiO	13.0	633.4	1.21×10^{-1}	-	6670.0
Al_2O_3	2.1	906.7	3.68×10^{-1}	-2.15×10^{7}	3630.0
CaO	8.5	746.6	3.61×10^{-1}	-8.06×10^{6}	3340.0
$CaCO_3$	2.3	823.2	4.97×10^{-1}	-1.29×10^{7}	2710.0

5.3.2 Heat transfer coefficient

Heat transfer coefficients relate to the resistance to heat transfer between the fluid and the solid matrix. They are functions of the fluid and solid properties and are usually expressed in terms of the Colburn factor j_H, which for fixed beds is a function of the Reynolds number and the mean bed voidage.

$$j_H = \frac{\alpha}{\rho_g C_{p,g} u_s}\left(\frac{C_{p,g}\mu_g}{\lambda_g}\right)^{2/3} \quad \textbf{(5.23)}$$

Various correlations are available for j_H, for the purpose of this analysis the expression proposed by Heggs and Handley [156] is used:

$$\varepsilon_b j_H = 0.255 Re^{-0.235} \quad \textbf{(5.24)}$$

5.3.3 Mean bed voidage

The mean bed voidage is a measure of the free volume within the fixed bed and is defined as the ratio of free volume to bed volume. This is a relevant parameter in the simulation and design of fixed beds as it has an important effect on the pressure drop in the system, and ultimately, on the length of packed bed required for a certain operation.

The estimation of the mean voidage in fixed beds of spherical packings can be attained theoretically for structured beds, based on the geometric arrangement of the pellets or by means of empirical correlations for randomly packed beds. For randomly packed beds, numerous investigations have been devoted to develop correlations to estimate the mean bed voidage [157, 158]. These investigations have produced several correlations applicable to various ranges of

diameter aspect ratio D_b/d_p, however, neglecting the contribution of the bed edges, i.e. the side wall and the top and bottom ends, a summary of these correlations is provided by Guo et al. [158]. Rwifa [159] proposed a correlation considering the contribution of the bed edges by incorporating in the expression the dependence of the mean voidage with the length aspect ratio L_b/d_p; such correlation is:

$$\varepsilon_b = \frac{d_p}{L_b}\left\{\varepsilon_1 + \left(\frac{L_b}{d_p} - 1\right)\varepsilon_\infty\right\} \quad \textbf{(5.25)}$$

$$\varepsilon_1 = 0.573 + 0.145e^{\left(-0.3175 D_b/d_p\right)} \quad \textbf{(5.26)}$$

$$\varepsilon_\infty = 0.352 + 0.145e^{\left(-0.1899 D_b/d_p\right)} \quad \textbf{(5.27)}$$

where ε_1 and ε_∞ are voidage at the end and core of the bed, respectively. Figure 5.2 is a plot of the mean bed voidage for spherical packings as function of the diameter aspect ratio, predicted by various correlations taken from [158] and in addition the values predicted by Equation (5.25) evaluated at the extreme values of the L_b/d_p ratio of its range of validity.

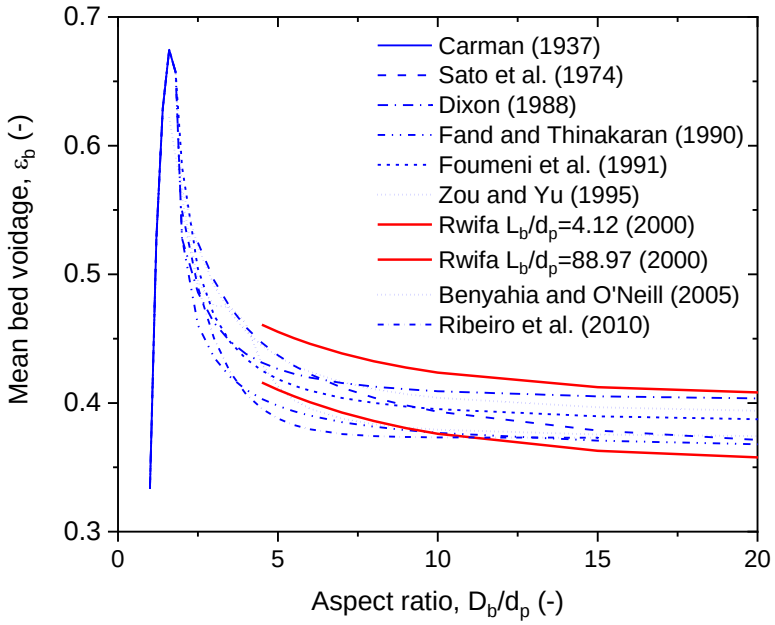

Figure 5.2 Mean bed voidage predicted by various correlations adapted from [158, 159].

The lack of agreement between the correlations on the prediction of mean bed porosity is evident from Figure 5.2, this is likely due to differences in the methods utilised in the investigations. The plots of values of ε_b predicted by Equation (5.25) were evaluated at the extreme values of the range of validity of L_b/d_p, giving

lines that seem to bound the majority of the values produced by other correlations for values of $D_b/d_p > 10$. Rwifa reported deviations in the range 5.25–13.31% in the prediction of bed voidage with the correlations of Dixon [160], Foumeny et al. [161], and Zou and Yu [162], for fixed beds with an aspect ratio $L_b/d_p > 20$; Guo et al. [158] compared the predictions of available correlations against experimental mean voidage data measured in the range $1.8 < D_b/d_p < 7.1$ at values of $L_b/d_p > 15$, and suggested that the disparity between the values of ε_b was related to the failure of the correlations to reconcile the oscillatory nature of the data.

The experimental data by Guo et al. [158], was compared in this work with predicted values of ε_b by Equation (5.25) assuming a value of $L_b/d_p = 20$, giving an average error of 2.05%, followed by the correlations of Foumeny and Zou and You with average errors of 2.09% and 2.26%. Therefore, Rwifa's correlation is applied in this study.

5.3.4 Pressure drop

The energy losses caused by the passage of the fluid through the channels of the packed bed are calculated by an Ergun type equation:

$$\frac{dP}{dz} = -\frac{A\mu_g u_s (1-\varepsilon_b)^2}{d_p^2 \varepsilon_b^3} - \frac{B\rho_g u_s^2 (1-\varepsilon_b)}{d_p \varepsilon_b^2} \qquad \textbf{(5.28)}$$

Where the first and second terms on the r.h.s. of Equation (5.28) relate to the kinetic and viscous losses, respectively.

The correlating parameters A and B have been fitted by various researchers and it has been found that they depend upon the shape of the packing [156]. For fixed beds of randomly dumped spherical pellets, Heggs [163] recommends to use the values provided by Macdonald et al. [164], yielding:

$$\frac{dP}{dz} = -\frac{180\mu_g u_s (1-\varepsilon_b)^2}{d_p^2 \varepsilon_b^3} - \frac{1.8\rho_g u_s^2 (1-\varepsilon_b)}{d_p \varepsilon_b^3} \qquad \textbf{(5.29)}$$

Equation (5.29) is valid for Reynolds numbers within $0.1 \leq Re/(1-\varepsilon_b) \leq 10000$.

5.3.5 Average pellet diameter

The estimation of the mean bed porosity and pressure drop requires information of the pellet diameter. The heat transfer model proposed here accounts for separate particles which can have different sizes; hence an average diameter (d_p) is used in Equations (5.25) – (5.29) which is estimated as [165]:

$$\frac{1}{d_p} = \frac{\gamma_1}{d_{p_1}} + \frac{\gamma_2}{d_{p_2}} \quad \textbf{(5.30)}$$

5.4 Methodology of solution

The heat transfer models developed in the previous section are sets of Linear Partial Differential and Algebraic Equations (PDAE). Analytical solutions can be obtained for these models and there are some available for the single pellet problem [146], however, the solution of the models produced in this thesis is sought by applying numerical techniques, which are a more practical and flexible approach.

Prior to develop the numerical solutions, the models are simplified by changing the time coordinate, then the finite differences method is applied to transform the set of PDAE into a set of algebraic equations; in addition, the models are solved by gPROMS.

5.4.1 Change of coordinate system: Lagrangian equations

The models set up in Section 5.2 are expressed in the Eulerian reference frame, which essentially provide a physical description of the system from a fixed point in space. The existence of two derivatives in the bulk gas energy balance equation, represents a challenge for the integration procedure due to the impending ratios of step sizes $\Delta t/\Delta z$ and $\Delta t/\Delta r$ that arise from the development of the finite differences approximation of the model equations, and can create instabilities and lack of convergence of the numerical solution.

An effective way to deal with these problems consists in changing the time coordinate from Eulerian to Lagrangian; in this way, only one of the aforementioned step size ratios appears on the solution; hence, in the Lagrangian reference frame the number of derivatives on models equations is lessened, thus reducing the sources of instabilities in the numerical scheme.

Lagrangian equations are obtained by redefining the time coordinate as per Equation (5.31):

$$\tau = t - \frac{z}{u_i} \quad \textbf{(5.31)}$$

where τ is the Lagrangian time coordinate, defined as the Eulerian time t, minus the residence time $\frac{z}{u_i}$. The substitution of Equation (5.31) in the distributed particle model equations (5.1) – (5.3) gives:

$$u_s \rho_g C_{p,g} \frac{\partial T}{\partial z} = -\alpha_1 a_{S_1} \left(T - T_1|_{r_1=R_1}\right) - \alpha_2 a_{S_2} \left(T - T_2|_{r_2=R_2}\right) \quad \textbf{(5.32)}$$

$$\rho_{p_1} C_{p_1} \frac{\partial T_1}{\partial \tau} = \lambda_{p_1} \left(\frac{\partial^2 T_1}{\partial r_1^2} + \frac{2}{r_1} \frac{\partial T_1}{\partial r_1} \right) \quad \textbf{(5.33)}$$

$$\rho_{p_2} C_{p_2} \frac{\partial T_2}{\partial \tau} = \lambda_{p_2} \left(\frac{\partial^2 T_2}{\partial r_2^2} + \frac{2}{r_2} \frac{\partial T_2}{\partial r_2} \right) \quad \textbf{(5.34)}$$

With initial conditions:

$$T(x,0) = T_1(x, r_1, 0) = T_2(x, r_2, 0) = T_i \quad \textbf{(5.35)}$$

And boundary conditions in the particle domain:

$$-\lambda_{p_1} \left.\frac{\partial T_1}{\partial r_1}\right|_{r_1=R_1} = \alpha_1 \left(T_1|_{r_1=R_1} - T\right)$$
$$\text{and } -\lambda_{p_2} \left.\frac{\partial T_2}{\partial r_2}\right|_{r_2=R_2} = \alpha_2 \left(T_2|_{r_2=R_2} - T\right) \quad \textbf{(5.36)}$$

$$\left.\frac{\partial T_1}{\partial r_1}\right|_{r_1=0} = 0 \text{ and } \left.\frac{\partial T_2}{\partial r_2}\right|_{r_2=0} = 0 \quad \textbf{(5.37)}$$

Similarly, the lumped model (Equations (5.18) – (5.20)) becomes:

$$u_s \rho_g C_{p,g} \frac{\partial T}{\partial z} = -\alpha_1 a_{S_1} \left(T - T_{S_1}\right) - \alpha_2 a_{S_2} \left(T - T_{S_2}\right) \quad \textbf{(5.38)}$$

$$\frac{\partial T_{S_1}}{\partial \tau} = \frac{\alpha_1 a_{S_1}}{\rho_{b_1} C_{p_1}} \left(T - T_{S_1}\right) \quad \textbf{(5.39)}$$

$$\frac{\partial T_{S_2}}{\partial \tau} = \frac{\alpha_2 a_{S_2}}{\rho_{b_2} C_{p_2}} \left(T - T_{S_2}\right) \quad \textbf{(5.40)}$$

Both models are solved for the square-step boundary condition (5.7), which is now a function of the Lagrangian time coordinate as follows:

$$T(0,\tau) = T_{in} \quad \textbf{(5.41)}$$

The solution to these models allows the analysis of the dynamic response of heat transfer in fixed beds, however the application of the Lagrangian formulation is limited to periods longer than the residence time and no changes in fluid velocity can be investigated.

5.4.2 Bed parameters

The analysis of the response of the fixed bed is attained by tracking the fluid temperature as a function of time at the outlet of the column. The comparison of different beds can be better approached in terms of dimensionless parameters that provide summarised information of the physical characteristics of the bed, namely the dimensionless bed length Y, the dimensionless time Z, and the intra-conduction parameter K_r, these numbers are defined for a single pellet type bed as follows:

$$Y = \frac{a_S \alpha L_b}{u_s \rho_g C_{p,g}} \tag{5.42}$$

$$Z = \frac{a_S \alpha t_P}{\rho_b C_{p,b}} \tag{5.43}$$

$$K_r = \frac{\lambda_p}{\alpha R} \tag{5.44}$$

Where a_S represents the surface area of the particle, α is the heat transfer coefficient, u_s is the surface velocity, ρ_g is the gas density, $C_{p,g}$ is the gas heat capacity, ρ_b is the packing bulk density, $C_{p,b}$ is the packing heat capacity, t_P represents the period time of the operation, L_b the length of the bed and R is the radius of the pellet.

A more significant parameter is the utilisation factor [166], which is the ratio of heat flowing into the fixed bed to the heat capacity of the packings within the bed. Thus, the utilisation factor U is a dimensionless group defined as:

$$U = \frac{u_g \rho_g C_{p,g} t_P}{\rho_b C_{p,b} L_b} \tag{5.45}$$

The significance of the utilisation factor in the analysis of breakthrough curves is that it relates the quickness of the response of the bed to a given inlet fluid temperature and forcing function. Figure 5.3 is a plot of breakthrough curves expressed in terms of the normalised temperature (θ) defined in Equation (5.46), as a function of the utilisation factor for various fixed-beds with different values of dimensionless length (Y), subjected to a square-step forcing function.

$$\theta = \frac{T - T_i}{T_{in} - T_i} \tag{5.46}$$

As indicated by Equation (5.42), Y is a direct function of the heat transfer coefficient α, therefore, as this parameter tends to infinity the shape of the breakthrough curve approaches that of the forcing function at a value of $U = 1$.

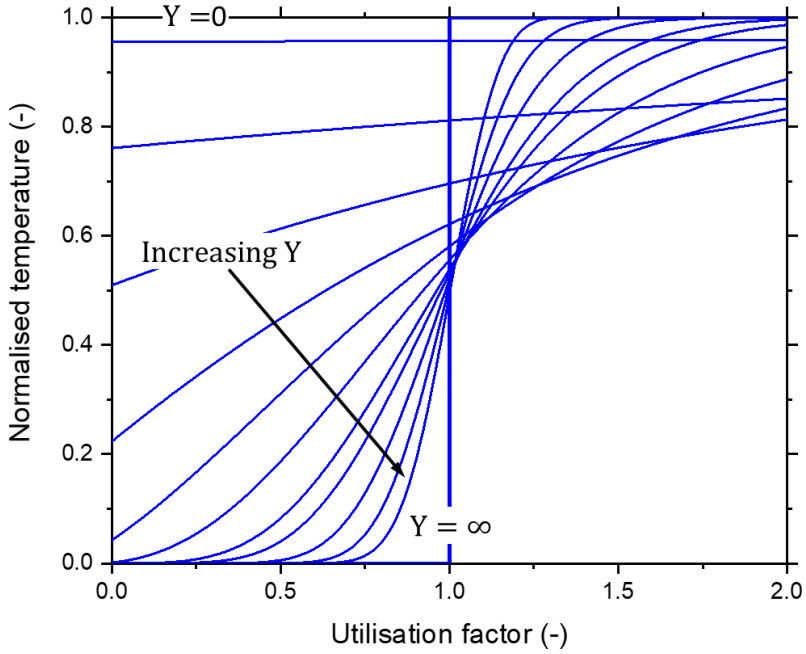

Figure 5.3 Breakthrough curves for a fixed bed of various Y.

The definition of utilisation factor in Equation (5.45) cannot be directly applied to a system with two type of packings as the one considered in this work. If the fixed bed is thought as a system comprised of two 'sub-beds' arranged in parallel, each of them with a characteristic dimensionless length and time, a utilisation factor for each packing can be written:

$$U_1 = \frac{u_g \rho_g C_{p,g} t_P}{\rho_{b_1} C_{p_1} L_b} \tag{5.47}$$

$$U_2 = \frac{u_g \rho_g C_{p,g} t_P}{\rho_{b_2} C_{p_2} L_b} \tag{5.48}$$

Where the parameters stand as defined before and the subindexes refer to the packings type 1 and 2. Equations (5.47) and (5.48) indicate that the utilisation of the heat capacity of each material on the bed will be different and dependent upon their thermal properties and the volumetric composition of that particular packing within the system. Hence the representation of the bed is related to an average utilisation factor, which is calculated by an harmonic expression as:

$$U = \frac{u_g \rho_g C_{p,g} t_P}{\left(\rho_{b_1} C_{p_1} + \rho_{b_2} C_{p_2}\right) L_b} \tag{5.49}$$

Equation (5.49) is consistent with Hausen's utilisation factor for a fixed bed packed with a single type of pellet. Noting that the volumetric heat capacities of

each type of packing are scaled by their respective volumetric fraction, the conditions $\gamma_1 = 0$ or $\gamma_1 = 1$ render Equation (5.45).

5.5 Numerical solution of the models

The Finite Differences Method is applied to develop a numerical solution of the Lagrangian Distributed Particle and Lumped models previously presented in section 5.4.1. The development of these solutions is discussed in this section.

5.5.1 Distributed particle model

The distributed model is a set of hyperbolic and parabolic PDE. The computational domain of this problem is a three dimensional mesh as illustrated in Figure 5.4. The mesh is subdivided into three separate domains namely the plane defined by the axis $N - I$ which physically represents the space-time region bounded by the period time τ and the bed length L, and the 3D regions formed by the axis $N - I - M$ and $N - I - P$, which incorporate the space region for each pellet radius r_1 and r_2. In these coordinated systems, N is the number of points in which the time period is divided and I is the number of subdivisions of the bed length; likewise, M and P are the number of subdivisions of the pellets' radii.

The solution for the gas temperature T_i^{n+1} at each node of the plane $N - I$ proceeds simultaneously with the solution for the solid temperatures ${T_1}_j^{n+1,i}$ and ${T_2}_k^{n+1,i}$ along the nodes of each row of the regions bounded by the axis $N - I - M$ and $N - I - P$; where the superscripts n, i represent the time and length coordinates of the gas and solid temperatures within the computational mesh at the bed scale, and the subscripts j, k represent the spatial coordinates of the solid temperatures nodes within the computational mesh at the particles' scale.

The discretisation of the heat balance at the fluid is worked out by central differences giving:

$$\begin{aligned} -C_{01}\Delta z {T_1}_m^{n+1,i} + [2 + \Delta z(C_{01} + C_{02})]T_i^{n+1} - C_{02}\Delta z {T_2}_p^{n+1,i} \\ = [2 - \Delta z(C_{01} + C_{02})]T_{i-1}^{n+1} + C_{01}\Delta z {T_1}_m^{n+1,i-1} \\ + C_{02}\Delta z {T_2}_p^{n+1,i-1} \end{aligned} \qquad \textbf{(5.50)}$$

For the heat conduction at the particles, the fully implicit backwards (FIB) finite differences (FD) scheme was applied, a solution with the Crank-Nicolson scheme [142] was also produced, the matrix solution for this method is presented in the **Appendix A**. The application of the FIB approach renders the following differences equations:

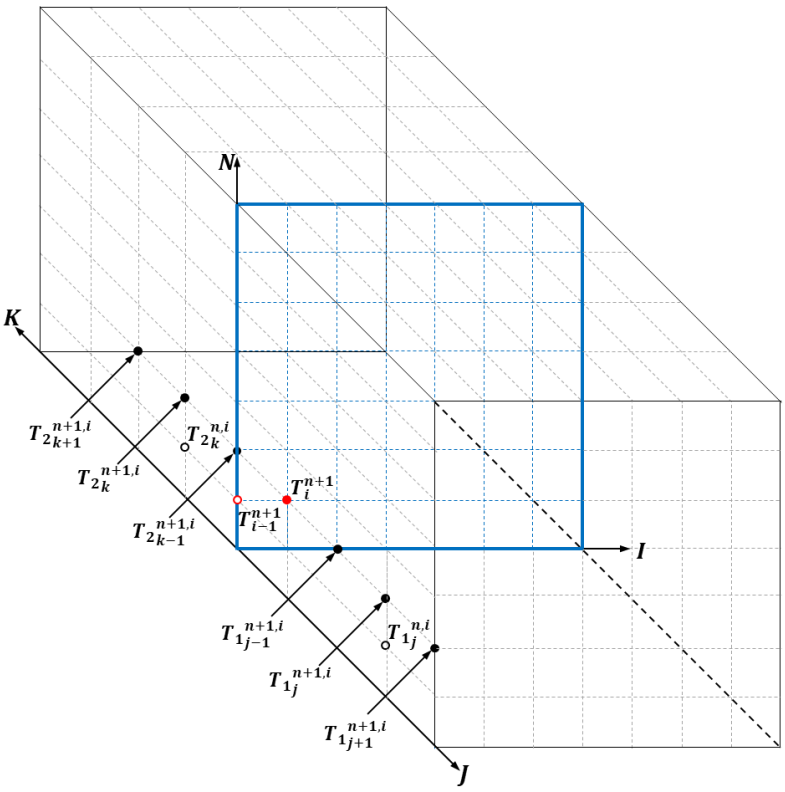

Figure 5.4 Computational domain of the numerical solution of the distributed particle model.

$$-\left(1+\frac{1}{j}\right)M_1 T_{1_{j+1}}^{n+1,i} + (1+2M_1)T_{1_j}^{n+1,i} - \left(1-\frac{1}{j}\right)M_1 T_{1_{j-1}}^{n+1,i} = T_{1_j}^{n,i} \qquad \textbf{(5.51)}$$

$$-\left(1+\frac{1}{k}\right)M_2 T_{2_{k+1}}^{n+1,i} + (1+2M_2)T_{2_k}^{n+1,i} - \left(1-\frac{1}{k}\right)M_2 T_{2_{k+1}}^{n+1,i} = T_{2_k}^{n,i} \qquad \textbf{(5.52)}$$

The parameters M_1 and M_2 are functions of the pellets' thermal diffusivities and the time and radius step sizes, and are defined as:

$$M_1 = \frac{\lambda_{p_1}}{\rho_{p_1} C_{p_1}} \frac{\Delta\tau}{(\Delta r_1)^2} \text{ and } M_2 = \frac{\lambda_{p_2}}{\rho_{p_1} C_{p_2}} \frac{\Delta\tau}{(\Delta r_2)^2} \qquad \textbf{(5.53)}$$

Equations (5.51) and (5.52) are valid in the regions $0 < r_1 < R_1$ and $0 < r_2 < R_2$, respectively; hence, their application at the packings surfaces result in the apparition of fictitious temperatures outside of the physical domain. These temperatures are eliminated by applying the boundary condition at $r_1 = R_1$ and at $r_2 = R_2$, represented in Equation (5.36); the discretised form of the boundary conditions is:

$$T_{1_{m+1}}^{n+1,i} - T_{1_{m-1}}^{n+1,i} = -C_1\left(T_{1_m}^{n+1,i} - T_i^{n+1}\right)$$
$$\text{and } T_{2_{p+1}}^{n+1,i} - T_{2_{p-1}}^{n+1,i} = -C_2\left(T_{2_p}^{n+1,i} - T_i^{n+1}\right) \qquad \textbf{(5.54)}$$

Where the constants C_1 and C_2 depend upon the step size, the heat transfer coefficient and the pellet thermal conductivity as follows:

$$C_1 = \frac{2\Delta r_1 \alpha_1}{\lambda_{p_1}} \text{ and } C_2 = \frac{2\Delta r_2 \alpha_2}{\lambda_{p_2}} \quad \textbf{(5.55)}$$

Substitution of Equation (5.54) in Equations (5.51) and (5.52) yields the final relationships to solve the pellets' temperatures at $r_1 = R_1$ and at $r_2 = R_2$:

$$-\left(1+\frac{1}{m}\right)C_1 M_1 T_i^{n+1} + \left[1 + M_1\left(2+\left(1+\frac{1}{m}\right)C_1\right)\right] T_{1_m}^{n+1,i} - 2M_1 T_{1_{m-1}}^{n+1,i} = T_{1_m}^{n,i} \quad \textbf{(5.56)}$$

$$-\left(1+\frac{1}{p}\right)C_2 M_2 T_i^{n+1} + \left[1 + M_2\left(2+\left(1+\frac{1}{p}\right)C_2\right)\right] T_{2_p}^{n+1,i} - 2M_2 T_{2_{p-1}}^{n+1,i} = T_{2_p}^{n,i} \quad \textbf{(5.57)}$$

At the centre of the particles, Equations (5.51) and (5.52) become indeterminate because of the substitution of the conditions $\frac{\partial T_k}{\partial r_k} = 0$ at $r_k = 0$ in the second term of the diffusive heat flux, where the index k refers to pellet 1 or 2. The indeterminate term $\frac{1}{r_k}\frac{\partial T_k}{\partial r_k}$ has the limit $\frac{\partial^2 T_k}{\partial r_k^2}$ so that Equations (5.33) and (5.34) become:

$$\rho_{p_1} C_{p_1} \frac{\partial T_1}{\partial \tau} = 3\lambda_{p_1} \frac{\partial^2 T_1}{\partial r_1^2} \; at \; r_1 = 0 \quad \textbf{(5.58)}$$

$$\rho_{p_2} C_{p_2} \frac{\partial T_2}{\partial \tau} = 3\lambda_{p_2} \frac{\partial^2 T_2}{\partial r_2^2} \; at \; r_2 = 0 \quad \textbf{(5.59)}$$

The application of FIB discretisation scheme to Equations (5.58) and (5.59) gives:

$$-3M_1 T_{1_1}^{n+1,i} + (1+6M_1) T_{1_0}^{n+1,i} - 3M_1 T_{1_{-1}}^{n+1,i} = T_{1_0}^{n,i} \quad \textbf{(5.60)}$$

$$-3M_2 T_{2_1}^{n+1,i} + (1+6M_2) T_{2_0}^{n+1,i} - 3M_2 T_{2_{-1}}^{n+1,i} = T_{2_0}^{n,i} \quad \textbf{(5.61)}$$

The hypothetical temperatures $T_{1_{-1}}^{n+1,i}$ and $T_{2_{-1}}^{n+1,i}$ obtained in Equations (5.60) and (5.61) are eliminated by incorporating the symmetry condition at $r_1 = 0$ and at $r_2 = 0$, which in its discretised form is:

$$\frac{T_{1_1}^{n+1,i} - T_{1_{-1}}^{n+1,i}}{2\Delta r_1} = 0 \text{ and } \frac{T_{2_1}^{n+1,i} - T_{2_{-1}}^{n+1,i}}{2\Delta r_2} = 0 \quad \textbf{(5.62)}$$

By substituting Equation (5.62) into Equations (5.60) and (5.61) the finite difference representation at the centre of the particles is obtained as follows:

$$-6M_1 T_{1_1}^{n+1,i} + (1+6M_1) T_{1_0}^{n+1,i} = T_{1_0}^{n,i} \quad \textbf{(5.63)}$$

$$-6M_2 T_{2_1}^{n+1,i} + (1 + 6M_2) T_{2_0}^{n+1,i} = T_{2_0}^{n,i} \quad \textbf{(5.64)}$$

The solution of the Distributed Particle model is mathematically represented by a linear system $Ax = b$ formed by Equations (5.50), (5.51), (5.52), (5.56), (5.57), (5.63) and (5.64), where A is a sparse matrix of $(J + K + 1) \times (J + K + 1)$ elements, x is the vector of unknown temperatures at the time level $n + 1$, and b is the independent vector calculated with known values at the time level n.

5.5.2 Lumped model

The lumped model is a system of first-order hyperbolic partial differential equations. The numerical integration of this class of PDEs for the square-step boundary condition is difficult to attain due to the propagative nature of the equations [139]. Heggs and Handley [152] presented an explicit numerical scheme of the lumped model for a single packing system based on the application of central finite differences evaluated at the half point. Their solution is implemented in this work and extended to the case of two types of packing.

The computational domain for this problem is a mesh formed in the plane defined by the axis $\tau - Z$ which physically represents the space-time region bounded by the period time τ and the bed length L as shown in Figure 5.5. The gas and the solid temperatures, T_i^{n+1}, $T_{1_i}^{n+1}$ and $T_{2_i}^{n+1}$ are calculated simultaneously at each node of the mesh, provided that values of T_i^n, $T_{1_i}^n$, $T_{2_i}^n$, and T_{i-1}^{n+1}, $T_{1_{i-1}}^{n+1}$, $T_{2_{i-1}}^{n+1}$ are available.

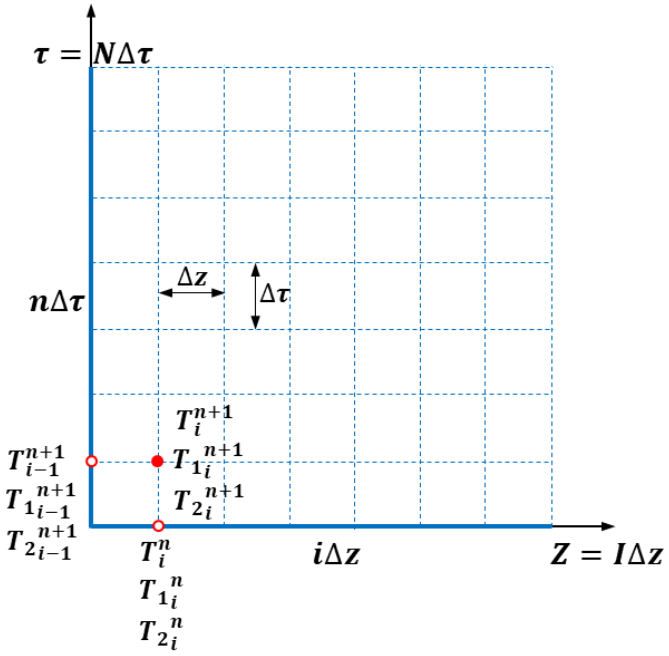

Figure 5.5 Computational domain of the numerical solution of the lumped model.

The application of central differences to Equations (5.38) to (5.40) yields the following system of linear algebraic equations:

$$[2 + A_1 + A_2]T_i^{n+1} - A_1 {T_{S_1}}_i^{n+1} - A_2 {T_{S_2}}_i^{n+1} = [2 - A_1 - A_2]T_{i-1}^{n+1} + A_1 {T_{S_1}}_{i-1}^{n+1} + A_2 {T_{S_2}}_{i-1}^{n+1} \quad \textbf{(5.65)}$$

$$-A_3 T_i^{n+1} + (2 + A_3){T_{S_1}}_i^{n+1} = A_3 T_i^n + (2 - A_3){T_{S_1}}_i^n \quad \textbf{(5.66)}$$

$$-A_4 T_i^{n+1} + (2 + A_4){T_{S_2}}_i^{n+1} = A_4 T_i^n + (2 - A_4){T_{S_2}}_i^n \quad \textbf{(5.67)}$$

Where A_1, A_2, A_3 and A_4 are model constants dependent upon the fluid and packings properties and the heat transfer coefficient, and are defined as:

$$A_1 = \frac{\alpha_1 a_{S_1} \Delta z}{u_s \rho_g C_{p,g}} \text{ and } A_2 = \frac{\alpha_2 a_{S_2} \Delta z}{u_s \rho_g C_{p,g}} \quad \textbf{(5.68)}$$

$$A_3 = \frac{\alpha_1 a_{S_1} \Delta \tau}{\rho_{b_1} C_{p_1}} \text{ and } A_4 = \frac{\alpha_1 a_{S_1} \Delta \tau}{\rho_{b_2} C_{p_2}} \quad \textbf{(5.69)}$$

5.5.3 Stability and convergence of the numerical solutions

When using numerical techniques, a sufficient condition to attain convergence to the solution of a set of PDE is to ensure the stability of the numerical scheme [138]. Thus, when developing numerical solutions it is necessary to incorporate mechanisms into the algorithm that guarantees this condition.

Various criteria can be applied to determine the condition of stability of parabolic and hyperbolic PDE. For the distributed particle model presented in this work, the Greschgorin [138] theorem is applied giving the following general stability criteria:

$$\Delta\tau_1 = \frac{(\Delta r_1)^2}{\frac{\lambda_{p_1}}{C_{p_1}\rho_{p_1}}\left[2 + \frac{2\Delta r_1 \alpha_1}{\lambda_{p_1}}\left(1 + \frac{1}{m}\right)\right]} \quad \textbf{(5.70)}$$

$$\Delta\tau_2 = \frac{(\Delta r_2)^2}{\frac{\lambda_{p_2}}{C_{p_2}\rho_{p_2}}\left[2 + \frac{2\Delta r_2 \alpha_2}{\lambda_{p_2}}\left(1 + \frac{1}{p}\right)\right]} \quad \textbf{(5.71)}$$

Where $\Delta\tau_1$ and $\Delta\tau_2$ are the time-step sizes that ensure stability of the algorithm and are dependent upon the physical properties, dimensions and the number of discretisation points of each pellet. Hence, for overall stability the minimum value between $\Delta\tau_1$ and $\Delta\tau_2$ should be selected, therefore:

$$\Delta\tau = min(\Delta\tau_1, \Delta\tau_2) \quad \textbf{(5.72)}$$

The time step size is calculated at the beginning of the calculation process and remains constant throughout the period time during the integration of the set of PDE.

For hyperbolic PDEs, Cockcroft [167] applied the Fourier series method to analyse different numerical schemes for the approximation of the pseudo-homogeneous and heterogeneous Lagrangian and Eulerian models of a single shot regenerator and found that the central-central approximation for the temporal and spatial partial derivatives of the Lagrangian model yielded a stable scheme, therefore, the numerical solution for the lumped model is deemed stable and convergent.

5.6 Results and discussion

5.6.1 Convergence of the model solutions

The convergence of the models was investigated to assess the quality of the numerical approximations. Although the implicit approach utilised in the numerical solution of the Distributed Particle Model is unconditionally stable, it can be affected by the values of the model parameters or the mesh size and, therefore, it is recommended to investigate the integration step size to ensure that the numerical solution is stable, and hence, convergent [138]. Series of simulations were conducted for packed beds whose parameters are summarised in Table 5.2.

Figure 5.6(a) and (b) are plots of the breakthrough curves for Case 1 of Table 5.2 obtained by the finite differences method implemented in this work (labelled as mCFDLF) and by gPROMS (labelled gCFDLF), respectively. Several length increments (5, 10, 20, and 50) have been considered and for the sake of comparison the discretisation scheme selected in gPROMS was the Central Differences of order 2. In addition the time step utilised in the mCFDLF algorithm was set to $\Delta t = 0.1$. The convergence of both algorithms was compared against the solution of gPROMS calculated with 100 discretisation points in length, which served as an “analytical” solution for this case. The results indicate that the numerical solution of the mCFDLF algorithm converges slightly more quickly than that obtained by the method of lines shown in Figure 5.6(b). However, for a very low number of length increment some degree of error is introduced in the prediction of the breakthrough curve with both methods. These errors might be related to the values taken by the eigenvalues of the matrices that represent the numerical solution to the problem, which are associated to the coefficients of the

differences equations defined in Equations (5.65)–(5.67), which relate to the step-size in the time and length domains.

Table 5.2 Parameters of the packed beds utilised for the analysis of the convergence of the numerical schemes.

Parameter	Case 1	Case 2
Gas temperature (K)	883.2	1073.2
Gas superficial velocity (m s^{-1})	1.1	6.0
Gas density (kg m^{-3})	6.97	0.32
Gas heat capacity (J kg^{-1} K^{--1})	2483.7	1157.6
Packing density (kg m^{-3})	3630.0	3340.0
Packing heat capacity (J kg^{-1} K^{--1})	1200.2	1051.5
Packing thermal conductivity (J kg^{-1} K^{-1} s^{-1})	2.1	8.5
Packing diameter (m)	0.010	0.010
Mean bed voidage (m^3 m^{-3})	0.37	0.37
Packing surface area (m^2 m^{-3})	373.0	370.8
Heat transfer coefficient (W m^{-2} K^{-1})	1124.2	227.9
Bed length (m)	0.45	0.25
Bed dimensionless length (-)	9.82	9.55
Dimensionless time (-)	23.22	19.47
Bed K_r number (-)	0.37	7.46

For the sake of comparison, both models where resolved with a coarse mesh for the same number of discretisation points in length as above, but in this case the time domain was discretised with a number of points that was set as the double of those used for the spatial domain. The convergence of the methods to the final solution is illustrated in Figure 5.7(a) and (b). Similarly to the previous solution, the algorithm developed in this thesis exhibited slightly better convergence than the algorithm of gPROMS, it is worth noting however, that the gPROMS algorithm losses efficiency when the temporal derivative is declared explicitly, thus the slower convergence in Figure 5.7(b).

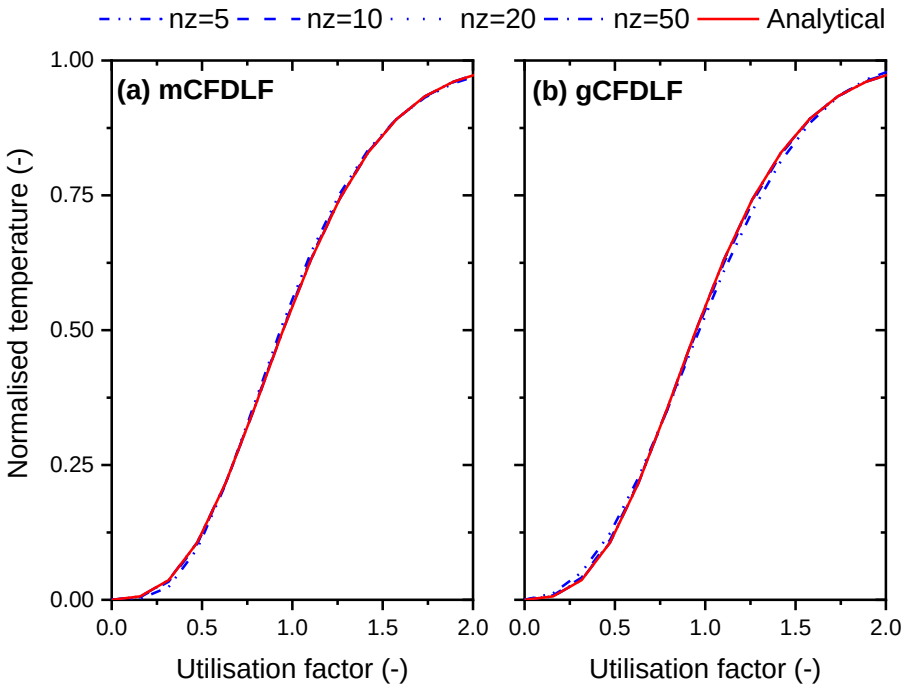

Figure 5.6 Breakthrough curves calculated from the numerical solution of the Lagrangian lumped model with the numerical scheme developed in this thesis (mCFDLF) and with gPROMS (gCFDLF); the solution is shown for Case 1 using a fine mesh.

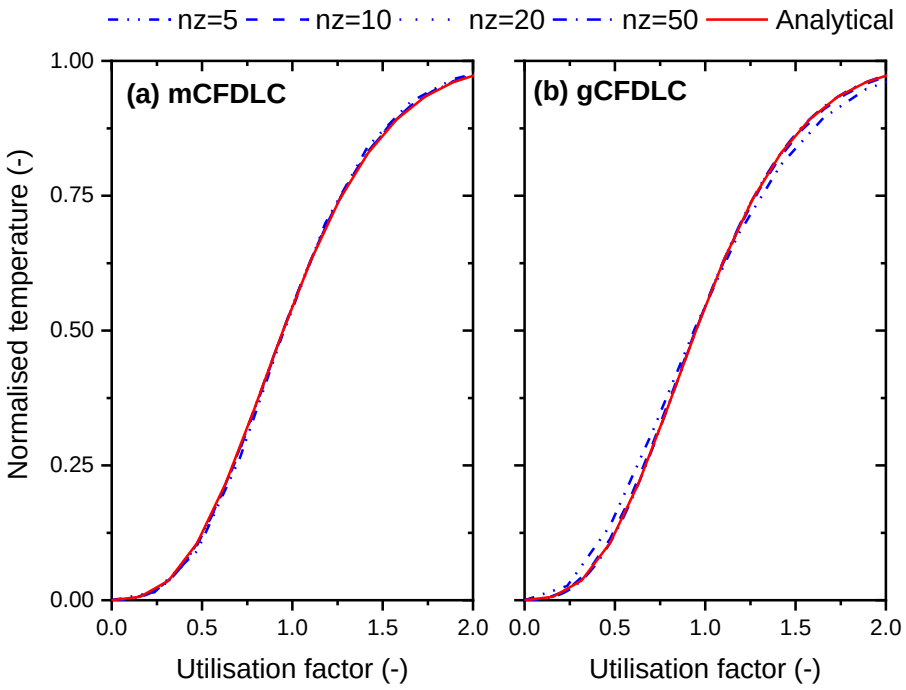

Figure 5.7 Breakthrough curves calculated from the numerical solution of the Lagrangian lumped model with the numerical scheme developed in this thesis (mCFDLF) and with gPROMS (gCFDLF); the solution is shown for Case 1 using a coarse mesh.

The distributed model was analysed in a similar fashion as the lumped model. Studies of convergence were performed varying the number of discretisation points in the bed and pellet domain from 5, 10, 20 and 50. In this case the time increment was determined by applying the Equations (5.70) – (5.72) for the FIB method (labelled as mFIBLF), while for the gPROMS solution (labelled gCFDLF) was determined by the software algorithm. In addition, a solution with the Crank-Nicholson scheme was calculated setting $\Delta t = 0.1$. The convergence of the three algorithms was compared against the solution of gPROMS calculated with 100 discretisation points in length and in the pellet radius, which served as an “analytical” solution for this case.

Unlike the lumped model, the convergence of the distributed model did not show a meaningful improvement with the increasing number of discretisation points, as it can be seen in Figure 5.8(a), (b) and (c). The reason for this might relate with different factors, namely the dimensions of the physical domain or the small time integration step selected to search the numerical solution. Moreover, the presence of the parabolic equation in the system produces a smooth solution as opposed to the hyperbolic system where the numerical integration struggles to handle the type of boundary condition imposed in this problem.

However, if the problem is solved in a coarse mesh where the number of discretisation points in time is set as $nt = 2 * nz$, with nz being the number of discretisation points in length, the FIB method (labelled mFIBLC) exhibits a much slower convergence, particularly in the leading zone of the breakthrough curve, in comparison with the Crank-Nicolson scheme (labelled mCNLC), as shown in Figure 5.9(a) and (b).

Therefore, it can be concluded that the schemes developed in this thesis are convergent and stable, and in order to ensure convergence the number of discretization points in length should be kept greater than 50, whereas for time an increment of $\Delta t = 0.1$ seems to suffice.

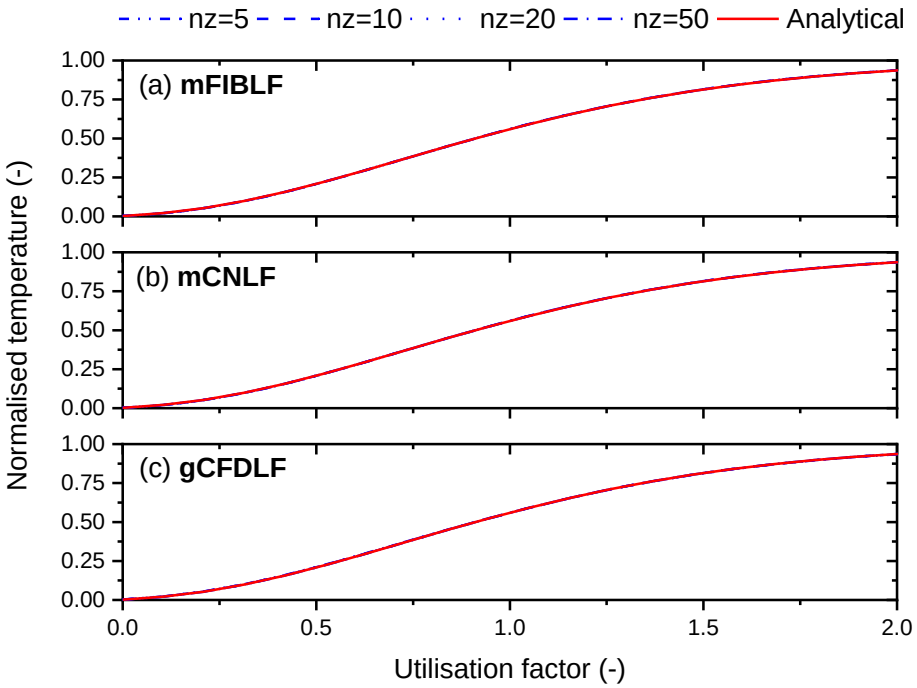

Figure 5.8 Breakthrough curves calculated with (a) the FIB algorithm of this work, (b) the Crank-Nicolson algorithm of this work and (c) the gPROMS solution.

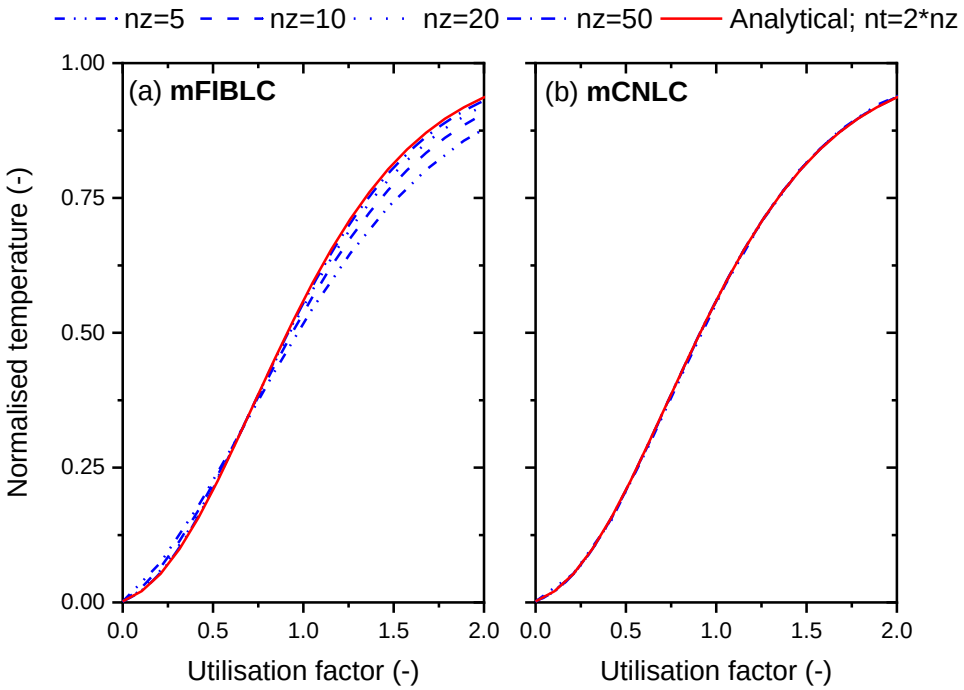

Figure 5.9 Breakthrough curves calculated with (a) the FIB algorithm of this work, (b) the Crank-Nicolson algorithm of this work using a coarse mesh.

5.6.2 Investigation of the modelling of packed beds with single packings of relevant materials for the SE-CLSR reactor.

The selection of the distributed or the lumped model to represent a packed bed can be supported with the analysis of the bed parameters. The Biot number ($Bi = \alpha d_p/\lambda_p$) has been used as the typical criteria to determine the presence of intrapellet conduction effects in a system, with $Bi \ll 1$ an indicator of a packing operating free of thermal gradients [168, 169]. For a single pellet type bed, Handley and Heggs (7) suggested that the use of the Biot number might lead to an inadequate assessment of the presence of intra-pellet conduction and proposed the dimensionless parameter YK_r defined by Equation (52), as a dividing line between the lumped and the distributed models; where Y is the dimensionless bed length and K_r is twice the reciprocal of the Biot number. A value of $YK_r > 60$ signifies that minimal or negligible conduction effects are present, thus the lumped model produces an appropriate description of the system.

$$YK_r = \frac{3\lambda_p(1-\varepsilon_b)L_b}{u_s\rho_g C_{p,g}R^2} \qquad \textbf{(5.73)}$$

Where λ_p is the packing thermal conductivity, L_b is the bed length, ε_b is the mean bed voidage, R is the packing radius, u_s is the superficial velocity, ρ_g is the bulk gas density and $C_{p,g}$ is the bulk gas heat capacity. To assess the presence of intra-particle gradients in packed beds filled with packing materials relevant to the SE-CLSR reactor, such as alumina, calcium oxide and calcium carbonate, three systems with characteristic values of YK_r above and below the dividing line were simulated with the distributed particle model, and with the lumped model. The parameters utilised in each simulation are summarised in Table 5.3.

Figure 5.10(a) and (b) are plots of breakthrough curves predicted with the distributed pellet and the lumped models for two fixed beds packed with alumina packings with $YK_r = 9.4$ and $YK_r = 90.5$ as indicated in Cases 1a and 1b in Table 5.3. According to these values, the system of Case 1a is likely to develop intra-pellet thermal gradients and would be better represented by the distributed particle model, whereas for Case 1b the lumped model would provide an accurate description of the system. However, an inspection of the Biot number for each case lead to the conclusion that both systems are likely to develop intra-pellet gradients and therefore, the distributed particle model should be utilised to simulate the system.

The plots of breakthrough curves for Case 1a are shown in Figure 5.10(a); it is visible that the distributed model predicts a breakthrough curve with a longer heat

transfer zone in comparison to that resulting from the solution of the lumped model; conversely, in Figure 5.10(b) the breakthrough curves of Case1b predicted with both models converge to the practical same solution, with an average difference less than 1%. As mentioned above, the difference between the systems of Cases 1a and 1b is the working fluid that exchange heat with the packings. Therefore, it is clear that in these cases the differences in the physical properties of the fluids are critical to define the thermal behaviour of each system and, consequently, it is useful to check the value of the YK_r parameter before deciding which model to implement. Moreover, Figure 5.10(a) indicate that if the prediction of the dynamic behaviour of the system with $YK_r = 9.4$, were simulated with the lumped model, it would introduce an error in the estimation of the temperature profiles and saturation time, thus impacting the modelling results of this unit and, most likely those of other models linked to it.

Similar results are obtained for Cases 2a and 2b; these systems contain calcium carbonate packings whose thermal properties are similar to those of the alumina packings used for the simulation of Cases 1a and 1b. Thus, the YK_r parameter for each bed as well as the Biot number are similar to Cases 1a and 1b, provided that the remaining simulation inputs are the same as shown in Table 5.3. The breakthrough curves obtained for Cases 2a and 2b are shown in Figure 5.11.

When the packing is made of calcium oxide as is for Cases 3a and 3b, higher values of the YK_r parameter are obtained due to the higher thermal conductivity of this material. In fact, this thermal property is about four fold that of alumina and calcium carbonate, therefore the values of K_r and YK_r are larger in these systems. This indicates that the system can be confidently modelled using the simple model as the main thermal resistance will be due to the gas film rather than the thermal gradients in the packing. This is confirmed in Figure 5.12(a) and (b) which are plots of the breakthrough curves of two packed beds filled with CaO packings. System (a) has a $YK_r = 37.9$, whereas system (b) has a $YK_r = 366.2$. The former is just below the threshold of $YK_r = 60$ and should exhibit the effect of thermal gradients to a certain degree, whereas the latter is well above $YK_r = 60$, and hence no thermal gradients are expected. In practice, both systems are fairly represented with the lumped model as shown in Figure 5.12(a) and (b). In fact, the average error in the models is barely 0.84% for Case 3a and 0.12% for Case 3b.

Table 5.3 Bed parameters and properties of the fluid and the particle for each of the cases analysed.

Parameter	Case 1a	Case 1b	Case 2a	Case 2b	Case 3a	Case 3b
Gas density (kg m^{-3})	6.9	1.6	6.9	1.6	6.9	1.6
Gas heat capacity (J kg^{-1} K^{--1})	2597.7	1149.6	2597.7	1149.6	2597.7	1149.6
Packing density (kg m^{-3})	3630.0	3630.0	2710.0	2710.0	3340.0	3340.0
Packing heat capacity (J kg^{-1} K^{--1})	1195.9	1195.9	1240.7	1240.7	943.4	943.4
Packing thermal conductivity (J kg^{-1} K^{-1} s^{-1})	2.1	2.1	2.3	2.3	8.5	8.5
Mean bed voidage (m^3 m^{-3})	0.37	0.37	0.37	0.37	0.37	0.37
Dimensionless bed length (-)	28.1	48.5	28.1	48.5	28.1	48.5
Dimensionless time (-)	57.5	99.3	58.3	99.7	56.6	101.3
Bed YK_r number (-)	9.4	90.5	10.0	96.9	37.9	366.2
Biot number (-)	6.0	1.1	5.6	1.0	1.5	0.3

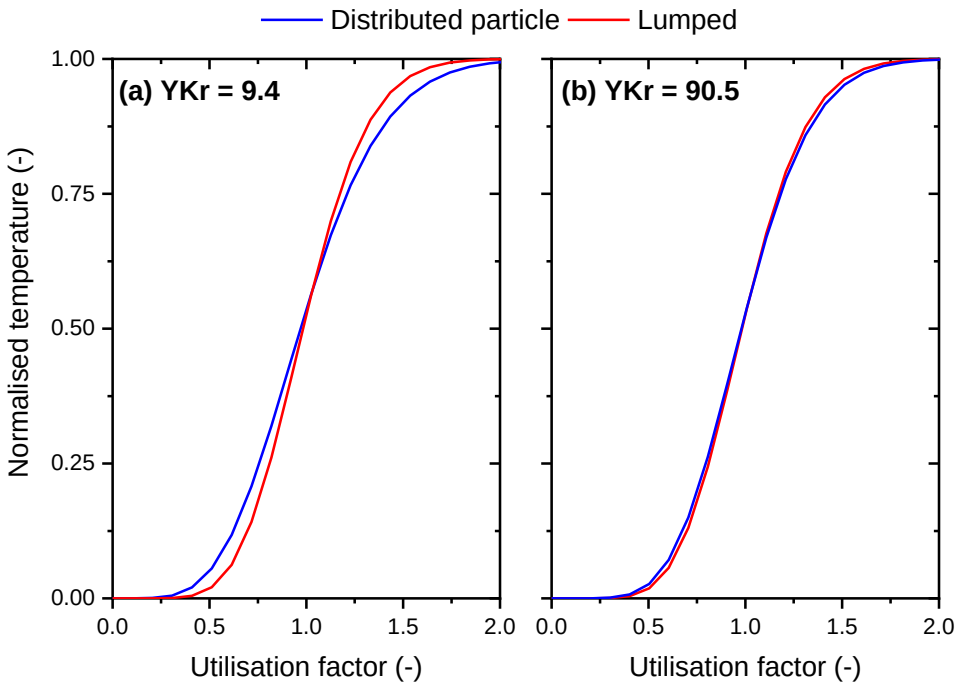

Figure 5.10 Breakthrough curves of a packed bed with 0.01 m diameter spherical alumina packings (a) Case 1a (b) Case 1b.

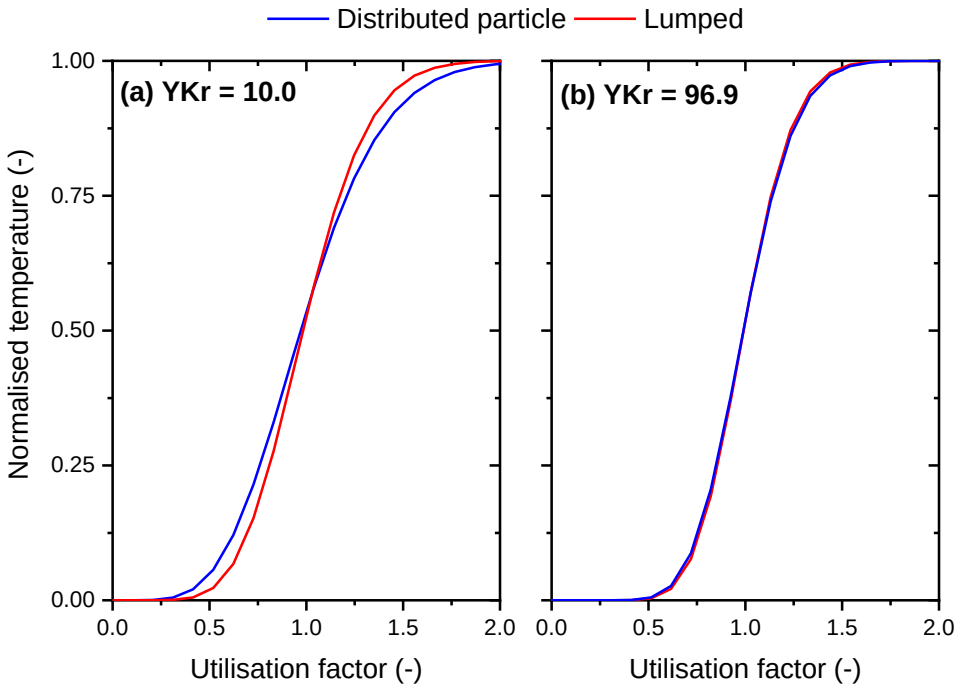

Figure 5.11 Breakthrough curves of a packed bed with 0.01 m diameter spherical calcium carbonate packings (a) Case 1a (b) Case 1b.

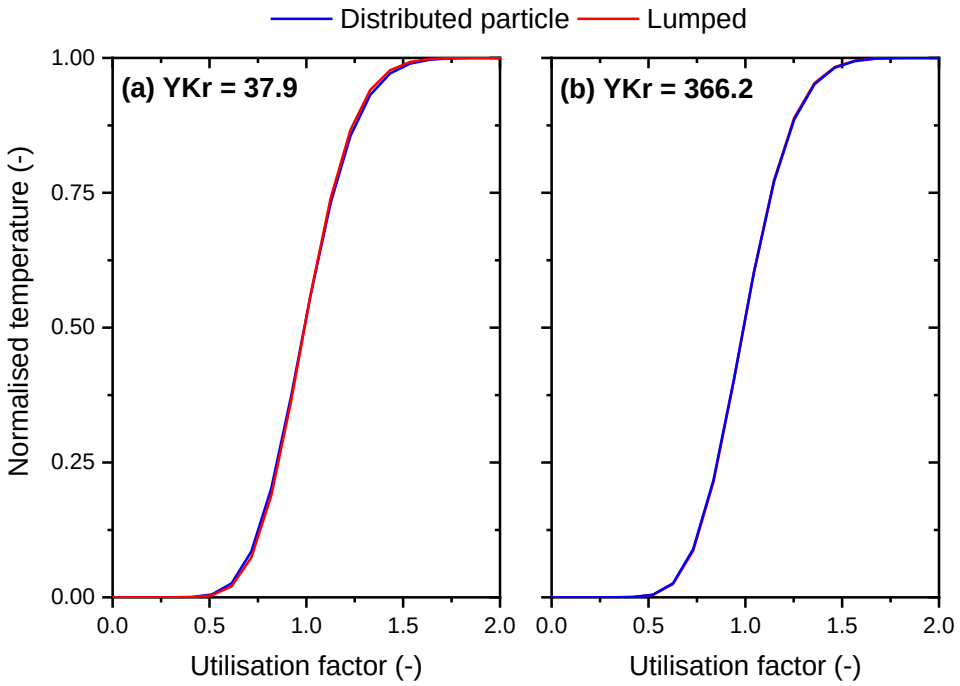

Figure 5.12 Breakthrough curves of a packed bed with 0.01 m diameter spherical calcium oxide packings (a) Case 1a (b) Case 1b.

5.6.3 Application of the models to fixed beds of mixtures of particles

5.6.3.1 Effect of the composition of the bed

In packed beds with mixtures of packings, the system is likely to exhibit a response that falls in between those of their individual packing materials. The extent of the change of the bed behaviour is related with the volumetric amount of each packing in the bed. The YK_r relationship of Equation (5.73) can be applied to assess a priori whether the system can be modelled with a lumped model or with the distributed particle model, if the weighted average thermal conductivity λ_p, and an average pellet diameter d_p obtained from Equation (5.30) are used; the weighted averaged thermal conductivity can be estimated as:

$$\lambda_p = \gamma_1 \lambda_{p,1} + \gamma_2 \lambda_{p,2} \qquad \textbf{(5.74)}$$

Where γ_1 represents the volumetric fraction of the packing of type 1, and $\gamma_2 = 1 - \gamma_1$ represents the volumetric fraction of the packing of the type 2. Table 5.4 summarises the values of YK_r obtained for a fixed bed of length 1 m, packed with different volumetric fractions alumina and calcium oxide packings

of 0.01 m of diameter, and exchanging heat with gas with $G = 7.59\ kg\ m^{-2}s^{-1}$, $C_{p,g} = 2597.7\ J\ kg^{-1}K^{-1}$.

Table 5.4 Packing average thermal conductivity λ_p and YK_r parameter of several packed beds with different volumetric fractions of packing 1 and 2. γ_1 represents the volumetric fraction of alumina.

Parameter	$\gamma_1 = 0$	$\gamma_1 = 0.25$	$\gamma_1 = 0.5$	$\gamma_1 = 0.75$	$\gamma_1 = 1.0$
$\lambda_p\ (J\ s^{-1}m^{-1}K^{-1})$	8.5	6.9	5.3	3.7	2.1
$YK_r\ (-)$	32.2	26.1	20.1	14.0	8.0

According to the values of the YK_r numbers shown in Table 5.4, the five beds should be simulated with the distributed model, however, for the sake of comparison, all systems were also simulated with the lumped model. Figure 5.13(a) and (b) are plots of breakthrough curves in dimensionless form of a packed bed filled with five combinations of alumina (packing 1) and calcium oxide (packing 2) according to the volumetric fraction of alumina listed in Table 5.4. The breakthrough curves presented in Figure 5.13(a) were calculated with the distributed particle model, which subsequently will be referred to as the DPM, whereas the breakthrough curves presented in Figure 5.13(b) where calculated with the lumped model (LM). As expected, two different behaviours where obtained for each modelling approach. When the DPM is utilised to predict the breakthrough curves (Figure 5.13(a)), the effects of the volumetric fraction of alumina in the bed are observed in the slope of the breakthrough curve, which decreases with the increasing value of γ_1, producing a curve with a gradient slightly smoother than that obtained from the simple model. This behaviour implicates an earlier breakthrough and a late saturation times, rendering a longer heat transfer zone, and a longer saturation period. Conversely, the LM predicts the same dimensionless response of the bed irrespective of the volumetric fraction of each packing (Figure 5.13(b)); thus the lumped model predicts a constant length of the heat transfer zone with the breakthrough and saturation points happening at approximately the same values of bed utilisation.

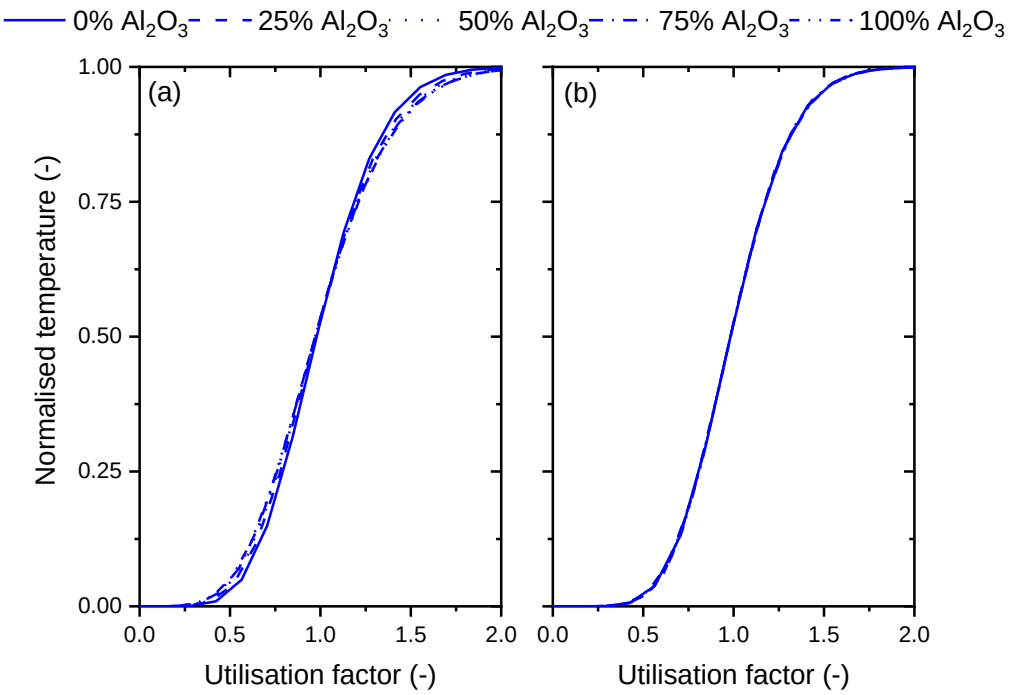

Figure 5.13 Breakthrough curves for various fixed beds with different volumetric fraction of alumina packings, calculated with the distributed particle model (a) and the lumped model (b).

Physically, the curves plotted in Figure 5.13 represent packed beds that will saturate at different velocities, with different breakthrough and saturation times. Figure 5.14 is a plot of the dimensional temperature versus the time of the various breakthrough curves calculated with the DPM and the LM approaches. This plot illustrates two situations, on the one hand, the saturation time increases with the increasing volumetric fraction of alumina in the bed γ_1, producing families of responses whose behaviour is intermediate of the cases of packed beds with either alumina ($\gamma_1 = 1$) or calcium oxide ($\gamma_1 = 0$). On the other hand, the response of the bed deviates from the simple model with the increase of γ_1, even in the cases where $\gamma_2 > \gamma_1$, with the greatest errors being exhibited in the rear zone of the breakthrough curve.

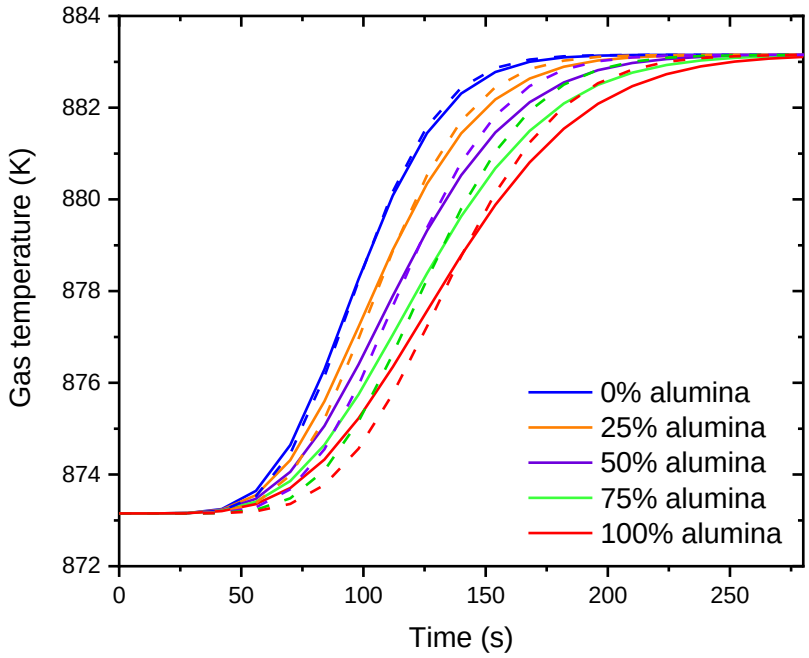

Figure 5.14 Temperature breakthrough curves for various fixed beds with different volumetric fraction of alumina packings, calculated with the distributed particle model (solid line) and the lumped model (dashed line).

The previous results indicate that for the type of materials utilised in the SE-CLSR reactor, the DPM approach should be applied when high accuracy of the temperature profile is required. This is not computationally expensive for linear systems. However, when non-linear systems are considered, the computational time might become prohibitive, and sway the decision to include or exclude certain physical features of the model.

In the particular application to the SE-CLSR reactor the various physical phenomena surrounding the system will result in a highly non-linear model and applying the DPM approach to this model might prove unaffordable from the computing time point of view. Moreover, the numerical solution of the model would increase the number of DAE involved raising the difficulty in establishing a set of solutions. Therefore, a modelling approach that simplifies the model solution maintaining the accuracy level should be sought.

Two approaches to render a simpler albeit accurate model are considered here, namely, the use of a hybrid model (HYM), in which the material exhibiting refractory properties is modelled with a distributed particle model, whereas the material exhibiting high thermal conductivity is modelled with a lumped model. The second approach is the application of an effective heat transfer

coefficient, this approach will be referred to as the EHTCM. Various expressions have been proposed for the effective heat transfer coefficient, the one used in this project is that of Xu et al. [168] who for spherical particles proposed the following expression:

$$\frac{1}{\alpha_e} = \frac{1}{\alpha} + \frac{d_p}{10\lambda_p} \quad \textbf{(5.75)}$$

Where $\alpha_e$is the effective heat transfer coefficient, α is the HTC calculated from one of the known correlations, λ_p is the thermal conductivity of the particle, and d_p is the particle diameter.

The aforementioned simplified approaches were applied to the five cases of packed beds listed in Table 5.4, and examples of the results are demonstrated in Figure 5.15 and Figure 5.16. Figure 5.15 is a plot of the breakthrough curves obtained with the DPM, the LM, the HYM and the EHTCM approaches for a packed bed filled with 25v/v% of alumina pellets of 0.01m of diameter and 75v/v% of calcium oxide particles of the same size. In Figure 5.16 the performance of each simplification is shown for the case of the packed be filled with 75v/v% of alumina packings and 25v/v% of calcium oxide packings, both with the same particle diameter of 0.01 m. For all the simulated cases, the highest error was obtained with the lumped model, and the lowest error was obtained with the EHTCM approach as summarised in Table 5.5. The HYM approach shows an improvement over the LM approach for all the cases, however with higher errors than the EHTCM approach in all the cases except that for $\gamma_1 = 1.0$ which represents the case of 100v/v% of alumina packings. Moreover, the accuracy obtained with this approach increases with the larger values of γ_1. The reason for this behaviour is that as the amount of the refractory packing increases the response of the bed to the heat transfer operation will be dominated by this material due to a higher heat transfer area, hence, the error induced by the use of the lumped model for the second material will be reduced.

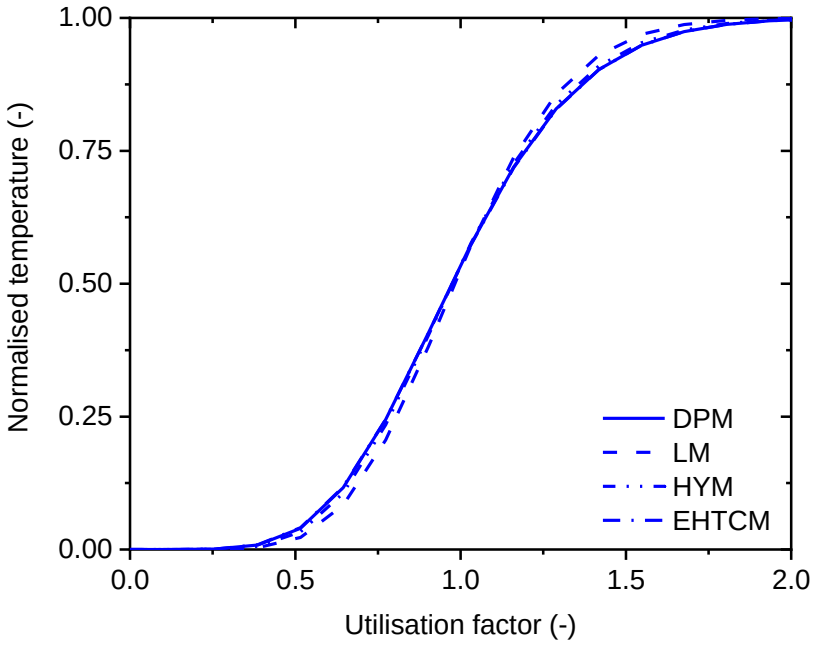

Figure 5.15 Breakthrough curve obtained with various modelling approaches for a fixed bed packed with a mixture of 25 v/v% of 0.01 m diameter alumina packings and 75 v/v% of 0.01 m diameter calcium oxide packings.

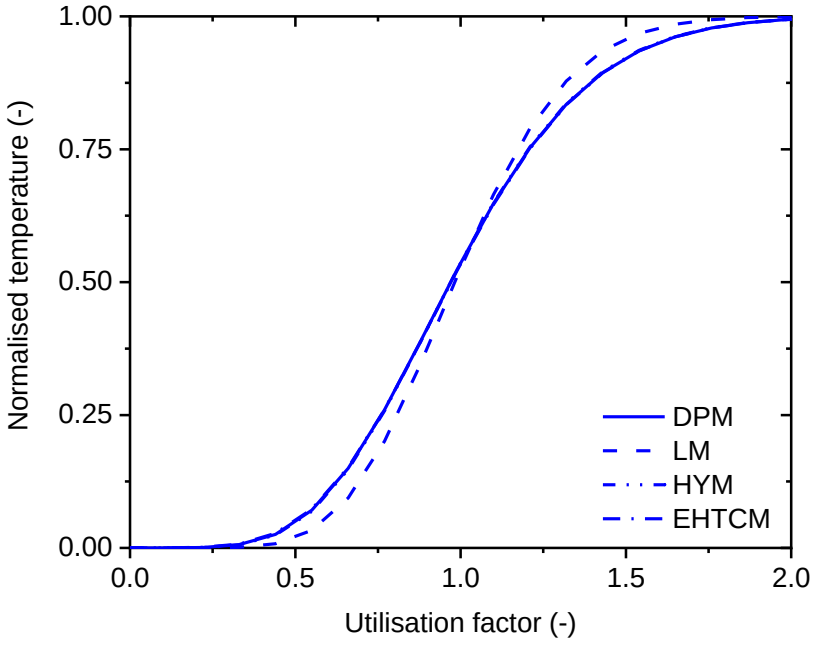

Figure 5.16 Breakthrough curve obtained with various modelling approaches for a fixed bed packed with a mixture of 75 v/v% of 0.01 m alumina packings and 25 %/vv of 0.01 m calcium oxide packings.

Table 5.5 Error percentage in the calculation of breakthrough curves with different modelling approaches for fixed beds packed with mixtures of 0.01m spherical packings exchanging heat with a stream of hot gas.

Case	**PBD10F00**						
Description	Fixed bed packed with 100% of calcium oxide pellets						
Breakthrough	DPM	LM	% Error	HYM	% Error	EHTCM	% Error
10%	0.636	0.659	**-3.63%**	0.659	**-3.64%**	0.636	**0.04%**
30%	0.835	0.848	**-1.60%**	0.848	**-1.60%**	0.835	**0.00%**
50%	0.980	0.983	**-0.30%**	0.983	**-0.29%**	0.980	**-0.01%**
70%	1.136	1.127	**0.76%**	1.127	**0.76%**	1.136	**-0.02%**
90%	1.385	1.363	**1.61%**	1.363	**1.60%**	1.385	**-0.01%**
Case	**PBD10F25**						
Description	Packed bed with 25% of alumina packings and 75% calcium oxide packings						
Breakthrough	DPM	LM	% Error	HYM	% Error	EHTCM	% Error
10%	0.617	0.662	**-7.28%**	0.634	**-2.78%**	0.615	**0.33%**
30%	0.818	0.843	**-3.07%**	0.824	**-0.76%**	0.818	**0.01%**
50%	0.974	0.983	**-0.89%**	0.975	**-0.08%**	0.975	**-0.08%**
70%	1.143	1.131	**1.05%**	1.138	**0.43%**	1.144	**-0.10%**
90%	1.413	1.366	**3.36%**	1.401	**0.85%**	1.414	**-0.04%**
Case	**PBD10F50**						
Description	Fixed bed packed with 50% of alumina packings and 50% calcium oxide packings						
Breakthrough	DPM	LM	% Error	HYM	% Error	EHTCM	% Error
10%	0.604	0.658	**-8.81%**	0.611	**-1.04%**	0.602	**0.35%**
30%	0.809	0.845	**-4.49%**	0.812	**-0.43%**	0.809	**-0.01%**
50%	0.971	0.983	**-1.22%**	0.971	**-0.02%**	0.972	**-0.12%**
70%	1.150	1.132	**1.54%**	1.147	**0.25%**	1.151	**-0.14%**
90%	1.433	1.365	**4.78%**	1.424	**0.65%**	1.434	**-0.08%**
Case	**PBD10F75**						
Description	Fixed bed packed with 75% of alumina packings and 25% calcium oxide packings						
Breakthrough	DPM	LM	% Error	HYM	% Error	EHTCM	% Error
10%	0.590	0.666	**-12.82%**	0.593	**-0.50%**	0.588	**0.46%**
30%	0.804	0.844	**-5.03%**	0.805	**-0.16%**	0.804	**-0.01%**
50%	0.970	0.982	**-1.26%**	0.970	**0.00%**	0.971	**-0.14%**
70%	1.154	1.131	**2.02%**	1.153	**0.11%**	1.156	**-0.16%**
90%	1.445	1.362	**5.80%**	1.442	**0.26%**	1.447	**-0.09%**
Case	**PBD10F100**						
Description	Fixed bed packed with 100% of alumina packings						
Breakthrough	DPM	LM	% Error	HYM	% Error	EHTCM	% Error
10%	0.585	0.663	**-13.31%**	0.585	**0.00%**	0.582	**0.57%**
30%	0.802	0.847	**-5.62%**	0.802	**0.00%**	0.802	**-0.02%**
50%	0.971	0.983	**-1.29%**	0.971	**0.00%**	0.972	**-0.15%**
70%	1.156	1.127	**2.50%**	1.156	**0.00%**	1.158	**-0.18%**
90%	1.451	1.356	**6.54%**	1.451	**0.00%**	1.453	**-0.09%**

The improvement on the prediction of the dimensional temperature breakthrough curves is illustrated in Figure 5.17(a) and (b). Figure 5.17(a) presents the results of the DPM and the HYM approaches, whereas Figure 5.17(b) presents the results of the DPM and the EHTCM approaches. In both

cases it is noticeable the accuracy of the results obtained with both simplifications, however, as discussed before, the HYM approach would still use a distributed particle approach for one of the materials, which will increase the computational burden. Hence, the EHTMC seems to be a better choice for both accuracy and computational efficiency.

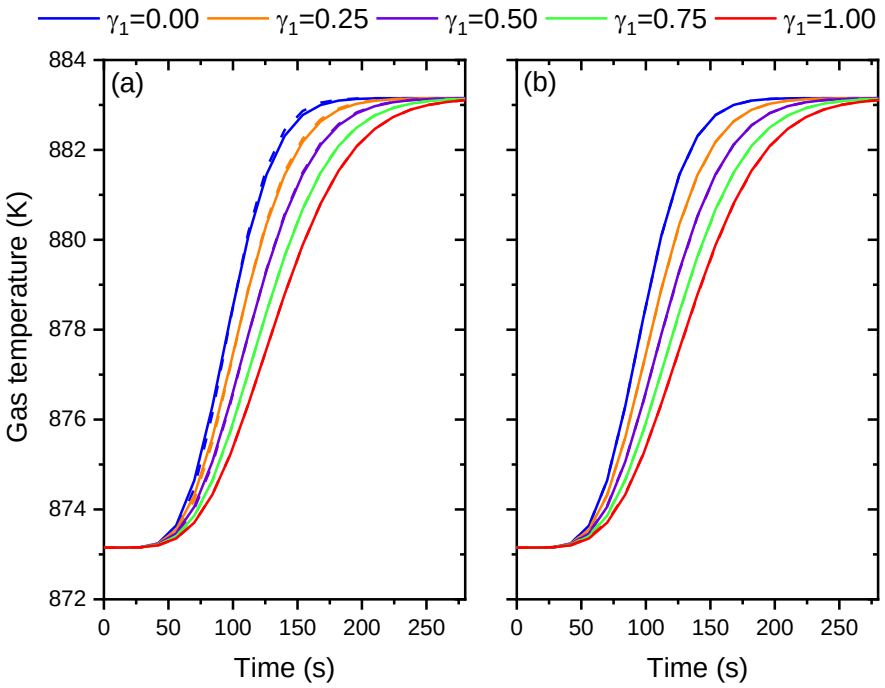

Figure 5.17 Temperature breakthrough curves for various fixed beds with different volumetric fraction of alumina packings (a) DPM vs HYM, (b) DPM vs EHTCM.

5.6.3.2 Effect of the change of particle size

The change of particle size will have an effect in the bed response to the heat transfer. From Equation (5.73) it is evident that, provided that all parameters (except the pellet size) and operating conditions are fixed, an increase of the pellet diameter will decrease the value of the YK_r number, whereas a decrease of the pellet size will increase the YK_r number. The former indicates that the likelihood of developing thermal gradients within the system will grow with the increasing particle size.

For the same packed bed previously analysed of length 1 m, filled with different volumetric fractions of alumina and calcium oxide packings, being heated with a gas with $G = 7.59\ kg\ m^{-2}s^{-1}$, $C_{p,g} = 2597.7\ J\ kg^{-1}K^{-1}$; the values of YK_r at two different pellet sizes are summarised in Table 5.6.

The values in Table 5.6 backup the latest observation, when the pellet diameter is set to $d_p = 0.005\ m$, the YK_r number indicates a system where the

heat transfer is controlled by the convection mechanism for mixtures with γ_1 as high as 50v/v%. Conversely, when the pellet diameter is set to $d_p = 0.02\ m$, the heat transfer operation will be controlled by the thermal conductivity of the packing for all values of γ_1.

Table 5.6 Effect of the pellet size on the YK_r number of several packed beds with different volumetric fractions of packing 1 and 2. γ_1 represents the volumetric fraction of alumina.

Parameter	$\gamma_1 = 0$	$\gamma_1 = 0.25$	$\gamma_1 = 0.5$	$\gamma_1 = 0.75$	$\gamma_1 = 1.0$
YK_r @ $d_p = 0.005$	128.8	104.6	80.3	56.1	31.8
YK_r @ $d_p = 0.02$	8.1	6.5	5.0	3.5	2.0

Figure 5.18(a) and (b) are plots the dimensionless and dimensional breakthrough curves for a packed bed filled with packings of diameter 0.02 m with an alumina volumetric fraction of $\gamma_1 = 0.25$. The fluid mass flux and properties are the same as in previous simulations. As expected, the time to saturate the bed increased with the particle diameter. The errors in the prediction by the LM and HYM approaches are more visible than in the previous case, the errors calculated based on the dimensionless curve are summarised in Table 5.7. A similar performance of the approaches was attained with the highest accuracy being obtained with the EHTCM approach, followed by the HYM and the LM approaches.

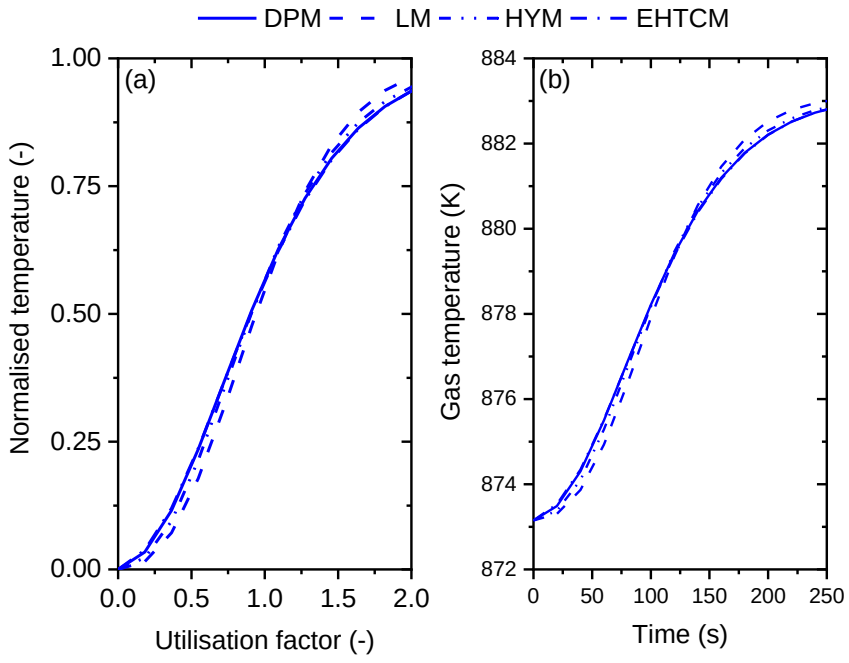

Figure 5.18 Breakthrough curve of a fixed bed packed with a mixture of 25 v% of 0.02 m alumina packings and 75 %v of 0.02 m calcium oxide packings (a) dimensionless form and (b) dimensional form.

Table 5.7 Error percentage in the calculation of breakthrough curves with different modelling approaches for fixed beds packed with mixtures of 0.02m spherical packings

Case	**PBD20F00**						
Description	Fixed bed packed with 100% of calcium oxide pellets						
Breakthrough	DPM	LM	% Error	HYM	% Error	LHTCM	% Error
10%	0.365	0.417	**-14.04%**	0.417	**-14.04%**	0.362	**0.85%**
30%	0.667	0.702	**-5.30%**	0.702	**-5.30%**	0.666	**0.06%**
60%	1.069	1.070	**-0.15%**	1.070	**-0.15%**	1.070	**-0.10%**
70%	1.229	1.214	**1.23%**	1.214	**1.23%**	1.230	**-0.11%**
90%	1.728	1.664	**3.69%**	1.664	**3.68%**	1.729	**-0.08%**
Case	**PBD20F25**						
Description	Packed bed with 25% of alumina packings and 75% calcium oxide packings						
Breakthrough	DPM	LM	% Error	HYM	% Error	LHTCM	% Error
10%	0.330	0.413	**-25.25%**	0.372	**-12.96%**	0.320	**2.79%**
30%	0.633	0.702	**-10.88%**	0.656	**-3.59%**	0.632	**0.11%**
50%	0.901	0.941	**-4.36%**	0.907	**-0.65%**	0.905	**-0.43%**
70%	1.226	1.214	**1.01%**	1.212	**1.13%**	1.232	**-0.51%**
90%	1.794	1.661	**7.42%**	1.751	**2.39%**	1.797	**-0.19%**
Case	**PBD20F50**						
Description	Fixed bed packed with 50% of alumina packings and 50% calcium oxide packings						
Breakthrough	DPM	LM	% Error	HYM	% Error	LHTCM	% Error
10%	0.299	0.411	**-37.70%**	0.326	**-9.05%**	0.286	**4.44%**
30%	0.605	0.703	**-16.06%**	0.618	**-2.08%**	0.606	**-0.05%**
50%	0.887	0.941	**-6.14%**	0.888	**-0.17%**	0.894	**-0.86%**
70%	1.230	1.209	**1.72%**	1.219	**0.91%**	1.241	**-0.87%**
90%	1.848	1.665	**9.91%**	1.825	**1.28%**	1.851	**-0.12%**
Case	**PBD20F75**						
Description	Fixed bed packed with 75% of alumina packings and 25% calcium oxide packings						
Breakthrough	DPM	LM	% Error	HYM	% Error	LHTCM	% Error
10%	0.272	0.412	**-51.62%**	0.284	**-4.32%**	0.256	**5.85%**
30%	0.584	0.702	**-20.27%**	0.589	**-0.86%**	0.586	**-0.38%**
50%	0.879	0.940	**-7.05%**	0.879	**0.01%**	0.889	**-1.13%**
70%	1.241	1.213	**2.26%**	1.237	**0.37%**	1.252	**-0.88%**
90%	1.889	1.660	**12.11%**	1.879	**0.54%**	1.889	**-0.03%**
Case	**PBD20F100**						
Description	Fixed bed packed with 100% of alumina packings						
Breakthrough	DPM	LM	% Error	HYM	% Error	LHTCM	% Error
10%	0.248	0.416	**-67.33%**	0.248	**0.00%**	0.231	**6.99%**
30%	0.568	0.703	**-23.76%**	0.568	**0.00%**	0.573	**-0.79%**
50%	0.875	0.941	**-7.55%**	0.875	**0.00%**	0.886	**-1.29%**
70%	1.248	1.211	**2.94%**	1.248	**0.00%**	1.260	**-1.00%**
90%	1.916	1.660	**13.38%**	1.916	**0.00%**	1.915	**0.06%**

5.6.3.3 Effect of the change of fluid

The effect of the change of fluid relates to the fluid's transport properties. At constant superficial velocity, particle diameter and bed length, a reduction of

the fluid's density and heat capacity will increase the YK_r number above the threshold that divides the regime of operation experiencing thermal gradients from the regime of operation free of gradients. A comparison of the values of the YK_r number for an operation with natural gas, and with air as working fluids is presented in Table 5.8; it is clear that by changing the fluid from natural gas to air, the system will operate free of thermal gradients for all values of γ_1. Therefore, in this situation, the lumped model would result in an accurate representation of the system. This is observed in Figure 5.19 which is a plot of the breakthrough curve corresponding to a packed bed with $\gamma_1 = 0.25$, $d_p = 0.01\,m$, $L_b = 1.0\,m$, with $G = 1.79\,kg\,m^{-2}s^{-1}$ and $C_{p,g} = 1158\,J\,kg^{-1}K^{-1}$; the four modelling approaches converge to the same practical solution with errors below 1.2% in all cases as summarised in Table 5.9.

Table 5.8 Effect of the fluid properties on the YK_r number of several packed beds with different volumetric fractions of packing 1 and 2. γ_1 represents the volumetric fraction of alumina.

Fluid	$\gamma_1 = 0$	$\gamma_1 = 0.25$	$\gamma_1 = 0.5$	$\gamma_1 = 0.75$	$\gamma_1 = 1.0$
Natural gas	32.2	26.1	20.1	14.0	8.0
Air	308.7	250.6	192.5	134.4	76.3

Table 5.9 Error percentage in the calculation of breakthrough curves with different modelling approaches for fixed beds packed with mixtures of 0.01m spherical packings exchanging heat with a stream of hot air.

Case:	**PB10F25A**						
Working fluid:	**Air at 1073K and 5 bar**						
Packing:	**25v/v% of alumina packings and 75v/v% CaO packings.**						
Breakthrough	DPM	LM	% Error	HYM	% Error	EHTCM	% Error
0.1	0.715	0.723	**-1.16%**	0.718	**-0.38%**	0.715	**0.00%**
0.3	0.873	0.877	**-0.40%**	0.874	**-0.12%**	0.873	**0.00%**
0.5	0.989	0.990	**-0.09%**	0.989	**-0.02%**	0.989	**0.00%**
0.7	1.112	1.110	**0.22%**	1.111	**0.08%**	1.112	**0.00%**
0.9	1.298	1.287	**0.79%**	1.294	**0.25%**	1.298	**0.00%**

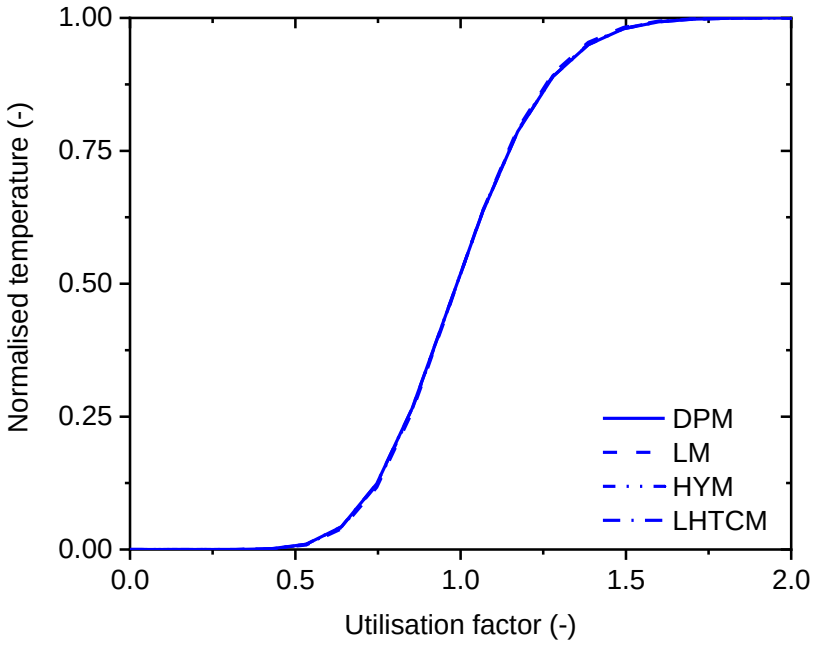

Figure 5.19 Breakthrough curve of a fixed bed packed with a mixture of 25 v% of 0.1 m alumina packings and 75 %v of 0.1 m calcium oxide packings, operating with air at 1073K and 5 bar.

5.7 Concluding remarks

The heat transfer from a hot fluid stream to a fixed bed packed with a single and two types of packings was analysed. Two modelling approaches were considered to represent the physical problem, namely a distributed particle model and a lumped model, and the numerical solutions of their Lagrangian representation were developed by the finite differences method. The numerical schemes proved to be convergent, and in particular the solution of the lumped model proved slightly superior to the solution of the models obtained in gPROMS; for the distributed particle models no significant difference was found between the finite differences method and the gPROMS solution.

The models were applied to simulate fixed beds packed with single type of packings, and with two different packings of refractory materials. The application of the distributed particle and the lumped models to fixed beds packed with a single and multiple packing revealed that the likelihood of developing temperature gradients within the packing not only depends of the thermal conductivity of the material, which in the case of catalysts and adsorbents is typically very low due to the particles' porosity and the fluid filling the pores, but it also depends upon the dimensions of the packing, the fixed bed length and fluid properties and flow conditions; the simulations conducted with values of the YK_r in the range 9.4 to 366.2 indicated that under certain circumstances the lumped model can represent the system regardless of the thermal conductivity of the packing material.

When applied to systems with mixtures of two different refractory materials of various sizes, the lumped model exhibited deviations from the distribute particle model ranging from 0.76 to 67.33% in absolute values. This was improved by introducing a hybrid model where the material exhibiting the most refractory nature was modelled with the distributed particle approach and the less refractory material with the lumped model, this approach indeed improved the results and reduced the absolute value of the error to the range 0.0 to 14.04%. Moreover, it was found that the application of the distributed particle model to fixed beds packed with two types of refractory materials can be avoided by incorporating an effective heat transfer coefficient along with the lumped model, this approach yielded errors ranging from 0.0 to 6.99% (in absolute value). Overall it was demonstrated that the latter approach was useful to simplify the heat transfer model for various particle sizes, thus it is recommended to be applied to the reactor model to reduce the mathematical complexity of the model and facilitate its solution.

Chapter 6 Modelling of the Fuel Reactor

6.1 Introduction

This chapter presents the development and application of the mathematical model representing the Fuel Reactor cycle of the process known as Sorption-Enhanced Chemical-Looping Steam Reforming. A heterogeneous model is developed here for methane as the feedstock ('fuel') for the production of hydrogen. The model considers separate gas, catalyst and adsorbent phases, and accounts for the variation of all physical properties of the gas and the transfer coefficients with time and space. It is to be used to simulate both, systems with small and large particles and investigate the pertinence of using the proposed modelling approach versus the use of simpler models previously proposed in the open literature (i.e. the pseudo-homogeneous and the pseudo-heterogeneous models).

The chapter has seven sections considering this Introduction. In section 6.2 the details of the model proposed in this work, along with the pseudo-homogeneous and pseudo-heterogeneous models used for comparison purposes and the closure relationships are presented. This section is followed by the description of the integration methodology followed to solve the model in gPROMS^{TM} in section 6.3, the method to check the model convergence (section 6.4) and the detail of the experimental data utilised to compare the models outputs (section 6.5). The results of the application of the model to systems with small and large packings are discussed in section 6.6. Finally, a summary of the conclusions of the investigations described in this chapter is provided in section 6.7.

6.2 Model development

The previous modelling work carried out by this research group considered a fixed bed packed with a homogeneous mixture of a steam reforming catalyst and a CO_2 adsorbent, and described the solid phase with a single local concentration and temperature. The modelling assumptions used by Abbas et al. [68] were the following:

1) The reactor is considered a plug flow reactor with axial dispersion of mass and heat.
2) The catalyst and adsorbent are exposed to the same local concentration and temperature profiles.
3) Temperature and concentration radial gradients are neglected.
4) The gas can be described by the ideal gas equation of state.

5) The operation is adiabatic.
6) Size of pellet is uniform and the porosity of the bed is constant.
7) The gas mas flux is constant.

The model produced from the application of the assumptions listed above resembles a system with a single bifunctional particle which has been proposed by various authors [33, 65, 170]. However, its application to a system that considers the catalyst and the adsorbent separately, thus exhibiting different thermophysical properties might prove unrealistic since assumption 2) neglects the transport of mass and heat from one material to the other, which can be hindered by the various transport resistances that are present in a packed bed. In addition, assumption 7) is valid in the case of a diluted adsorbable specie, nevertheless, in bulk separation applications the total mass varies as a result of one or more components being stripped from the gas phase, hence a large variation of the mass flux is expected, making this assumption questionable for the modelling of the reactor considered in this work.

Figure 6.1 is a scheme of the processes occurring during the Fuel Reactor in each material as well as the interaction between them. In the Fuel Reactor, the gaseous mixture of the methane and steam flow through the interstices of the packed bed to eventually reach the active sites of the catalyst. The transfer of these species from the bulk towards the surface of the catalyst faces inter- and intra-pellet resistances to mass and heat transport. Rostrup-Nielsen [171] has reported that the primary resistances in steam reforming are the diffusion of reactants in the catalyst pore for mass transfer, and heat transfer over the fluid film. However, for an adiabatic steam reformer, Christiansen [172] indicates that the heterogeneous model is needed, although with the disadvantages of the increased complexity of the mathematical model and its solution. Once in the active sites, the reactants are adsorbed and the steam reforming reactions happen. The reforming products then are desorbed and diffuse from the active sites to the catalyst surface, and from the surface through the fluid film to the bulk. The CO_2 then is transported from the bulk to the adsorbent surface, where it is adsorbed at the adsorbent grain surfaces starting from the most external layer of grains and progressively moving towards the adsorbent centre. The adsorption of CO_2 has a twofold effect; on one side, it depletes the bulk mass inducing gradients in the velocity field; on the other hand it produces a significant amount of heat of adsorption which is transferred by convection to the bulk, and carried towards the catalyst where it is consumed by the steam reforming reactions.

Based on the previous description, the model will consider an axial flow reactor of cylindrical shape (Figure 6.2), packed with a mixture of catalyst and the adsorbent and will account for the mass and heat transport individually for each

phase present in the reactor. Therefore, the following set of modelling assumptions are proposed:

a) The system is adiabatic and well insulated, moreover the reactor diameter-to-particle diameter ratio is held above 30, hence no radial thermal gradients are developed.
b) The velocity profile is deemed flat and therefore, no radial velocity or concentration gradients are accounted for.
c) The basic model is deemed as an ideal plug flow, however the impact of the axial dispersion term in the representation of experimental data will be assessed.
d) No intrapellet transport resistances are considered, intra-conductivity is represented by an effective heat transfer coefficient as indicated in **Chapter 5**.
e) In this study side reactions that occur under steam methane reforming (SMR) operating conditions such as methane decomposition, carbon formation or dry reforming are not considered. This is valid an excess of steam conditions (super-stoichiometric steam to carbon ratio) will be held.
f) The fluid is a multicomponent mixture with one adsorbable component only. Adsorption of other species such as water depends upon the operating pressure and temperature, moreover, however this mechanism is not considered in the model.
g) Catalyst and adsorbent particles are deemed spherical. Where simulations are run with different shapes, an equivalent diameter is used.
h) The basic model will consider a constant particle porosity fraction for both materials. In addition, the pellets sizes are considered constant.
i) A mean bed voidage is considered throughout the reactor.
j) The volumetric fraction of each material in the reactor is deemed constant throughout the length regardless of the packing being structured or unstructured.

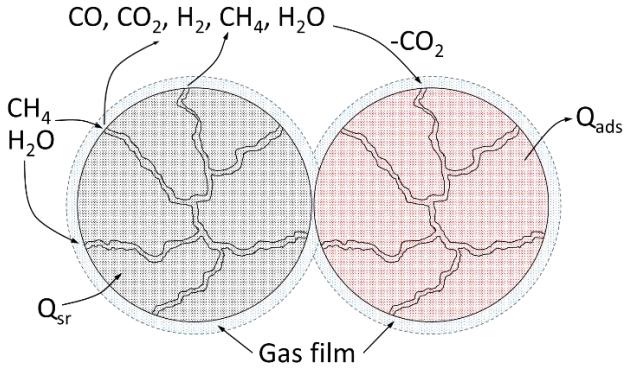

Figure 6.1 Scheme of the physical interaction between the adsorbent and the catalyst during Fuel Reactor mode.

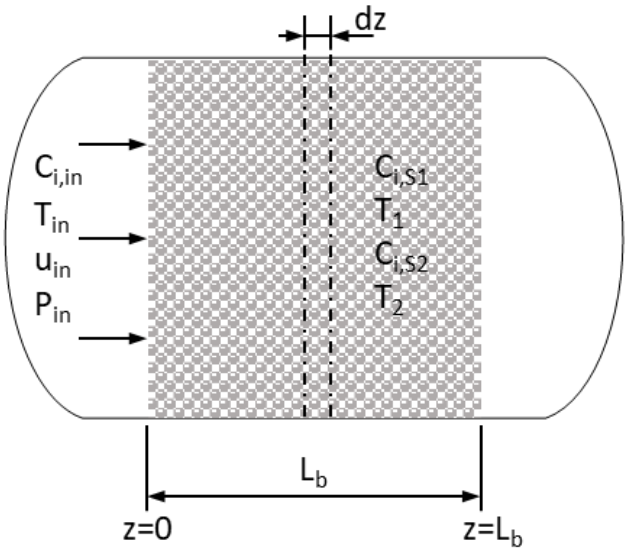

Figure 6.2 Scheme of the fixed bed reactor indicating the domain of interest for the deployment of the model equations, the boundary conditions and the initial conditions of the packed bed.

6.2.1 Heterogeneous model

6.2.1.1 Base plug flow model

The heterogeneous model accounts separately for each of the phases in the reactor. Three phases can be recognised, namely the bulk gas, the catalyst and the adsorbent. Therefore, each phase needs to be mathematically described by the relevant conservation equations. The species continuity equation is defined in the region of interest $t > 0$ and $0 < z \leq L_b$ as follows:

$$\varepsilon_b \frac{\partial C_i}{\partial t} + \varepsilon_b \frac{\partial (u_i C_i)}{\partial z} = -\beta_1 a_{S_1}\left(C_i - C_{i,S_1}\right) - \beta_2 a_{S_2}\left(C_i - C_{i,S_2}\right) \qquad \textbf{(6.1)}$$

where ε_b is the mean bed voidage, C_i is the mole concentration of the $i-th$ specie in the bulk, C_{i,S_1} and C_{i,S_2} are the mole concentrations of the $i-th$ specie at the catalyst and adsorbent surfaces, and β_1 and β_2 are the mass transfer coefficients and the expressions to estimate them are given in section 6.2.3. The first term in the r.h.s. of Equation (6.1) accounts for the mass transfer between the bulk fluid and the catalyst and the second term of the r.h.s. accounts for the mass transfer between the bulk fluid and the adsorbent. The volumetric fraction of each material within the bed is accounted for as part of the superficial area per unit of bed of the catalyst (a_{S_1}) and the adsorbent (a_{S_2}) as:

$$a_{S_1} = \frac{6\gamma_1(1-\varepsilon_b)}{d_1} \text{ and } a_{S_2} = \frac{6(1-\gamma_1)(1-\varepsilon_b)}{d_2} \qquad \textbf{(6.2)}$$

The bulk energy balance is represented within the region of interest $t > 0$ and $0 < z \leq L_b$ in a similar way as in **Chapter 5**, with the main difference being that now the bulk gas physical properties and velocity are allowed to vary axially:

$$\varepsilon_b \frac{\partial(\rho_g C_{p,g} T)}{\partial t} + \varepsilon_b \frac{\partial(u_i \rho_g C_{p,g} T)}{\partial z} = -\alpha_1 a_{S_1}(T - T_{S_1}) - \alpha_2 a_{S_2}(T - T_{S_2}) \quad \textbf{(6.3)}$$

Where u_i is the interstitial velocity of the gas, ρ_g the gas density and $C_{p,g}$ the gas heat capacity; α_1 and α_2 are the film heat transfer coefficients at the catalyst and at the adsorbent. Equation (6.3) represents an adiabatic system; for a system that is being heated, an additional term accounting for the heat transfer at the reactor wall is needed, then, the bulk energy balance is:

$$\varepsilon_b \frac{\partial(\rho_g C_{p,g} T)}{\partial t} + \varepsilon_b \frac{\partial(u_i \rho_g C_{p,g} T)}{\partial z} = -\alpha_1 a_{S_1}(T - T_{S_1}) - \alpha_2 a_{S_2}(T - T_{S_2}) - \frac{4U_w}{d_r}(T - T_f) \quad \textbf{(6.4)}$$

where U_w is the overall wall heat transfer coefficient, d_r is the reactor diameter and T_f is the temperature of the source of heat.

At the particle level, the mass and energy balances are accounted for separately, rendering a set of equations for the catalyst, and another for the adsorbent; the concentrations and temperatures at the surface of the materials are deemed as functions of time, hence, these balances are represented within the region $t > 0$ and $0 \leq z \leq L_b$ by Equations (6.5) to (6.8) as:

$$\varepsilon_{p_1}(1 - \varepsilon_b)\frac{\partial C_{i,S_1}}{\partial t} = \beta_1 a_{S_1}(C_i - C_{i,S_1}) + \rho_{b_1}\sum_{j=1}^{m}\eta_j \nu_{ij} r_j \quad \textbf{(6.5)}$$

$$\varepsilon_{p_2}(1 - \varepsilon_b)\frac{\partial C_{i,S_2}}{\partial t} = \beta_2 a_{S_2}(C_i - C_{i,S_2}) + \rho_{b_2}\sum_{k=1}^{n}\eta_k \nu_{ik} r_k \quad \textbf{(6.6)}$$

$$\rho_{b_1} C_{p_1}\frac{\partial T_{S_1}}{\partial t} = \alpha_1 a_{S_1}(T - T_{S_1}) + \rho_{b_1}\sum_{j=1}^{m}\eta_j r_j(-\Delta H_j) \quad \textbf{(6.7)}$$

$$\rho_{b_2} C_{p_2}\frac{\partial T_{S_2}}{\partial t} = \alpha_2 a_{S_2}(T - T_{S_2}) + \rho_{b_2}\sum_{k=1}^{n}\eta_k r_k(-\Delta H_k) \quad \textbf{(6.8)}$$

where ε_{p_i} with i=1,2 is the porosity of packing types 1 and 2, ρ_{b_i} is the bulk density of packing type 1 and 2 and C_{p_i} is the heat capacity of packings type 1 and 2. The solution of equations (6.1) to (6.8) requires information of the values of the gas density ρ_g and the interstitial velocity u_i at each within the bed length. These

variables maintain an inverse relationship expressed through the continuity equation. Moreover, the various non-catalytic processes occurring during the two stages of the reactor cyclic operation promote the variation of the bulk mass flux throughout the bed; this is expressed as:

$$\frac{\partial \rho_g}{\partial t} + \frac{\partial (\rho_g u_i)}{\partial z} = S_m \qquad \textbf{(6.9)}$$

Where S_m is the source term and its nature depends upon the process being simulated. During the Fuel Reactor mode, the reduction of NiO will add mass to the bulk owing to the formation of H_2O and CO_2; the amount of these species depends upon the available NiO in the packed bed and the prevalent mechanism to reduce the OTM. On the other hand, the carbonation of CaO will exhaust the CO_2 as it is being formed; under certain conditions of pressure and temperature, water can also be adsorbed by the Ca-based adsorbent forming $Ca(OH)_2$ [69, 173], this reaction consumes one molecule of H_2O as previously discussed in **Chapter 2**. The calcium hydroxide reacts subsequently with CO_2 releasing one molecule of H_2O, therefore it is assumed that this process does not affect significantly the variation of mass in the reactor, hence the source term is defined only by the capture of CO_2 as:

$$S_m = -\frac{\rho_{b_2}}{\varepsilon_b} M_{CO_2} \eta_{Carb} r_{Carb} \qquad \textbf{(6.10)}$$

The solution of the velocity field in Equation (6.9) requires the simultaneous integration of the momentum equation, which for a fixed bed can be represented within the domain $t > 0$ and $0 < z \leq L$ as:

$$\rho_g \frac{\partial u_i}{\partial t} + \rho_g u_i \frac{\partial u_i}{\partial z} + u_i S_m + \frac{\partial P}{\partial z} = -\frac{A \mu_g u_i (1-\varepsilon_b)^2}{d_p^2 \varepsilon_b^2} - \frac{B \rho_g u_i^2 (1-\varepsilon_b)}{d_p \varepsilon_b} \qquad \textbf{(6.11)}$$

In Equation (6.11), A and B are packing shape dependent correlating parameters, whose values for spheres are dependent upon the correlation used, as mentioned in **Chapter 5**, in this work the McDonald's correlation is used with values of $A = 180$ and $B = 1.8$.

The model presented in Equations (6.1) to (6.11) is a stiff model due to the very strong correlation between the various variables involved, producing a highly non-linear system. Since the gas velocity changes with time and position, the slope of the characteristics of this system will vary and could intersect, leading to a multivalued solution for the gas velocity [174, 175]; this in turn can create problems during the integration of the set of PDE, preventing its solution. In fact, no convergence was achieved with Equations (6.9) and (6.11) and their

simplification was needed to attain a model solution. By neglecting the accumulation terms in Equations (6.9) and (6.11), the final continuity and momentum equations are:

$$\frac{\partial(\rho_g u_i)}{\partial z} = S_m \tag{6.12}$$

$$\rho_g u_i \frac{\partial u_i}{\partial z} + u_i S_m + \frac{\partial P}{\partial z} = -\frac{A\mu_g u_i (1-\varepsilon_b)^2}{d_p^2 \varepsilon_b^2} - \frac{B\rho_g u_i^2 (1-\varepsilon_b)}{d_p \varepsilon_b} \tag{6.13}$$

where the average packing diameter d_p is calculated as indicated in **Chapter 5**, and used to estimate the mean bed voidage ε_b. The initial conditions of the set of PDE (6.1)–(6.8), (6.12) and (6.13) represent an unloaded thermally equilibrated bed and are expressed as:

$$C_i(z,0) = C_{i,S_1}(z,0) = C_{i,S_2}(z,0) = 0 \tag{6.14}$$

$$T(z,0) = T_{S_1}(z,0) = T_{S_2}(z,0) = T_i \tag{6.15}$$

The boundary conditions are a square step input for the gas concentration, temperature, pressure and velocity as:

$$C_i(0,t) = C_{i,in} \qquad T(0,t) = T_{in} \qquad u_i(0,t) = \frac{u_{s,in}}{\varepsilon_b} \qquad P(0,t) = P_{in} \tag{6.16}$$

Additional information is required to relate the total reactor pressure with the gas total concentration and the individual partial pressures for each component, the thermodynamic and transport properties in this thesis are estimated with the aid of the third party software Multiflash [176]; the method selected to predict the thermodynamic properties is the Advanced Peng-Robinson which is based on the original Peng-Robinson equation of state:

$$P = \frac{NRT}{V-b} + \frac{a}{V^2 + 2bV - b^2} \tag{6.17}$$

6.2.1.2 Heterogeneous model accounting for axial dispersion

If axial dispersion in the fluid is accounted for, the fluid species and energy balances of equations (6.1) and (6.3) are replaced by:

$$\varepsilon_b \frac{\partial C_i}{\partial t} - \varepsilon_b D_{z,i} \frac{\partial^2 C_i}{\partial z^2} + \varepsilon_b \frac{\partial (u_i C_i)}{\partial z} = -\beta_1 a_{S_1}(C_i - C_{i,S_1}) - \beta_2 a_{S_2}(C_i - C_{i,S_2}) \tag{6.18}$$

$$\varepsilon_b \frac{\partial(\rho_g C_{p,g} T)}{\partial t} - \varepsilon_b \lambda_{z,g} \frac{\partial^2 T}{\partial z^2} + \varepsilon_b \frac{\partial(u_i \rho_g C_{p,g} T)}{\partial z} = -\alpha_1 a_{S_1}(T - T_{S_1}) - \alpha_2 a_{S_2}(T - T_{S_2}) \quad \textbf{(6.19)}$$

Where $D_{z,i}$ and $\lambda_{z,g}$ are the effective diffusion and the effective thermal conductivity coefficients in the axial direction. Equations(6.18) and (6.19) are second order PDE within the domain of interest $t > 0$ and $0 < z < L$ and require two boundary conditions, which are given by:

$$C_i(0,t) = C_{i,in} \qquad T(0,t) = T_{in} \qquad \left.\frac{\partial C_i}{\partial z}\right|_{z=L_b} = \left.\frac{\partial T}{\partial z}\right|_{z=L_b} = 0 \quad \textbf{(6.20)}$$

6.2.2 Models for benchmarking

6.2.2.1 Pseudo-homogeneous model

A pseudo-homogeneous model is implemented to relax the assumptions of different concentration and temperature profiles at the catalyst and adsorbent particles. Several previous investigations have relied on the validity of the assumption of a single concentration and temperature profiles in the modelling of the sorption enhanced steam reforming process with and without including the chemical looping [6, 31, 32, 50, 177, 178], however, the available models of the SE-CLSMR process provided by [50, 177, 178] have not accounted for the variations of bulk gas mass flux resulting from the adsorption of CO_2. The pseudo-homogeneous model implemented in this research is the following:

$$\varepsilon_b \frac{\partial C_i}{\partial t} + \varepsilon_b \frac{\partial(u_i C_i)}{\partial z} = \rho_{b_1} \sum_{j=1}^{m} \eta_j \nu_{ij} r_j + \rho_{b_2} \sum_{k=1}^{n} \eta_k \nu_{ik} r_k \quad \textbf{(6.21)}$$

$$\left(\varepsilon_b \rho_g C_{p,g} + \rho_{b_1} C_{p_1} + \rho_{b_2} C_{p_2}\right) \frac{\partial T}{\partial t} + \varepsilon_b \frac{\partial(u_i \rho_g C_{p,g} T)}{\partial z} = \rho_{b_1} \sum_{j=1}^{m} \eta_j r_j(-\Delta H_j) + \rho_{b_2} \sum_{k=1}^{n} \eta_k r_k(-\Delta H_k) \quad \textbf{(6.22)}$$

$$\frac{\partial(\rho_g u_i)}{\partial z} = -\frac{\rho_{b_2}}{\varepsilon_b} M_{CO_2} \eta_{Carb} r_{Carb} \quad \textbf{(6.23)}$$

$$\rho_g u_i \frac{\partial u_i}{\partial z} - \frac{u_i \rho_{b_2}}{\varepsilon_b} M_{CO_2} \eta_{Carb} r_{Carb} + \frac{\partial P}{\partial z} = -\frac{A \mu_g u_i (1 - \varepsilon_b)^2}{d_p^2 \varepsilon_b^2} - \frac{B \rho_g u_i^2 (1 - \varepsilon_b)}{d_p \varepsilon_b} \quad \textbf{(6.24)}$$

with initial conditions:

$$C_i(z,0) = 0 \tag{6.25}$$

$$T(z,0) = T_i \tag{6.26}$$

and boundary conditions:

$$C_i(0,t) = C_{i,in} \qquad T(0,t) = T_{in} \qquad u_i(0,t) = \frac{u_{s,in}}{\varepsilon_b} \qquad P(0,t) = P_{in} \tag{6.27}$$

6.2.2.2 Pseudo-heterogeneous model

The model developed by Abbas et al. [68] is relevant to this research. The main differences between the aforementioned investigation and the approach presented in this work are the that the former considers a constant mass flux and does not distinguish between the catalyst and the adsorbent in the solid phase; in addition, this work considers the variation of the gas properties and models the fluid as a real gas as opposed to the premises of Abbas' model. The pseudo-heterogeneous model of Abbas et al. [68] is:

$$\varepsilon_b \frac{\partial C_i}{\partial t} - \varepsilon_b D_z \frac{\partial^2 C_i}{\partial z^2} + \frac{\partial (u_s C_i)}{\partial z} = -\beta a_S \left(C_i - C_{i,S}\right) \tag{6.28}$$

$$\varepsilon_b \rho_g C_p \frac{\partial T}{\partial t} - \varepsilon_b \lambda_{z,g} \frac{\partial^2 T}{\partial z^2} + u_s \rho_g C_p \frac{\partial T}{\partial z} = -\alpha a_S (T - T_S) \tag{6.29}$$

$$\varepsilon_{p_s}(1-\varepsilon_b)\frac{\partial C_{i,S}}{\partial t} = \beta a_S \left(C_i - C_{i,S}\right) + \rho_{b_1} \sum_{j=1}^{m} \eta_j \nu_{ij} r_j + \rho_{b_2} \sum_{k=1}^{n} \eta_k \nu_{ik} r_k \tag{6.30}$$

$$\rho_b C_{p_s} \frac{\partial T_S}{\partial t} = \alpha a_S (T - T_S) + \rho_{b_1} \sum_{j=1}^{m} \eta_j r_j \left(-\Delta H_j\right) + \rho_{b_2} \sum_{k=1}^{n} \eta_k r_k (-\Delta H_k) \tag{6.31}$$

$$\frac{\partial P}{\partial z} = -\frac{A \mu_g u_i (1-\varepsilon_b)^2}{d_p^2 \varepsilon_b^2} - \frac{B \rho_g u_i^2 (1-\varepsilon_b)}{d_p \varepsilon_b} \tag{6.32}$$

with initial conditions:

$$C_i(z,0) = C_{i,S}(z,0) = 0 \tag{6.33}$$

$$T(z,0) = T_S(z,0) = T_i \tag{6.34}$$

and boundary conditions:

$$C_i(0,t) = C_{i,in} \qquad T(0,t) = T_{in} \qquad u_i(0,t) = \frac{u_{s,in}}{\varepsilon_b} \qquad P(0,t) = P_{in} \qquad \textbf{(6.35)}$$

6.2.3 Closure relationships

6.2.3.1 Kinetics

The solution of the models proposed in sections 6.2.1 and 6.2.2 requires information of the kinetics for the main reactions involved in the process. A summary of the relevant chemical reactions considered in the modelling of the Fuel Reactor is presented in Table 6.1.

Table 6.1 Main processes occurring during the Fuel Reactor cycle.

Reaction	Material	Process	Standard heat of reaction (ΔH^0)
R1	Catalyst/OTM	$CH_{4(g)} + H_2O_{(g)} \leftrightarrows CO_{(g)} + 3H_{2(g)}$	$206\ kJ\ mol_{CH_4}^{-1}$
R2	Catalyst/OTM	$CO_{(g)} + H_2O_{(g)} \leftrightarrows CO_{2(g)} + H_{2(g)}$	$-41\ kJ\ mol_{CO}^{-1}$
R3	Catalyst/OTM	$CH_{4(g)} + H_2O_{(g)} \leftrightarrows CO_{(g)} + 3H_{2(g)}$	$165\ kJ\ mol_{CH_4}^{-1}$
R4	Catalyst/OTM	$CH_{4(g)} + NiO_{(s)} \leftrightarrows CO_{(g)} + 2H_{2(g)} + Ni_{(s)}$	$203\ kJ\ mol_{CH_4}^{-1}$
R5	Catalyst/OTM	$CH_{4(g)} + 4NiO_{(s)} \leftrightarrows CO_{2(g)} + 2H_2O_{(g)} + 4Ni_{(s)}$	$31\ kJ\ mol_{CH_4}^{-1}$
R6	Catalyst/OTM	$H_{2(g)} + NiO_{(s)} \leftrightarrows H_2O_{(g)} + Ni_{(s)}$	$-2\ kJ\ mol_{H_2}^{-1}$
R7	Catalyst/OTM	$CO_{(g)} + NiO_{(s)} \leftrightarrows CO_{2(g)} + Ni_{(s)}$	$-43\ kJ\ mol_{CO}^{-1}$
R8	Adsorbent	$CO_{2(g)} + CaO_{(s)} \leftrightarrows CaCO_{3(s)}$	$-178.8\ kJ\ mol_{CO_2}^{-1}$

Based on the review of the available kinetic rate expressions presented in **Chapter 2** the kinetic expressions of Xu and Froment [86] are selected as the base models for the reforming reactions R1 to R3:

$$r_{SMR} = \frac{k_{SMR}}{p_{H_2}^{2.5}} \frac{\left(p_{CH_4} p_{H_2O} - \frac{p_{H_2}^3 p_{CO}}{K_{SMR}}\right)}{DEN^2} \qquad \textbf{(6.36)}$$

$$r_{WGS} = \frac{k_{WGS}}{p_{H_2}} \frac{\left(p_{CO} p_{H_2O} - \frac{p_{H_2} p_{CO_2}}{K_{WGS}}\right)}{DEN^2} \qquad \textbf{(6.37)}$$

$$r_{SMRC} = \frac{k_{SMRC}}{p_{H_2}^{3.5}} \frac{\left(p_{CH_4} p_{H_2O}^2 - \frac{p_{H_2}^4 p_{CO_2}}{K_{SMRC}}\right)}{DEN^2} \qquad \textbf{(6.38)}$$

$$DEN = 1 + K_{CO}p_{CO} + K_{H_2}p_{H_2} + K_{CH_4}p_{CH_4} + \frac{K_{H_2O}p_{H_2O}}{p_{H_2}} \quad \textbf{(6.39)}$$

Where r_{SMR} is the rate of reaction of steam methane reforming (R1), r_{WGS} is the rate of reaction of the water-gas shift (R2) and r_{SMRC} is the rate of reaction of complete steam methane reforming (R3). The partial pressures (p_{CH_4}, p_{H_2O}, p_{H_2}, p_{CO}, p_{CO_2}) kinetic constants (k_{SMR}, k_{WGS}, k_{SMRC}) and adsorption constants (K_{CH_4}, K_{H_2O}, K_{H_2}, K_{CO}) involved in Equations (6.36)–(6.39) should be calculated at the local operating pressure and temperature at the catalyst.

For the reduction of nickel oxide (NiO), the kinetic expressions proposed by Iliuta et al. [119] are used:

$$r_{CH_4c} = -2k_{CH_4c}S_{g,f}(1 - X_{NiO})C_{CH_4}w_{NiO}w_{Ni}M_{NiO} \quad \textbf{(6.40)}$$

$$r_{CH_4p} = -k_{CH_4p}S_{g,f}(1 - X_{NiO})C_{CH_4}w_{NiO}w_{Ni}M_{NiO} \quad \textbf{(6.41)}$$

$$r_{H_2} = -k_{H_2}S_{g,f}(1 - X_{NiO})C_{H_2}w_{NiO}M_{NiO} \quad \textbf{(6.42)}$$

$$r_{CO} = -2k_{CO}S_{g,f}(1 - X_{NiO})C_{CO}w_{NiO}M_{NiO} \quad \textbf{(6.43)}$$

where r_{CH_4c} is the rate of reduction of NiO with CH_4 via unmixed combustion (R4), r_{CH_4p} is the rate of reduction of NiO with CH_4 via unmixed partial oxidation (R5), r_{H_2} is the rate of reduction of NiO with H_2 (R6) and r_{CO} is the rate of reduction of NiO with CO (R7). The fractional conversion of NiO (X_{NiO}) is calculated from the expression:

$$\frac{dX_{NiO}}{dt} = \frac{S_{g,f}(1 - X_{NiO})}{C_{0,NiO}}\left[\left(2k_{CH_4c} + k_{CH_4p}\right)C_{CH_4}w_{NiO}w_{Ni} + \left(k_{H_2}C_{H_2} + k_{CO}C_{CO}\right)w_{NiO}\right] \quad \textbf{(6.44)}$$

Where w_{NiO} is the weight fraction of NiO and w_{Ni} is the weight fraction of Ni in the catalyst and are calculated from:

$$\frac{dw_{NiO}}{dt} = -S_{g,f}M_{NiO}(1 - X_{NiO})\left[\left(2k_{CH_4c} + k_{CH_4p}\right)C_{CH_4}w_{NiO}w_{Ni} + \left(k_{H_2}C_{H_2} + k_{CO}C_{CO}\right)w_{NiO}\right] \quad \textbf{(6.45)}$$

$$\frac{dw_{Ni}}{dt} = S_{g,f}M_{Ni}(1 - X_{NiO})\left[\left(2k_{CH_4c} + k_{CH_4p}\right)C_{CH_4}w_{NiO}w_{Ni} + \left(k_{H_2}C_{H_2} + k_{CO}C_{CO}\right)w_{NiO}\right] \quad \textbf{(6.46)}$$

The initial conditions required to integrate Equations (6.44)–(6.46) are:

$$X_{NiO}(z, 0) = 0 \qquad w_{NiO}(z, 0) = w_{NiO,0} \qquad w_{Ni}(z, 0) = 0 \quad \textbf{(6.47)}$$

The rate of carbonation of calcium oxide (r_{Carb}) represented in R8 of Table 6.1 is modelled by the intrinsic kinetics proposed by Sun et al. [96]:

$$r_{Carb} = \frac{1}{M_{CaO}} \frac{dX_{CaO}}{dt} \quad \textbf{(6.48)}$$

Where M_{CaO} is the molecular weight of CaO and the fractional conversion of the adsorbent X_{CaO} is calculated from:

$$\frac{dX_{CaO}}{dt} = k_{Carb} S_{g,f} M_{CaO} (1 - X_{CaO}) \quad \textbf{(6.49)}$$

Where k_{Carb} is the kinetic constant of carbonation and $S_{g,f}$ is the B.E.T. surface area of the fresh adsorbent. Equation (6.49) predicts a maximum conversion of the adsorbent of 100%, this is not consistent with the experimental evidence that shows an incomplete conversion of this material [179, 180]. Hence, in order to enforce the equation to adjust to the maximum conversion, a modification is introduced by substituting the value of 1 within the bracket, which in fact represents an availability of the whole grain for conversion, by the value of X_{max} giving the final expression used in this work:

$$\frac{dX_{CaO}}{dt} = k_{Carb} S_{g,f} M_{CaO} (X_{CaO,max} - X_{CaO}) \quad \textbf{(6.50)}$$

Initially, the adsorbent is assumed to be completely calcinated, therefore, the initial condition of equation (6.50) is:

$$X_{CaO}(z, 0) = 0 \quad \textbf{(6.51)}$$

6.2.3.2 Mass and heat transfer coefficients

The film transfer coefficients were calculated based on the Colburn correlations for heat and mass transfer. For the design of adsorption systems, the following correlation is recommended [181, 182]:

$$j_D = \frac{0.458}{\varepsilon_b Re^{0.407}} \quad \textbf{(6.52)}$$

Where j_D is the Colburn factor for mass transfer; equation (6.52) is valid for $Re > 10$. For $Re < 10$ the correlation by Petrovic and Thodos is used [182]:

$$j_D = \frac{0.357}{\varepsilon_b Re^{0.359}} \quad \textbf{(6.53)}$$

The Colburn factor for heat transfer was obtained from the Colburn analogy for heat and mass transfer [183]:

$$j_D = j_H \quad \textbf{(6.54)}$$

Where j_H is the Colburn factor for heat transfer; these factors are related to the mass and heat transfer coefficients as follows [184]:

$$j_D = \frac{\beta}{u_s}\left(\frac{\mu_g}{D_m \rho_g}\right)^{2/3} \quad \textbf{(6.55)}$$

$$j_H = \frac{\alpha}{C_{p,g}\rho_g u_s}\left(\frac{C_{p,g}\mu_g}{\lambda_g}\right)^{2/3} \quad \textbf{(6.56)}$$

6.2.3.3 Heat transfer at the wall

The experimental work selected to validate the models is conducted in reactors enclosed by electrical furnaces that supply the energy required to maintain the temperature at a certain level. Equation (6.4) accounts for this energy supply and requires the calculation of a parameter U_w which is the overall wall heat transfer coefficient. Previous modelling work have used a wall film heat transfer α_w [6, 35, 44, 59], however this approach requires knowledge of the wall internal temperature which is not always readily available. Other investigations have looked at the development and use of an overall heat transfer coefficient U_w that accounts for the radial heat transfer [31, 65, 185, 186], in this case the estimation of the effective radial thermal conductivity leads to the calculation of a large number of parameters that impose an unnecessary computational burden for the purpose of the modelling work of this project; a third approach [187], in which the overall wall heat transfer is estimated based on the temperature at the furnace is used here, where U_w is estimated based on the individual resistances around the reactor wall as:

$$\frac{1}{U_w} = \frac{1}{\alpha_w} + d_{ri}\frac{\ln(d_{ro}/d_{ri})}{2\lambda_w} + \frac{d_{ri}}{\alpha_r d_{ro}} \quad \textbf{(6.57)}$$

Where α_w is the wall film heat transfer coefficient, λ_w is the thermal conductivity of the reactor material, d_{ri} is the reactor internal diameter, d_{ro} is the outside reactor diameter, and α_r is the radiative heat transfer coefficient. The internal wall heat transfer coefficient was calculated with the correlation by Li and Finlayson [188, 189] for spherical particles valid for $0.05 < d_p < 0.3$ and $20 < Re < 7600$:

$$\alpha_w = 2.03\frac{\lambda_g}{d_r}\left(\frac{\rho_g u_s d_p}{\mu_g}\right)^{0.8} exp\left(-\frac{6d_p}{d_r}\right) \quad \textbf{(6.58)}$$

The radiative heat transfer coefficient α_r is estimated from:

$$\alpha_r = \sigma \Im_{f \to ro} (T_{ro}^4 - T_f^4)/(T_{ro} - T_f) \quad \textbf{(6.59)}$$

Where $\sigma = 5.67x10^{-8}\, Js^{-1}m^{-2}K^{-4}$ is the Boltzmann constant, $\Im_{f \to ro}$ is the grey body view factor between the reactor and the furnace surfaces, and is a measure of the energy intercepted by the body subjected to radiation out of the total energy emitted by the radiant body [190], and T_{ro} is the temperature at the outside of the wall. The grey body view factor is estimated from the emissivity of the reactor outside wall (ε_{ro}) and the emissivity of the furnace (ε_f) as:

$$\frac{1}{\Im_{ro \to f}} = \frac{d_{ro}}{d_f}\left(\frac{1}{\varepsilon_f} - 1\right) + \frac{1}{\varepsilon_{ro}} \quad \textbf{(6.60)}$$

ε_{ro} and ε_f are functions of T_{ro} and T_f and are correlated by a second order polynomial considering quartz for the reactor and refractory material for the furnace [191] as:

$$\varepsilon_{ro}(T_{ro}) = 0.61 + 2.58 \times 10^{-4} T_{ro} - 3.14 \times 10^{-7} T_{ro}^2 \quad \textbf{(6.61)}$$

$$\varepsilon_f(T_f) = 1.17 - 5.06 \times 10^{-4} T_f \quad \textbf{(6.62)}$$

6.2.3.4 Axial dispersion coefficients

The mass axial dispersion coefficient is calculated from the Peclet number ($Pe_{i,m}$) defined as [84]:

$$Pe_{i,m} = \frac{d_p u_g}{D_{i,z}} \quad \textbf{(6.63)}$$

Where $D_{i,z}$ is the mass axial dispersion coefficient. The Peclet number is calculated from the correlation proposed by Edwards and Richardson [181] as:

$$\frac{1}{Pe_{i,m}} = \frac{0.3}{ReSc_i} + \frac{0.5}{1 + 3.8/ReSc_i} \quad \textbf{(6.64)}$$

Where $Re = \frac{\rho_g u_g d_p}{\mu_g}$ and $Sc_i = \frac{\mu_g}{\rho_g D_{i,m}}$ are the Reynolds and Schmidt numbers.

For the effective thermal conductivity, the following expression is used [31, 68]:

$$\frac{\lambda_{z,g}}{\lambda_g} = \frac{\lambda_{z,0}}{\lambda_g} + 0.75 PrRe \quad \textbf{(6.65)}$$

with:

$$\frac{\lambda_{z,0}}{\lambda_g} = \varepsilon_b + \frac{1-\varepsilon_b}{0.139\varepsilon_b - 0.0339 + \frac{2}{3}\lambda_g/\lambda_s} \quad \textbf{(6.66)}$$

6.3 Model integration

The transient models were implemented and solved in gPROMS™. For a strongly convective system, Process Systems Enterprise recommends the use of upwind discretisation schemes [136]; in this work, the First Order Backward Finite Differences discretisation scheme was utilised.

The integration of the system of partial differential and algebraic equations (PDAE) required the formulation of an initialisation strategy in order to improve the initial estimates given for the problem and ensured a solution. The strategy consisted of the following steps:

1. Solution of the isothermal version of the model with the following considerations:
    - The derivative of velocity with respect to the axial position is neglected.
    - The source term in the continuity equation is set to zero.
    - The mass transfer coefficient (MTC) is independent of position.
    - Gas properties are allowed to vary with position but their derivatives are neglected.
2. The model from step 1 is upgraded by including the rate of change of the interstitial velocity and enables the calculation of the source term in the continuity equation.
3. The procedure enables the variation of the MTC with the axial position and the energy balance with the following restriction:
    - The gas properties are allowed to vary with the axial position but their derivatives in the energy balance are neglected.
    - The heat transfer coefficient is evaluated at inlet conditions and kept independent of the axial position.
4. The model of step 3 is upgraded by enabling the variation of the HTC with the axial position and the derivatives of the gas density and heat capacity into the energy balance.
5. For the models that account for the changes in adsorbent structure as it is being converted, an additional step including the variations in the adsorbent porosity, heat capacity and density is included.

6.4 Convergence of the model

The convergence of the model was checked by varying the number of discretisation points in the spatial domain. This is an important step due to the highly non-linear nature of the reactor model being investigated and the strong sensitivity of the method of lines to the mesh size [139].

6.5 Model validation

The models are validated by comparing the predicted breakthrough curve and, where available, the temperature profile, against experimental data gathered from the open literature. The Fuel Reactor model or enhanced steam reforming cycle model, is validated against the data published by Grasa et al. [44]. Other sets of experimental data are available for the Fuel Reactor cycle in [192], however the level of detail of experimental conditions presented in the paper is rather limited and its utilisation required the assumption of various parameters needed for the simulation, therefore it was not selected for the model validation process.

6.5.1 SE-SR experimental details

Grasa et al. [44] conducted experiments of Sorption Enhanced Steam Reforming of Methane over a mixture of commercial Ni-based catalyst supported on $CaAl_2O_4$ and a Ca-based adsorbent reinforced with a 10 wt.% of $Ca_{12}Al_{14}O_{33}$. The materials were mixed and packed in a tubular stainless steel reactor equipped with a thermocouple located on top of the bed. The reactor temperature was enclosed by an electrical furnace and controlled by a PID temperature controller; the temperature set point was 923 K. In addition, the reactor has a control valve that allows to regulate the reactor pressure from 3–10 bar. The researchers did not provide details of the way the materials were allocated in the reactor (e.g. if they mixed the materials or used layers), therefore, for the purpose of the simulation, it is assumed that the materials are homogeneously mixed and that the volumetric fraction of each material in the bed is constant throughout the bed length. The experimental data provided by this research group comprise the compositions of hydrogen and carbon dioxide in dry basis free of nitrogen in the effluent (breakthrough curves), and are available for a fixed temperature and steam-to-carbon molar ratio, and a range of operating pressures and CH_4 space velocities. The experimental conditions used by the researchers is summarised in Table 6.2.

Table 6.2 Conditions used in the Fuel Reactor experiments.

Parameter	Value
Temperature (K)	923
Total Pressure (bar)	3, 5, 7 and 9
CH_4 space velocity ($kg\ CH_4\ kg^{-1}cat - h^{-1}$)	2.5
Steam-to-carbon molar ratio ($kmol\ H_2O\ kmol^{-1}\ C$)	3.2
Adsorbent-to-catalyst weight ratio ($g\ ads\ g^{-1}cat$)	5
Catalyst loading ($g\ cat$)	4.4
Adsorbent loading ($g\ ads$)	22
Reactor bed length (m)	0.15
Reactor diameter (m)	0.0164
Particle diameter (m)	0.0006 – 0.0010

The textural properties of the catalyst and adsorbent utilised in the experiments are also reported in [44] and are summarised in Table 6.3.

Table 6.3 Summary of properties of materials utilised in the experiments used for model validation.

Property	Catalyst	Adsorbent
Active material content ($wt.\%$)	15.9 – 20	90
Particle density ($kg\ m^{-3}$)	3451	2710
B.E.T. surface area ($m^2\ g^{-1}$)	25	16
Particle porosity ($m_f^3\ m_p^{-3}$)	0.41	0.48
Mean pore size (nm)	14	80

The thermal properties of the catalyst were estimated based on an average content of 17.95 wt.% of nickel oxide; the thermal properties of the adsorbent at the beginning of the first cycle were assumed as those of 100 wt.% calcium oxide.

6.6 Results and discussion

6.6.1 Convergence of the model

The independence of the model solution from the mesh size was checked through series of simulations varying the number of discretisation points of the spatial domain. Two reactors of different dimensions and with different particle sizes were simulated for this purpose, the simulation parameters are summarised in

Table 6.4. The nomenclature of case R4VL0.15-3/5/7/9 refers to a lab-scale reactor of 0.15m long operated at 3, 5, 7 and 9 bar. Whereas the case R4SL1.0 refers to a reactor with a bed of 1.0m of length operated at 25 bar.

Table 6.4 Parameters utilised to run the various simulations described in this chapter.

Parameter	Case R4VL0.15-3/5/7/9	Case R4SL1.0
Gas composition (mole%)		
Methane	21.46	17.78
Water	68.68	72.64
Hydrogen	2.55	4.87
Carbon Monoxide	0.0	0.01
Carbon Dioxide	2.55	1.66
Nitrogen	4.75	3.04
Pellets properties (cat./ads.)		
Density (kg m^{-3})	3450/2710	3400/3340
Heat capacity (J $kg^{-1}K^{-1}$)	1102.5/1070.7	1102.5/1070.7
Porosity (m^3 m^{-3})	0.41/0.48	0.41/0.48
Avg. particle diameter (m)	0.0008	0.01
Reactor length (m)	0.15	1.0
Reactor diameter (m)	0.0264	0.35
Time period (s)	3600	1000
Inlet temperature (K)	923	973
Inlet pressure (bar)	3, 5, 7, 9	25
Inlet velocity	0.1, 0.06, 0.042 0.033	1.48
Vol. fraction of catalyst (m^3 m^{-3})	0.123	0.123
Discretisation method and order	1st order Backwards Finite Differences	1st order Backwards Finite Differences
Discretisation points	25, 50, 75, 100, 125	60, 75, 100, 125, 150

The response of the solution for the outlet hydrogen composition and the gas temperature profile along the bed at 1800s for case R4VL0.15-5 are shown in Figure 6.3(a) and (b); similarly, the gas velocity and the gas density profiles throughout the bed at 1800s are shown in Figure 6.4(a) and (b). For all four variables, it is apparent that 100 discretisation points suffice for an accurate solution of the system at a reasonable computing time. Below 100 discretisation points, the solution exhibits strong dependence on the mesh size, particularly in the prediction of the gas temperature profile as can be observed in Figure 6.3(b). For case R4SL1.0 the simulations were ran for 60, 75, 100, 125, and 150 points and the results are illustrated in Figure 6.5(a) and (b), and Figure 6.6(a) and (b). For this case, the results seem to be independent from the mesh size for a

number of discretisation points greater than $nz = 75$, thus for both cases 100 discretisation points will be used to establish the model solution.

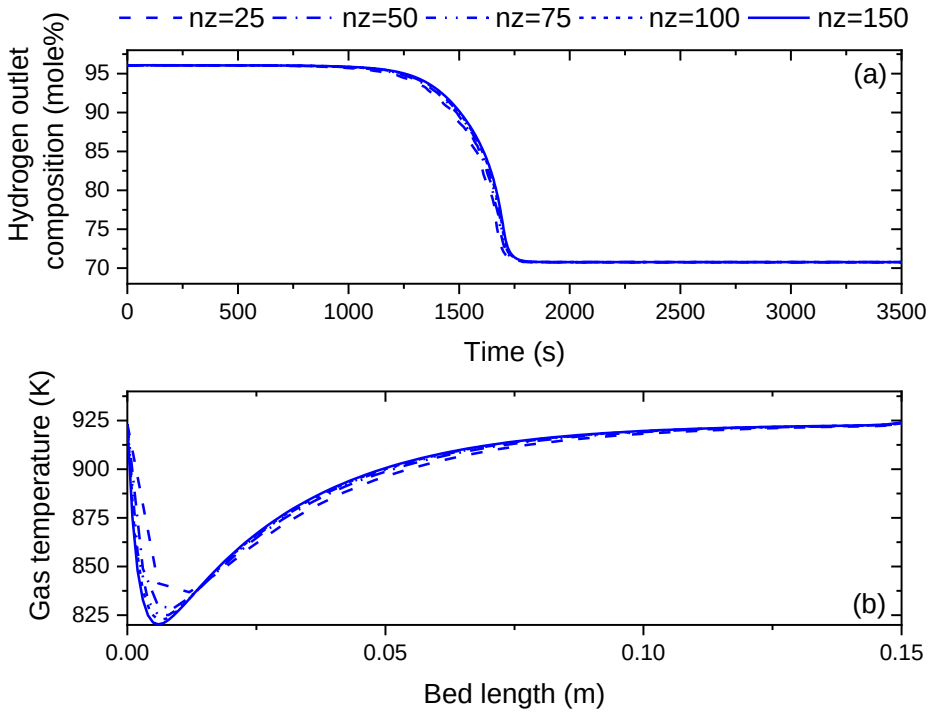

Figure 6.3 Convergence checks of model solution for case R4VL0.15-5 by (a) hydrogen outlet dry composition and (b) gas temperature profile at 1800 s, calculated for 25, 50, 75, 100, and 150 discretisation points.

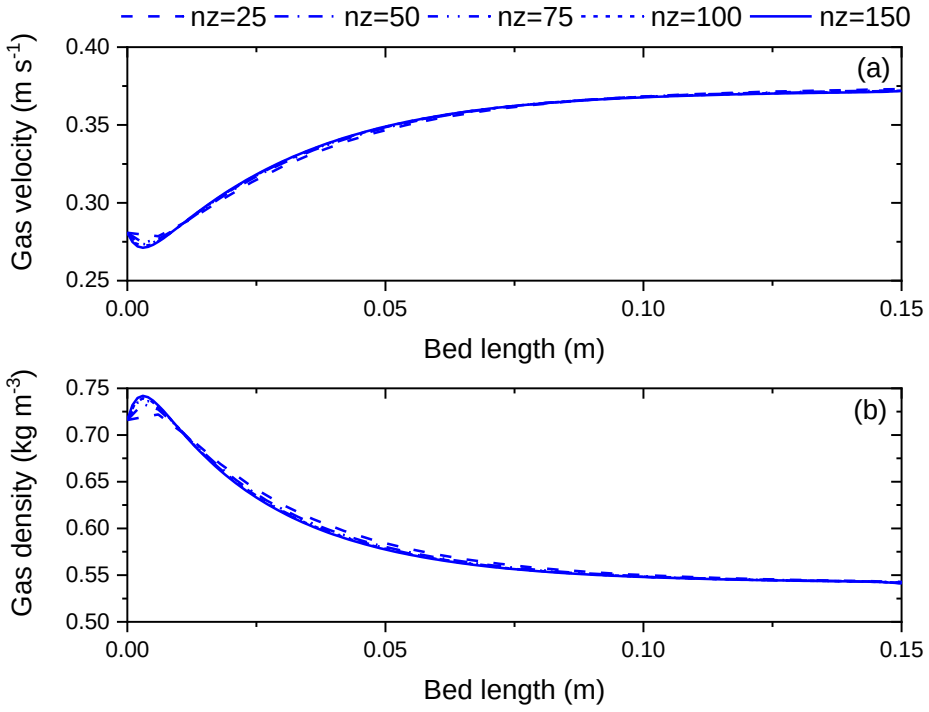

Figure 6.4 Convergence checks of model solution for case R4VL0.15-5 by (a) gas velocity profile at t=1800 s and (b) gas density profile at t=1800 s, calculated for 25, 50, 75, 100, and 150 discretisation points.

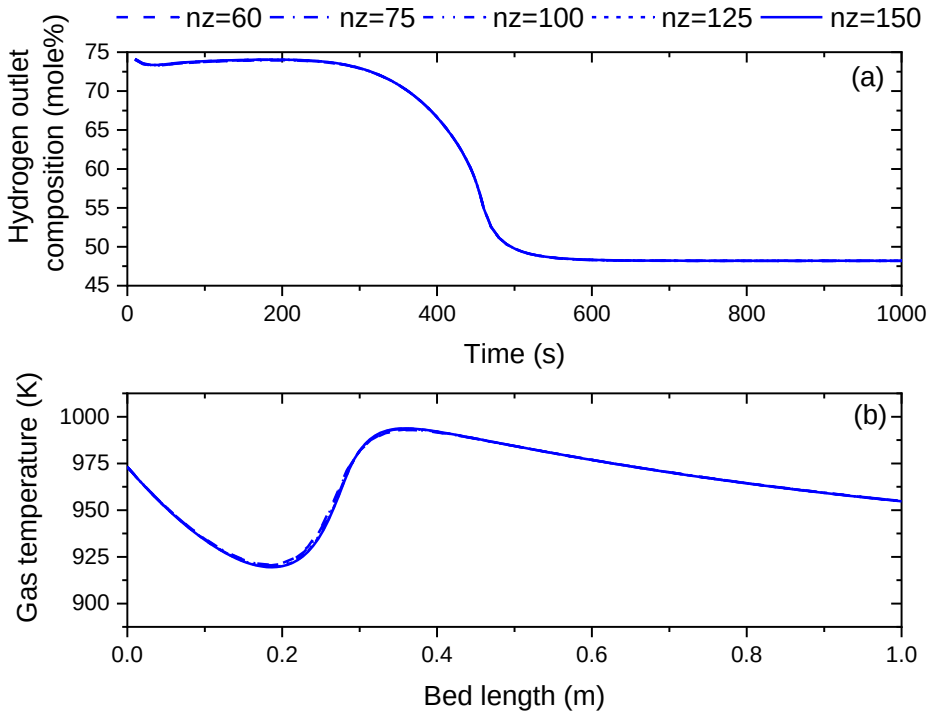

Figure 6.5 Convergence checks of model solution for case R4SL1.0 by (a) hydrogen outlet dry composition and (b) gas temperature profile at 250 s, calculated for 60, 75, 100, 125, and 150 discretisation points.

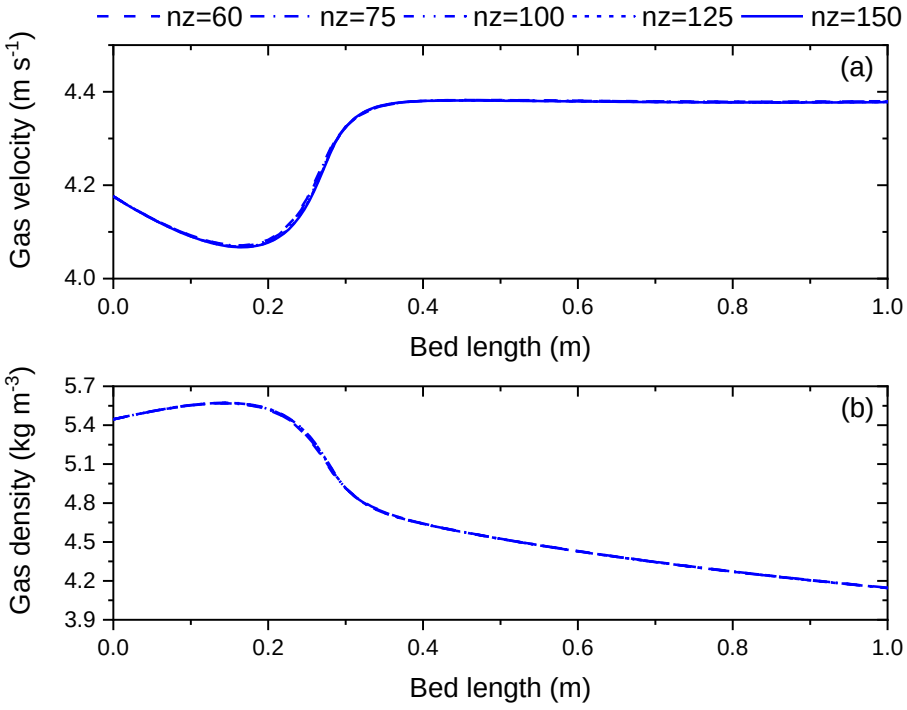

Figure 6.6 Convergence checks of model solution for case R4SL1.0 (a) gas velocity profile at t=250 s and (b) gas density profile at t=250 s, calculated for 60, 75, 100, 125, and 150 discretisation points.

6.6.2 The Fuel Reactor model

In this section the results of the application of the basic model described in 6.2.1 to simulate the experiments of Grasa et al. (32) are presented and compared with the predictions of the pseudo-homogeneous and the pseudo-heterogeneous models described in section 6.2.2. Prior to simulate the experiments, the sensitivity of the Fuel Reactor model to various kinetic rate expressions of the steam reforming reactions and the carbonation reaction is conducted.

6.6.2.1 Sensitivity of the kinetic rate expressions

The sensitivity of the model to the kinetic rate expressions was evaluated by comparing the outputs of various simulations ran with different kinetic expressions. The reforming kinetic rate expressions were assessed by simulating the Fuel Reactor model at a fixed temperature with the input data of Case R4VL0.15-3 (Table 6.4). The kinetic rate of carbonation presented in Equation (6.50) was used and kept fixed for this exercise. Figure 6.7(a) and (b) illustrate the effect of the different kinetic models in the simulation of the Fuel Reactor mode. Clearly, only the results of the models of Xu and Froment [86], and Hou and Hughes [88] (models XF and HH hereafter, respectively) produce a similar simulation output, whilst the models of Abbas et al. [89], and Soliman et al. [87] (models AB and SO) predict slower processes.

The hydrogen concentration profiles predicted by the AB and SO models are well below the hydrogen equilibrium concentration at the operating pressure and temperature elected for the simulation as shown in Figure 6.7(a), which is contrary to the expected approach to equilibrium of this process [172]. This anomalous behaviour might be related to the application of these models outside the range of operating conditions at which their kinetic parameters were estimated, although in the particular case of the SO model, the elimination of the mechanism of the formation of CO from the reaction network might affect the overall reactor concentrations. Conversely, the XF and HH models did approach the hydrogen equilibrium concentration, and produced comparable concentration profiles. The kinetic parameters of the latter models were estimated for a wider range of operating conditions, particularly those of the XF model, which was adjusted for a broader range of pressures.

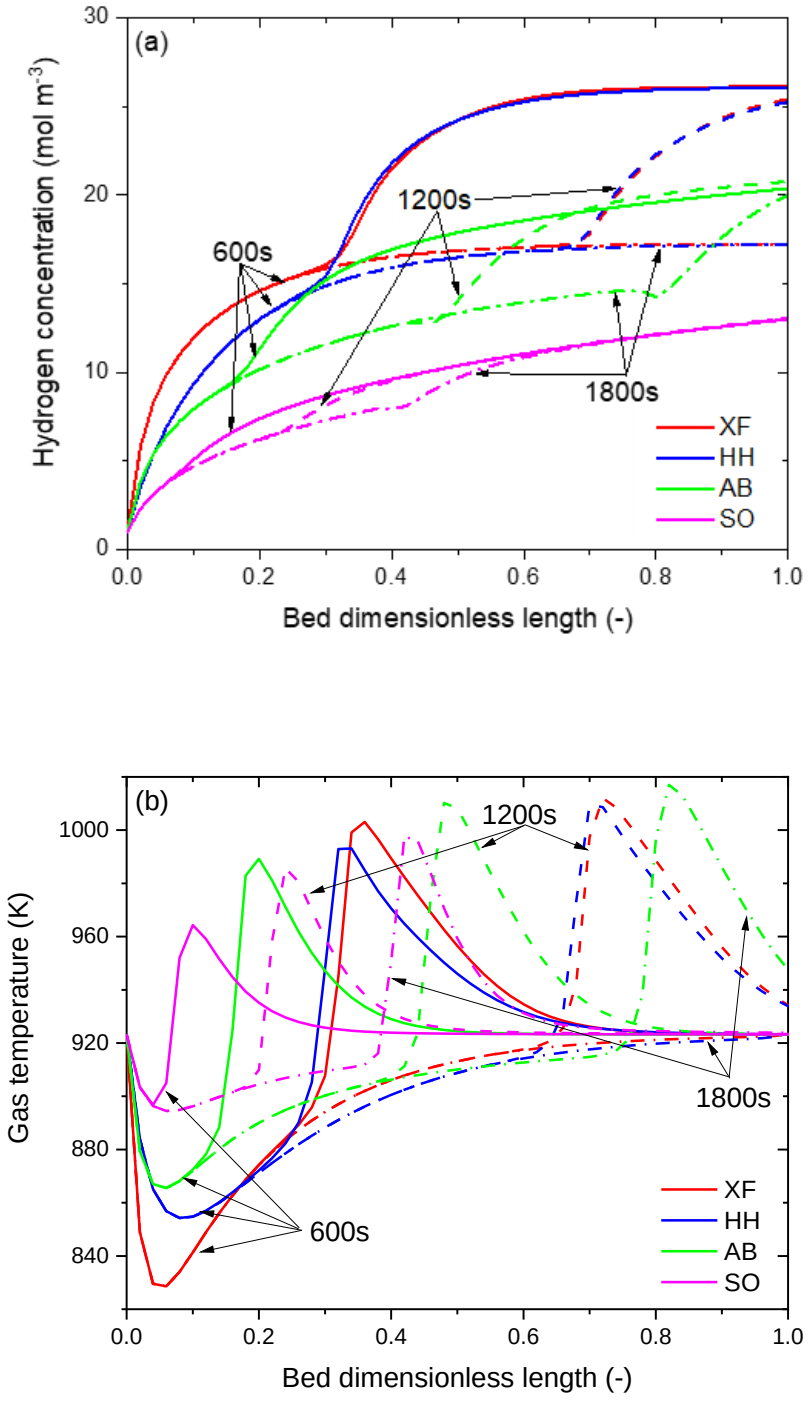

Figure 6.7 (a) Hydrogen concentration profiles (b) Gas temperature profiles, results of the simulation of Case R4VL0.15-3 bar and initial temperature of 923 K.

The rates of reaction also affect other variables, such as the gas temperature. Figure 6.7(b) shows the temperature profiles predicted with the four models. For all the cases a temperature drop near the reactor inlet is observed, which is expected given the endothermic nature of the reforming reactions. Nevertheless, the magnitude of the temperature drop differs among the models, with the XF

model giving the most severe temperature drop prediction. As with the concentration profile, the predictions of the temperature profile obtained with the XF model and with the HH model, are comparable; particularly as the thermal front approaches the bed outlet. The AB and SO models predict a less severe initial temperature drop, and consequently the temperature recovers more quickly owing to the heat of reaction released by the adsorption of CO_2 and the additional energy input to the reactor. Moreover, the AB and SO models predict slower kinetics than the XF and HH models, which is indicated by the hot spot shown at 1800 seconds; at this time, the XF and HH models predict that the saturation of the adsorbent has been reached, hence the predicted temperature profile corresponds to a system operating as a conventional reformer.

The previous results indicate some uncertainty in the utilisation of the AB and SO models within the SE-CLSMR model. The XF and HH model seem to produce a more consistent output, aside from the prediction of the temperature profile close to the bed inlet which can prove to be critical to assess the performance of the reactor concept. A final comparison of the simulation output of the four models against the experimental breakthrough data of the dry mole fraction of hydrogen was carried out and the results of the times for the 10%, 30%, 50%, 70%, and 90% of the breakthrough are summarised in Table 6.5 along with the error for each breakthrough time and the overall error. The magnitudes of the average errors are in accordance with the trends shown in the plots presented in Figure 6.7, the HH model presents the lowest average error with the experimental breakthrough data, closely followed by the XF model. However, the XF model will be used in the following analyses due to the wider range of operating temperature and pressure over which its parameters were estimated.

A similar analysis has been conducted for the carbonation model keeping fixed the reforming kinetic rate model of XF. The models of Sun et al. [96] hereafter termed GM1, Stendardo et al. [106] also referred to as GM2, and the empirical model (EM) of Rodriguez et al. [109] were implemented in the SE-CLSMR reactor model, and their effect on the model output is illustrated in Figure 6.8, Figure 6.9, and Figure 6.10. The random-pore model of Bhatia and Perlmutter [95] was also implemented., nevertheless gPROMS^{TM} could not establish a set of solutions, as it encountered many difficulties to integrate the equations during the initialisation step.

Figure 6.8 is a plot of the adsorbent conversion profiles predicted with the various carbonation kinetic models at different simulation times. All of the assessed models produce similar outputs, particularly below 20% of conversion of the adsorbent. Above this value, the grain models predict a slightly faster conversion of the material than the empirical model, which is indicative of a higher rate of

carbonation being predicted by the grain models. In fact, the EM model exhibits the lowest rate of carbonation, while the GM1 and the GM2 models exhibit peak rates of carbonation trending in opposite direction as illustrated in Figure 6.9.

The latter affects the temperature rise of the system since a higher rate of adsorbent conversion yields a faster generation of heat of adsorption, thus increasing the bulk gas and bed temperatures; simultaneously the local temperature of the adsorbent enhances the kinetic rate constant, hence the rate of carbonation. Figure 6.10 illustrates the gas temperature profiles predicted with the various models of carbonation kinetics. The location of the peak temperatures at each simulation time is consistent with the peak carbonation rates showed in Figure 6.9.

The breakthrough curves of this system were used as an additional criterion to compare the effect of the carbonation model in the output of the SE-CLSMR model. The times for 10%, 30%, 50%, 70% and 90% of the breakthrough curve were calculated by linear interpolation and compared against the experimental data, the results are summarised in Table 6.6 along with average error in the prediction of the curve. The overall average error is less than 10% for the three models, and the empirical model (EM) recorded the lowest error, followed by the model GM1. The highest errors for all the models are located close to the leading and the rear zones of the breakthrough curve, whereas in the mass transfer zone the error drops below 5% for the EM and the GM1 models. Thus the empirical model seem to produce a better fit of the experimental data. However, the level of physical detail of this type of model is a drawback as it would not allow to investigate the sensitivity of certain adsorbent properties (e.g. the surface area) on the behaviour of the system as its mathematical structure accommodates all the effects within the kinetic rate constant. In this sense, the grain models provide a better investigative tool that allows to explore the properties of the adsorbent that would produce a certain output. Thus, the GM1 model is chosen to simulate the different study cases.

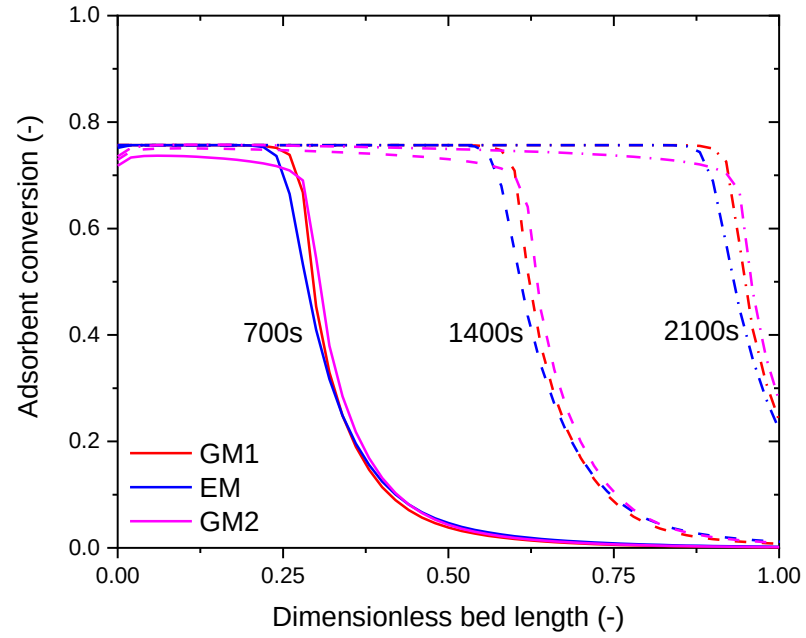

Figure 6.8 Adsorbent conversion profiles predicted with the GM1, GM2 and EM models at various simulation times.

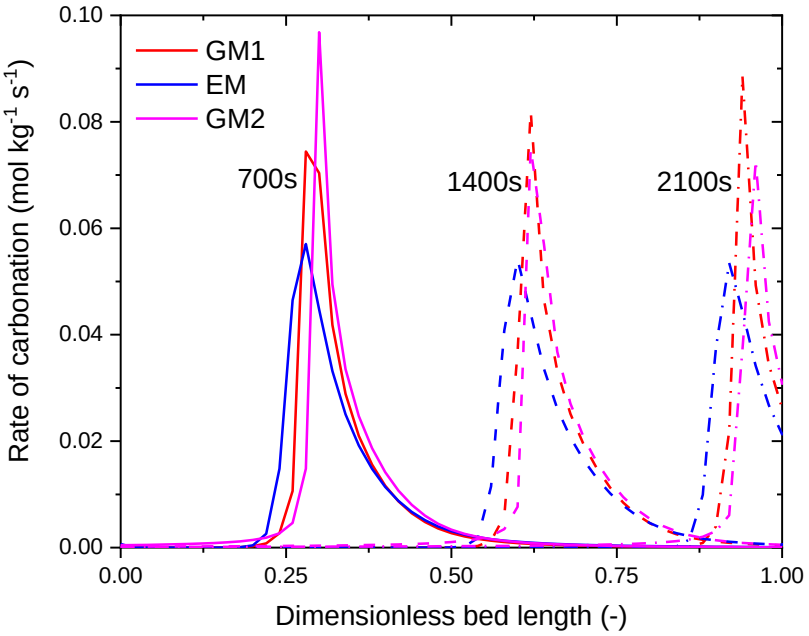

Figure 6.9 Adsorption reaction rate predicted with the GM1, GM2 and EM models at various simulation times.

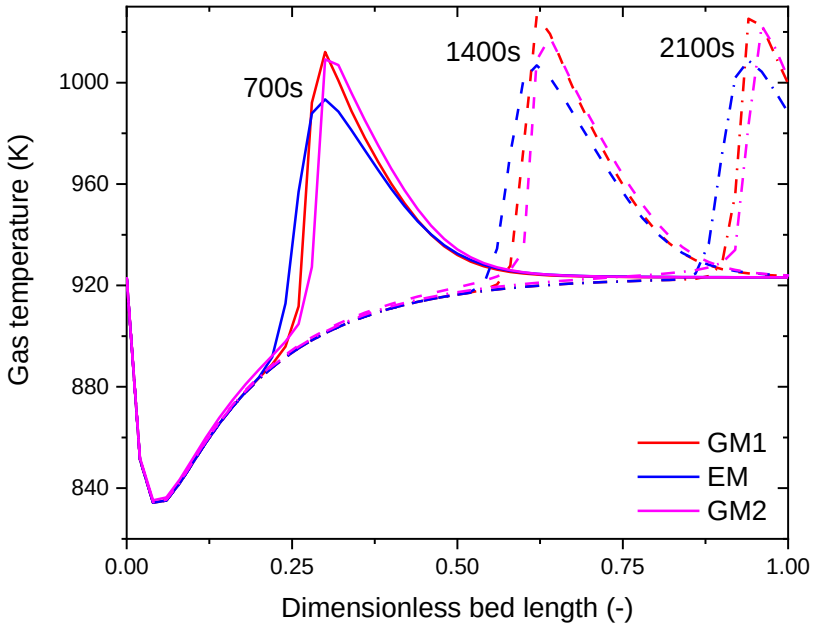

Figure 6.10 Gas temperature profiles predicted with the GM1, GM2 and EM models at various simulation times.

Table 6.5 Effect of the steam reforming kinetic rate expressions on the prediction of hydrogen breakthrough curves with the heterogeneous Fuel Reactor model.

Case	**R4VL0.15-3**								
Description	**Sorption Enhanced Steam Reforming experiments at 3 bar and 923 K.**								
Breakthrough	**Experimental time (s)**	**Xu and Froment (1989)**	**% Error**	**Soliman et al. (1992)**	**% Error**	**Hou and Hughes (2001)**	**% Error**	**Abbas et al. (2017)**	**% Error**
0.1	1980.2	1698.1	14.25%	3367.9	70.07%	1718.0	13.24%	2150.0	8.57%
0.3	1798.8	1663.5	7.52%	3328.4	85.03%	1681.4	6.53%	2107.5	17.16%
0.5	1671.5	1614.6	3.41%	3265.8	95.38%	1630.0	2.48%	2048.2	22.54%
0.7	1588.4	1525.9	3.93%	3156.9	98.75%	1536.0	3.30%	1972.8	24.21%
0.9	1489.2	1349.1	9.41%	2776.0	86.41%	1338.0	10.15%	1841.5	23.66%
		Avg. Error	**6.97%**		**88.91%**		**6.34%**		**19.75%**

Table 6.6 Effect of the carbonation kinetic rate expressions on the prediction of hydrogen breakthrough curves with the heterogeneous Fuel Reactor model.

Case	**R4VL0.15-5**						
Description	**Sorption Enhanced Steam Reforming experiments at 5 bar and 923 K.**						
Breakthrough	**Experimental time (s)**	**Sun et al. (2008)**	**% Error**	**Stenardo and Foscolo (2009)**	**% Error**	**Rodriguez et al. (2011)**	**% Error**
0.1	2569.2	2273.2	11.52%	2254.6	12.24%	2337.9	9.00%
0.3	2363.4	2248.8	4.85%	2222.5	5.96%	2287.2	3.22%
0.5	2292.3	2206.1	3.76%	2179.5	4.92%	2231.4	2.66%
0.7	2214.3	2126.2	3.98%	2097.7	5.27%	2141.4	3.29%
0.9	2109.2	1951.5	7.48%	1918.3	9.05%	1936.0	8.21%
		Avg. Error	**5.91%**		**7.07%**		**4.76%**

6.6.2.2 Validation of the heterogeneous Fuel Reactor model and the benchmarking models

The validation of the Fuel Reactor model is attained by comparing the simulated breakthrough curve of hydrogen and carbon dioxide against the experimental breakthrough data. The simulations were conducted with the input data summarised in Table 6.4 corresponding to the cases R4VL0.15-3/5/7/9, and the outputs are shown in Figure 6.11 – Figure 6.14. To afford clarity and quick reference in the discussion of the results and in the reading of plots, the nomenclature indicated in Table 6.7 is used for each of the models utilised:

Table 6.7 Nomenclature utilised for reference to the models.

Model nomenclature	Description
HTG-2P-PF	Plug flow base model described in section 6.2.1.1.
HTG-2P-AD	Base model plus axial dispersion described in section 6.2.1.2.
PHG-2P-PF	Pseudo-homogeneous plug flow model described in section 6.2.2.1.
PHTG-1P-PF	Pseudo-heterogeneous model described in section 6.2.2.2 without the axial dispersion term.
PHTG-1P-AD	Pseudo-heterogeneous model described in section 6.2.2.2.

Figure 6.11 is a plot of the breakthrough curves of the dry composition of hydrogen and carbon dioxide predicted for case R4VL0.15-3 with various approaches of the Fuel Reactor model; the last number of the case code indicates the pressure at which the experimental data was obtained, hence the pressure at which the simulation was conducted. Similarly, R4VL0.15-5, R4VL0.15-7, and R4VL0.15-9, refer to those cases simulated at 5, 7, and 9 bar, respectively, and the results are shown in Figure 6.12, Figure 6.13, and Figure 6.14.

At 3 bar (Figure 6.11) the carbonation effectiveness factor can be utilised in the different Fuel Reactor models as an adjustable parameter to approximate the output of the simulation to the experimental breakthrough data. In fact, the average errors calculated for the approximation of the breakthrough curves are below 10%. As shown in Figure 6.11, all the models represent poorly the leading zone of the breakthrough curve; a better approximation is obtained for the rear zone, particularly for the dry mole percentage of hydrogen. Nevertheless, the models represented with good accuracy the pre- and post-breakthrough zones. The accuracy of the breakthrough curve was improved by manipulating the effectiveness factor of the carbonation reaction, whose effect on the simulation

results is to reduce or increase the time required to saturate the adsorbent. For the experiments ran at 3 bar and 923 K, the models HTG-2P-PF, HTG-2P-AD, PHG-2P-PF were adjusted with $\eta_{Carb} = 0.85$, whereas the models PHTG-1P-PF and PHTG-1P-AD required $\eta_{Carb} = 0.90$. These effectiveness factor values seem very high for this reaction since the CO_2 has to overcome the diffusional resistance imposed by the product layer to reach the reaction zone. In fact, the effectiveness factors utilised here are higher than those used by Grasa et al. [44] who reported a good fit of their pseudo-homogeneous model with $\eta_{Carb} = 0.30$, these differences might be justified by the model assumptions used by the researchers, and possibly, by the use of different inputs into the model.

The performance of each model was measured by the average error in the estimation of the breakthrough curve. At 3 bar, the HTG-2P-PF model produced the output with the lowest error (4.73%), followed by the PHG-2P-PF and the PHTG-1P-PF models, with 6.30% and 9.00%, respectively. The incorporation of axial dispersion in the models showed improvement only in the case of the PHTG-1P-AD model, increasing the accuracy by 0.36%; in the case of the heterogeneous model HTG-2P-AD the incorporation of axial dispersion resulted in an increase of the average error to 6.63%. These errors must be taken with care since the manipulation of the effectiveness factor to adjust the model output was attained by trial and error, and the final value was chosen by visually inspecting the approach of the simulation to the experimental data. This is by no means the most advisable way to proceed; a parameter estimation algorithm should render a more accurate and reliable output, unfortunately, the version of gPROMS^{TM} utilised in this work does not handle distributed variables in parameter estimation problems and the case could not be set up.

At higher pressures, the models did not adjust well to the experimental data. The predicted breakthrough curves presented in Figure 6.12, Figure 6.13, and Figure 6.14, exhibit an increasing average error with respect to the data as summarised in Table 6.9 to Table 6.11. At 5 bar the HTG-2P-PF model exhibits the lowest average error (5.91%), whereas at 7 and 9 bar the HTG-2P-AD model yielded slightly better results, with errors of 13.26% and 14.65%, respectively. The shorter adsorbent saturation time predicted with the models can be related to the need of accounting for the reduction of the porosity due to the progress of the adsorbent conversion with time. The net effect of loss of porosity is a process controlled by the diffusion of CO_2 through the product layer, thus increasing the time required to approach the maximum conversion of the adsorbent. Nevertheless, the experimental error should not be disregarded as the inspection of the data reveals an anomalous behaviour; for example, at 7 bar the dry mole percentage of hydrogen breaks through a few seconds after the data

corresponding to the experiment at 9 bar, this behaviour is unexpected as the inlet velocity of the experiment at 7 bar is higher than the corresponding velocity at 9 bar. The effect of the velocity on the breakthrough curve has been reported in [6], a higher velocity shortens the adsorbent saturation time, hence it would have been reasonable to expect that the experimental data at 9 bar exhibited a longer pre-breakthrough zone.

In addition, the experimental data exhibit a different degree of diffusion, which implicates a different mass zone transfer length, with the data at 5 bar being the only one approaching the shape of a sharp front. This might be an indication of an incorrect inlet forcing function in the modelling work as well as some uncertainty in the experimental conditions at the bed inlet. Nevertheless, the performance of the models based on the plug flow behaviour is acceptable as their output approaches the data reasonably well. Moreover, the plug flow-based models produce a similar output to that of the models considering axial dispersion, this is not surprising, since the length-to-particle diameter ratio for this particular system ($L_b/d_p = 187.5$) surpass the threshold $L_b/d_p = 50$, thus highlighting the strong convective character of the process.

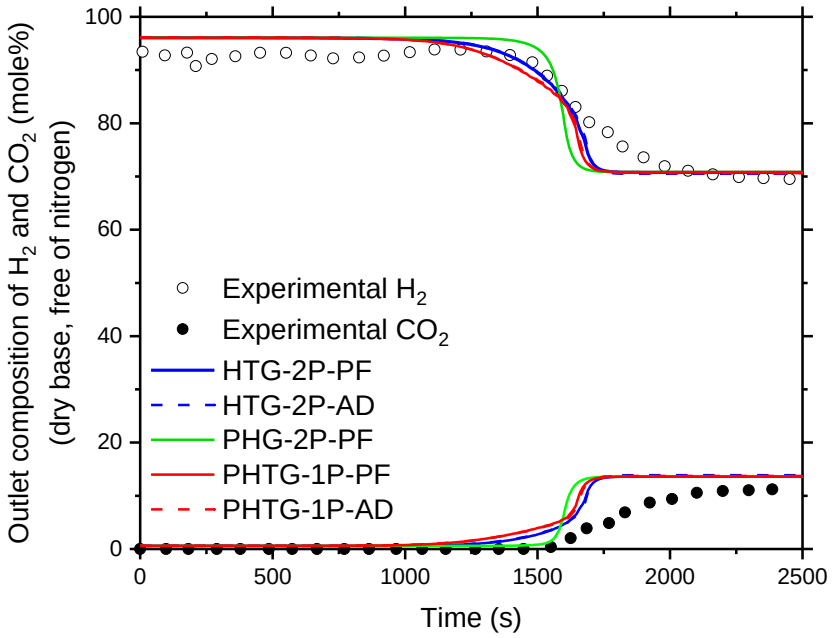

Figure 6.11 Breakthrough curves of H_2 and CO_2 at 3 bar and 923 K calculated with the various modelling approaches.

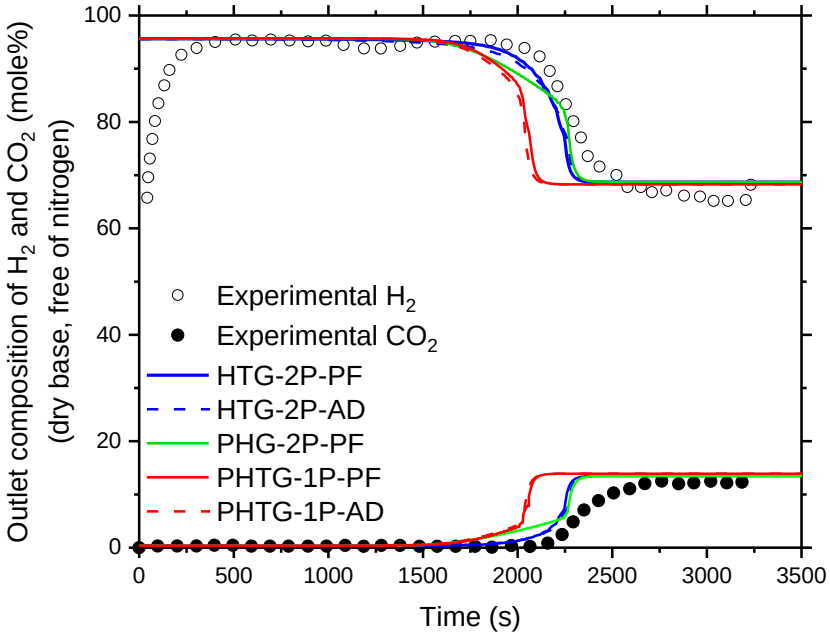

Figure 6.12 Breakthrough curves of H_2 and CO_2 at 5 bar and 923 K calculated with the various modelling approaches.

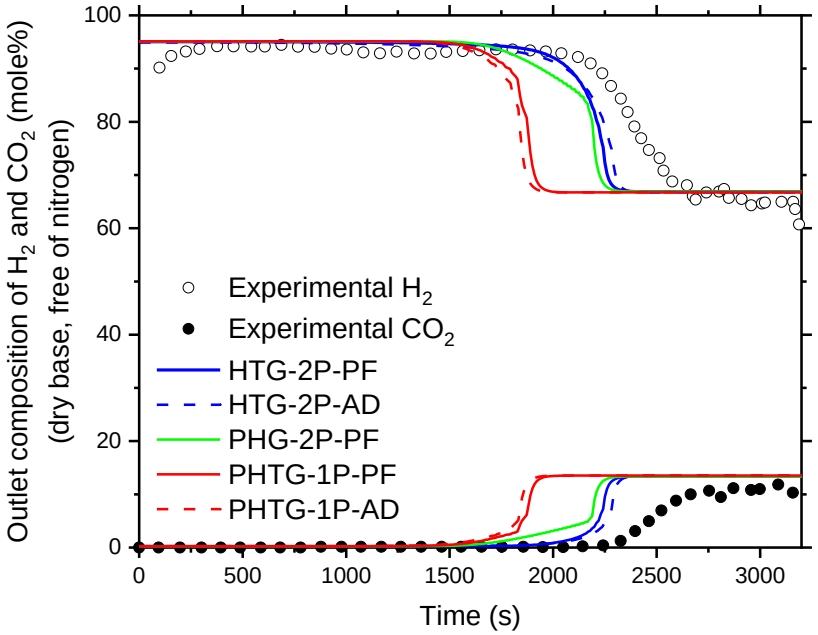

Figure 6.13 Breakthrough curves of H_2 and CO_2 at 7 bar and 923 K calculated with the various modelling approaches.

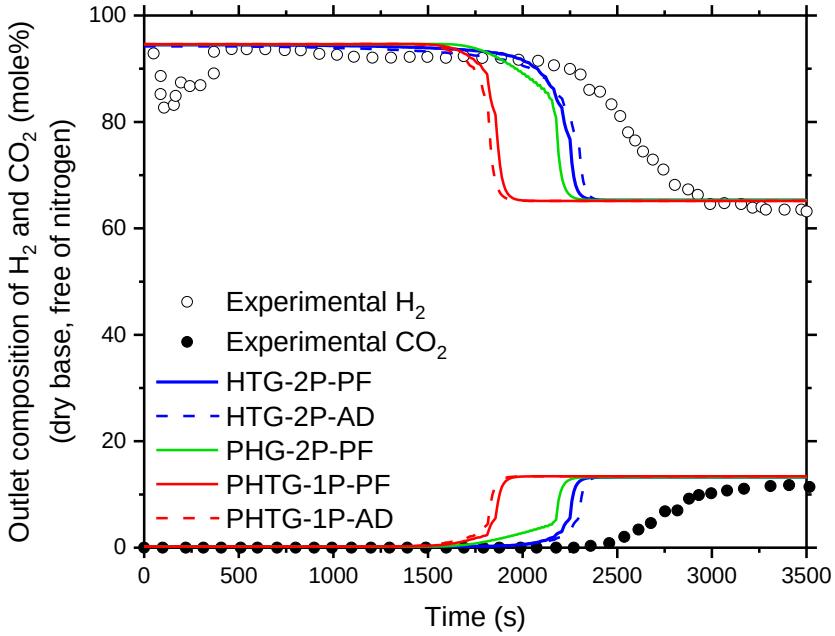

Figure 6.14 Breakthrough curves of H_2 and CO_2 at 9 bar and 923 K calculated with the various modelling approaches.

Table 6.8 Average error of the various modelling approaches in the prediction of the mass transfer zone of the breakthrough curve of hydrogen at 3 bar and 923 K.

Case	R4VL0.15-3										
Description	Sorption Enhanced Steam Reforming experiments at 3 bar and 923 K.										
Breakthrough	**Experimental time (s)**	**HTG-2P-PF**	**% Error**	**HTG-2P-AD**	**% Error**	**PHG-2P-PF**	**% Error**	**HTG-1P-PF**	**% Error**	**HTG-1P-AD**	**% Error**
0.1	1980.2	1735.1	12.38%	1703.3	13.98%	1636.9	17.34%	1675.8	15.37%	1682.3	15.04%
0.3	1798.8	1701.5	5.41%	1672.5	7.02%	1606.6	10.68%	1646.8	8.45%	1653.9	8.06%
0.5	1671.5	1653.1	1.11%	1620.6	3.05%	1589.9	4.89%	1604.0	4.04%	1611.5	3.59%
0.7	1588.4	1561.9	1.67%	1529.6	3.70%	1567.9	1.29%	1483.9	6.57%	1491.4	6.10%
0.9	1489.2	1388.1	6.79%	1354.5	9.04%	1511.3	-1.49%	1269.7	14.74%	1271.5	14.62%
		Avg. Error	**4.73%**		**6.63%**		**6.30%**		**9.00%**		**8.64%**

Table 6.9 Average error of the various modelling approaches in the prediction of the mass transfer zone of the breakthrough curve of hydrogen at 5 bar and 923 K.

Case	R4VL0.15-5										
Description	Sorption Enhanced Steam Reforming experiments at 5 bar and 923 K.										
Breakthrough	**Experimental time (s)**	**HTG-2P-PF**	**% Error**	**HTG-2P-AD**	**% Error**	**PHG-2P-PF**	**% Error**	**HTG-1P-PF**	**% Error**	**HTG-1P-AD**	**% Error**
0.1	2569.2	2273.2	11.52%	2288.5	10.93%	2299.2	10.51%	2092.3	18.56%	2070.0	19.43%
0.3	2363.4	2248.8	4.85%	2264.1	4.20%	2272.3	3.85%	2065.8	12.59%	2043.3	13.54%
0.5	2292.3	2206.1	3.76%	2207.1	3.72%	2244.3	2.09%	2036.6	11.16%	2024.3	11.69%
0.7	2214.3	2126.2	3.98%	2111.5	4.64%	2066.0	6.70%	1992.0	10.04%	1962.2	11.39%
0.9	2109.2	1951.5	7.48%	1885.8	10.59%	1790.6	15.10%	1795.6	14.87%	1765.9	16.28%
		Avg. Error	**5.91%**		**6.19%**		**6.91%**		**12.99%**		**13.98%**

Table 6.10 Average error of the various modelling approaches in the prediction of the mass transfer zone of the breakthrough curve of hydrogen at 7 bar and 923 K.

Case	**R4VL0.15-7**										
Description	**Sorption Enhanced Steam Reforming experiments at 7 bar and 923 K.**										
Breakthrough	**Experimental time (s)**	**HTG-2P-PF**	**% Error**	**HTG-2P-AD**	**% Error**	**PHG-2P-PF**	**% Error**	**HTG-1P-PF**	**% Error**	**HTG-1P-AD**	**% Error**
0.1	3166.0	2174.8	31.31%	2204.6	30.37%	2127.3	32.81%	1914.2	39.54%	1808.9	42.87%
0.3	2533.4	2150.7	15.11%	2180.7	13.92%	2097.3	17.21%	1887.2	25.51%	1780.8	29.71%
0.5	2415.4	2119.6	12.25%	2141.5	11.34%	2083.9	13.72%	1870.4	22.56%	1767.9	26.81%
0.7	2327.2	2067.0	11.18%	2072.5	10.95%	2061.2	11.43%	1833.3	21.22%	1732.0	25.58%
0.9	2175.3	1930.5	11.25%	1892.8	12.99%	1981.2	8.93%	1699.9	21.86%	1594.7	26.69%
		Avg. Error	**15.11%**		**14.65%**		**15.89%**		**25.12%**		**29.32%**

Table 6.11 Average error of the various modelling approaches in the prediction of the mass transfer zone of the breakthrough curve of hydrogen at 9 bar and 923 K.

Case	**R4VL0.15-9**										
Description	**Sorption Enhanced Steam Reforming experiments at 9 bar and 923 K.**										
Breakthrough	**Experimental time (s)**	**HTG-2P-PF**	**% Error**	**HTG-2P-AD**	**% Error**	**PHG-2P-PF**	**% Error**	**HTG-1P-PF**	**% Error**	**HTG-1P-AD**	**% Error**
0.1	2939.9	2279.4	22.47%	2326.4	20.87%	2217.6	24.57%	1900.4	35.36%	1862.4	36.65%
0.3	2713.1	2256.2	16.84%	2302.8	15.12%	2189.6	19.30%	1873.9	30.93%	1834.7	32.38%
0.5	2554.6	2219.9	13.10%	2260.0	11.53%	2178.0	14.74%	1859.6	27.21%	1821.9	28.68%
0.7	2440.9	2167.6	11.20%	2179.3	10.72%	2117.1	13.27%	1824.5	25.25%	1790.6	26.64%
0.9	2170.8	2001.7	7.79%	1946.9	10.32%	1884.5	13.19%	1742.5	19.73%	1689.2	22.19%
		Avg. Error	**13.99%**		**13.26%**		**16.70%**		**27.61%**		**29.19%**

6.6.2.3 Comparison of the heterogeneous model, the pseudo-homogeneous model and the pseudo-heterogeneous model for a reactor with small pellets.

The breakthrough profiles showed in Figure 6.12, Figure 6.13, and Figure 6.14, revealed that the pseudo-heterogeneous models (PHTG-1P-PF and PHTG-1P-AD) predict a faster saturation of the bed, whereas the pseudo-homogeneous model (PHG-2P-PF) and the heterogeneous models (HTG-2P-PF and HTG-2P-AD) predict a similar bed response. Furthermore, it was also observed that the models accounting for axial dispersion (PHTG-1P-AD and HTG-2P-AD) did not improve the prediction of the breakthrough curve, therefore in this section the focus will be in comparing the plug flow-based models. The aforementioned reported behaviour of the models' responses is associated with the assumption of a constant mass flux taken in the development of the models based in the pseudo-heterogeneous approach. As the process progresses, the total bulk mass is depleted owing to the adsorption of CO_2 as illustrated in Figure 6.15; at the same time, the density of the bulk gas decreases due to the increasing fraction of H_2 present in the mixture, this situation effects the velocity of the bulk gas due to a higher volume of gas flowing through the bed pores, this is expressed by the continuity equation.

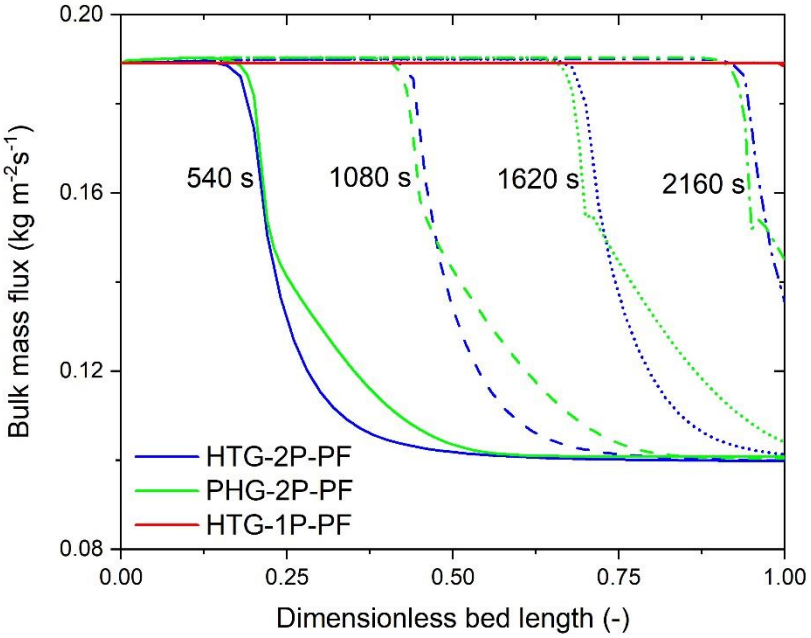

Figure 6.15 Bulk mass flux profiles predicted with the heterogeneous model (HTG-2P-PF), the pseudo-homogeneous model (PHG-2P-PF), and the pseudo-heterogeneous model (HTG-1P-PF), at inlet gas conditions of 5 bar, 923 K and 0.06 m s^{-1}; the initial bed temperature is 923 K.

The bulk density and velocity at different simulation times predicted with the plug flow models PHTG-1P-PF, PHG-2P-PF, and HTG-2P-PF are illustrated in Figure 6.16 and Figure 6.17. Similar density profiles are shown in Figure 6.16 with the three models, whose main difference is the position of the discontinuity; this is another effect of the differences in the modelling assumptions as it will be seen later. The velocity profile at different simulation times predicted with the various models are illustrated in Figure 6.17; a much higher velocity was predicted with the PHTG-1P-PF plug flow model, which proceeds from the assumption of constant mass flux throughout the bed, in combination with the decrease of the gas density. Conversely, the velocity profiles obtained with the HTG-2P-PF and the PHG-2P-PF models were calculated by accounting for the depletion of the total bulk gas mass as modelled by Equations (6.12) and (6.13). The incorporation of this phenomenon into the model led to the prediction of ca. 30% - 41.6% lower peak velocities than the PHTG-1P-PF model. In addition, it is observed that the pseudo-homogeneous plug flow model (PHG-2P-PF) predicts a higher velocity profile than the heterogeneous plug flow model (HTG-2P-PF), the reason for this behaviour being a combination of the differences in bulk gas density due primarily to the higher temperature predicted by the pseudo-homogenous model as shown in Figure 6.18(a).

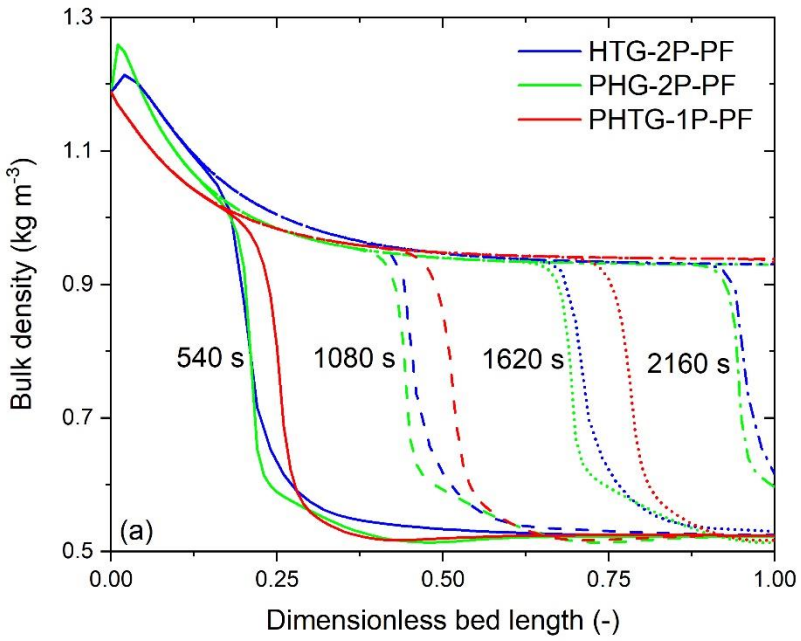

Figure 6.16 Bulk density profiles at several simulation times predicted with the heterogeneous model (HTG-2P-PF), the pseudo-homogeneous model (PHG-2P-PF), and the pseudo-heterogeneous model (HTG-1P-PF), at inlet gas conditions of 5 bar, 923 K and 0.06 m s-1; the initial bed temperature is 923 K.

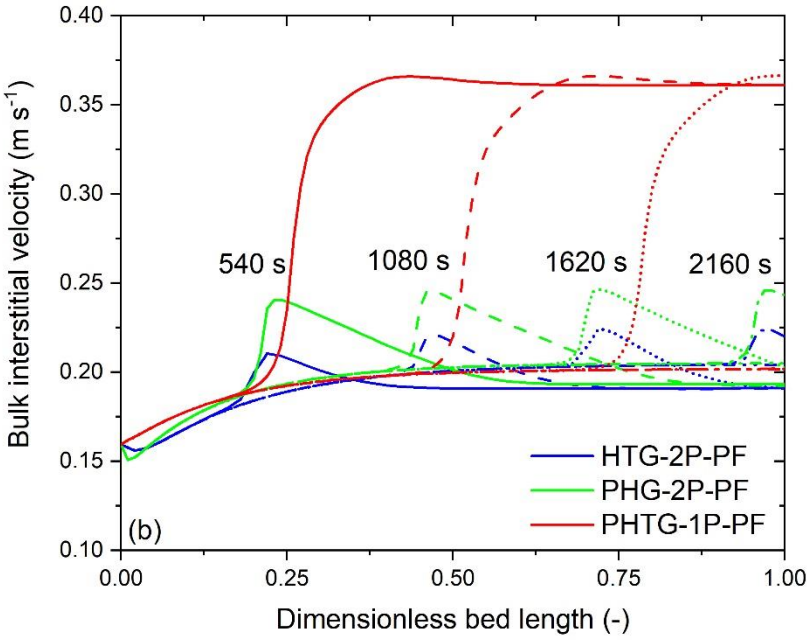

Figure 6.17 Gas interstitial velocity profiles at several simulation times predicted with the heterogeneous model (HTG-2P-PF), the pseudo-homogeneous model (PHG-2P-PF), and the pseudo-heterogeneous model (HTG-1P-PF), at inlet gas conditions of 5 bar, 923 K and 0.06 m s^{-1}; the initial bed temperature is 923 K.

Figure 6.18(a) and (b) present the temperature profiles predicted with the plug flow-based heterogeneous (HTG-2P-PF), pseudo-heterogeneous (PHTG-1P-PF), and pseudo-homogeneous (PHG-2P-PF) models. Figure 6.18(a) illustrates the profiles of the bulk gas temperature with the three different models, at several simulation times; the prediction of the three models indicate a hot spot moving downstream in the bed, however, significant differences are observed among the various temperature profiles, either in the magnitude of the temperature or in the location of the maximum temperature in the bed. The pseudo-homogeneous model (PHG-2P-PF) predicts peak bulk gas temperatures 30.8 – 43.4 K higher than those predicted with the HTG-2P-PF model. However, it is more interesting to compare the temperature profile predicted with the pseudo-homogeneous model with the catalyst temperature profile predicted with the heterogeneous model, since these temperatures are ultimately used to calculate the reaction rate constant, therefore the activity of the catalyst. The heterogeneous model predicts peak catalyst temperatures in the range 966.5 – 998.8 K; these temperatures are significantly lower than the bulk gas peak temperatures predicted by the pseudo-homogeneous model which are in the range 1048.9 – 1057.3 K; this clearly effects the expected rate of reaction and ultimately the length of bed needed to attain the desired conversion.

Conversely, the magnitude of the bulk gas temperature profiles predicted with the pseudo-heterogeneous model (PHTG-1P-PF) is similar to that of the corresponding temperature obtained with the HTG-2P-PF model; the former model predicts bulk gas temperatures that are 1.6 – 12.1 K higher than those obtained with the heterogeneous plug flow model. However, it is noticeable that the velocity of thermal front moves faster for the pseudo-heterogeneous model and at 1620 s the leading edge of the front has already reached the bed exit.

In Figure 6.18(b) the temperature profiles of the solid phases obtained with the heterogeneous and pseudo-heterogeneous approaches are shown. Similarly to the bulk gas temperature, both models predict a hot spot moving throughout the solid phases. The heterogeneous model allows for the prediction of two different profiles, one at the adsorbent surface, and one at the catalyst surface. This model predicts that the temperature of the adsorbent is ca. 5.44% higher than the temperature at the catalyst surface. This suggest that a fraction the heat of reaction released by the adsorbent during the carbonation of CaO is in fact being utilised to heat-up the catalyst, however, with some part of the available heat being lost. In fact, a comparison of the bulk gas temperature profile with the adsorbent temperature profile predicted with this model reveals that the peak temperature of the latter is just ca. 1.39% higher than the peak temperature of the bulk gas; this suggest in principle, that a significant amount of the heat of adsorption exits in the system within the bulk gas. Nevertheless, it should be remembered that these simulations considered a system externally heated by a furnace, hence it is difficult to establish to what extent the temperature of the catalyst is being raised by the effect of the heat of adsorption, and to what extent is the external heating offsetting the endothermicity of the steam reforming processes.

The temperature profile of the adsorbent/catalyst predicted by the PHTG-1P-PF is also illustrated in Figure 6.18(b). The peak temperatures predicted with this model are of comparable magnitude to the peak temperatures of the adsorbent predicted by the HTG-2P-PF model. However, the location of the maximum temperature vary, with the thermal front being located ahead in the case of the PHTG-1P-PF model as a consequence of the higher gas velocity profile, which accelerates the velocity of the thermal front.

The results of the temperature profiles calculated with the various modelling approaches affect significantly other variables that are temperature-dependent such as the fluid properties or the kinetic rates. As discussed before, if the full reactor or the solid phases are considered homogeneous, the rate constants (and thus the rates of reaction) might be overestimated, rendering a different performance of the reactor as shown in Figure 6.19. Figure 6.20 shows an

example of the rates of reaction of the reforming processes and the carbonation of CaO at 1080 s predicted with the various models; clearly the lowest rates correspond to those calculated based on the heterogeneous model.

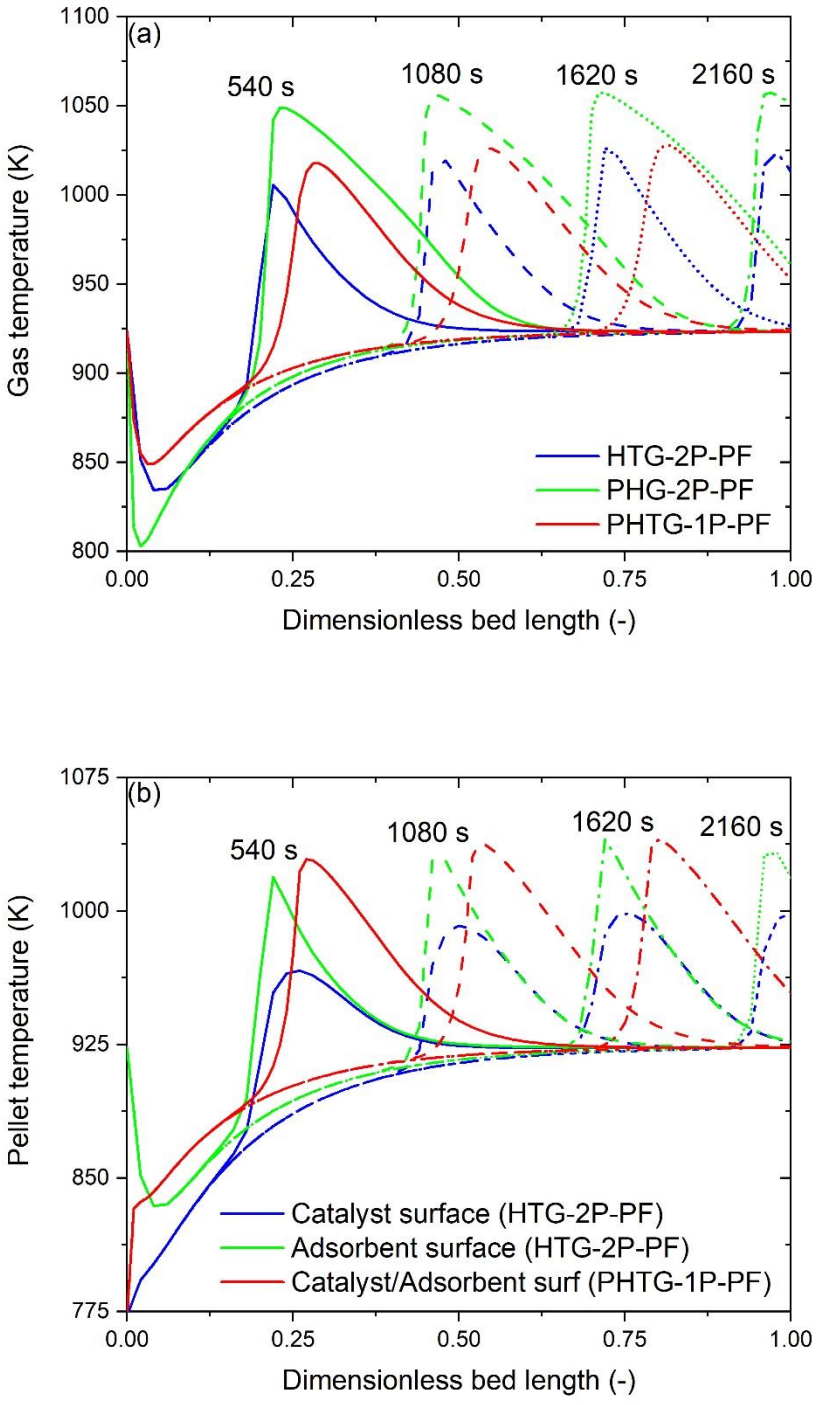

Figure 6.18 (a) Bulk gas temperature and (b) Solid phase temperature at several simulation times predicted with the heterogeneous model (HTG-2P-PF), the pseudo-homogeneous model (PHG-2P-PF), and the pseudo-heterogeneous model (HTG-1P-PF), at inlet gas conditions of 5 bar, 923 K and 0.06 m s^{-1}; the initial bed temperature is 923 K.

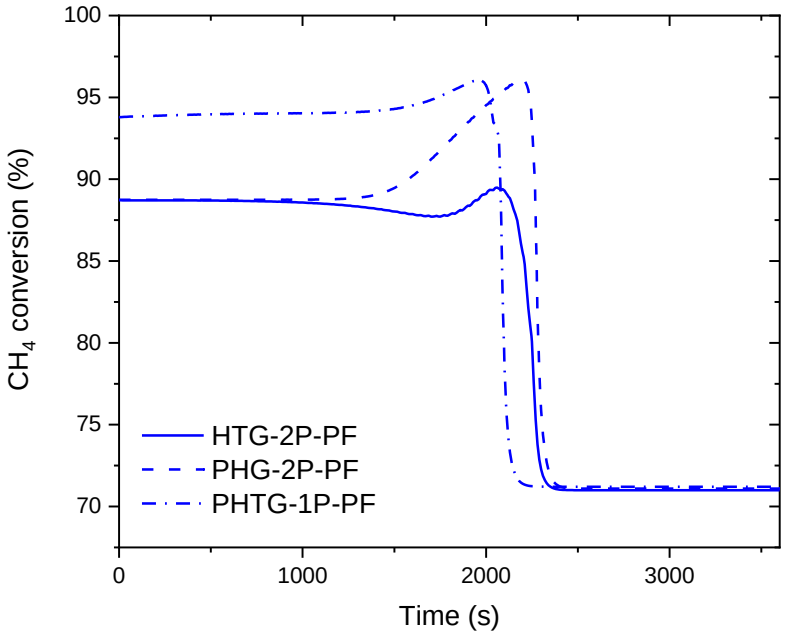

Figure 6.19 Methane conversion predicted with the heterogeneous model (HTG-2P-PF), the pseudo-homogeneous model (PHG-2P-PF), and the pseudo-heterogeneous model (HTG-1P-PF), at inlet gas conditions of 5 bar, 923 K and 0.06 m s^{-1}; the initial bed temperature is 923 K.

The rate of reaction (Figure 6.20) is also affected by the partial pressure of the different chemical species at the nickel active sites for the reforming reactions, and the CaO active surface for the capture of CO_2. Figure 6.21 and Figure 6.22 display various profiles of the partial pressure of CH_4 and CO_2, respectively. Similar profiles have been previously presented in [6, 65], albeit with slightly different shape in the breakthrough zone which is likely related with the treatment of the velocity field as neither of the studies accounted for the depletion of mass in their approach. In the same fashion as with temperature, Figure 6.21(a) and Figure 6.22(a) compare the partial pressure profiles of CH_4 and CO_2, predicted with the heterogeneous, the pseudo-homogeneous, and the pseudo-heterogeneous models, whereas Figure 6.21(b) and Figure 6.22(b) compare the partial pressure profiles in the solid phases which were obtained with the plug flow heterogeneous (HTG-2P-PF) and the plug flow pseudo-heterogeneous (PHTG-1P-PF) models. For the bulk gas, the models produce similar responses with the HTG-2P-PF model showing the higher partial pressure of CH_4, and the lowest partial pressure of CO_2 within the first half of the bed. This behaviour is consistent with that of the temperature, as the HTG-2P-PF model predicts that the catalyst will have the lowest temperature at the bed inlet, thus reducing the rate of disappearance of CH_4 and the rate of production of CO_2. In the case of the solid phase, the HTG-2P-PF model predicts a slightly lower partial pressure

of CH_4 in the catalyst surface with respect to that at the adsorbent surface, whereas for CO_2, the opposite behaviour is observed. In both cases, the partial pressure profiles were higher when calculated with the HTG-2P-PF model in comparison to those obtained with the PHTG-1P-PF model.

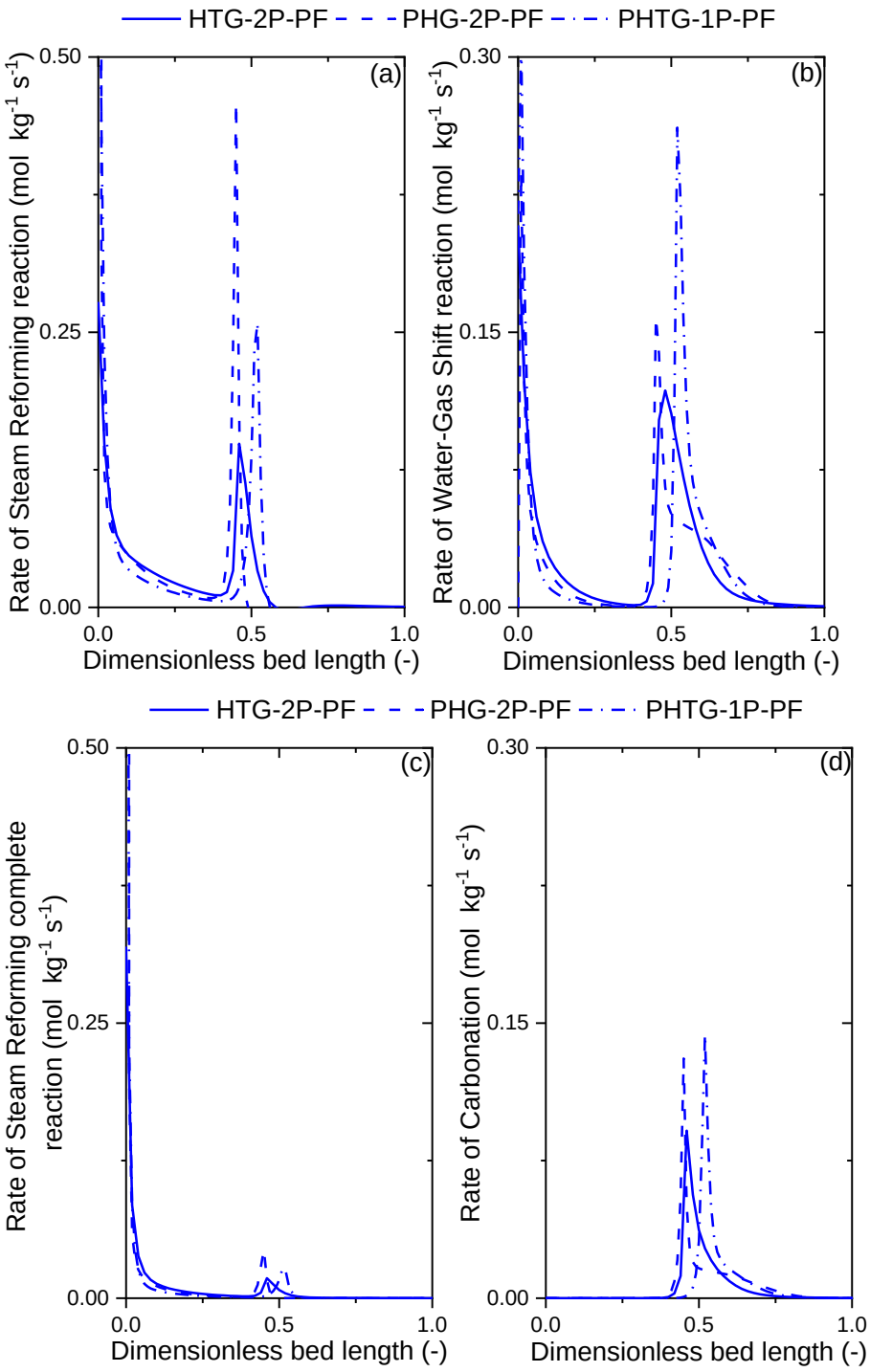

Figure 6.20 Rate of reaction profiles of: (a) the steam methane reforming reaction, (b) the water-gas shift reaction, (c) the complete steam reforming reaction, and (d) the carbonation reaction. The profiles correspond to a simulation time of 1080s, and are predicted at inlet gas conditions of 5 bar, 923 K and 0.06 m s^{-1}; the initial bed temperature is 923 K.

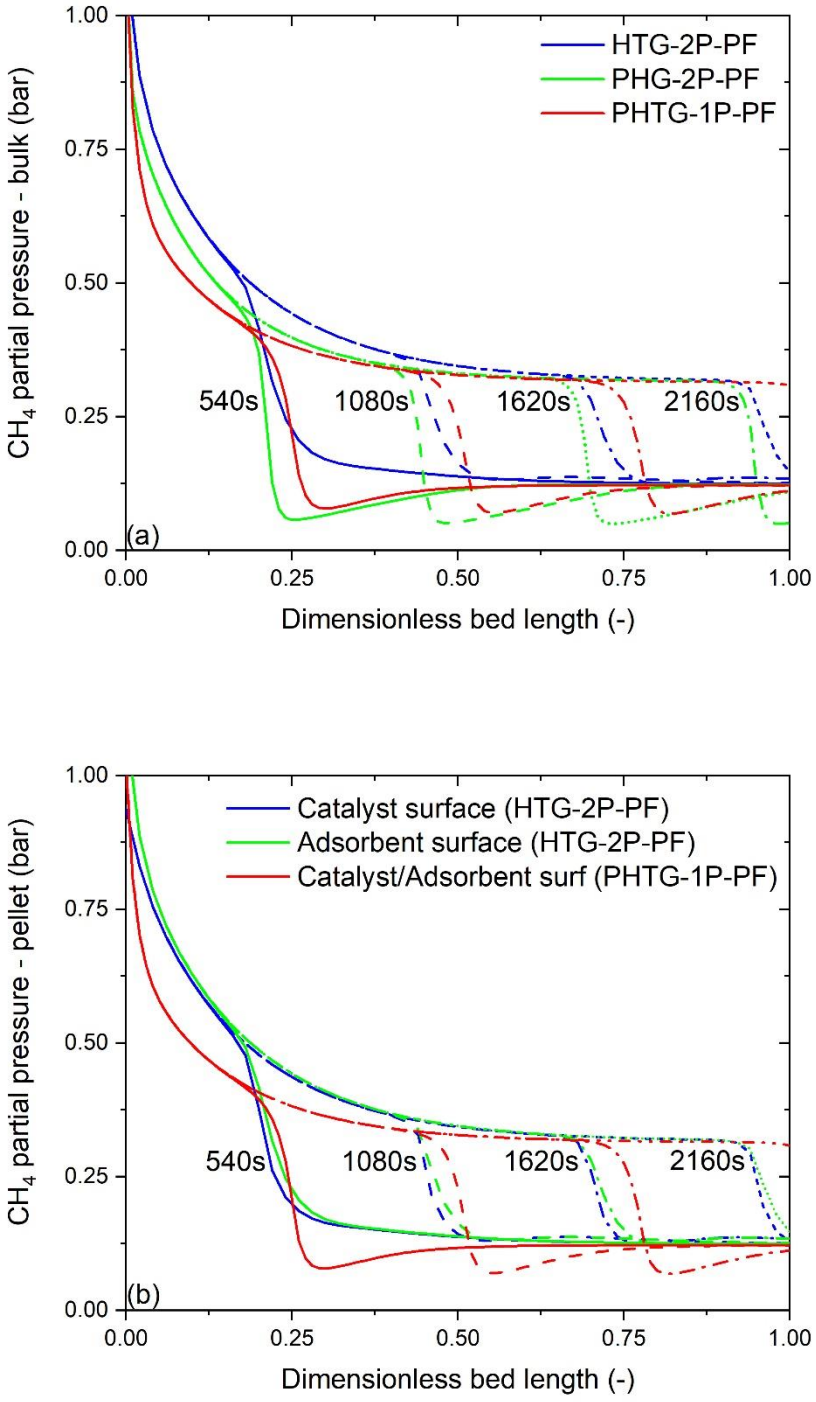

Figure 6.21 CH_4 concentration profiles at several simulation times predicted with: (a) the heterogeneous model (HTG-2P-PF), (b) the pseudo-homogeneous model (PHG-2P-PF), and (c) the pseudo-heterogeneous model (HTG-1P-PF), at inlet gas conditions of 5 bar, 923 K and 0.06 m s^{-1}; the initial bed temperature is 923 K.

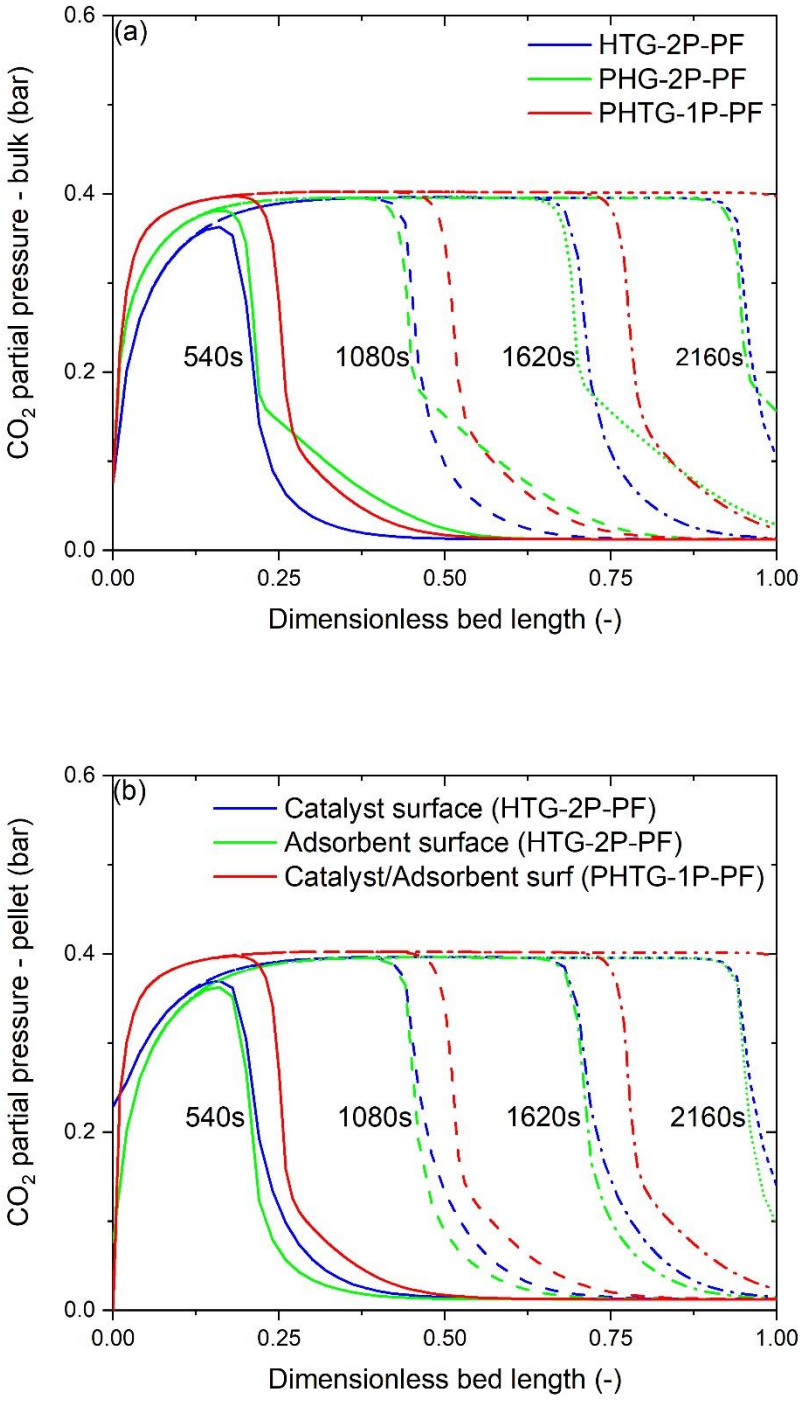

Figure 6.22 CO_2 concentration profiles at several simulation times predicted with: (a) the heterogeneous model (HTG-2P-PF), (b) the pseudo-homogeneous model (PHG-2P-PF), and (c) the pseudo-heterogeneous model (HTG-1P-PF), at inlet gas conditions of 5 bar, 923 K and 0.06 m s^{-1}; the initial bed temperature is 923 K.

The variables discussed previously have a cascade effect over the saturation time of the adsorbent. The higher velocity predicted with the model PHTG-1P-PF leads to the prediction of a faster saturation of the CaO-adsorbent as shown in

Figure 6.23, which is the primary cause of the shorter breakthrough times previously shown in Figure 6.12 – Figure 6.14 for this model. Figure 6.23 also shows that the reaction front is slower when predicted by the PHG-2P-PF and the HTG-2P-PF models. Moreover, the pseudo-homogeneous plug flow model response approaches a square-step indicating an almost even saturation of the bed; this seem unrealistic given the various resistances that the CO_2 molecules generated at the catalyst active sites have to overcome to reach the reaction front within the adsorbent, particularly the intra-particle effects. On the other hand, the heterogeneous and pseudo-heterogenous models show a degree of diffusion which can be associated with the fact that these models accounted for the film resistance to mass and heat transfer.

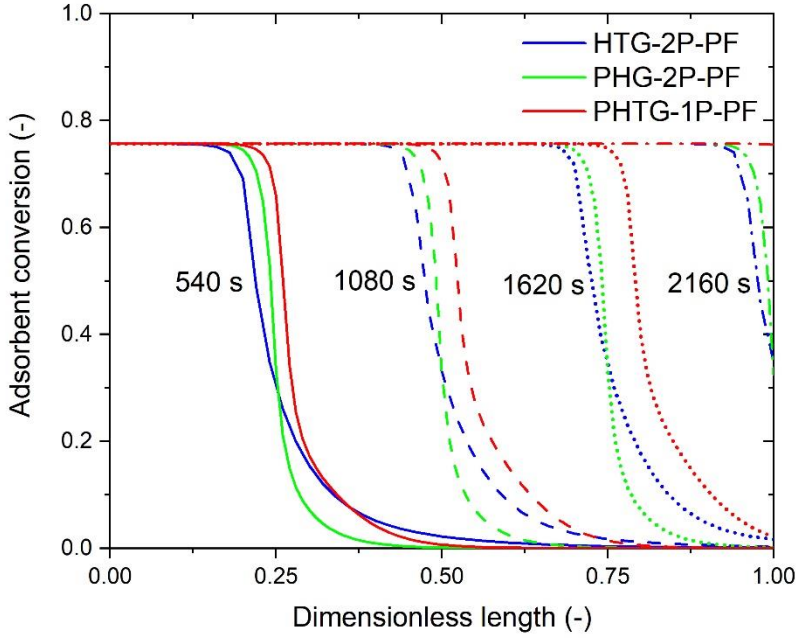

Figure 6.23 Adsorbent conversion profiles at several simulation times predicted with the heterogeneous model (HTG-2P-PF), the pseudo-homogeneous model (PHG-2P-PF), and the pseudo-heterogeneous model (HTG-1P-PF), at inlet gas conditions of 5 bar, 923 K and 0.06 m s^{-1}; the initial bed temperature is 923 K.

The selection of the physical assumptions to be included within the model also affects the predicted pressure drop in the packed bed reactor. This is an important variable to consider, as it effects the performance of the reactor, but also has design implications regarding the size of the reactor. Figure 6.24 illustrates the gas pressure profile predicted with the HTG-2P-PF, PHG-2P-PF and PHTG-1P-PF models; the largest pressure drop is obtained when the reactor is simulated with the PHTG-1P-PF model, owing to the higher velocity profile predicted with this model, followed by the prediction of the PHG-2P-PF and the HTG-2P-PF

models. Unfortunately, no experimental information regarding the pressure drop throughout the lab reactor is provided in the source utilised to validate the models, thus the pressure drop model cannot be corroborated.

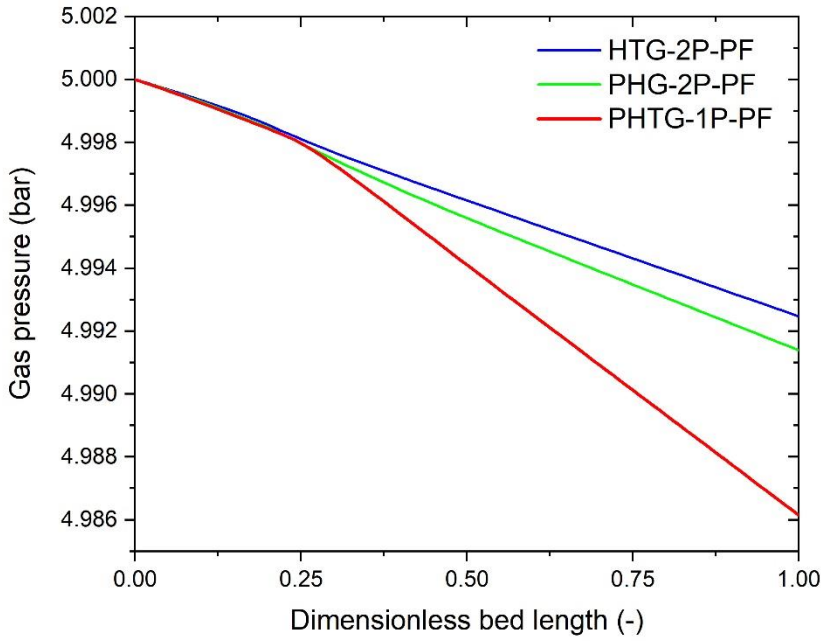

Figure 6.24 Gas pressure profiles predicted with the heterogeneous model (HTG-2P-PF), the pseudo-homogeneous model (PHG-2P-PF), and the pseudo-heterogeneous model (HTG-1P-PF), at inlet gas conditions of 5 bar, 923 K and 0.06 m s^{-1}; the initial bed temperature is 923 K.

6.6.2.4 Comparison of the heterogeneous model, the pseudo-homogeneous model and the pseudo-heterogeneous model for a reactor with large pellets.

The heterogeneous plug flow model (HTG-2P-PF), the pseudo-homogeneous plug flow model (PHG-2P-PF), and the pseudo-heterogeneous plug flow model (PHTG-1P-PF) were applied to simulate the Fuel Reactor packed with larger pellets. The dimensions of the reactor and the catalyst and adsorbent pellets were selected to fulfil the criteria of a plug flow reactor (i.e. $L_b/d_p > 50$ and $D_b/d_p > 30$), whilst ensuring that the particle size selected was in the range of sizes typically encountered in the industrial application. The simulation parameters utilised in this analysis are summarised in Table 6.12.

The simulation of the reactor was conducted for adiabatic conditions, and since these computational experiments were conducted with larger particles, appropriate values of the effectiveness factors were required for the various processes, particularly the reforming reactions and the carbonation reaction.

Table 6.12 Simulation parameters for the analysis of the models in reactor packed with larger packings.

Parameter	Value
Gas composition (mole%)	
Methane	17.78
Water	72.64
Hydrogen	4.87
Carbon Monoxide	0.01
Carbon Dioxide	1.66
Nitrogen	3.04
Pellets properties (cat./ads.)	
Density (kg m^{-3})	3450/2710
Heat capacity (J $kg^{-1}K^{-1}$)	1102.5/1070.7
Porosity (m^3 m^{-3})	0.41/0.48
Avg. particle diameter (m)	0.01
Reactor length (m)	1.0
Reactor diameter (m)	0.35
Time period (s)	800
Inlet temperature (K)	923
Inlet pressure (bar)	9
Inlet velocity	0.5
Vol. fraction of catalyst (m^3 m^{-3})	0.25

It is well known that the steam reforming reactions are diffusion-controlled processes, thus with very low effectiveness factors. Rostrup-Nielsen [20, 29] reported that the effectiveness factor of the reforming reactor decreases away from the inlet with values typically below 0.1. This range of values has been confirmed in other theoretical studies [18, 25, 193, 194], therefore an effectiveness of 0.1 is used in this analysis. The carbonation effectiveness has also been studied and for particles of similar size to that used in these simulations, Solsvik and Jakobsen [85] estimated a value of ca. 0.6 for 0.007 m particles, whilst Lugo and Wilhite [33] reported values of 0.68 for 0.0077 m particles; for 0.01 m Fernandez et al. [6] used a value of effectiveness of 0.3. Ishida and Wen [195, 196] developed an equation to estimate the effectiveness factor of non-catalytic reactions as:

$$\eta_{Carb} = \begin{cases} \dfrac{3}{\phi^2}[\phi_{ads}coth(\phi_{ads}) - 1] \; if \; X_{CaO} < X_{CaO,0} \\ \dfrac{3r_{CaO}^3}{(\phi_{ads}r_{CaO})^2} \dfrac{\phi_{ads}r_{CaO}coth(\phi_{ads}r_{CaO}) - 1}{1 + (1 - r_{CaO})[\phi_{ads}r_{CaO}coth(\phi_{ads}r_{CaO}) - 1]} \; if \; X_{CaO} \geq X_{CaO,0} \end{cases} \quad \textbf{(6.67)}$$

where X_{CaO} is the conversion of the adsorbent, $X_{CaO,0}$ is the conversion at the end of the first stage, r_{CaO} is the radius of the unreacted core, and ϕ_{Carb} is the Thiele module for the carbonation reaction which is calculated as:

$$\phi_{Carb} = r_{CaO}\sqrt{\frac{k_{Carb}}{D_{e,CO_2}}} \quad \textbf{(6.68)}$$

The application of Equation (6.67) with the simulation inputs indicated in Table 6.12 gives a value of 0.54 estimated at inlet conditions; this value represents the effectiveness factor at the start of the carbonation of the adsorbent and is likely to decrease as a result of the reduction of the adsorbent porosity, thus a value of 0.4 has been selected for this analysis.

Figure 6.25 and Figure 6.26 show the profiles of the partial pressure of methane and carbon dioxide as a function of time. Figure 6.25(a) illustrates the partial pressure of methane in the bulk predicted by the different models; clearly, the output is different for each model, particularly at the early stage of the process in which the pseudo-homogeneous model predicts a sharp profile, whereas the heterogeneous model exhibits a high degree of diffusion, resulting in a smoother consumption of methane. In Figure 6.25(b), the profiles of the partial pressure of methane at the catalyst, and at the adsorbent surfaces predicted with the heterogeneous model are shown; additionally, the output of the pseudo-heterogeneous model is presented. The similarity of these profiles with the corresponding partial pressure of methane in the bulk is visible, however, the average differences between the profiles at the solid surfaces and the bulk range 1.4%-10.4% in the heterogeneous model, and 0.4%-4.2% in the pseudo-heterogeneous model; in both cases, the error is larger in the mass transfer zone, and decreases as the process is approaching the behaviour of a conventional steam reformer, this is important since the rate of reaction (and its thermal effects) are dependent upon the partial pressure of the different species at the catalyst surface.

Figure 6.26(a) presents the partial pressure of CO_2 in the bulk; as in the case of the CH_4 profile, the predictions of each model are significantly different. The pseudo-homogeneous model (PHG-2P-PF) initially predicts two mass transfer zones; this is not the case with the heterogeneous (HTG-2P-PF) and pseudo-heterogeneous (PHTG-1P-PF) models which predict a single mass transfer zone throughout the duration of the simulation. The average differences between the profiles at the solid surfaces and the bulk gas for the heterogeneous model range 7.8% to 112.1% with respect to the catalyst, and 0.01% to 41.0% with respect to the adsorbent. The higher differences in the former reflect the poor transfer of

CO_2 from the catalyst to the bulk gas; indeed the mass transfer is reduced owing to the lower transfer area of this material in the bed, leading to the accumulation of CO_2 in the catalyst surface as it is formed. This is detrimental to the reforming processes since the increase of CO_2 will shift the equilibrium, thus limiting the production of H_2. In the case of the partial pressure of CO_2 at the adsorbent surface, the lower values will reduce the rate of carbonation, hence the availability of heat of reaction to heat-up the system and enhance the rate of reaction of the reforming processes. On the other hand, the pseudo-heterogeneous model predictions are different by 0.03% to 5.23%.

The differences between the models also lead to the prediction of significantly different temperatures. Figure 6.27(a) and (b) illustrate the temperature profile in the bulk gas and in the solid phases as a function of time. The neglect of the interfacial resistances in the pseudo-homogeneous model steers to the prediction of a very high reactor temperature, this is not surprising since the assumption of a local concentration also enhances the rate of reaction of both the reforming and the carbonation processes. Moreover, the pseudo-homogeneous model (PHG-2P-PF) assumes intimate contact between all the phases, therefore no losses of heat are expected due to the limitations imposed by the structure of the packed bed. The pseudo-homogeneous model (PHG-2P-PF) predicts the formation of a bulk gas temperature plateau at ca. 1074.5 K, while the pseudo-heterogenous model (PHTG-1P-PF) predicts a plateau at ca. 1041.6 K after 100 s. This behaviour is not observed with the heterogeneous model HTG-2P-PF, which initially predicts a quasi-constant bulk gas temperature profile as the gas moves towards the exit of the bed. A drop of bulk gas temperature is observed in the section of the bed, where the fraction of adsorbent has already been saturated and then followed by an increase of the bulk gas temperature due to the carbonation of CaO. Eventually, the profile reaches a maximum at ca. 1018.1 K and then decreases smoothly towards the exit of the bed.

Figure 6.27(b) illustrates the temperature profiles of the adsorbent and the catalyst predicted with the heterogeneous model HTG-2P-PF, and the temperature profile of the particle predicted with the pseudo-heterogeneous model PHT-1P-PF. The heterogeneous model (HTG-2P-PF) forecasts a significant difference between the adsorbent and the catalyst temperatures (up to 141.4K) which in principle confirm the need of accounting for separate phases. The temperature difference between the phases creates a hot zone in the adsorbent and cold zone in the catalyst that move along the bed. Behind this zone, the temperature of both particles tend to approach to each other as a result of the adsorbent capacity being exhausted as shown in Figure 6.28, and the system being thermally equilibrated to the adiabatic temperature of a

conventional reformer. Ahead of this zone the temperature of both particles approach each other as the front reaches the bed exit, with a minimum difference of 13K between them. This value is constrained by the physical resistances to heat transfer, but also by the reduced transfer area of the catalyst as in the case of the mass transfer. This suggests that the catalyst-to-adsorbent ratio can be increased or the catalyst particle size can be reduced to augment the transfer area, thus enhancing the heat transfer rate. Conversely, the pseudo-heterogeneous model (PHTG-1P-PF) predicts a particle temperature profile with a more pronounced temperature drop behind the mass transfer zone, and a higher temperature rise ahead of it.

The effect of the concentration and temperature on the performance of the reactor is illustrated in Figure 6.29 and Figure 6.30. Figure 6.29 shows the conversion of methane predicted with the various models. The heterogeneous model (HTG-2P-PF) predicts a lower conversion in the pre-breakthrough zone, whereas the PHG-2P-PF and PHTG-1P-PF predict similar values, albeit slightly above the equilibrium conversion (92.7%); in the post-breakthrough zone, all the models approach the equilibrium value of a conventional reformer. The mass transfer zone or breakthrough zone features two main behaviours, on one hand, a sharp profile with the pseudo-homogeneous model is predicted, as opposed to a diffusive front calculated by the heterogeneous model. On the other hand, a much shorter saturation time is exhibited by the prediction of the pseudo-heterogeneous model.

The product purity (Figure 6.30) exhibits very different profiles for each modelling approach. When estimated with the pseudo-homogeneous model (PHG-2P-PF), the purity is initially higher than 95%, but suddenly drops to values below 90%. As shown in Figure 6.26(a), this model predicts the formation of two reaction zones; the first reaction zone appears at ca. 10 s and moves downstream until it exits the bed at ca.120 s. During this time period the very low CO_2 pressure seems to favour the formation of H_2, however, as the first transfer zone exits the bed the CO_2 partial pressure increases, thus reducing the rate of H_2 production and therefore the product purity. The purity obtained with the heterogeneous model averages 91.4% in the pre-breakthrough zone, whereas the pseudo-heterogeneous predicts an average purity of 95.9%. For reference, the equilibrium value of purity at 923 K is 92.7% which is above the values predicted by the pseudo-homogeneous (PHG-2P-PF) and heterogeneous models (HTG-2P-PF), but below the prediction of the pseudo-heterogeneous model (PHTG-1P-PF).

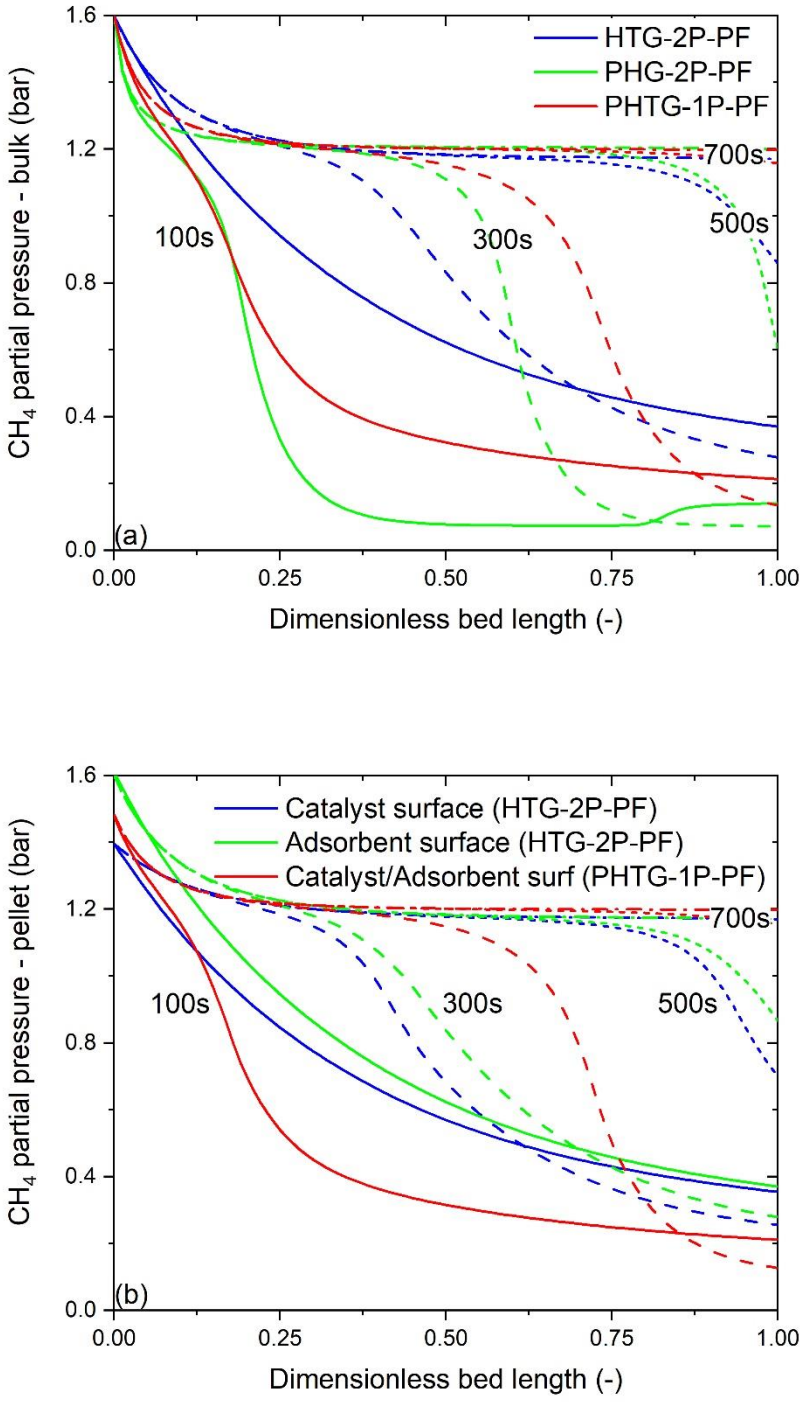

Figure 6.25 (a) CH_4 partial pressure in the bulk, and (b) CH_4 partial pressure in the solid phases predicted with the heterogeneous model (HTG-2P-PF), the pseudo-homogeneous model (PHG-2P-PF), and the pseudo-heterogeneous model (HTG-1P-PF), at inlet gas conditions of 9 bar, 923 K and 0.5 m s^{-1}; the initial bed temperature is 923 K.

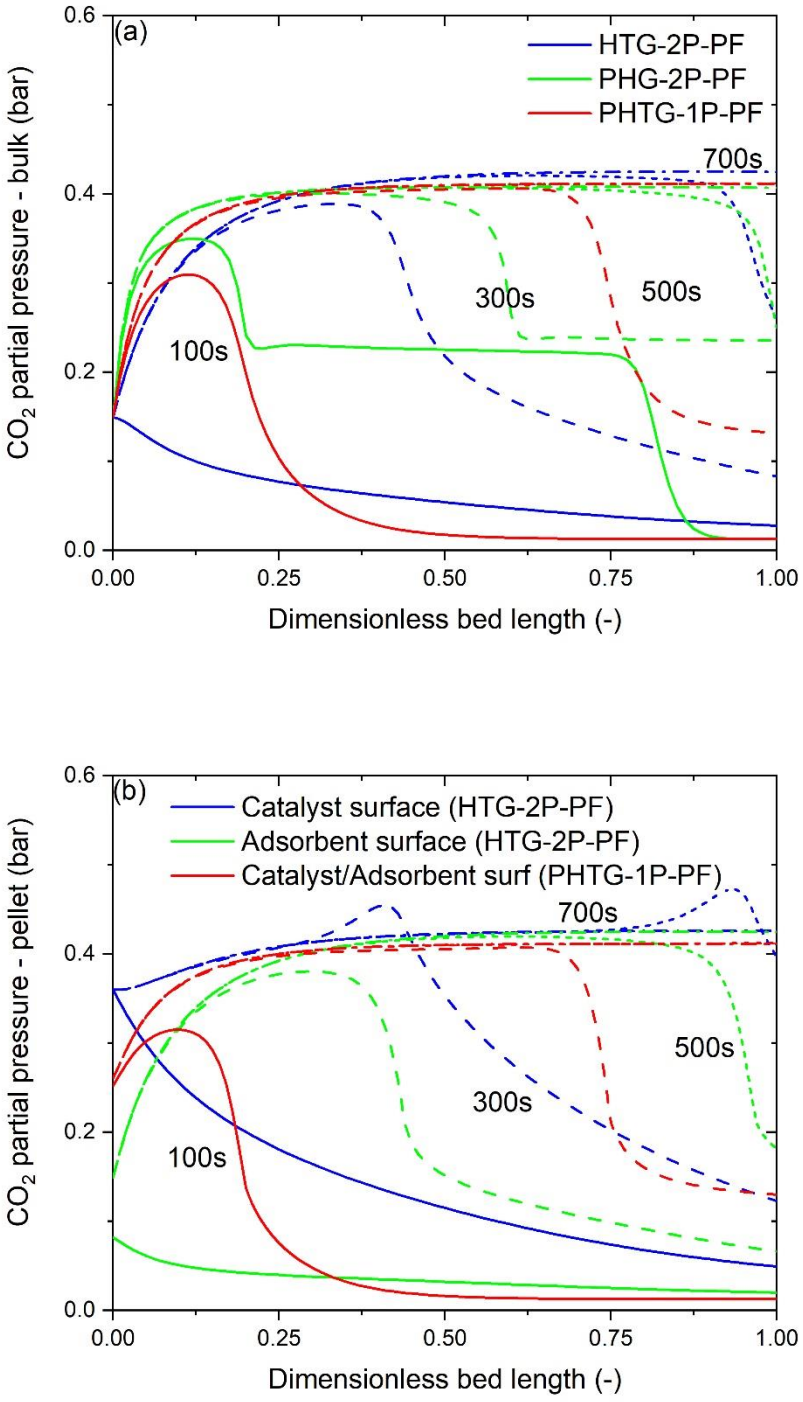

Figure 6.26 (a) CO_2 partial pressure in the bulk, and (b) CO2 partial pressure in the solid phases predicted with the heterogeneous model (HTG-2P-PF), the pseudo-homogeneous model (PHG-2P-PF), and the pseudo-heterogeneous model (HTG-1P-PF), at inlet gas conditions of 9 bar, 923 K and 0.5 m s-1; the initial bed temperature is 923 K.

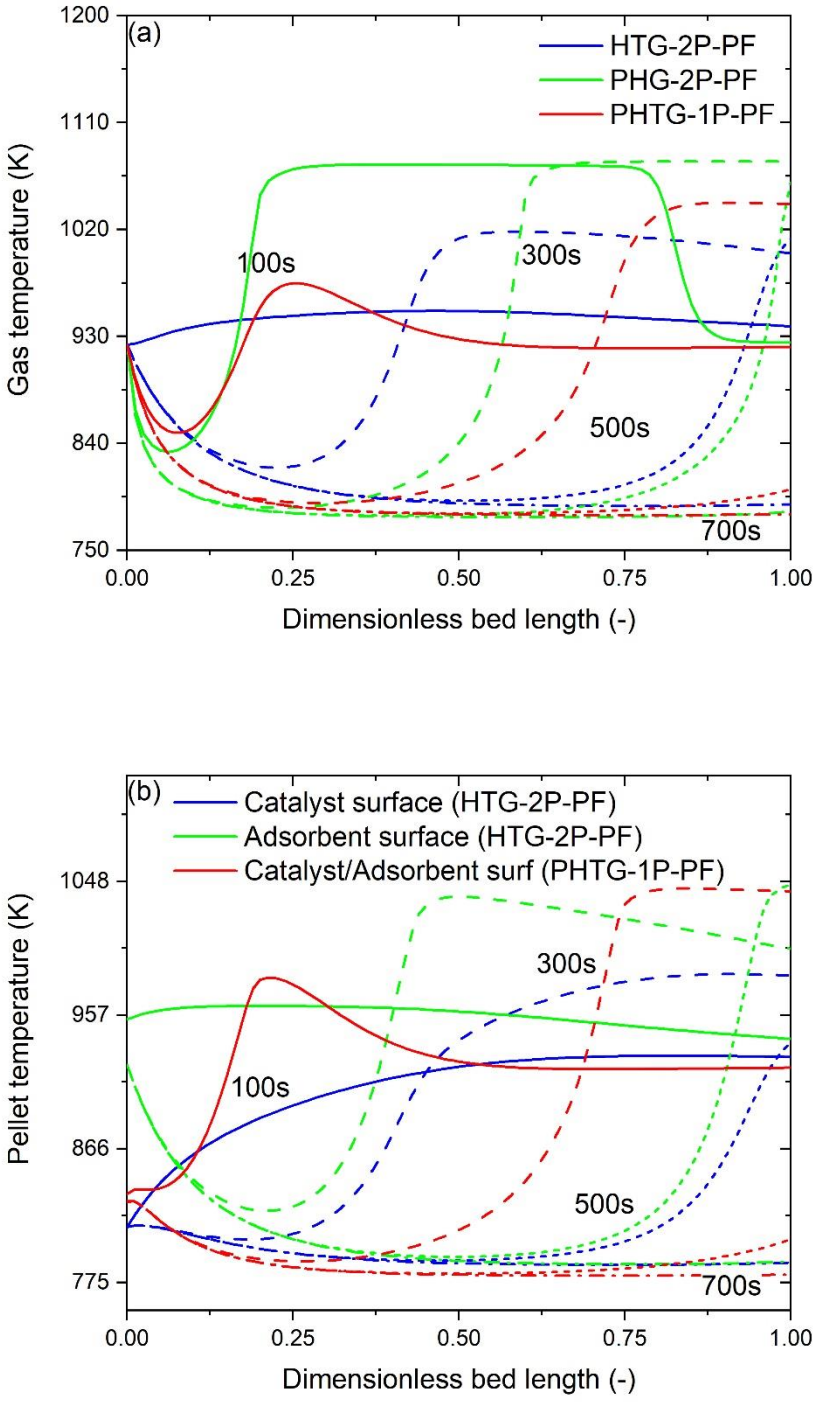

Figure 6.27 (a) Bulk temperature profiles, and (b) Solid phases temperature profiles predicted with the heterogeneous model (HTG-2P-PF), the pseudo-homogeneous model (PHG-2P-PF), and the pseudo-heterogeneous model (HTG-1P-PF), at inlet gas conditions of 9 bar, 923 K and 0.5 m s^{-1}; the initial bed temperature is 923 K.

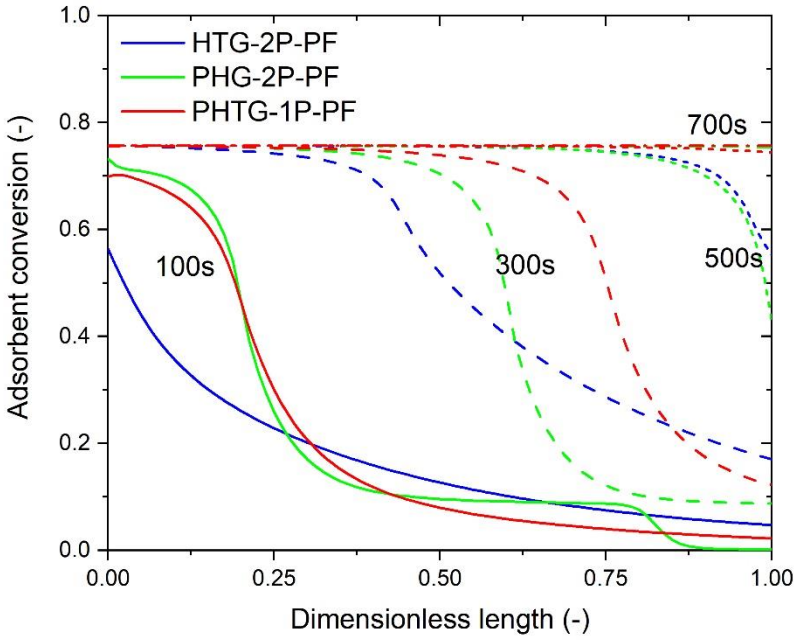

Figure 6.28 Adsorbent conversion profiles predicted with the heterogeneous model (HTG-2P-PF), the pseudo-homogeneous model (PHG-2P-PF), and the pseudo-heterogeneous model (HTG-1P-PF), at inlet gas conditions of 9 bar, 923 K and 0.5 m s^{-1}; the initial bed temperature is 923 K.

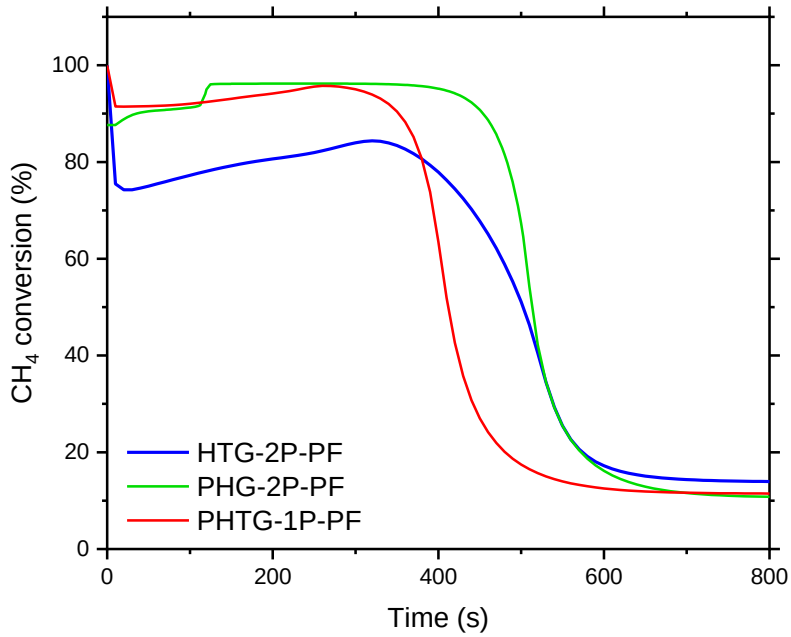

Figure 6.29 Methane conversion predicted with the heterogeneous model (HTG-2P-PF), the pseudo-homogeneous model (PHG-2P-PF), and the pseudo-heterogeneous model (HTG-1P-PF), at inlet gas conditions of 9 bar, 923 K and 0.5 m s^{-1}; the initial bed temperature is 923 K.

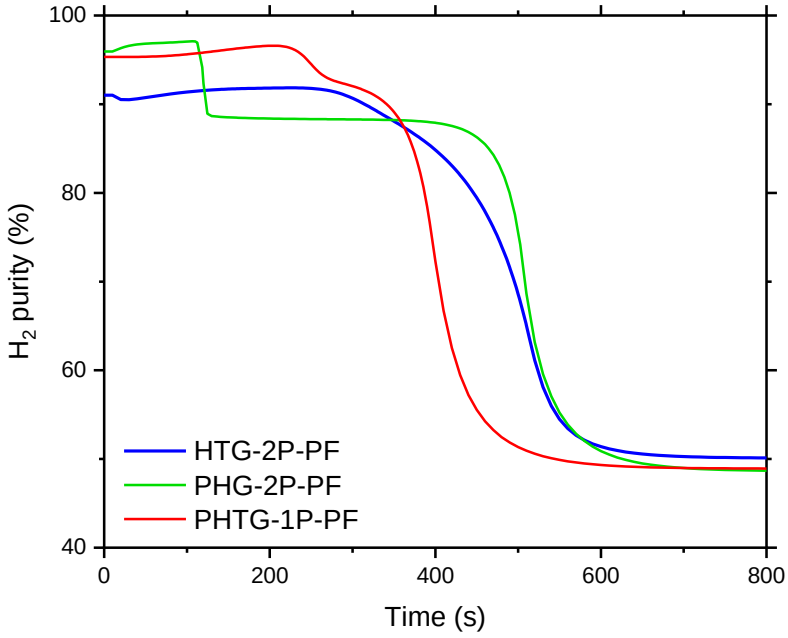

Figure 6.30 Hydrogen purity in dry basis predicted with the heterogeneous model (HTG-2P-PF), the pseudo-homogeneous model (PHG-2P-PF), and the pseudo-heterogeneous model (HTG-1P-PF), at inlet gas conditions of 9 bar, 923 K and 0.5 m s^{-1}; the initial bed temperature is 923 K.

6.7 Concluding remarks

In this chapter, a transient heterogeneous model of a reactor for hydrogen production with in-situ carbon capture known as the Fuel Reactor cycle of the Sorption Enhanced Chemical Looping Steam Reforming was developed. The development considered separate equations for the catalyst (or oxygen transfer material), the adsorbent and the bulk gas, and represented the intra-pellet resistances by means of an adjustable effectiveness factor. Moreover, the model considered the reactor as an ideal plug flow and a plug flow with axial dispersion effects. Additionally, the pseudo-homogeneous and pseudo-heterogeneous models were tested for comparison purposes.

Various differences in terms of the prediction of the breakthrough curves of H_2 and other variable profiles (e.g. velocity, temperature and concentration) were spotted and explained in terms of the different assumptions taken for the development of each type of model. Regarding the validation of the model, errors in the prediction of the breakthrough curve of H_2 ranged from 4.73% to 29.32%, with the deviations increasing as the pressure of the experimental data increased. Regarding the comparison of specific profiles, the pseudo-heterogeneous models (PHTG-1P-PF and PHTG-1P-PF) produced velocity profiles ranging 30% to 41.6% higher than the heterogeneous models (HTG-2P-PF and HTG-2P-AD) and the pseudo-homogeneous model. Conversely, the PHG-2P-PF model reported the highest temperature profiles with values that were in excess of 30.8 – 43.4 K with respect to the bulk gas temperature predicted by the HTG-2P-PF model. When comparing the profile obtained by the former with that predicted by the heterogeneous model for the catalyst surface this differences increase ranging from 58.8 – 82.4 K. Conversely, the temperatures predicted by the heterogeneous models (HTG-2P-PF) and pseudo-heterogeneous model (PHTG-1P-PF) were very close, with differences in the range 1.2 to 12.1 K. These differences in the temperature profile worsen when the models are applied to particle sizes close to those encountered in typical industrial applications.

The models were applied to conduct computational experiments with systems considering lab-scale particles (typical sizes in the order of sub millimetre) and with larger particles in the order those utilised at industrial scale. When applied to simulate the experiments at lab-scale, the three type of models failed to predict the position of the breakthrough zone of the curve in those experiments conducted at pressures above 3 bar; the errors in the prediction of the breakthrough curve of H_2 ranged from 4.73% to 29.32%; the least accurate performance in all cases was obtained with the pseudo-heterogeneous model (PHTG-1P-PF and PHTG-1PAD), presumably due to the inadequacy of the

assumption of constant mass flux, whose effect on the simulation is the prediction of a higher superficial velocity and a shorter adsorbent saturation time. Conversely, the heterogeneous models (HTG-2P-PF and HTG-2P-AD) and pseudo-homogeneous model (PHG-2P-PF) predicted a similar saturation time, with the main difference being the higher bulk gas temperature predicted by the latter. However, these models failed too to reproduce accurately the experimental data at pressures greater than 3 bar.

The models considered in this chapter did not take into account the reduction of porosity and pore size in the adsorbent, presumably affecting the ability of the models to adjust to the experimental breakthrough curve of hydrogen, since for all the experimental data available at pressures higher than 3 bar the effectiveness factor of carbonation was set to 1.0 which represent a situation free intra-particle mass transfer resistance which clearly is an unrealistic scenario. Since the variations of adsorbent porosity and pore size affect the rate of transport CO_2 from the surface of the adsorbent to the reaction zone, it can be expected that as the adsorbent approaches its saturation, the reduction of its porosity and pore size will control the process, increasing the time required to convert the adsorbent, thus moving the breakthrough zone to the right, allowing for a better adjustment of the experimental data.

The differences obtained in the prediction of the concentration and temperature profiles with the heterogeneous (HTG-2P-PF) and the pseudo-homogeneous (PHG-2P-PF) models, might be considered within the expected error since the heterogeneous approach relies on the application of correlations for the mass and heat transfer coefficients that were typically determined in the absence of chemical reactions. However, given the experimental conditions and dimensions of the lab reactor and the particle simulated to validate the model, the influence of external or internal diffusion is expected to be negligible, under these circumstances any of the three models could be used to represent the reactor at this scale, provided that the pseudo-heterogeneous model (PHTG-1P-PF) is modified to account for the depletion of bulk gas mass in the bed.

When applied to a reactor with larger particles, the models' outputs are significantly different. The differences are particularly important when comparing the output of the heterogeneous model (HTG-2P-PF) with that of the pseudo-homogeneous model (PHG-2P-PF). This is not surprising considering the set of assumptions that produces each model; furthermore, by applying of the pseudo-homogeneous approach to simulate the Fuel Reactor the heat transfer from the adsorbent to the catalyst is overestimated, yielding significantly higher bulk gas temperatures and affecting the prediction of the conversion of methane and hydrogen yield. This contradicts the expected behaviour since the pellet size and

the composition of each material in the bed affect the mass and heat transfer processes due to a reduction of the transfer area, and the effective heat transfer coefficient. The pseudo-heterogeneous model predicts an intermediate output in comparison with the aforementioned models, however, it carries the drawback of the assumption of constant gas mass flux, and the over-simplification of equal local temperature and concentration in both materials.

The results presented in this chapter suggest that at small scale all the approaches analysed can be applied. For larger particles, however, the results reflect uncertainty regarding the correct choice; unfortunately, the available experimental work regarding this type of reactor has been conducted with small particles since researching groups working on this topic envision the application of this concept in a fluidised system. Therefore there is currently a lack of data to conduct a more definitive validation of the model. Nevertheless, in the following chapters the heterogeneous model proposed in this work will be considered since it is deemed to represent the system in a more realistic fashion.

Chapter 7 Effect of the adsorbent structure changes on the Fuel Reactor model, validation, and sensitivity study.

7.1 Introduction

In this chapter the heterogeneous model of the Fuel Reactor presented in **Chapter 6** is extended to account for the changes in the structure and properties of the CO_2-adsorbent. The development considers in first instance the reduction of the adsorbent porosity due to the adsorption of CO_2, and in second place the variation of the adsorbent density and heat capacity due to the formation of the product layer.

The development of the proposed modifications is presented in section 7.2. The models are applied to simulate the experiments referred in Chapter 6 and compared among them and with the base model to choose the right level of detail to represent the Fuel Reactor mode; these results are presented in section 7.6.1. The selected model is then applied to conduct a sensitivity analysis and the results are presented in section 7.6.2.

Finally, a summary of the conclusions of the investigations described in this chapter is provided in section 7.7.

7.2 Model development

The modification of the base model affects only the model equations of the adsorbent, thus the bulk gas and the catalyst are modelled by the same equations presented in **Chapter 6**. The species and energy balances for the bulk gas in the region of interest $t > 0$ and $0 < z \leq L_b$ are:

$$\varepsilon_b \frac{\partial C_i}{\partial t} + \varepsilon_b \frac{\partial (u_i C_i)}{\partial z} = -\beta_1 a_{S_1}\left(C_i - C_{i,S_1}\right) - \beta_2 a_{S_2}\left(C_i - C_{i,S_2}\right) \qquad \textbf{(7.1)}$$

$$\varepsilon_b \frac{\partial \left(\rho_g C_{p,g} T\right)}{\partial t} + \varepsilon_b \frac{\partial \left(u_i \rho_g C_{p,g} T\right)}{\partial z} = -\alpha_1 a_{S_1}\left(T - T_{S_1}\right) - \alpha_2 a_{S_2}\left(T - T_{S_2}\right) \qquad \textbf{(7.2)}$$

And for the catalyst in the region $t > 0$ and $0 \leq z \leq L_b$:

$$\varepsilon_{p_1}(1 - \varepsilon_b)\frac{\partial C_{i,S_1}}{\partial t} = \beta_1 a_{S_1}\left(C_i - C_{i,S_1}\right) + \rho_{b_1} \sum_{j=1}^{m} \eta_j \nu_{ij} r_j \qquad \textbf{(7.3)}$$

$$\rho_{b_1} C_{p_1} \frac{\partial T_{S_1}}{\partial t} = \alpha_1 a_{S_1} \left(T - T_{S_1}\right) + \rho_{b_1} \sum_{j=1}^{m} \eta_j r_j \left(-\Delta H_j\right) \quad \textbf{(7.4)}$$

The continuity and momentum equations proposed in **Chapter 6** also apply:

$$\frac{\partial \left(\rho_g u_i\right)}{\partial z} = S_m \quad \textbf{(7.5)}$$

$$\rho_g u_i \frac{\partial u_i}{\partial z} + u_i S_m + \frac{\partial P}{\partial z} = -\frac{A\mu_g u_i (1-\varepsilon_b)^2}{d_p^2 \varepsilon_b^2} - \frac{B\rho_g u_i^2 (1-\varepsilon_b)}{d_p \varepsilon_b} \quad \textbf{(7.6)}$$

With the source term S_m being defined as:

$$S_m = -\frac{\rho_{b_2}}{\varepsilon_b} M_{CO_2} \eta_{Carb} r_{Carb} \quad \textbf{(7.7)}$$

The initial and boundary conditions of Equations (7.1)–(7.7) are the same as for the base plug flow model:

$$C_i(z,0) = C_{i,S_2}(z,0) = 0 \quad \textbf{(7.8)}$$

$$T(z,0) = T_{S_2}(z,0) = T_i \quad \textbf{(7.9)}$$

And:

$$C_i(0,t) = C_{i,in} \qquad T(0,t) = T_{in} \qquad u_i(0,t) = \frac{u_{s,in}}{\varepsilon_b} \qquad P(0,t) = P_{in} \quad \textbf{(7.10)}$$

7.2.1 Changes of porosity in adsorbent

The available data regarding the carbonation of Ca-based adsorbents demonstrates that during the adsorption of CO_2 the adsorbent undergoes structural changes due to the formation of an ash layer of lower density than the adsorbent, promoting the progressive decrease of porosity of the material and increasing the resistance to CO_2 diffusion [58, 106]. This effects the controlling rate of the whole process and impacts the time required to attain the maximum conversion of the adsorbent, and ultimately the breakthrough time.

The porosity of the adsorbent relates with the morphology of the material, which in turn determines the activity of the adsorbent and that is affected by the conditions selected for the calcination of the sample. The SEM images obtained in various experimental studies indicate that the adsorbent morphology consists of an array of quasi-spherical grains [42, 96]. Thus in this work the adsorbent is

thought as a collection of spherical grains accommodated within a grain matrix as shown in Figure 7.1.

Figure 7.1(a) shows a slice of the adsorbent before the carbonation process starts. At this point, all the grains are deemed of equal initial diameter $d_{g,0}$, and the spaces between them gives the adsorbent an initial porosity which is represented by $\varepsilon_{p_2,0}$. After the process has initiated the reaction of CO_2 with CaO produces a layer of $CaCO_3$ whose thickness increases with the conversion of calcium oxide represented by X_{CaO}, whilst the unreacted grain core shrinks as illustrated in Table 7.1(b). Since the product layer has a lower density than the unreacted core, the radius of the grain increases, reducing the mean porosity of the particle.

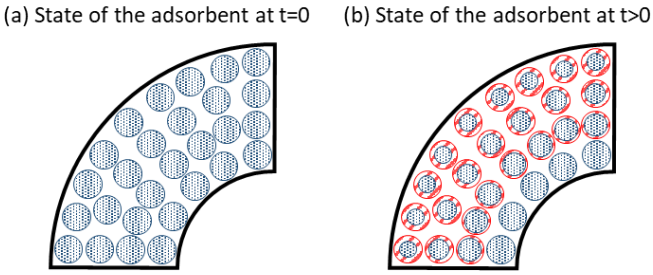

Figure 7.1 Model of a) the initial adsorbent state and b) the adsorbent state after reaction has started.

Therefore, the species and energy balances in the adsorbent are modified to include the variation of the adsorbent porosity with time, thus becoming:

$$(1-\varepsilon_b)\frac{\partial\left(\varepsilon_{p_2}C_{i,S_2}\right)}{\partial t} = \beta_2 a_{S_2}\left(C_i - C_{i,S_2}\right) + \rho_{b_2}\sum_{k=1}^{n}\eta_k \nu_{ik} r_k \qquad \textbf{(7.11)}$$

$$(1-\varepsilon_b)\rho_{p_2}C_{p_2}\frac{\partial\left(1-\varepsilon_{p_2}\right)T_{S_2}}{\partial t} = \alpha_2 a_{S_2}\left(T - T_{S_2}\right) + \rho_{b_2}\sum_{k=1}^{n}\eta_k r_k(-\Delta H_k) \qquad \textbf{(7.12)}$$

Where ρ_{p_2} is the true density of the adsorbent. The solution of Equations (7.11) and (7.12) require the definition of the relationship of the adsorbent porosity with time; Stenardo and Foscolo [106] proposed the following relationship which relates the time derivative of the adsorbent porosity with the time derivative of the adsorbent conversion:

$$\frac{\partial \varepsilon_{p_2}}{\partial t} = -N_{Ca}V_{CaO}(Z-1)\frac{\partial X_{CaO}}{\partial t} \qquad \textbf{(7.13)}$$

where N_{Ca} is the molar concentration of calcium in the adsorbent, V_{CaO} is the molar volume of CaO, and Z is the ratio of the molar volume of $CaCO_3$ to the

molar volume of CaO. The substitution of (7.13) in (7.11) and (7.12) renders the final model equations to account for the changes in adsorbent porosity:

$$\varepsilon_{p_2}\frac{\partial C_{i,S_2}}{\partial t} - C_{i,S_2}N_{Ca}V_{CaO}(Z-1)\frac{\partial X_{CaO}}{\partial t} = \frac{\beta_2 a_{S_2}}{(1-\varepsilon_b)}\left(C_i - C_{i,S_2}\right) + \frac{\rho_{b_2}}{(1-\varepsilon_b)}\sum_{k=1}^{n}\eta_k \nu_{ik} r_k \tag{7.14}$$

$$\left(1-\varepsilon_{p_2}\right)\frac{\partial T_{S_2}}{\partial t} + T_{S_2}N_{Ca}V_{CaO}(Z-1)\frac{\partial X_{CaO}}{\partial t} = \frac{\alpha_2 a_{S_2}\left(T - T_{S_2}\right)}{(1-\varepsilon_b)\rho_{p_2}C_{p_2}} + \frac{\left(1-\varepsilon_{p_2}\right)}{(1-\varepsilon_b)C_{p_2}}\sum_{k=1}^{n}\eta_k r_k(-\Delta H_k) \tag{7.15}$$

With initial conditions:

$$C_{i,S_2}(z,0) = 0 \qquad T_{S_2}(z,0) = T_i \qquad \varepsilon_{p_2}(z,0) = \varepsilon_{p_2,0} \tag{7.16}$$

7.2.2 Changes in adsorbent density and heat capacity

Along with the changes in the adsorbent porosity, the density and heat capacity of the material undergo variations owing to the formation of the ash layer with different physical properties from the unreacted adsorbent. These differences might affect the rate at which the heat of adsorption is transferred from the adsorbent to the bulk gas. Rigorously speaking, a distributed particle model at the grain level should be applied to account for the differences in thermal properties between the unreacted grain core and the ash layer; however, the approach followed in this work is to consider averaged density and heat capacity values. The procedure to estimate the average properties is given in **Appendix B**.

The variation of the adsorbent true density and heat capacity, in addition to the variation of the adsorbent porosity implies that Equation (7.12) becomes:

$$(1-\varepsilon_b)\frac{\partial\left[\left(1-\varepsilon_{p_2}\right)\rho_{p_2}C_{p_2}T_{S_2}\right]}{\partial t} = \alpha_2 a_{S_2}\left(T - T_{S_2}\right) + \rho_{b_2}\sum_{k=1}^{n}\eta_k r_k(-\Delta H_k) \tag{7.17}$$

Additional relationships are needed to complete the system as the partial differentials of the adsorbent true density ρ_{p_2}, and the adsorbent heat capacity C_{p_2} appear now on the l.h.s. of Equation (7.17). From **Appendix B**, the following

expressions relating the adsorbent heat capacity and true density with the adsorbent conversion are used:

$$\frac{\partial \rho_{p_2}}{\partial t} = -\left(\rho_{CaO} - \rho_{CaCO_3}\right)\left\{\frac{Z}{[1 + X_{CaO}(Z-1)]^2}\right\}\frac{\partial X_{CaO}}{\partial t} \qquad \textbf{(7.18)}$$

$$\frac{\partial C_{p_2}}{\partial t} = -\left(C_{p,CaO} - C_{p,CaCO_3}\right)\left\{\frac{Z\phi}{[1 + X_{CaO}(Z\phi-1)]^2}\right\}\frac{\partial X_{CaO}}{\partial t} \qquad \textbf{(7.19)}$$

The heat transfer model of the adsorbent is now outlined by Equations (7.13) and (7.17)–(7.19). These equations incorporate the information of the variation of porosity, density and heat capacity of the adsorbent into the reactor model. The new PDE system requires the specification of initial conditions for the additional differential variables to attain a well posed mathematical problem. At the beginning of each cycle, the initial values of the porosity, density and heat capacity of the adsorbent are dependent upon the degree of conversion of the pellet in the previous cycle, therefore, the following initial conditions apply:

$$T_{S_2}(z,0) = T_i \quad \varepsilon_{p_2}(z,0) = \varepsilon_{p_2,0} \quad \rho_{p_2}(z,0) = \rho_{p_2,0} \quad C_{p_2}(z,0) = C_{p_2,0} \qquad \textbf{(7.20)}$$

7.3 Closure relationships

The relationships required to complete the model such as the reaction rate expressions, the mass and heat transfer coefficients and axial dispersion coefficients are calculated with the correlations provided in **Chapter 6**.

7.4 Model integration and convergence

The model is integrated following the procedure outlined in **Chapter 6**. To ensure convergence, 100 mesh points were utilised following the analysis made for the Fuel Reactor base model.

7.5 Model Validation

The models' outputs were compared against the experimental data described in **Chapter 6**.

7.6 Results and discussion

7.6.1 Effect of the changes of porosity, density, and heat capacity on the Fuel Reactor model's predictions

The application of the heterogeneous model to simulate the experiments of sorption enhanced steam methane reforming showed that the basic version of

the model does not reproduce accurately the experimental breakthrough curves of H_2 or CO_2 at pressures above at 3 bar. Moreover, the effectiveness factor value obtained from the manipulation of the model output to approach the experiments at 3 bar is high in comparison to the reported value of Grasa et al. [44]. Other studies based on a bifunctional pellet have determined the carbonation effectiveness factors, Rout et al. [65] suggested $\eta_{Carb} = 0.81$ for 5 mm diameter particles, Di Carlo et al. [41] suggested $\eta_{Carb} = 0.9$ for 0.5 mm diameter pellets, Solsvik and Jakobsen [85] determined a range of $\eta_{Carb} = 0 - 2.1$ for 0.5 mm diameter particles, and a range of $\eta_{Carb} = 0.3 - 1.2$ for a two pellet system considering a mole fraction of CO_2 of 0.1, whilst Lugo and Wilhite [33] reported values of $\eta_{Carb} = 0.68 - 0.77$ at 5% of conversion of the adsorbent, and $\eta_{Carb} = 0.38 - 0.47$ at 95% of the adsorbent conversion.

Although the values of effectiveness vary from one study to another, there is a consensus between the different data that indicates a drop of the effectiveness factor as the conversion of the adsorbent progresses. This trend is related with the structural changes suffered by the adsorbent due to the adsorption of CO_2. The chemisorption of CO_2 produces a product layer of $CaCO_3$ on top of the active CaO, the lower density of the product layer implicates that this phase will occupy a larger volume within the pellet. This expansion reduces the particle porosity, thus decreasing the pore diffusion from the bulk gas towards the centre of the particle. Additionally, at the grain level the CO_2 molecule has to travel through the product layer towards the interface between the ash layer and the active phase. The effect of these structural changes is to reduce the rate of conversion of the adsorbent and increase the time period for saturation. Another implication of the formation of the product layer is the change of the adsorbent's physical properties, i.e. its density and heat capacity.

The incorporation of the structural changes in the plug flow heterogeneous model HTG-2P-PF enables a better fit of the experimental data. Similarly to the basic model, the output of the models considering the loss of adsorbent porosity and the variations of the density and heat capacity of the adsorbent was adjusted by manipulating the value of the carbonation effectiveness factor, Table 7.1 summarises the values of effectiveness factor utilised to adjust the models' outputs to the experimental breakthrough curves.

Figure 7.2 is a plot of the breakthrough curves of the dry composition of hydrogen and carbon dioxide predicted for case R4VL0.15-5, predicted with the basic plug flow heterogeneous model (HTG-2P-PF), the basic model plus the effect of the decrease of the adsorbent porosity (hereafter HTG-2P-PFP), and the basic model plus all the structural changes in the adsorbent properties (i.e. change of porosity, density and heat capacity) or model HTG-2P-PFS. As shown in Figure 7.2 the

basic model response is improved when the changes in the adsorbent properties are incorporated, allowing to fit the simulation to the experimental data. As indicated in Table 7.1, the effectiveness factor necessary to adjust the response of the model HTG-2P-PFP is slightly higher than the corresponding adjusting value of the model HTG-2P-PFS (0.77 vs 0.71, respectively); this indicates a priori that the velocity of propagation of the mass transfer zone is reduced as can be inferred from Equation (7.21) which represents the mass transfer front velocity for a very simplified pseudo-homogeneous system[1].

$$\left(\frac{dz}{dt}\right)_{C_i} = \frac{u_i}{1 + \frac{\rho_{b_1} V_r}{\varepsilon_b W_c} + \frac{\rho_{b_2} \eta_{Carb}}{\varepsilon_b M_{CaO}} \frac{\partial X_{CaO}}{\partial C_i}} \qquad \textbf{(7.21)}$$

Table 7.1 Carbonation effectiveness factor used to fit the experiments of sorption-enhanced steam methane reforming at 3, 5, 7, and 9 bar with the basic model and the incorporation of the structural changes in the adsorbent.

Pressure	Effectiveness factor		
(bar)	HTG-2P-PF	HTG-2P-PFP	HTG-2P-PFS
3	0.85	0.60	0.49
5	1.00	0.77	0.71
7	1.00	0.80	0.62
9	1.00	0.80	0.70

The denominator of Equation (7.21) contains the bulk density of the adsorbent $\rho_{b_2} = \gamma_2(1 - \varepsilon_{p_2})(1 - \varepsilon_b)\rho_{p_2}$, where both, the porosity of the adsorbent ε_{p_2}, and the solid density ρ_{p_2}decrease with the increasing conversion. This is shown in Figure 7.3 and Figure 7.4, which plots of the evolution of the adsorbent properties (porosity, true density and heat capacity) as functions of time and bed position. Since in the denominator of Equation (1.88) all the other parameters are kept constant, and the term $\frac{\partial X_{CaO}}{\partial C_i}$ is positive for the first order reaction, the net effect of the changes in porosity and density of the adsorbent lead to an increase in the numerical value of the denominator and a decrease of the front velocity, thus delaying the saturation of the bed and displacing the breakthrough curves beyond the location shown by the experimental values.

It is worth noting that Equation (7.21) is only valid for CO_2, for other species the third term of the denominator vanishes since the adsorbent conversion depends

[1] It is acknowledged that the model utilised to simulate the reactor is of a heterogeneous nature, however, for the purpose of verifying the effect of the changing adsorbent properties in the mass transfer front velocity a homogeneous version is considered sufficient.

only upon the concentration of carbon dioxide, thus the partial derivative $\frac{\partial X_{CaO}}{\partial C_i}$ is zero for other components. Thus, Equation (7.21) indicates a faster mass transfer zone for the remainder of the bulk components. This is observed by comparing the position of the mass transfer zones of CH_4 (Figure 7.5), and H_2 (Figure 7.6), with that of CO_2 (Figure 7.7).

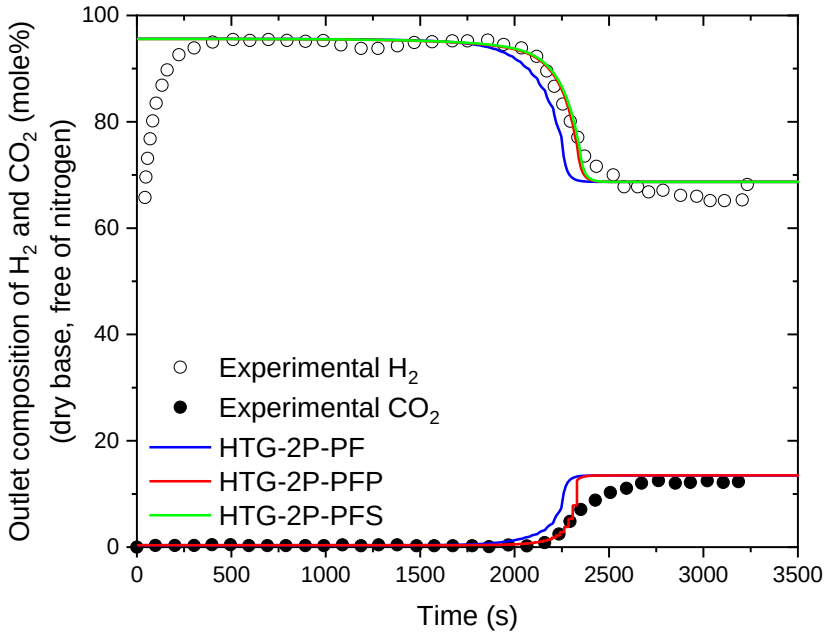

Figure 7.2 Breakthrough curves of H_2 and CO_2 at 5 bar and 923K predicted with the heterogeneous model (HTG-2P-PF), the heterogeneous model with adsorbent porosity changes (HTG-2P-PFP), and the heterogeneous model with full structural changes (HTG-2P-PFS).

Table 7.2 Average error of the HTG-2P-PF, HTG-2P-PF and HTG-2P-PF models in the prediction of the mass transfer zone of the breakthrough curve of hydrogen at 5 bar and 923 K.

Case	**SESR5C**						
Description	**Effect of the incorporation of the changes of the adsorbent porosity and adsorbent thermal properties in the breakthrough curves prediction.**						
Breakthrough	**Experimental time (s)**	**HTG-2P-PF**	**% Error**	**HTG-2P-PFP**	**% Error**	**HTG-2P-PFS**	**% Error**
0.1	2569.2	2273.2	11.52%	2351.1	8.49%	2363.3	8.02%
0.3	2363.4	2248.8	4.85%	2323.0	1.71%	2333.9	1.25%
0.5	2292.3	2206.1	3.76%	2288.5	0.17%	2298.4	0.26%
0.7	2214.3	2126.2	3.98%	2228.5	0.64%	2236.2	0.99%
0.9	2109.2	1951.5	7.48%	2064.6	2.11%	2075.7	1.59%
		Avg. Error	**5.91%**		**2.17%**		**2.03%**

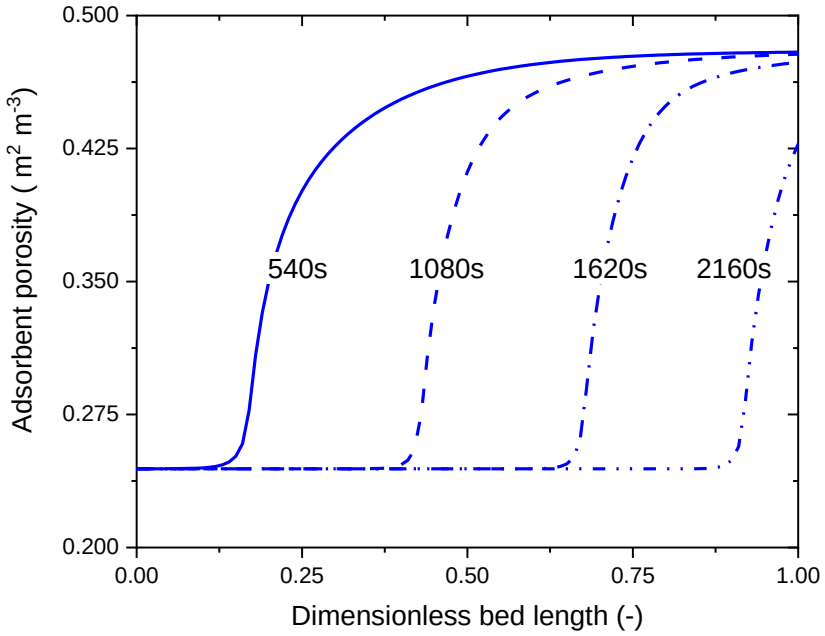

Figure 7.3 Evolution of the adsorbent porosity with time and bed position,

The average errors in the prediction of the breakthrough curves with the different levels of models are summarised in Table 7.2 for 10%, 30%, 50%, 70%, and 90% of the mass transfer zone, and the overall average value. Despite the improvement in the model adjustment, the results reveal that the model continues to exhibit a poor accuracy near the region of the complete saturation of the adsorbent (i.e. at 90% of breakthrough). However, the global error of the prediction is reduced from 5.91% down to 2.17% when the only structural change considered is the loss of porosity, and down to 2.03% when the loss of porosity, the change of density and the change of heat capacity are all accounted for. The small difference in the error introduced by the HTG-2P-PFP and the HTG-2P-PFS models is likely to be due to the manual adjustment of the breakthrough curve, therefore both models can render an acceptable simulation output.

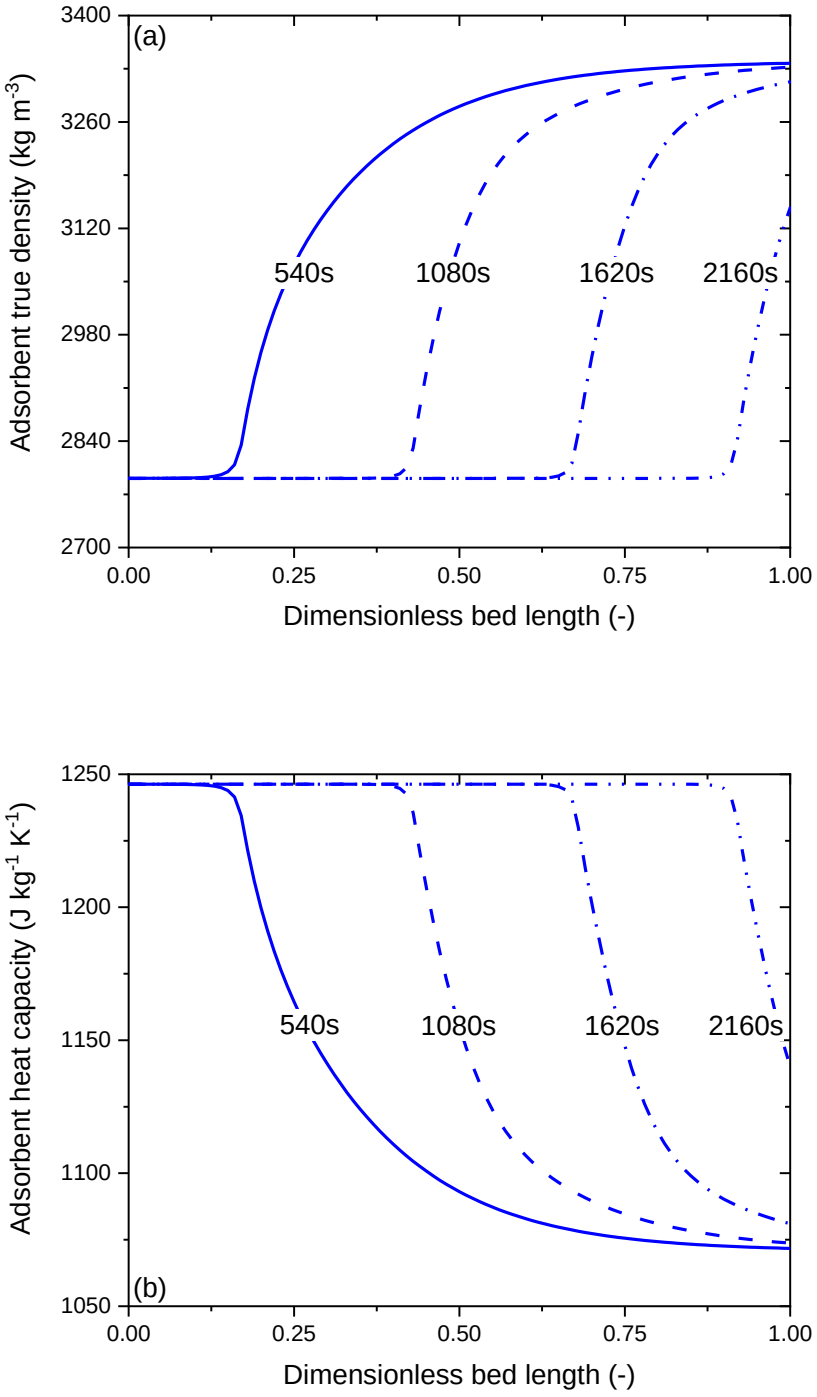

Figure 7.4 (a) Evolution of the adsorbent true density with time and bed position, (b) Evolution of the adsorbent heat capacity with time and position.

The effect of the incorporation of the adsorbent structural changes on the temperature of the bulk, the catalyst and the adsorbent, the gas velocity and the bulk concentration of various chemical species are shown in Figure 7.5 to Figure 7.11. The profiles obtained with the HTG-2P-PFP and HTG-2P-PFS models exhibit a marginal difference between them, but differ considerably from the

profiles obtained with the basic model HTG-2P-PF, predicting different maxima of the various variables and their position within the bed, and a narrower transfer zone. Regarding the temperatures of the different phases (Figure 7.8 – Figure 7.10), the bulk gas and the catalyst surface temperature profiles exhibit lower peak temperatures when predicted with the models HTG-2P-PFP and HTG-2P-PFS, whereas the adsorbent surface temperature shows initially a lower maximum temperature, but as time progresses higher peak temperatures to those predicted by the simple model (HTG-2P-PF). This would indicate some accumulation of heat within the adsorbent that is not effectively removed by the gas, owing to the increase of the adsorbent volumetric capacity $\rho_{b_2} C_{p_2}$ which reduces the transfer rate of the heat of adsorption to the bulk gas; this has a cascade effect to other variables such as the velocity as shown in Figure 7.11.

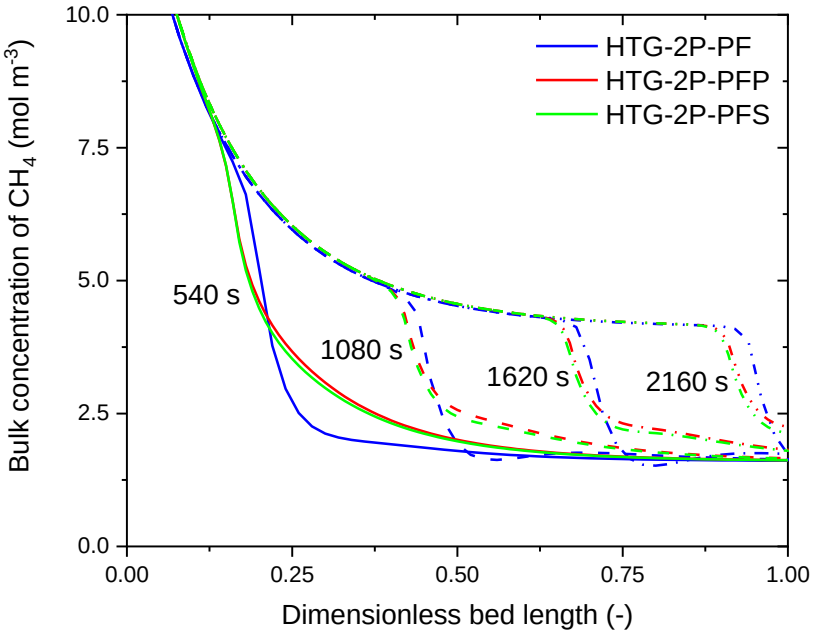

Figure 7.5 CH_4 concentration profiles predicted with the heterogeneous model (HTG-2P-PF), the heterogeneous model with adsorbent porosity changes (HTG-2P-PFP), and the heterogeneous model with full structural changes (HTG-2P-PFS) at inlet gas pressure of 5 bar, gas and bed temperature of 923 K and inlet gas velocity of 0.06 m s^{-1}.

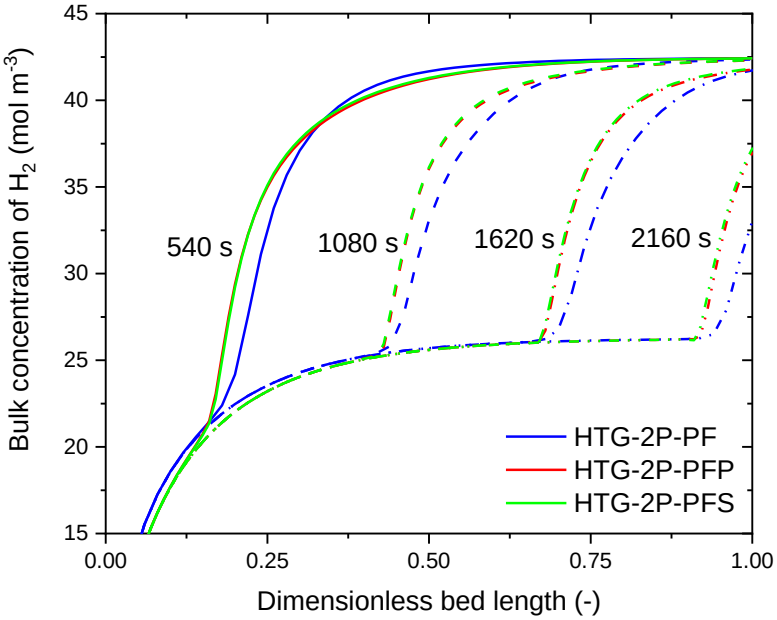

Figure 7.6 H_2 concentration profiles predicted with the heterogeneous model (HTG-2P-PF), the heterogeneous model with adsorbent porosity changes (HTG-2P-PFP), and the heterogeneous model with full structural changes (HTG-2P-PFS) at inlet gas pressure of 5 bar, gas and bed temperature of 923 K and inlet gas velocity of 0.06 m s^{-1}.

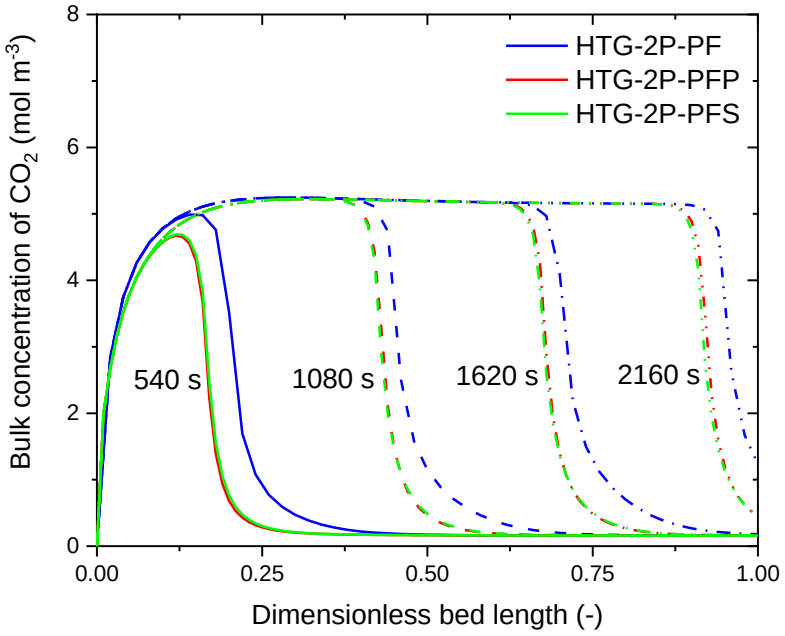

Figure 7.7 CO_2 concentration profiles predicted with the heterogeneous model (HTG-2P-PF), the heterogeneous model with adsorbent porosity changes (HTG-2P-PFP), and the heterogeneous model with full structural changes (HTG-2P-PFS) at inlet gas pressure of 5 bar, gas and bed temperature of 923 K and inlet gas velocity of 0.06 m s^{-1}.

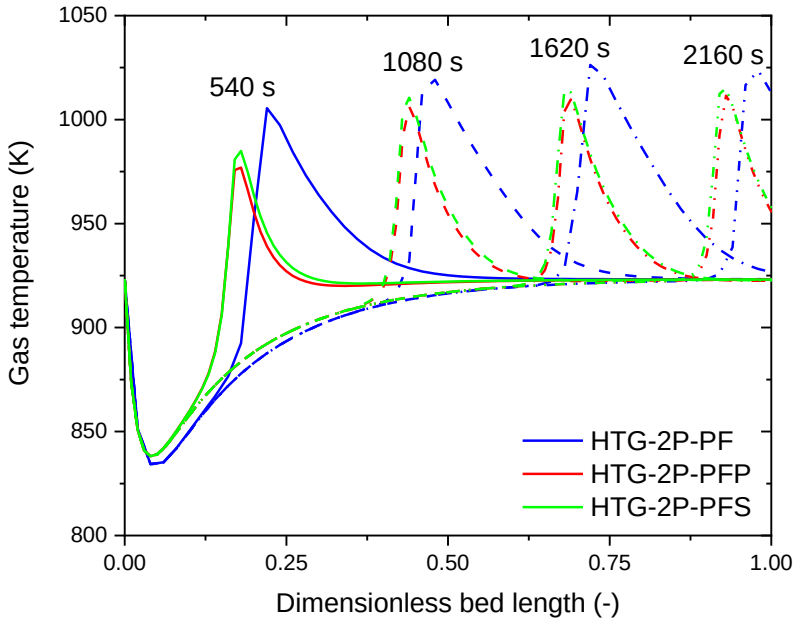

Figure 7.8 Gas temperature profiles predicted with the heterogeneous model (HTG-2P-PF), the heterogeneous model with adsorbent porosity changes (HTG-2P-PFP), and the heterogeneous model with full structural changes (HTG-2P-PFS) at inlet gas pressure of 5 bar, gas and bed temperature of 923 K and inlet gas velocity of 0.06 m s^{-1}.

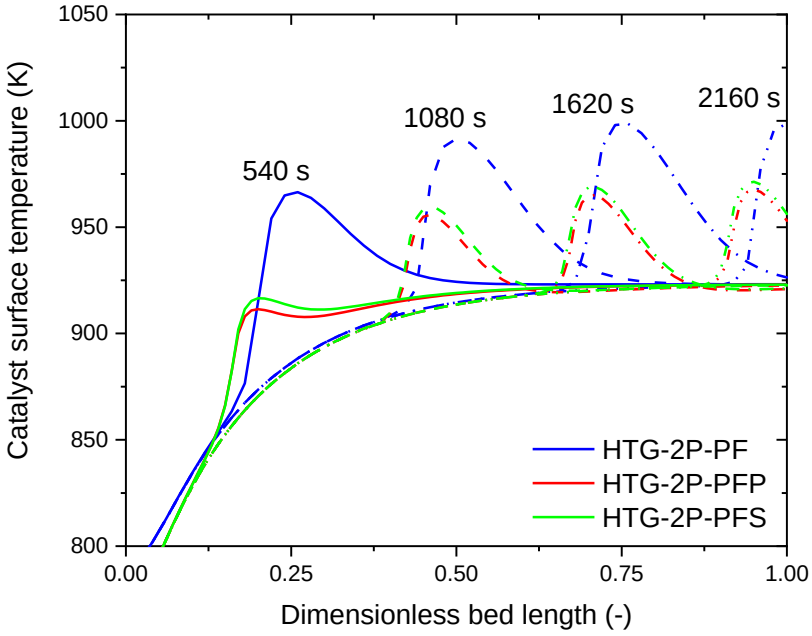

Figure 7.9 Catalyst surface temperature profiles predicted with the heterogeneous model (HTG-2P-PF), the heterogeneous model with adsorbent porosity changes (HTG-2P-PFP), and the heterogeneous model with full structural changes (HTG-2P-PFS) at inlet gas pressure of 5 bar, gas and bed temperature of 923 K and inlet gas velocity of 0.06 m s^{-1}.

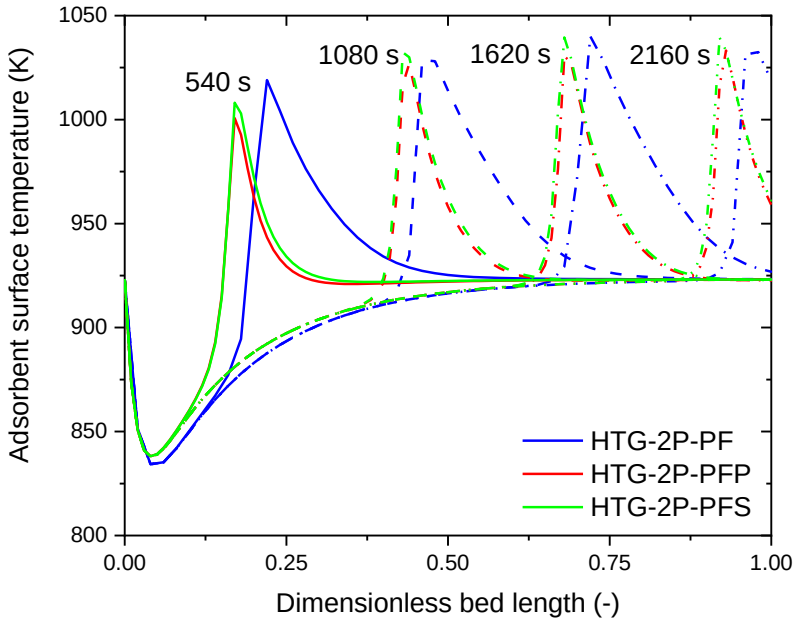

Figure 7.10 Adsorbent surface temperature profiles predicted with the heterogeneous model (HTG-2P-PF), the heterogeneous model with adsorbent porosity changes (HTG-2P-PFP), and the heterogeneous model with full structural changes (HTG-2P-PFS) at inlet gas pressure of 5 bar, gas and bed temperature of 923 K and inlet gas velocity of 0.06 m s^{-1}.

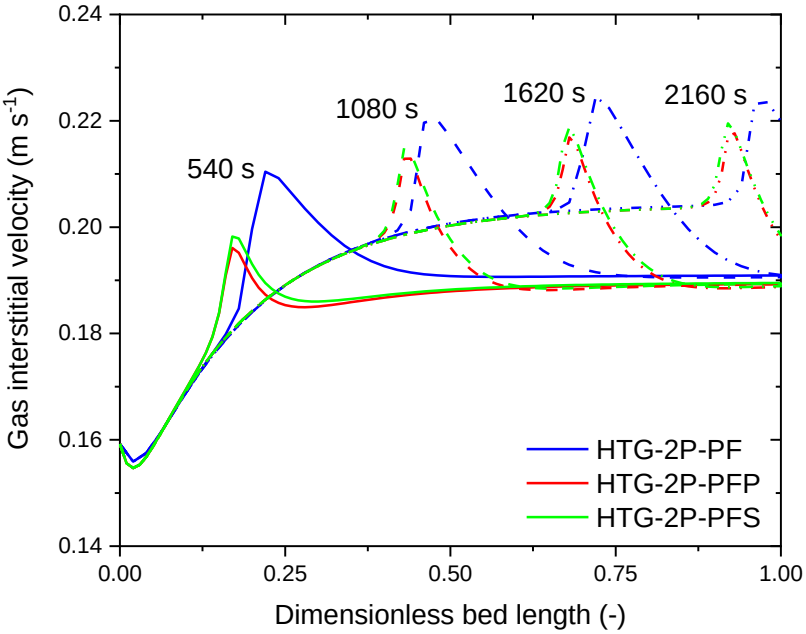

Figure 7.11 Gas velocity profiles predicted with the heterogeneous model (HTG-2P-PF), the heterogeneous model with adsorbent porosity changes (HTG-2P-PFP), and the heterogeneous model with full structural changes (HTG-2P-PFS) at inlet gas pressure of 5 bar, gas and bed temperature of 923 K and inlet gas velocity of 0.06 m s^{-1}.

7.6.2 Sensitivity analysis for the Fuel Reactor mode

The heterogeneous plug flow reactor model in fuel mode accounting for the reduction of adsorbent porosity (HTG-2P-PFP) was applied to a reactor packed with pellets whose dimensions approach those of industrial application to analyse the effect of varying different parameters in the reactor performance, and identify the regions where the heat transfer efficiency is high, thus the conversion of methane and hydrogen yield.

Ideally, the Fuel Reactor is expected to operate as an autothermal reactor, this would mean that the heat of reaction released by the adsorbent during the adsorption of CO_2 is transferred without losses and matches the heat of reaction required by the reforming processes. In practice this is difficult to achieve due to the physical limitations imposed by the physical properties of the materials, the fluid flow phenomena and the structure of the packed bed. Nevertheless, assuming that neither of these physical limitations are present (the homogeneous case) the following equations describing the velocity of the mass and thermal fronts can be derived:

$$\left(\frac{dz}{dt}\right)_{C_i} = \frac{u_i}{1 + \frac{1}{\varepsilon_b} + \frac{\rho_{b_2}\eta_{Carb}}{\varepsilon_b M_{CaO}}\frac{\partial X_{ads}}{\partial C_i}} \tag{7.22}$$

$$\left(\frac{dz}{dt}\right)_{T} = \frac{u_i}{1 + \frac{\rho_b C_{p,b}}{\varepsilon_b \rho_g C_{p,g}} - \frac{\sum_{j=1}^{m}\eta_j \Delta H_j \frac{\partial C_j}{\partial T}}{\varepsilon_b \rho_g C_{p,g}} - \frac{\Delta H_{Carb}\rho_{b_2}\eta_{Carb}}{\varepsilon_b \rho_g C_{p,g} M_{CaO}}\frac{\partial X_{CaO}}{\partial T}} \tag{7.23}$$

These expressions differ significantly from those proposed by Fernandez et al. [52], who derived expressions for the velocity of the reaction and thermal fronts assuming fast reactions. Equation (7.22) has been utilised in the previous section to explain the effect of the decrease of adsorbent porosity upon the velocity of the mass transfer front, giving a longer saturation time. Equation (7.23) represents the velocity of the thermal front as it travels downstream the bed, it also provides information regarding the ability of the reactor of operating under autothermal conditions. The derivation of these equations is available in the Appendix C, Section C.1. By inspecting Equation (7.23), it can be realised that the third and four terms of the denominator carry the thermal effects of the reforming reactions and the adsorption of CO_2, respectively. If the reactor is to be operated as an autothermal system, the aforementioned terms should cancel between them, this means that, if the Fuel Reactor is autothermal, the velocity of the thermal front will correspond to that of a pure thermal wave when:

$$\frac{1}{\rho_{b_2}} = \frac{\eta_{Carb}\Delta H_{Carb}E_{Carb}k_{Carb}S_{g,f}t}{100M_{CaO}\sum_{j=1}^{m}\eta_j\Delta H_j p_j\, e^{k_{Carb}S_{g,f}t}} \quad \textbf{(7.24)}$$

Equation (7.24) suggest that the thermal effects in the bed are defined by the adsorbent density in the bulk (ρ_{b_2}), the adsorbent surface area ($S_{g,f}$), and the reactivity of the adsorbent expressed by means of the rate constant of carbonation (k_{Carb}). If the R.H.S. is greater than the L.H.S. the system will be dominated by the heat of adsorption, this would happen at the early stage of the process when the adsorbent has enough capture capacity. Conversely, if the R.H.S. is lower than the L.H.S. the reforming process will dominate the thermal effects in the bed.

The aforementioned adsorbent properties can be targeted during the design of the adsorbent, by selecting suitable supports that maximise the adsorbent surface area and provide enough porosity, therefore increasing its reactivity and affecting its density. In any case, it could prove useful to analyse the effect of varying such parameters in the simulation output. Previous studies have addressed the effect of the operating parameters over the reactor performance; Abbas et al. [68] conducted a sensitivity analysis varying the operating temperature and pressure, and the steam-to-carbon ratio, Fernandez et al. [50] studied the effect of temperature, pressure, space velocity, steam-to-carbon ratio, and catalyst-to-adsorbent ratio over the performance of a reactor operating with a Ca/Cu looping with in-situ CO_2 adsorption, however their analysis neglected the inter-pellet resistance and therefore, no discussion regarding the importance of the available transfer area was provided. Rout and Jakobsen [65] studied the effects of the pressure, temperature, gas flowrate and steam-to-carbon ratio on the product composition during on the start-up of the reactor. In this analysis the effect of the available heat transfer area, mass flux, feedstock composition, temperature catalyst density and adsorbent density over the methane conversion, hydrogen purity, hydrogen yield and hydrogen productivity is studied; these variables were calculated with Equations (7.25) - (7.28). The simulation parameters utilised for the simulations conducted in this study are summarised in Table 7.3.

$$X_{CH_4} = \left(\frac{u_S^{in}C_{C_{CH_4}}^{in} - u_S^{out}C_{C_{CH_4}}^{out}}{u_S^{in}C_{C_{CH_4}}^{in}}\right) \times 100 \quad \textbf{(7.25)}$$

$$P_{H_2} = \frac{C_{H_2}^{out}}{C_{CH_4}^{out} + C_{H_2}^{out} + C_{CO_2}^{out} + C_{CO}^{out}} \times 100 \quad \textbf{(7.26)}$$

$$Y_{H_2} = \frac{u_S^{out} C_{H_2}^{out}}{4 u_S^{in} C_{CH_4}^{in}} \times 100 \quad \textbf{(7.27)}$$

$$Pr_{H_2} = 2 \times 10^{-3} A_r \left[\int_0^t u_S C_{H_2} dt - u_S^{in} C_{H_2}^{in} t \right] \quad \textbf{(7.28)}$$

Table 7.3 Simulation parameters for the sensitivity study of the Fuel Reactor model.

Parameter	Value
Gas composition (mole%)	
Methane	17.78
Water	72.64
Hydrogen	4.87
Carbon Monoxide	0.01
Carbon Dioxide	1.66
Nitrogen	3.04
Pellets properties (cat./ads.)	
Density (kg m^{-3})	3450/2710
Heat capacity (J $kg^{-1}K^{-1}$)	1102.5/1070.7
Porosity (m^3 m^{-3})	0.41/0.48
Avg. particle diameter (m)	0.01
Reactor length (m)	1.0
Reactor diameter (m)	0.35
Time period (s)	800
Inlet temperature (K)	923
Inlet pressure (bar)	9
Inlet velocity	0.5
Vol. fraction of catalyst (m^3 m^{-3})	0.25

7.6.2.1 Effect of transfer area of the catalyst/adsorbent

The integration of the heat of adsorption of CO_2 and the heat of reaction of reforming is constrained by the physics of the reactor, particularly the velocity of the flow and the rate of heat transfer between the phases. The application of the Fuel Reactor concept considering separate particles implies that the thermal contact between the heat source particle and the heat sink particle is not intimate due to the structure of the packed bed; furthermore, the contact points between the particles are zones might control the heat transfer in the bed at low Reynolds numbers due to the stagnated fluid surrounding these areas, which reduces the thermal conductivity of the packed bed [197]. Equation (6.3) indicates that the

heat transfer with either particle can be influenced by manipulating the heat transfer area or by enhancing the heat transfer coefficient. The former can be attained by varying the volumetric fraction of each material in the packed bed or by varying the particle size, or a combination of both. The latter is a function of the Reynolds number and the bed porosity and, at a fixed inlet velocity, is also affected by the particle size.

Figure 7.12 shows the reactor performance indicators of the Fuel Reactor as function of time and the volumetric factor of catalyst in the packed bed. Two clear trends can be identified, firstly, the duration of the pre-breakthrough period decreases with the increasing amount of catalyst in the bed; the shorter pre-breakthrough period is due the lower CO_2 capture capacity in the packed bed owing to the decreasing volumetric fraction of adsorbent in each case. Secondly, the three indicators (i.e. hydrogen yield, methane conversion and hydrogen purity) increase with the increasing volumetric fraction, however, the reactor performance is well below the predicted performance at equilibrium at 923 K as reported in **Chapter 3** and by Abbas et al. [68] and Fernandez et al. [6], among others.

The very low values of the reactor performance indicators are likely a consequence of the limitations of mass and heat transfer between the catalyst and the adsorbent. Figure 7.13 illustrate the temperature profiles of the bulk gas, the catalyst surface and the adsorbent surface at 400 s for the various cases of volumetric fraction of catalyst simulated. For each case, the position of the thermal front in the bed is different, this is due to the volumetric fraction affecting the duration of the pre-breakthrough zone, since all the curves shown are a snapshot of the system at the same simulation time, some cases exhibit a thermal front closer to the bed exit than others. More relevant is the position of the temperature profiles with respect to each other for each case of volumetric fraction simulated. For $\gamma_1 = 0.1\ m^3 m^{-3}$ the bulk gas temperature profile is closer to the adsorbent temperature profile than it is to the catalyst temperature profile which increases ca. 35 K from its value at the bed inlet but exhibits a temperature difference with the adsorbent of 130.3 K close to the bed inlet. This situation suggests that at this very low catalyst content, the heat transfer may be constrained by a reduced transfer area. Moreover, the closeness between the adsorbent and bulk gas temperature suggests that in this situation most of the heat of adsorption will leak from the reactor. As the fraction of catalyst in the bed increases, the bulk gas temperature profile in the rear zone of the thermal front departs from the adsorbent temperature profile and approaches the catalyst temperature profile, this could be interpreted as a sign of a tendency of the system to equilibrate its temperature owing to a better transfer of heat from the

adsorbent to the catalyst. This is evident from the peak zone formed in the catalyst which indicates that this phase is being heated up.

The transfer area also affects the mass transfer as shown in Figure 7.15 and Figure 7.16, which are plots of the partial pressures of CH_4 and CO_2, respectively. Figure 7.15 presents the partial pressure of CH_4 in the bulk gas and in the catalyst. The profile in the adsorbent is not shown for this variable because no physical or chemical process affecting the CH_4 profiles happen in that phase and thus is not relevant for the reactor performance. However, similarly to the temperature behaviour, significant differences between the profiles of CH_4 in the bulk gas and in the catalyst are observed for low values of volumetric fraction of catalyst. Similarly, in Figure 7.16 the profiles of partial pressure of CO_2 are illustrated. In this case, the profiles of the three phases are shown since the CO_2 is generated in the catalyst, and has to diffuse from the catalyst pore towards the bulk gas and from there diffuse into the adsorbent particle until it reaches the reaction front. Like in the case of CH_4, the differences in the partial pressure from one phase to another are more significant as the volumetric fraction of catalyst is reduced. This also has a double effect on the reactor operation. On one hand, since the mass transfer is reduced by a lower transfer area, the partial pressure of CO_2 in the catalyst surface may limit the rate of the reforming reactions owing to the thermodynamic equilibrium. This will favour the reverse reaction due to the high concentration of CO_2 and the high operating pressure. On the other hand, the lower concentration of CO_2 in the adsorbent affects the rate of carbonation, thus the availability of heat of adsorption. The latter effect is not necessarily evident in these simulation outputs since the chosen carbonation model predicts a carbonation rate that is independent of the CO_2 concentration when the difference between the actual partial pressure of CO_2 and the equilibrium pressure is less than 0.1 bar, since the total pressure selected for this exercise is 25 bar, the likelihood of being above the aforementioned threshold is considerably high.

With regards to the gas pressure (Figure 7.17), the effect of varying the catalyst volumetric fraction is barely significant. The pressure drop throughout the packed bed is very low, owing to the low gas superficial velocity and varies from 0.0060 – 0.0063 bar m^{-1}, which is acceptable as it barely represents less than 1% of the inlet pressure in all the cases. Thus, this is unlikely to affect the process significantly.

The best choice of volumetric fraction of catalyst depends on several factors. As mentioned above, this parameter will affect the duration of the cycle and thus, its proper selection should be made as part of the analysis of the integral system, including the regeneration or air reactor cycle. However, for the purposes of this

exercise, the selection of $\gamma_1 = 0.5\ m^3 m^{-3}$ seems to render the best case scenario for all the parameters, but the hydrogen production, according to the data summarised in Table 7.4. Considering the active material present in the catalyst and the adsorbent, this would correspond to a NiO-to-CaO molar ratio of 0.16; for comparison, the NiO-to-CaO ratio determined from thermodynamic analysis was 0.5.

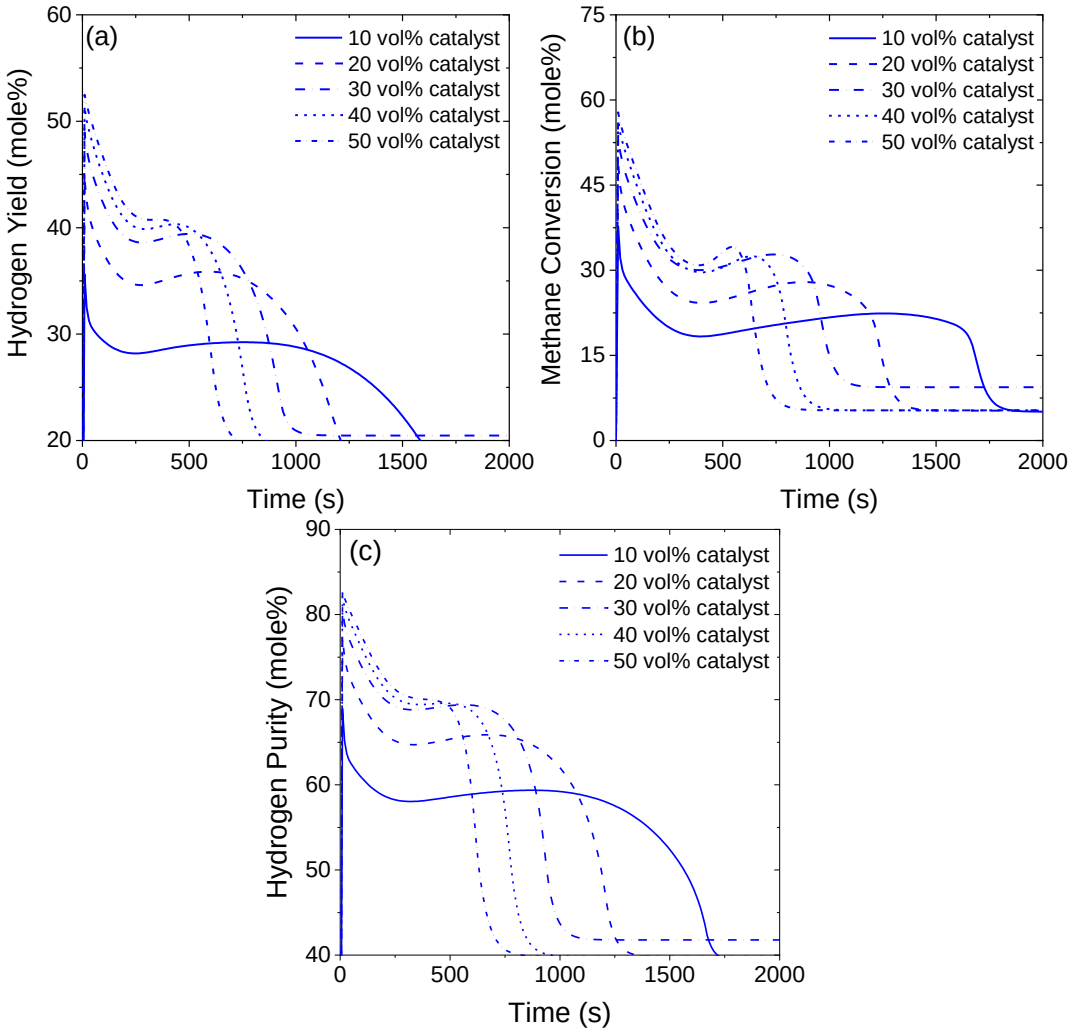

Figure 7.12 Reactor performance indicators of the Fuel Reactor as function of the volumetric fraction of catalyst in the bed. (a) Hydrogen yield, (b) Methane conversion, (c) Hydrogen purity (free of nitrogen).

Table 7.4 Average performance indicators for various values of volumetric fraction of catalyst.

Vol. fraction of catalyst (m^3m^{-3})	H_2 purity (mole%)	CH_4 conversion (mole%)	H_2 yield (mole%)	H_2 productivity (kg x 10^{-3})
0.10	59.0	21.3	28.7	1960.6
0.20	66.1	28.2	35.5	1923.8
0.30	70.3	34.1	39.7	1786.6
0.40	71.7	36.5	40.7	1573.5
0.50	73.2	39.3	42.0	1349.4

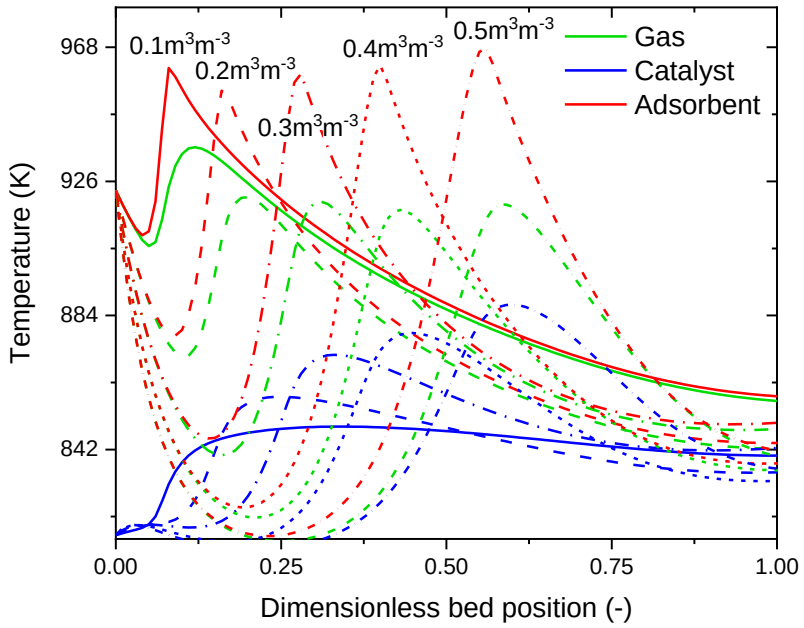

Figure 7.13 Temperature profiles at 400 s as function of the volumetric fraction of catalyst in the packed bed reactor.

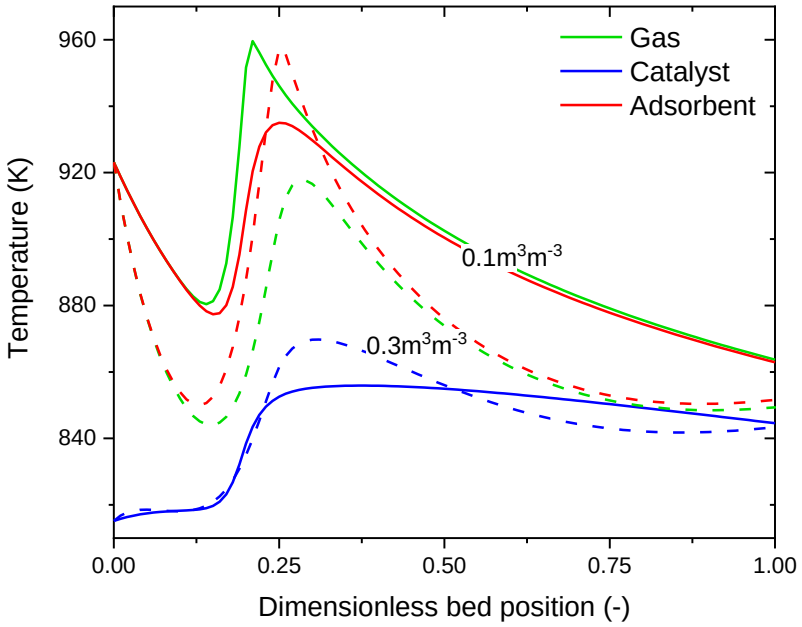

Figure 7.14 Temperature profiles at 50% of the breakthrough time for two cases of the volumetric fraction of catalyst in the packed bed reactor.

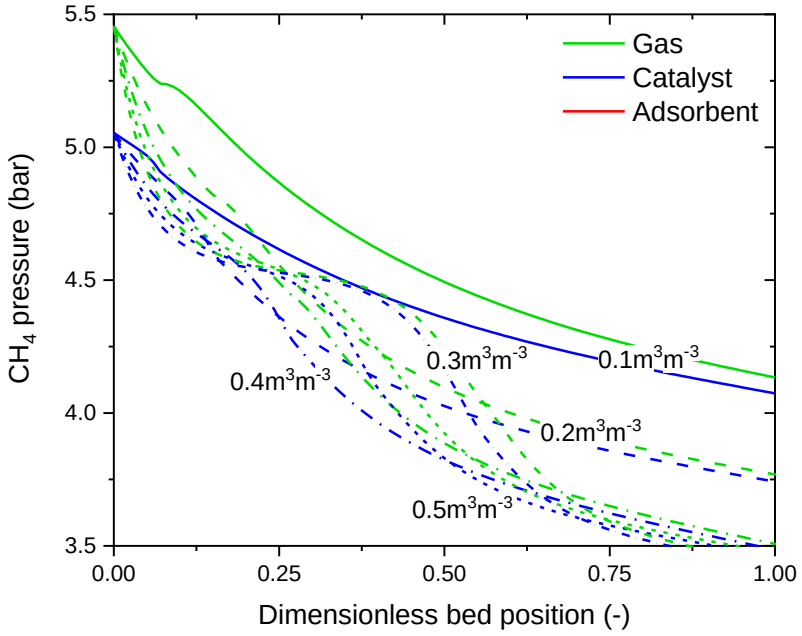

Figure 7.15 CH_4 partial pressure profiles at 400 s as function of the volumetric fraction of catalyst in the packed bed reactor.

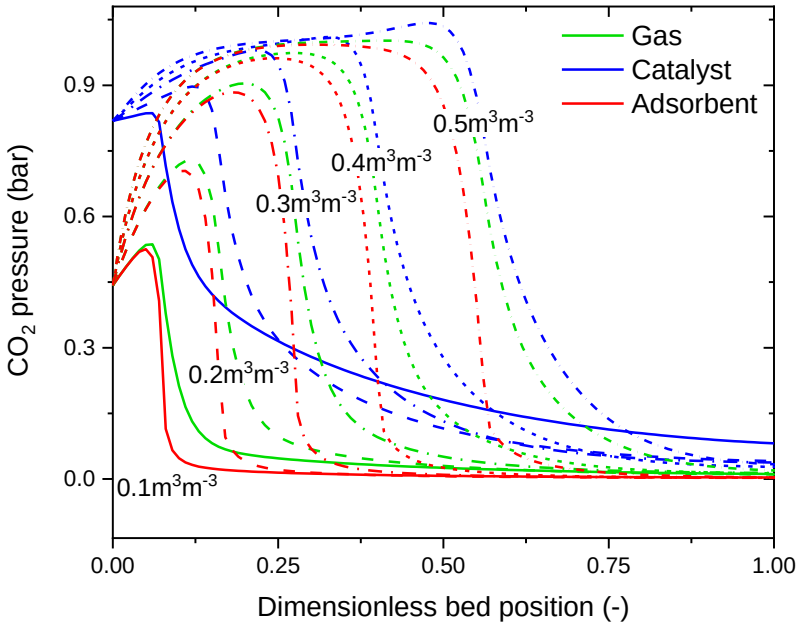

Figure 7.16 CO_2 partial pressure profiles at 400 s as function of the volumetric fraction of catalyst in the packed bed reactor.

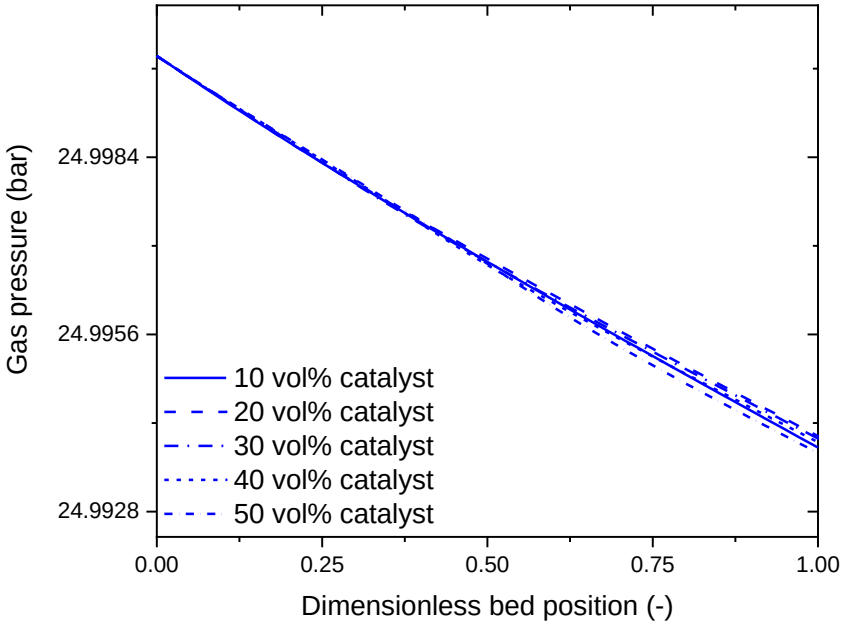

Figure 7.17 Gas pressure profiles at 400 s as function of the volumetric fraction of catalyst in the packed bed reactor.

As mentioned above, the transfer area can also be manipulated by reducing the pellet diameter which in principle should enhance the heat transfer rate, moreover, reducing the pellet diameter also reduces the Reynolds number and enhances the heat transfer coefficient. Two situations are analysed, firstly, the

case of reducing the catalyst size only in such a manner that the catalyst-to-adsorbent diameter ratio is reduced from the base case of 1.0, to 0.75 and 0.5; the second scenario considers the reduction of the diameter of both particles.

Figure 7.18 illustrates the effect of reducing the particle diameter on the reactor performance indicators and Table 7.5 summarises the average values of the performance indicators. By reducing only the catalyst pellet diameter, a slight enhancement of the reactor performance is achieved. The improvement of H_2 yield, CH_4 conversion and H_2 purity increased up to 5.1%, 6.3% and 2.3% above their values for the base case with both packings sizes of 0.01 m. When both particles sizes (i.e. catalyst and adsorbent) are reduced, the performance of the reactor improves up to 7.7%, 22.0% and 16.6% for the hydrogen purity, methane conversion and hydrogen yield, respectively. This is relevant not only for the design of the reactor, but also for the design of downstream units for purification (e.g. a pressure swing adsorption unit), and it would be worthy to analyse how the selection of the final reactor design parameters affect the design of such units aiming at optimising the design of the coupled system.

Regarding the temperature, the catalyst peak temperature rose from the value predicted with the base case simulation parameters. When the catalyst particle size is reduced keeping the adsorbent particle size fixed, the catalyst peak temperature increases up to 880.9 K as shown in Figure 7.19, representing an increase of ca. 10 K. When both particles sizes are reduced, the catalyst temperature increases more significantly as shown in Figure 7.20; for the lowest particle size of 0.0025 m (corresponding to a transfer area of 1553.9 m^2m^{-3}), the peak temperature reaches 917.7K and the temperature difference with respect to the adsorbent is clearly reduced. This demonstrates that the transfer area is a key parameter in achieving an efficient process, and suggests that a future investigation could be devoted to the design and optimisation of the shapes of particles to maximise the transfer area whilst minimising the pressure drop.

The counterpart side of the improvement of the heat transfer by reducing the packing size is the increase of pressure drop as illustrated in Figure 7.21. It is evident that the lowest size tested (i.e. 0.0025 m) renders the highest pressure drop, however, since the inlet velocity value utilised for these simulations is low (0.2 m s^{-1}), the maximum pressure drop per unit of length obtained was 0.035 bar m^{-1}, representing barely 0.14% of the inlet pressure. The effect of the larger pressure drop can be also noticed in Figure 7.18 and Figure 7.20; a higher pressure drop in the system renders sharper mass and thermal fronts which result in reduced lengths of the mass and heat transfer zones.

The results presented in this section indicate that the best case scenario for the reactor performance corresponds to a distribution of 50/50 vol% of each material in the bed and the lowest practical particle sizes; from a pure simulation standpoint, choosing particle sizes of 0.0025 m renders the best case scenario for reactor performance and yields a very low pressure drop. However, the use of particles of this size at the industrial scale is impractical, primarily because any eventual attrition of the materials can cause blocking of the packed bed leading to a poor flow distribution and utilisation of the materials. Therefore, in the following studies a particle size of 0.005 m is used, since this particle size is more realistic according to the equivalent sphere diameters of commercial catalyst reported in [171].

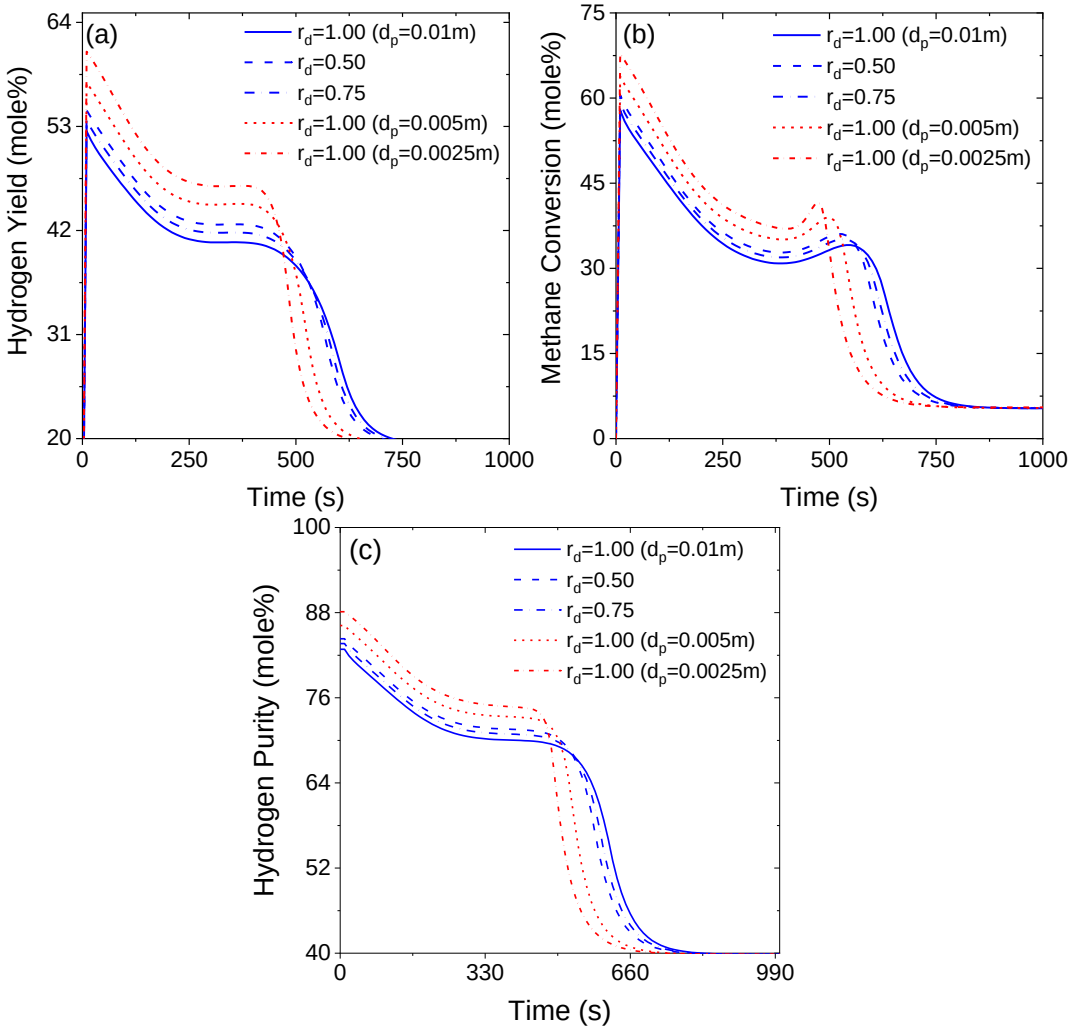

Figure 7.18 Reactor performance indicators of the Fuel Reactor as function of the ratio of catalyst diameter to adsorbent diameter in the packed bed reactor. (a) Hydrogen yield, (b) Methane conversion, (c) Hydrogen purity (free of nitrogen).

Table 7.5 Average performance indicators for three values of catalyst-to-adsorbent diameter ratios.

Catalyst-to-adsorbent diameter ratio (-)	Particle diameter cat./ads. (m)	H_2 purity (mole%)	CH_4 conversion (mole%)	H_2 yield (mole%)	H_2 productivity (kg x 10^{-3})
0.50	0.005/0.01	74.7	40.5	45.0	1398.8
0.75	0.0075/0.01	73.9	39.4	44.0	1381.5
1.00	0.01/0.01	73.0	38.1	42.8	1357.8
1.00	0.005/0.005	76.7	43.5	47.4	1400.3
1.00	0.0025/0.0025	78.6	46.5	49.9	1432.2

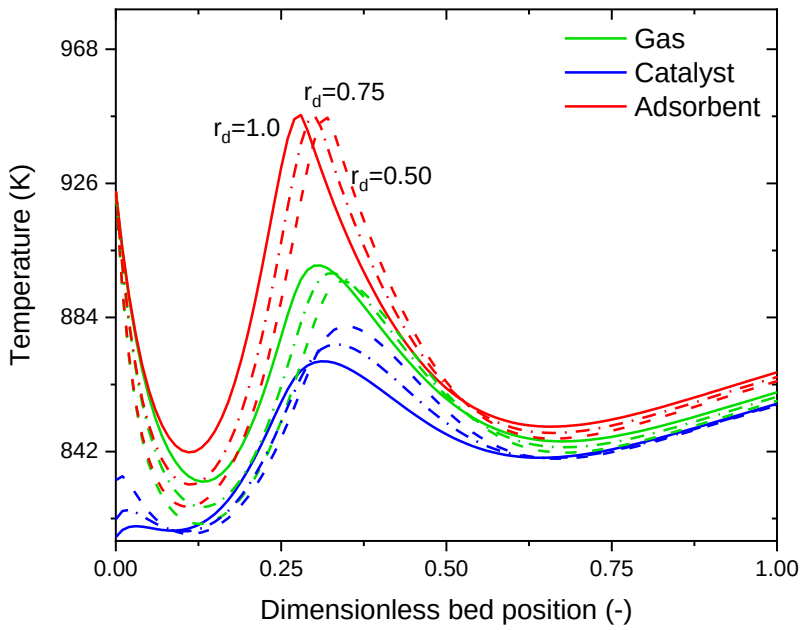

Figure 7.19 Temperature profiles at 250 s as function of the ratio of catalyst diameter to adsorbent diameter in the packed bed reactor.

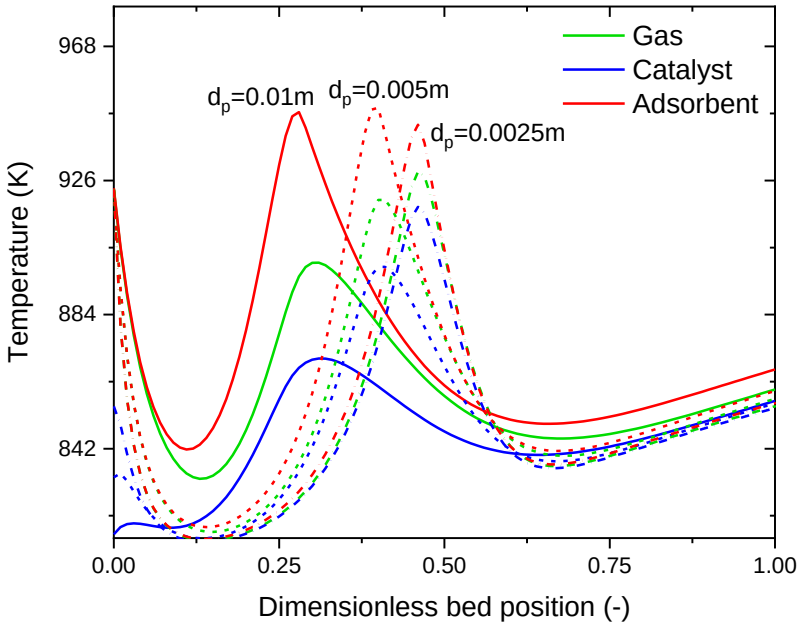

Figure 7.20 Temperature profiles at 250 s as function of the packing diameter in the packed bed reactor.

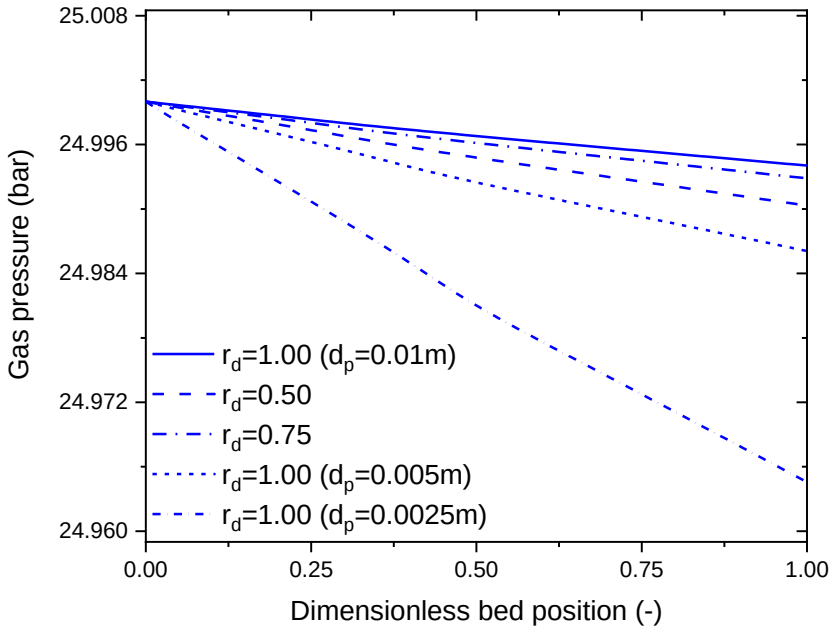

Figure 7.21 Gas pressure profiles at 400 s as function of the ratio of catalyst diameter to adsorbent diameter in the packed bed reactor.

7.6.2.2 Effect of the inlet mass flux

The effect of the inlet gas mass flux was analysed by varying the gas inlet velocity; this variable essentially lengthens or shortens the residence time of the gas in

the packed bed reactor, thus affecting the contact time of the species with the catalyst and the adsorbent. The increase of the inlet gas velocity results in a) a shorter time available to saturate the adsorbent to its maximum conversion, and b) a reduction of the conversion of methane, the hydrogen purity and the hydrogen yield, as illustrated in Figure 7.22. Abbas et al. [68] reported a similar behaviour regarding the duration of the pre-breakthrough stage; but they found that the reactor performance was independent of the gas mass flux. Fernandez et al. [6] indicated that a high adsorbent reactivity is needed to achieve equilibrium as the gas mass flux is increased; they argued that this behaviour is related to the reduced time for the sorbent to adsorb the CO_2 present in the bulk gas.

The results observed in Figure 7.22 clearly differ in the second aspect from the former investigation, but seem to agree with the description provided by the latter. The differences in the findings might be associated to the different nature of the models utilised to simulate the system. Abbas et al. [68] utilised a pseudo-heterogeneous model described previously in **Chapter 6**. Fernandez et al. [6, 50] and other researching groups [32, 65, 177] have modelled the reactor as a pseudo-homogeneous system. In both cases, it was assumed that the contact between the catalyst and the adsorbent is intimate, thus transferring all the heat of reaction generated in the adsorbent to the catalyst; this leads to a situation in which the catalyst operates at higher temperature levels, therefore with a higher reactivity. Conversely, the heterogeneous model proposed in this work accounts for the inter-pellet resistances, as well as the intra-pellet resistances through the use of an effective heat transfer coefficient [168]. It is well known, that even at high mass velocities the heat transfer in the interphase fluid-solid is limited by the low thermal conductivity of the bed caused by the stagnated fluid film surrounding the pellet [129, 171], hence it can be expected that the heat transport from the adsorbent towards the catalyst will occur at a reduced rate. Under these circumstances, the assumption of intimate contact between the materials may be invalid, thus it is reasonable to expect an inefficient heat transfer from the adsorbent to the catalyst, rendering a lower conversion of the fuel, hence a lower yield of hydrogen.

Figure 7.23 and Figure 7.24 are plots of the evolution of the temperature profiles of the gas bulk, the catalyst and the adsorbent, at different simulation times as a function of the axial position in the bed. Figure 7.23 presents the profiles obtained with an inlet gas velocity of 0.12 m s^{-1}, and Figure 7.24 presents those corresponding to an inlet velocity of 0.4 m s^{-1}; the initial bed temperature has been indicated as a reference. In both cases, the operating catalyst temperature is well below the initial bed temperature, this happens because of the initial drop of temperature due to the endothermicity of the reforming reactions. Although the

adsorption of CO_2 increases the temperature of the system, the increase is not enough to return the bed temperature to the initial level, in fact as it can be seen in both plots, the temperature rise happens in a narrow section of the bed. These low catalyst temperatures affect the final reactor performance as can be expected.

An additional effect of the inlet velocity on the reactor physics can also be noticed in Figure 7.23 and Figure 7.24. As the inlet velocity increases, the shape of the thermal front becomes diffuse, this could be an effect of the increased pressure drop in the system as it was pointed out in the section 7.6.2.1. The pressure drop per unit of length increases due to the higher mass handled in the same cross sectional area as illustrated in Figure 7.25, varying between 0.006–0.18 bar m^{-1}.

The results presented in this section indicate that the reactor should be operated at the lowest practical value of mass flux to achieve the highest reactor performance in terms of the methane conversion, hydrogen purity, hydrogen yield and hydrogen productivity (Table 7.6). The optimum velocity should be determined as part of the design of the cyclic operation of the reactor in order to attain a continuous system whilst targeting the desired throughput capacity. The selection of the final mass flux (or reactor throughput) will be critical to the process economics, since it will determine the minimum number of reaction units and the reactor dimensions required to operate continuously.

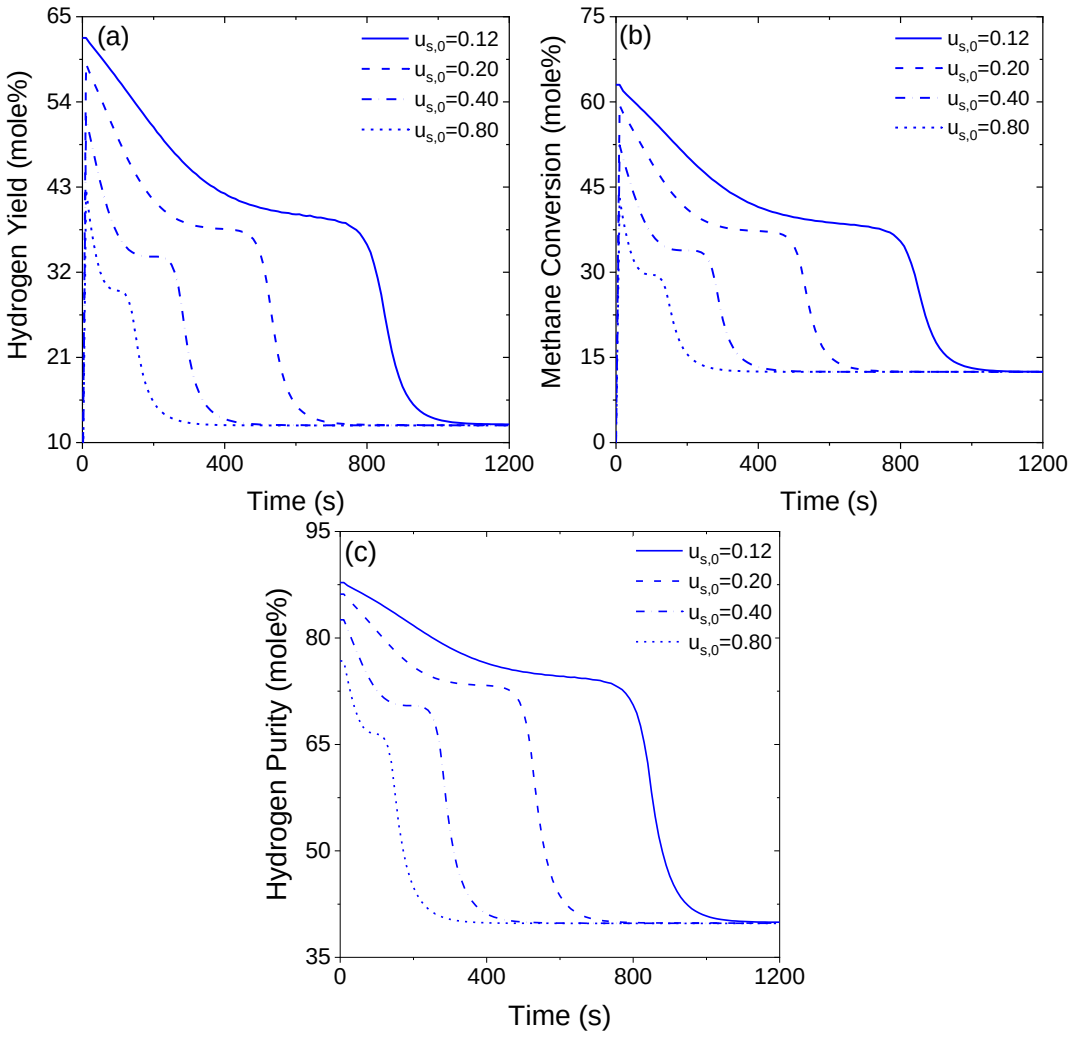

Figure 7.22 Reactor performance indicators of the Fuel Reactor mode as function of the gas inlet velocity. (a) Hydrogen yield, (b) Methane conversion, (c) Hydrogen purity (free of nitrogen).

Table 7.6 Average performance indicators at various values of gas inlet velocity.

Inlet gas velocity ($m\ s^{-1}$)	H_2 purity (mole%)	CH_4 conversion (mole%)	H_2 yield (mole%)	H_2 productivity ($kg \times 10^{-3}$)
0.50	78.3	45.1	45.6	2007.1
0.75	76.7	42.8	42.9	1910.3
1.00	73.4	38.1	38.1	1816.9
1.00	69.3	33.1	33.0	1597.5

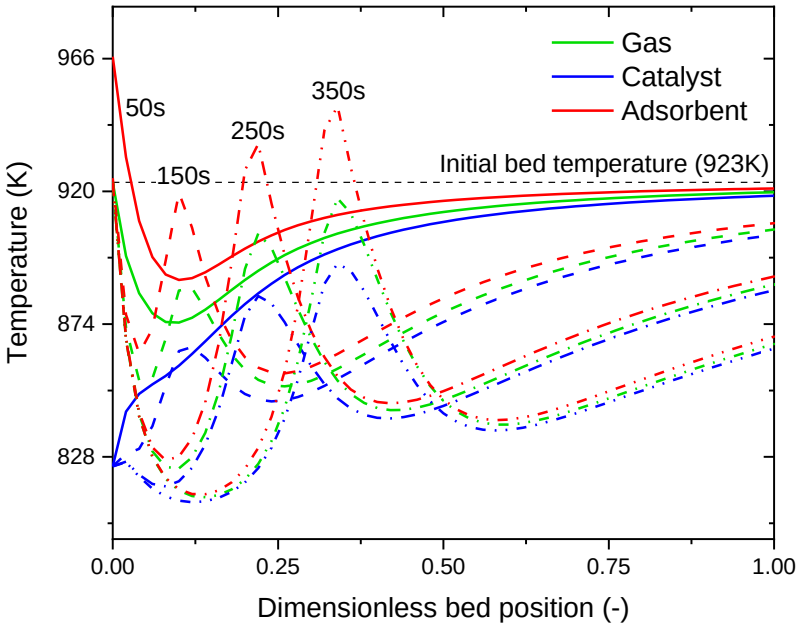

Figure 7.23 Temperature profiles evolution evaluated with an inlet velocity of 0.12 m s^{-1}, inlet gas temperature of 923 K and initial packing temperature of 923 K.

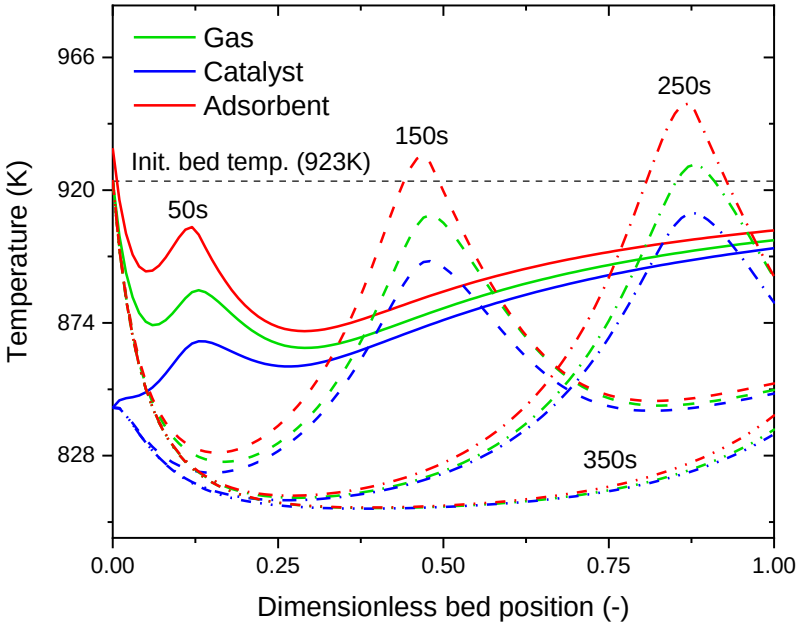

Figure 7.24 Temperature profiles evolution evaluated with an inlet velocity of 0.4 m s^{-1}, inlet gas temperature of 923 K and initial packing temperature of 923 K.

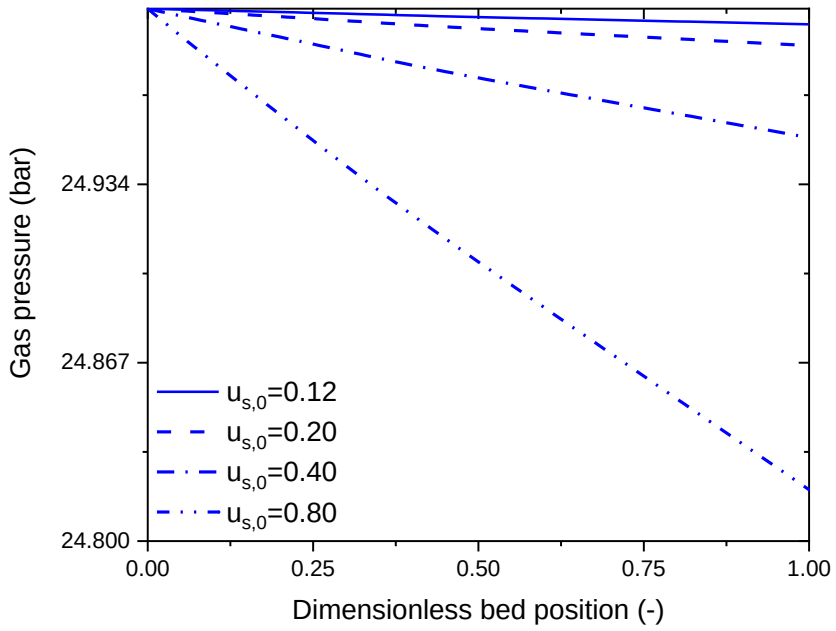

Figure 7.25 Gas pressure at 50% of the time for saturation of the adsorbent to its maximum conversion as function of the axial position in the bed and the inlet gas velocity. Gas inlet temperature and initial bed temperature of 923 K.

7.6.2.3 Effect of temperature

The temperature of the gas and the initial bed temperature profile were varied within ±5% from the base case scenario value of 923 K, and the effect on the reactor performance was studied. Figure 7.26 illustrates the reactor performance indicators when the inlet gas temperature is varied, whilst the initial bed temperature is kept at 923 K, and when the gas inlet temperature is fixed at 923 K and initial temperature of the bed is varied. It is clear that operating the reactor at lower temperature, will lead to lower hydrogen yield, methane conversion and hydrogen purity. Conversely operating either the gas inlet temperature or the initial bed temperature at higher levels will enhance the performance indicators. The main difference between the two scenarios is that when the gas inlet temperature is varied, the effect over the performance indicators happens earlier during the cycle, whereas when the manipulated temperature is that of the bed, the effect is seen later in the operation. In addition, manipulating the gas inlet temperature also effects the duration of the Fuel Reactor step. Abbas et al. [68] found similar enhancements when increasing the operating temperature from 873 K to 973 K, but a detrimental effect at temperatures as high as 1073 K. The latter condition was not considered in this work due to its closeness to the calcination temperature of $CaCO_3$, since operating close to this limit hinders the rate of

carbonation, thus the enhancement of the reforming reactions. Table 7.7 summarises the average values of H_2 purity, CH_4 conversion and H_2 yield, the production of H_2 is also reported. The best case scenario correspond to the situation where either the gas inlet temperature or the initial bed temperature are set to 969 K whilst the other parameter is set to 923 K, rendering very similar performance indexes, with variations of circa 1%.

When both parameters, the gas inlet temperature and the bed initial temperature are increased or decreased by the same factor, the resultant profiles change as shown in Figure 7.27. When the temperature increases, the reactor performance indices also increase and the pre-breakthrough period becomes shorter. This is clearly due a higher reaction rate of reforming which promotes the production of CO_2, leading to a higher carbonation rate, thus a faster consumption of the adsorbent. Conversely, when the temperature is reduced, the reactor performance worsens and the pre-breakthrough period is lengthened. The best case scenario renders a highest 83.1 mol% of H_2 purity, 53.7 mol% of CH_4 conversion and 54.2 mol% of H_2 yield as indicated in Table 7.8.

However, the values of the performance indicators reported by Abbas et al. [68] are well above those determined in this work. The average H_2 purity compares well with at 83.1 mol% in this work versus 87.3 mole% in the reference, whilst the conversion differs by a larger margin at 53.7 mole% vs 71.7 mole%, both values have been calculated at similar temperatures but different pressures (25 bar in this work vs 30 bar in the reference). Numerous reasons might be causing these discrepancies, however, the fundamental differences on the modelling approach seem to be the underlying cause, particularly the assumption of a single temperature for the packing in the pseudo-heterogeneous model. By characterising the packing with a single temperature the dynamics of heat transfer and the inter-pellet resistances are neglected, thus the expectation is that the catalyst will utilise all the heat of adsorption being released by the adsorbent. This implies that the temperature utilised to estimate the rate of the reforming reactions will be higher as discussed in **Chapter 6**, hence the higher conversion of methane and hydrogen purity.

Similarly to the mass flux, the selected operating temperature should be a trade-off between the performance of the reactor and the CAPEX and OPEX. It is clear that increasing the temperature renders a better case scenario from the performance standpoint, however, the feasibility of operating at such temperature levels should be investigated to understand the potential of the reactor concept to efficiently integrate heat and reduce the heat imports required to condition the reactor and feedstock the desired levels. For the remainder of the simulating work

of the Fuel Reactor in this project the highest combination of temperatures (i.e. 969 K / 969 K for gas inlet/bed) will be considered.

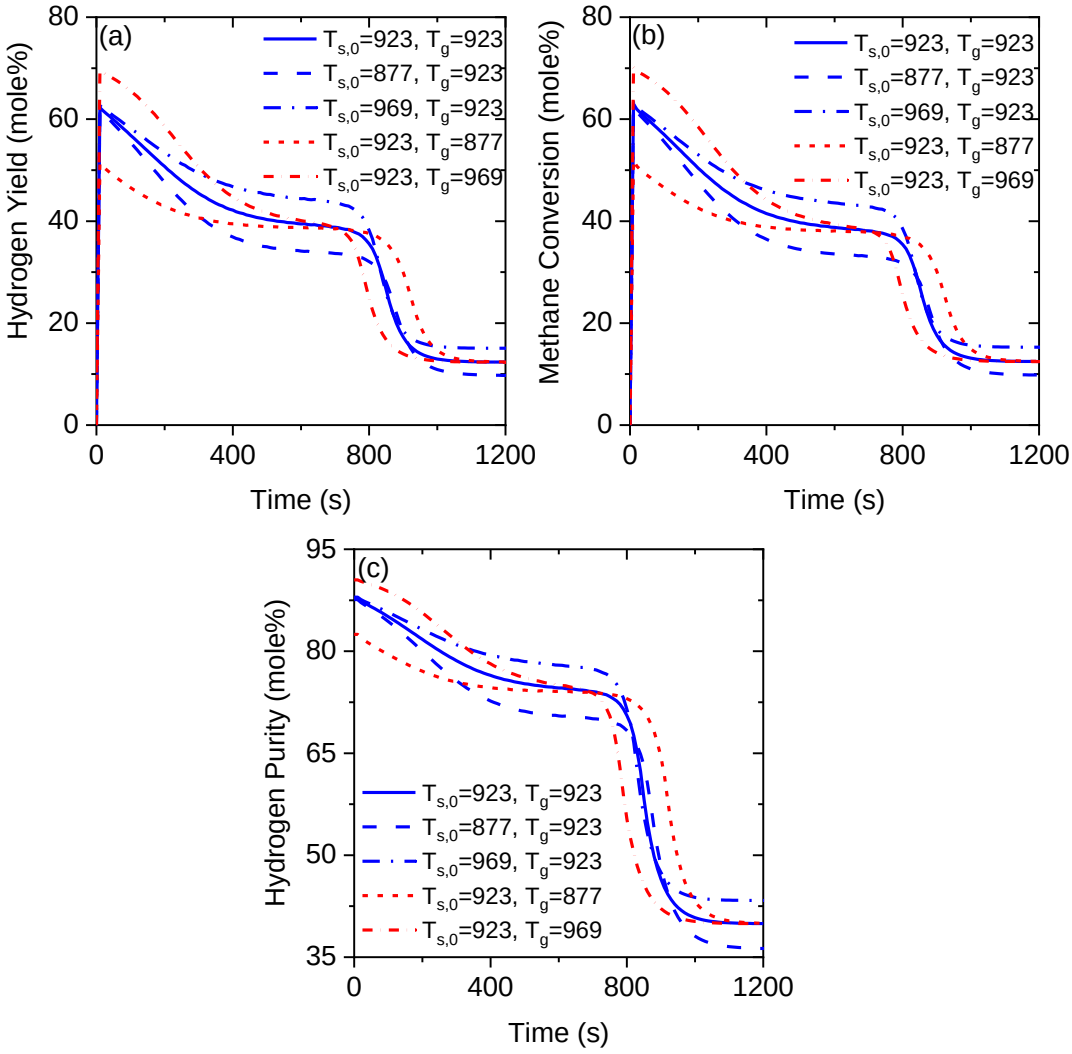

Figure 7.26 Effect of the variation of the gas inlet temperature or the initial bed temperature by ±5% on the reactor performance indicators. (a) Hydrogen yield, (b) Methane conversion, (c) Hydrogen purity (free of nitrogen).

Table 7.7 Average performance of the reactor for various combinations of gas inlet temperature and packing initial temperature.

Gas inlet temp. (K)	Bed initial temp. (K)	H_2 purity (mole%)	CH_4 conversion (mole%)	H_2 yield (mole%)	H_2 productivity (kg x 10^{-3})
923	877	75.7	40.6	41.0	1429.5
923	923	78.3	45.1	45.6	1447.0
923	969	80.7	49.9	50.2	1451.5
877	923	75.3	41.0	41.3	1371.0
969	923	80.8	48.9	49.5	1495.2

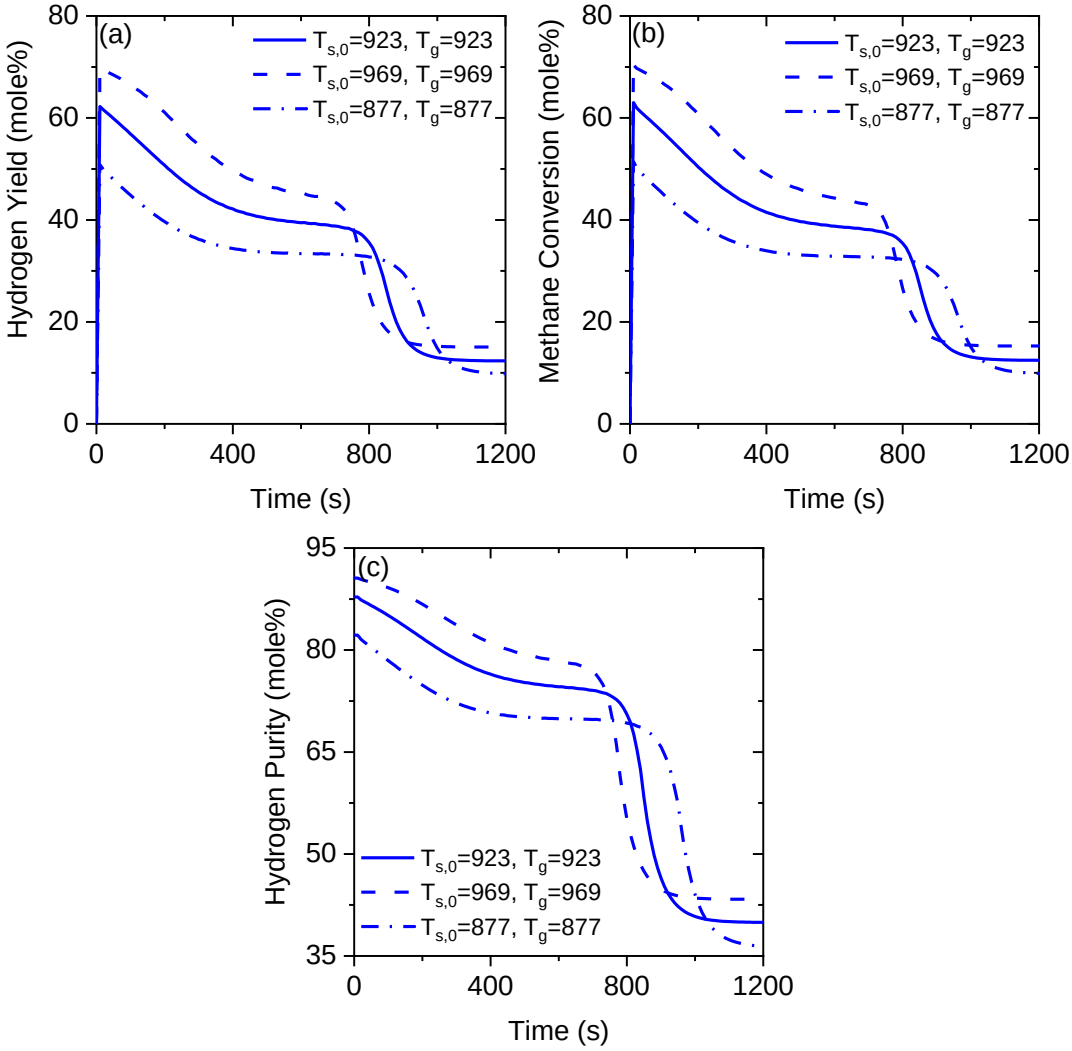

Figure 7.27 Effect of the variation of the gas inlet temperature and the initial bed temperature by ±5% at the same time on the reactor performance indicators. (a) Hydrogen yield, (b) Methane conversion, (c) Hydrogen purity (free of nitrogen).

Table 7.8 Average performance of the reactor for various conditions of equal gas inlet temperature and packing initial temperature.

Gas inlet temp. (K)	Bed initial temp. (K)	H_2 purity (mole%)	CH_4 conversion (mole%)	H_2 yield (mole%)	H_2 productivity (kg x 10^{-3})
877	877	72.3	36.3	36.7	1357.8
923	923	78.3	45.1	45.6	1447.0
969	969	83.1	53.7	54.2	1499.5

7.6.2.4 Inlet gas composition

The composition of unconventional gas varies as a function of the source [12]. Typically, the natural gas transported by pipeline from the production sites should comply with a certain specification of specific gravity and higher heating value, among others properties. However, if the gas streams were processed close to the production sites, then the composition might impact the final performance of the Fuel Reactor.

Figure 7.28 presents plots of the reactor performance indices for three samples of gas with different composition at the inlet of the Fuel Reactor. The composition of the Fuel Reactor feedstock was calculated in Aspen Plus™ by simulating the adiabatic pre-reforming of the three gas samples assuming an operating temperature of 723 K which is within the range of typical operating conditions of pre-reformers as indicated in [21]. The gas UG1 corresponds to the base case and is a feedstock produced from a sample of gas with a steam-to-carbon ratio of 3. The UG2 feedstock corresponds to a sample of gas with a nitrogen content of 29%, pre-reformed with a S/C ratio of 3, and the UG3 corresponds to a sample of gas with 14.2 vol% of C_2+ components pre-reformed with a S/C ratio of 4. The compositions of the feedstocks to the Fuel Reactor are summarised in Table 7.10.

Table 7.9 Composition of samples of gas fed utilised to study the effect of feedstock on the Fuel Reactor performance.

Component	UG1 (mole%)	UG2 (mole%)	UG3 (mole%)
CH_4	21.82	19.82	17.69
H_2O	67.77	64.40	75.04
H_2	4.94	4.61	5.14
CO	0.01	0.02	0.01
CO_2	1.77	2.72	2.07
N_2	3.69	8.43	0.05
HHV (MJ m^{-3})[2]	27.4	22.6	29.3

The nature of the feedstock has a slight impact on the duration of the Fuel Reactor step, but a significant effect on the performance indices; particularly when the S/C ratio is increased from 3 to 4. The benefits of increasing the S/C ratio have already been discussed in **Chapter 3**, and were reported by Abbas et al. [68], and are related to the increased partial pressure of steam in the reactor, which favours the production of H_2.

Regarding the UG2 feedstock, there could be a combination of factors that favours the reforming reactions. Firstly, the initial lower content of H_2 is beneficial to move the equilibrium towards the production of syngas. Secondly, the higher content of CO_2 in the feedstock increases the initial rate of carbonation and as a cascade effect the temperature of the system. Figure 7.29 illustrates the rate of reaction of carbonation for the three cases at 50% of the time required to saturate the adsorbent, where the higher rate corresponds to the system processing the gas UG2. As a result the temperature of the system, particularly that of the catalyst is increased as shown in Figure 7.30. It is worth noting how for the gas UG2 the thermal front is wider than for the gases UG1 and UG3, thus heating up a larger portion of the catalyst in the bed and enhancing the rate constants of the reforming reaction.

[2] Values of HHV obtained considering a composition free of water.

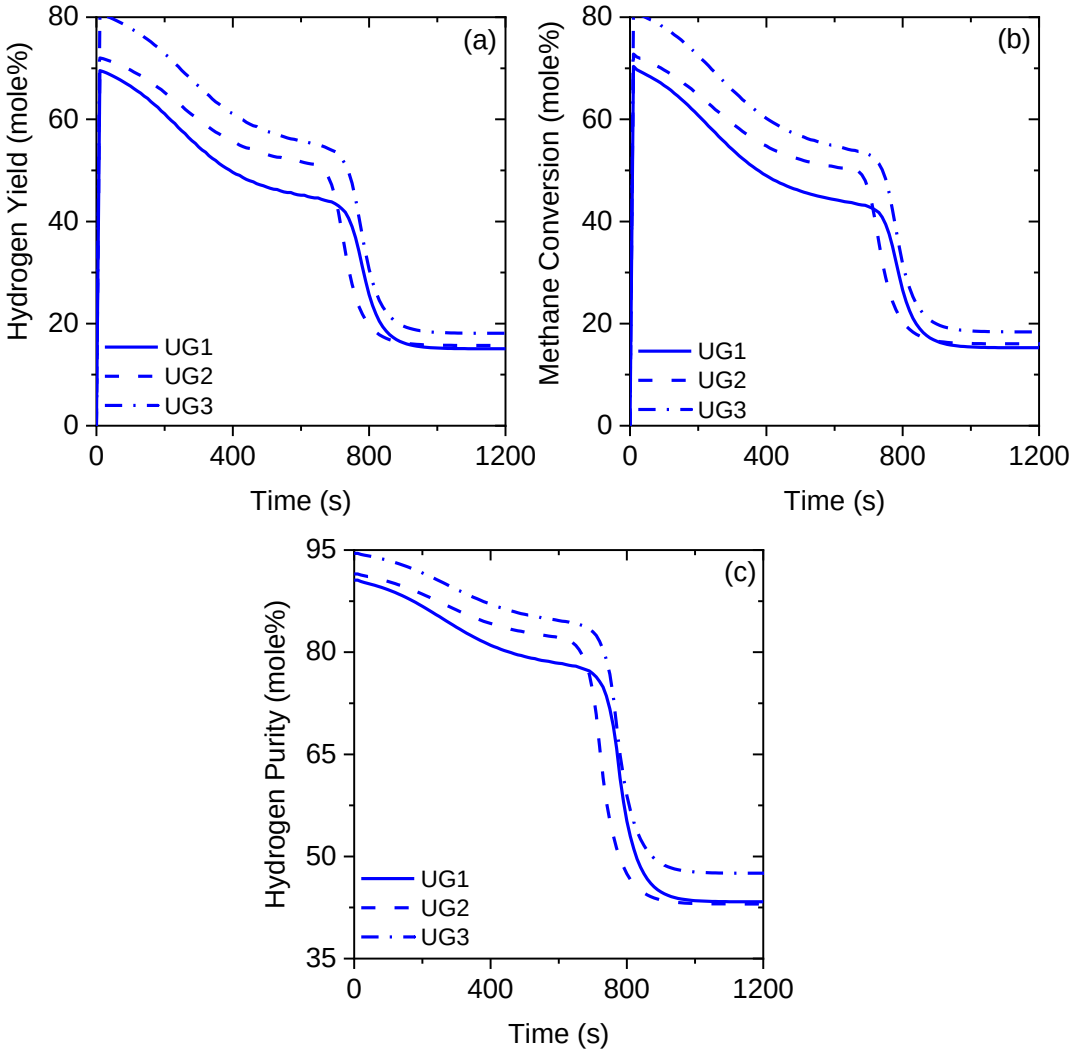

Figure 7.28 Effect of the gas composition on the reactor performance indicators. (a) Hydrogen yield, (b) Methane conversion, (c) Hydrogen purity (free of nitrogen).

Table 7.10 Average performance indicators for various Fuel Reactor feedstock compositions.

Feedstock	H_2 purity (mole%)	CH_4 conversion (mole%)	H_2 yield (mole%)	H_2 productivity (kg x 10^{-3})
UG1	83.1	53.7	54.2	1357.8
UG2	86.1	59.4	60.0	1447.0
UG3	88.6	64.8	65.4	1499.5

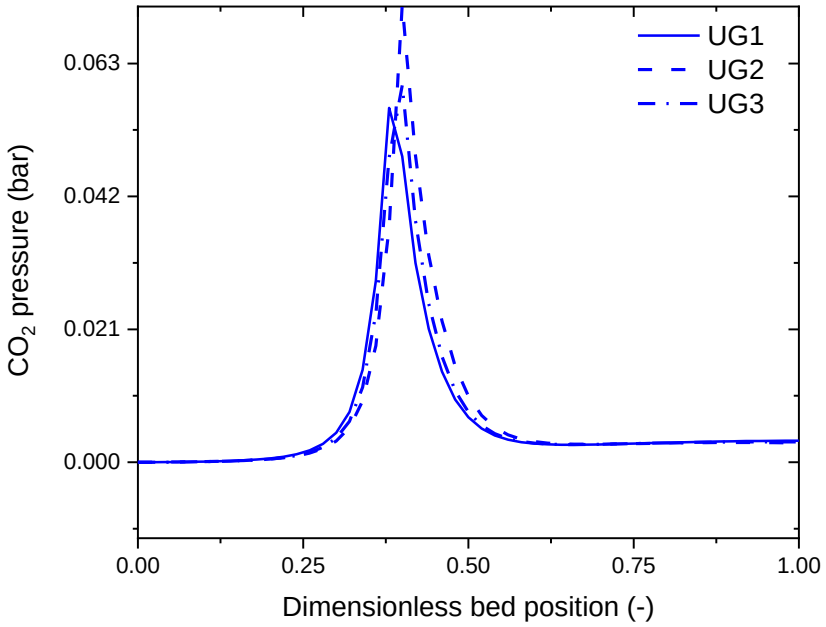

Figure 7.29 Rate of carbonation at 50% of the adsorbent saturation time for the three simulated feedstocks.

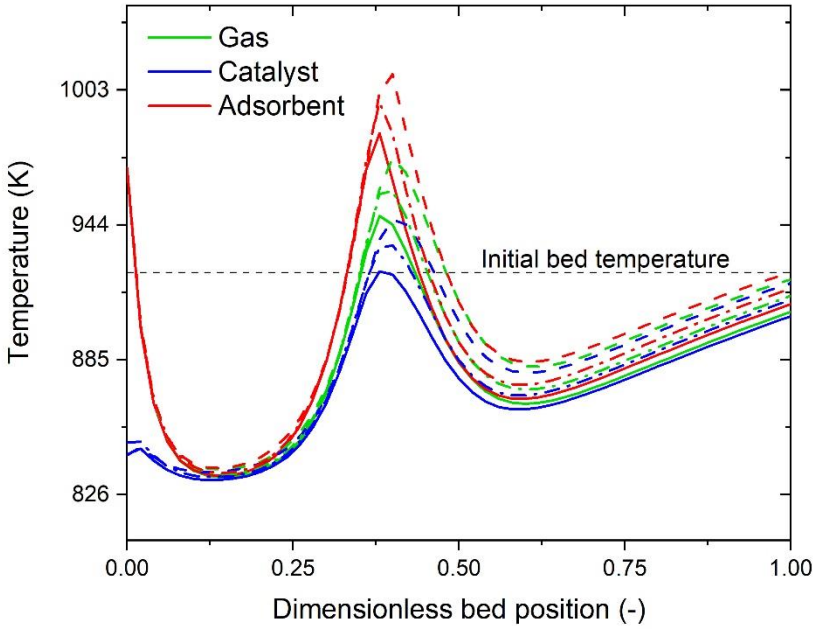

Figure 7.30 Temperature profile of the gas, catalyst and adsorbent at 50% of the adsorbent saturation time for the three simulated feedstocks.

7.6.2.5 Density and heat capacity of the adsorbent and catalyst

As expressed in Equations (7.22) – (7.24), the density and heat capacity of the packing materials effect the velocity of the reaction and thermal fronts, therefore

in this section the response of the reactor to the variation of the density and heat capacity of the adsorbent and the catalyst is analysed.

The effect of the adsorbent density on the temperature is illustrated in Figure 7.31. By increasing the adsorbent density by 10% the temperature of the adsorbent decreases and so the temperatures of the bulk and the catalyst. Conversely, a decrease of the density by 10% implies an increase of the temperature of the adsorbent, catalyst and bulk. A higher adsorbent density implies that the heat capacity of the material per unit of volume will be higher and therefore a higher amount of heat of adsorption is required to elevate the temperature of this material. Moreover, the rate of heat exchange between the material and the bulk depends upon the value of ratio $\frac{\alpha_2 a_{S_2}}{\rho_{b_2} C_{p_2}}$, thus a reduction of this ratio leads to a slower rate of heat transfer with the bulk gas, and consequently a poor transfer of heat from the adsorbent to the catalyst.

A less significant effect is observed in the profile of the concentration of CO_2 in the bulk, catalyst and adsorbent as shown in Figure 7.32, however, a similar trend is observed. This is a consequence of the system temperature since a higher temperature at the catalyst surface will enhance the rate of reaction of reforming, thus the CO_2 concentration will increase, meaning an improved rate of either the water-gas shift reaction, the complete reforming reaction or both. In turn these higher concentrations of CO_2 increase the partial pressure of the adsorbate at the adsorbent surface and enhances the rate of carbonation, leading to the release of a higher amount of heat of adsorption available to heat up the reactor packing.

As expected the higher temperature of the system influences other variables such as the gas velocity and the gas pressure, as illustrated in Figure 7.33 and Figure 7.34, respectively. Since a less dense adsorbent promotes the heat transfer from the adsorbent to the bulk gas, it follows that the bulk density decreases, and the volume of gases flowing through the interstices builds up leading to a higher velocity. In fact, Figure 7.33 shows that the highest velocity corresponds to the situation where the adsorbent density is reduced by 10%. Hence a highest pressure drop in the system is observed. Nevertheless, the low gas velocity allows that the system operates with a pressure drop of 0.0059 bar m^{-1} representing only 0.02% of the reactor inlet pressure; this pressure drop is just slightly higher than that estimated for the base case scenario (0.0057 bar m^{-1}).

The enhancement of the heat and mass transfer when operating the reactor with an adsorbent packing of lower density is reflected in the reactor performance indicators in Figure 7.35. The effect of varying the initial density of the adsorbent is similar to that discussed in section 7.6.1 regarding the change of adsorbent porosity, whose effect for all what is worth is a change in the bulk density of the

adsorbent. Figure 7.35 shows that the effect of increasing the adsorbent density is a slight decrease of the indicators during the pre-breakthrough zone and the enlargement of this period. Conversely, a decrease of 10% of the adsorbent density leads to a slightly increase of the pre-breakthrough zone, accompanied by a shorter pre-breakthrough period. The average values of the performance indicators of the Fuel Reactor are summarised in Table 7.11; the stream with the highest H_2 purity is obtained in the case of the lowest initial adsorbent density; the same trend is observed for the CH_4 conversion and the H_2 yield. However, since for this case the duration of the pre-breakthrough is 15.7% shorter with respect to the base case, the productivity of this hypothetical bed will be reduced by 11.8%, which will affect the number and size of the reactors for a given throughput.

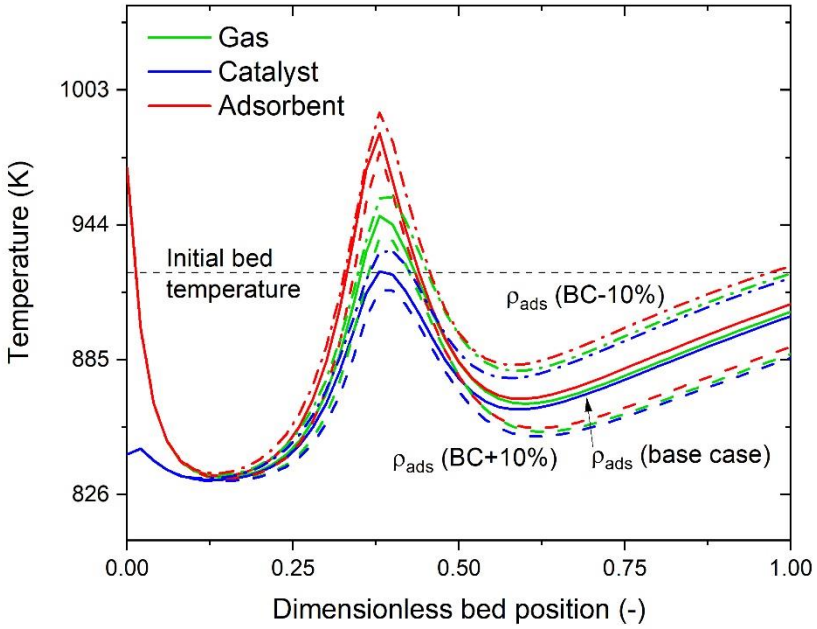

Figure 7.31 Effect of the variation of ±10% of the adsorbent density on the temperature profile of the gas, catalyst and adsorbent at 50% of the adsorbent saturation time.

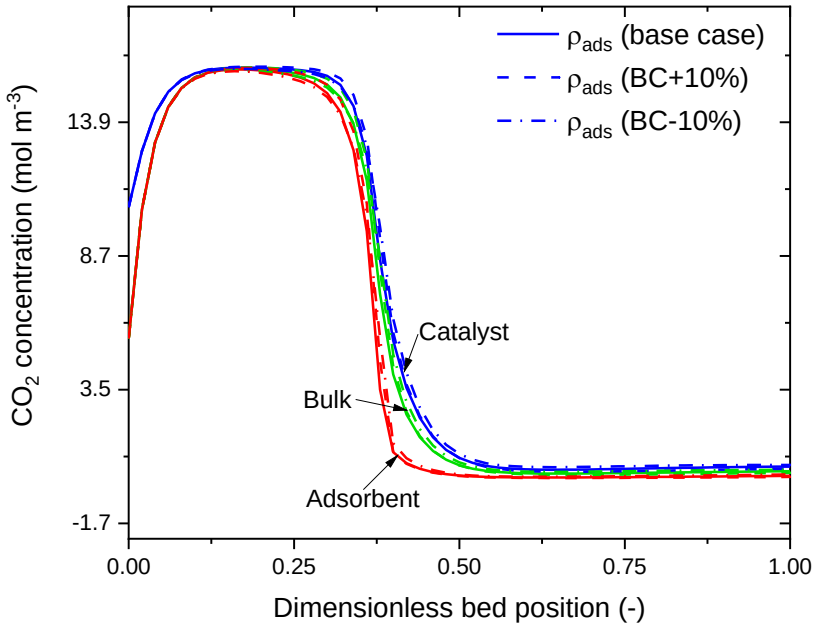

Figure 7.32 Effect of the variation of ±10% of the adsorbent density on the concentration profile of CO2 in the gas, catalyst and adsorbent at 50% of the adsorbent saturation time.

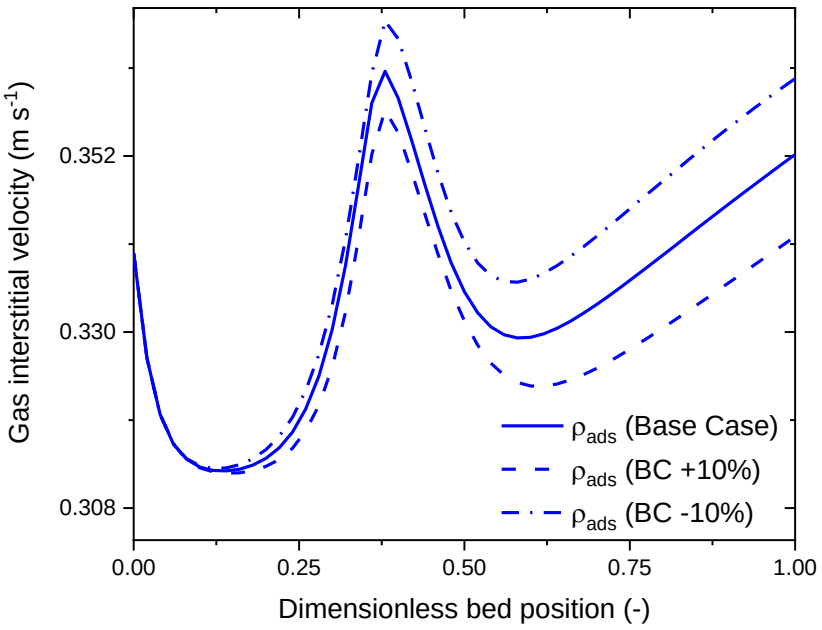

Figure 7.33 Effect of the variation of ±10% of the adsorbent density on the gas interstitial velocity at 50% of the adsorbent saturation time.

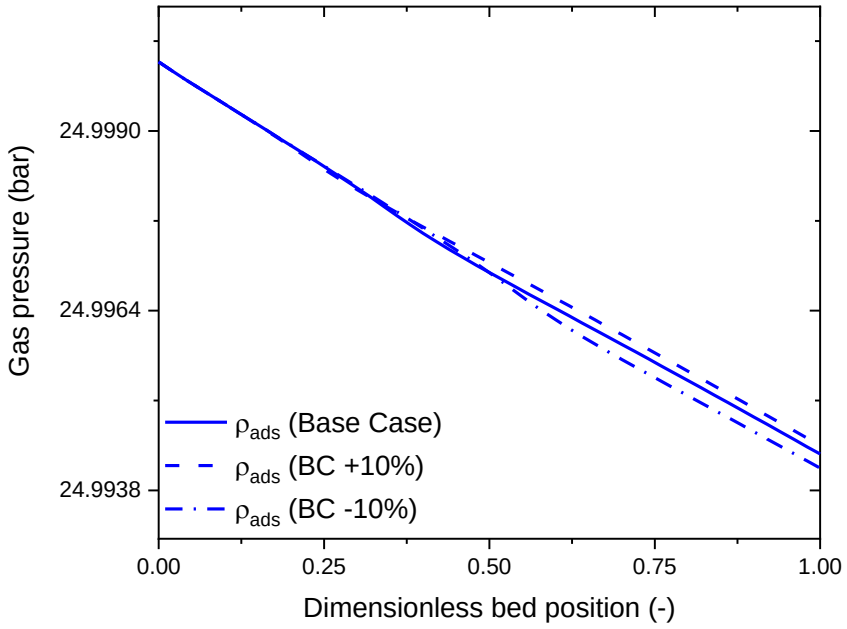

Figure 7.34 Effect of the variation of ±10% of the adsorbent density on the gas pressure at 50% of the adsorbent saturation time.

Table 7.11 Average performance of the Fuel Reactor for various values of initial adsorbent density.

Case	H_2 purity (mole%)	CH_4 conversion (mole%)	H_2 yield (mole%)	H_2 productivity (kg x 10^{-3})
ρ_{ads} – 10%	84.5	56.4	56.9	1332.0
ρ_{ads}, cat	83.1	53.7	54.2	1510.3
ρ_{ads} + 10%	81.7	51.2	51.6	1706.0

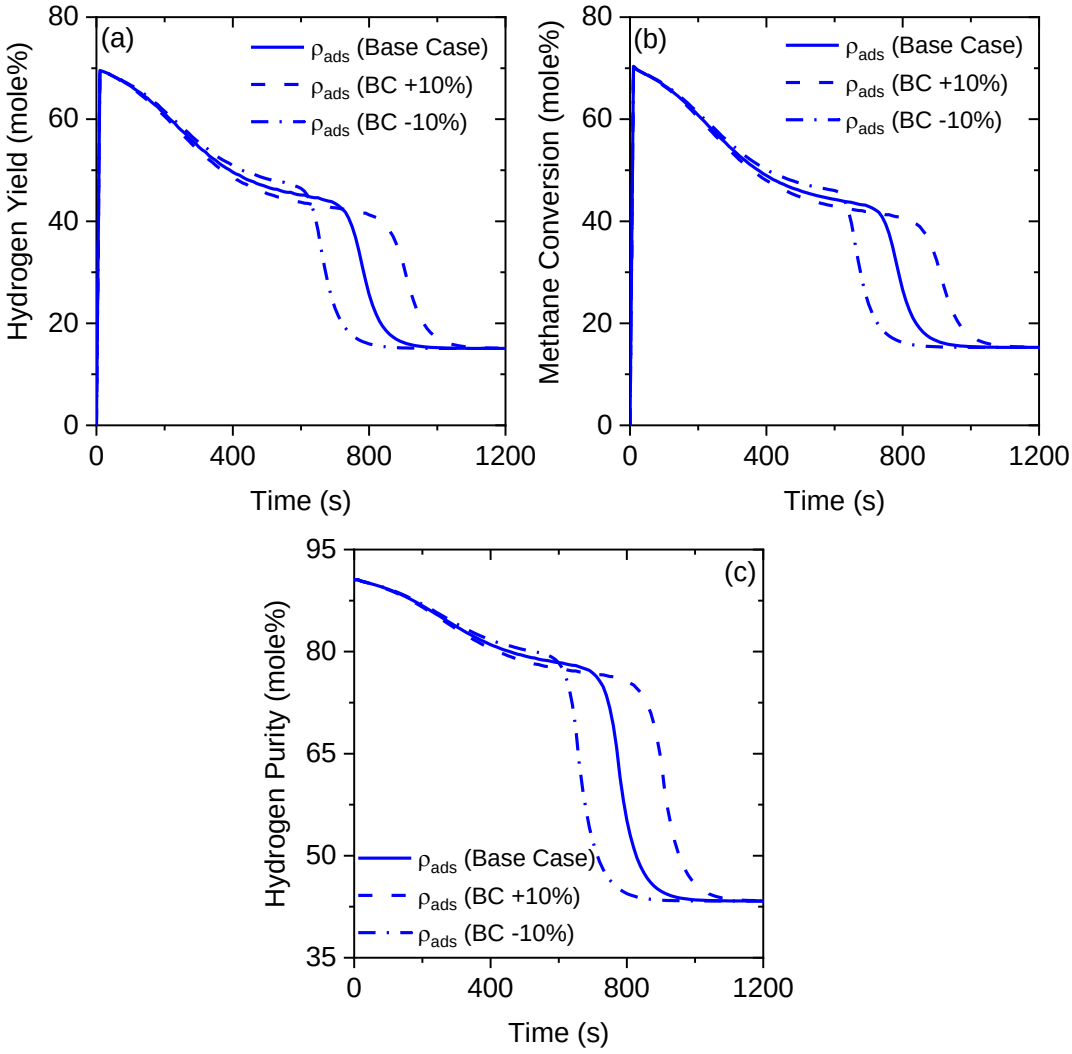

Figure 7.35 Effect of the adsorbent density on the reactor performance indicators. (a) Hydrogen yield, (b) Methane conversion, (c) Hydrogen purity (free of nitrogen).

The adsorbent heat capacity effects the performance of the system in a similar fashion but to a lesser extent than the adsorbent initial density. Plots of temperature are illustrated in Figure 7.36. Evidently, a smaller value of heat capacity reduces the volumetric heat capacity allowing the adsorbent to utilise a lower amount of the heat of adsorption to increase its temperature. This is the same effect as discussed above for the density.

The effect of varying the adsorbent heat capacity on the concentration of CO_2 in the bulk gas, catalyst and adsorbent is less significant than that of density and is illustrated in Figure 7.37. Similar trends are obtained for the gas velocity and pressure, however, the effect of heat capacity on these variables is less pronounced than the effect of the adsorbent density, a sample of the profiles is presented in Figure 7.38 and Figure 7.39.

Finally, the effect of varying the adsorbent heat capacity on the reactor performance is illustrated in Figure 7.40, and the average values of the indicators is summarised in Table 7.12. It can be seen that the trends are the same as with the variation of the adsorbent density, with the only difference of lower magnitudes. A heat capacity variation of -10% renders a stream with an average H_2 purity of up to 84.1% which could benefit the design of the purification stage. However, as with the adsorbent initial density, a lower adsorbent heat capacity results in a shorter cycle and reactor productivity.

Simulations were ran under the same premises of varying the density and heat capacity of the catalyst by ±10%. No significant effect over the reactor performance is observed. Figure 7.41 and Figure 7.42 illustrate the output of these simulations; Table 7.13 and Table 7.14 summarise the average values of the indicators. Evidently, the effect of varying the properties of this packing changes the output very little. However, the trend observed is opposed to that of varying the adsorbent properties. Interestingly, increasing the catalyst density or heat capacity render the best case scenario for the reactor performance, which is the opposite effect of that obtained with the adsorbent properties. Following the same reasoning than for the adsorbent, by augmenting the volumetric heat capacity of the material (i.e. the product $\rho_{b_1} C_{p_1}$) the amount of heat dissipated needed to cool down the catalyst is higher, thus the material could be capable of maintaining its energy for longer, enhancing the rate of reaction of reforming.

The properties of these materials can be manipulated by selecting suitable supports and by optimising the load of active phase on the material. This has been the subject of several investigations aiming to enhance the mechanical properties of CaO-based adsorbents [43-46, 128, 198] and oxygen carriers to allow multicyclic operation with minimal loss of activity. Nevertheless, the results presented here suggest that the design of the packings should aim also towards the optimisation of their thermal properties to increase the feasibility of this reactor concept.

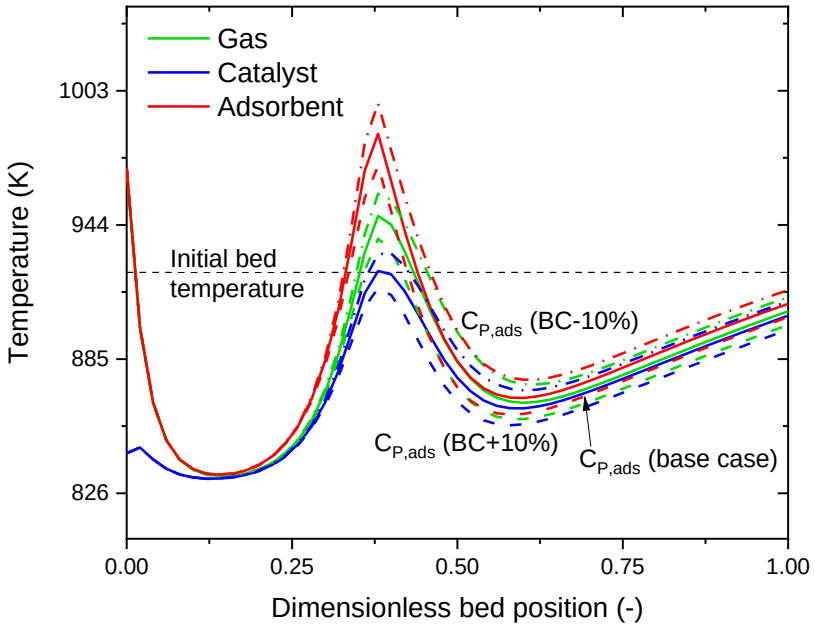

Figure 7.36 Effect of the variation of ±10% of the adsorbent heat capacity on the temperature profile of the gas, catalyst and adsorbent at 50% of the adsorbent saturation time.

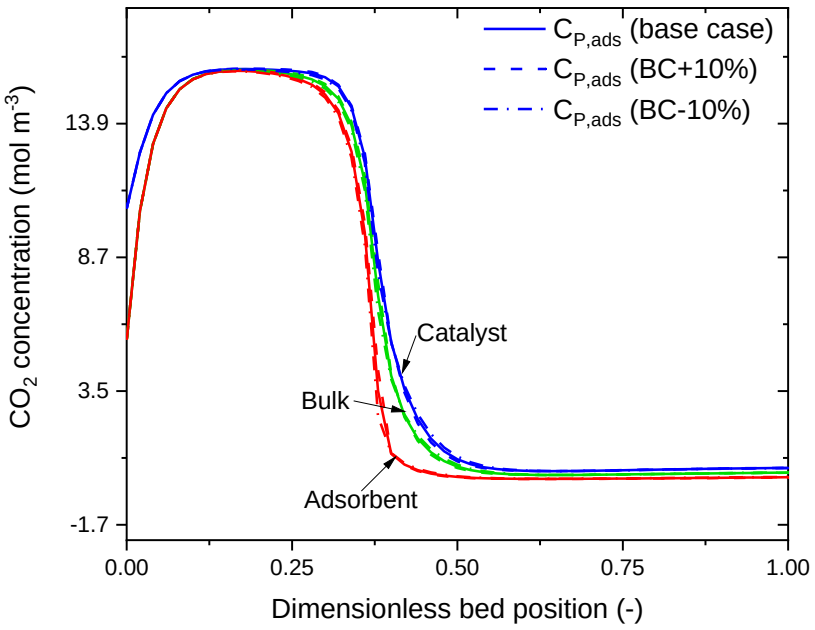

Figure 7.37 Effect of the variation of ±10% of the adsorbent heat capacity on the concentration profile of CO_2 in the gas, catalyst and adsorbent at 50% of the adsorbent saturation time.

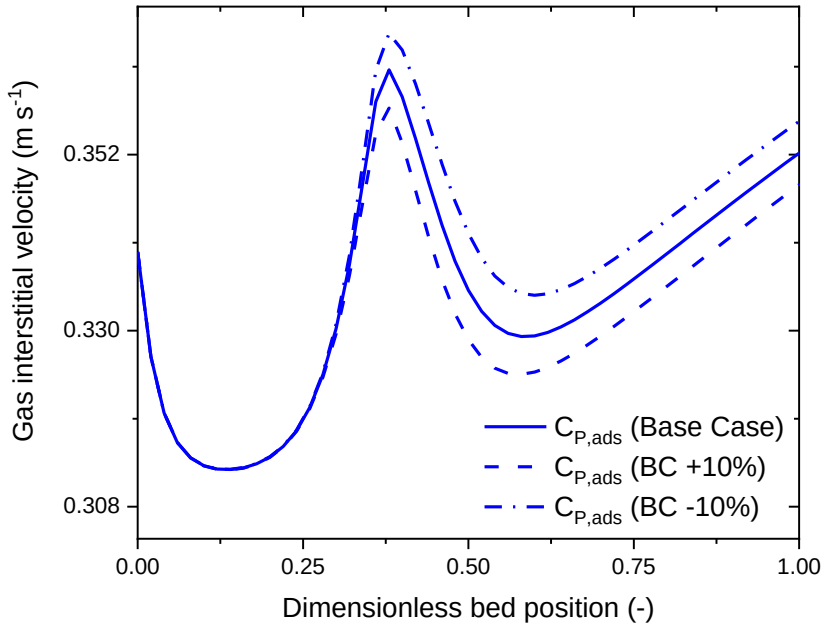

Figure 7.38 Effect of the variation of ±10% of the adsorbent heat capacity on the gas interstitial velocity at 50% of the adsorbent saturation time.

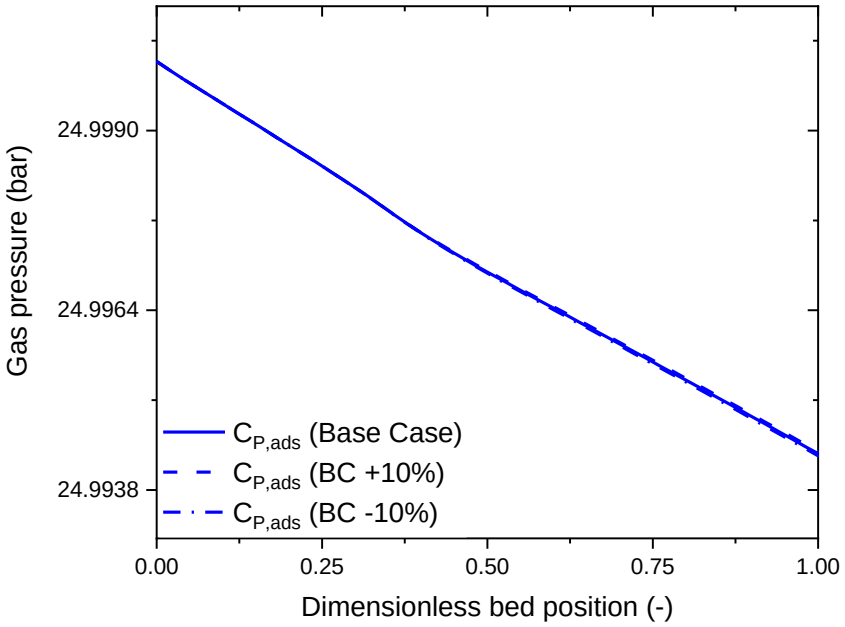

Figure 7.39 Effect of the variation of ±10% of the adsorbent heat capacity on the gas pressure at 50% of the adsorbent saturation time.

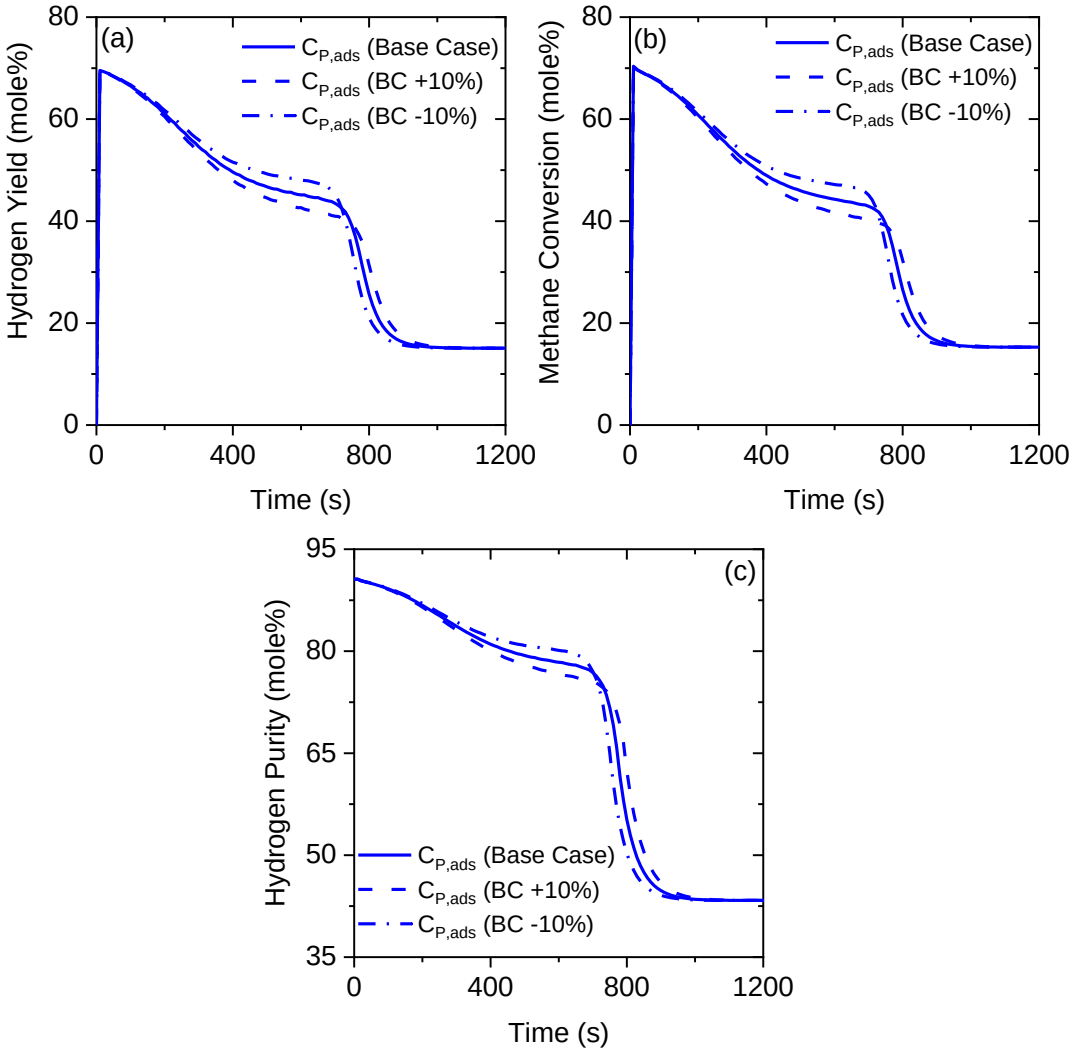

Figure 7.40Effect of the adsorbent heat capacity on the reactor performance indicators. (a) Hydrogen yield, (b) Methane conversion, (c) Hydrogen purity (free of nitrogen).

Table 7.12 Average performance of the Fuel Reactor for various values of initial adsorbent heat capacity.

Case	H_2 purity (mole%)	CH_4 conversion (mole%)	H_2 yield (mole%)	H_2 productivity (kg x 10^{-3})
$C_{P,\,ads}$ – 10%	84.1	55.5	56.0	1508.7
$C_{P,\,ads}$	83.1	53.7	54.2	1510.3
$C_{P,\,ads}$ + 10%	82.1	52.0	52.4	1511.4

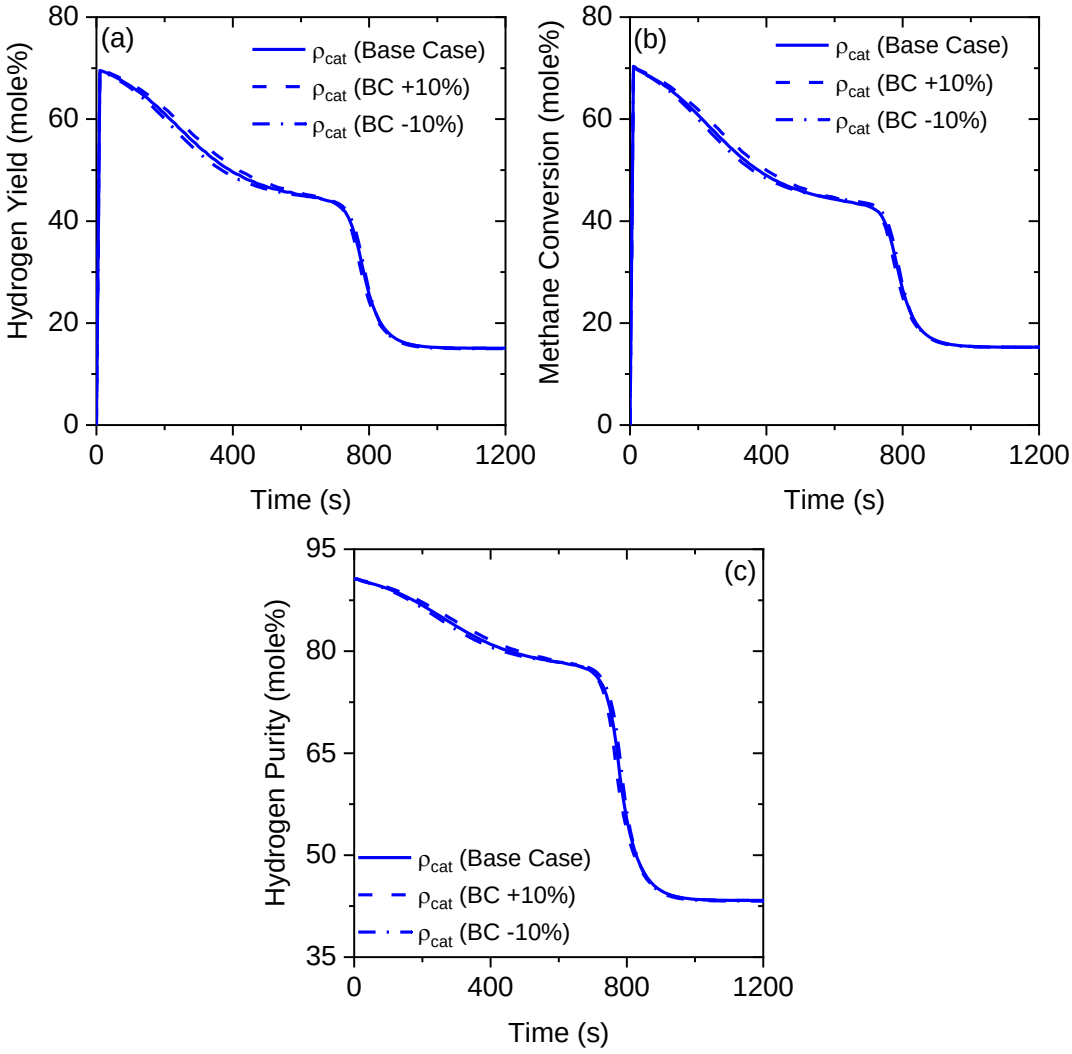

Figure 7.41 Effect of the catalyst density on the reactor performance indicators. (a) Hydrogen yield, (b) Methane conversion, (c) Hydrogen purity (free of nitrogen).

Table 7.13 Average performance of the Fuel Reactor for various values of catalyst density.

Case	H_2 purity (mole%)	CH_4 conversion (mole%)	H_2 yield (mole%)	H_2 productivity (kg x 10^{-3})
ρ_{cat} – 10%	82.8	53.2	53.4	1511.7
ρ_{cat}, cat	83.1	53.7	54.2	1510.3
ρ_{cat} + 10%	83.5	54.6	55.0	1512.9

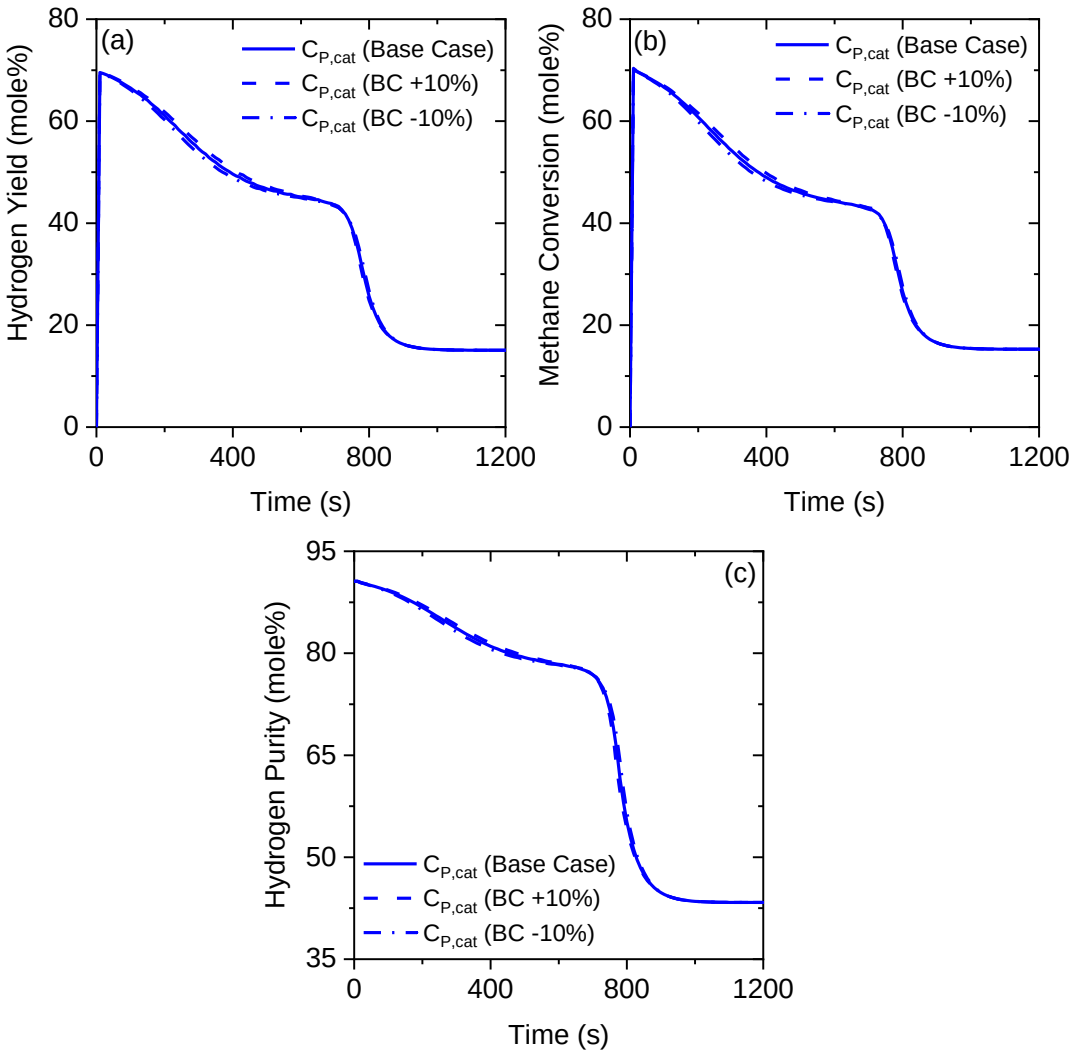

Figure 7.42 Effect of the catalyst heat capacity on the reactor performance indicators. (a) Hydrogen yield, (b) Methane conversion, (c) Hydrogen purity (free of nitrogen).

Table 7.14 Average performance of the Fuel Reactor for various values of catalyst heat capacity.

Case	H_2 purity (mole%)	CH_4 conversion (mole%)	H_2 yield (mole%)	H_2 productivity (kg x 10^{-3})
$C_{P,\,cat}$ – 10%	82.7	53.0	53.5	1511.5
$C_{P,\,cat}$	83.1	53.7	54.2	1510.3
$C_{P,\,cat}$ + 10%	83.3	54.2	54.7	1520.3

7.7 Concluding remarks

In this chapter, the transient model of the Fuel Reactor was modified to include in the mathematical description of the variation of the adsorbent's porosity, density and heat capacity. The development of this feature considered a case to assess the effect of including the variation of the porosity only, and another considering the variation of the three variables altogether. Both developments allow the heterogeneous model presented in Chapter 6 (HTG-2P-PF) to fit the experimental breakthrough curves of H_2, reducing the errors reported in the previous chapter from 5.91% at 5 bar down to 2.17% when considering only the variation of porosity, and down to 2.03% when considering also the variation of the adsorbent density and heat capacity.

Based on the aforementioned results, the heterogeneous model accounting for porosity only (model HTG-2P-PFP) was applied to run a sensitivity analysis of the main parameters affecting the performance of the fuel reactor at 25 bar, such a pressure was selected based on the results of the thermodynamic analysis presented in Chapter 2. It was found that the best case scenario is obtained with the following parameters: volumetric fraction of catalyst of 0.5 m^3m^{-3}, with packings whose surface area corresponds to that of spherical packings of 5 mm of diameter and operating the reactor at the lowest possible gas superficial velocity, in the particular cases analysed in this investigation a velocity of 0.12 m s^{-1} was selected. Regarding the temperature the best case scenario was obtained when setting the gas inlet temperature to 923K and the bed initial temperature to 969 K.

The incorporation of the adsorbent structural changes into the mathematical model proved to be important to adjust the simulated output to the experimental data. The effectiveness factor values that gave the better fit are in agreement with those values suggested in previous studies for systems with packing sizes of similar order to those utilised in the validation of the model in this work ranging from 0.49 to 0.80. When considering the full description of the variation of the adsorbent's properties the apparition of the breakthrough zone is delayed, thus requiring smaller values of the effectiveness factor to fit the experimental breakthrough curve in comparison to the case of considering only the variation of the adsorbent porosity. However, the simulation output of both approaches can be fitted to the same practical solution.

Conversely, not accounting for the structural changes leads to simulation outputs that could have implications in the final design of the reactor. The saturation time is an important variable that needs to be estimated accurately as it will define the duration of the Fuel Reactor step, and ultimately the design of the complete

operation, including the regeneration step (air reactor mode), and any other times required to set up the reactor to the required levels of pressure and temperature to perform the operation efficiently. Moreover, it has implications in the definition of the length of the reactor bed and the fraction of adsorbent to be contained in the system. Therefore, utilising the basic model would likely give an oversized system.

Mathematically, the addition of the equations representing the variation of the adsorbent porosity, density and heat capacity, did not create problems for the integrator within the range of simulated conditions. However, a significantly higher simulation time is needed to solve the rigorous model for the adsorbent in comparison to the base model presented in **Chapter 6** (3.2 times when considering the variation of porosity only, and 3.7 times when considering all the variations). The percentage change of the adsorbent density and heat capacity was 16.42% and 16.45% respectively, whilst the variation of their product was only ca. 2.61%; these variations change the response of the model for a fixed value of effectiveness factor; however, there is uncertainty in the correct value of this parameter and therefore it is advisable to further develop the model to account explicitly for the mass transfer resistances in both the catalyst and the adsorbent, and study the effect of the reduction of the adsorbent porosity, pore size and the product layer diffusivity on the reactor model response.

The Fuel Reactor model with porosity variation was utilised to investigate the effect of operating and structural parameters over the performance of the Fuel Reactor. Regarding the operating parameters, the study investigated the effect of the mass flux, temperature and gas composition. It was found that the reactor should be operated at the lowest feasible throughput so that the total number of reactors required to meet the plant capacity whilst maintaining continuous operation results in an optimum CAPEX and OPEX. Regarding the temperature, the best case scenario of performance of the reactor is obtained when the both the bulk and the packing are set at the same temperature level. The reactor performance is improved by increasing the temperature, but care should be taken to avoid reaching temperatures that would promote the calcination of the adsorbent as this would be detrimental for the operation. Finally, the variations on the gas composition will lead to different reactor performance but no particular trend was identified other than the fact that a higher steam content in the feedstock improves the reactor performance. However, the benefits of operating at high S/C ratios should be analysed with an economic perspective on top of the technical analysis.

Regarding the structural parameters of the system, the analysis of the available surface area of the catalyst and the adsorbent in the packing bed indicates that

in order to improve the utilisation of the heat of adsorption by the steam reforming reactions, the surface area of both materials should be maximised. Thus it is advisable to look at the design of packing shapes that provide surface areas equivalent to those of the smallest spheres. In this work the packings were considered to be spherical and the sensitivity of the diameter of the packing revealed that the approach of the catalyst temperature to the adsorbent temperature is enhanced as the diameter is reduced. The use of foams as supports for steam reforming catalyst is an enticing alternative due to their better mass and heat transfer properties which result from their very high specific surface area [199, 200].

In addition, it was demonstrated that the physical properties of the materials affect the final performance of the reactor. Some enhancement was obtained in particular when the density and heat capacity of the adsorbent were set below the values of those of unsupported calcium oxide, which suggest that the investigation on the synthesis of adsorbents should look also at the selection and investigation of supports that, when mixed with calcium oxide, render a material whose physical properties are below those of the active phase. However, the performance of this material should be analysed in the context of the air reactor since during the material regeneration catalyst and adsorbent swap functions, and a material with certain properties working in the Fuel Reactor mode might be detrimental for the performance of the reactor during the regeneration step.

Chapter 8 Modelling, validation, and sensitivity study of the Air Reactor

8.1 Introduction

This chapter presents the development and application of the mathematical model that represents the Air Reactor cycle the Sorption-Enhanced Chemical-Looping Steam Reforming process. A heterogeneous plug flow model is developed here for air as the oxidant agent for the regeneration of the reactor packing materials (catalyst and adsorbent). It is to be used to investigate the effect of the operating conditions during the air cycle of the process over the reoxidation of the oxygen transfer material and the calcination of the CaO-based adsorbent.

The chapter is structured in seven sections considering this Introduction. In section 8.2 the details of the Air Reactor model proposed in this work, along with the closure relationships are presented. Section 8.3 refers to the methodology of integration of the model and the measures taken to ensure convergence of the solution. The detail of the experiments and experimental data utilised validate the Air Reactor model are presented in section 8.4. The results of model validation and its application analyse the sensitivity of the reactor performance to various operating parameters are discussed in section 8.5. Finally, a summary of the conclusions of the investigations described in this chapter is provided in section 8.6.

8.2 Model development

The Air Reactor cycle follows after the fuel reactor cycle studied in **Chapter 6** and **Chapter 7**. When the fuel reactor cycle is completed, the reactor operating mode switches to the air feed to regenerate the adsorbent, Figure 8.1 is a scheme of the physical phenomena occurring during the Air Reactor mode. In the Air Reactor, an oxidant agent (e.g. air) enters the packed bed and the oxygen reacts with the oxygen transfer material (nickel) contained in the catalyst, releasing heat of oxidation which is transferred to the bulk and carried towards the adsorbent, where it is utilised to decompose (regenerate) the $CaCO_3$ into CaO and CO_2. The transport of oxygen from the bulk gas to the nickel surface is by convection to the catalyst surface, and by diffusion from the catalyst surface to the reactive sites. This is a non-catalytic process and results in the mass of oxygen in the bulk being depleted during the time period required to complete the conversion of nickel to nickel oxide. Simultaneously, the adsorbent is indirectly heated-up using the heat

of reaction of oxidation of nickel. The increase of temperature of the adsorbent promotes the desorption of CO_2, thus adding mass to bulk.

Based on the previous description, the model will consider an axial flow reactor of cylindrical shape as shown in Figure 8.2, packed with a mixture of catalyst and the adsorbent and will account for the mass and heat transport individually for each phase present in the reactor. Therefore, the following set of modelling assumptions are proposed:

a) The system is adiabatic and well insulated, moreover the reactor diameter-to-particle diameter ratio is held above 30, hence no radial thermal gradients are developed.
b) The velocity profile is deemed flat and therefore, no radial velocity or concentration gradients are accounted for.
c) The basic model is deemed as an ideal plug flow, however the impact of the axial dispersion term in the representation of experimental data will be assessed.
d) No intrapellet transport resistances are considered, intra-conductivity is represented by an effective heat transfer.
e) The base case considers only the reaction of oxygen with nickel in the catalyst and the decomposition of the adsorbent in calcium oxide and carbon dioxide.
f) Catalyst and adsorbent particles are deemed spherical. Where simulations are run with different shapes, an equivalent diameter is used.
g) A mean bed voidage is considered throughout the reactor.
h) The volumetric fraction of each material in the reactor is deemed constant throughout the length regardless of the packing being structured or unstructured.

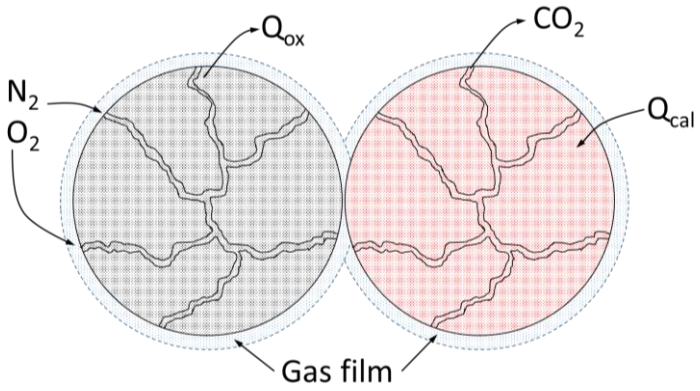

Figure 8.1 Scheme of the physical interaction between the adsorbent and the catalyst during Air Reactor mode.

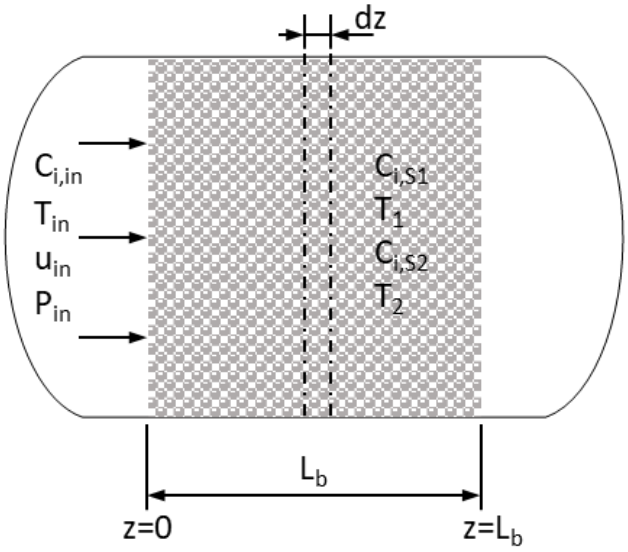

Figure 8.2 Scheme of the fixed bed reactor indicating the domain of interest for the deployment of the model equations, the boundary conditions and the initial conditions of the packed bed

8.2.1 Model equations

8.2.1.1 Heterogeneous plug flow model

The Air Reactor base model is essentially the same as the Fuel Reactor base model, hence for $t > 0$ and $0 < z \leq L_b$ the species balance is represented as:

$$\varepsilon_b \frac{\partial C_i}{\partial t} + \varepsilon_b \frac{\partial (u_i C_i)}{\partial z} = -\beta_1 a_{S_1}(C_i - C_{i,S_1}) - \beta_2 a_{S_2}(C_i - C_{i,S_2}) \quad \textbf{(8.1)}$$

Where ε_b is the bed mean voidage, C_i is the mole concentration of the $i-th$ specie in the bulk, C_{i,S_1} and C_{i,S_2} are the mole concentrations of the $i-th$ specie at the catalyst and adsorbent surfaces, and β_1 and β_2 are the mass transfer coefficients, calculated with the expressions presented in **Chapter 6**.

The gas energy balance in adiabatic conditions is represented as:

$$\varepsilon_b \frac{\partial (\rho_g C_{p,g} T)}{\partial t} + \varepsilon_b \frac{\partial (u_i \rho_g C_{p,g} T)}{\partial z} = -\alpha_1 a_{S_1}(T - T_{S_1}) - \alpha_2 a_{S_2}(T - T_{S_2}) \quad \textbf{(8.2)}$$

And for a diabatic reactor:

$$\varepsilon_b \frac{\partial (\rho_g C_{p,g} T)}{\partial t} + \varepsilon_b \frac{\partial (u_i \rho_g C_{p,g} T)}{\partial z} = -\alpha_1 a_{S_1}(T - T_{S_1}) - \alpha_2 a_{S_2}(T - T_{S_2}) - \frac{4U_w}{d_r}(T - T_f) \quad \textbf{(8.3)}$$

Where u_i is the interstitial velocity of the gas, ρ_g the gas density and $C_{p,g}$ the gas heat capacity; α_1 and α_2 are the film heat transfer coefficients at the catalyst and

at the adsorbent, U_w is the overall wall heat transfer coefficient, d_r is the reactor diameter and T_f is the temperature of the source of heat.

The mass and energy balances at the particle level remain the same as those defined for the base model in **Chapter 6** as follows:

$$\varepsilon_{p_1}(1-\varepsilon_b)\frac{\partial C_{i,S_1}}{\partial t} = \beta_1 a_{S_1}\left(C_i - C_{i,S_1}\right) + \rho_{b_1}\sum_{j=1}^{m}\eta_j \nu_{ij} r_j \qquad \textbf{(8.4)}$$

$$\varepsilon_{p_2}(1-\varepsilon_b)\frac{\partial C_{i,S_2}}{\partial t} = \beta_2 a_{S_2}\left(C_i - C_{i,S_2}\right) + \rho_{b_2}\sum_{k=1}^{n}\eta_k \nu_{ik} r_k \qquad \textbf{(8.5)}$$

$$\rho_{b_1} C_{p_1}\frac{\partial T_{S_1}}{\partial t} = \alpha_1 a_{S_1}\left(T - T_{S_1}\right) + \rho_{b_1}\sum_{j=1}^{m}\eta_j r_j\left(-\Delta H_j\right) \qquad \textbf{(8.6)}$$

$$\rho_{b_2} C_{p_2}\frac{\partial T_{S_2}}{\partial t} = \alpha_2 a_{S_2}\left(T - T_{S_2}\right) + \rho_{b_2}\sum_{k=1}^{n}\eta_k r_k(-\Delta H_k) \qquad \textbf{(8.7)}$$

Where ε_{p_1} and ε_{p_2} are the catalyst and adsorbent porosities; ρ_{b_1} and ρ_{b_2} are the catalyst and adsorbent bulk densities; C_{p_1} and C_{p_2} are the catalyst and adsorbent heat capacities; η_j represents the effectiveness factor of the reaction j in the catalyst, ν_{ij} is the stoichiometric coefficient of the specie i in the reaction j and r_j is the rate of reaction of the $j-th$ reaction in the catalyst; similarly, η_k represents the effectiveness factor of the reaction k in the adsorbent, ν_{ik} is the stoichiometric coefficient of the specie i in the reaction k and r_k is the rate of reaction of the $k-th$ reaction in the adsorbent.

The continuity and momentum equations are the same as in **Chapter 6**:

$$\frac{\partial\left(\rho_g u_i\right)}{\partial z} = S_m \qquad \textbf{(8.8)}$$

$$\rho_g u_i\frac{\partial u_i}{\partial z} + u_i S_m + \frac{\partial P}{\partial z} = -\frac{A\mu_g u_i(1-\varepsilon_b)^2}{d_p^2\varepsilon_b^2} - \frac{B\rho_g u_i^2(1-\varepsilon_b)}{d_p\varepsilon_b} \qquad \textbf{(8.9)}$$

For the Air Reactor the main difference is the source term S_m, which now accounts for the effects of the depletion of oxygen from the air due to the re-oxidation of nickel, and the release of carbon dioxide to the bulk gas due to the decomposition of $CaCO_3$; this is expressed as:

$$S_m = \frac{\rho_{b_2}}{\varepsilon_b}M_{CO_2}\eta_{Calc}r_{Calc} - \frac{\rho_{b_1}}{\varepsilon_b}M_{O_2}\eta_{Oxi}r_{Oxi} \qquad \textbf{(8.10)}$$

Where M_{CO_2} is the molecular weight of CO_2, η_{Calc} is the effectiveness factor of the calcination of calcium carbonate, r_{Calc} is the rate of reaction of calcination, M_{O_2} is the molecular weight of O_2, η_{Oxi} is the effectiveness factor of the oxidation of nickel and r_{Oxi} is the rate of reaction of oxidation.

The initial conditions of the set of PDE (8.1), (8.2) and (8.4) – (8.7) represent an unloaded thermally equilibrated bed and are expressed as:

$$C_i(z,0) = C_{i,S_1}(z,0) = C_{i,S_2}(z,0) = 0 \qquad \textbf{(8.11)}$$

$$T(z,0) = T_{S_1}(z,0) = T_{S_2}(z,0) = T_i \qquad \textbf{(8.12)}$$

The boundary conditions are a square step input for the gas concentration, temperature, pressure and velocity as:

$$C_i(0,t) = C_{i,in} \qquad T(0,t) = T_{in} \qquad u_i(0,t) = u_{i,f} \qquad P(0,t) = P_{in} \qquad \textbf{(8.13)}$$

In addition, the total reactor pressure is related to the gas total concentration and the individual partial pressures for each component, through an advanced version of the Peng-Robinson equation of state which is implemented in the Multiflash software [176].

8.2.1.2 Heterogeneous model accounting for axial dispersion

Axial dispersion is included in the Air Reactor model in the same fashion as for the fuel reactor mode, thus equations (8.1) and (8.2) are replaced by:

$$\varepsilon_b \frac{\partial C_i}{\partial t} - \varepsilon_b D_{z,i} \frac{\partial^2 C_i}{\partial z^2} + \varepsilon_b \frac{\partial (u_i C_i)}{\partial z} = -\beta_1 a_{S_1}\left(C_i - C_{i,S_1}\right) - \beta_2 a_{S_2}\left(C_i - C_{i,S_2}\right) \qquad \textbf{(8.14)}$$

$$\varepsilon_b \frac{\partial \left(\rho_g C_{p,g} T\right)}{\partial t} - \varepsilon_b \lambda_{z,g} \frac{\partial^2 T}{\partial z^2} + \varepsilon_b \frac{\partial \left(u_i \rho_g C_{p,g} T\right)}{\partial z} = -\alpha_1 a_{S_1}\left(T - T_{S_1}\right) - \alpha_2 a_{S_2}\left(T - T_{S_2}\right) \qquad \textbf{(8.15)}$$

Where $D_{e,z}$ and $\lambda_{e,z}$ are the effective diffusion and the effective thermal conductivity coefficients in the axial direction. Equations (8.14) and (8.15) are second order PDE within the domain of interest $t > 0$ and $0 < z < L$ and require two boundary conditions, which are given by:

$$C_i(0,t) = C_{i,in} \qquad T(0,t) = T_{in} \qquad \left.\frac{\partial C_i}{\partial z}\right|_{z=L_b} = \left.\frac{\partial T}{\partial z}\right|_{z=L_b} = 0 \qquad \textbf{(8.16)}$$

8.2.1.3 Heterogeneous model accounting for the variation of the adsorbent porosity

During the regeneration of the adsorbent, the structure of the particle changes due to the conversion of the $CaCO_3$ layer into CaO, resulting in the increase of the particle porosity. These effects are modelled in a similar way to the reduction of porosity due to the adsorption of CO_2 presented in **Chapter 7**. Hence, when considering the porosity changes in the Air Reactor model Equations (8.5) and (8.7) are replaced by:

$$\varepsilon_{p_2}\frac{\partial C_{i,S_2}}{\partial t} - C_{i,S_2}N_{Ca}V_{CaCO_3}(Z'-1)\frac{\partial X_{CaCO_3}}{\partial t} = \frac{\beta_2 a_{S_2}}{(1-\varepsilon_b)}\left(C_i - C_{i,S_2}\right) + \frac{\rho_{b_2}}{(1-\varepsilon_b)}\sum_{k=1}^{n}\eta_k \nu_{ik} r_k \quad \textbf{(8.17)}$$

$$\left(1-\varepsilon_{p_2}\right)\frac{\partial T_{S_2}}{\partial t} + T_{S_2}N_{Ca}V_{CaCO_3}(Z'-1)\frac{\partial X_{CaCO_3}}{\partial t} = \frac{\alpha_2 a_{S_2}\left(T - T_{S_2}\right)}{(1-\varepsilon_b)\rho_{p_2}C_{p_2}} + \frac{\left(1-\varepsilon_{p_2}\right)}{(1-\varepsilon_b)C_{p_2}}\sum_{k=1}^{n}\eta_k r_k(-\Delta H_k) \quad \textbf{(8.18)}$$

where N_{Ca} is the molar concentration of calcium in the adsorbent, V_{CaCO_3} is the molar volume of $CaCO_3$, and Z' is the ratio of the molar volume of CaO to the molar volume of $CaCO_3$. The adsorbent porosity ε_{p_2} is related to the conversion of calcium carbonate X_{CaCO_3} through the following expression:

$$\frac{\partial \varepsilon_{p_2}}{\partial t} = -N_{Ca}V_{CaCO_3}(Z'-1)\frac{\partial X_{CaCO_3}}{\partial t} \quad \textbf{(8.19)}$$

The following initial conditions apply for the solution of Equations (8.17) - (7.13):

$$C_{i,S_2}(z,0) = 0 \qquad T_{S_2}(z,0) = T_i \qquad \varepsilon_{p_2}(z,0) = \varepsilon_{p_2,0} \quad \textbf{(8.20)}$$

8.2.2 Closure relationships

8.2.2.1 Kinetics of the processes involved in the Air Reactor mode

The Air Reactor model considers the reactions summarised in Table 8.1.

Table 8.1 Main processes occurring during the Air Reactor cycle.

Reaction	Material	Process	Standard heat of reaction (ΔH^0)
R1	OTM	$O_{2(g)} + 2Ni_{(s)} \leftrightarrows 2NiO_{(s)}$	$-479.4\ kJ\ mol_{Ni}^{-1}$
R2	Adsorbent	$CaCO_{3(s)} \leftrightarrows CO_{2(g)} + CaO_{(s)}$	$178.8\ kJ\ mol_{CaCO_3}^{-1}$

For the kinetics of nickel oxidation the base model is that of Medrano et al. [57]:

$$r_{Oxi} = \frac{w_{Ni,0}}{M_{Ni}} \frac{dX_{Ni}}{dt} \quad \textbf{(8.21)}$$

$$\frac{dX_{Ni}}{dt} = \frac{3C_{O_2}^{0.9}}{2r_{g,Ni}\rho_{m,Ni}\left[\frac{1}{k_{Oxi}}(1-X_{Ni})^{-\frac{2}{3}} + r_{g,Ni}(1-X_{Ni})^{-\frac{1}{3}} - r_{g,Ni}\right]} \quad \textbf{(8.22)}$$

The initial conversion of the nickel in the catalyst is determined based on the conversion of nickel oxide during its reduction in the previous fuel reactor cycle. Hence, the initial condition of Equation (2.59) can be expressed as:

$$X_{Ni}(z,0) = f(z,\pi_{n-1}) \quad \textbf{(8.23)}$$

where π_{n-1} is time period of the previous cycle of operation of the system. If it is assumed that nickel oxide is completely converted towards nickel, then the initial condition is:

$$X_{Ni}(z,0) = 0 \quad \textbf{(8.24)}$$

For the calcination of calcium carbonate the expression proposed by Martinez et al. [116] is used:

$$r_{Calc} = \frac{1}{M_{CaCO_3}} \frac{dX_{CaCO_3}}{dt} \quad \textbf{(8.25)}$$

$$\frac{dX_{CaCO_3}}{dt} = k_{Calc}\left(1 - X_{CaCO_3}\right)^{2/3}\left(C_{CO_2,eq} - C_{CO_2}\right) \quad \textbf{(8.26)}$$

Similarly to the initial conversion of nickel, the initial conversion of calcium carbonate in Equation (8.26) depend upon the conversion of adsorbent attained during the carbonation of CaO, as discussed in **Chapter 6** the carbonation process is an incomplete process, thus the initial condition of (8.26) can be expressed in general as:

$$X_{CaCO_3}(z,0) = g(z,\pi_{n-1}) \quad \textbf{(8.27)}$$

8.2.2.2 Other relationships

The remaining relationships required to complete the model such as the mass and heat transfer coefficients, and axial dispersion coefficients are calculated with the correlations provided in **Chapter 6**.

8.3 Model integration and convergence

The model is integrated following the procedure outlined in **Chapter 6**. To ensure convergence, 100 mesh points were utilised following the analysis made for the fuel reactor model.

8.4 Model validation

The validation of the reactor model was attained by comparing the simulation output against the experimental data reported by Antzara et al. [58] who carried out experimental work to prove the feasibility of the SE-CLSMR process.

Their work was focused on the demonstration of both a high H_2 production in the fuel cycle, and the regeneration of the adsorbent without putting additional heat into the reactor. Their experiments were conducted over a mixture of a Ni-based catalyst and a Ca-based catalyst supported on ZrO_2 in a bench-scale fixed bed reactor. No detail of the packing distribution was provided by the researchers, hence the assumption of a homogeneous mixture is made. These experiments were conducted at a pressure slightly above the atmospheric and temperature of 1073 K in a quartz reactor enclosed by an electrical furnace with three heating zones independently controlled, the experimental conditions are listed in Table 8.2 and the properties of the catalyst and the adsorbent utilised in the experiment are summarised in Table 8.3. The reactor was equipped with three thermocouples located at three different locations in the bed (at the entrance, in the middle and at the outlet) and an on-line gas analyser, thus the experimental data for the Air Reactor experiments comprised a set of temperatures for each location of the reactor, along with the measurement of the standard flow of CO_2 at the reactor outlet.

Each experimental run consisted of a fuel cycle followed by an air cycle. At the end of each fuel cycle, the fuel gas was replaced by an inert gas to purge the reactor while maintaining the reactor at the reforming temperature utilised for this cycle, and monitoring the signals of CO and CO_2 in the analyser. Once the gas analyser indicated that the content of CO and CO_2 in the effluent was minimal, the inert gas was replaced by air and the re-oxidation of nickel started without increasing the reactor temperature and allowing the system to absorb the heat of reaction of oxidation of nickel, thus heating up the bed and promoting the calcination of the adsorbent. This condition was maintained until the nickel was completely oxidised; at this point, the reactor temperature set point was increased to 1073 K to complete the calcination of $CaCO_3$.

Table 8.2 Experimental conditions of the SE-CLSMR runs utilized to validate the air model.

Parameter	Fuel reactor	Air Reactor
Temperature (K)	873–973	1073
Total Pressure (bar)	1	1
Gas space hourly velocity (h^{-1})	250	430
S/C molar ratio ($kmol\ H_2O\ kmol^{-1}\ C$)	3	-
NiO-to-CaO molar ratio ($mol\ NiO\ mol^{-1} CaO$)	0.5	
Reactor bed length (m)	0.1	
Reactor diameter (m)	0.02	
Particle diameter (m)	0.0018 – 0.0035	

Table 8.3 Summary of properties of materials utilised in the experiments by Antzara et al. [58, 198] used for model validation.

Property	Catalyst		Adsorbent	
	Fresh	Spent	Fresh	Spent
Active material content ($wt.\%$)	40	-	66	-
B.E.T. surface area ($m^2\ g^{-1}$)	22	9.3	15.3	3.9
Pore volume ($cm^3\ g^{-1}$)	0.15	0.13	0.05	0.02

8.5 Results and discussion

The validation of the reactor model in air mode ('Air Reactor') was attained by comparing the predicted temperature profiles at three different locations in the reactor and the breakthrough curve of CO_2 with the experimental data recovered from [60]; the selected data corresponded to the Air Reactor experiments starting from an initial bed temperature at 923 K and atmospheric pressure. The computational experiment was run with the input data summarised in Table 8.4, which was obtained by processing the experimental data detailed the previous section.

Table 8.4 Simulation inputs for the validation of the Air Reactor model.

Parameter	Value
Gas composition (mole%)	
Nitrogen	79.0
Oxygen	21.0
Pellets properties (cat./ads.)	
Density (kg m^{-3})	4163.6/2934.8
Heat capacity (J $kg^{-1}K^{-1}$)	589.7/1108.0
Porosity (m^3 m^{-3})	0.35/0.05
Avg. particle diameter (m)	0.00027
Reactor length (m)	0.10
Reactor diameter (m)	0.02
Time period (s)	3600
Inlet temperature (K)	923
Inlet pressure (bar)	Atmospheric
Inlet velocity	0.029
Vol. fraction of catalyst (m^3 m^{-3})	0.502

8.5.1 Sensitivity of the kinetic rate expressions

Prior to the validation of the Air Reactor model, the sensitivity of the model to the kinetic rate expressions of the oxidation of nickel and the calcination of calcium carbonate was assessed. For the oxidation of nickel the models of Medrano et al. [57] and Zafar et al. [118] are compared, both models are based on the shrinking core model and will be referred to as SCM1 and SCM2; the models reported by Abad et al. [117] and Dueso et al. [122] were also tested but no convergence was obtained with the former, whereas the mathematical form of the latter led to a numerical run away from the maximum conversion of the material, thus these two models could not be assessed in this work. These simulations were conducted fixing the calcination kinetics to the model of Martinez et al. [113].

The conversion profiles of nickel predicted with models SCM1 and SCM2 at various simulation times are illustrated in Figure 8.3. The model SCM1 predicts a front that exhibits a degree of diffusion, resulting in a slower re-oxidation of the oxygen carrier. Conversely, the model SCM2 predicts a sharper front and the conversion of the bed seems to progress evenly. The rate of reaction profiles (Figure 8.4) confirm this situation and exhibit that the reaction moves downstream as a pulse with different features for each model. The SCM1 model predicts a lower rate with a longer mass transfer zone, whereas the SCM2 rate predicts a higher peak (roughly 3.2 times that predicted by the SCM1 model), and a shorter

length of the mass transfer zone. The shape of the oxidation front affects the temperature profiles in the bed as illustrated in Figure 8.5, which shows that the two models predict a hot spot moving downstream the bed. The magnitude of the temperature rise is associated to the rate of oxidation, therefore it is understandable to obtain a profile with higher peak temperature with the SCM2 model; however, in the context of the Air Reactor, not only the re-oxidation of nickel is occurring, but also the calcination of calcium carbonate, which in itself is an endothermic process, thus the final temperature profile is influenced also by the regeneration of the adsorbent.

The results shown for both the SCM1 and the SMC2 models suggest that any of the models can be used to represent the re-oxidation of nickel in the Air Reactor model. The final selection of the model being dependent upon the validation of the simulation against measurable variables such as the temperature and by comparing the breakthrough curves of the different species emerging from the reactor. Nevertheless, because the SCM1 kinetic model data were obtained from experiments with a reforming catalyst with an initial content of NiO in the range of interest of this particular application, it is going to be deemed as the base model in the following simulation work.

Regarding the calcination of calcium carbonate, the models of Martinez et al. [113] hereafter UCM1, Borgwardt et al. [111] referred to as UCM2, and Escardino et al. [116] referred to as GM, were assessed, and their outputs are illustrated in Figure 8.6 and Figure 8.7. As mentioned above, the kinetic model of nickel oxidation selected for this exercise was the SCM1 model as per the nomenclature stated before.

Figure 8.6 shows the conversion profiles of calcium carbonate at three different simulation times. The discrepancies between the calcination models are evident in Figure 8.6; the fastest conversion is predicted with the UCM2 model, followed by the GM model, and the UCM1 model. The UCM2 model prediction might be unrealistic since its derivation was based on the analysis of data obtained from experiments in which the atmosphere did not influence the rate of calcination, therefore the rate expression does not consider the effect of the concentration of CO_2 in the reactor atmosphere. Normally, the latter tends to limit the conversion of $CaCO_3$ when its value is close to the equilibrium concentration [113, 116]. Conversely, the models UCM1 and GM predict a high conversion close to the bed inlet that decreases as the reaction front moves downstream; interestingly, the GM model predicts zones within the bed with a negative conversion, this can be interpreted as a re-carbonation of the adsorbent due to a CO_2 concentration higher than equilibrium. The rate of reaction profiles (Figure 8.7) are in accordance with the behaviour described for the conversion of $CaCO_3$. The

model UC2 predicts a positive reaction rate at 200 s, and reaction rates of zero for 400 s and 600 s which are indicative of a complete conversion of $CaCO_3$. The UC1 and GM model predict zones of positive values of calcination rate followed by zones of negative values (as before, in these zones the bulk concentration of CO_2 is higher than the equilibrium concentration); moreover, in the prediction of GM model, the magnitude of the rate of calcination is considerably larger than in the prediction of the UCM1 model, for both zones of positive and negative values. The differences observed in the predictions of these two models might relate to the experimental conditions at which their kinetic parameters were determined. For both models, the experiments were conducted at a minimum temperature of 1098 K, whereas the simulation was conducted at a fixed temperature of 923 K well below the range of validity of the kinetic parameters of the models.

From the three models of calcination kinetics, the UCM1 model seems to predict the less extreme scenario, as opposed to the UCM2 model which predicts a very fast calcination but fails to account for the mass transfer limitations, and the GM model which predicts a very high rate of re-carbonation of the adsorbent. Thus, the UCM1 model is used as the base model to validate the Air Reactor model.

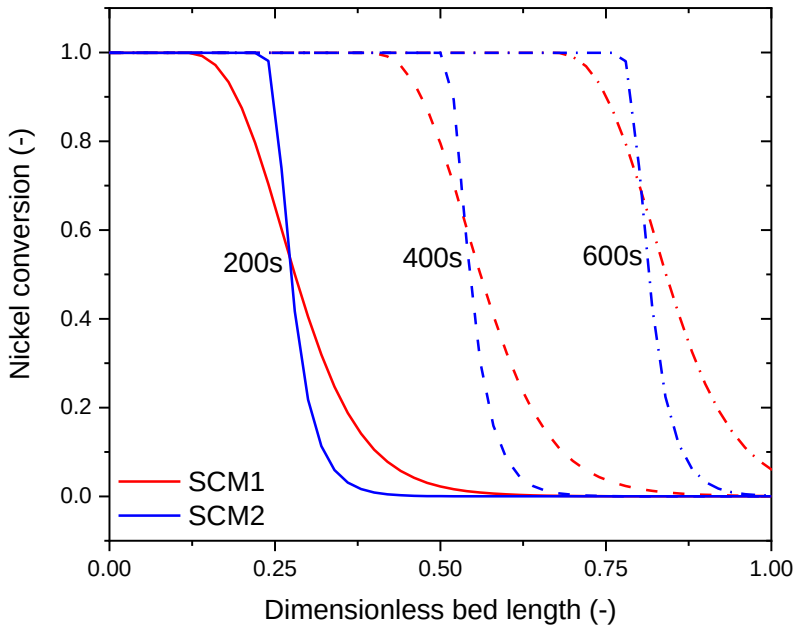

Figure 8.3 Conversion profiles of nickel predicted with the SCM1 and SCM2 models at t=200 s, 400 s, and 600 s.

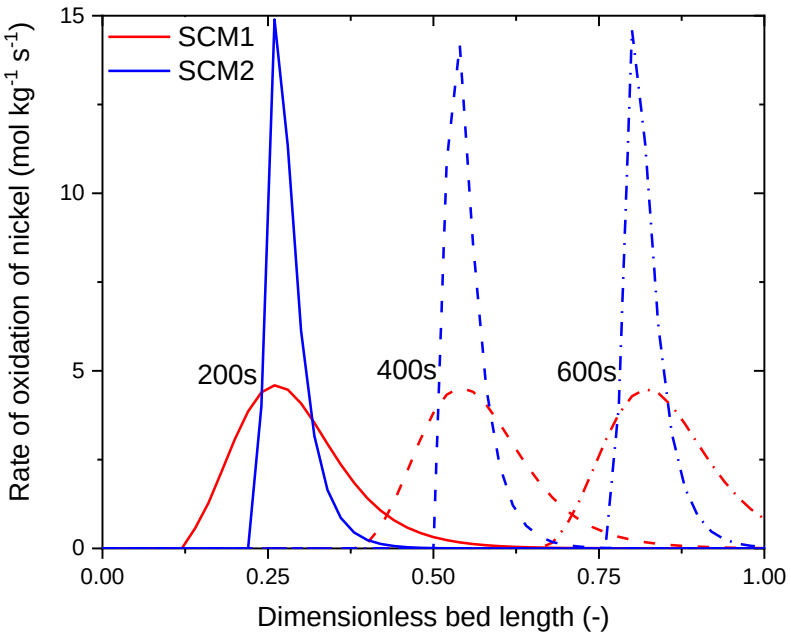

Figure 8.4 Rate of oxidation of nickel predicted with the SCM1 and SCM2 models at t=200 s, 400 s, and 600 s.

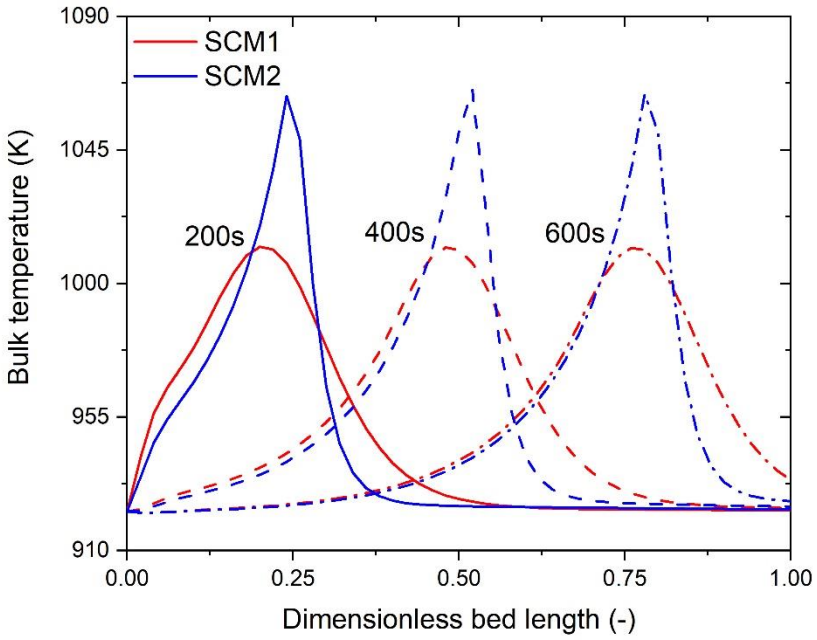

Figure 8.5 Bulk gas temperature profiles predicted with the SCM1 and SCM2 models at t=200 s, 400 s, and 600 s.

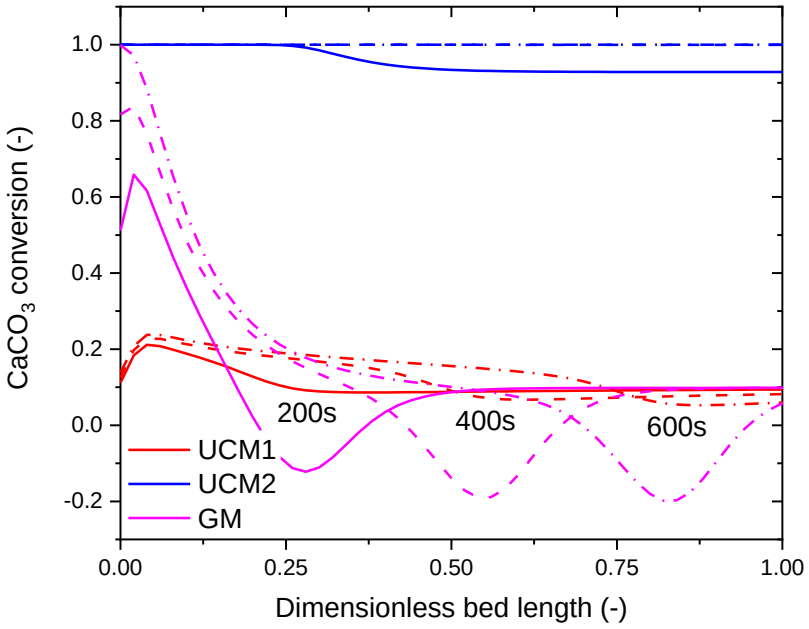

Figure 8.6 Conversion profiles of calcium carbonate predicted with the UCM1, UCM2 and GM models at t=200 s, 400 s, and 600 s

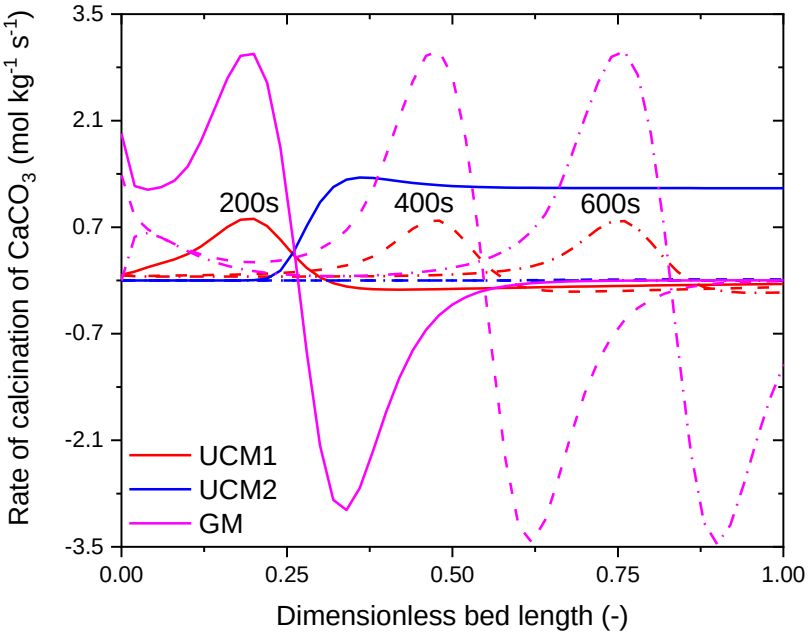

Figure 8.7 Rate of calcination of calcium carbonate predicted with the SCM1 and SCM2 models at t=200 s, 400 s, and 600 s.

8.5.2 Validation of the Air Reactor model

Various versions of the Air Reactor model considering a range of physical phenomena were assessed during the validation process. Table 8.5 summarises

the models considered along with the description of the physical phenomena incorporated in each of them.

Table 8.5 Nomenclature utilised for reference to the models utilised to simulate the Air Reactor.

Case nomenclature	Description
AR-PF-SF00	Plug flow heterogeneous model with simple correlation for the film heat transfer coefficient.
AR-PF-SF01	Plug flow heterogeneous model with simple correlation for the film heat transfer coefficient. Porosity changes of the adsorbent are included.
AR-PF-EF01	Plug flow heterogeneous model with effective correlation for the film heat transfer coefficient. Porosity changes of the adsorbent are included.
AR-AD-SF01	Plug flow with axial dispersion heterogeneous model with simple correlation for the film heat transfer coefficient. The kinetics of oxidation was represented by the SCM1 model, and the kinetics of calcination was represented by the UCM1 model. Porosity changes of the adsorbent are included.
AR-AD-SF02	Plug flow with axial dispersion heterogeneous model with simple correlation for the film heat transfer coefficient. The kinetics of oxidation was represented by the SCM1 model, and the kinetics of calcination was represented by the GM model. Porosity changes of the adsorbent are included.
AR-AD-SF03	Plug flow with axial dispersion heterogeneous model with simple correlation for the film heat transfer coefficient. The kinetics of oxidation was represented by the SCM2 model, and the kinetics of calcination was represented by the UCM1 model. Porosity changes of the adsorbent are included.
AR-AD-SF04	Plug flow with axial dispersion heterogeneous model with simple correlation for the film heat transfer coefficient. The kinetics of oxidation was represented by the SCM2 model, and the kinetics of calcination was represented by the GM model. Porosity changes of the adsorbent are included.

Table 8.6 summarises the average error of the prediction of the temperature profiles at various bed locations and the flowrate of CO_2 desorbed measured at the bed outlet; in addition, the peak temperature predicted with each model and the corresponding error is listed. All the modelling options listed in Table 8.5 produce an acceptable output in the prediction of the temperature profiles, with errors in the range 0.99% - 6.20% when considering the complete temperature profile. When considering the peak temperature only, the highest errors are

obtained in the prediction of the temperature at the bed inlet, however, in all cases the error was less than 10% which in principle indicates a fair representation of the system. Regarding the CO_2 desorbed, none of the predictions was accurate. The large errors in the approximation of this variable are due to the erroneous prediction of the flowrate of CO_2 during the first stage of the experiment, and its overprediction during the second part of the experiment, as observed in Figure 8.8.

The results summarised in Table 8.6 indicate similar outputs for all the modelling options based in the plug flow model. The incorporation in the model of the increase of adsorbent's porosity, improves the prediction of the breakthrough of CO_2, although with a marginal enhancement of the temperature prediction. Similar results are obtained when the conductivity of the materials is considered through an effective heat transfer coefficient. When the axial dispersion effects are considered, the prediction of the temperature profiles is slightly improved although this seems to be detrimental for the prediction of the CO_2 breakthrough curve. These results highlight the very high uncertainty associated with the kinetic models, particularly those representing the calcination of $CaCO_3$.

Figure 8.9, Figure 8.10 and Figure 8.11 illustrate the experimental and simulated temperature profiles of the bulk gas and solids at three different locations in the packed bed. Two zones can be identified in all the plots corresponding to the two different stages of the experiment. During the first step, the experiment is being conducted by controlling the supply of heat to the reactor to maintain the base temperature of the bed at 923 K, and allowing the system to absorb part of the heat of reaction released during the re-oxidation of nickel, i.e. during this stage the reactor operates according to the Air Reactor concept. This produces a hot zone moving towards the bed exit. The second stage starts after 1440 s and entails an increase of the heat supply to the reactor to raise the temperature to 1073 K in order to complete the regeneration of the adsorbent.

It is visible that the simulation output resembles correctly the shape of the experimental data profile; of particular interest is the first stage of the experiment, in which the agreement of the simulation with the experiment is reasonably good. Similarly to the validation of the fuel reactor models, the effectiveness factors of nickel oxidation and calcium oxide calcination were handled as adjustable parameters to tune the Air Reactor model simulation output to the experimental data. The best output was obtained by setting the effectiveness factors of the oxidation of nickel to $\eta_{ox} = 0.2$, and of the calcination of calcium carbonate to $\eta_{cal} = 1.0$. These values are consistent with the theoretical values estimated with the effectiveness factor models of Ishida and Wen [195] previously presented in **Chapter 6**, which rendered values of $\eta_{ox} = 0.205$ and $\eta_{cal} = 0.999$ at inlet

conditions. Fernandez et al. [178] reported a value of effectiveness for the calcination of $CaCO_3$ of $\eta_{cal} = 1.0$, albeit for particles sizes an order of magnitude larger than those utilised in the experiments used for the validation of the Air Reactor model in this project; Diglio et al. [177] utilised values of $\eta_{ox} = 0.3$ and $\eta_{cal} = 1.0$.

As mentioned above, the Air Reactor model failed to reproduce accurately the breakthrough curve of CO_2. Various reasons might be argued, there is uncertainty associated with various key properties of the materials since they have been estimated from the properties of their individual components and other textural properties reported by Antzara et al. [58] as mentioned previously. Another possibility, is that the available calcination kinetic rate models are unsuitable to represent the synthetic adsorbent utilised in the Air Reactor experiments. The profiles of concentration of CO_2, temperature and reaction rate give an insight of what the model is predicting about the reactor behaviour.

Figure 8.12 illustrates the actual concentration profile of CO_2 in the bed at several simulation times; for comparison purposes, the equilibrium concentration profile has been included. It is evident in Figure 8.12 that the concentration front of CO_2 is travelling faster toward the exit of the bed than the corresponding equilibrium concentration front. The reason for this behaviour is that the equilibrium concentration depends upon the system temperature (Figure 8.13) and since the thermal front is moving slower than the concentration front, it follows that the CO_2 equilibrium concentration profile moves behind the CO_2 actual concentration front. This is mathematically expressed in Equations (8.28), and (8.30) which represent the velocity of the concentration front of CO_2 and the thermal front, respectively; these equations were derived in a similar fashion to those of the Fuel Reactor and the derivation process is presented in Appendix C, Section C.2. If the gradients $\frac{\partial X_{Calc}}{\partial C_{CO_2}}$, $\frac{\partial X_{Calc}}{\partial T}$ and $\frac{\partial X_{Oxi}}{\partial T}$ are positive, then the denominator of Equation (8.28) will decrease and the velocity of the reaction front of CO_2 will increase with a limit at $\left(\frac{dz}{dt}\right)_{C_{CO_2}} = u_i$; the velocity of the thermal front will depend upon the magnitude of the third and fourth terms in the denominator of Equation (8.30), however, it is limited at $\left(\frac{dz}{dt}\right)_T = \frac{u_i}{1+\frac{\rho_s C_{p,s}}{\varepsilon_b \rho_g C_{p,g}}}$, which in fact indicates that it will travel at a slower velocity. Similarly, the velocity of the concentration front of O_2 will vary according to the sign and magnitude of $\frac{\partial X_{Oxi}}{\partial C_{O_2}}$; for positive values of this gradient, the velocity of this front will be less than that of CO_2, hence the concentration front of CO_2 will travel ahead of the concentration front of O_2 and the thermal front.

$$\left(\frac{dz}{dt}\right)_{C_{CO_2}} = \frac{u_i}{1 - \frac{\rho_{b_2}\eta_{Calc}}{\varepsilon_b M_{CaCO_3}}\frac{\partial X_{CaCO_3}}{\partial C_{CO_2}}} \quad \textbf{(8.28)}$$

$$\left(\frac{dz}{dt}\right)_{C_{O_2}} = \frac{u_i}{1 + \frac{\rho_{b_1}\eta_{Oxi}}{2\varepsilon_b M_{Ni}}\frac{\partial X_{Ni}}{\partial C_{O_2}}} \quad \textbf{(8.29)}$$

$$\left(\frac{dz}{dt}\right)_{T} = \frac{u_i}{1 + \frac{\rho_b C_{p,b}}{\varepsilon_b \rho_g C_{p,g}} + \frac{\rho_{b_2}\eta_{Calc}\Delta H_{Calc}}{M_{CaCO_3}\varepsilon_b \rho_g C_{p,g}}\frac{\partial X_{CaCO_3}}{\partial T} - \frac{\rho_{b_1}\eta_{Oxi}\Delta H_{Oxi}}{2M_{Ni}\varepsilon_b \rho_g C_{p,g}}\frac{\partial X_{Ni}}{\partial T}} \quad \textbf{(8.30)}$$

Consequently, the adsorbent will be subjected to cycles of re-carbonation in those zones where the actual concentration CO_2 exceeds the equilibrium concentration of CO_2.This can be observed in Figure 8.14 which is a plot of the profiles of the rate of calcination at 100 s, 300 s, 500 s and 600 s. The profiles show two zones, a rear zone in which the rate of calcination increases up to a maximum which is bounded by the maximum temperature of the system and by the approach of the CO_2 concentration that is building up in the system to the equilibrium limit. The leading zone is formed where the rate of calcination decreases down to negative values which coincides with the zone observed in Figure 8.12 in which the bulk concentration of CO_2 is above its equilibrium value, this zone would represent a situation where the adsorbent undergoes a re-carbonation as was mentioned before.

Equations (8.28), (8.29) and (8.30) also express the impact of the interstitial velocity of the gas over the velocity of the various fronts. Figure 8.16 presents profiles of the gas interstitial velocity at several simulation times. The shape of the velocity profile reflects the expected variation of total mass in the bulk gas according to the behaviour of the concentration fronts of CO_2 and O_2 shown in Figure 8.12 and Figure 8.15, and the variation of the gas density due to the changes in the bulk gas composition and temperature. The velocity initial increase is caused by the addition of the mass of CO_2 to the bulk gas, although at the early stage of the process this is offset by the depletion of O_2 which is consumed in the oxidation of nickel, this is the reason why the velocity barely increases at the beginning of the process. As the oxidation of nickel is completed, the depletion of oxygen in the bulk gas is reduced, whilst the addition of carbon dioxide increases, thus the velocity reaches higher peaks as the time passes by. Nevertheless, since the model predicts a re-carbonation of the adsorbent, the peak of velocity is followed by a reduction of this variable down to a minimum value that corresponds with the presence of a nitrogen rich bulk gas.

Table 8.6 Average error in the prediction of the desorbed CO_2 and of the temperature profile at 0.02 m, 0.06 m and 0.095 m with various versions of the Air Reactor model.

Case	T_1 @ z=0.02 m			T_2 @ z=0.06 m			T_3 @ z=0.095 m			CO_2 desorbed
	Temp. profile error	Peak temperature		Temp. profile error	Peak temperature		Temp. profile error	Peak temperature		Error
		Value (K)	Error		Value (K)	Error		Value (K)	Error	
Experiment	-	999.2	-	-	1053.6	-	-	1075.5	-	-
AR-PF-SF00	2.23%	1050.5	5.13%	2.35%	1072.7	1.81%	5.19%	1076.6	0.11%	693.3%
AR-PF-SF01	2.29%	1049.4	5.02%	2.36%	1069.9	1.54%	5.17%	1073.1	0.22%	390.9%
AR-PF-EF01	2.29%	1049.4	5.02%	2.36%	1069.9	1.54%	5.17%	1073.1	0.22%	390.9%
AR-AD-SF01	1.93%	1034.2	3.50%	2.05%	1057.6	0.38%	4.71%	1067.3	0.76%	649.2%
AR-AD-SF02	1.72%	1032.7	3.35%	0.99%	1058.7	0.48%	6.20%	1063.8	1.08%	812.7%
AR-AD-SF03	1.85%	1066.1	6.69%	2.09%	1093.9	3.82%	5.91%	1106.0	2.84%	643.7%
AR-AD-SF04	1.69%	1066.9	6.78%	1.16%	1084.0	2.88%	5.84%	1085.8	0.96%	780.4%

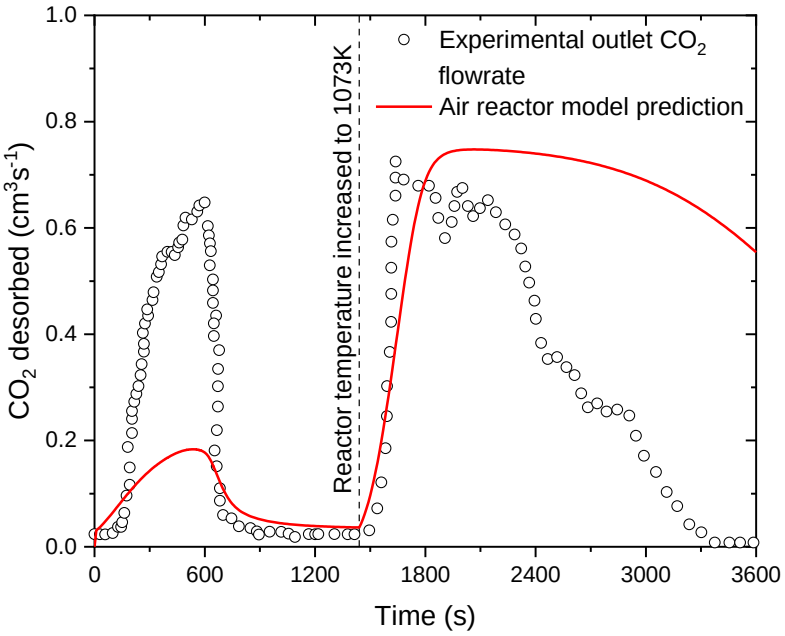

Figure 8.8 Air Reactor model prediction of the outlet standard CO_2 flowrate against the experimental data. The initial bed temperature and the air inlet temperature were set up to 923 K and the model used was the AR-PF-SF01 model.

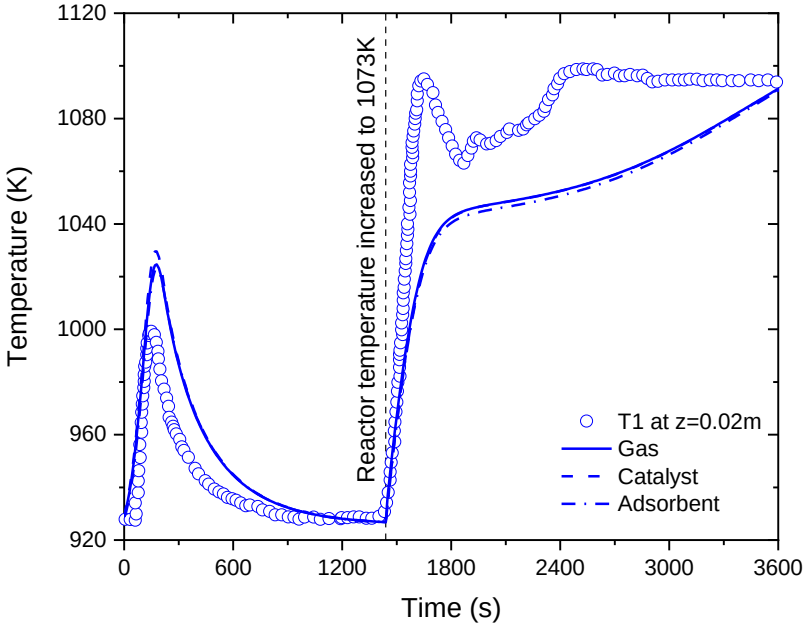

Figure 8.9 Experimental and predicted temperature dynamic profiles at z=0.02 m. The simulation output for the bulk gas, the catalyst and the adsorbent are shown for the AR-PF-SF01 model are shown.

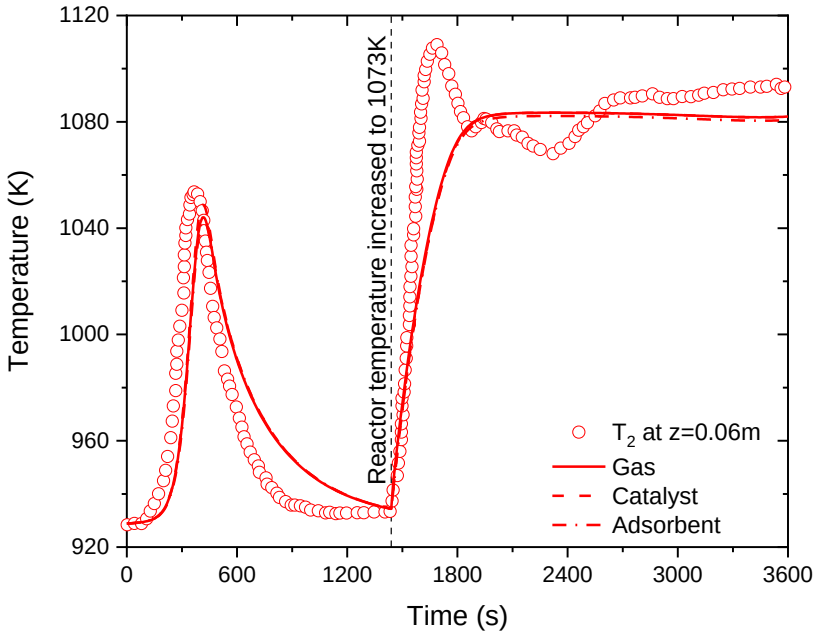

Figure 8.10 Experimental and predicted temperature dynamic profiles at z=0.06 m. The simulation output for the bulk gas, the catalyst and the adsorbent are shown for the AR-PF-SF01 model are shown.

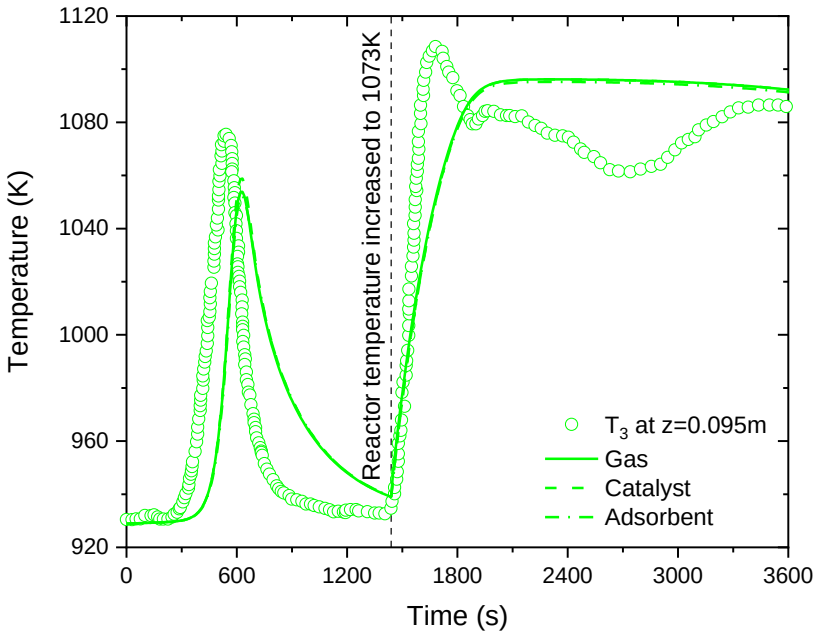

Figure 8.11 Experimental and predicted temperature dynamic profile at z=0.095 m. The simulation output for the bulk gas, the catalyst and the adsorbent are shown for the AR-PF-SF01 model are shown.

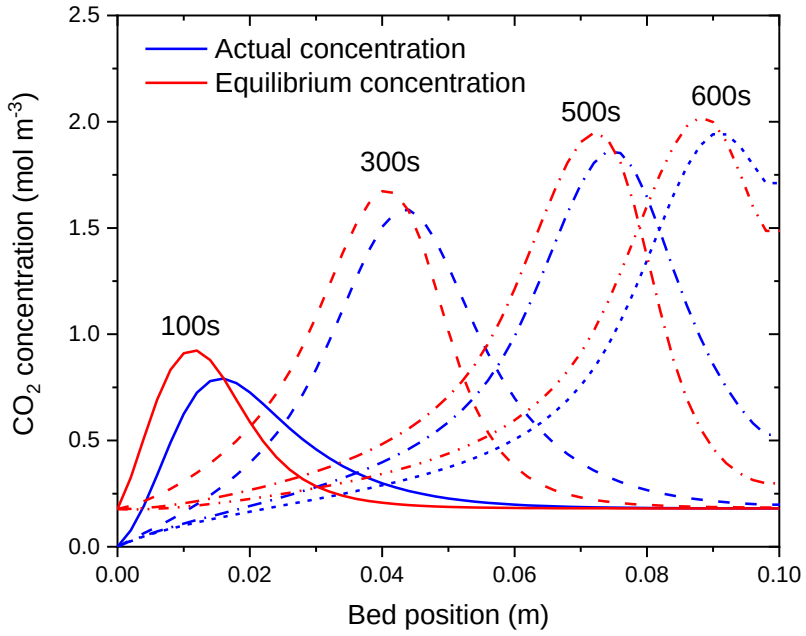

Figure 8.12 Actual and equilibrium CO_2 concentration profiles for various simulation times as function of the axial position in the bed. The profiles were obtained with the AR-PF-SF01 model.

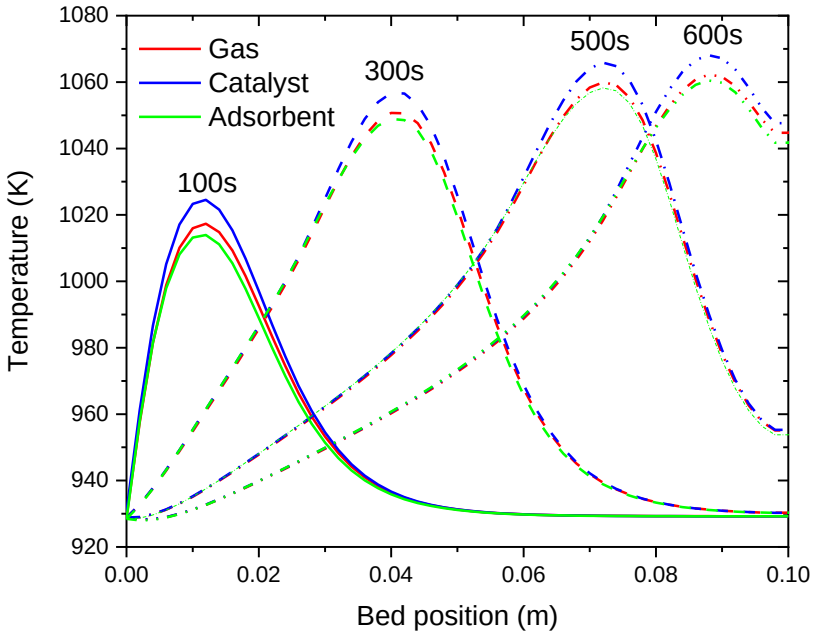

Figure 8.13 Temperature profiles of the bulk gas, catalyst and adsorbent for various simulation times as function of the axial position in the bed. The profiles were obtained with the AR-PF-SF01 model.

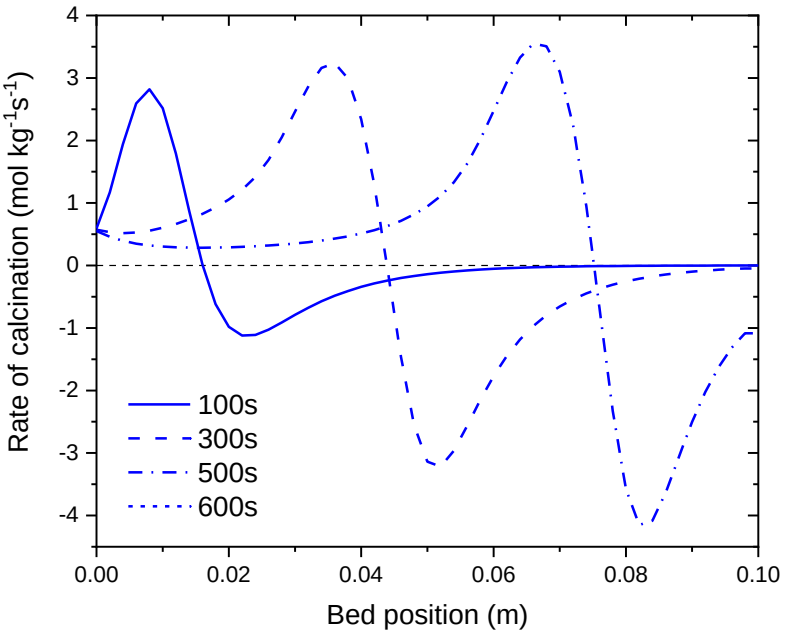

Figure 8.14 Rate of $CaCO_3$ calcination profiles for various simulation times as function of the axial position in the bed. The profiles were obtained with the AR-PF-SF01 model.

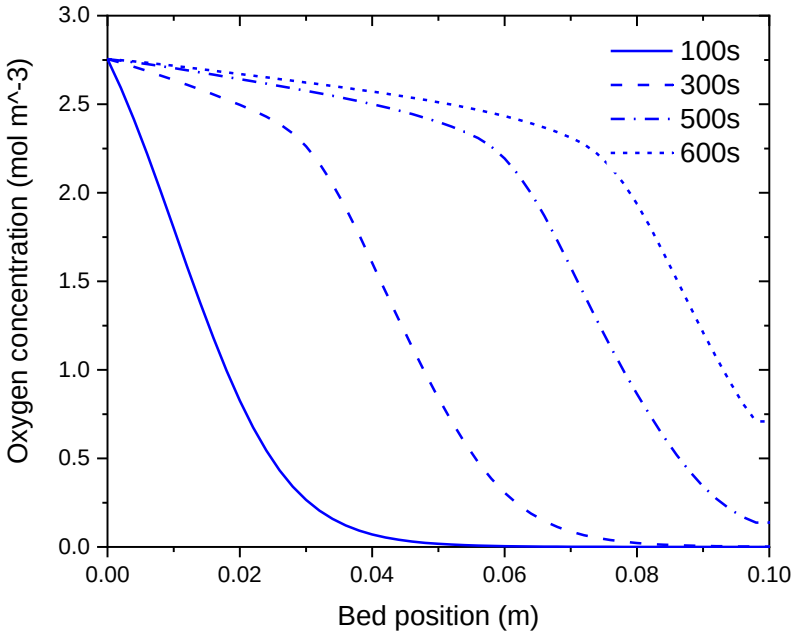

Figure 8.15 O_2 concentration profiles for various simulation times as function of the axial position in the bed. The profiles were obtained with the AR-PF-SF01 model.

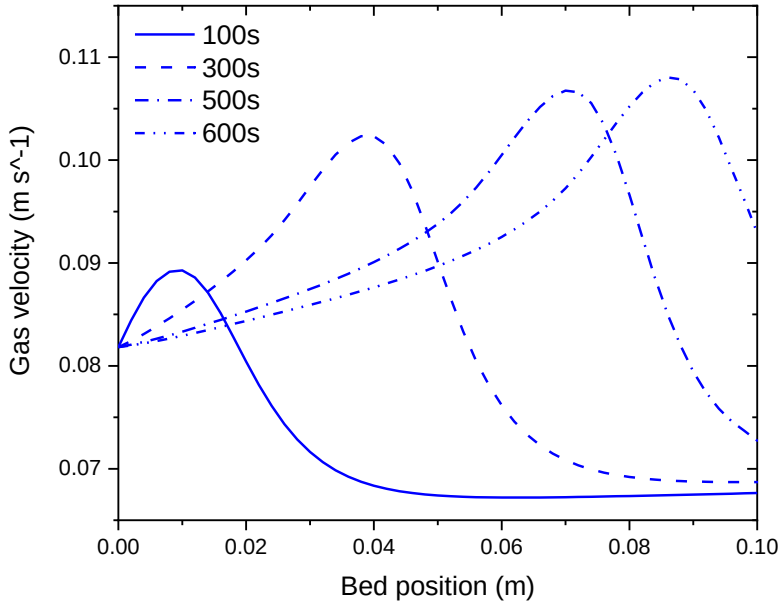

Figure 8.16 Gas interstitial velocity profiles for various simulation times as function of the axial position in the bed. The profiles were obtained with the AR-PF-SF01 model.

8.5.3 Sensitivity analysis of the Air Reactor

The heterogeneous plug flow Air Reactor model accounting for the increase of adsorbent porosity (AR-PF-SF01) was applied to conduct a sensitivity analysis of the bed regeneration cycle. Similarly to the Fuel Reactor, the Air Reactor is aimed to operate auto-thermally, with the heat of reaction released from the oxidation of nickel being the source of energy to calcinate the $CaCO_3$ in the adsorbent. This task presents the same physical restrictions to heat transfer as in the Fuel Reactor, since the transfer area is now fixed due to the selection of an optimal catalyst-to-adsorbent ratio to maximise hydrogen production. Moreover, the success of the operation of this stage relies on the rate of oxidation and the rate of calcination. Likewise the case of the fuel reactor, the Air Reactor thermal front in equation (8.30) describes how the thermal effects of the oxidation and calcination processes affect the velocity at which the thermal wave travels down the bed. Since the auto-thermal operation is achieved when the thermal effects compensate each other, the following expression arises:

$$\frac{\rho_{b_2}}{\rho_{b_1}} = \frac{M_{CaCO_3}\eta_{Oxi}\Delta H_{Oxi}}{2M_{Ni}\eta_{Cal}\Delta H_{Cal}} \frac{\frac{\partial X_{Ni}}{\partial T}}{\frac{\partial X_{CaCO_3}}{\partial T}} \qquad \textbf{(8.31)}$$

Equation (8.31) establishes the condition to be fulfilled to attain an auto-thermal Air Reactor. If the variation of the bulk density of the catalyst ρ_{b_1}, and the dependence of the heat of reaction of oxidation ΔH_{Oxi} and calcination ΔH_{Calc} upon the temperature are neglected, the behaviour of the reactor is defined by the values of the bulk density of the adsorbent ρ_{b_2}, and the partial derivatives of the catalyst conversion X_{Oxi} and the adsorbent conversion X_{Calc} with respect to the temperature. Thus, since the aforementioned variables are functions of time, it is unlikely to meet the criterion for auto-thermal operation.

Nevertheless, it is of interest to analyse the effect of several operating parameters in the performance of the Air Reactor. Previous studies have looked at the sorbent regeneration stage of reactor systems involving a Ca-Cu looping concept and have modelled the system using a pseudo-homogeneous model [177, 178, 201], but no study regarding the effect of the operating parameters over the Air Reactor performance is available for a reactor considering a Ni-Ca looping. Hence, a study is conducted to investigate the effect of the gas mass flux, temperature, the nickel load in the catalyst, the concentration of oxygen in the oxidant agent and the adsorbent and catalyst densities over the regeneration of the materials. The analysis of an additional scenario regarding the presence of hydrogen traces adsorbed in the catalyst at the beginning of the Air Reactor cycle is presented in the last part of this section. The simulation inputs are summarised in Table 8.7.

Table 8.7 Simulation inputs for the sensitivity analysis of the Air Reactor.

Parameter	Value
Gas composition (mole%)	
Nitrogen	79.0, 90.0, 95.0, 98.0, 99.0
Oxygen	21.0, 10.0, 5.0, 2.0, 1.0
Pellets properties (cat./ads.)	
Density (kg m^{-3})	3487/2791
Heat capacity (J $kg^{-1}K^{-1}$)	1102.5/1246.3
Porosity (m^3 m^{-3})	0.41/0.23
Avg. particle diameter (m)	0.005
Reactor length (m)	1.0
Reactor diameter (m)	0.35
Time period (s)	3600
Inlet temperature/initial bed temperature (K)	923, 1023, 1073, 1098, 1113
Inlet pressure (bar)	1.5
Inlet velocity (m s^{-1})	0.1, 0.2, 0.5, 1.0, 2.0
Vol. fraction of catalyst (m^3 m^{-3})	0.50
Nickel content in the reduced catalyst (wt.%)	14.1, 30.0, 45.0

8.5.3.1 Effect of the inlet gas mass flux

The effect of the inlet gas mass flux was studied by varying the inlet superficial velocity of the air, while keeping the inlet gas temperature constant, thus its density. Figure 8.17 and Figure 8.18 illustrate the average conversion profiles obtained for the active phases of the catalyst and the adsorbent (i.e. Ni and $CaCO_3$, respectively) as a function of time at various values of inlet gas superficial velocity. Conversely to the trend found in the Fuel Reactor (FR), the increase of the inlet gas velocity favours the regeneration of the packed bed reactor. Two situations are observed in Figure 8.17; firstly, the increase of inlet velocity reduces the time for complete re-oxidation of nickel, and secondly, the data shows that this parameter seems to behave asymptotically with the increasing inlet velocity, this would impose a limit to the maximum velocity at which the conversion of nickel will be affected by the gas mass flux. On the other hand, the conversion of $CaCO_3$ to CaO (i.e. the regeneration of the adsorbent) is poor at the temperature conditions simulated in this exercise. The extent of the effect of the inlet gas velocity over the conversion of the adsorbent is illustrated in Figure 8.18. At the simulated conditions, a very low conversion of the adsorbent is attained; the maximum conversion is 35% at the highest velocity (i.e. 2.0 m s^{-1}), this value represents an effective conversion of 12.3% considering that the initial state of the adsorbent is a partially carbonated material, due to the incomplete carbonation of the adsorbent attained during the fuel reactor cycle.

The very low conversion of the adsorbent is due to the combined effect of the initial temperature of the system and the heat of reaction released during the re-oxidation of nickel. Figure 8.19 illustrates the temperature profiles of the catalyst surface and at the adsorbent surface as function of the bed position, at 50% of the time required for the complete conversion of nickel for the various values of inlet gas velocity simulated. In all the cases the simulation was conducted at an initial bed and air inlet temperature of 923 K, and the rise of the temperature above this level is due to the heat of oxidation absorbed by the packing. It is evident that as the air velocity increases, the thermal front moves faster down the bed. Moreover, for all scenarios of air velocity, the rise of temperature in the adsorbent is not high enough to reach the temperature of decomposition of $CaCO_3$ at 1.5 bar, whose value is circa 1200 K. However, a higher air velocity reduces the gap between the catalyst and the adsorbent temperatures, and heats up evenly the whole packed bed, albeit the peak temperature in the adsorbent is lower than that obtained at low air velocities.

Nevertheless, the selection of the feasible air velocity is constrained by the pressure losses throughout the packed bed and the minimum fluidisation velocity, which for the packed bed considered here varies between 9.6 and 10.6 m s^{-1}.

Figure 8.20 illustrate the profiles of air pressure for the several air velocities simulated. As expected, the higher the air velocity, the higher the pressure losses through the packed bed. If a maximum allowable pressure drop of 10% of the inlet air pressure is selected as the criterion to choose the operating air velocity, then the maximum eligible value for this parameter is 1.0m s^{-1}, which renders a pressure drop of 0.061bar m^{-1}, representing 4% of the total pressure. Under these conditions, the predicted temperature approach between the catalyst and the adsorbent is less than 20 K.

Increasing the velocity seems to improve the utilization of the heat of oxidation released by the catalyst, favouring the regeneration of the adsorbent. However, care should be taken in the selection of the operating air velocity since a very high pressure drop would made necessary to increase the system total pressure to avoid operating under vacuum conditions, thus increasing the equilibrium temperature of $CaCO_3$ decomposition and the necessary heat load to attain complete conversion of de adsorbent.

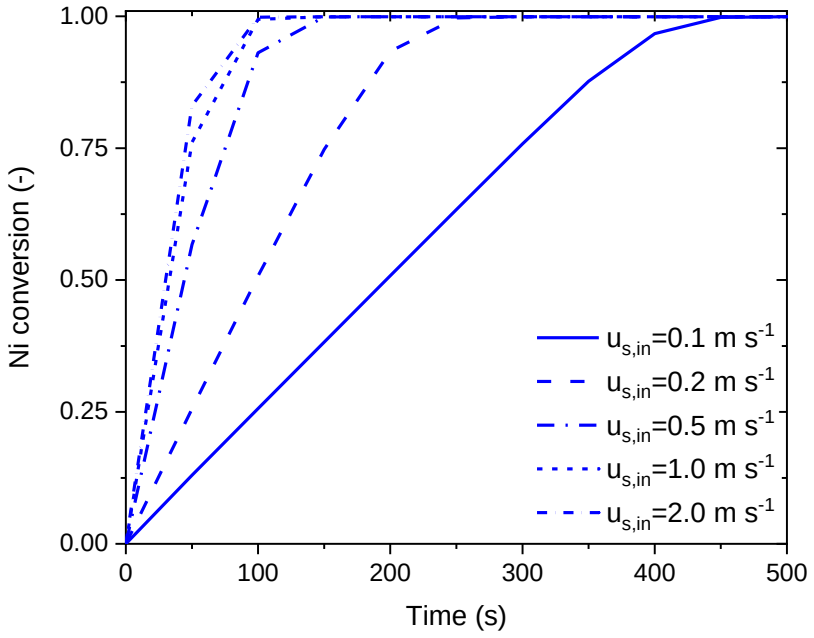

Figure 8.17 Average conversion of nickel to nickel oxide as function of time and inlet velocity. The air inlet conditions were 923 K and 1.5 bar, and the initial bed temperature was 923 K.

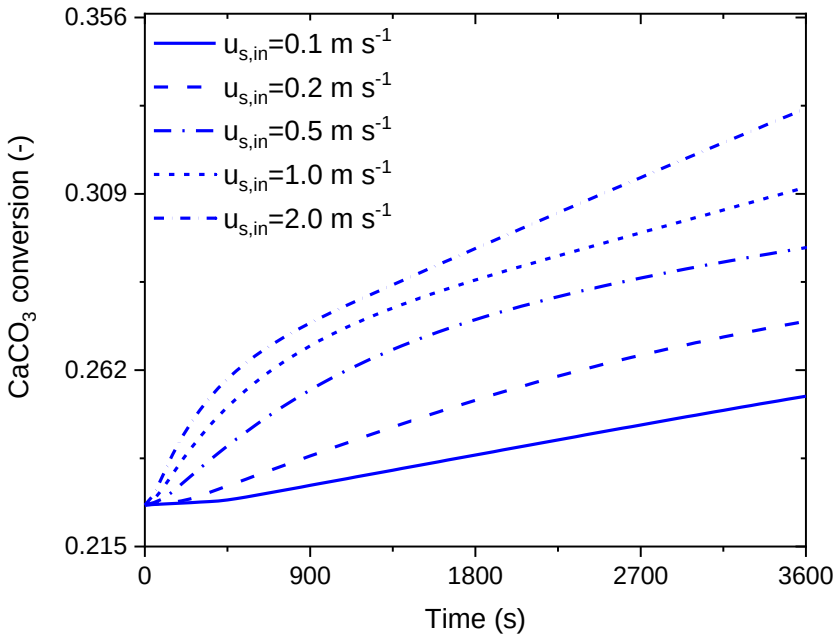

Figure 8.18 Average conversion of calcium carbonate to calcium oxide as function of time and inlet velocity. The air inlet conditions were 923 K and 1.5 bar, and the initial bed temperature was 923 K.

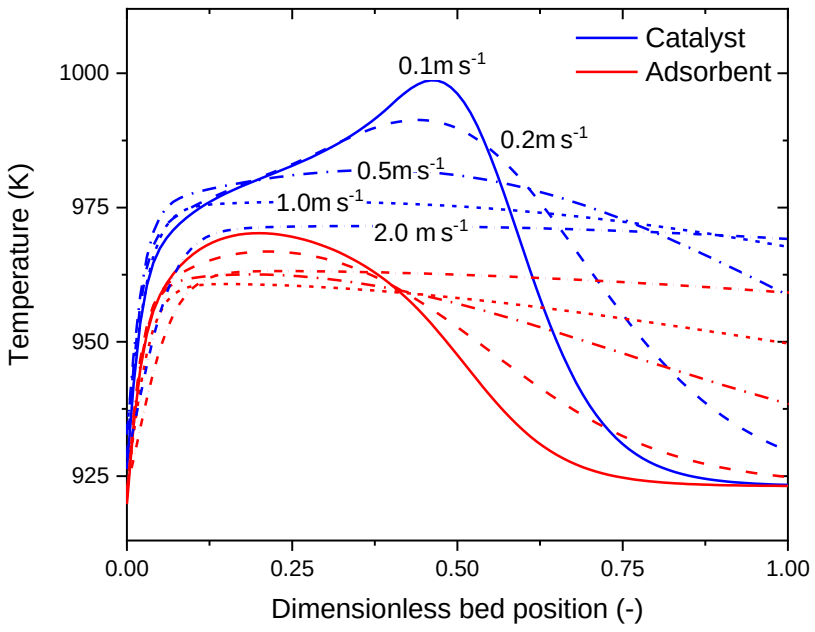

Figure 8.19 Temperature profiles of catalyst and sorbent as function of the bed position and the inlet gas velocity. The profiles are shown at 50% of the time required for the complete re-oxidation of nickel.

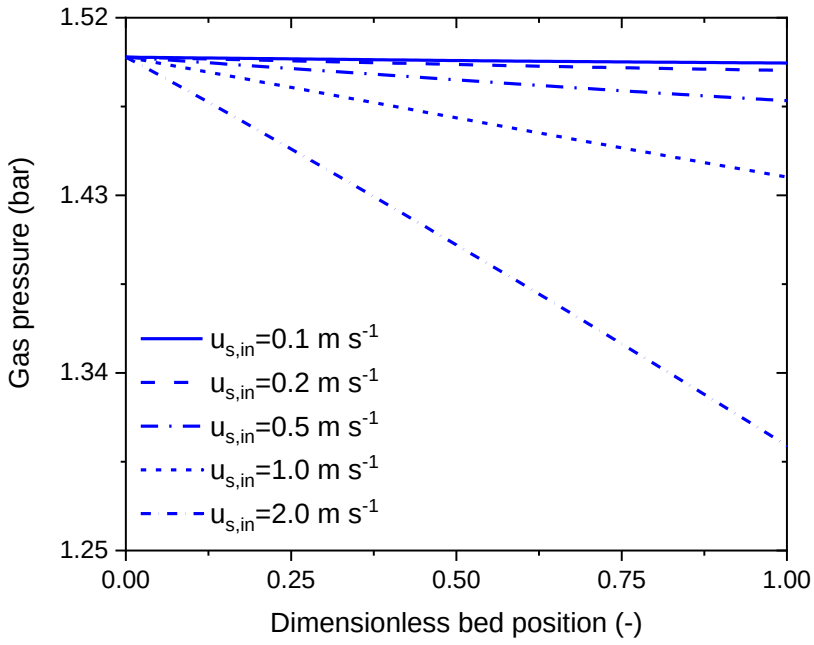

Figure 8.20 Gas pressure profiles as function of the bed position and the inlet gas velocity. The profiles are shown at 50% of the time required for the complete re-oxidation of nickel.

8.5.3.2 Effect of the temperature

The packed bed and air temperature are a key factor to achieve a high performance on the Air Reactor. Several simulations were conducted increasing the temperature of the packing and the air to 1023 K, 1073 K, 1098 K and 1113 K; some simulations at higher initial temperature values were attempted, however, no convergence could be attained for the air velocity selected (1.0 m s^{-1}), due to a very high pressure drop predicted during the initialisation of the problem solution.

The main effect of the temperature on the operation of the Air Reactor relates to the regeneration of the adsorbent. Figure 8.21 Illustrates the profiles of the average conversion of $CaCO_3$ to CaO as a function of time for several air and bed initial temperatures. Clearly, as the temperature increases the conversion of the adsorbent increases, although an incomplete regeneration of the bed is achieved. A maximum regeneration of 63.6% of the bed is obtained when the air and bed temperatures are both set at 1113K. The incomplete conversion predicted by the model is consistent with the equilibrium calculations presented in **Chapter 3**, which indicated a maximum conversion of $CaCO_3$ of 96.7%, provided that the NiO/CaO molar ratio in the packed bed is 0.5 mol NiO/mol CaO; for the current case, the NiO load in the catalyst is 17.95 wt.%, whilst for the adsorbent a content of CaO of 97 wt.% was considered, since the volumetric

fraction of each material in the reactor considered for these simulations is 50v/v%, the NiO/CaO molar ratio is just 0.16 mol NiO/mol CaO, thus indicating that the presence of nickel in the system does not meet the minimum required to generate enough heat of reaction for the calcination of $CaCO_3$.

The predicted $CaCO_3$ conversion results are also in agreement with the experimental data provided by Fernandez and Abanades [178], who conducted experiments to validate the concept of calcinating $CaCO_3$ with the heat of reaction released from the reduction of CuO with CH_4, and achieved a conversion of $CaCO_3$ up to 60% at an initial bed temperature of 1033 K.

Figure 8.22 illustrates the predicted temperature profiles at the catalyst surface and at the adsorbent surface at 50% of the time needed to achieve the complete oxidation of nickel and for various values of air inlet and bed initial temperatures. For initial temperatures up to 1023 K, the adsorbent is heated up and reaches a plateau that moves downstream, however, the plateau temperature is very low in comparison with the equilibrium temperature of $CaCO_3$/CaO at 1.5 bar (ca. 1200 K), thus a very low rate of carbonation is expected under this conditions. When the simulation is run with air and bed temperatures above 1073 K, a temperature drop is observed close to the bed inlet, which is an indication of higher rates of calcination as illustrated in Figure 8.23. After the initial temperature drop, the bed is heated-up and both materials show a temperature increase, owing to the combined effect of heat of oxidation of the nickel being released downstream in the bed and the low calcination rate. Although the adsorbent temperature recovers to values close to the initial bed temperature, the rate of calcination slows down because of the concentration of CO_2 building-up as it is released from the adsorbent. This closes the gap with the CO_2 equilibrium concentration as time passes by, as illustrated in Figure 8.24, thus reducing the driving force for the calcination of the adsorbent.

The calcination of $CaCO_3$ proceeds fast during the first 160 s of the run, since during this time period the oxidation of nickel is ongoing as is illustrated in Figure 8.25, therefore the heat released by this reaction is transferred to the packed bed enhancing the rate of calcination. The effect of decreasing the temperatures of the air and of the bed on the nickel oxidation is to increase the time required to convert the nickel to nickel oxide; as expressed in Equation (2.59), the kinetics of nickel oxidation depends upon the concentration of oxygen; therefore, operating at high temperature slows down the conversion of nickel, since augmenting the bulk gas temperature increases decreases the oxygen concentration, thus the longer time required to convert the nickel in the packed bed. However, the timescale of the oxidation of nickel is too short in comparison with the timescale of the calcination of calcium carbonate, thus the availability of Ni oxidation's heat

of reaction does not meet the demand to calcinate fully the calcium carbonate in the packed bed. Moreover, the rate of calcination after 160 s is slower and is propelled by the sensible heat of the gas being fed to the reactor.

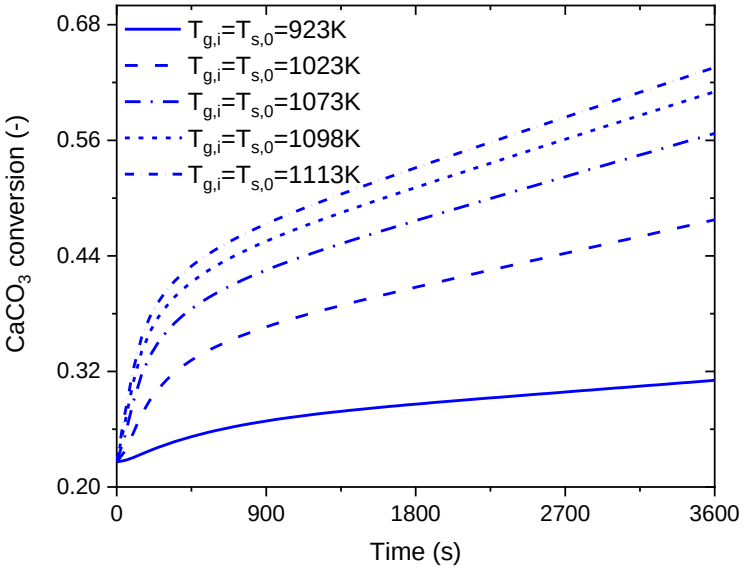

Figure 8.21 Effect of air and bed inlet initial temperatures on the profiles of the average $CaCO_3$ conversion.

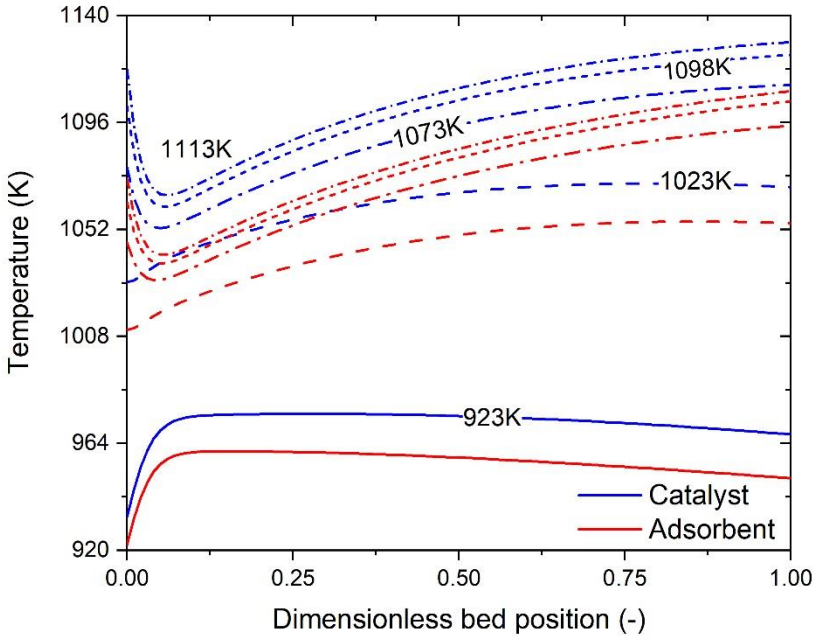

Figure 8.22 Adsorbent and catalyst temperature profiles as function of the bed position for various air and bed initial temperature values. The profiles are shown at 50% of the time required for the complete re-oxidation of nickel.

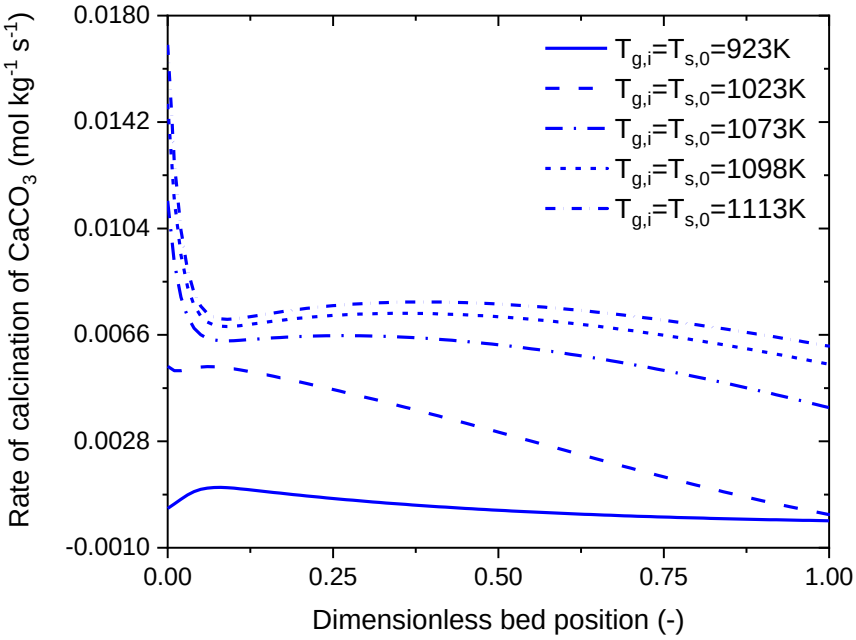

Figure 8.23 Rate of calcination of $CaCO_3$ as function of the bed position for various air and bed initial temperature values. The profiles shown correspond to the temperature of the packings at 50% of the time required for the complete re-oxidation of nickel.

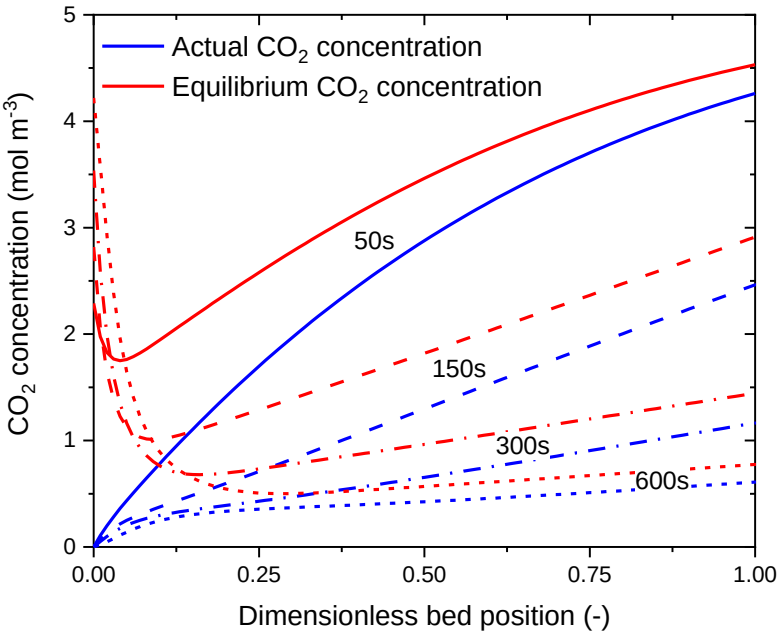

Figure 8.24 Actual and equilibrium concentrations of CO_2 in the Air Reactor predicted for the case of air and bed initial temperatures of 1113K.

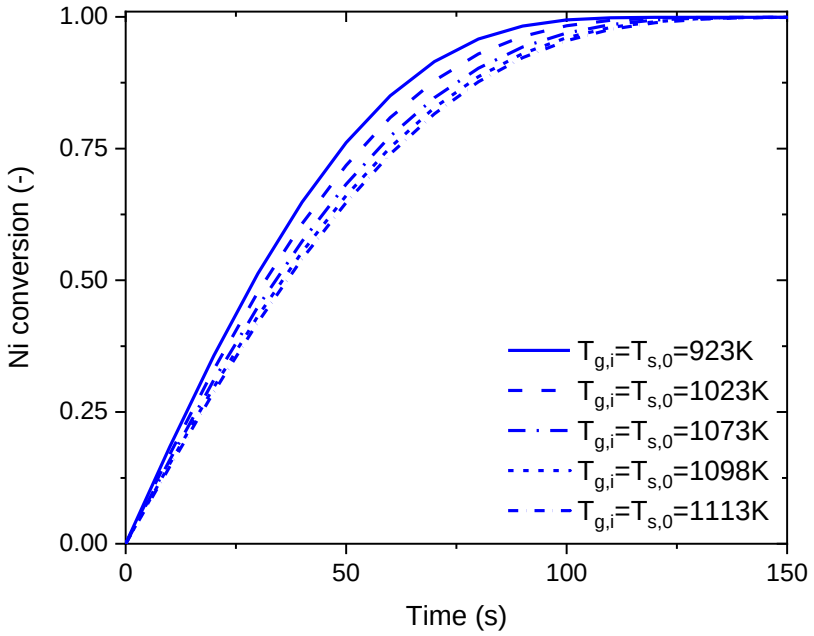

Figure 8.25 Effect of the air and bed initial temperatures on the profiles of the average Ni conversion during the oxidation of nickel.

8.5.3.3 Effect of the initial load of Ni in the reduced catalyst

The results presented in the previous sections suggest that the nickel content typically encountered in commercial catalysts for steam reforming is insufficient to produce the thermal load required by the reactor to attain the complete calcination of the adsorbent. Increasing the nickel content in the catalyst might help reducing the external heat input and obtaining a more cost-effective process, albeit with the penalty of augmenting the time period and gas consumption for the reduction of the steam reforming catalyst in the fuel reactor cycle.

To illustrate the effect of increasing the content of active nickel in the catalyst over the conversion of $CaCO_3$ to CaO, the Air Reactor was simulated with a nickel content of 30 wt.% and 45 wt.%, these values corresponds to an initial load of nickel oxide of 40 wt.% and 60 wt.% which are typical in oxygen carriers for chemical looping combustion, although some studies regarding their application to chemical looping reforming have been conducted [76]. Figure 8.26 is a plot of the average conversion of the bed, which increases from 63.6% for the base case, to 74.3% for the case of nickel load of 45 wt.%; moreover, improvement of the $CaCO_3$ conversion is observed during the stage of fast calcination, attaining a regeneration of 47.2% of the total amount of adsorbent in the bed when the initial content of nickel in the oxygen carrier is 45%, versus 36.1% when the initial nickel content is 14.1w%, i.e. when the oxygen carrier is a typical commercial steam reforming catalyst. Furthermore, the adsorbent conversion is even lower

when considering that the initial state of the adsorbent during the Air Reactor run is that of a partially carbonated particle; for the simulations of this work, the initial value of conversion was estimated at 22.6%, this means that the real conversion of the adsorbent during the fast calcination stage is barely 24.6% when utilising an oxygen carrier with 45 wt.% of nickel, and 13.5% when utilising an oxygen carrier with 14.1 wt.% of nickel.

The effect of increasing of nickel content in the oxygen carrier over its conversion is to augment the time required to complete the oxidation, as illustrated in Figure 8.27. This obviously increases the time during which heat of oxidation is available, which is the reason why the adsorbent conversion is improved during the fast stage of the bed regeneration. Evidently, this also impacts the temperature profile in the bed; as illustrated in Figure 8.28, the higher the initial content of nickel in the oxygen carrier, the higher the temperature of the adsorbent. However, utilising a material with a very high load of nickel (e.g. 45 wt.%) seems to have the disadvantage of promoting some accumulation of heat in the catalyst (oxygen carrier) due to the combined effect of the very fast rate of oxidation (thus the release of heat of reaction) and the limitations for heat transfer imposed by the low transfer area, giving place to the formation of a hot zone in the catalyst that moves down the bed as illustrated in Figure 8.29.

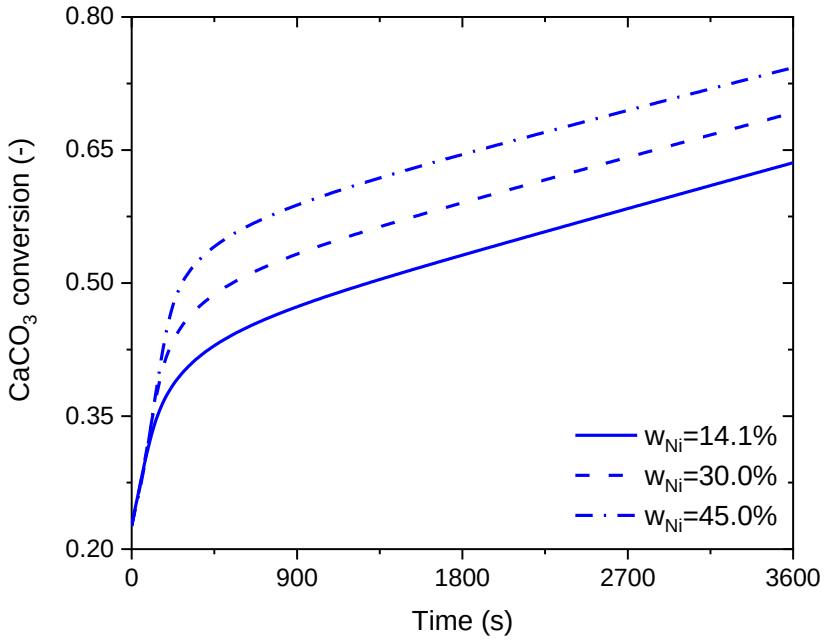

Figure 8.26 Average conversion of $CaCO_3$ to CaO as function of time for three cases of Ni content in the oxygen carrier. The air inlet conditions were 1113K and 1.5 bar, and the initial bed temperature was 1113K.

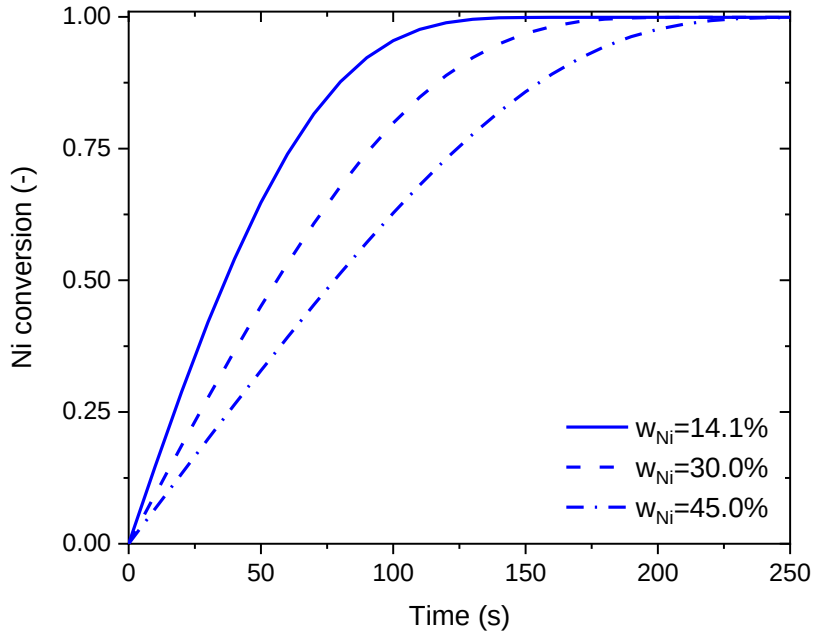

Figure 8.27 Average conversion of Ni to NiO as function of time for three cases of Ni content in the oxygen carrier. The air inlet conditions were 1113K and 1.5 bar, and the initial bed temperature was 1113K.

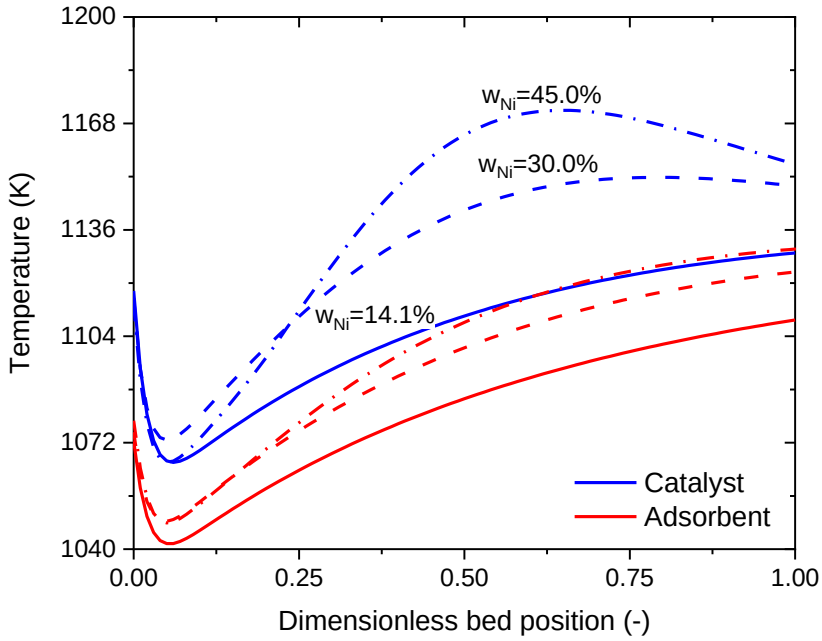

Figure 8.28 Adsorbent and catalyst temperature profiles as function of the bed position for various cases of Ni content in the oxygen carrier. The profiles are shown at 50% of the time required for the complete re-oxidation of nickel.

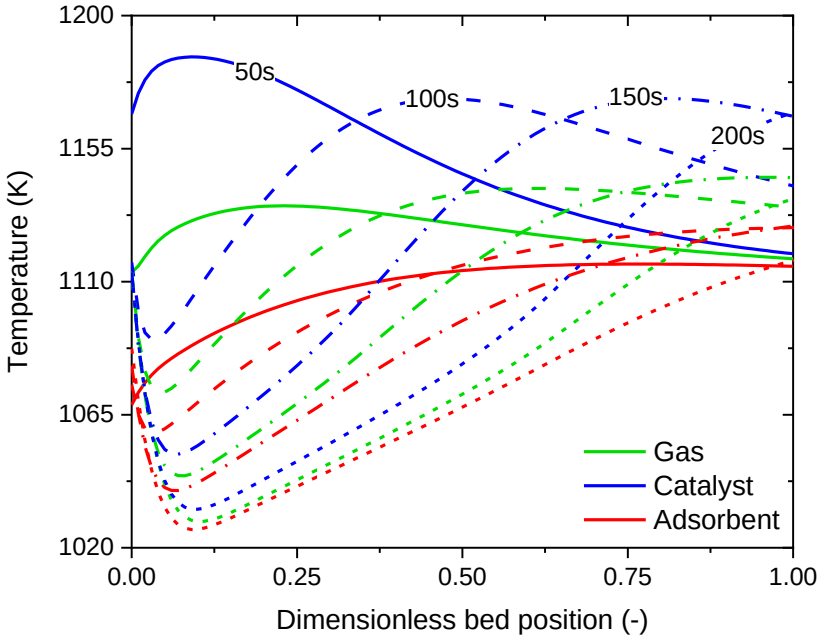

Figure 8.29 Temperature profiles of the bulk gas, catalyst and adsorbent obtained from the simulation of the Air Reactor with an initial nickel content of 45w%.

8.5.3.4 Effect of reducing the concentration of oxidant

The formation of hot zones when operating with oxygen carriers with a high load with nickel can be prevented by controlling the rate of oxidation of nickel. This can be attained by utilising a lean oxidant agent, i.e. by reducing the concentration of oxygen in the gaseous stream utilised for regenerating the materials. Figure 8.30 illustrates the effect of the concentration of oxygen on the temperature profiles of the gas, catalyst and adsorbent at 50% of the time required to oxidise all the nickel in the packed bed. The profiles were obtained by assuming the use of an oxygen carrier with 45 wt.% of nickel. Figure 8.30 shows three consequences of regenerating the bed with a gas containing a low concentration of oxygen; firstly, the initial temperature drop is larger than in the operation with a more concentrated sweep gas, indicating a higher conversion of the adsorbent. Secondly, the gap between the temperature of the catalyst and the adsorbent is reduced. Thirdly, the predicted temperature of the various phases in the reactor with an oxygen concentration of 5 mole% is the lowest among the three cases. The second and third situations are likely due to the heat of reaction from the oxidation of nickel being released at a slower rate, thus preventing the bed to recover to a higher temperature level.

Regarding the regeneration of the materials, reducing the oxygen concentration in the sweep gas augments the time period required for complete oxidation of

nickel as shown in Figure 8.31, this seems to slow down the rate of calcination of $CaCO_3$ as indicated by the slope of the initial fast stage of calcination as can be seen in Figure 8.32. However, slight improvement is predicted in the achieved conversion at the end of the fast calcination period during which the heat of oxidation is transferred to the adsorbent, since the conversion increases from 49% when operating with a concentration 21 mole% of oxygen, to 57.2% when the oxygen concentration is reduced to 5 mole%.

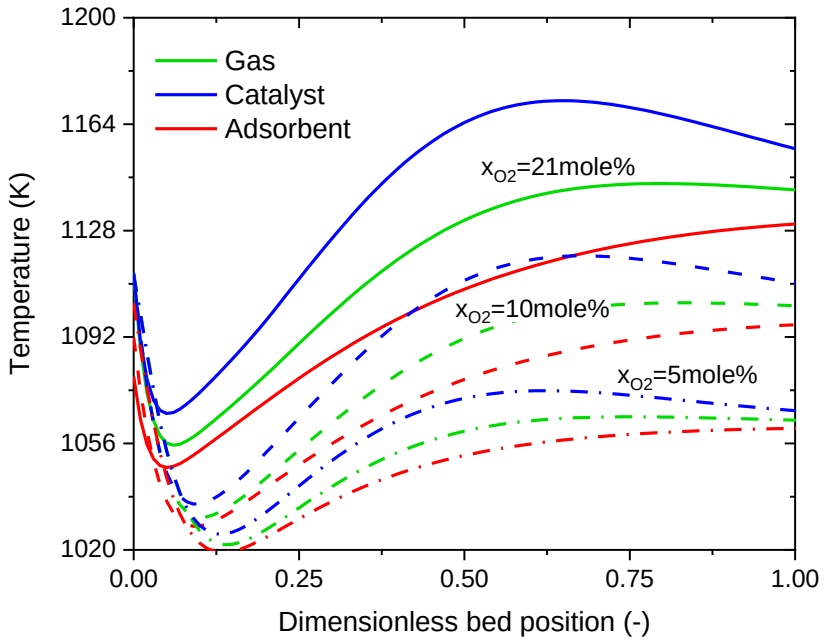

Figure 8.30 Temperature profiles of bulk gas, catalyst and adsorbent for three cases of oxygen concentration in the sweep gas. The profiles are shown at 50% of the time required for the complete re-oxidation of nickel.

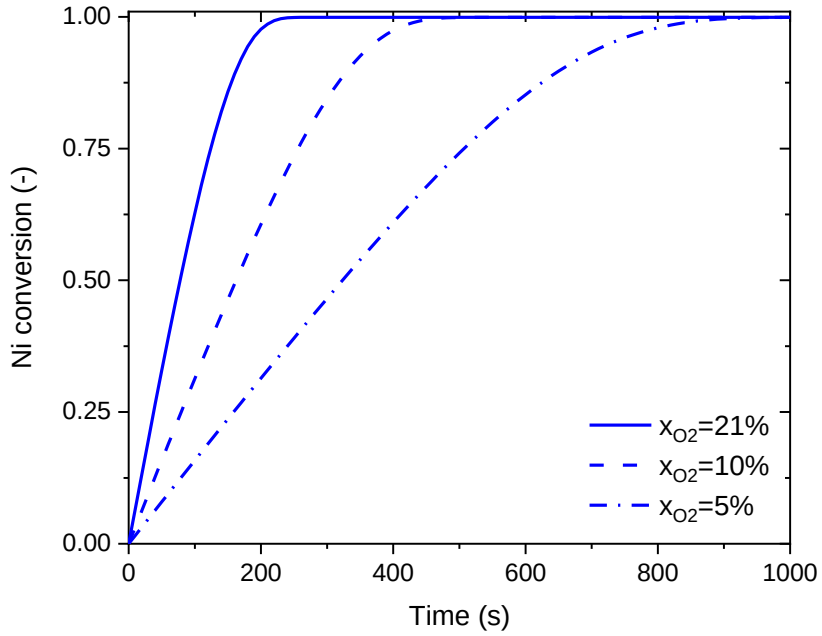

Figure 8.31 Average conversion of Ni to NiO as function of time for three cases of oxygen concentration in the sweep gas. The air inlet conditions were 1113 K and 1.5 bar, and the initial bed temperature was 1113 K.

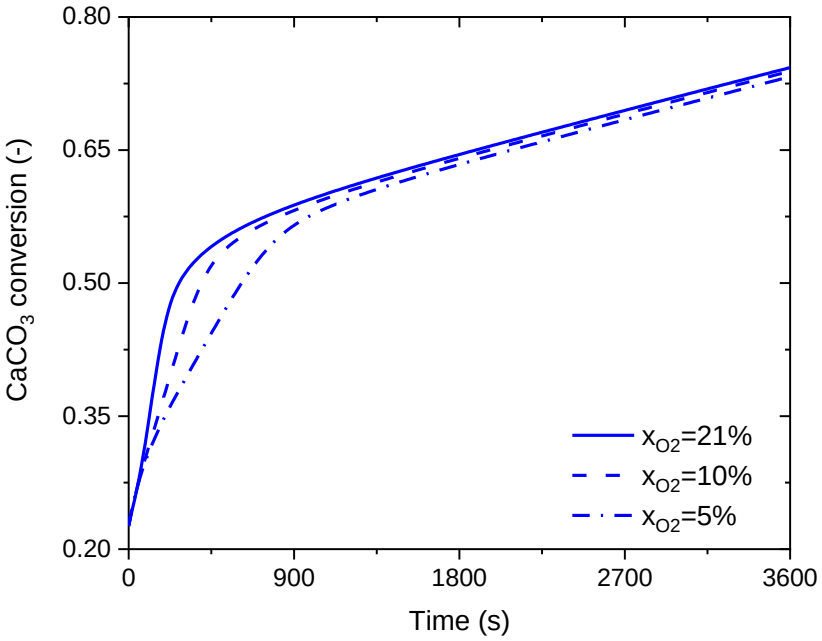

Figure 8.32 Average conversion of CaCO3 to CaO as function of time for three cases of oxygen concentration in the sweep gas. The air inlet conditions were 1113 K and 1.5 bar, and the initial bed temperature was 1113 K.

8.5.3.5 Effect of the adsorbent and catalyst densities

The assessment of the effect of the catalyst and adsorbent properties on the performance of the Fuel Reactor reported in **Chapter 7** indicated that the catalyst density has little effect on the reactor performance, whereas reducing the adsorbent density improves it. In the Air Reactor both densities seem to play a key role according to Equation (8.31), therefore, simulations were conducted varying both densities by ±10%. No significant effect of varying the density of the catalyst and the adsorbent over the conversion of $CaCO_3$ to CaO is observed (Figure 8.33), in fact, during the stage of fast calcination a minimal departure from the base case profile is observed as the end of the stage is approached. The variation of the catalyst density does affect, albeit with little impact, the second stage of calcination. It is observed that by augmenting the catalyst density by 10%, the conversion profile exhibits an increase and the final conversion of $CaCO_3$ is augmented slightly from 63.6% to 64.5%. Conversely, decreasing the catalyst density by 10% would reduce the final conversion from 63.6% to 62.6%. The effect of varying the density of the adsorbent is even less significant than varying the density of the catalyst. An increase of adsorbent temperature by 10% will reduce the final conversion from 63.6% to 63.1%; contrarily, a decrease of the adsorbent density by 10% will increase the final $CaCO_3$ conversion from 63.6% to 64.0%. Regarding the conversion of Ni to NiO, only the variation of catalyst density effects the profile as illustrated in Figure 8.34.

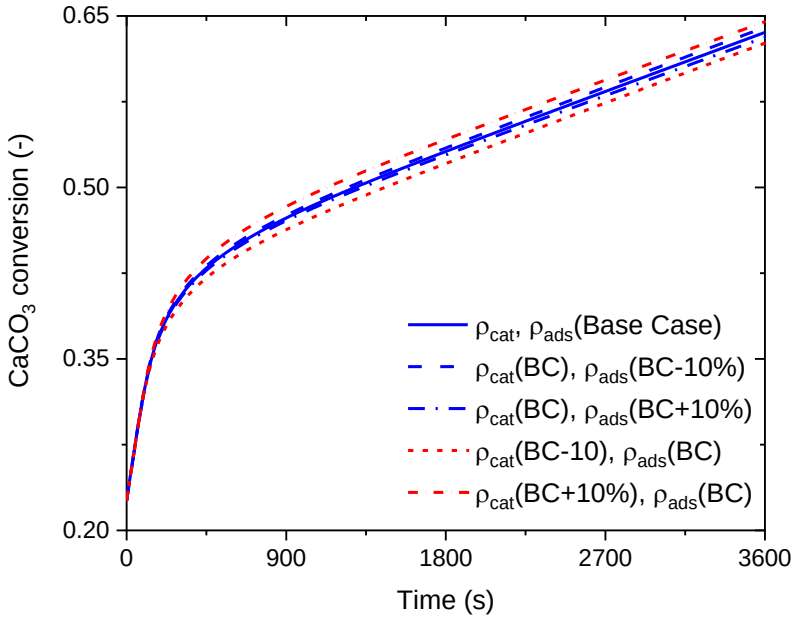

Figure 8.33 Effect of the varying the catalyst and adsorbent densities by ±10% over the conversion of $CaCO_3$ to CaO. The simulation considered an initial load of Ni of 14.1 wt.%, gas temperature and initial bed temperature of 1113 K and inlet gas velocity of 1.0 m s^{-1}.

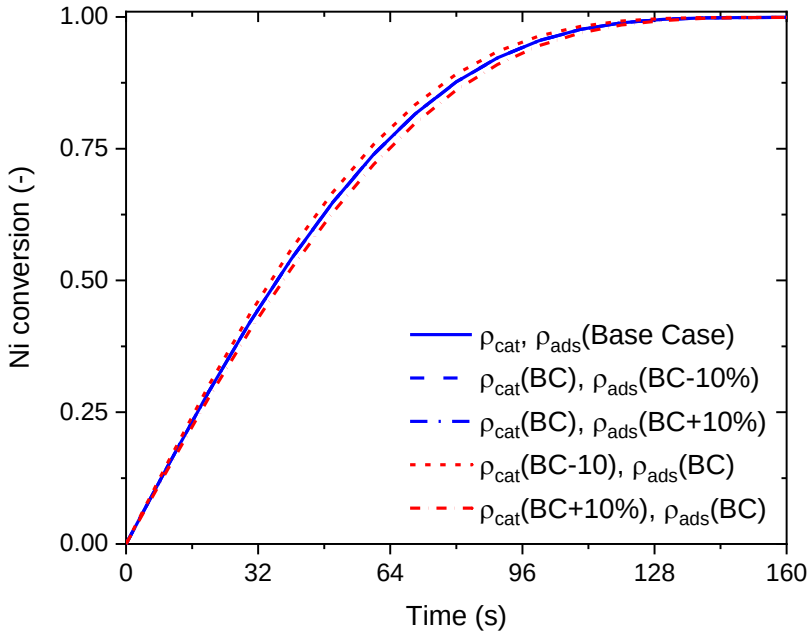

Figure 8.34 Effect of varying the catalyst and adsorbent densities by ±10% over the conversion of Ni to NiO. The simulation considered an initial load of Ni of 14.1 wt.%, gas temperature and initial bed temperature of 1113 K and inlet gas velocity of 1.0 m s^{-1}.

8.5.3.6 What if the bed contains traces of hydrogen?

The past simulations considered a clean bed in which the only reactants were the solid phases (i.e. nickel in the catalyst and calcium carbonate in the adsorbent), and oxygen. After the fuel reactor step, it is likely that the packed bed undergoes a pre-treatment with steam or other inert gas to eliminate undesired materials deposited in the catalyst or to condition the temperature of the packing to the required level for the Air Reactor cycle to run; this operation might be detrimental for the process economics since a sweeping gas at a minimum temperature equal to that of the fuel reactor would be needed to avoid wasting the heat stored in the packing at the end of the cycle. Nevertheless, if the aforementioned operation were to be conducted, the gases stored in the pores of the packings and the voids of the packed bed will be stripped by the sweeping gas, although it is probable that some amounts of hydrogen remain adsorbed in the surface of the nickel as pointed out by Hatcher et al. [202]. Hence, as the air is fed to the reactor, a fast reaction between the oxygen and the adsorbed hydrogen occurs according to Equation (8.32), forming of a thermal wave whose maximum temperature depends upon the amount of hydrogen available and the concentration of oxygen in the air.

$$H_{2(g)} + {}^{1}/_{2}\, O_{2(g)} \leftrightarrows H_2O_{(g)} \quad \Delta H^0 = -241.8\ kJ\ mol_{H_2}^{-1} \tag{8.32}$$

If the reactor is packed with catalyst only, then the latter situation poses a number of operational and safety risks, e.g. the rise of temperature to levels above the melting point of nickel that can cause agglomeration, or the risk of explosion due to the highly reactive atmosphere within the reactor. However, in the context of the Air Reactor, the calcination of $CaCO_3$ occurring simultaneously with the combustion of hydrogen/oxidation of nickel, might have a dampening effect on the temperature rise, whilst taking advantage of the increased availability of heat of reactions due to the combustion of hydrogen and the oxidation of nickel.

Following [202], the rate of disappearance of hydrogen in the reactor is infinite and depends upon the concentration of oxygen in the bulk gas, thus:

$$\frac{\partial \bar{C}_{H_2}}{\partial t} = -\frac{\beta_1 a_{S_1} C_{O_2}}{\rho_{b_1}} \tag{8.33}$$

where $\bar{C}_{H_2}$ represents the moles of adsorbed hydrogen on the nickel surface per unit of mass of catalyst. The initial condition of Equation (8.34) corresponds to a concentration of H_2 adsorbed in the surface of the catalyst expressed as:

$$\bar{C}_{H_2}(0, z) = \bar{C}^0_{H_2} \tag{8.34}$$

The results presented in this section were obtained from simulations of the Air Reactor with the parameters of Table 8.7, the value of the initial concentration of hydrogen of 0.93 mol kg^{-1} is taken from [202] and belongs to a reforming catalyst with a content of nickel slightly than the catalyst used as the base case for these studies (21 wt.% in the reference against 18.0 wt.% in the base case).

Figure 8.35 and Figure 8.36 are plots of the temperature profiles of the gas, catalyst and adsorbent obtained by assuming initial bed and gas temperatures of 923K and 1073K, respectively, and a concentration of oxygen of 1.0 mole% in both cases. The differences in the shape of the thermal fronts are evident. When the initial temperature of the packing materials and the inlet gas temperature are 923 K (Figure 8.35), the simulation of the Air Reactor predicts the development of a thermal front that increases the temperature of the catalyst by more than 100K and that of the adsorbent by more than 85 K; these increments imply that the temperature of the catalyst reach values in the range 1034–1050 K, whereas the adsorbent temperature reach maximum values in the range 1001–1008 K. The temperatures attained by the adsorbent are well below the equilibrium temperature of $CaCO_3$ decomposition and therefore a very low conversion is predicted (Figure 8.37). It is worth noting in Figure 8.35 the slight drop of

temperature in the rear edge of the thermal front at 1500 s and 2000 s, which indicates the dominance of the endothermic calcination process. Conversely, the leading edge of the front denote a higher temperature of the different phases present in the reactor, this behaviour seems to be caused by the possible the re-carbonation of CaO observed in the leading front of the conversion profiles in Figure 8.37 which drop below the initial value of the adsorbent conversion; this suggest that the concentration of CO_2 in the bulk gas builds up above the equilibrium concentration (Figure 8.38), thus reversing the calcination process and increasing the system energy due to the release of heat of reaction of carbonation which adds to the heat of combustion of H_2 and the heat of oxidation of Ni. The maximum average $CaCO_3$ conversion attained in this scenario is 36.8% which is higher than that obtained when the presence of hydrogen is not considered.

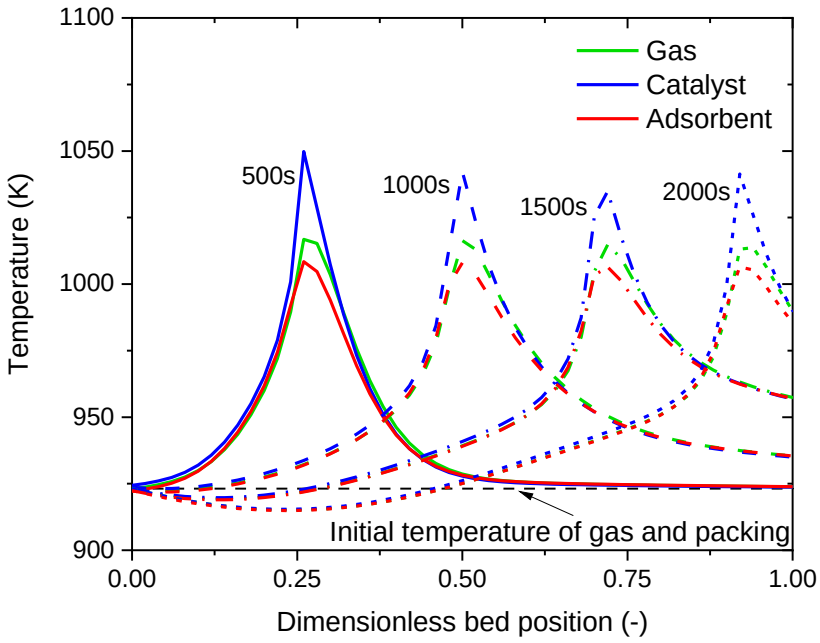

Figure 8.35 Temperature profiles of the sweep gas, the catalyst and the adsorbent at various times during the period of combustion of H_2; the sweep gas contains 1 mol% of O_2 and the balance of N_2 and is fed at 923 K. The initial bed temperature is 923 K.

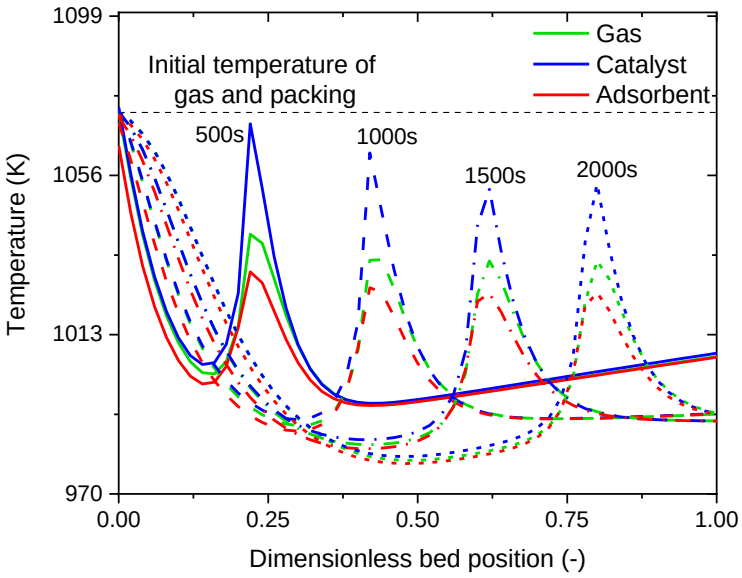

Figure 8.36 Temperature profiles of the sweep gas, the catalyst and the adsorbent at various times during the period of combustion of H_2; the sweep gas contains 1 mol% of O_2 and the balance of N_2 and is fed at 1073 K. The initial bed temperature is 1073 K.

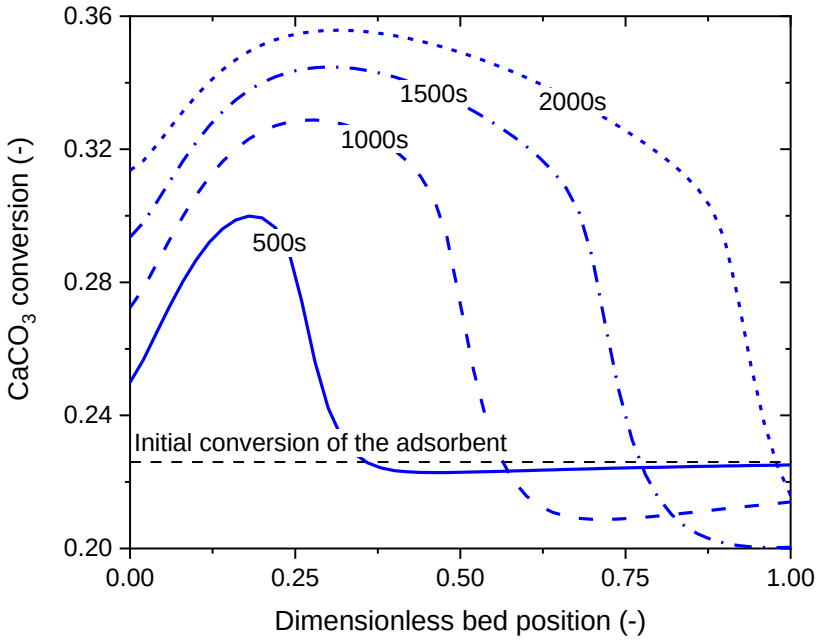

Figure 8.37 Conversion profiles of $CaCO_3$ to CaO during the period of combustion of H_2; the sweep gas contains 1 mol% of O_2 and the balance of N_2 and is fed at 923 K. The initial bed temperature is 923 K.

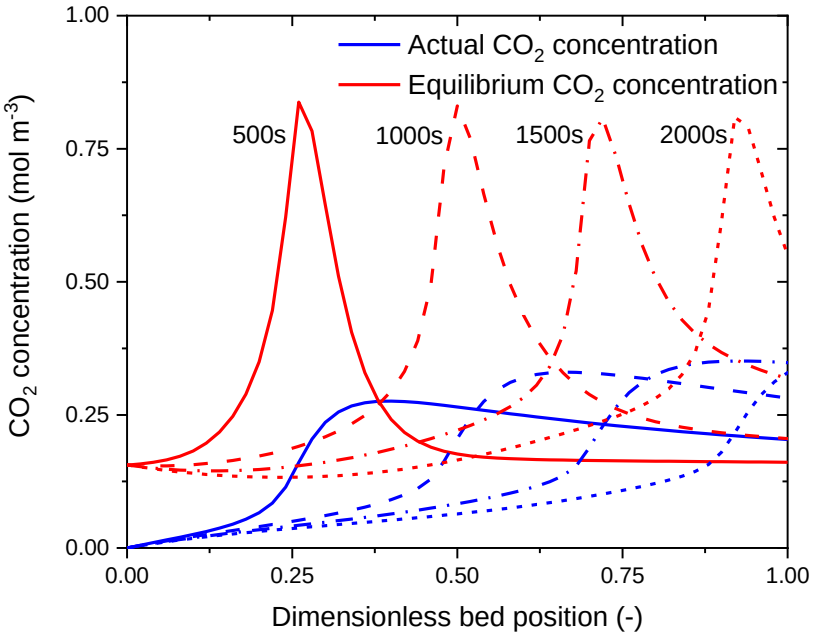

Figure 8.38 Actual and equilibrium concentration of CO_2 at various times during the period of combustion of H_2; the sweep gas contains 1 mol% of O_2 and the balance of N_2 and is fed at 923 K. The initial bed temperature is 923 K.

The increase of the oxidant agent inlet temperature and the initial bed temperature to 1073 K naturally favours the calcination of $CaCO_3$ since the initial energy content of the system is higher. Figure 8.36 shows the temperature profiles of the bulk gas, catalyst and adsorbent when the packing and gas inlet temperatures are set up at 1073 K. The observed initial temperature drop denotes the high initial rate of calcination of the adsorbent, this process consumes a significant amount of energy and cools down the system below the temperature base line. The effect of the higher initial temperature on the shape of the thermal front is noticeable, forming a narrower region than that obtained when the system's initial temperature is 923 K; moreover, the thermal front velocity is slower at 1073 K than at 923 K, presumably due to the lower oxygen concentration in the reactor, since it affects the rates of both the hydrogen combustion and nickel oxidation.

In this scenario only 97.8% of the nickel in the packed bed reactor is re-oxidised, whereas 62.9% of the calcium carbonate is calcinated. The latter is an improvement in comparison to the 56.7% of adsorbent regenerated when starting from the same initial temperature but no hydrogen is considered to be adsorbed in the packed bed. The increase in conversion of the adsorbent owes to the higher temperature reached by the adsorbent as shown in Figure 8.35, which despite the initial temperature drop, recovers up to values in the range 1024 – 1030 K.

This sustains the adsorbent conversion albeit at a lower rate. Moreover, the oxygen reacts first with hydrogen during the first 2000 seconds of the simulation, which is the period of time required to consume the major part the hydrogen available in the packed bed (Figure 8.39). Up to this point, the nickel in the packed has been partially oxidised as illustrated in Figure 8.40. Hence, from this moment onwards, the calcination of $CaCO_3$ is sustained by a combination of the gas entering the system at high temperature and the availability of heat of reaction of the oxidation of nickel. The presence of hydrogen on the nickel's surface affects the pattern of consumption of oxygen, forming two mass transfer zones of different length as shown in Figure 8.41.

The conversion profile of the adsorbent exhibits two mass transfer zones (Figure 8.42); the first mass zone is formed due to the increase of the adsorbent temperature owing to the exothermic combustion of hydrogen and the oxidation of nickel, this is confirmed in Figure 8.43 which reveal that the position of the increase of CO_2 concentration coincides with the position in which a peak of the equilibrium concentration of CO_2 is formed. This peak corresponds with the position of the thermal front since the equilibrium concentration is a function of the adsorbent temperature. The second transfer zone seems to be propelled by the gas being fed at higher temperature which heats-up the bed promoting the calcination of $CaCO_3$.

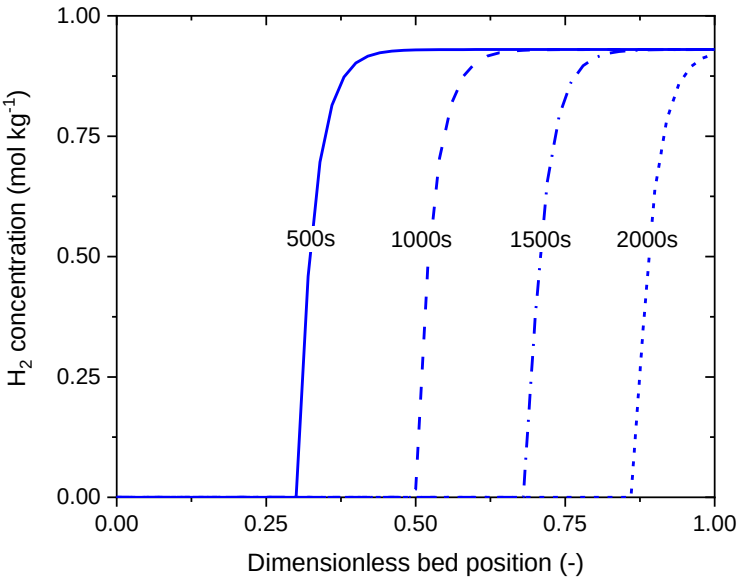

Figure 8.39 Hydrogen profiles in the reactor at various times. The sweep gas contains 1 mol% of O_2 and the balance of N_2 and is fed at 1073 K. The initial bed temperature is 1073 K.

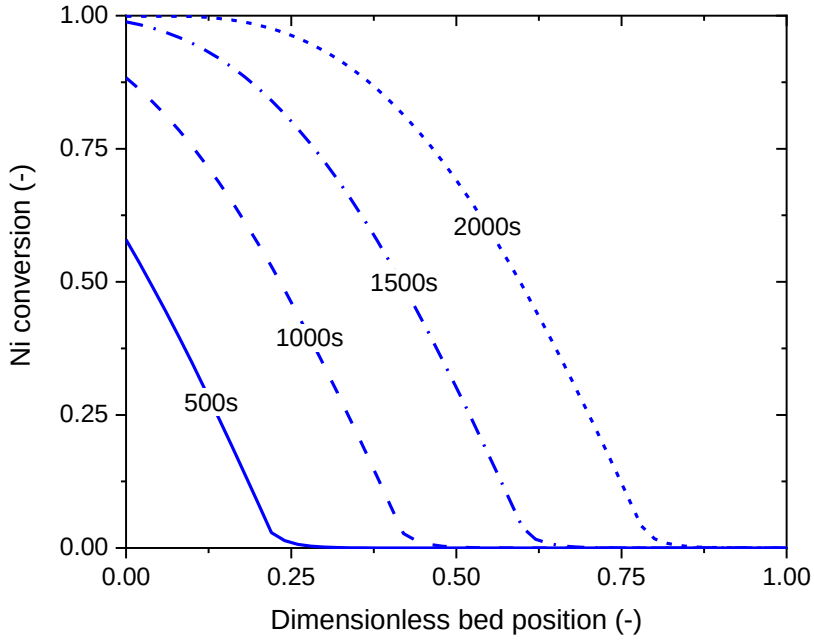

Figure 8.40 Conversion profiles of Ni to NiO during the period of combustion of H_2; the sweep gas contains 1 mol% of O_2 and the balance of N_2 and is fed at 1073 K. The initial bed temperature is 1073 K.

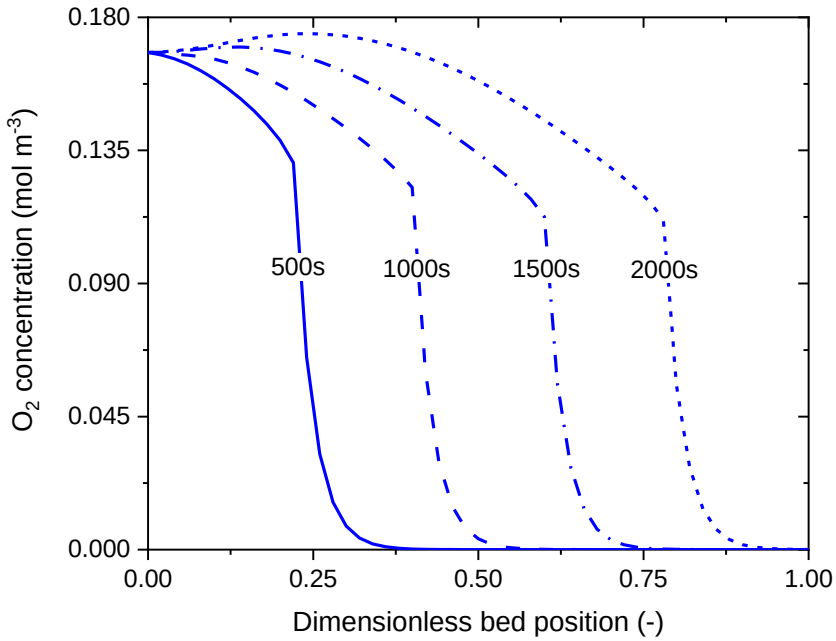

Figure 8.41 Oxygen concentration profiles in the reactor at various times during the period of combustion of H_2; the sweep gas contains 1 mol% of O_2 and the balance of N_2 and is fed at 1073 K. The initial bed temperature is 1073 K.

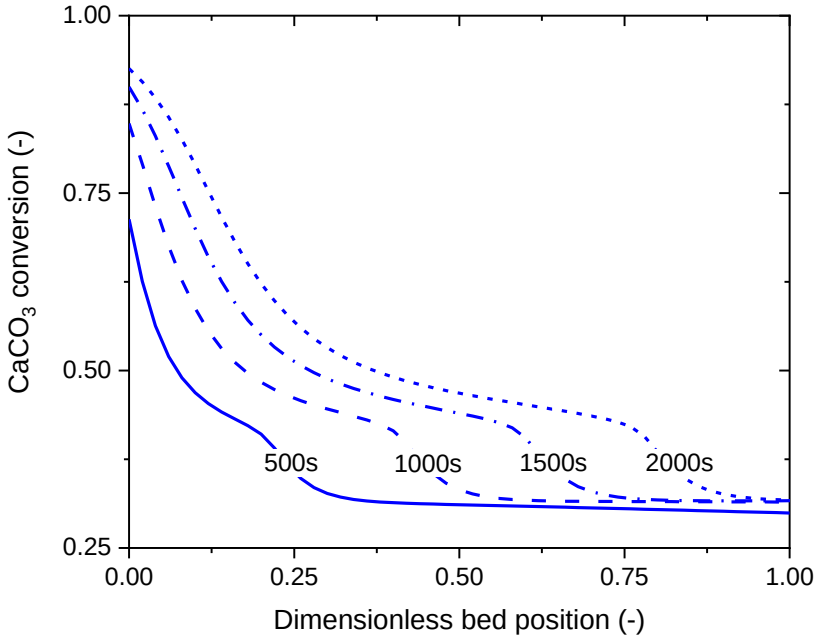

Figure 8.42 Conversion profiles of $CaCO_3$ to CaO during the period of combustion of H_2; the sweep gas contains 1 mole% of O_2 and the balance of N_2 and is fed at 1073 K. The initial bed temperature is 1073 K.

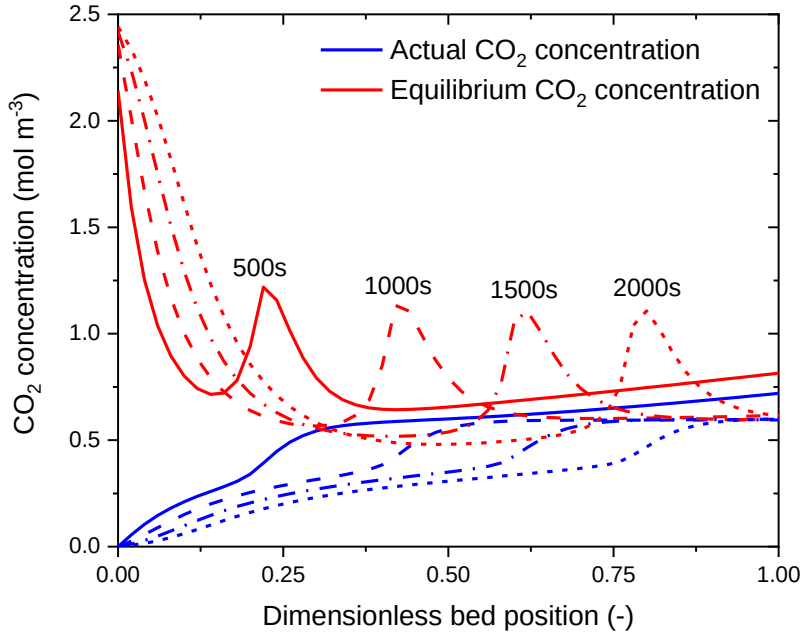

Figure 8.43 CO_2 actual and equilibrium concentration profiles during the period of combustion of H_2; the sweep gas contains 1 mol% of O_2 and the balance of N_2 and is fed at 1073 K. The initial bed temperature is 1073 K.

Other simulations were performed considering the effect of the increase of the mole fraction of oxygen in the sweep gas, and the effect of increasing and

decreasing the initial mass concentration of hydrogen adsorbed in the packed bed. The variation of the oxygen content in the sweep gas affects the time required to consume the available hydrogen in the packed bed and to complete the oxidation of nickel. Table 8.8 summarises indicators regarding the conversion of $CaCO_3$, the time required to exhaust the available hydrogen and nickel in the bed, the catalyst temperature and the temperature difference between the catalyst and the adsorbent; the data reveals that as the concentration of oxygen in the oxidant agent is increased, less $CaCO_3$ is being converted during the time period in which the hydrogen combustion and the nickel oxidation provide energy to heat up the packed bed. This suggest a poor transfer of the available heat of reaction from the catalyst to the adsorbent, which is also indicated by the increasing temperature differences and the overheating of the catalyst due to the violent reaction between oxygen and hydrogen, producing a temperature rise in the catalyst as high as 1225 K; this temperature is well below the melting point of the catalyst materials and the possibility of agglomeration might be low, however, it might surpass the recommended maximum operating temperature for certain commercial steam reforming catalysts, thus it becomes critical to control the temperature rise of the catalyst, in order to maximise its lifetime and that of the reacting system.

The trend followed by the conversion of $CaCO_3$ is also noticeable, when considering only the time period during which the packed bed is heated by the heat of reaction of oxidation of hydrogen and nickel. The conversion of $CaCO_3$ drops from 62.9% down to 47.1% as the content of oxygen in the gas increases. Conversely, when considering the total simulation time (3600 s), the conversion of $CaCO_3$ increases from 62.9% to 65.4%. Nevertheless, the need to supply high temperature gas for the whole period of time required to attain the maximum achievable conversion of the adsorbent represents a drawback for the economy of the process, since the heat to condition the sweep gas will need to be imported from burning a fuel or recovered from waste heat sources. However, the Air Reactor operation is limited structurally by the heat transfer area and by the thermodynamic equilibrium of the decomposition of $CaCO_3$, hence will require additional external heating to complete the conversion of the adsorbent. On the other hand, it is relevant to recall that the product stream will contain a mixture of N_2, CO_2, O_2 and steam, posing challenges for the optimal design of downstream units, particularly where condensate water is formed, since the presence of CO_2 and condensate promotes corrosion [203].

Figure 8.44, Figure 8.45, Figure 8.46 and Figure 8.47 are plots of the hydrogen profiles, the nickel conversion profile, the $CaCO_3$ conversion profile and the temperature of profiles of the gas, the catalyst and the adsorbent, for the

simulation case with an oxygen concentration of 5.0 mol%. The similarity with the profiles obtained with an oxygen concentration of 1.0 mol% presented earlier is evident, with the main difference being the shorter time required for the reaction fronts to travel through the bed. Note the changes in the temperature profiles, which now exhibit larger differences between the catalyst and adsorbent temperatures.

Table 8.8 Effect of the oxygen concentration over the conversion of $CaCO_3$, the times required for complete conversion of hydrogen and nickel, the catalyst temperature and the temperature difference between the catalyst and the adsorbent.

Concentration of O_2 (mole%)	Conversion of $CaCO_3$[1] (%)	Conversion of $CaCO_3$[2] (%)	Time to convert 100% of H_2 (s)	Time to convert 100% of Ni (s)	Max. temp. difference $T_{cat} - T_{ads}$ (K)	Max. catalyst temp. (K)
1.0	62.9	62.9	2590	>3600	40.0	1096.7
2.0	57.4	63.9	1300	2290	72.2	1123.7
5.0	50.8	64.9	510	930	112.7	1187.1
10.0	47.1	65.4	260	480	126.4	1225.1

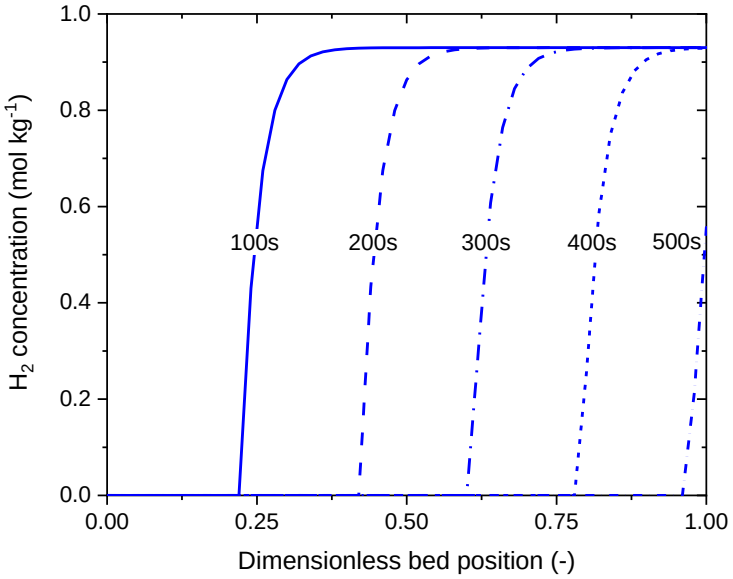

Figure 8.44 Hydrogen profiles in the reactor at various times. The sweep gas contains 5 mol% of O_2 and the balance of N_2 and is fed at 1073 K. The initial bed temperature is 1073 K.

[1] Estimated at the end of the period of oxidation of hydrogen and nickel.
[2] Estimated at the end of the simulation run.

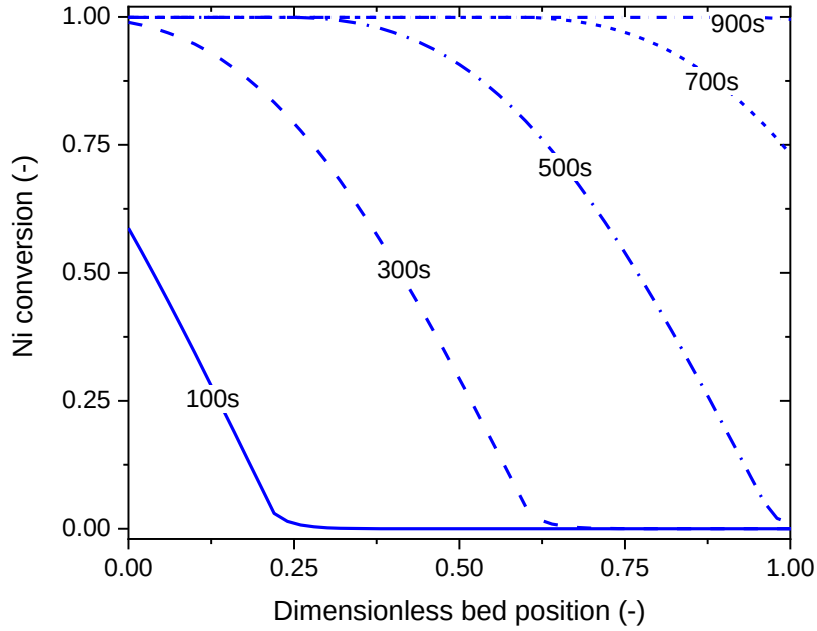

Figure 8.45 Conversion profiles of Ni to NiO during the period of combustion of H_2; the sweep gas contains 5 mole% of O_2 and the balance of N_2 and is fed at 1073 K. The initial bed temperature is 1073 K.

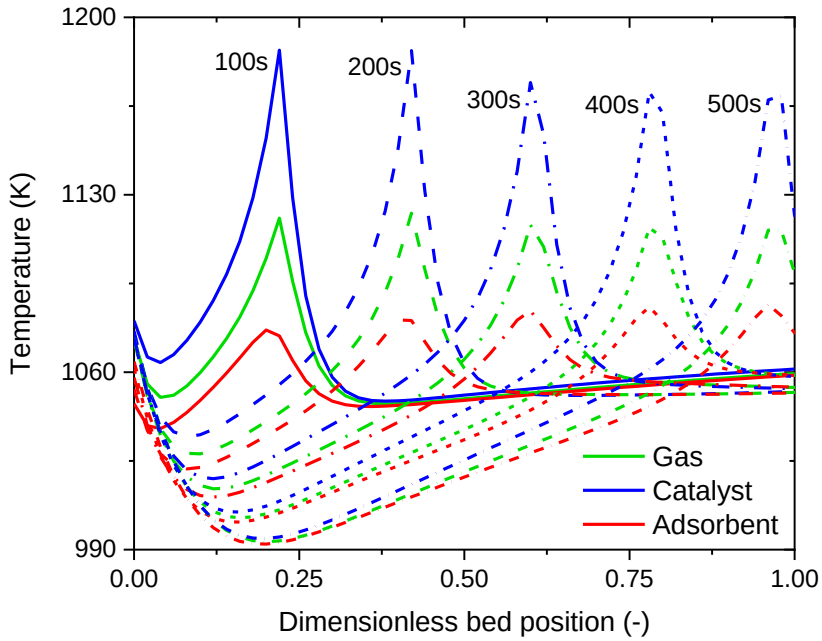

Figure 8.46 Temperature profiles of the sweep gas, the catalyst and the adsorbent at various times during the period of combustion of H_2; the sweep gas contains 5 mol% of O_2 and the balance of N_2 and is fed at 1073 K. The initial bed temperature is 1073 K.

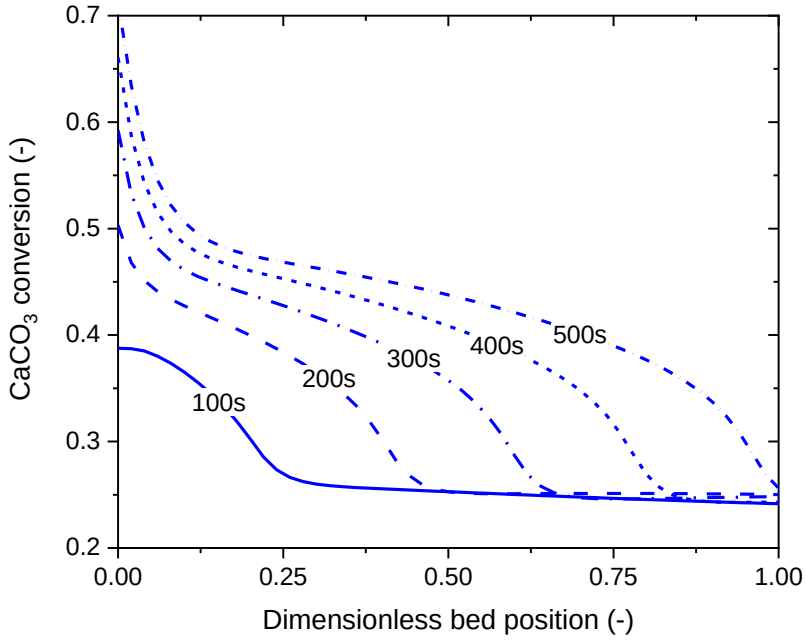

Figure 8.47 Conversion profiles of $CaCO_3$ to CaO during the period of combustion of H_2 with oxidant agent containing 5 mol% of O_2 and the balance of N2; the gas is fed at 1073 K. The initial bed temperature is 1073 K.

A similar pattern is observed when the amount of H_2 adsorbed in the packed bed varies. Table 8.9 summarises the same list of indicators previously presented in Table 8.8 for three cases of hydrogen concentration. A concentration of O_2 of 5.0 mole% was assumed for the simulations. As expected, if the H_2 concentration in the bed increases, the conversion of $CaCO_3$ increases, but so does the catalyst temperature and the temperature difference between catalyst and adsorbent. The temperature profiles for the case of an initial concentration of H_2 of 0.46 mol kg^{-1} adsorbed in the catalyst are illustrated in Figure 8.48 and the corresponding profiles for the case of an of the initial concentration of H_2 to 1.86 mol kg^{-1} adsorbed in the catalyst are illustrated in Figure 8.49. Higher temperatures are obtained in the latter case. It is also interesting to note how the shape of the profiles change, broader profiles are obtained with lower H_2 concentration, whereas as this parameter increases, the temperature profiles become sharper; this suggests the need of design internal devices to improve the mixing of the gas stream and remove the excess of heat from the catalyst more efficiently.

Table 8.9 Effect of the hydrogen concentration over the conversion of $CaCO_3$, the times required for complete conversion of hydrogen and nickel, the catalyst temperature and the temperature difference between the catalyst and the adsorbent.

Concentration of H_2 (mol kg^{-1})	Conversion of $CaCO_3$[3] (%)	Conversion of $CaCO_3$[4] (%)	Time to convert 100% of H_2 (s)	Time to convert 100% of Ni (s)	Max. temp. difference $T_{cat} - T_{ads}$ (K)	Max. catalyst temp. (K)
0.47	45.1	60.8	300	750	64.0	1137.5
0.93	50.8	64.9	510	930	112.7	1187.1
1.86	56.9	72.6	900	1280	162.0	1257.2

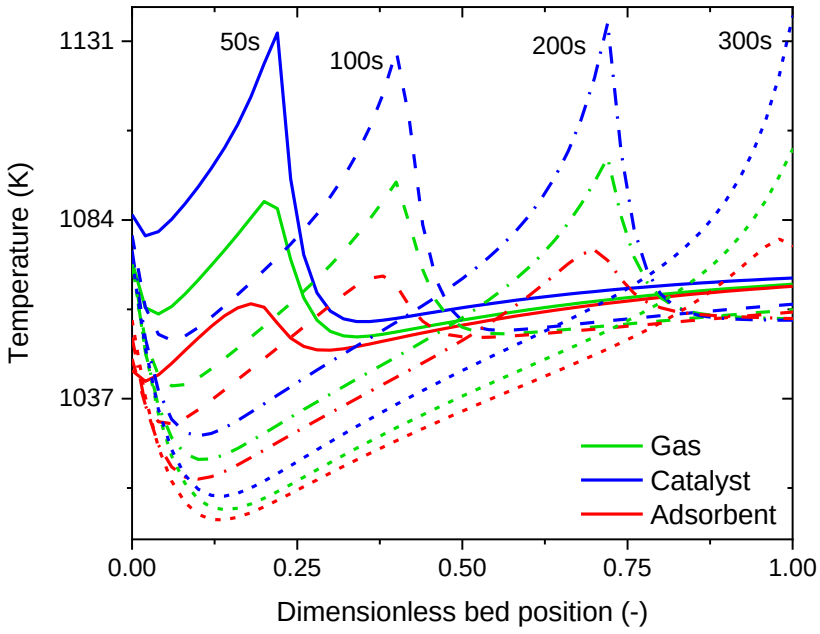

Figure 8.48 Temperature profiles of the bulk gas, the catalyst and the adsorbent at various times during the period of combustion of H_2; the bed has an initial concentration of H_2 of 0.47 mol kg-cat-1. The initial bed temperature is 1073 K.

[3] Estimated at the end of the period of oxidation of hydrogen and nickel.
[4] Estimated at the end of the simulation run.

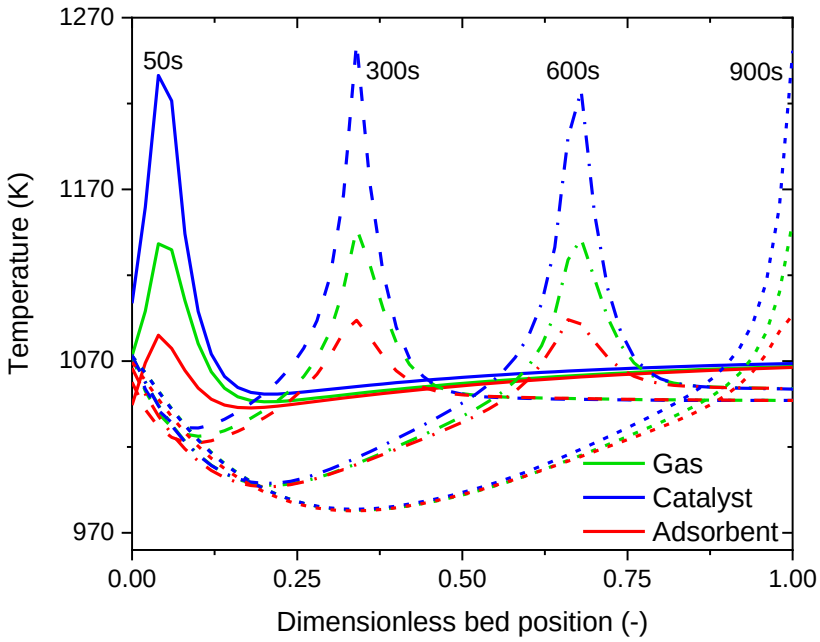

Figure 8.49 Temperature profiles of the gas, the catalyst and the adsorbent at various times during the period of combustion of H_2; the bed has an initial concentration of H_2 of 1.86 mol kg-cat-1. The initial bed temperature is 1073 K.

8.6 Concluding remarks

In this chapter, a transient heterogeneous model of a reactor for regeneration of the oxygen transfer material and the adsorbent known as the Air Reactor cycle of the Sorption Enhanced Chemical Looping Steam Reforming was developed. Similarly to the Fuel Reactor model, the development considered separate equations for the catalyst (or oxygen transfer material), the adsorbent and the bulk gas, and represented the intra-pellet resistances by means of an adjustable effectiveness factor. Moreover, the base case model considered the reactor as an ideal plug flow, but the axial dispersion effects were also assessed.

The various models produced were validated against experimental data gathered from the open literature that included temperature profiles measured at different positions within the reactor. The models' output reported an accuracy in the prediction of the temperature profiles within 5% for all the variants of the model. Whereas no version of the model was capable of reproducing with accuracy the profile of the CO_2 desorbed and exhibited very large errors in the range 390.9% to 812.5%. The misrepresentation of this variable is deemed to be related to inaccurate simulation inputs of various parameters that either were not available in the published paper or were estimated or assumed. Another source of error relates to the uncertainty carried by the kinetic models of calcination utilised to represent the system. Therefore, the model output was accepted albeit with a high degree of error, being the heterogeneous plug flow model accounting for axial dispersion and variation of the adsorbent porosity the best alternative to simulate the experimental data.

The aforementioned version of the Air Reactor model was applied to study the effect of various operating and structural parameters over the reoxidation of the active metal in the oxygen transfer material and the calcination of the active phase in the adsorbent. The sensitivity of the Air Reactor performance to the operating parameters considered the mass flux, the air temperature and the bed initial temperature; the effect of the pressure was not analysed since it is well known that increasing this parameter is detrimental for the regeneration of the adsorbent due to an increased energy requirement to overcome the limitations imposed by the chemical equilibrium. However, a proper optimisation of the operating pressure strongly depends upon the final use of the CO_2 produced during the bed regeneration. Moreover, if the feasible process of regeneration turns out to be using air, the outlet stream will be a mixture of CO_2, N_2 and O_2 which will require further separation to utilise or capture the CO_2. Therefore, the determination optimal pressure of the Air Reactor is not a trivial question, as the stream can be used for myriad of options, including enhanced oil recovery,

production of chemicals, carbonation, mineralisation, etc. In this context, the pressure utilised in this exercise was arbitrarily selected to assess the potential of the integration of the heat of oxidation and the heat of calcination without any consideration of downstream processing schemes. Regarding the parameters analysed in the sensitivity analysis, it was determined that the reactor should be operated at the highest feasible throughput of air to enhance the utilisation of the heat of oxidation of nickel in the calcination of calcium oxide; however, a very high air velocity should be avoided in order to prevent the possibility of fluidisation of the packing and to maintain the pressure drop as low as possible, since this parameter is critical to maintain a low operating pressure, thus reducing the heat load required to calcine the $CaCO_3$ in the adsorbent, for the particular case of this study a value of air velocity at the reactor inlet of 2.0 m s^{-1} was selected. Regarding the air and packing temperatures, these operating parameters should be set at the highest possible value to promote the regeneration of the packings, particularly the adsorbent. An increase of the inlet temperature of the air, the initial bed temperature or both will accelerate the oxidation of nickel, thus reducing the window during which heat of reaction of oxidation is available to heat up the adsorbent. However, a techno-economic analysis is required to determine the optimal operating temperature since a very high temperature might imply a very high OPEX. The simulations conducted here indicated that to achieve the maximum conversion of $CaCO_3$ the temperature should be set at least at 1200K.

The sensitivity analysis also considered varying the content of nickel in the catalyst/OTM since the molar ratio NiO-to-CaO in the bed is low when using a commercial steam reforming catalyst, reducing the potential amount of heat of oxidation available to achieve high $CaCO_3$ conversion. It was found that augmenting the nickel content in the catalyst renders a best scenario for the calcination of $CaCO_3$. However, the mole composition of oxygen in the sweep gas requires to be low to control the excessive increase of the catalyst temperature due to a very fast rate of reaction of oxidation, and avoid local overheating of the material and temperature gradients throughout the bed, to this end a concentration of O_2 in the sweep gas of 5% will render reasonably well heat management. Finally, the effect of varying the density of the adsorbent and the catalyst was analysed, however, no significant improvement in the reactor performance was observed.

In addition to the aforementioned studies, the scenario where the catalyst in the packed bed is loaded with traces of hydrogen was revised. The presence of hydrogen in the bed permits the reduction of the operating temperature of the reactor from ca. 1200 to 1073K, however, under these conditions the composition of oxygen in the sweep gas should be kept low to control the sudden increase of

the temperature due to the very fast reaction of combustion of hydrogen, for the cases analysed her a concentration of O_2 as low as 1 mole% was required to avoid overheating of the catalyst. Moreover, the likelihood of this operating scenario must be considered for the purposes of selecting adequate materials of construction, since the gaseous product stream leaving the reactor will contain a mixture of N_2, steam, and CO_2 released from the calcination of the adsorbent, increasing the possibility of a corrosive environment in downstream condensers and separation equipment.

Chapter 9 Conclusions and recommendations

9.1 Conclusions

The investigation carried out in this project has looked at the development of mathematical models for the simulation of the fuel and air cycles of the process concept known as the Sorption Enhanced Chemical Looping Steam Reforming of Methane. The proposed models considered a heterogeneous system and accounted for separate gas, catalyst/OTM and adsorbent phases. The project motivation for this project arises from the need of developing technologies to produce hydrogen more efficiently and with a lesser environmental blueprint and the unanswered questions regarding the ability of the reactor concept to integrate the heats of reaction and adsorption without losses as has been assumed in previous models.

To achieve the objective of the project, a literature review was conducted focusing on the chemistry of the process, including the main and side chemical reactions, and documenting whether all of these processes are likely to happen at typical reactor operating conditions suggested in the literature. The kinetic rate expressions of the catalytic and non-catalytic processes of relevance to the process were also collected from the literature along their parameters. The different types of rate expressions were discussed a priori in the literature review and their use within the models was analysed in Chapter 6 for the Fuel Reactor and Chapter 8 for the Air Reactor as part of the model calibration.

A thermodynamic study of the process was carried out to investigate the potential performance of the Fuel and Air Reactors within selected operating conditions and to identify the operating window that maximise the conversion of the fuel towards hydrogen and the regeneration of the materials to their initial state. The study also looked at the convenience of pre-reforming the feedstock and it was found that operating the fuel reactor with a pre-processed feed yields a better operating case scenario since the product temperature is increased.

The reactor models were developed in two stages. First a transient heat transfer model was set up and tested with various examples of fixed beds considering packing materials relevant to the reactor concept of interest. Then the reactor model was set up for both the Fuel and Air reactors and solved in gPROMS^{TM}. The conclusions of these investigations are outlined in the following sections.

9.1.1 Heat transfer model

The problem of heat transfer in a packed bed comprising two different types of refractory packing materials was studied with a heterogeneous model that accounted explicitly for intra-particle conductivity. A stable, convergent, compatible solution of the model was developed by the finite differences method and was successfully compared against the solution by the method of lines obtained from the model implementation in gPROMS^{TM}. The model was then applied to analyse the response of series of packed beds with different bed parameters. The results suggested that the packing materials of interest for the application of the chemical reactor are likely to develop intra-conduction gradients, and therefore the model should account for these effects. Nevertheless, the application of the intra-particle model can be avoided by selecting appropriate dimensions of the packings and reactor length, which would allow for the use of a lumped type model without losing accuracy in the representation of the heat transfer operation. Moreover, the accuracy of the lumped model to represent the fixed bed with packings containing alumina, calcium oxide or calcium carbonate, which are relevant for the reactor concept of this research, can be improved by incorporating an effective heat transfer coefficient into the heat transfer model.

9.1.2 Fuel reactor

The mathematical model of the fuel reactor mode was studied under the optics of three different modelling approaches, namely: the pseudo-homogeneous model, the pseudo-heterogeneous model and the heterogeneous model. These models were applied to simulate various sets of experimental data, however all of them failed to reproduce all the simulated conditions. A comparison between the models indicated that when applied to a system with small particles, e.g. to simulate a lab-scale experiment, the three models produce similar profiles with the exception of the temperature and the gas velocity profiles. This was attributed to the differences in the key assumptions of each model. However, when applied to systems with large particles, i.e. particles with typical industrial sizes, the models exhibit strong differences; the highest reactor performances are predicted by the pseudo-homogeneous model and the worst case scenario is predicted by the heterogeneous model proposed in this work. This has not been observed experimentally since the published data have considered only lab-scale reactors with particle sizes with sub millimetre scales, operated with an influx of heat to compensate the reactor temperature. Hence, the validity of the different models to represent realistically the industrial situation has a strong degree of uncertainty, however, it was deemed that the pseudo-homogeneous and pseudo-

heterogeneous models provided an unrealistic representation of the heat transfer in the system. Therefore, the heterogeneous model was selected since its mathematical structure reflects more accurately the various phenomena and interactions occurring in the Fuel Reactor.

The heterogeneous model was further developed to include in the mathematical description the variations of porosity, density and heat capacity in the adsorbent that occur as a consequence of the capture of CO_2. The resultant models were applied to simulate experiments of a lab-scale rig and their output was fitted by manually adjusting the effectiveness factor of carbonation. It was found that by adding the variations of the adsorbent structure into the mathematical model, the model output is improved, allowing to match the experimental breakthrough curve of H_2 at all the simulated conditions, furthermore, the values of effectiveness factor of carbonation required to fit the model compared well with those previously reported in the open literature.

The heterogeneous model accounting for the adsorbent porosity variation was then applied to conduct a sensitivity analysis to study the effect of the available heat transfer area, mass flux, feedstock composition, gas and packing temperature, catalyst density and adsorbent density over the methane conversion, hydrogen purity, hydrogen yield and hydrogen productivity. Similar results to previous studies were found during the analysis of the operating conditions. In general, it was determined that the reactor should operate at the lowest possible gas mass flux condition, and the highest possible temperature below the calcination temperature of the adsorbent. Moreover, it is recommended that the inlet temperature of the gas and the initial temperature of the bed are set at the same level as these conditions render the best reactor performance.

The results of the computational experiments varying the volumetric fraction of the materials in the packed bed (hence the transfer area) suggested that the heat transfer from the adsorbent to the catalyst is enhanced as the fraction of catalyst is augmented, however, augmenting the volumetric fraction of catalyst implies to reduce the volumetric fraction of adsorbent in the fixed bed, thus the duration of the Fuel Reactor cycle is reduced (i.e. a shorter pre-breakthrough time) due to less CO_2 capture capacity available in the reactor. Increasing the fraction of catalyst also increases the transfer area of the catalyst, allowing for an improved heat transfer and enhancing the performance indicators of the reactor. It was also demonstrated that packing the reactor with smaller sized packings improves the performance, owing to the higher transfer area, however, with the penalty of an increased pressure drop throughout the packing bed. These results suggest that future work should look at an investigation of packing shapes that maximise the superficial area whilst minimising the pressure drop in the system.

9.1.3 Air reactor

The work conducted regarding the modelling of the air reactor entailed the assessment of the plug flow heterogeneous model with and without axial dispersion, and with the incorporation of the increase of adsorbent porosity during the calcination of the adsorbent. The model was validated against experimental data and produced a fair representation of the temperature profiles, but failed to produce an accurate breakthrough curve of the desorbed CO_2. The lack of precision was deemed to be a consequence of the uncertainty of the application of the available models of the rate of reaction of calcination, but also to the necessity of assuming a great number of parameters of the experiment that were not available in the original source.

A sensitivity study of the air reactor to the variation of the mass flux, temperature, the nickel load in the catalyst, the concentration of oxygen in the oxidant agent and the adsorbent and catalyst densities was conducted. It was found that operating at a high air throughput is beneficial for the conversion of nickel to nickel oxide, and calcium carbonate to calcium oxide, particularly the latter. Care should be taken however, to avoid a very large high pressure loss since it would imply the need of operating the reactor at higher pressure, thus increasing the thermal load required for the calcination of calcium carbonate. Moreover, the selected air throughput should be such that the air velocity inside the reactor falls below the minimum bed fluidisation velocity.

The air and initial bed temperatures should be set at the maximum possible value to promote the calcination of the adsorbent; the temperature of the oxidant agent and the packed bed should be kept at the same level at the beginning of the cycle. However, similar to the fuel reactor the transfer of the heat of reaction of oxidation of nickel to the adsorbent is limited by the available heat transfer area. Moreover, the release of heat of oxidation is fast in comparison to the rate of consumption of heat by the adsorbent, all these factors promote the loss of heat, which is carried out of the reactor by the bulk gas.

The calcination of calcium carbonate was found to be incomplete at all conditions of temperature and air throughput simulated. The reason for this relates partially with the aforementioned loss of heat to the bulk gas, but also to the limited amount of nickel to be oxidised, which ultimately represent the source of heat. The effect of increasing the nickel content in the catalyst/OTM was analysed and it was founded that the performance of the reactor is enhanced. Nevertheless, a higher content of nickel implies the formation of strong gradients of temperature along the bed due to the poor heat transfer from the catalyst to the adsorbent, hence the overheating of the catalyst. The amount of heat of reaction of oxidation can

be managed by diluting the oxygen in the air, helping to control the temperature rise in the catalyst/OTM, albeit reducing the calcination degree of the adsorbent.

A similar scenario is obtained when assuming that the bed contains traces of hydrogen adsorbed in the surface of nickel. In this situation is possible to operate the reactor at lower air and bed initial temperatures and attain conversions of the adsorbent comparable to those obtained when considering a clean bed operating at a higher air and bed temperatures. Therefore, switching from the Fuel Reactor to the Air Reactor cycle without sweeping the fuel gas from the bed pores might prove beneficial for the economics of the reactor operation. However, safety measures should be taken to ensure the design of a safe operation in such a scenario.

9.2 Recommendations for future work

The development of more efficient methods for the production of hydrogen is an area of interest due to its key role in the decarbonisation of the energy system. Currently, the so called “blue hydrogen” technologies are particularly relevant since they take advantage of mature technologies like steam reforming in combination with some CO_2 capture method. As such, the reactor concept investigated in this thesis has scope for further research.

The mathematical models could be extended to account explicitly for the intra-particle resistance to mass and heat transfer. Such investigation is relevant to improve the predictive capabilities of the models, which in their current state require information of the effectiveness factor to adjust the experimental data. The modelling of the intra-particle mass and heat transfer would permit a more accurate description of the progress of the non-catalytic processes involved in the redox reactions of the oxygen transfer material, and the adsorption/desorption of the adsorbent.

Another branch of investigation is use of Computational Fluid Dynamics (CFD) coupled with the gPROMS^{TM} reactor model. The relevance of this investigation is twofold. On one hand, the incorporation of the full description of the fluid flow field into the model would provide information on how the hydrodynamics effects the performance of the reactor. On the other hand, the use of CFD would allow to investigate different shapes of structural packing that allow to maximise the heat and mass transfer area, thus enhancing the integration of heat of reaction within the packed bed.

Further development of the models is recommended to include the reaction kinetics of side processes such as carbon formation or the adsorption of water in the sorbent. While carbon formation is unlikely to occur whenever there is

availability of adsorption capacity, the sections of the bed in which the adsorbent has been exhausted might operate at low temperatures due to the adiabatic nature of the reactor and the endothermic nature of the reforming processes, this could lead to conditions in which these undesired reactions are present, and hinder the process by blocking the packed bed causing flow maldistribution or by forming carbon deposits inside the catalyst causing deactivation or breaking of the material. Therefore the results of this investigation would be valuable to select the appropriate steam-to-carbon ratio from the operation standpoint and from the process economics standpoint.

The cyclic operation could also be investigated to study the complete operation and determine the optimal design of the reaction system to achieve continuous production of H_2. This is of paramount importance to ensure the successful design of the process plant. It is also worthwhile to research the integration of the reactor within a H_2 production plant, and within different industrial sites that demand large amounts of H_2. This would provide valuable information regarding the optimum plant configuration that renders a highly efficient process.

Finally, the experimental demonstrations of this concept have been conducted at scales that are not useful to validate the models for their use in the simulation of industrial sized packings. Hence it would be worthwhile to conduct experiments at conditions closer to those of an actual application of a packed bed reactor. The results of this effort would be valuable from a model validation perspective and to attest the validity of the concept in conditions similar to those of an actual reactor.

List of References

1. United Nations and P.D. Department of Economic and Social Affairs, *World Population Prospects 2019: Highlights*. 2019.

2. International Energy Agency (IEA), *World Energy Outlook 2019*. 2019, IEA: Paris.

3. UNFCCC, *Kyoto Protocol Reference Manual on Accounting of Emissions and Assigned Amount.* 2008.

4. Mansilla, C., et al., *CO2-free hydrogen as a substitute to fossil fuels: What are the targets? Prospective assessment of the hydrogen market attractiveness.* International Journal of Hydrogen Energy, 2012. **37**(12): p. 9451-9458.

5. Iruretagoyena, D., *Supported Layered Double Hydroxides as CO2 Adsorbents for Sorption Enhanced H2 Production*. 2014, Imperial College of London.

6. Fernandez, J.R., J.C. Abanades, and R. Murillo, *Modeling of sorption enhanced steam methane reforming in an adiabatic fixed bed reactor.* Chemical Engineering Science, 2012. **84**: p. 1-11.

7. IRENA, *Hydrogen: A Renewable Energy Perspective*. 2019, International Energy Agency: Abu Dhabi.

8. Da Silva Veras, T., et al., *Hydrogen: Trends, production and characterization of the main process worldwide.* International Journal of Hydrogen Energy, 2017. **42**(4): p. 2018-2033.

9. Saeidi, S., et al., *Hydrogen production: Perspectives, separation with special emphasis on kinetics of WGS reaction: A state-of-the-art review.* Journal of Industrial and Engineering Chemistry, 2017. **49**: p. 1-25.

10. Adiya, Z., V. Dupont, and T. Mahmud, *Chemical equilibrium analysis of hydrogen production from shale gas using sorption enhanced chemical looping steam reforming.* Fuel Processing Technology, 2017. **159**: p. 128-144.

11. BP, *BP Statistical Review of World Energy*. 2020, British Petroleum.

12. Noureldin, M.M.B., N.O. Elbashir, and M.M. El-Halwagi, *Optimization and Selection of Reforming Approaches for Syngas Generation from Natural/Shale Gas.* Industrial & Engineering Chemistry Research, 2014. **53**(5): p. 1841-1855.

13. Dupont, V., et al., *Production of hydrogen by unmixed steam reforming of methane.* Chemical Engineering Science, 2008. **63**(11): p. 2966-2979.

14. Holladay, J.D., et al., *An overview of hydrogen production technologies.* Catalysis Today, 2009. **139**(4): p. 244-260.

15. Kalamaras, C.M. and A.M. Efstathiou, *Hydrogen Production Technologies: Current State and Future Developments.* Conference Papers in Energy, 2013. **2013**: p. 1-9.

16. Energy Research Partnership, *Potential Role of Hydrogen in the UK Energy System*. 2016, ERP Reports: UK.

17. Kumar, R.V., J.A. Cole, and R.K. Lyon, *Unmixed reforming: An advanced steam-reforming process.* Abstracts of Papers of the American Chemical Society, 1999. **218**: p. U631-U632.

18. Dedeken, J.C., E.F. Devos, and G.F. Froment, *Steam Reforming of Natural Gas - Intrinsic Kinetics, Diffusional Influences, and reactor Design.* Acs Symposium Series, 1982. **196**: p. 181-197.

19. Rostrup-Nielsen, J.R., *Production of synthesis gas.* Catalysis Today, 1993. **18**(4): p. 305-324.

20. Rostrup-Nielsen, J.R., *An industrial perspective on the impact of Haldor Topsøe on research and development in synthesis gas production.* Journal of Catalysis, 2015. **328**: p. 5-10.

21. Ritter, J.A. and A.D. Ebner, *State-of-the-art adsorption and membrane separation processes for hydrogen production in the chemical and petrochemical industries.* Separation Science and Technology, 2007. **42**(6): p. 1123-1193.

22. Sperle, T., et al., *Pre-reforming of natural gas on a Ni catalyst - Criteria for carbon free operation.* Applied Catalysis a-General, 2005. **282**(1-2): p. 195-204.

23. Christensen, T.S., *Adiabatic prereforming of hydrocarbons - An important step in syngas production.* Applied Catalysis a-General, 1996. **138**(2): p. 285-309.

24. Cross, J., G. Jones, and M.A. Kent, *An introduction to pre-reforming catalysis*, in *Nitrogen+Syngas*. 2016. p. 40-48.

25. Rout, K.R. and H.A. Jakobsen, *A numerical study of fixed bed reactor modelling for steam methane reforming process.* The Canadian Journal of Chemical Engineering, 2015. **93**(7): p. 1222-1238.

26. De Wilde, J. and G.F. Froment, *Computational Fluid Dynamics in chemical reactor analysis and design: Application to the ZoneFlow (TM) reactor for methane steam reforming.* Fuel, 2012. **100**: p. 48-56.

27. Nikolaidis, P. and A. Poullikkas, *A comparative overview of hydrogen production processes.* Renewable & Sustainable Energy Reviews, 2017. **67**: p. 597-611.

28. Guandalini, G., S. Campanari, and G. Valenti, *Comparative assessment and safety issues in state-of-the-art hydrogen production technologies.* International Journal of Hydrogen Energy, 2016. **41**(42): p. 18901-18920.

29. Rostrup-Nielsen, J.R. and T. Rostrup-Nielsen, *Large-Scale Hydrogen Production.* CATTECH, 2002. **6**(4): p. 150-159.

30. Barelli, L., et al., *Hydrogen production through sorption-enhanced steam methane reforming and membrane technology: A review.* Energy, 2008. **33**(4): p. 554-570.

31. Ochoa-Fernández, E., et al., *Sorption enhanced hydrogen production by steam methane reforming using Li2ZrO3 as sorbent: Sorption kinetics and reactor simulation.* Catalysis Today, 2005. **106**(1-4): p. 41-46.

32. Diglio, G., et al., *Modelling of sorption-enhanced steam methane reforming in a fixed bed reactor network integrated with fuel cell.* Applied Energy, 2018. **210**: p. 1-15.

33. Lugo, E.L. and B.A. Wilhite, *A theoretical comparison of multifunctional catalyst for sorption-enhanced reforming process.* Chemical Engineering Science, 2016. **150**: p. 1-15.

34. Martinez, I., et al., *Process design of a hydrogen production plant from natural gas with CO2 capture based on a novel Ca/Cu chemical loop.* Applied Energy, 2014. **114**: p. 192-208.

35. Xiu, G., P. Li, and A.E. Rodrigues, *Adsorption-enhanced steam-methane reforming with intraparticle-diffusion limitations.* Chemical Engineering Journal, 2003. **95**(1-3): p. 83-93.

36. Martavaltzi, C.S., T.D. Pefkos, and A.A. Lemonidou, *Operational Window of Sorption Enhanced Steam Reforming of Methane over CaO-Ca12Al14O33.* Industrial & Engineering Chemistry Research, 2011. **50**(2): p. 539-545.

37. Coenen, K., et al., *Chemisorption working capacity and kinetics of CO2 and H2O of hydrotalcite-based adsorbents for sorption-enhanced water-gas-shift applications.* Chemical Engineering Journal, 2016. **293**: p. 9-23.

38. Bamiduro, F., et al., *Spray-Dried Sodium Zirconate: A Rapid Absorption Powder for CO2 Capture with Enhanced Cyclic Stability.* ChemSusChem, 2017. **10**(9): p. 2059-2067.

39. Halabi, M.H., et al., *Kinetic and structural requirements for a CO2 adsorbent in sorption enhanced catalytic reforming of methane – Part I: Reaction kinetics and sorbent capacity.* 2012. **99**: p. 154-164.

40. Dean, C.C., et al., *The calcium looping cycle for CO2 capture from power generation, cement manufacture and hydrogen production.* Chemical Engineering Research & Design, 2011. **89**(6A): p. 836-855.

41. Di Carlo, A., et al., *Sorption enhanced steam methane reforming on catalyst-sorbent bifunctional particles: A CFD fluidized bed reactor model.* Chemical Engineering Science, 2017. **173**: p. 428-442.

42. Butler, J.W., C. Jim Lim, and J.R. Grace, *Kinetics of CO2 absorption by CaO through pressure swing cycling.* Fuel, 2014. **127**: p. 78-87.

43. Ramirez-Solis, S., V. Dupont, and S.J. Milne, *Preparation and Evaluation of CaO-Based CO2 Sorbents Deposited on Saffil Fiber Supports.* Energy & Fuels, 2018. **32**(8): p. 8631-8640.

44. Grasa, G., et al., *Validation of the H2 production stage via SER under relevant conditions for the Ca/Cu reforming process practical application.* Chemical Engineering Journal, 2017. **324**: p. 266-278.

45. Skoufa, Z., et al., *Evaluating the activity and stability of CaO-based sorbents for post-combustion CO2 capture in fixed-bed reactor experiments*, in *8th Trondheim Conference on Co2 Capture, Transport and Storage*, R. Aarlien, N.A. Rokke, and H.F. Svendsen, Editors. 2016. p. 171-180.

46. Salaudeen, S.A., B. Acharya, and A. Dutta, *CaO-based CO2 sorbents: A review on screening, enhancement, cyclic stability, regeneration and kinetics modelling.* Journal of CO2 Utilization, 2018. **23**: p. 179-199.

47. Ochoa-Fernandez, E., et al., *Process design simulation of H-2 production by sorption enhanced steam methane reforming: evaluation of potential CO2 acceptors.* Green Chemistry, 2007. **9**(6): p. 654-662.

48. Alcántar-Vázquez, B.-C. and R.-M. Ramírez-Zamora, *Lithium silicates synthetized from iron and steel slags as high temperature CO2 adsorbent materials.* Adsorption, 2020. **26**(5): p. 687-699.

49. Zhang, Y., et al., *Recent advances in lithium containing ceramic based sorbents for high-temperature CO2 capture.* Journal of Materials Chemistry A, 2019. **7**(14): p. 7962-8005.

50. Fernandez, J.R., J.C. Abanades, and G. Grasa, *Modeling of sorption enhanced steam methane reforming—Part II: Simulation within a novel Ca/Cu*

chemical loop process for hydrogen production. Chemical Engineering Science, 2012. **84**: p. 12-20.

51. Papalas, T., A.N. Antzaras, and A.A. Lemonidou, *Intensified steam methane reforming coupled with Ca-Ni looping in a dual fluidized bed reactor system: A conceptual design.* Chemical Engineering Journal, 2020. **382**.

52. Fernandez, J.R., et al., *Conceptual design of a hydrogen production process from natural gas with CO2 capture using a Ca-Cu chemical loop.* International Journal of Greenhouse Gas Control, 2012. **6**: p. 126-141.

53. Protasova, L. and F. Snijkers, *Recent developments in oxygen carrier materials for hydrogen production via chemical looping processes.* Fuel, 2016. **181**: p. 75-93.

54. Diglio, G., et al., *Simulation of hydrogen production through chemical looping reforming process in a packed-bed reactor.* Chemical Engineering Research and Design, 2016. **105**: p. 137-151.

55. Sanchez, R.A. and H.A. Jakobsen, *Modeling the Chemical Looping Reforming Process Operated in a Circulating Fluidized Bed Reactor Consisting of Two Bubbling Bed Units: Model Validation.* Industrial & Engineering Chemistry Research, 2014. **53**(23): p. 9616-9630.

56. Rydén, M. and P. Ramos, *H2 production with CO2 capture by sorption enhanced chemical-looping reforming using NiO as oxygen carrier and CaO as CO2 sorbent.* Fuel Processing Technology, 2012. **96**: p. 27-36.

57. Medrano, J.A., et al., *NiO/CaAl2O4 as active oxygen carrier for low temperature chemical looping applications.* Applied Energy, 2015. **158**: p. 86-96.

58. Antzara, A., E. Heracleous, and A.A. Lemonidou, *Energy efficient sorption enhanced-chemical looping methane reforming process for high-purity H2 production: Experimental proof-of-concept.* Applied Energy, 2016. **180**: p. 457-471.

59. Spallina, V., et al., *Chemical looping reforming in packed-bed reactors: Modelling, experimental validation and large-scale reactor design.* Fuel Processing Technology, 2017. **156**: p. 156-170.

60. Antzara, A., et al., *Thermodynamic analysis of hydrogen production via chemical looping steam methane reforming coupled with in situ CO2 capture.* International Journal of Greenhouse Gas Control, 2015. **32**: p. 115-128.

61. Snoeck, J.W., G.F. Froment, and M. Fowles, *Steam/CO2Reforming of Methane. Carbon Filament Formation by the Boudouard Reaction and*

Gasification by CO2, by H2, and by Steam: Kinetic Study. Industrial & Engineering Chemistry Research, 2002. **41**(17): p. 4252-4265.

62. Piña, J., V. Bucalá, and D.O. Borio, *Optimization of Steam Reformers: Heat Flux Distribution and Carbon Formation.* International Journal of Chemical Reactor Engineering, 2003. **1**(1).

63. Snoeck, J.W., G.F. Froment, and M. Fowles, *Kinetic Study of the Carbon Filament Formation by Methane Cracking on a Nickel Catalyst.* Journal of Catalysis, 1997. **169**(1): p. 250-262.

64. Meloni, E., M. Martino, and V. Palma, *A Short Review on Ni Based Catalysts and Related Engineering Issues for Methane Steam Reforming.* Catalysts, 2020. **10**(3).

65. Rout, K.R. and H.A. Jakobsen, *Reactor performance optimization by the use of a novel combined pellet reflecting both catalyst and adsorbent properties.* Fuel Processing Technology, 2012. **99**: p. 13-34.

66. Phuluanglue, A., W. Khaodee, and S. Assabumrungrat, *Simulation of intensified process of sorption enhanced chemical-looping reforming of methane: Comparison with conventional processes.* Computers & Chemical Engineering, 2017. **105**: p. 237-245.

67. Zhu, L. and J.M. Fan, *Thermodynamic analysis of H-2 production from CaO sorption-enhanced methane steam reforming thermally coupled with chemical looping combustion as a novel technology.* International Journal of Energy Research, 2015. **39**(3): p. 356-369.

68. Abbas, S.Z., V. Dupont, and T. Mahmud, *Modelling of high purity H2 production via sorption enhanced chemical looping steam reforming of methane in a packed bed reactor.* Fuel, 2017. **202**: p. 271-286.

69. Ghosh, S., et al., *Kinetics Modeling, Development, and Comparison for the Reaction of Calcium Oxide with Steam.* Energy & Fuels, 2019. **33**(6): p. 5505-5517.

70. Fan, L.-S., *Chemical looping systems for fossil energy conversions*. 2010, Hoboken, N.J: AIChE.

71. Deshpande, A. and A. Arya, *Comparative CFD simulation studies on monolith and packed bed reactors for oxidation of Cu in unmixed combustion (UMC) process.* Chemical Engineering Research and Design, 2020. **160**: p. 521-532.

72. Di Giuliano, A., et al., *Multicycle sorption enhanced steam methane reforming with different sorbent regeneration conditions: Experimental and modelling study.* Chemical Engineering Journal, 2019. **377**: p. 119874.

73. Chao, Z., et al., *Numerical Investigation of the Sorption Enhanced Steam Methane Reforming in a Fluidized Bed Reactor.* Energy Procedia, 2012. **26**: p. 15-21.

74. Phuakpunk, K., et al., *Parametric study of hydrogen production via sorption enhanced steam methane reforming in a circulating fluidized bed riser.* Chemical Engineering Science, 2018. **192**: p. 1041-1057.

75. Wang, J., Y. Wang, and H.A. Jakobsen, *The modeling of circulating fluidized bed reactors for SE-SMR process and sorbent regeneration.* Chemical Engineering Science, 2014. **108**: p. 57-65.

76. Adanez, J., et al., *Progress in Chemical-Looping Combustion and Reforming technologies.* Progress in Energy and Combustion Science, 2012. **38**(2): p. 215-282.

77. Mattisson, T., et al., *Chemical-looping technologies using circulating fluidized bed systems: Status of development.* Fuel Processing Technology, 2018. **172**: p. 1-12.

78. García-Díez, E., et al., *Autothermal chemical looping reforming process of different fossil liquid fuels.* 2017.

79. Önsan, Z.I. and A.K. Avci, *Multiphase Catalytic Reactors: Theory, Design, Manufacturing, and Applications*. 2016, Hoboken: John Wiley & Sons, Incorporated.

80. Zhou, Z., L. Han, and G.M. Bollas, *Overview of Chemical-Looping Reduction in Fixed Bed and Fluidized Bed Reactors Focused on Oxygen Carrier Utilization and Reactor Efficiency.* 2014.

81. Krishnaswamy, S., A. Deshpande, and K.N. Ponnani, *Modeling of unmixed combustion based packed bed reactor system for heat transfer applications.* Chemical Engineering Science, 2018. **178**: p. 367-376.

82. Hamers, H.P., et al., *A novel reactor configuration for packed bed chemical-looping combustion of syngas.* 2013. **16**: p. 1-12.

83. De Vos, Y., et al., *Development of Stable Oxygen Carrier Materials for Chemical Looping Processes-A Review.* Catalysts, 2020. **10**(8).

84. Smith, J.M., *Chemical engineering kinetics*. Third edition. ed. McGraw-Hill chemical engineering series. 1981, New York ;: McGraw-Hill.

85. Solsvik, J. and H.A. Jakobsen, *A numerical study of a two property catalyst/sorbent pellet design for the sorption-enhanced steam-methane reforming process: Modeling complexity and parameter sensitivity study.* Chemical Engineering Journal, 2011. **178**: p. 407-422.

86. Xu, J.G. and G.F. Froment, *Methane Steam Reforming, Methanation and Water-Gas Shift. 1.Intrinsinc Kinectics.* Aiche Journal, 1989. **35**(1): p. 88-96.

87. Soliman, M.A., et al., *Intrinsinc Kinetics of Nickel Calcium Aluminate Catalyst for Methane Steam Reforming.* Journal of Chemical Technology and Biotechnology, 1992. **55**(2): p. 131-138.

88. Hou, K.H. and R. Hughes, *The kinetics of methane steam reforming over a Ni/alpha-Al2O catalyst.* Chemical Engineering Journal, 2001. **82**(1-3): p. 311-328.

89. Abbas, S.Z., V. Dupont, and T. Mahmud, *Kinetics study and modelling of steam methane reforming process over a NiO/Al2O3 catalyst in an adiabatic packed bed reactor.* International Journal of Hydrogen Energy, 2017. **42**(5): p. 2889-2903.

90. Fedunik-Hofman, L., A. Bayon, and S.W. Donne, *Kinetics of Solid-Gas Reactions and Their Application to Carbonate Looping Systems.* Energies, 2019. **12**(15): p. 35.

91. Fedunik-Hofman, L., et al., *Friedman method kinetic analysis of CaO-based sorbent for high-temperature thermochemical energy storage.* Chemical Engineering Science, 2019. **200**: p. 236-247.

92. Tian, H.C., et al., *Study of kinetic characteristics of limestone decomposition under different atmospheres and heating conditions.* Journal of Thermal Analysis and Calorimetry, 2017. **130**(3): p. 2351-2358.

93. Zhou, Z., L. Han, and G.M. Bollas, *Kinetics of NiO reduction by H2 and Ni oxidation at conditions relevant to chemical-looping combustion and reforming.* International Journal of Hydrogen Energy, 2014. **39**(16): p. 8535-8556.

94. Ipsakis, D., et al., *Reduction and oxidation kinetic modeling of NiO-based oxygen transfer materials.* Chemical Engineering Journal, 2017. **308**: p. 840-852.

95. Bhatia, S.K. and D.D. Perlmutter, *Effect of the Poduct Layer on the Kinetics of the CO2-Lime Reaction.* Aiche Journal, 1983. **29**(1): p. 79-86.

96. Sun, P., et al., *Determination of intrinsic rate constants of the CaO–CO2 reaction.* Chemical Engineering Science, 2008. **63**(1): p. 47-56.

97. Bhatia, S.K. and D.D. Perlmutter, *A Random Pore Model for Fluid-Solid Reactions. 1. Isothermal, Kinetic Control.* Aiche Journal, 1980. **26**(3): p. 379-386.

98. Grasa, G., et al., *Application of the random pore model to the carbonation cyclic reaction.* AIChE Journal, 2009. **55**(5): p. 1246-1255.

99. Zhou, Z., et al., *Modeling of the carbonation kinetics of a synthetic CaO-based sorbent.* Chemical Engineering Science, 2013. **95**: p. 283-290.

100. Nouri, S., H. Ebrahim, and B. Nejad, *A modified random pore model for carbonation reaction of calcium oxide with carbon dioxide.* Hemijska industrija, 2015. **69**(2): p. 209-217.

101. Jiang, L., et al., *Performance and Carbonation Kinetics of Modified CaO-Based Sorbents Derived from Different Precursors in Multiple CO2 Capture Cycles.* Energy & Fuels, 2016. **30**(11): p. 9563-9571.

102. Szekely, J. and J.W. Evans, *Structural Model For Gas-Solid Reactions With a Moving Boundary. 2. Effect of Grain Size, Porosity and Temperature on Reaction of Porous Pellets.* Chemical Engineering Science, 1971. **26**(11): p. 1901-&.

103. Sohn, N.Y. and J. Szekely, *General Grain Model for Gas-Solid Reactions Involving a Moving Boundary.* Canadian Mining and Metallurgical Bulletin, 1971. **64**(712): p. 28-&.

104. Yu, F.-C. and L.-S. Fan, *Kinetic Study of High-Pressure Carbonation Reaction of Calcium-Based Sorbents in the Calcium Looping Process (CLP).* Industrial & Engineering Chemistry Research, 2011. **50**(20): p. 11528-11536.

105. Yin, J., et al., *Calcium Looping for CO2 Capture at a Constant High Temperature.* Energy & Fuels, 2013. **28**(1): p. 307-318.

106. Stendardo, S. and P.U. Foscolo, *Carbon dioxide capture with dolomite: A model for gas–solid reaction within the grains of a particulate sorbent.* Chemical Engineering Science, 2009. **64**(10): p. 2343-2352.

107. Lee, D., *An apparent kinetic model for the carbonation of calcium oxide by carbon dioxide.* Chemical Engineering Journal, 2004. **100**(1-3): p. 71-77.

108. Gupta, H. and L.S. Fan, *Carbonation-calcination cycle using high reactivity calcium oxide for carbon dioxide separation from flue gas.* Industrial & Engineering Chemistry Research, 2002. **41**(16): p. 4035-4042.

109. Rodriguez, N., M. Alonso, and J.C. Abanades, *Experimental Investigation of a Circulating Fluidized-Bed Reactor to Capture CO2 with CaO.* Aiche Journal, 2011. **57**(5): p. 1356-1366.

110. Satterfield, C.N. and F. Feakes, *Kinetics of the thermal decomposition of calcium carbonate.* 1959. **5**(1): p. 115-122.

111. Borgwardt, R.H., *Calcination Kinetics and Surface-Area of Dispersed Limeston Particles.* Aiche Journal, 1985. **31**(1): p. 103-111.

112. Fedunik-Hofman, L., A. Bayon, and S.W. Donne, *Comparative Kinetic Analysis of CaCO3/CaO Reaction System for Energy Storage and Carbon Capture.* Applied Sciences-Basel, 2019. **9**(21).

113. Martínez, I., et al., *Kinetics of Calcination of Partially Carbonated Particles in a Ca-Looping System for CO2 Capture.* Energy & Fuels, 2012. **26**(2): p. 1432-1440.

114. Rao, T.R., D.J. Gunn, and J.H. Bowen, *Kinetics of Calcium-Carbonate Decomposition.* Chemical Engineering Research & Design, 1989. **67**(1): p. 38-47.

115. Murthy, M.S., et al., *Investigation on the kinetics of thermal decomposition of calcium carbonate.* 1994. **49**(13): p. 2198-2204.

116. Escardino, A., et al., *Kinetic study of the thermal decomposition process of calcite particles in air and CO2 atmosphere.* 2013. **19**(3): p. 886-897.

117. Abad, A., et al., *Mapping of the range of operational conditions for Cu-, Fe-, and Ni-based oxygen carriers in chemical-looping combustion.* Chemical Engineering Science, 2007. **62**(1-2): p. 533-549.

118. Zafar, Q., et al., *Reaction Kinetics of Freeze-Granulated NiO/MgAl2O4Oxygen Carrier Particles for Chemical-Looping Combustion.* Energy & Fuels, 2007. **21**(2): p. 610-618.

119. Iliuta, I., et al., *Chemical-looping combustion process: Kinetics and mathematical modeling.* AIChE Journal, 2010: p. NA-NA.

120. Rao, T.R., *Kinetic-Parameters For Decomposition of Calcium-Carbonate.* Canadian Journal of Chemical Engineering, 1993. **71**(3): p. 481-484.

121. Fernandez, J.R., S. Turrado, and J.C. Abanades, *Calcination kinetics of cement raw meals under various CO2 concentrations.* Reaction Chemistry & Engineering, 2019. **4**(12): p. 2129-2140.

122. Dueso, C., et al., *Reduction and oxidation kinetics of nickel-based oxygen-carriers for chemical-looping combustion and chemical-looping reforming.* Chemical Engineering Journal, 2012. **188**: p. 142-154.

123. Zhou, Z., L. Han, and G.M. Bollas, *Model-based analysis of bench-scale fixed-bed units for chemical-looping combustion.* 2013. **233**: p. 331-348.

124. Ehlinger, V.M., et al., *Process Design and Integration of Shale Gas to Methanol.* Acs Sustainable Chemistry & Engineering, 2014. **2**(1): p. 30-37.

125. Spragg, J., T. Mahmud, and V. Dupont, *Hydrogen production from bio-oil: A thermodynamic analysis of sorption-enhanced chemical looping steam reforming.* International Journal of Hydrogen Energy, 2018. **43**(49): p. 22032-22045.

126. Dybkjaer, I., *Tubular Reforming and Autothermal Reforming of Natural Gas - An Overview of Available Processes.* Fuel Processing Technology, 1995. **42**(2-3): p. 85-107.

127. Cuéllar-Franca, R.M. and A. Azapagic, *Carbon capture, storage and utilisation technologies: A critical analysis and comparison of their life cycle environmental impacts.* Journal of CO2 Utilization, 2015. **9**: p. 82-102.

128. Angeli, S.D., C.S. Martavaltzi, and A.A. Lemonidou, *Development of a novel-synthesized Ca-based CO2 sorbent for multicycle operation: Parametric study of sorption.* 2014. **127**: p. 62-69.

129. Froment, G.F., *Chemical reactor analysis and design*. Second edition. ed. Wiley series in chemical engineering, ed. K.B. Bischoff. 1990, New York ;: Wiley.

130. Young, L.C. and B.A. Finlayson, *Axial Dispersion in Nonisothermal Packed Bed Chemical Reactors.* Ind. Eng. Chem. Fundam., 1973. **12**(412).

131. Mears, D.E., *On Criteria for Axial Dispersion in Nonisothermal Packed-Bed Catalytic Reactors.* 1976. **15**(1): p. 20-23.

132. Achenbach, E., *Heat and Flow Characteristics of Packed-Beds.* Experimental Thermal and Fluid Science, 1995. **10**(1): p. 17-27.

133. Dixon, A.G., *Fixed Bed Catalytic Reactor Modelling-The Radial Heat Transfer Problem.* Canadian Journal of Chemical Engineering, 2012. **90**(3): p. 507-527.

134. Iordanis, A.A., *Mathematical Modeling of Catalytic Fixed Bed Reactors*. 2002, University of Twente.

135. Mears, D.E., *Tests for Transport Limitations in Experimental Catalytic Reactors.* 1971. **10**(4): p. 541-547.

136. Process Systems Enterprise, *gPROMS*. 1997 - 2018.

137. Versteeg, H.K., *An introduction to computational fluid dynamics : the finite volume method*. Second edition. ed, ed. W. Malalasekera. 2007, Harlow: Pearson Prentice Hall.

138. Smith, G.D., *Numerical solutions of partial differential equations.* Oxford University Press, London, UK, 2004.

139. Schiesser, W., *The Numerical Method of Lines.* Academic Press, London, UK, 1991.

140. Carpenter, K.J., *An investigation of thermal regenerator design*. 1976, University of Leeds, UK.

141. Beers, K.J., *Numerical Methods for Chemical Engineering*. 2006: Cambridge University Press - M.U.A.

142. Crank, J. and P. Nicolson, *A Practical Metod for Numerical Evaluation of Solutions of Partial Differential Equations of the Heat-Conduction Type.* Proceedings of the Cambridge Philosophical Society, 1947. **43**(1): p. 50-67.

143. Oh, M., *Modelling and Simulation of Combined Lumped and Distributed Processes*. 1995, Imperial College London.

144. Jarvis, R.B., *Robust Dynamic Simulation of Chemical Engineering Processes*. 1993, Imperial College London.

145. Abbott, M.B., *An introduction to the method of characteristics*. 1966, London: Thames & Hudson.

146. Schumann, T.E.W., *Heat transfer: A liquid flowing through a porous prism.* Journal of the Franklin Institute, 1929. **208**: p. 405-416.

147. Kuznetsov, A.V., *An analytical solution for heating a 2-Dimensional porous packed bed by a non-thermal equilibrium fluid flow.* Applied Scientific Research, 1995. **55**(1): p. 83-93.

148. Ferreira, L.M., J.A.M. Castro, and A.E. Rodrigues, *An analytical and experimental study of heat transfer in fixed bed.* International Journal of Heat and Mass Transfer, 2002. **45**(5): p. 951-961.

149. Amundson, N.R., *Fixed beds with large particles.* Industrial and Engineering Chemistry, 1956. **48**(1): p. 35-43.

150. Amundson, N.R., *Folid-fluid interactions in fixed and moving beds - Fixed beds with small particles.* Industrial and Engineering Chemistry, 1956. **48**(1): p. 26-35.

151. Anzelius, A., *Heating by means of streaming media.* Zeitschrift Fur Angewandte Mathematik Und Mechanik, 1926. **6**: p. 291-294.

152. Handley, D. and P.J. Heggs, *Effect of Thermal Conductivity of Packing Material on Transient Heat Transfer in a Fixed Bed.* International Journal of Heat and Mass Transfer, 1969. **12**(5): p. 549-&.

153. Aspentech, *Aspen Plus*. 1981-2021.

154. Green, D.W. and R.H. Perry, *Perry's Chemical Engineers' Handbook*. 8th Edition ed. 2007: McGraw-Hill Professional. 2703.

155. Han, L., *Dynamyc Simulation, Optimization, and Control of Flexible Chemical-Looping Combustion Processes*. 2016, University of Connecticut.

156. Handley, D. and P.J. Heggs, *Momentum and Heat Transfer Mechanisms in Regular Shaped Packings.* Transactions of the Institution of Chemical Engineers and the Chemical Engineer, 1968. **46**(9): p. T251-&.

157. Benyahia, F. and K.E. O'Neill, *Enhanced Voidage Correlations for Packed Beds of Various Particle Shapes and Sizes.* Particulate Science and Technology, 2005. **23**(2): p. 169-177.

158. Guo, Z.H., et al., *Mean porosity variations in packed bed of monosized spheres with small tube-to-particle diameter ratios.* Powder Technology, 2019. **354**: p. 842-853.

159. Rwifa, S.B., *Mean Voidage and Momentum Transfer in Packed Beds*. 2000, University of Manchester.

160. Dixon, A.G., *Correlations for Wall and Particle-Shape Effects on Fixed-Bed Bulk Voidage.* Canadian Journal of Chemical Engineering, 1988. **66**(5): p. 705-708.

161. Foumeny, E.A., et al., *Elucidation of Mean Voidage in Packed-Beds.* Canadian Journal of Chemical Engineering, 1991. **69**(4): p. 1010-1015.

162. Zou, R.P. and A.B. Yu, *The Packing of Spheres in a Cylindrical Container - The Thickness Effect.* Chemical Engineering Science, 1995. **50**(9): p. 1504-1507.

163. Heggs, P.J., *Fixed Beds*, in *Handbook of Heat Exchanger Design*, G.F. Hewitt, Editor. 1998, BEGELL House: New York.

164. Macdonald, I.F., et al., *Flow Through Porous-Media - Ergun Equation Revisited.* Industrial & Engineering Chemistry Fundamentals, 1979. **18**(3): p. 199-208.

165. Rase, H.F., *Fixed-bed reactor design and diagnostics: gas-phase reactions*. 2013: Butterworth-Heinemann.

166. Baclic, B.S. and P.J. Heggs, *Unified regenerator theory and reexamination of the unidirectional regenerator performance.* Advances in Heat Transfer, 1990. **20**: p. 133-179.

167. Cockcroft, C.S., *Investigation of a thermally regenerative reactor system.*, in *University of Leeds, UK*. 1976.

168. Xu, B., P.W. Li, and C.L. Chan, *Extending the validity of lumped capacitance method for large Biot number in thermal storage application.* Solar Energy, 2012. **86**(6): p. 1709-1724.

169. Zarrinehkafsh, M.T. and S.M. Sadrameli, *Simulation of fixed bed regenerative heat exchangers for flue gas heat recovery.* Applied Thermal Engineering, 2004. **24**(2-3): p. 373-382.

170. Aloisi, I., et al., *Hydrogen by sorption enhanced methane reforming: A grain model to study the behavior of bi-functional sorbent-catalyst particles.* Chemical Engineering Science, 2016. **149**: p. 22-34.

171. Rostrup-Nielsen, J.R., *Catalytic Steam Reforming.* Catalysis 1984. **5**: p. 130.

172. Christiansen, L.J., *Use of modeling in scale-up of steam reforming technology.* Catalysis Today, 2016. **272**: p. 14-18.

173. Molinder, R., et al., *In situ X-ray diffraction of CaO based CO2 sorbents.* Energy & Environmental Science, 2012. **5**(10): p. 8958.

174. Ockendon, H. and J.R. Ockendon, *Waves and compressible flow*. Texts in applied mathematics ; 47. 2004, New York ;: Springer.

175. Morton, K.W. and D.F. Mayers, *Numerical solution of partial differential equations*. Second edition. ed. 2005, Cambridge: Cambridge University Press.

176. KBC. *Advanced Thermodynamics*. 2020 13/05/2020]; Available from: https://www.kbc.global/software/advanced-thermodynamics/.

177. Diglio, G., et al., *Feasibility of CaO/CuO/NiO sorption-enhanced steam methane reforming integrated with solid-oxide fuel cell for near-zero-CO2 emissions cogeneration system.* Applied Energy, 2018. **230**: p. 241-256.

178. Fernández, J.R. and J.C. Abanades, *Experimental testing and model validation of the calcination of calcium carbonate by the reduction of copper oxide with CH4.* Chemical Engineering Science, 2019. **193**: p. 120-132.

179. Biasin, A., et al., *Investigation of CaO–CO2 reaction kinetics by in-situ XRD using synchrotron radiation.* Chemical Engineering Science, 2015. **127**: p. 13-24.

180. Fan, Y., et al., *Pressurized calcium looping in the presence of steam in a spout-fluidized-bed reactor with DFT analysis.* Fuel Processing Technology, 2018. **169**: p. 24-41.

181. Yang, R.T., *Gas Separation by Adsorption Processes*. First Edition ed. Series on Chemical Engineering. Vol. I. 1997, London: Imperial College Press.

182. Dwivedi, P.N. and S.N. Upadhyay, *Particle-Fluid Mass Transfer in Fixed and Fluidized Beds.* 1977. **16**(2): p. 157-165.

183. Brodkey, R.S., *Transport Phenomena: A Unified Approach*. McGraw-Hill chemical engineering series, ed. H.C. Hershey. 1988, Boston, Mass: McGraw-Hill.

184. Procter, I.C., *An assessment of design techniques for fixed bed adsorption/desorption systems*. 1985, Thesis (Ph.D.) -- University of Leeds (Department of Chemical Engineering), 1985.: Leeds.

185. Jakobsen, H.A., H. Lindborg, and V. Handeland, *A numerical study of the interactions between viscous flow, transport and kinetics in fixed bed reactors.* Computers & Chemical Engineering, 2002. **26**(3): p. 333-357.

186. Dixon, A.G., *An improved equation for the overall heat transfer coefficient in packed beds.* Chemical Engineering and Processing: Process Intensification, 1996. **35**(5): p. 323-331.

187. Jorge, L.M.M., et al., *Evaluation of heat transfer in a catalytic fixed bed reactor at high temperatures.* Brazilian Journal of Chemical Engineering, 1999. **16**(4): p. 407-420.

188. Li, C.-H. and B.A. Finlayson, *Heat transfer in packed beds—a reevaluation.* Chemical Engineering Science, 1977. **32**(9): p. 1055-1066.

189. Gutiérrez Ortiz, F.J., M. Barragán Rodríguez, and R.T. Yang, *Modeling of fixed-bed columns for gas physical adsorption.* Chemical Engineering Journal, 2019. **378**: p. 121985.

190. Modest, M.F., *Radiative heat transfer*. 3rd ed. ed. 2013, New York: Academic Press.

191. Jones, J.M., P.E. Mason, and A. Williams, *A compilation of data on the radiant emissivity of some materials at high temperatures.* Journal of the Energy Institute, 2019. **92**(3): p. 523-534.

192. García-Lario, A.L., et al., *Experimental study of the application of a NiO/NiAl2O4 catalyst and a CaO-based synthetic sorbent on the Sorption Enhanced Reforming process.* International Journal of Hydrogen Energy, 2015. **40**(1): p. 219-232.

193. da Cruz, F.E., S. Karagöz, and V.I. Manousiouthakis, *Parametric Studies of Steam Methane Reforming Using a Multiscale Reactor Model.* Industrial & Engineering Chemistry Research, 2017. **56**(47): p. 14123-14139.

194. Baek, S.M., et al., *A numerical study of the effectiveness factors of nickel catalyst pellets used in steam methane reforming for residential fuel cell*

applications. International Journal of Hydrogen Energy, 2014. **39**(17): p. 9180-9192.

195. Ishida, M. and C.Y. Wen, *Comparison of kinetic and diffusional models for solid-gas reactions.* AIChE Journal, 1968. **14**(2): p. 311-317.

196. Yang, W., et al., *An Effective Reaction Rate Model for Gas-Solid Reactions with High Intra-Particle Diffusion Resistance.* International Journal of Chemical Reactor Engineering, 2016. **14**(1): p. 331-342.

197. Yagi, S. and D. Kunii, *Studies on effective thermal conductivities in packed beds.* AIChE Journal, 1957. **3**(3): p. 373-381.

198. Antzara, A., E. Heracleous, and A.A. Lemonidou, *Improving the stability of synthetic CaO-based CO2 sorbents by structural promoters.* 2015. **156**: p. 331-343.

199. Twigg, M.V. and J.T. Richardson, *Theory and Applications of Ceramic Foam Catalysts.* Chemical Engineering Research and Design, 2002. **80**(2): p. 183-189.

200. Xu, X., P. Li, and Y. Shen, *Small-scale reforming of diesel and jet fuels to make hydrogen and syngas for fuel cells: A review.* Applied Energy, 2013. **108**: p. 202-217.

201. Alarcón, J.M. and J.R. Fernández, *CaCO3 calcination by the simultaneous reduction of CuO in a Ca/Cu chemical looping process.* Chemical Engineering Science, 2015. **137**: p. 254-267.

202. Hatcher, W.J., L. Viville, and G.F. Froment, *Reoxidation of a Nickel Reforming Catalyst - Kinetic Analysis and Fixed Bed Ssimulation.* Industrial & Engineering Chemistry Process Design and Development, 1978. **17**(4): p. 491-500.

203. Nickel Institute, *Stainless Steels in Ammonia Production - A Designers' Handbook Series No 9013*. 2020, Nickel Institute.

Appendix A Matrix form of the numerical solution of the intra-conduction heat transfer problem of presented in Chapter 5.

The following matrices are the components of the system $Ax = b$ representing the set of linear equations obtained from the application of the Fully Implicit Backwards and the Crank-Nicolson methods to the intra-particle model presented in Chapter 5.

For both methods of discretisation the following parameters are defined:

$$M_1 = \frac{\lambda_{p_1}}{\rho_{p_1} C_{p_1}} \frac{\Delta\tau}{(\Delta r_1)^2} \text{ and } M_2 = \frac{\lambda_{p_2}}{\rho_{p_1} C_{p_2}} \frac{\Delta\tau}{(\Delta r_2)^2} \quad \textbf{(A.1)}$$

$$C_{01} = \frac{\alpha_1 a_{S_1} \Delta z}{u_g \rho_g C_p} \text{ and } C_{02} = \frac{\alpha_2 a_{S_2} \Delta z}{u_g \rho_g C_p} \quad \textbf{(A.2)}$$

$$C_1 = \frac{2\Delta r_1 \alpha_1}{\lambda_{p_1}} \text{ and } C_2 = \frac{2\Delta r_2 \alpha_2}{\lambda_{p_2}} \quad \textbf{(A.3)}$$

Where $\Delta\tau$ is the time-step increment in the Lagrangian coordinate, Δz is the length-step increment, Δr_1 and Δr_2 are the radius-step increments for particle type 1 and 2, α_1 and α_2 are the heat transfer coefficients in the interphase of the bulk gas with the particles type 1 and 2, a_{S_1} and a_{S_2} are the surface area of the particles type 1 and 2, u_g is the superficial gas velocity, ρ_g is the gas density, C_p is the gas heat capacity; ρ_{p_1}, C_{p_1} and λ_{p_1} are the density, heat capacity and thermal conductivity of particle type 1, and ρ_{p_2}, C_{p_2} and λ_{p_2} are the density, heat capacity and thermal conductivity of particle type 2.

a) Fully Implicit Backwards (FIB) method

$$A = \begin{bmatrix} (1+6M_1) & -6M_1 & 0 & 0 & 0 & 0 & 0 & 0 \\ -\left(1-\frac{1}{j}\right)M_1 & (1+2M_1) & -\left(1+\frac{1}{j}\right)M_1 & 0 & 0 & 0 & 0 & 0 \\ 0 & \ddots & \ddots & \ddots & 0 & 0 & 0 & 0 \\ 0 & -2M_1 & 1+M_1\left(2+\left(1+\frac{1}{m}\right)C_1\right) & -\left(1+\frac{1}{m}\right)C_1M_1 & 0 & 0 & 0 & 0 \\ 0 & 0 & -C_{01}\Delta z & 2+\Delta z(C_{01}+C_{02}) & -C_{02}\Delta z & 0 & 0 & 0 \\ 0 & 0 & 0 & -\left(1+\frac{1}{p}\right)C_2M_2 & 1+M_2\left(2+\left(1+\frac{1}{p}\right)C_2\right) & -2M_2 & 0 & 0 \\ 0 & 0 & 0 & 0 & -\left(1+\frac{1}{k}\right)M_2 & (1+2M_2) & -\left(1-\frac{1}{k}\right)M_2 & 0 \\ 0 & 0 & 0 & 0 & 0 & \ddots & \ddots & \ddots \\ 0 & 0 & 0 & 0 & 0 & 0 & -6M_2 & (1+6M_2) \end{bmatrix}$$

$$x = \begin{bmatrix} T_{1_0}^{n+1,i} \\ T_{1_1}^{n+1,i} \\ \vdots \\ T_{1_m}^{n+1,i} \\ T_i^{n+1} \\ T_{2_p}^{n+1,i} \\ \vdots \\ T_{2_1}^{n+1,i} \\ T_{2_0}^{n+1,i} \end{bmatrix} \quad b = \begin{bmatrix} T_{1_0}^{n,i} \\ T_{1_1}^{n,i} \\ \vdots \\ T_{1_m}^{n,i} \\ [2-\Delta z(C_{01}+C_{02})]T_{i-1}^{n+1} + C_{01}\Delta z T_{1_m}^{n+1,i-1} + C_{02}\Delta z T_{2_p}^{n+1,i-1} \\ T_{2_p}^{n,i} \\ \vdots \\ T_{2_1}^{n,i} \\ T_{2_0}^{n,i} \end{bmatrix}$$

b) Crank-Nicolson method

$$A=\begin{bmatrix}
(1+3M_1) & -3M_1 & 0 & 0 & 0 & 0 & 0 & 0\\
-\left(1-\frac{1}{j}\right)M_1 & (2+2M_1) & -\left(1+\frac{1}{j}\right)M_1 & 0 & 0 & 0 & 0 & 0\\
0 & \ddots & \ddots & \ddots & 0 & 0 & 0 & 0\\
0 & -2M_1 & 2+M_1\left(2+\left(1+\frac{1}{m}\right)C_1\right) & -\left(1+\frac{1}{m}\right)C_1M_1 & 0 & 0 & 0 & 0\\
0 & 0 & -C_{01}\Delta z & 2+\Delta z(C_{01}+C_{02}) & -C_{02}\Delta z & 0 & 0 & 0\\
0 & 0 & 0 & -\left(1+\frac{1}{p}\right)C_2M_2 & 2+M_2\left(2+\left(1+\frac{1}{p}\right)C_2\right) & -2M_2 & 0 & 0\\
0 & 0 & 0 & 0 & -\left(1+\frac{1}{k}\right)M_2 & (2+2M_2) & -\left(1-\frac{1}{k}\right)M_2 & 0\\
0 & 0 & 0 & 0 & 0 & \ddots & \ddots & \ddots\\
0 & 0 & 0 & 0 & 0 & 0 & -3M_2 & (1+3M_2)
\end{bmatrix}$$

$$x=\begin{bmatrix}
{T_1}_0^{n+1,i}\\
{T_1}_1^{n+1,i}\\
\vdots\\
{T_1}_m^{n+1,i}\\
T_i^{n+1}\\
{T_2}_p^{n+1,i}\\
\vdots\\
{T_2}_1^{n+1,i}\\
{T_2}_0^{n+1,i}
\end{bmatrix}\qquad
b=\begin{bmatrix}
3M_1{T_1}_1^{n,i}+(1-3M_1){T_1}_0^{n,i}\\
\left(1+\frac{1}{j}\right)M_1{T_1}_2^{n,i}+(2-2M_1){T_1}_1^{n,i}+\left(1-\frac{1}{j}\right)M_1{T_1}_0^{n,i}\\
\vdots\\
\left(1+\frac{1}{m}\right)C_1M_1T_i^n+\left[2-M_1\left(2+\left(1+\frac{1}{m}\right)C_1\right)\right]{T_1}_m^{n,i}+2M_1{T_1}_{m-1}^{n,i}\\
[2-\Delta z(C_{01}+C_{02})]T_{i-1}^{n+1}+C_{01}\Delta z{T_1}_m^{n+1,i-1}+C_{02}\Delta z{T_2}_p^{n+1,i-1}\\
\left(1+\frac{1}{p}\right)C_2M_2T_i^n+\left[2-M_2\left(2+\left(1+\frac{1}{p}\right)C_2\right)\right]{T_2}_p^{n,i}+2M_2{T_2}_{p-1}^{n,i}\\
\vdots\\
\left(1+\frac{1}{k}\right)M_2{T_2}_2^{n,i}+(2-2M_2){T_2}_1^{n,i}+\left(1-\frac{1}{k}\right)M_2{T_2}_0^{n,i}\\
3M_2{T_2}_1^{n,i}+(1-3M_2){T_2}_0^{n,i}
\end{bmatrix}$$

Appendix B Derivation of the model to account for changes in adsorbent physical properties.

The conversion of the adsorbent during the carbonation of CaO leads to structural changes that affect the porosity, heat capacity and density of the material and impact the thermal behaviour of the pellet, thus, the energy balance at a particle accounting for these changes become:

$$\frac{\partial\left(\rho_{b_2} C_{p_2} T_{S_2}\right)}{\partial t} = \alpha_2 a_{S_2}\left(T - T_{S_2}\right) + \rho_{b_2} \sum_{k=1}^{n} \eta_k r_k (-\Delta H_k) \qquad \textbf{(B.1)}$$

Thus, Equation (6.8) needs information about the evolution of the adsorbent density and mass heat capacity. These properties are related to the conversion of the material and therefore, are functions of time. If it is assumed that the thermal properties can be estimated by a weighted average of the properties of the pure materials that compose the pellet and that the particle is constituted by non-porous spherical grains that follows a shrinking core behaviour, then the average density of the adsorbent can be estimated as:

$$\rho_{p_2} = \varphi_{CaO}\rho_{CaO} + \varphi_{CaCO_3}\rho_{CaCO_3} \qquad \textbf{(B.2)}$$

$$\varphi_{CaO} + \varphi_{CaCO_3} = 1 \qquad \textbf{(B.3)}$$

Where ρ_{p_2} is the density of the adsorbent pellet, ρ_{CaO} is the density of the fresh adsorbent, ρ_{CaCO_3} is the density of the ash layer, φ_{CaO} and φ_{CaCO_3} are the volumetric fractions of fresh and ash layer.

The volumetric fraction of fresh adsorbent φ_{CaO} is the ratio of the volume of fresh adsorbent to the total volume of the grain. For spherical grains that follow the shrinking core model the following relationship apply:

$$\varphi_{CaO} = \frac{\bar{V}_{CaO}}{\bar{V}_{total}} = \frac{\bar{V}_{CaO}}{\bar{V}_{CaO} + \bar{V}_{CaCO_3}} \qquad \textbf{(B.4)}$$

Where the volumes of fresh and spend adsorbent, $\bar{V}_{CaO}$ and $\bar{V}_{CaCO_3}$, respectively, are calculated as:

$$\bar{V}_{CaO} = \frac{4}{3}\pi r_{g,CaO}^3 (1 - X_{CaO})$$
$$\bar{V}_{CaCO_3} = \frac{4}{3}\pi r_{g,CaO}^3 X_{CaO} Z \quad \textbf{(B.5)}$$

Where X_{CaO} is the molar conversion of the adsorbent and Z is the ratio of the molar density of $CaCO_3$ to the molar density of CaO, thus, the volumetric fraction of CaO in the grain is:

$$\varphi_{CaO} = \frac{(1 - X_{CaO})}{1 + X_{CaO}(Z - 1)} \quad \textbf{(B.6)}$$

And for the product layer ($CaCO_3$):

$$\varphi_{CaCO_3} = \frac{X_{CaO} Z}{1 + X_{CaO}(Z - 1)} \quad \textbf{(B.7)}$$

Which has been also reported as the volumetric conversion of a growing grain by Stenardo and Foscolo [106]. Therefore, combining Equation (6.10) with Equation (B.3) and substituting the result from Equation (B.6) we obtain:

$$\rho_{p_2} = \rho_{CaCO_3} + \frac{(1 - X_{CaO})}{1 + X_{CaO}(Z - 1)} \left(\rho_{CaO} - \rho_{CaCO_3}\right) \quad \textbf{(B.8)}$$

Similarly, the average thermal conductivity is estimated by:

$$\lambda_{p_2} = \lambda_{CaCO_3} + \frac{(1 - X_{CaO})}{1 + X_{CaO}(Z - 1)} \left(\lambda_{CaO} - \lambda_{CaCO_3}\right) \quad \textbf{(B.9)}$$

The average heat capacity is calculated based on the weight fraction of the material during the process:

$$C_{p_2} = w_{CaO} C_{p,CaO} + w_{CaCO_3} C_{p,CaCO_3} \quad \textbf{(B.10)}$$

$$w_{CaO} + w_{CaCO_3} = 1 \quad \textbf{(B.11)}$$

Where $C_{p,ads}$ is the heat capacity of the adsorbent per unit of mass, w_{CaO} and w_{CaCO_3} are the weight fractions of CaO and $CaCO_3$, $C_{p,CaO}$ and $C_{p,CaCO_3}$ are the heat capacity per unit of mass of CaO and $CaCO_3$ in the grain.

The expression of the weight fraction is obtained following a similar procedure to that of the volumetric fraction, with the main difference being that now the mass of each specie in the adsorbent grains is needed, these masses can be expressed in terms of the density and volume of each chemical specie in the grain as:

$$w_{CaO} = \frac{\rho_{CaO}\bar{V}_{CaO}}{\rho_{CaO}\bar{V}_{CaO} + \rho_{CaCO_3}\bar{V}_{CaCO_3}} \quad \textbf{(B.12)}$$

Substitution of Equation (B.5) in Equation (B.12) yields:

$$w_{CaO} = \frac{\rho_{CaO}(1 - X_{CaO})}{\rho_{CaO}(1 - X_{CaO}) + \rho_{CaCO_3}X_{CaO}Z} \quad \textbf{(B.13)}$$

Finally, multiplying and dividing Equation (B.13) by $1/\rho_{CaO}$ renders the sought expression:

$$w_{CaO} = \frac{(1 - X_{CaO})}{1 + X_{CaO}(Z\phi - 1)} \quad \textbf{(B.14)}$$

Where ϕ is the ratio of the mass density of $CaCO_3$ to the mass density of CaO.

Combining Equations (B.10) with (B.11) and (B.14) the expression to calculate the heat capacity of the adsorbent as function of the adsorbent conversion is obtained as follows:

$$C_{p,ads} = C_{p,CaCO_3} + \frac{(1 - X_{CaO})}{1 + X_{CaO}(Z\phi - 1)}\left(C_{p,CaO} - C_{p,CaCO_3}\right) \quad \textbf{(B.15)}$$

The expressions for the adsorbent density and mass heat capacity are applied then in the heat balance of the adsorbent

By deriving Equations (B.8), (B.9) and (B.15) with respect to the conversion X_{CaO} the final expressions are obtained as:

$$\partial\rho_{p_2} = -\left(\rho_{CaO} - \rho_{CaCO_3}\right)\left\{\frac{Z}{[1 + X_{CaO}(Z - 1)]^2}\right\}\partial X_{CaO} \quad \textbf{(B.16)}$$

$$\partial\lambda_{p_2} = -\left(\lambda_{CaO} - \lambda_{CaCO_3}\right)\left\{\frac{Z}{[1 + X_{CaO}(Z - 1)]^2}\right\}\partial X_{CaO} \quad \textbf{(B.17)}$$

$$\partial C_{p_2} = -\left(C_{p,CaO} - C_{p,CaCO_3}\right)\left\{\frac{Z\phi}{[1 + X_{CaO}(Z\phi - 1)]^2}\right\}\partial X_{CaO} \quad \textbf{(B.18)}$$

Appendix C Derivation of the expressions of velocity of the reaction and thermal fronts

C.1 Fuel Reactor

Assuming that the reactor can be represented by a pseudo-homogeneous model, with constant parameters, and that the pressure drop is negligible, the governing equations for mass and energy are:

$$\varepsilon_b \frac{\partial C_i}{\partial t} + u_s \frac{\partial C_i}{\partial z} = \rho_{b_1} \sum_{j=1}^{m} \eta_j \nu_{ij} r_j + \rho_{b_2} \sum_{k=1}^{n} \eta_k \nu_{ik} r_k \qquad \textbf{(C.1)}$$

$$\left(1 + \frac{\rho_b C_{p,b}}{\varepsilon_b \rho_g C_{p,g}}\right) \frac{\partial T}{\partial t} + \frac{u_s}{\varepsilon_b} \frac{\partial T}{\partial z} = \frac{\rho_{b_1}}{\varepsilon_b} \sum_{j=1}^{m} \eta_j r_j \left(-\Delta H_j\right) + \frac{\rho_{b_2}}{\varepsilon_b} \sum_{k=1}^{n} \eta_k r_k (-\Delta H_k) \qquad \textbf{(C.2)}$$

In Equation (C.1), the sum indicated in the first term of the r.h.s. correspond to the rate of disappearance/appearance of an specie in the system, therefore, it can be replaced by:

$$\sum_{j=1}^{m} \eta_j \nu_{ij} r_j = r_i = -\frac{V_r}{W_c} \frac{\partial C_i}{\partial t} \qquad \textbf{(C.3)}$$

where V_r is the reactor volume and W_c is the mass of catalyst. Similarly, the sum indicated in the second term of the r.h.s. of Equation (C.1) represents the rate of adsorption of a specie. According to the scope of this thesis, only CO_2 has been considered as an adsorbable component, hence:

$$\sum_{k=1}^{n} \eta_k \nu_{ik} r_k = r_{Carb} = -\frac{\eta_{Carb}}{M_{CaO}} \frac{dX_{CaO}}{dt} \qquad \textbf{(C.4)}$$

By substituting these identities in Equations (C.1) and (C.2)) the governing mass and energy balances become:

$$\frac{\partial C_i}{\partial t} + \frac{u_s}{\varepsilon_b} \frac{\partial C_i}{\partial z} = -\frac{\rho_{b_1} V_r}{\varepsilon_b W_c} \frac{\partial C_i}{\partial t} - \frac{\rho_{b_2} \eta_{Carb}}{\varepsilon_b M_{CaO}} \frac{\partial X_{CaO}}{\partial t} \qquad \textbf{(C.5)}$$

$$\left(1+\frac{\rho_b C_{p,b}}{\varepsilon_b \rho_g C_{p,g}}\right)\frac{\partial T}{\partial t}+\frac{u_s}{\varepsilon_b}\frac{\partial T}{\partial z} = \frac{\rho_{b_1} V_r}{\varepsilon_b \rho_g C_{p,g} W_c}\sum_{j=1}^{m}\eta_j \Delta H_j \frac{\partial C_j}{\partial t}+\frac{\Delta H_{Carb}\rho_{b_2}\eta_{Carb}}{\varepsilon_b \rho_g C_{p,g} M_{CaO}}\frac{\partial X_{CaO}}{\partial t} \quad \textbf{(C.6)}$$

In addition, the following identities are defined:

$$\frac{\partial C_j}{\partial t}=\frac{\partial C_j}{\partial T}\frac{\partial T}{\partial t} \qquad \frac{\partial X_{CaO}}{\partial t}=\frac{\partial X_{CaO}}{\partial C_i}\frac{\partial C_i}{\partial t} \qquad \frac{\partial X_{CaO}}{\partial t}=\frac{\partial X_{CaO}}{\partial T}\frac{\partial T}{\partial t} \quad \textbf{(C.7)}$$

The substitution of Equation (C.7) in Equations (C.5) and (C.6) renders:

$$\frac{\partial C_i}{\partial t}+\frac{u_s}{\varepsilon_b}\frac{\partial C_i}{\partial z}=-\frac{\rho_{b_1} V_r}{\varepsilon_b W_c}\frac{\partial C_i}{\partial t}-\frac{\rho_{b_2}\eta_{Carb}}{\varepsilon_b M_{CaO}}\frac{\partial X_{ads}}{\partial C_i}\frac{\partial C_i}{\partial t} \quad \textbf{(C.8)}$$

$$\left(1+\frac{\rho_b C_{p,b}}{\varepsilon_b \rho_g C_{p,g}}\right)\frac{\partial T}{\partial t}+\frac{u_s}{\varepsilon_b}\frac{\partial T}{\partial z} = \frac{\rho_{b_1} V_r}{\varepsilon_b \rho_g C_{p,g} W_c}\sum_{j=1}^{m}\eta_j \Delta H_j \frac{\partial C_j}{\partial T}\frac{\partial T}{\partial t}+\frac{\Delta H_{Carb}\rho_{b_2}\eta_{Carb}}{\varepsilon_b \rho_g C_{p,g} M_{CaO}}\frac{\partial X_{ads}}{\partial T}\frac{\partial T}{\partial t} \quad \textbf{(C.9)}$$

Rearranging (C.8) and (C.9):

$$\left(1+\frac{\rho_{b_1} V_r}{\varepsilon_b W_c}+\frac{\rho_{b_2}\eta_{Carb}}{\varepsilon_b M_{CaO}}\frac{\partial X_{CaO}}{\partial C_i}\right)\frac{\partial C_i}{\partial t}+\frac{u_s}{\varepsilon_b}\frac{\partial C_i}{\partial z}=0 \quad \textbf{(C.10)}$$

$$\left(1+\frac{\rho_b C_{p,b}}{\varepsilon_b \rho_g C_{p,g}}-\frac{\rho_{b_1} V_r}{\varepsilon_b \rho_g C_{p,g} W_c}\sum_{j=1}^{m}\eta_j \Delta H_j \frac{\partial C_j}{\partial T}-\frac{\Delta H_{Carb}\rho_{b_2}\eta_{Carb}}{\varepsilon_b \rho_g C_{p,g} M_{CaO}}\frac{\partial X_{CaO}}{\partial T}\right)\frac{\partial T}{\partial t}+\frac{u_s}{\varepsilon_b}\frac{\partial T}{\partial z}=0 \quad \textbf{(C.11)}$$

Equations ((C.10) and (C.11) can be analysed by the method of characteristics; by arranging the coefficients in matrix form, yields:

$$\begin{vmatrix} 1+\frac{\rho_{b_1} V_r}{\varepsilon_b W_c}+\frac{\rho_{b_2}\eta_{Carb}}{\varepsilon_b M_{CaO}}\frac{\partial X_{CaO}}{\partial C_i} & \frac{u_s}{\varepsilon_b} & 0 & 0 \\ 0 & 0 & 1+\frac{\rho_b C_{p,b}}{\varepsilon_b \rho_g C_{p,g}}-\frac{\rho_{b_1} V_r \sum_{j=1}^{m}\eta_j \Delta H_j \frac{\partial C_j}{\partial T}}{\varepsilon_b \rho_g C_{p,g} W_c}-\frac{\Delta H_{Carb}\rho_{b_2}\eta_{Carb}}{\varepsilon_b \rho_g C_{p,g} M_{CaO}}\frac{\partial X_{CaO}}{\partial T} & \frac{u_s}{\varepsilon_b} \\ dt & dz & 0 & 0 \\ 0 & 0 & dt & dz \end{vmatrix} \begin{vmatrix} \frac{\partial C_i}{\partial t} \\ \frac{\partial C_i}{\partial z} \\ \frac{\partial T}{\partial t} \\ \frac{\partial T}{\partial z} \end{vmatrix} = \begin{vmatrix} 0 \\ 0 \\ dC_i \\ dT \end{vmatrix}$$

(C.12)

By setting the coefficient matrix to zero and solving the determinant, the sought front velocities are obtained:

$$\left(\frac{dz}{dt}\right)_{C_i}=\frac{u_i}{1+\frac{\rho_{b_1} V_r}{\varepsilon_b W_c}+\frac{\rho_{b_2}\eta_{Carb}}{\varepsilon_b M_{CaO}}\frac{\partial X_{CaO}}{\partial C_i}} \quad \textbf{(C.13)}$$

$$\left(\frac{dz}{dt}\right)_T = \frac{u_i}{1 + \frac{\rho_s C_{p,s}}{\varepsilon_b \rho_g C_{p,g}} - \frac{\rho_{b_1} V_r}{\varepsilon_b \rho_g C_{p,g} W_c} \sum_{j=1}^{m} \eta_j \Delta H_j \frac{\partial C_j}{\partial T} - \frac{\Delta H_{Carb} \rho_{b_2} \eta_{Carb}}{\varepsilon_b \rho_g C_{p,g} M_{CaO}} \frac{\partial X_{CaO}}{\partial T}} \quad \textbf{(C.14)}$$

C.2 Air Reactor

The reaction and thermal fronts that represent the Air Reactor process differ slightly from Equations (C.13) and (C.14) owing to the non-catalytic nature of the re-oxidation of nickel and the calcination of calcium carbonate. If it is assumed that the only species involved in the process are the oxygen as the oxidant agent and the carbon dioxide released from the regeneration of the adsorbent, the governing equations representing this reactor are:

$$\frac{\partial C_{CO_2}}{\partial t} + \frac{u_s}{\varepsilon_b} \frac{\partial C_{CO_2}}{\partial z} = \frac{\rho_{b_2}}{\varepsilon_b} \eta_{Calc} r_{Calc} \quad \textbf{(C.15)}$$

$$\frac{\partial C_{O_2}}{\partial t} + \frac{u_s}{\varepsilon_b} \frac{\partial C_{O_2}}{\partial z} = -\frac{\rho_{b_1}}{\varepsilon_b} \eta_{Oxi} r_{Oxi} \quad \textbf{(C.16)}$$

$$\left(1 + \frac{\rho_b C_{p,b}}{\varepsilon_b \rho_g C_{p,g}}\right) \frac{\partial T}{\partial t} + \frac{u_s}{\varepsilon_b} \frac{\partial T}{\partial z} = -\frac{\rho_{b_2} \eta_{Calc} r_{Calc} \Delta H_{Calc}}{\varepsilon_b \rho_g C_{p,g}} + \frac{\rho_{b_1} \eta_{Oxi} r_{Oxi} \Delta H_{Oxi}}{\varepsilon_b \rho_g C_{p,g} \varepsilon_b} \quad \textbf{(C.17)}$$

The rates of calcination r_{Calc} and oxidation r_{Oxi} are defined in a similar fashion as the rate of carbonation in Equation (C.4), giving:

$$r_{Calc} = \frac{1}{M_{CaCO_3}} \frac{dX_{CaCO_3}}{dt} \quad \textbf{(C.18)}$$

$$r_{Oxi} = \frac{1}{2M_{Ni}} \frac{dX_{Ni}}{dt} \quad \textbf{(C.19)}$$

Substituting (C.18) and (C.19) in Equations (C.15) – (C.17):

$$\frac{\partial C_{CO_2}}{\partial t} + \frac{u_s}{\varepsilon_b} \frac{\partial C_{CO_2}}{\partial z} = \frac{\rho_{b_2} \eta_{Calc}}{\varepsilon_b M_{CaCO_3}} \frac{\partial X_{CaCO_3}}{\partial t} \quad \textbf{(C.20)}$$

$$\frac{\partial C_{O_2}}{\partial t} + \frac{u_s}{\varepsilon_b} \frac{\partial C_{O_2}}{\partial z} = -\frac{\rho_{b_1} \eta_{Oxi}}{2\varepsilon_b M_{Ni}} \frac{\partial X_{Ni}}{\partial t} \quad \textbf{(C.21)}$$

$$\left(1+\frac{\rho_b C_{p,b}}{\varepsilon_b \rho_g C_{p,g}}\right)\frac{\partial T}{\partial t}+\frac{u_s}{\varepsilon_b}\frac{\partial T}{\partial z} = -\frac{\rho_{b_2}\eta_{Calc}\Delta H_{Calc}}{M_{CaCO_3}\varepsilon_b \rho_g C_{p,g}}\frac{\partial X_{CaCO_3}}{\partial t}+\frac{\rho_{b_1}\eta_{Oxi}\Delta H_{Oxi}}{2M_{Ni}\varepsilon_b \rho_g C_{p,g}}\frac{\partial X_{Ni}}{\partial t} \quad \textbf{(C.22)}$$

Similarly to Eq.(C.7) the following identities are defined:

$$\frac{\partial X_{CaCO_3}}{\partial t}=\frac{\partial X_{CaCO_3}}{\partial C_{CO_2}}\frac{\partial C_{CO_2}}{\partial t} \qquad \frac{\partial X_{CaCO_3}}{\partial t}=\frac{\partial X_{CaCO_3}}{\partial T}\frac{\partial T}{\partial t}$$
$$\frac{\partial X_{Ni}}{\partial t}=\frac{\partial X_{Ni}}{\partial C_{O_2}}\frac{\partial C_{O_2}}{\partial t} \qquad \frac{\partial X_{Ni}}{\partial t}=\frac{\partial X_{Ni}}{\partial T}\frac{\partial T}{\partial t} \quad \textbf{(C.23)}$$

Substituting (C.23) in (C.20) – (C.22) and re-arranging gives the final equations:

$$\left(1-\frac{\rho_{b_2}\eta_{Calc}}{\varepsilon_b M_{CaCO_3}}\frac{\partial X_{CaCO_3}}{\partial C_{CO_2}}\right)\frac{\partial C_{CO_2}}{\partial t}+\frac{u_s}{\varepsilon_b}\frac{\partial C_{CO_2}}{\partial z}=0 \quad \textbf{(C.24)}$$

$$\left(1+\frac{\rho_{b_1}\eta_{Oxi}}{2\varepsilon_b M_{Ni}}\frac{\partial X_{Ni}}{\partial C_{O_2}}\right)\frac{\partial C_{O_2}}{\partial t}+\frac{u_s}{\varepsilon_b}\frac{\partial C_{O_2}}{\partial z}=0 \quad \textbf{(C.25)}$$

$$\left(1+\frac{\rho_s C_{p,s}}{\varepsilon_b \rho_g C_{p,g}}+\frac{\rho_{b_2}\eta_{Calc}\Delta H_{Calc}}{M_{CaCO_3}\varepsilon_b \rho_g C_{p,g}}\frac{\partial X_{CaCO_3}}{\partial T}-\frac{\rho_{b_1}\eta_{Oxi}\Delta H_{Oxi}}{2M_{Ni}\varepsilon_b \rho_g C_{p,g}}\frac{\partial X_{Ni}}{\partial T}\right)\frac{\partial T}{\partial t}+\frac{u_s}{\varepsilon_b}\frac{\partial T}{\partial z}=0 \quad \textbf{(C.26)}$$

The system is expressed in matrix form as:

$$\begin{vmatrix} 1-\frac{\rho_{b_2}\eta_{Calc}}{\varepsilon_b M_{CaCO_3}}\frac{\partial X_{CaCO_3}}{\partial C_{CO_2}} & \frac{u_s}{\varepsilon_b} & 0 & 0 & 0 & 0 \\ 0 & 0 & 1+\frac{\rho_{b_1}\eta_{Oxi}}{2\varepsilon_b M_{Ni}}\frac{\partial X_{Ni}}{\partial C_{O_2}} & \frac{u_s}{\varepsilon_b} & 0 & 0 \\ 0 & 0 & 0 & 0 & 1+\frac{\rho_b C_{p,b}}{\varepsilon_b \rho_g C_{p,g}}+\frac{\rho_{b_2}\eta_{Calc}\Delta H_{Calc}}{M_{CaCO_3}\varepsilon_b \rho_g C_{p,g}}\frac{\partial X_{CaCO_3}}{\partial T}-\frac{\rho_{b_1}\eta_{Oxi}\Delta H_{Oxi}}{2M_{Ni}\varepsilon_b \rho_g C_{p,g}}\frac{\partial X_{Ni}}{\partial T} & \frac{u_s}{\varepsilon_b} \\ dt & dz & 0 & 0 & 0 & 0 \\ 0 & 0 & dt & dz & 0 & 0 \\ 0 & 0 & 0 & 0 & dt & dz \end{vmatrix} \begin{vmatrix} \frac{\partial C_{CO_2}}{\partial t} \\ \frac{\partial C_{CO_2}}{\partial z} \\ \frac{\partial C_{O_2}}{\partial t} \\ \frac{\partial C_{O_2}}{\partial z} \\ \frac{\partial T}{\partial t} \\ \frac{\partial T}{\partial z} \end{vmatrix} = \begin{vmatrix} 0 \\ 0 \\ 0 \\ 0 \\ dC_i \\ dT \end{vmatrix} \quad \textbf{(C.27)}$$

By setting the coefficient matrix to zero and solving the determinant, the sought front velocities are:

$$\left(\frac{dz}{dt}\right)_{C_{CO_2}}=\frac{u_i}{1-\frac{\rho_{b_2}\eta_{Calc}}{\varepsilon_b M_{CaCO_3}}\frac{\partial X_{CaCO_3}}{\partial C_{CO_2}}} \quad \textbf{(C.28)}$$

$$\left(\frac{dz}{dt}\right)_{C_{O_2}} = \frac{u_i}{1 + \frac{\rho_{b_1}\eta_{Oxi}}{2\varepsilon_b M_{Ni}}\frac{\partial X_{Ni}}{\partial C_{O_2}}} \quad \textbf{(C.29)}$$

$$\left(\frac{dz}{dt}\right)_{T} = \frac{u_i}{1 + \frac{\rho_b C_{p,b}}{\varepsilon_b \rho_g C_{p,g}} + \frac{\rho_{b_2}\eta_{Calc}\Delta H_{Calc}}{M_{CaCO_3}\varepsilon_b \rho_g C_{p,g}}\frac{\partial X_{CaCO_3}}{\partial T} - \frac{\rho_{b_1}\eta_{Oxi}\Delta H_{Oxi}}{2M_{Ni}\varepsilon_b \rho_g C_{p,g}}\frac{\partial X_{Ni}}{\partial T}} \quad \textbf{(C.30)}$$